Topology optimization for energy problems

Doctoral Dissertation
Doctoral Program in Energy Engineering (30^{th}cycle)

Topology optimization for energy problems

Thermal storage with phase change, district heating networks and PEM fuel cells

By

Alberto Pizzolato

******

Supervisor(s):
Prof. Vittorio Verda, Supervisor
Prof. Adriano Sciacovelli, Co-Supervisor
Prof. Kurt Maute, Co-Supervisor

Doctoral Examination Committee:
Prof. Casper Andreasen , Referee, Technical University of Denmark
Prof. Oronzio Manca, Referee, Universita' degli Studi della Campania
Prof. Niels Aage, Technical University of Denmark
Prof. Perumal Nithiarasu, Swansea University
Prof. Pierluigi Leone, Politecnico di Torino

Politecnico di Torino
June 28, 2018

Declaration

I hereby declare that the contents and organization of this dissertation constitute my own original work and does not compromise in any way the rights of third parties, including those relating to the security of personal data.

Alberto Pizzolato
June 28, 2018

* This dissertation is presented in partial fulfillment of the requirements for **Ph.D. degree** in the Graduate School of Politecnico di Torino (ScuDo).

To my parents and Ludovica,
constant sources of support and inspiration

Acknowledgements

This thesis is the result of three years of research at the Department of Energy at Politecnico di Torino and at the Department of Aerospace Sciences at University of Colorado. During this period, I benefited from the contributions of a number of remarkable people that I wish to acknowledge.

First and foremost, I would like to thank my supervisors: Vittorio Verda, Adriano Sciacovelli and Kurt Maute. Vittorio has three extraordinary and rare abilities among others: analyzing the big picture, identifying promising research moves and spotting potential high-impact innovations. Thanks for sharing these gifts with me in our revealing brainstormings, for giving me both guidance, support and freedom in pursuing my research curiosity and also for being a good friend. It was simply great to have you as a supervisor. Adriano has an exceptional passion and enthusiasm for science that makes him an expert on various engineering topics. Thanks for teaching me the art of multi-disciplinary research, for the long-distance stimulating discussions over Skype and for coming at my desk three years back with a topology optimization paper [13], saying "we should do this". Kurt couples a true talent for research and a passion for clear teaching that impressed me from the first moment at DTU. During my stay at CU Boulder, I benefited from countless suggestions that cleared long-standing doubts on optimization in the time span of a meeting. Thanks for framing my mind as a scientist and for fueling my ambition to push research frontiers a little bit further.

During these Ph.D. years, I learned the importance of constructing a network of "allies" that I truly trust. At CU Boulder, I was lucky enough to meet three excellent individuals that I consider as milestones in this network. Their feedback is essential on any novel idea, research progress and professional move that I have in mind. First, I would like to acknowledge Ashesh Sharma as this thesis greatly benefited from his contributions. Thanks for being always there to help, from the first FEMDOC

compilation to the recent multi-scale hacks. Second, I am immensely grateful to Reza Behrou for his rigorous and timely feedbacks and for his exemplary devotion to our research. Working with you on our "little kid" fuel cell framework was a great learning experience but also a great fun. Last, I am extremely grateful to Lamberto Dell'Elce that I sincerely consider my most trusted research advisor. Thanks for your neat tips and instructions on the most disparate aspects of the academic life.

I owe a great deal of recognition also to my fellow office mates over the years. Each of them helped me either by listening and discussing research issues or simply by creating a positive and amusing atmosphere. At Polito, a special mention is deserved to Sara, Elisa, Jesus and Stefano. At CU Boulder, I would like to thank in particular Markus, Jorge Luis and Matthew.

Every single day spent on this thesis, I realized the importance of the values I learned from my family. I would like to thank my sister Elisa, for showing me the need for perseverance; my mother Fiorenza, for teaching me the art of curiosity; and my father Loris, for shaping my ambitions and for truly being my mentor in every aspect of life. I am grateful also to my new family: Francesco, Giovanna and Baldo, for demonstrating their interest in this research and their enthusiasm about my passion for science. Many thanks are owed to my loyal friends: Francesco, Luca, Lorenzo, Gabriele and Giacomo, for being an awesome distraction from research.

Finally, I want to thank my beloved soulmate Ludovica. This work would have been impossible without your unconditional and endless support, encouragement and inspiration. Thanks for constantly expanding my mind and motivating me to pursue my life dreams.

Abstract

The optimal design of energy systems is a challenge due to the large design space and the complexity of the tightly-coupled multi-physics phenomena involved. Standard design methods consider a reduced design space, which heavily constrains the final geometry, suppressing the emergence of design trends. On the other hand, advanced design methods are often applied to academic examples with reduced physics complexity that seldom provide guidelines for real-world applications. This dissertation offers a systematic framework for the optimal design of energy systems by coupling detailed physical analysis and topology optimization.

Contributions entail both method-related and application-oriented innovations. The method-related advances stem from the modification of topology optimization approaches in order to make practical improvements to selected energy systems. We develop optimization models that respond to realistic design needs, analysis models that consider full physics complexity and design models that allow dramatic design changes, avoiding convergence to unsatisfactory local minima and retaining analysis stability. The application-oriented advances comprise the identification of novel optimized geometries that largely outperform industrial solutions. A thorough analysis of these configurations gives insights into the relationship between design and physics, revealing unexplored design trends and suggesting useful guidelines for practitioners.

Three different problems along the energy chain are tackled. The first one concerns thermal storage with latent heat units. The topology of mono-scale and multi-scale conducting structures is optimized using both density-based and level-set descriptions. The system response is predicted through a transient conjugate heat transfer model that accounts for phase change and natural convection. The optimization results yield a large acceleration of charge and discharge dynamics through three-dimensional geometries, specific convective features and optimized assemblies

of periodic cellular materials. The second problem regards energy distribution with district heating networks. A fully deterministic robust design model and an adjoint-based control model are proposed, both coupled to a thermal and fluid-dynamic analysis framework constructed using a graph representation of the network. The numerical results demonstrate an increased resilience of the infrastructure thanks to particular connectivity layouts and its rapidity in handling mechanical failures. Finally, energy conversion with proton exchange membrane fuel cells is considered. An analysis model is developed that considers fluid flow, chemical species transport and electrochemistry and accounts for geometry modifications through a density-based description. The optimization results consist of intricate flow field layouts that promote both the efficiency and durability of the cell.

Publications

The following publications constitute part of this thesis:

[J1] Pizzolato, A., Sharma, A., Maute, K., Sciacovelli, A., & Verda, V. (2017). Design of effective fins for fast PCM melting and solidification in shell-and-tube latent heat thermal energy storage through topology optimization. Applied Energy, 208, 210-227.

[J2] Pizzolato, A., Sharma, A., Maute, K., Sciacovelli, A., & Verda, V. (2017). Topology optimization for heat transfer enhancement in Latent Heat Thermal Energy Storage. International Journal of Heat and Mass Transfer, 113, 875-888.

[J3] Pizzolato, A., Sciacovelli, A., & Verda, V. (in press), Centralized control of district heating networks during failure events using discrete adjoint sensitivities, Energy.

[J4] Pizzolato, A., Sciacovelli, A., & Verda, V. (2017). Topology optimization of robust district theating networks. Journal of Energy Resource Technology, 140-2, 020905.

[J5] Behrou, R. & Pizzolato, A. Topology optimization of gas flow channels in Proton Exchange Membrane fuel cells. Submitted to Applied Energy.

[J6] Pizzolato, A., Sharma, A., Maute, K., Sciacovelli, A., & Verda, V. Multi-scale topology optimization of multi-material machinable structures using geometric primitives. In preparation for submission to Computer Methods in Applied Mechanics and Engineering.

[C1] Pizzolato, A., Sharma, A., Maute, K., Sciacovelli, A., & Verda, V. (2017). Multi-scale concurrent material and structure design of a metal matrix for heat transfer enhancement in phase change materials. In Proceedings of the 12th World Congress of Structural and Multidisciplinary Optimisation, Braunschweig, Germany.

[C2] Pizzolato, A., Sharma, A., Maute, K., Sciacovelli, A., & Verda, V. (2017). Improved melting and solidification in thermal energy storage through topology optimization of highly conductive fins. In Proceedings of the 2017 ASME Summer Heat Transfer Conference, Bellevue, Washington, USA

[C3] Pizzolato, A., Sciacovelli, A., & Verda, V. (2016). Discrete Adjoint Sensitivities for the Real-Time Optimal Control of Large District Heating Networks During Failure Events. In Proceedings of the ASME 2016 International Mechanical Engineering Congress and Exposition, Phoenix, USA.

[C4] Pizzolato, A., Sciacovelli, A., & Verda, V. (2016). Heat transfer enhancement in PCM storage tanks through topology optimization of finning material distribution. In Proceedings of the 4th International Conference on Computational Methods for Thermal Problems, Atlanta, USA.

[C5] Pizzolato, A., Sciacovelli, A., & Verda, V. (2016). Robust design of large district heating networks through topology optimization. In Proceedings of the 29th International Conference on Efficiency, Cost, Optimisation, Simulation and Environmental Impact of Energy Systems, Portorož, Slovenia.

[C6] Behrou, R. & Pizzolato, A. (2018). A computational approach for the design of high-power performance Proton Exchange Membrane fuel cells. In Proceedings of the 18th U.S. National Congress for Theoretical and Applied Mechanics, Chicago, USA.

The following publications were published within the Ph.D. research but do not constitute part of this thesis:

[J7] Pizzolato, A., Donato, F., Verda, V., Santarelli, M., & Sciacovelli, A. (2017) CSP plants with thermocline thermal energy storage and integrated steam generator – Techno-economic modeling and design optimization, Energy 139, 231–246.

[J8] Pizzolato, A., Sciacovelli, A., & Verda, V. (2016). Transient local entropy generation analysis for the design improvement of a thermocline thermal energy storage. Applied Thermal Engineering, 101, 622-629.

[J9] Pizzolato, A., Donato, F., Verda, V., & Santarelli, M. (2015). CFD-based reduced model for the simulation of thermocline thermal energy storage systems. Applied Thermal Engineering, 76, 391-399.

[C7] Pizzolato, A., Sciacovelli, A., & Verda, V. (2015). Transient local entropy generation analysis for the design improvement of a thermocline thermal energy storage. In Proceedings of the ASME-ATI-UIT 2015 Conference on Thermal Energy Systems: Production, Storage, Utilization and the Environment, Napoli, Italy.

[C8] Pizzolato, A., Sciacovelli, A., & Verda, V. (2015). Local entropy generation analysis of transient processes-an innovative approach for the design improvement of a Thermal Energy Storage with Integrated Steam Generator. In Proceedings of the 9th Constructal and Second Law Conferernce, Parma, Italy.

[C9] Pizzolato, A., Sciacovelli, A., & Verda, V. (2015). Techno-economic optimization of Concentrated Solar Power plants with thermocline thermal energy storage and integrated steam generator. In Proceedings of the 28th International Conference on Efficiency,Cost, Optimisation, Simulation and Environmental Impact of Energy Systems, Pau, France.

Contents

List of Figures

List of Tables

Abbreviations and acronyms

ACO	Ant Colony Optimization
AM	Additive Manufacturing
ANN	Artificial Neural Network
BDF	Backward Differentiation Formula
BESO	Bi-directional Evolutionary Structural Optimization
BM	Background Material
BPP	BiPolar Plate
CAD	Computer Aided Design
CDS	Central Differencing Scheme
CEG	Compressed Expanded Graphite
CFD	Computational Fluid-Dynamics
CHP	Combined Heat and Power
CL	Catalyst Layer
CONLIN	CONvex LINearization
CU	University of Colorado
CSP	Concentrating Solar Power
CVD	Chemical Vapor Deposition

CWD	Cross-Wind Diffusion
DH	District Heating
DHN	District Heating Network
DMO	Discrete Material Optimization
EM	Energy Minization
FE	Finite Element
FEM	Finite Element Method
FEMDOC	Finite Element Multi-disciplinary Design Optimization Code
FMO	Free Material Optimization
GA	Genetic Algorithm
GCMMA	Globally Convergent Method of Moving Asymptotes
GDL	Gas Diffusion Layer
GGLS	Gradient Galerkin Least Squares
GLS	Galerkin Least Squares
GRG	Generalized Reduced Gradient
HTF	Heat Transfer Fluid
HCM	High Conducting Material
HS	Hasin-Shtrikman
HSM	Heat Storage Medium
IP	Interior Point
KKT	Karush-Kuhn-Tucker
KS	Kreisselmeier Steinhauser
LCA	Linear Cellular Alloys

LDS	Limited Discrepancy Search
LHTES	Latent Heat Thermal Energy Storage
LMD	Least Maximum Discomfort
LP	Linear Programming
LSF	Level-Set Function
MEMS	Micro-Electro-Mechanical System
MILP	Mixed Integer Linear Programming
MK	Milton-Kohn
MMA	Method of Moving Asymptotes
MMC	Moving Morphable Component
MPC	Model Predictive Control
MUMPS	MUltifrontal Massively Parallel sparse direct Solver
NAND	Nested ANalysis and Design
NECODOC	NEtwork COntrol and Design Optimization Code
NEG	Natural Expanded Graphite
NGTO	Non-Gradient Topology Optimization
NLP	Non-Linear Programming
ODE	Ordinary Differential Equation
ORR	Oxygen Reduction Reaction
PAMP	Porous Anisotropic Material with Penalization
PCE	Polynomial Chaos Expansion
PCM	Phase Change Material
PDE	Partial Differential Equation

PDF	Probability Density Function
PEG	Polyethylene glycol
PEM	Proton Exchange Membrane
PEMFC	Proton Exchange Membrane Fuel Cell
PID	Proportional Integral Derivative
PPI	Pores Per Inch
POD	Proper Orthogonal Decomposition
PoliTo	Politecnico di Torino
PS	Particle Swarm
PSPG	Pressure Stabilized Petrov-Galerkin
RAMP	Rational Approximation of Material Properties
RHS	Right-Hand Side
RTI	Real Time Iteration
RVE	Representative Volume Element
SA	Simulated Annealing
SAND	Simultaneous ANalysis and Design
SCADA	Supervisory Control And Data Acquisition
SCP	Sequential Convex Programming
SET	Strategic Energy Technology
SIMP	Simplified Isotropic Material with Penalization
SLP	Sequential Linear Programming
SM	Steadiness Maximization
SQP	Sequential Quadratic Programming

SS	Solar Salt
ScS	Scatter Search
STL	STereoLithography
SUPG	Streamline Upwind Petrov-Galerkin
TES	Thermal Energy Storage
TM	Time Minimization
TRL	Technology Readiness Level
TTHX	Triplex Tube Heat eXchanger
VTS	Variable Thickness Sheet
WDN	Water Distribution Network
XFEM	eXtended Finite element Method

Chapter 1

Introduction

In this chapter, we first present the context in which this research has been conducted. Then, we describe how we intend to overcome technological barriers and enunciate the research questions that this thesis aims to address. Finally, we illustrate the structure of the dissertation.

1.1 Context

Constantly growing energy needs, rising climate concerns and the rapid depletion of fossil-based resources demand a fast development of alternative energy technologies. Providing an affordable supply of clean, reliable and efficient energy was identified as one of the seven great societal challenges in the research agenda of the European Union [122]. However, abandoning a fossil-based economy is a complicated task. The energy market relies on the trading of fuel, which is accumulated and transported to be used for power generation and energy conversion. The development of renewables is hampered by an absent control on *when* and *where* the energy is available. To cure the *temporal* mismatch between supply and demand, there is an urgent need to substitute the accumulation potential of fossil fuels with clean alternatives. This is the primary motivation for the widespread interest in energy storage. Thermal Energy Storage (TES) deserves particular attention due to the wide availability of thermal byproducts from industrial processes [22], the technological difficulties in achieving a full electrification of heat [343] and the limited cost of stored energy [490]. Within state-of-the-art options for TES, latent heat units are gaining mo-

mentum in recent years [490]. This technology relies on inexpensive and largely available Phase Change Materials (PCMs), yields high energy density and allows charge/discharge at a nearly constant temperature [134]. Storage alone can hardly exploit the full potential of clean energy technologies as it cannot cope with the *spatial* mismatch between supply and demand. The distributed nature of renewable sources demands a transition to smart energy systems in which consumers can act as producers [479]. To make this possible, it is crucial to find solutions for transferring and distributing large amounts of energy. District Heating (DH) infrastructures are central to accomplishing this task. They allow any source of heat to be used economically, including the low-temperature residual heat of industrial processes and the distributed geothermal and solar resources [281]. Static energy grids cannot feed movable units such as those utilized in transport applications. The limited distance range and large recharge time of electric vehicles powered by batteries [172] has led to research into alternatives that allow a fuel-based infrastructure to be retained. The utilization of hydrogen as energy vector and Proton Exchange Membrane Fuel Cells (PEMFCs) for conversion constitutes a promising option in this direction [379]. The interest in this technology is also high for distributed stationary applications due to its high efficiency of chemical-to-electrical conversion, absent harmful emissions, prompt load following, low temperature and silent operation [379]. Although it is acknowledged that Latent Heat Thermal Energy Storage (LHTES) units, District Heating Networks (DHNs) and PEMFCs may play a crucial role in future energy scenarios, their employment is still impeded by specific technological barriers:

- Most of the PCMs feature a low thermal conductivity, which limits their power density and thus the range of feasible applications [298].
- The consequences of failures of DHNs in harsh climates may be dramatic [370, 378, 244], raising concerns about the resilience of the infrastructure.
- PEMFCs are characterized by high costs and limited durability [379], preventing their large-scale penetration into the market of energy conversion devices.

1.2 Beyond barriers with topology optimization

The low-carbon transition requires both radical and incremental innovations. The former refer to disruptive technological advancements that open research frontiers *creating* new potential for change [316]. The latter refer to improvements to well-identified solutions and aim at *fully exploiting* the established potential for change [316]. Among the ten key actions identified by the European Union [124] to accelerate the accomplishment of the energy and climate goals, three belong to the category of radical innovations while seven are improvements intended to reduce costs and to increase the efficiency and resilience of clean technologies. This suggests that after decades of research efforts in the direction of a low-carbon society, it is now time to get the most from the past technological breakthroughs by overcoming the established barriers.

Improving LHTES units, DHNs and PEMFCs is a challenge for two main reasons: the complexity of the analysis and the ineffectiveness of enhancement methodologies. Regarding the analysis complexity, predicting responses with high accuracy involves the development of sophisticated numerical tools. Physical phenomena are based on strongly coupled heat transfer, fluid flow and electrochemical interactions. Most interest is focused on the system response over time and requires a transient analysis. Addressing resilience demands the inclusion of uncertainty, which may be hard to characterize and quantify in complex systems. Regarding ineffective enhancement strategies, the industrial status quo encompasses methods that generate a multitude of (largely) different "optimized" configurations and hardly handle systems with a large design and control space. The extremely simplified schematics in Figure 1.1 show why the classical approaches may fail in this regard. The design engineers start with the formulation of an initial "design concept" based on personal experience, insights on physical phenomena and manufacturing limitations. This initial step defines a "concept region" as the space of design specifications in which the concept can be uniquely identified (Figure 1.1(a)). The designers conduct analyses within this region to investigate the effect of a few parameters and propose an "optimized" design. However, the search is bounded to a poorly parametrized space enclosed within the "concept region". Figure 1.1(b) shows that this procedure easily leads to different "optimized designs" when starting with different initial "design concepts". Furthermore, only a tiny fraction of the design space is explored.

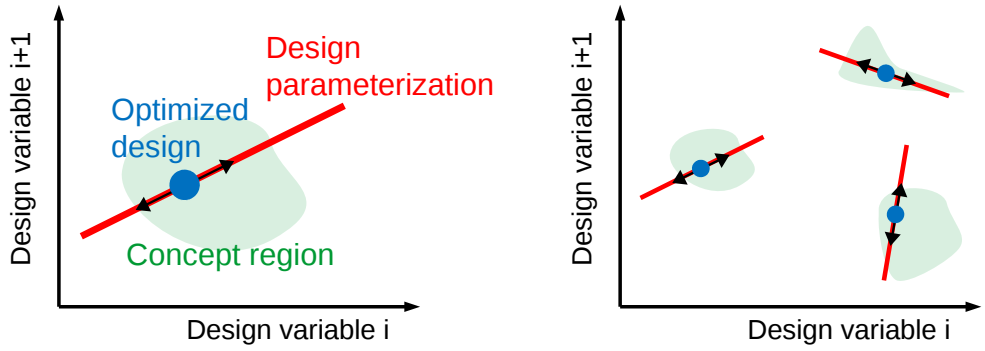

(a) (b)

Fig. 1.1. Schematics of classical design procedures. (a): Design concept formulation and search for optimized configurations; (b): bias of the "optimized designs" towards the initial design concept

To advance energy technologies it is essential to develop computational frameworks that couple accurate analysis with thorough and affordable optimization procedures. Although the research on analysis strategies is rapidly progressing, advances in optimization for the design of energy systems are largely unexplored in the published literature. The modification of the high-fidelity analysis frameworks to allow dramatic design changes is a compelling task due to the complexity and tight coupling of the physical phenomena involved. Within this context, the aim of this thesis is to adapt topology optimization for the practical design of LHTES units, DHNs and PEMFCs. Topology optimization is a powerful and affordable form-finding methodology that allows full design freedom to be retained with no need to formulate an initial design concept. The geometries freely evolve along the optimization process leading to unexpected topologies, shapes and configurations. We intend to exploit this tool to (i) identify enhancement avenues, (ii) assess their technological potential, (iii) catch design trends, (iv) provide guidelines to practitioners. Specifically, we attempt to address four research questions:

Q1 *How and how much can we improve the performance of LHTES units through the design of high conducting structures?*

Q2 *How are optimized fin layouts and performance affected by natural convection, storage unit configuration and materials choice?*

Q3 *How can we enhance the resilience of district heating infrastructures through the design of the network layout and the control of user valves?*

Q4 *How and how much can we improve the efficiency and durability of PEMFCs through the design of reactants flow paths?*

1.3 Outline of the dissertation

The outline of this dissertation is represented in Figure 1.2.

Chapter 2 describes the fundamental mathematical background of topology optimization and discusses how it can be used as a **practical design tool** to conceive highly crafted devices. This discussion allows the creation of a common ground for notation and terminology that will be used throughout the monograph. We describe material interpolation and regularization strategies and review selected approaches for sensitivity analysis and numerical optimization. The effect of the most important parameters is illustrated through demonstrative numerical examples.

Chapters 3 and 4 address research question **Q1**. The former deals with the design **optimization of fins**. After reviewing the state-of-the-art extended surface layouts, we describe how to solve the Stefan problem using a model with reduced physics complexity and discuss the advantages and drawbacks of the available solution strategies. We then present three original optimization problem formulations, responding to three different design criteria in TES. The numerical results allow the exploration of relevant design trends, such as the trade-off between discharge time and discharged energy, the effect of material properties on the optimized designs and the differences between 2D and 3D layouts. Chapter 4 extends the research of Chapter 3 to **multi-scale structures**. Here, we develop a novel one-shot optimization procedure where the microscopic structure of materials, their aggregation layout and the macroscopic structure are optimized concurrently. First, we review potential applications of cellular metals as heat transfer enhancers. Second, we discuss how to obtain the cell and the homogenized problem through a two-scale asymptotic expansion and we present strategies for multi-scale and multi-material design. Then, we present a geometric description of the macroscopic shapes based on level-sets parametrized by a smoothed union of geometric primitives that allows machinable

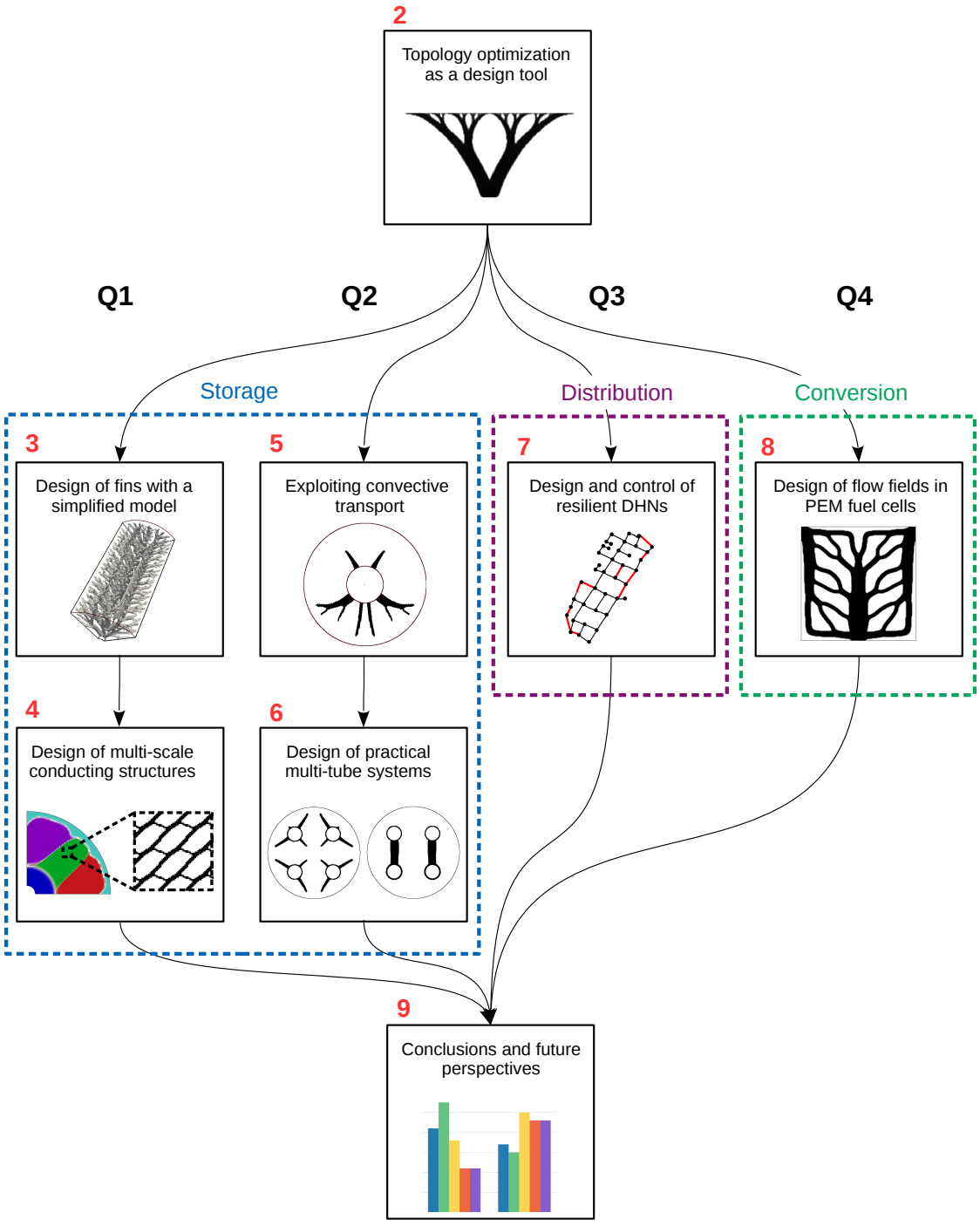

Fig. 1.2. Flowchart of the dissertation

configurations to be obtained. Finally, we present and discuss the numerical results and design trends obtained for a heat sink and an LHTES unit.

Chapters 5 and 6 address research question **Q2**. The former is devoted to the investigation of the mutual **influence** between **natural convection** and the optimized fin designs. Similarly to Chapter 3, we start by describing the relevant governing equations and solution strategies. Special care is dedicated to the verification and validation of the code in steps of increasing physics complexity. We then discuss a few flaws of density-based topology optimization in conjugate heat transfer. Those are illustrated through a natural convection and a forced convection example. Last, we describe the optimized designs obtained for melting and solidification enhancement, discussing the differences and similarities with conventional fin layouts. Chapter 6 builds on this framework and reports some **practical design** considerations for **multi-tube** shell-and-tube LHTESs. For this purpose, the possible options for storage and conducting materials are reviewed, including economic considerations. We then introduce a heuristic method that allows design trends to be anticipated and that can be used for rule-of-thumb design verifications. The predictions of this methodology are compared to the design trends obtained with topology optimization. The first numerical example sheds light on the effect of considering a circular periodicity assumption instead of the full domain in design studies. We then optimize a conducting geometry for units with separate hydraulic loops. Finally, we discuss possible High Conducting Material (HCM) choices and present optimized fin layouts for different combinations of HCM and PCM.

Chapter 7 addresses research question **Q3**, focusing on the use of topology optimization to increase the resilience of DHNs. We first review the optimization strategies that were used to date for both the design and control of fluid distribution networks. Then, we present a graph-based numerical framework able to predict the thermal and fluid-dynamic responses of the system. Last, we describe two different optimization problem formulations and discuss algorithmic details for their numerical implementation. These include a **robust design** and a **real-time control**. Numerical examples considering the Turin district heating networks are solved and the performance gains with respect to the conventional design and control strategies are discussed.

Chapter 8 addresses research question **Q4**, dealing with the design **optimization of cathodic flow fields** in Proton Exchange Membrane (PEM) fuel cells. We start by

describing a number of different geometric configurations of BiPolar Plates (BPPs) that were used to date at both the commercial and research levels. After introducing an averaging method that allows analyses in reduced dimensionality to be conducted, we present the governing equations and numerical model used to predict fluid flow, species transport and electrochemistry. A design optimization problem is then formulated to account for both the amount of power generation and durability of the cell. Last, we verify the analysis framework and conduct several design examples discussing the differences in layout and performance between the topology-optimized and conventional geometries.

Chapter 9 discusses the achievements and limitations of this work and identifies the topics that deserve attention in future research.

Chapter 2

Topology optimization as a design tool

Topology optimization is a powerful design tool that does not require any close-to-optimal geometry guess to start with. The design freely evolves throughout the optimization process, leading to non-intuitive topologies, shapes and configurations. This chapter presents the fundamentals of this method and establishes a common ground for all the design studies presented in this thesis.

The plan of the chapter is as follows. After discussing design freedom in conventional design methodologies (Section 2.1), in Section 2.2 we illustrate two alternatives to describe the geometry in order to allow topology modifications: the density and level-set approaches. Section 2.3 describes the optimization framework, focusing on the gradient-based algorithm of choice and sensitivity analysis. Then, in Section 2.4 we introduce popular strategies to account for layout modifications into the analysis model. Last, Section 2.5 shows the effect of a few selected topology optimization parameters with a steady-state diffusion example.

2.1 Increasing design freedom

Topology optimization responds to the fundamental question of engineering design: how shall we distribute the material in a specific region to obtain a device with maximum performance and minimum cost?

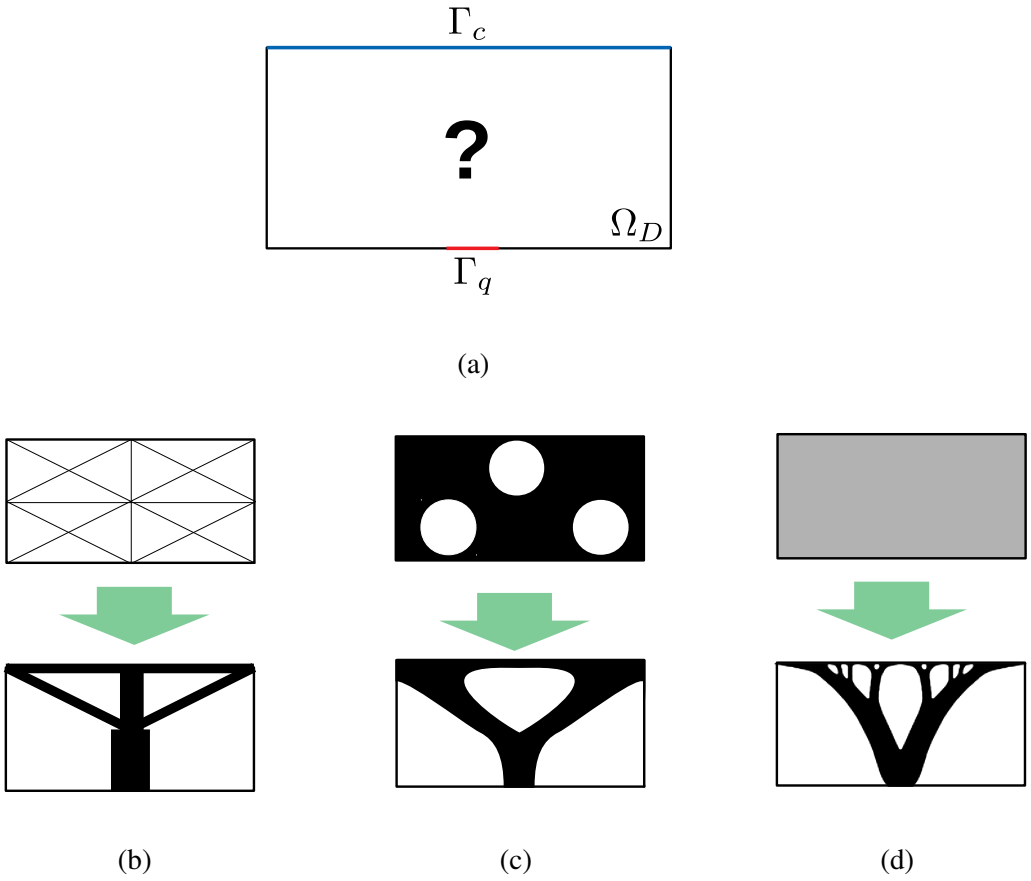

Fig. 2.1. Possible design optimization routes to obtain a heat dissipator with minimal heat transfer resistance. (a): Schematic of the design optimization problem; (b): sizing optimization; (c): shape optimization; (d): topology optimization

The key feature that distinguishes this method from the alternative design routes is freedom. Consider the design optimization problem presented in Figure 2.1(a). A square domain, Ω_D, is heated on Γ_q by an inward heat flux and is connected to a boundary, Γ_c, that is cooled by convection. We aim at finding the optimal layout of HCM within Ω_D such that the average integral temperature, T_q, of the heat source is minimized. The quantity of usable HCM is limited in order to comply with cost requirements. A classical option is to solve a sizing optimization problem (Figure 2.1(b)). The optimization procedure starts by filling the design domain with a number of candidate bar connections. Sizing optimization deals with finding the optimal thickness of each HCM bar element. Here, the original structure from which the optimization evolves is known a priori. A popular alternative is shape optimization

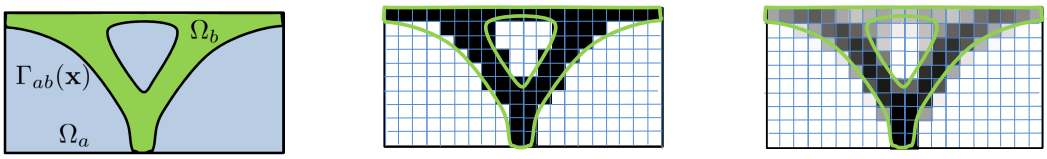

(a) (b) (c)

Fig. 2.2. The density design model. (a): Simplified dissipator schematics; (b): integer density description; (c): smoothed density description

(Figure 2.1(c)), which consists in drilling some holes in a block of HCM and finding the optimal shape and size of each hole through boundary variation techniques. Here, the number of holes and HCM domains is known a priori. Hence, this procedure leads to optimized layouts that are topologically equivalent to the starting guess. Topology optimization (Figure 2.1(d)) searches for the optimal shape, number and connectivity of the holes and HCM domains. No a-priori assumption is made on the optimal layout.

When solving a design optimization problem, designers need three tools: a design model that defines how the layout is controlled by the optimization variables, an analysis model that computes the system response using multi-scale/multi-physics analysis, an optimization model that defines the objective, constraints and search strategy. In the following sections of this chapter, we will describe the fundamentals of the design and optimization model for a topology optimization framework. As different energy systems and devices are considered in this thesis, the analysis model is discussed on a chapter-by-chapter basis.

2.2 The design model

In topology optimization, the design model should be formulated in such a way to allow topology changes. Let us consider a reference geometry (Figure 2.2(a)) based on a simplified version of the dissipator device considered in the previous section. A HCM fills Ω_a and a Background Material (BM) (can represent also void) fills Ω_b, such that $\Omega_D = \Omega_a \cup \Omega_b$. The interface between the two materials is referred to as Γ_{ab}. There are mainly two approaches that allow this geometry to be described with

sufficient design freedom: the density and level-set representations. In the following sections, we briefly summarize the main features of the two methods. For a thorough overview, the readers are referred to the comprehensive review paper of Sigmund and Maute [395].

2.2.1 Density approach

The density concept makes use of a scalar indicator function, $\chi(\mathbf{x})$, that allows switching between material phases (or material and void) as follows:

$$\chi(\mathbf{x}) = \begin{cases} 1 & \forall \mathbf{x} \in \Omega_a \\ 0 & \forall \mathbf{x} \in \Omega_D / \Omega_a \end{cases} . \tag{2.1}$$

Most commonly, the indicator function is discretized using the computational mesh such that the design variables, $\mathbf{s}$, are associated with either the elements or the nodes. The two material phases are generally represented through a raster black-and-white description like the one presented in Figure 2.2(b). The binary $\{0;\ 1\}$ nature of (2.1) can be smoothed to a continuous representation $[0, 1]$ (Figure 2.2(c)) so that the topology optimization problem is converted into a sizing problem. Now also a composite "gray" material exists to allow the transition between the black and the white phase. Using this artifact gives our indicator function a precise physical meaning: it now represents the normalized density of HCM within the other material/void. For this reason, the discretized indicator function is widely referred to as density and indicated with $\rho_s(\mathbf{x})$. The geometry changes should be somehow reflected in the analysis model. In the seminal paper of Bendsoe and Kikuchi [55], the authors considered a composite with periodically distributed microscopic voids and optimized its macroscopic density at each element of the mesh. The functional relation between macroscopic property and density was obtained by the homogenization theory [364]. Bendsoe [51] and later Zhou and Rozvany [500] showed that the composite abstraction can be abandoned if one aims at obtaining $\{0;\ 1\}$ binary designs with no regions occupied by intermediate density material. The functional relation density-property was then replaced by a differentiable artificial law. This law was chosen in such a way that the intermediate values of ρ_s are unattractive, providing low performance (small conductivity or stiffness) at high cost (volume of material). The available strategies for interpolating the material properties

are discussed in detail in Section 2.4.1. The convexity of the material interpolation law is crucial to prevent a premature convergence to unsatisfactory local minima in continuous density-based topology optimization. The effects of this choice can be alleviated by retaining the original binary $\{0;1\}$ geometry description, as in the Bi-directional Evolutionary Structural Optimization (BESO) method. However, as noted by the authors of [395], discrete approaches often generate an oscillating non-converging sequence of solutions and hardly deal with multiple non-trivial constraints. For these reasons, discrete density-based geometry descriptions are not considered in this monograph.

As this thesis deal with the design optimization of realistic devices whose analysis involves a considerable physics complexity, we adopted the continuous density-based geometry representation as the primary design model, due to its ease of implementation. It is used for the optimization of HCM fins (Chapters 3, 5 and 6) and periodic micro-structures (Chapter 4) in LHTES units, pipe loops in DHNs (Chapter 7) and flow fields in PEMFCs (Chapter 8). However, the design model developed in Chapter 4 makes use also of the level-set description to evolve the macroscopic layout. This geometry representation is described in the next section.

2.2.2 Level-set approach

The layout description of a n-dimensional body through the level-set method uses an $(n+1)$-dimensional auxiliary function, $\phi(\mathbf{x})$, defined such that:

$$\phi(\mathbf{x}) = \begin{cases} > 0 & \forall x \in \Omega_a \\ = 0 & \forall x \in \Gamma_{ab} \\ < 0 & \forall x \in \Omega_b \end{cases}. \tag{2.2}$$

A graphical representation for the simplified dissipator geometry is reported in Figure 2.3(a). The horizontal cutting plane is positioned at $z = 0$. The most popular ways to map a level-set description on a mechanical model are the deforming mesh, immersed boundaries or Ersatz material approach. A graphical comparison is reported in Figure 2.3. The former (Lagrangian) approach requires an update of the Finite Element (FE) mesh after every geometry modification. This may be prohibitively expensive for solving topology optimization problems. Furthermore, the change of

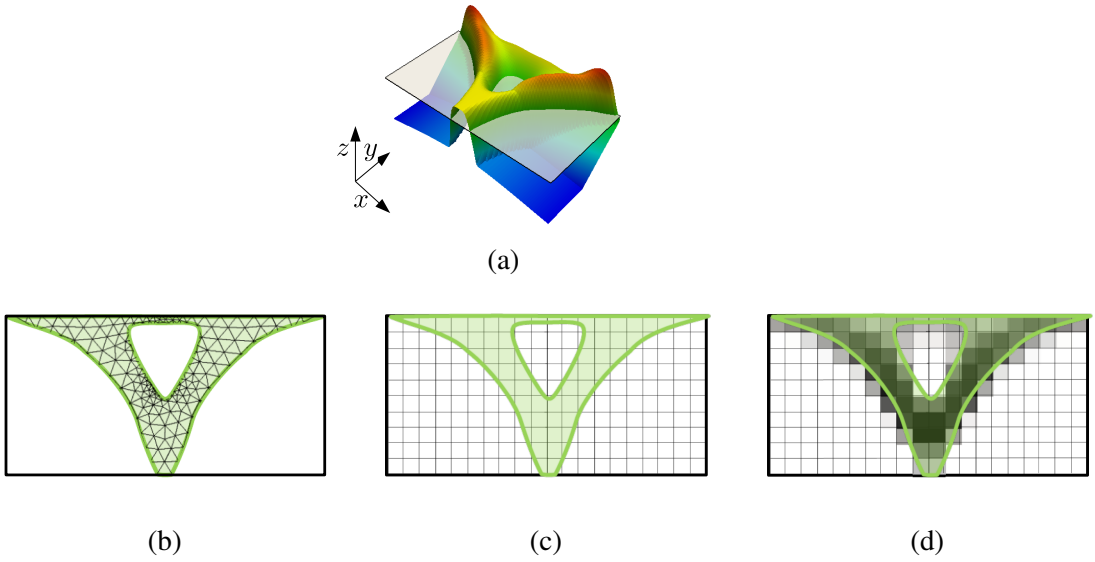

(a) (b) (c) (d)

Fig. 2.3. The level-set design model. (a): Level-set geometry description; (b): deforming grid; (c): immersed boundaries; (d): Ersatz material

the discretization introduces numerical noise in the optimization process that may significantly affect the optimization results [427]. Immersed boundary techniques are Eulerian approaches that do not require geometry re-meshing but retain a crisp representation of the material interface in the mechanical model. The eXtended Finite element Method (XFEM) approach, stemming from the partition of unity method, was applied to topology optimization with great success; for a comprehensive overview, the readers can consult the review paper of Van Dijk et al. [427]. The Ersatz material approach is an alternative Eulerian description that is based on the density concept. A nodal Level-Set Function (LSF) can be projected on a density field in two steps. First, the LSF must be mapped to the $[0,\ 1]$ interval. This can be done through a smoothed Heaviside function of the form [337]:

$$\tilde{H}(\phi) = \begin{cases} 0 & \text{if } \phi < -\xi \\ \frac{1}{2}\left(1 + \frac{\phi}{\xi} + \frac{1}{\pi}\sin\left(\frac{\pi\phi}{\xi}\right)\right) & \text{if } -\xi \leq \phi \leq \xi \\ 1 & \text{if } \phi > \xi \end{cases}, \tag{2.3}$$

where ξ represents the half-bandwidth of the Heaviside smearing. Various alternatives to (2.3) based on polynomials and other trigonometric functions were considered, see for instance [194, 428]. Second, the projected nodal LSF, $\tilde{H}$, should be transformed into an element-wise constant density field. The easiest method is a

direct point-wise mapping [337]:

$$\rho_s(\phi) = \tilde{H}(\phi(\mathbf{x}^e)), \tag{2.4}$$

where $\mathbf{x}^e$ is the position of the element centroid. Alternatively, the elemental density can be obtained as an integral average of the (smoothed) Heaviside function:

$$\rho_s(\phi) = \frac{1}{|\Omega_e|}\int_{\Omega_e} \tilde{H}(\phi)\, d\mathbf{x}. \tag{2.5}$$

Note that some authors, e.g. those of [19], used the exact Heaviside function and integrated it analytically in (2.5). The numerical integration of the exact Heaviside requires either XFEM-like techniques or a large number of integration points so that the Heaviside discontinuity is properly captured.

The most attractive feature of the level-set method is that the geometry description (2.2) allows the explicit tracking of the material interface, represented by the iso-contour of the LSF at $\phi = 0$. The interface cannot be described explicitly with the density approach (2.1). This yields an important competitive advantage for solving physical problems that rely on critical interface conditions, such as boundary layers in fluid flow at high Reynolds number. If the mechanical model is constructed using the Ersatz material approach, the level-set description in principle leads to inaccuracies similar to those of the density concept. However, in practice it is possible to control the size of the blurred region such that the areas interested by the physics inaccuracies are reduced. Another advantage of the level-set method is the high flexibility in the LSF parametrization. Differently from the density-based methods, the spatial resolution of the analysis and design models can be easily decoupled. This allows a finer control over the design space, which can be tailored to prevent the formation of numerical artifacts and increase the computational efficiency of the optimization process, at no cost of reduced accuracy of the mechanical response [427]. Most commonly, the LSF is computed using basis functions with local support such as the Finite Element Method (FEM), radial or spectral basis functions [427]. Recently, some researchers [188] started to use LSFs parametrized by smooth combinations of geometric primitives, in the spirit of an even tighter control on the geometric complexity of the optimized layouts. We will adopt this approach to produce "well-behaved" machinable assemblies of periodic cellular materials in the multi-scale multi-material design studies presented in Chapter 4. A detailed description of this

concept is given in Section 4.4.2. The most acknowledged drawbacks of the level-set methods are their strong dependence on the starting guess, inability to generate new holes, mesh dependence and slow convergence due to extremely localized sensitivities [395]. The concept of level-sets parametrized by geometric primitives used in this thesis cure both the last two issues [381].

2.3 The optimization model

In most Partial Differential Equation (PDE)-constrained optimization problems, the function evaluations are very expensive in that they involve costly numerical analyses [196]. Hence, designers are interested in obtaining an optimized layout with a limited number of computed system responses [245]. For this reason, the gradient-based routines are the preferred choice in topology optimization [393]. The need for design sensitivities is the primary reason for the formulation of a material interpolation law (see Section 2.4.1). Non-gradient approaches are "hopelessly inefficient" in topology optimization as argued by Sigmund in a recent Forum Discussion paper [393]. The author pointed out that there are at least three valid reasons to discard non-gradient routes. First, it is unlikely that global-search techniques converge to the global optimum in typical topology optimization problems. In a cantilever beam numerical example that he conducted, a conventional gradient-based technique with 60 analysis led to a better optimum than a non-gradient method using 15730 analysis. Second, although Non-Gradient Topology Optimization (NGTO) algorithms do not need the unphysical "gray" material, the coarse discretization of the design required to reduce the computational complexity leads to inaccurate FE analysis. This strongly limits the applications to real-world problems such as those considered in this thesis. A last common argument in favor of NGTO is that it does not need gradients. However, Section 2.3.2 will show that the objective and constraint sensitivities can be calculated cheaply using adjoint calculus, which makes the computational complexity of the gradients nearly insensitive to the optimization problem dimension.

A generic design optimization problem with PDE constraints can be casted in the following form:

$$\begin{aligned} \underset{\mathbf{s}}{\text{minimize}} \quad & z(\mathbf{s},\mathbf{u}(\mathbf{s})) \\ \text{subject to} \quad & g_i(\mathbf{s},\mathbf{u}(\mathbf{s})) = 0,\ i = 1,\ldots,N_{eq}. \\ & h_j(\mathbf{s},\mathbf{u}(\mathbf{s})) \leq 0,\ j = 1,\ldots,N_{ieq}. \\ & \mathbf{R}(\mathbf{s},\mathbf{u}(\mathbf{s})) = \mathbf{0} \\ & \mathbf{s} \in \mathbf{S} = \left\{ \mathbb{R}^{N_s} \mid s_{min} \leq s_i \leq s_{max}, i = 1,...,N_s \right\} \end{aligned} \quad , \tag{2.6}$$

where $\mathbf{u}$ is the vector of degrees of freedom of the physical problem, g_i is one of the N_{eq} generic equality constraints, h_i is one of the N_{ieq} generic inequality constraints, $\mathbf{R}$ is the vector of residuals of the discretized physical problem and N_s is the number of design variables with upper and lower bounds denoted by s_{max} and s_{min}. There are two possible routes for solving (2.6). The classical approach is based on the so-called Nested ANalysis and Design (NAND). Here, the optimizer does not "see" the state equations, $\mathbf{R} = \mathbf{0}$, and the states variables are treated as implicit function of the design variables [31]. Hence, in NAND $\mathbf{R} = \mathbf{0}$ does not appear in the set of constraints of (2.6). The state variables, $\mathbf{u}$, are calculated at each optimization iteration by computing the physical response of the system [31]. This decoupled approach results in the integration of analysis codes into a topology optimization code with minimal intrusiveness [58]. The alternative method is referred to as Simultaneous ANalysis and Design (SAND). In this case, the state equations are included in the optimization problem as constraints and both the state and design variables are treated as independent variables of the optimization problem [54]. This approach generally yields a simplified sensitivity analysis [356], as the objective and constraints are explicitly dependent on both the state and design variables. However, it dramatically enlarges the size of the design space and introduces non-linear equality constraints which may complicate convergence [245]. Furthermore, intermediate SAND iterations lack of physical interpretation as the state constraints may be violated [31]. Finally, this option is highly intrusive and does not allow a straightforward integration with existing analysis codes [54]. This monograph considers only NAND formulations. This choice results in the flow of computations depicted in Figure 2.4:

1. Make an initial design variable guess, e.g. a homogeneous density distribution.

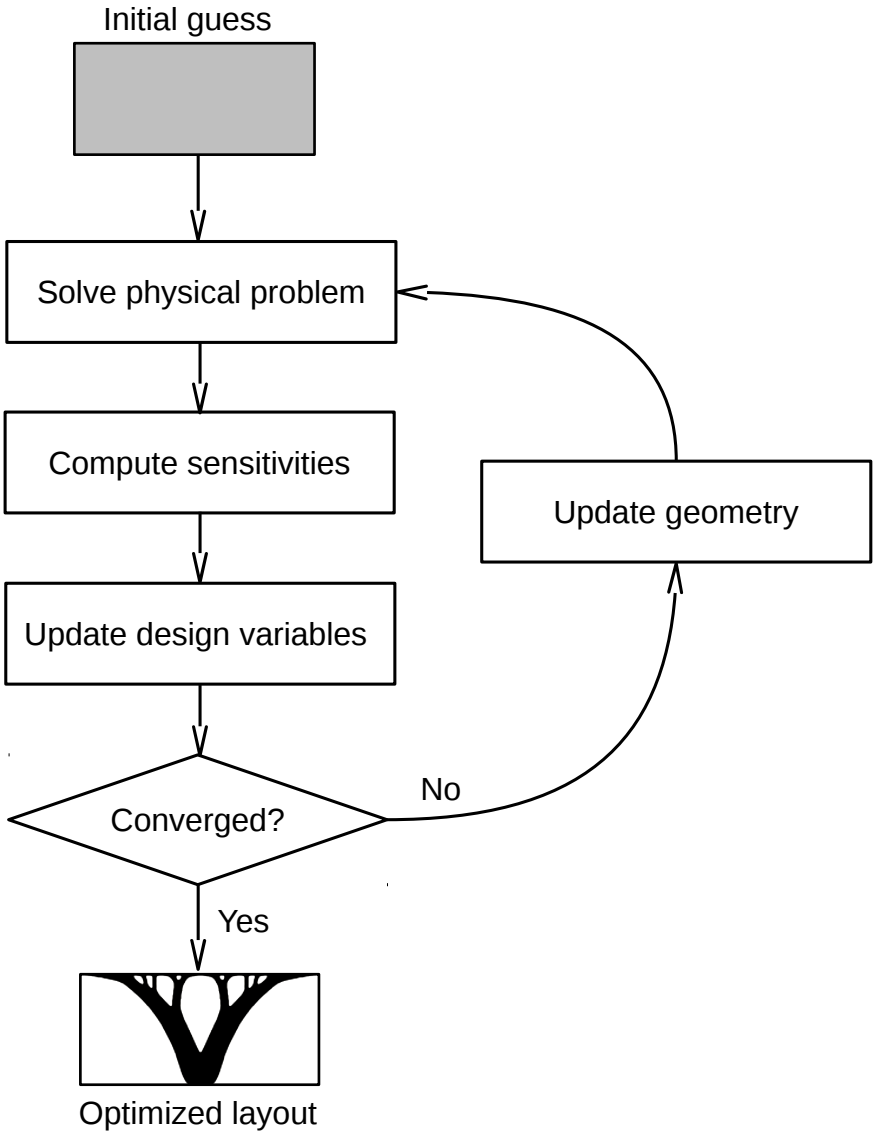

Fig. 2.4. Schematic of the flow of computations when solving a topology optimization problem with the NAND approach

2. Solve the physical problem by numerical analysis.

3. Compute the objective and constraint(s) sensitivities. In this monograph, we use the discrete adjoint method.

4. Update the design variables using a gradient-based optimizer. The Non-Linear Programming (NLP) routines of choice are the Method of Moving Asymptotes (MMA) and the Globally Convergent Method of Moving Asymptotes (GCMMA).

5. Check for convergence. If the convergence criteria are not satisfied, update the geometry and go back to step 2; otherwise, stop the optimization process and post-process the optimized design for manufacturing.

Note that a geometry update in step 5 is not needed when the design variable field is used to describe directly the geometry. However, this is necessary when using either a level-set (Section 2.2.2) or a multi-field density description (Section 2.4.2). In Section 2.3.2 and Section 2.3.1 we will discuss step 3 and step 4 of this iterative procedure. The governing equations and numerical models needed for step 2 are discussed in each chapter.

2.3.1 Method of Moving Asymptotes and its extension

The MMA builds on the idea of Sequential Linear Programming (SLP) and Sequential Quadratic Programming (SQP) in that a highly non-convex optimization problem is replaced by a sequence of "easier" approximate subproblems. Differences lie in the way these subproblems are constructed and solved.

The objective and constraints are linearized with respect to the reciprocals of the optimization variables as follows:

$$f^k(\mathbf{s}) = f(\mathbf{s}^k) + \sum_{i \in N_{s+}} \left(\frac{(U_i^k - s_i^k)^2}{U_i^k - s_i} - (U_i^k - s_i^k) \right) \frac{\partial f}{\partial s_i} - \sum_{i \in N_{s-}} \left(\frac{(s_i^k - L_i^k)^2}{s_i - L_i^k} - (s_i^k - L_i^k) \right) \frac{\partial f}{\partial s_i} \quad , \tag{2.7}$$

where f denotes either the objective or one of the constraints at optimization iteration "k", f^k denotes its approximation, N_{s-} and N_{s+} are the set of design variables with

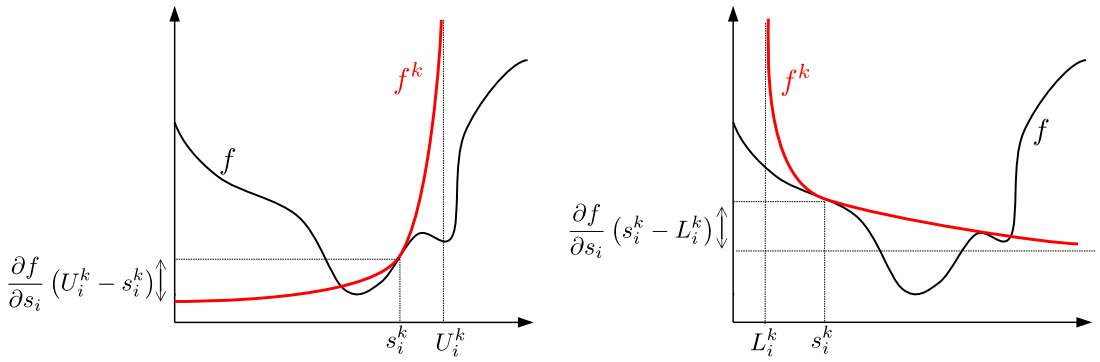

Fig. 2.5. MMA function approximation with positive (a) and negative (b) gradient.

respect to which the sensitivities are negative and strictly positive, respectively. The approximation (2.7) requires the functional gradients with respect to the design variables, s_i, that can be computed using the adjoint method described in Section 2.3.2 and the material interpolation and regularization laws presented in Section 2.4. Using reciprocal sizing variables in structural optimization is motivated by the fact that stresses and displacements are exact linear functions with respect to these quantities for statically determinate structures [141]. The parameters U_i^k and L_i^k represent local bounds of the approximated problem such that $f^k \to \infty$ when $s_i \to U_i^k$ in increasing functions and when $s_i \to L_i^k$ in decreasing functions. The values of L_i^k and U_i^k are different for each design variable and are dynamically updated along the optimization process. For these reasons, L_i^k and U_i^k are referred to as (lower and upper) "moving asymptotes". Moving the asymptotes allows the tuning of the curvature of the approximation: as L_i^k or U_i^k approach s_i^k, the curvature of f^k increases, yielding a more conservative approximation. For $L_i^k \to \infty$ or $U_i^k \to \infty$, a linear function is recovered and the MMA approximations reduce to SLP approximations. The CONvex LINearization (CONLIN) approximation of Fleury and Braibant [142] is recovered for $L_i^k = 0$ and $U_i^k \to \infty$ [507]. Note that (2.7) is an exact first-order approximation of the original function f such that $f^k(\mathbf{s}^k) = f(\mathbf{s}^k)$ and $\nabla_s f^k(\mathbf{s}^k) = \nabla_s f(\mathbf{s}^k)$. A schematic representation of the MMA approximation for a function f in a point s_i^k with a positive and a negative gradient is depicted in Figure 2.5. The function f^k is strictly convex when the asymptotes are finite and the sensitivities are non-zero. Furthermore, the approximation is separable,

allowing a reduced computational complexity in large-scale problems even when the Hessians of the objective and constraints are dense [410].

Let us consider the all-inequality version of (2.6) where the state equations are not listed as constraints due to the NAND solution approach. At iteration "k" the MMA subproblem reads [410]:

$$\begin{aligned} \underset{\mathbf{s},\mathbf{y},r}{\text{minimize}} \quad & z^k + a_0 r + \sum_{i=1}^{N_{ieq}} \left(c_i y_i + \frac{d_i}{2} y_i^2 \right) \\ \text{subject to} \quad & h_j^k - a_j r - y_j \leq 0, \; j = 1, \ldots, N_{ieq}, \\ & \mathbf{y} \geq \mathbf{0}, \; r \geq 0 \\ & \boldsymbol{\alpha}^k \leq \mathbf{s} \leq \boldsymbol{\beta}^k \end{aligned} \tag{2.8}$$

where r and $\mathbf{y}$ are artificial optimization variables, $\mathbf{c}$, $\mathbf{d}$, $\mathbf{a}$ and a_0 are user-defined constants and $\boldsymbol{\alpha}^k$ and $\boldsymbol{\beta}^k$ are referred to as lower and upper move limits. These prevent the division by zero when solving the subproblem. They should be chosen in such a way that $L_i^k < \alpha_i^k < s_i^k < \beta_i^k < U_i^k$ [409]. A popular possibility is [411]:

$$\begin{aligned} \alpha_i^k &= \max\left(s_{min}, \; L_i^k + 0.1(s_i^k - L_i^k), \; s_i^k - \Delta s(s_{max} - s_{min}) \right) \\ \beta_i^k &= \min\left(s_{max}, \; U_i^k - 0.1(U_i^k - s_i^k), \; s_i^k + \Delta s(s_{max} - s_{min}) \right) \end{aligned}, \tag{2.9}$$

where Δs is a user-defined relative step-size. The artificial variable, r, and the constants $\mathbf{d}$, a_0 and $\mathbf{a}$ allows a simplified treatment of minimax and least squares problems. As this is not of interest in this dissertation, we consider $a_0 = 1$, $\mathbf{d} = \mathbf{0}$ and $\mathbf{a} = \mathbf{0}$ such that $r = 0$ for the optimal solution of (2.8). The elastic variables, $\mathbf{y}$, enlarge the feasibility region of the original problem. Svanberg [410] proved that there exist at least one point satisfying the Karush-Kuhn-Tucker (KKT) conditions of (2.8). It is customary to set $\mathbf{c}$ to large values such that the non-feasibility becomes expensive. However, these constants may retain engineering interest when the bounds on the inequality constraints are uncertain.

The update of the asymptotes position during the optimization process relies on the following test:

$$t_i^k = \left(s_i^k - s_i^{k-1} \right) \left(s_i^{k-1} - s_i^{k-2} \right). \tag{2.10}$$

Svanberg [410] proposed to:

- tighten the approximation when a design variable oscillation is detected, i.e. $t_i^k < 0$. This can be done as following [409]:

$$\begin{aligned} L_i^{k+1} &= s_i^k - \alpha_- \left(s_i^k - L_i^k \right), \\ U_i^{k+1} &= s_i^k + \alpha_- \left(U_i^k - s_i^k \right), \end{aligned} \tag{2.11}$$

  where $\alpha_- \in [0,\ 1]$ is a user-defined parameter, set to 0.7 in this thesis.

- relax the approximation when the convergence is monotone, i.e. $t_i^k > 0$. This can be done as following [409]:

$$\begin{aligned} L_i^{k+1} &= s_i^k - \alpha_+ \left(s_i^k - L_i^k \right), \\ U_i^{k+1} &= s_i^k + \alpha_+ \left(U_i^k - s_i^k \right), \end{aligned} \tag{2.12}$$

  where $\alpha_+ > 1$ is a user-defined parameter, set to 1.43 in this thesis.

- conserve the original approximation when the design variable did not change within the last two iterations, i.e. $t_i^k = 0$

During the first two iterations the test t_i^k cannot be computed. The asymptotes are initialized as [411]:

$$\begin{aligned} L_i^k &= s_i^k - \sigma_{MMA} \left(s_{max} - s_{min} \right), \\ U_i^k &= s_i^k + \sigma_{MMA} \left(s_{max} - s_{min} \right), \end{aligned} \tag{2.13}$$

with $k \in \{1;\ 2\}$ and σ_{MMA} is a user-defined parameter generally set to 0.5 [411].

Although the original MMA algorithm [409] worked well in practice, convergence cannot be guaranteed, leading to unsatisfactory results in a few practical problems [507]. This deficiency was cured by Zillober in [507] and later in [508] with a line-search procedure, ensuring that the search direction is a descent direction of an augmented Lagrangian merit function. On the other hand, Svanberg [410] extended his original MMA algorithm through the addition of an inner iteration loop that does not require a line-search. The reworked version is referred to as GCMMA in literature. The curvatures of the objective and constraints approximations are modified with inner iterations until specific stopping criteria are satisfied. A basic algorithm of the inner iteration loop at the outer iteration "k" can be summarized as follows [410]:

1. Let the inner iteration counter $l \leftarrow 0$.

2. Assemble and solve the GCMMA approximate problem to obtain the solution $(\mathbf{x}^{lk}, \mathbf{y}^{lk}, z^{lk})$

3. Compute the objective and constraints in both the original and approximate problem and check that:
$$z^{lk}(x^{lk}) \geq z(x^{lk}) \tag{2.14}$$
and
$$h_i^{lk}(x^{lk}) \geq h_i(x^{lk}) \quad i = 1, \ldots, N_{ieq}. \tag{2.15}$$
If both criteria (2.14) and (2.15) are satisfied or the maximum number of inner iterations, N_{in}, is reached, proceed to the next outer iteration and let $(\mathbf{x}^{k+1}, \mathbf{y}^{k+1}, z^{k+1}) \leftarrow (\mathbf{x}^{lk}, \mathbf{y}^{lk}, z^{lk})$. Otherwise, modify the GCMMA approximation, let $l \leftarrow l+1$ and go to step 2.

The inner iterations do not require sensitivity analysis as the objective and constraints gradients are updated at each outer iteration. However, the inner loop does require the objective and constraints values, meaning that the physical response needs to be re-computed. This slows down convergence as compared to the ordinary MMA implementation. Criteria (2.14) and (2.15) imply that the solution of the subproblem is a feasible point with a lower objective function than the previous iteration [410]. The author referred to this property as conservativeness. In GCMMA, the approximation described in (2.7) for MMA and hereafter denoted as f^k_{MMA} is modified through the addition of a function w_c such that [410]:

$$f^k(\mathbf{s}) = f^k_{MMA}(\mathbf{s}) + \underbrace{\sum_{i \in N_s} \frac{1}{4}\rho_c \left(\frac{U_i^k - s_i^k}{U_i^k - s_i} + \frac{s_i^k - L_i^K}{s_i - L_i^k} - 2 \right)}_{w_c}, \tag{2.16}$$

where ρ_c is a conservative parameter that differs for the objective and each constraint. This is updated during the optimization procedure using the following rule [410]:

$$\rho_c^{l+1,k} = \begin{cases} \min\left(10\rho_c^{lk}, 1.1(\rho_c^{lk} + \delta_c^{lk})\right) & \text{if } \delta_c^{lk} > 0 \\ \rho_c^{lk} & \text{if } \delta_c^{lk} \leq 0 \end{cases}, \tag{2.17}$$

where the value of δ_c^{lk} is obtained through an extrapolation of the w_c function as follow [410]:

$$\delta_c^{lk} = \frac{f(x^{lk}) - f^{lk}(x^{lk})}{w_c}. \tag{2.18}$$

At each inner iteration, ρ_c is initialized based on the converged solution of the previous iterate [410]:

$$\rho_c^{0,k+1} = \max\left(0.1\rho_c^{N_l,k}, \rho_c^{min}\right), \tag{2.19}$$

where N_l is the number of inner iterations of the previous iterate and ρ_c^{min} is a user-defined minimum bound.

The GCMMA subproblems can be solved by either a dual approach or a primal-dual Interior Point (IP) approach. The latter is the method of choice in this thesis. The KKT conditions of each GCMMA subproblem are relaxed in two ways: first, the right-hand side of the complementary slackness equations is replaced by a small parameter, $\varepsilon_{cs} > 0$; second, the inequality constraints are transformed into equality constraints through the use of slack optimization variables. This removes the combinatorial issue of determining which constraints are active. The relaxed KKT conditions are mathematically equivalent to those of a log-barrier problem, typical in IP methods [411]. A damped Newton method is adopted to solve the KKT system. Due to the separability of the approximation, the resulting system can be solved only with respect to $\boldsymbol{\lambda}_{ieq}$ (the vector of Lagrange multipliers of the inequality constraints) and r. Hence, it has dimensions $(N_{ieq}+1) \times (N_{ieq}+1)$. The parameter ε_{ck} is decreased during the Newton convergence through heuristic rules [411] in a central-path fashion [313]. The iterative algorithm is stopped when both the norm of the KKT residuals and ε_{ck} are sufficiently small.

2.3.2 Adjoint sensitivity analysis

The MMA, the GCMMA and any other gradient-based numerical optimization algorithm require the objective and constraints gradients to update the design variable set. In the following, let us denote by $q_j(\mathbf{s}, \mathbf{u}(\mathbf{s}))$ a generic optimization criterion and by N_q the total number of optimization criteria. The objective and constraints can be formulated as a function of these optimization criteria.

A possible and straightforward approach to obtain the objective and constraints gradients is to evaluate the derivatives through finite differences. If a central difference scheme is adopted, the design sensitivities are computed as [196]:

$$\frac{dq_j}{ds_i} = \frac{q_j(s_i + \varepsilon_{s_i}) - q_j(s_i - \varepsilon_{s_i})}{2\varepsilon_{s_i}}, \tag{2.20}$$

where ε_{s_i} is the perturbation size of the design variable i. To compute the optimization criterion, the physical problem $\mathbf{R} = \mathbf{0}$ should be solved. Hence, the central finite difference strategy requires at least $2 \times N_s$ system evaluations. The consequence is a computational burden that makes impractical to solve high-dimensional problems (such as topology or shape optimization) using this route. Plus, the accuracy of a finite difference framework strongly depends on the degree of non-linearity of the problem and on the choice of the perturbation size, ε_{s_i}. Large values may lead to inaccuracies related to truncation errors [196]; the accuracy at small values gets affected by cancellation error due to machine limits [196]. Despite these downsides, finite difference sensitivities are still used throughout this monograph to cross-check the accuracy of analytical sensitivities.

Analytical differentiation is an alternative to finite differences, allowing a reduced computational complexity. The direct differentiation of a generic optimization criterion through the chain rule leads to:

$$\frac{dq_j}{ds_i} = \underbrace{\frac{\partial q_j}{\partial s_i}}_{\text{(i)}} + \underbrace{\left(\frac{\partial q_j}{\partial \mathbf{u}}\right)^T}_{\text{(ii)}} \underbrace{\frac{d\mathbf{u}}{ds_i}}_{\text{(iii)}}. \tag{2.21}$$

When dealing with smooth optimization criteria, terms (i) and (ii) in Eq. (2.21) are generally easy to compute. Evaluating term (iii) is much more involving. One may require that the state sensitivities satisfy the linearized state equations as follows [164]:

$$\frac{d\mathbf{R}}{ds_i} = \frac{\partial \mathbf{R}}{\partial s_i} + \underbrace{\frac{\partial \mathbf{R}}{\partial \mathbf{u}}}_{\mathbf{J}} \frac{d\mathbf{u}}{ds_i} = \mathbf{0}, \tag{2.22}$$

where $\mathbf{J}$ indicates the Jacobian of the residual vector with respect to the state variables. Solving (2.22) for term (iii) we obtain [293]:

$$\frac{d\mathbf{u}}{ds_i} = -\left(\frac{\partial \mathbf{R}}{\partial \mathbf{u}}\right)^{-1} \frac{\partial \mathbf{R}}{\partial s_i}. \tag{2.23}$$

Solving (2.23) and substituting back into (2.21) yields the criterion sensitivities. This route is known as direct method. Similarly to finite differencing, the computational complexity of this approach is insensitive to the number of optimization criteria. However, it requires as many system solutions as the number of design variables: Eq. (2.23) should be solved for $i = 1,\ 2, \ldots,\ N_s$. Hence, the direct method is still impractical for topology optimization problems. A much cheaper option is to use a *symbolic* substitution yielding:

$$\frac{dq_j}{ds_i} = \frac{\partial q_j}{\partial s_i} - \left(\frac{\partial q_j}{\partial \mathbf{u}}\right)^T \left(\frac{\partial \mathbf{R}}{\partial \mathbf{u}}\right)^{-1} \frac{\partial \mathbf{R}}{\partial s_i}, \tag{2.24}$$

which can be rearranged through transposition properties as:

$$\frac{dq_j}{ds_i} = \frac{\partial q_j}{\partial s_i} - \left(\underbrace{\left(\frac{\partial \mathbf{R}}{\partial \mathbf{u}}\right)^{-T} \frac{\partial q_j}{\partial \mathbf{u}}}_{\text{Adjoint problem}} \right)^T \frac{\partial \mathbf{R}}{\partial s_i}. \tag{2.25}$$

The term in bracket is referred to as adjoint problem. To simplify the computations, we introduce the adjoint equation [293]:

$$\left(\frac{\partial \mathbf{R}}{\partial \mathbf{u}}\right)^T \boldsymbol{\lambda} = \frac{\partial q_j}{\partial \mathbf{u}}, \tag{2.26}$$

where $\boldsymbol{\lambda}$ is the vector of adjoint variables or Lagrange multipliers. Now Eq. (2.25) can be restated as [293]:

$$\frac{dq_j}{ds_i} = \underbrace{\frac{\partial q_j}{\partial s_i}}_{\text{(i)}} - \boldsymbol{\lambda}^T \underbrace{\frac{\partial \mathbf{R}}{\partial s_i}}_{\text{(ii)}}. \tag{2.27}$$

The adjoint problem (2.26) is insensitive to the optimization problem dimension as it does not depend on s_i. It requires as many systems solutions as the number of optimization criteria, i.e. it should be solved for $j = 1,\ 2, \ldots,\ N_q$. This is the preferred method for sensitivity analysis in topology optimization problems since generally $N_s >> N_q$. Note also that (2.26) is linear meaning that the sensitivity analysis is consistently cheaper than forward analysis of nonlinear problems.

The computation of the adjoint sensitivities used in this thesis is done with the following steps:

1. Recover the Jacobian, **J**, from the last Newton iteration of the forward analysis and compute the adjoint Right-Hand Side (RHS).
2. Solve the adjoint equation (2.26).
3. Compute terms (i) and (ii) of Eq. (2.27) for every design variable s_i.
4. Compute (2.27) by post-multiplication.

2.4 Mapping the design model on the analysis model

This section presents two fundamental features of any density-based topology optimization code used to map the density-based (and Ersatz material level-set) geometry representation on the analysis model. First, we describe a few functions that are commonly adopted in literature as artificial laws material property-density. Then, we discuss how to regularize the topology optimization problem to obtain a unique solution that is free of numerical instabilities.

2.4.1 Material interpolation

The continuous $[0,\ 1]$ density setting requires a continuous and differentiable relation material property-density such that both the physical response and design sensitivities can be computed. For instance, to solve our dissipator example using a steady-state diffusion model, the conductivity, k, within Ω_D needs to be defined also for the intermediate "gray" material. Interpolating the material properties with an artificial law is referred to as material interpolation. Various techniques were developed over the years. All the methods aim at "penalizing" the intermediate density values such that the optimization process converges to a manufacturable binary $\{0;\ 1\}$ design.

The Simplified Isotropic Material with Penalization (SIMP) or power-law approach introduced by Bendsoe [51] is arguably the most popular material interpolation model in the topology optimization community. Referring to the dissipator design problem, the conductivity k in Ω_D is expressed as:

$$k(\rho_s) = k_{BM} + (k_{HCM} - k_{BM})\rho_s^p \tag{2.28}$$

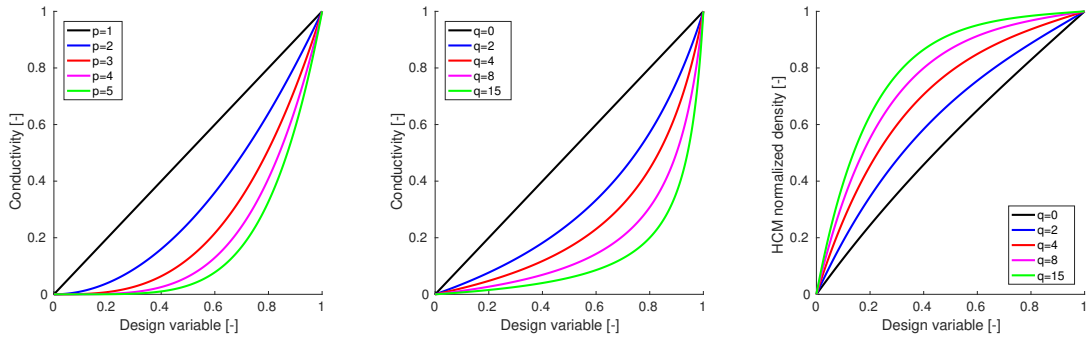

(a) (b) (c)

Fig. 2.6. Comparison of material interpolation models. (a): SIMP model; (b): RAMP model; (c): SINH model

where k_{HCM} and k_{BM} are the conductivities of the two materials and p is a penalization exponent. The latter defines the steepness of the interpolation: $p = 1$ allows a linear function (the Voigt bound) to be recovered while the interpolation convexity increases for $p > 1$. Note that when Eq. (2.28) is used in material-void problems, a minimum value of $k_{BM} > 0$ should be set in order to avoid singularities in the solution of the physical problem. The SIMP interpolation function in the case $k_{HCM} = 1$ and $k_{BM} = 1e-6$ is represented in Figure 2.6(a). The conductivity interpolation does not provide penalization by itself. This effect is obtained only in the presence of a (linear) volume constraint of the type:

$$\int_{\Omega_D} \rho_s \, d\mathbf{x} - V^* \leq 0, \tag{2.29}$$

where V^* is a maximum prescribed volume of HCM. When considering both Eq. (2.28) and (2.29), intermediate densities become inefficient: they provide small conductivity per unit of material expense. The SIMP interpolation model originated as artificial and somewhat heuristic strategy to obtain binary designs. However, Bendsoe and Sigmund [53] showed that it is possible to construct micro-structures that physically realize the SIMP interpolation model. This discovery can be of interest when interpreting premature designs along the optimization process, having large regions with intermediate ρ_s material, or when searching for physical reasons behind non-convergence to binary $\{0;\ 1\}$ designs.

An alternative to SIMP is the RAMP model, which was first introduced by Stolpe and Svanberg [406]. The authors showed that SIMP does not in general lead

to a concave compliance with respect to the feasible set. Hence, it can be debated whether a solution to the "relaxed" continuous problem is also a solution to the original discrete-valued problem. To cure this issue, they proposed to interpolate the generic material property as follows:

$$k(\rho_s) = k_{BM} + (k_{HCM} - k_{BM}) \frac{\rho_s}{1 + q(1 - \rho_s)}, \tag{2.30}$$

where q is a penalization parameter that plays a role similar to the SIMP exponent, p. The RAMP interpolation function in the case $k_{HCM} = 1$ and $K_{BM} = 1e-6$ is represented in Figure 2.6(b). Later experience showed that ensuring concavity with respect to the feasible set does not hold relevance for practical problems [395]. The most interesting feature of the RAMP approximation is that it preserves non-nil gradients at $\rho_s = 0$. This can increase convergence to binary designs and, in our experience, plays a significant role when dealing with large k_{HCM}/k_{BM} ratios. Furthermore, the RAMP model satisfies the Hasin-Shtrikman (HS) bounds for all $0 \leq \rho_s \leq 1$ in a certain range of q [54].

Instead of using a convex property-density relation coupled with the linear equality constraint (2.29), one could use a linear property-density relation coupled with a concave volume constraint to achieve the penalization effect. For instance, Bruns [69] proposed the SINH (standing for hyperbolic sine) method, in which the material law and volume constraint take the form:

$$k(\rho_s) = k_{BM} + (k_{HCM} - k_{BM})\rho_s, \tag{2.31}$$

$$\int_{\Omega_D} \left(1 - \frac{\sinh(p(1-\rho_s))}{\sinh(p)}\right) d\mathbf{x} - V^* \leq 0, \tag{2.32}$$

where the term in brackets in (2.32) is a normalized HCM density, quantifying the HCM expense per unit volume. A graphical representation of the SINH material interpolation strategy is given in Figure 2.6(c). This approach did not encounter broad acceptance for two main reasons. First, specifying V^* is tricky since the term in brackets in (2.32) may not represent the true volume. Second, the linear relation (2.31) does not satisfy the HS bounds.

Choosing suitable values of the penalization parameters can be a non-trivial task. The best set-up, provided that it exists, strongly depends on the physics and objective function considered. Since the (thermal) compliance minimization problem

is convex with $p = 1$ in (2.28), a popular approach is to slowly raise the penalization parameters following a continuation scheme. A sequence of optimization problems with increasing penalty values are solved. The solution of each continuation step is used as initial guess for the next continuation step. This method works well in many practical problems where it avoids unsatisfactory local minima. However, there is no theoretical proof that this approach leads to the global optimum. Stolpe and Svanberg [406] showed with some truss optimization examples that the trajectories of the optimal solutions of the penalized problems are in general discontinuous during a continuation scheme. The interpolation and continuation strategies in complex multi-physics problems are even more complicated to formulate. If the penalization is not "balanced" among the material properties governing competitive physics, there is a chance of favoring one physical phenomenon over the others at intermediate optimization steps and obtain trivial local minima. More detailed discussions on this issue are left for Section 5.4, where we investigate some possible continuation schemes in coupled problems involving heat transfer and fluid flow.

2.4.2 Regularization

The numerical instabilities arising in density-based topology optimization can be divided in two categories: checkerboards and mesh-dependence. The first category indicates the formation of black-white checkerboard patterns in the optimized layouts. The second one refers to the issue of obtaining different solutions when the mesh is refined.

Diaz and Sigmund [114] demonstrated that the reason for the creation of checkerboards is the numerical approximation of the FE discretization. Checkerboard patterns were found to produce numerical stiffness that makes these artifacts locally stronger than any layered arrangement of the two material constituents. This instability can be mitigated by the use of higher order elements, patches and filtering [387]. As the latter also solves mesh-dependence issues, it is the method of choice adopted in this thesis. Mesh-dependence is related to the fact that some design optimization problems are ill-posed in nature. The creation of micro-structural holes with a fixed amount of structural volume is beneficial to the compliance of structures. Similarly, the creation of small HCM features in general improves the performance of heat transfer enhancers as heat can be distributed more efficiently. Figure 2.7 shows how the numerical solution of the dissipator problem changes when the mesh is refined.

(a) (b) (c)

Fig. 2.7. Optimized dissipator geometries with different meshes. (a): 25 x 50 elements; (b): 50 x 100 elements; (c): 100 x 200 elements

More and more HCM branches are created connecting the heat source in Γ_q with the cooled boundary, Γ_c. This means that the feasible set is not closed and a solution does not exist [387]. Although this trend agrees with the intuition, obtaining a unique manufacturable structure is desirable for design engineers. Note that these numerical issues are highly problem and physics-dependent. For instance, the minimization of pressure drop in flow problems is not ill-posed. The objective function worsens with small structural details and layouts with large channels are generally privileged.

The methods available to cure the non-existence issue are of two kinds: relaxation and restriction. Relaxation refers to the enlargement of the design space so that the "gray" material is allowed in the solution. This should be interpreted as a composite material, whose micro-structural topology is optimized. The homogenization method for topology optimization described in the seminal work of Bendsoe and Kicuchi [55] belongs to this category. The optimization variables parametrize the micro-structural layout determining macroscopic properties. These are then used to solve the FE problem at the macro-scale. The homogenization theory was later used for material design [390] by topology optimization, where the microscopic layout of periodic structures with prescribed mechanical properties are sought. Following this flourishing line of development, relaxation based on homogenization was later extended [355] to multi-scale topology optimization frameworks, where both the material and structure are optimized. An alternative to the homogenization method to achieve the relaxation of the design space is to convert the problem into a Variable Thickness Sheet (VTS) optimization [332]. Here, the density should be interpreted as a thickness function and can take intermediate values in the optimized design.

Restriction considers a smaller design set of the original problem in which rapid oscillations of the design field are limited. Ambrosio and Buttazzo [24] added a

penalization term, z_p, to their objective function accounting for perimeter:

$$z_p = \alpha_p \int_{\Omega_D} ||\nabla \rho||_q \, dV, \tag{2.33}$$

where $q = 1$ is the norm exponent and α_p is the penalization weight. Selecting a proper α_p value is not easy and requires some tuning. Other authors [62] defined a maximum design perimeter and augmented the optimization problem with a perimeter constraint. However, choosing a maximum value for the constraint presents similar difficulties to the selection of a proper α_p. Note that the generalization of the notion of norm in Eq. (2.33) allows the computation of an approximate maximum *local* slope when $q \to \infty$. A much more popular alternative to these perimeter/variation strategies is to employ filtering. Intuitively, filtering spreads the spatial influence of each design variable such that rapid oscillations of the design field are prevented. A straightforward but heuristic implementation of this idea was presented in [391], where a convolution operator is adopted to modify the sensitivity field:

$$\frac{\partial \tilde{q}_j}{\partial \rho_s} = \frac{\sum_{i \in N^e} w_i \rho_{s_i} \frac{\partial q_j}{\partial \rho_{s_i}}}{\sum_{i \in N^e} \rho_{s_i} w_i}, \tag{2.34}$$

where w_i is the filter weight and the index i spans the design variables, elemental or nodal, located in the neighborhood N^e of the element. This set is defined as:

$$i \in N^e \quad \text{if } ||\mathbf{x}_i - \mathbf{x}^e|| \leq r_f, \tag{2.35}$$

where r_f is the filter radius and $\mathbf{x}_i$ is the position of the design variable. The weight is defined as a linearly-decaying function:

$$w_i = r_f - ||\mathbf{x}_i - \mathbf{x}^e||, \tag{2.36}$$

which is a distance function centered in $\mathbf{x}^e$ and locally supported within the filter radius. A schematic representation of the linear filter operator with nodal design variables is represented in Figure 2.8(a). The nodal positions belonging to N^e are marked in green. The filter weight function varies linearly between 0 and r_f and does not depend upon the mesh size. Researchers often questioned the mathematical rationale behind the sensitivity filter as it was not possible to identify which objective function was being actually optimized. Lately, Sigmund and Maute [394] revealed

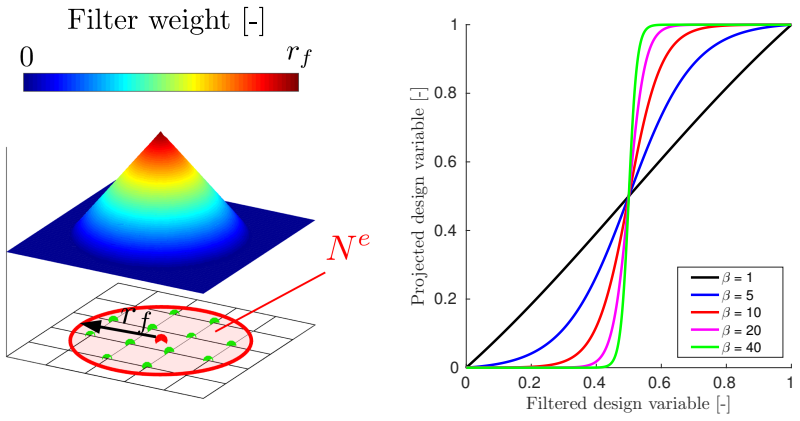

(a) (b)

Fig. 2.8. (a): Schematic representation of the linear filter operator; (b): generalized tanh projection with $\eta = 0.5$

that using the sensitivity filter in structural optimization corresponds to minimizing the compliance in non-local elasticity problems.

Taking inspiration from the sensitivity filter approach, Bruns and Tortorelli [70] proposed to filter the design variable field. In the original view of the authors, this method has the advantage that designers "know exactly what optimization problem is being solved". A new filtered design variable, $\tilde{s}$, is introduced in the optimization problem. For this reason, the authors of [393] refer to this method as "two-field SIMP". The additional design variable field is defined as:

$$\tilde{s} = \frac{\sum_{i \in N^e} w_i s_i}{\sum_{i \in N^e} w_i}. \tag{2.37}$$

Note that this approach does not enlarge the design set. The filtered field can be obtained explicitly from s through (2.37). Now the density indicator is represented by this additional field such that $\rho_s = \tilde{s}$. For this reason, we will refer to s and ρ_s as abstract and physical design variables throughout this monograph. As with the homogenization method for topology optimization, this approach relies on the separation of the design space, where the abstract design variables, s, live, and the FE space, where the physical design variables, ρ_s, live and the system response is computed.

Using the filter (2.37) blurs the boundary of the geometry representation, ρ_s, and gives at best regions with intermediate density values of thickness $2r_f$ (sufficiently far from the design domain boundaries) even for well penalized problems. One may reduce the related inaccuracies in the analysis by using a continuation approach where the filter radius is slowly decreased. As an alternative, Guest [176] proposed a projection scheme, where a third field is introduced as:

$$\bar{s} = 1 - e^{-\beta \tilde{s}}, \tag{2.38}$$

where β corresponds to a projection steepness parameter. This method works with three different design variable fields. The projected design variable field is used to describe the geometry and interpolate the material properties, hence $\rho_s = \bar{s}$. Equation (2.38) is a smoothed version of a Heaviside function. Using filtering followed by projection with (2.38) guarantees a minimum length-scale on the optimized designs. To understand how this is possible consider the 1D example of Figure 2.9, where s is defined at the nodes and $\tilde{s}$ and $\bar{s}$ are defined at the elements and are element-wise constant. The geometry discretization consists of 7 equally spaced nodes and 6 elements with characteristic size $h = 1$. The filter has radius $r_f = 2$. Consider the situation presented in Figure 2.9(a), where $s = 1$ in one node and $s = 0$ in neighbor nodes. Filtering produces a smoothed layout with $\tilde{s} > 0$ in a region with width $2r_f$, i.e. spanning 4 elements. This whole region is then projected to a structural member of width $2r_f$ when using (2.38). Hence, geometries with features smaller than $2r_f$ are not allowed for HCM elements sufficiently far from the design domain boundaries. Close to the boundaries, the region spanned by the filter operator is reduced. For instance, if the node with $s = 1$ belongs to a design domain boundary (Fig 2.9(b)), an r_f wide smoothing is obtained. This shows that structural features with width $r_f \leq w_{HCM} \leq 2r_f$ can appear close to the design domain boundaries.

Sigmund [392] later revisited the problem to obtain a minimum length-scale of the BM layout. This is achieved by simply modifying the Heaviside to be centered at $\tilde{s} = 1$ as following:

$$\bar{s} = 1 - e^{-\beta(1-\tilde{s})}. \tag{2.39}$$

The effect of projection (2.39) is presented in Figure 2.9(c). A single $s = 0$ node positioned sufficiently far from the boundaries is surrounded by an $s = 1$ neighborhood. After filtering and projection, the hole in the structure has width $2r_f$. Smaller holes

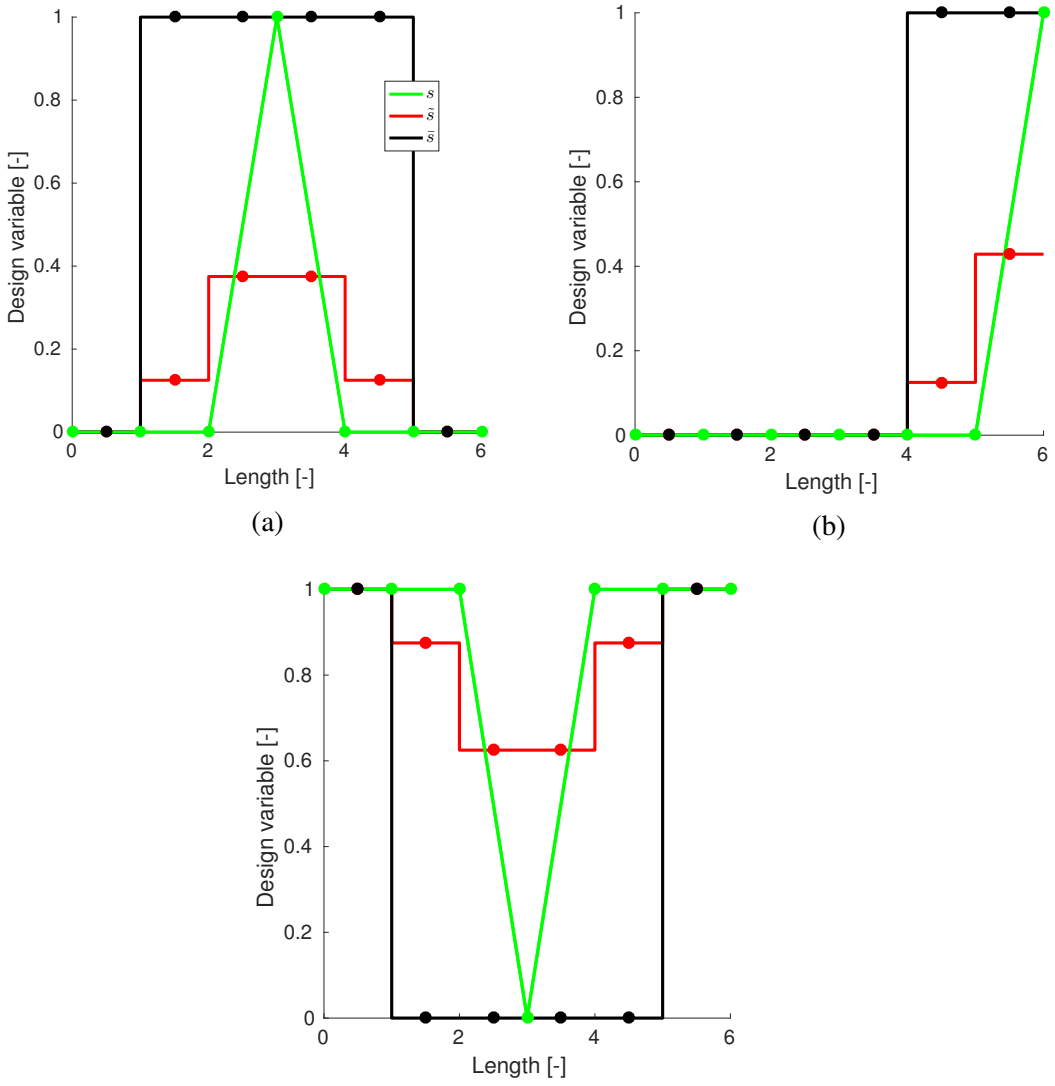

Fig. 2.9. Filtering and projection 1D example. (a): Preservation of the minimum feature size of HCM; (b): boundary effect on the minimum feature size of HCM; (c): preservation of the minimum feature size of BM

can appear close to the design domain boundaries for the same reasons discussed for Figure (2.9)(b).

Wang et al. [446] later generalized the previous approaches with a hyperbolic tangent formulation where the projection thresholds, η, can be varied continuously between 0 and 1.

$$\bar{s} = \frac{\tanh(\beta\eta) + \tanh\left(\beta(\tilde{s} - \eta)\right)}{\tanh(\beta\eta) + \tanh\left(\beta(1 - \eta)\right)}. \tag{2.40}$$

This generalized projection with variable threshold and steepness is represented in Figure 2.8(b) for the case with $\eta = 0.5$. When $\eta \in (0,1)$, Eq. (2.40) does not guarantee a minimum feature size on neither of the two phases but has shown to provide mesh-independent and crisp results in practical cases [393]. Methods that guarantee minimum length-scale on both phases involve the use of four design variable fields. One example was demonstrated in [177]. Note that the projection only helps to obtain crisp boundaries when a filtering scheme is adopted. This should not be used to improve the convergence to binary $\{0;\ 1\}$ designs in poorly penalized problems [395]. In the best case, the abstract design variable field would morph such that the intermediate values of the physical design variable field are still present. In most cases, using high projection values and a small penalization parameter leads to premature convergence to poor local minima. Continuation schemes are generally adopted to slowly raise the projection steepness parameter, β. This helps to avoid wiggling in the optimization history and premature convergence to local minima. However, in a recent paper [178], Guest showed that it is possible to avoid such a continuation by tightening the initial asymptotes position in the MMA routine as follows:

$$\sigma_{MMA} = \frac{0.5}{\beta + 1}. \tag{2.41}$$

Both asymptotes initialization strategies (2.13) and (2.41) are used throughout this monograph. The choice will be clarified on a case-by-case basis.

When using the three-field density methods, all the computations described for adjoint sensitivity analysis in Section 2.3.2 are performed with respect to the physical design variable, $\rho_s = \bar{s}$. Then, the sensitivity field should be modified to ensure consistent optimization criteria gradients with respect to the abstract design variable, s. In this monograph, we account for filtering and projection in the sensitivity

analysis using the chain rule as follows:

$$\frac{dq_j}{ds_i} = \sum_{l=1}^{N_s} \sum_{k=1}^{N_s} \frac{dq_j}{d\bar{s}_k} \frac{\partial \bar{s}_k}{\partial \tilde{s}_l} \frac{\partial \tilde{s}_l}{\partial s_i}, \tag{2.42}$$

where the first term on the RHS is the one computed through adjoint calculus.

2.5 Steady-state diffusion example

In this section, we investigate and discuss the effect of the most relevant topology optimization parameters introduced in this chapter. To this aim, we consider our dissipator example. The design optimization problem can be stated as:

$$\begin{aligned} \underset{\mathbf{s}}{\text{minimize}} \quad & \int_{\Gamma_q} T \, d\mathbf{x}' \\ \text{subject to} \quad & \int_{\Omega_D} \rho_s \, d\mathbf{x} - V^* \leq 0 \\ & \mathbf{s} \in \mathbf{S} = \left\{ \mathbb{R}^{N_s} \mid s_{min} \leq s_i \leq s_{max}, i = 1, \ldots, N_s \right\} \end{aligned} \quad , \tag{2.43}$$

where the maximum volume of HCM, V^*, is set to 25 % of the total volume available. The design domain has width $W = 2$ and height $H = 1$. The heat source boundary has width $w_q = 0.2$. The focus here is exclusively on the topology optimization parameters; we are not interested in obtaining an optimized device for practical use. Hence, we limit the physics complexity. Heat transfer is governed by steady-state diffusion within Ω_D:

$$-\frac{\partial}{\partial x_i}\left(k(s)\delta_{ij}\frac{\partial T}{\partial x_j}\right) = q_v, \tag{2.44}$$

where δ_{ij} is the Kronecker delta and $k(s)$ is the design-dependent conductivity interpolated with (2.28) between $k_{BM} = 1$ and $k_{HCM} = 1000$ and $q_v = 0$ is the volumetric heat generation. A constant heat flux is imposed through a Neumann boundary condition on Γ_q:

$$-k(s)\delta_{ij}\frac{\partial T}{\partial x_j}n_i = q_{hs}, \tag{2.45}$$

Table 2.1. GCMMA parameters utilized in this monograph

Description	Symbol	Value
Relative step-size	Δs	0.03
Maximum inner iterations	N_{in}	2
Initial asymptote position parameter	σ_{MMA}	0.5
Lower asymptote adaptivity	α_{-}	0.7
Upper asymptote adaptivity	α_{+}	1.43
Constraint penalty	c_i	1000
Parameters	a_i	0
Parameter	a_0	1
Parameters	d_i	0
Minimum conservativeness parameter	ρ_c^{min}	1e-5

where n_i is the inward-pointing normal and $q_{hs} = 1$ is the applied heat flux. The top boundary is cooled by convection, hence a mixed-type (Robin) condition is applied on Γ_c:

$$-k(s)\delta_{ij}\frac{\partial T}{\partial x_j}n_i = h(T_{ext} - T), \tag{2.46}$$

where $T_{ext} = 0$. The governing equations are discretized with $2e4$ bilinear quadrilateral elements and solved in COMSOL Multiphysics [101]. The optimization problems are solved using GCMMA in Matlab [292]. The most relevant GCMMA parameters are summarized in Table 2.1. Unless otherwise stated, these values are used to produce all the results presented in this thesis. Limiting the number of maximum inner iterations, N_{in}, to 2 does not guarantee the "globally convergent" feature of the GCMMA algorithm. However, a high N_{in} was often found to lead to slow convergence, requiring a large number of analyses. In specific numerical examples, N_{in} is raised from this default value only to stabilize convergence and avoid dramatic oscillations along the optimization process. In this section, we will investigate the effect of the penalization exponent, p, filter radius, r_f, projection steepness parameter, β, and projection threshold, η. The default values of these parameters are listed in Table 2.2.

The COMSOL-Matlab design optimization framework used here was developed in cooperation with Dr. Reza Behrou and used to produce the results presented in Chapter 8. The design studies presented in Chapters 3, 4, 5 and 6 are solved using the Finite Element Multi-disciplinary Design Optimization Code (FEMDOC), a C++ design optimization framework developed at University of Colorado (CU)

Table 2.2. Default topology optimization parameters of the dissipator example

Description	Symbol	Value
SIMP exponent	p	3
Filter radius	r_f	0.021
Projection steepness	β	1
Projection threshold	η	0.5

Boulder. The design and control studies presented in Chapter 7 are solved using the NEtwork COntrol and Design Optimization Code (NECODOC), a design and control optimization framework developed at Politecnico di Torino (PoliTo).

The topology optimization results for the different values of the SIMP exponent, p, are presented in Figure 2.10. The same colorbar displayed in Figure 2.10 is used for all the layouts presented in this chapter. The design obtained using $p = 1$ can be interpreted in a VTS perspective. The width of the HCM connection increases along the y direction to link a thin to a wide boundary. As a consequence, the heat flux per unit width diminishes along the y direction and so does the optimized thickness of the dissipator. Large areas with intermediate gray material are present in this layout. The convergence to binary $\{0;\ 1\}$ designs is gradually improved when increasing the SIMP exponent. The layout obtained with $p = 2$ shows gray areas close to the top boundary that nearly disappear with $p = 3$. No substantial differences in the degree of convergence is observed for $p > 3$. However, the optimized geometry changes consistently. Since designers should select a unique geometry for manufacturing, one may identify the best one according to the performance. For this reason, we post-process the optimized ρ_s field using (2.40) with $\beta = 1e6$ such that a steep Heaviside function is obtained. The projection threshold is iteratively chosen to weakly conserve the HCM volume:

$$\left| \frac{\int_{\Omega_D} \rho_s \, d\mathbf{x} - V^*}{V^*} \right| \leq 1e-3. \tag{2.47}$$

Figure 2.11 shows an example of post-processing for the layout obtained with $p = 2$. The gray areas disappear when projecting the optimized design variable field. The design obtained by a projection with $\eta = 0.5$ (Figure 2.11(b)) results in a volume fraction of 19.74 %. Hence, the projection has reduced the amount of HCM in the design domain and likely affected the performance, complicating comparisons.

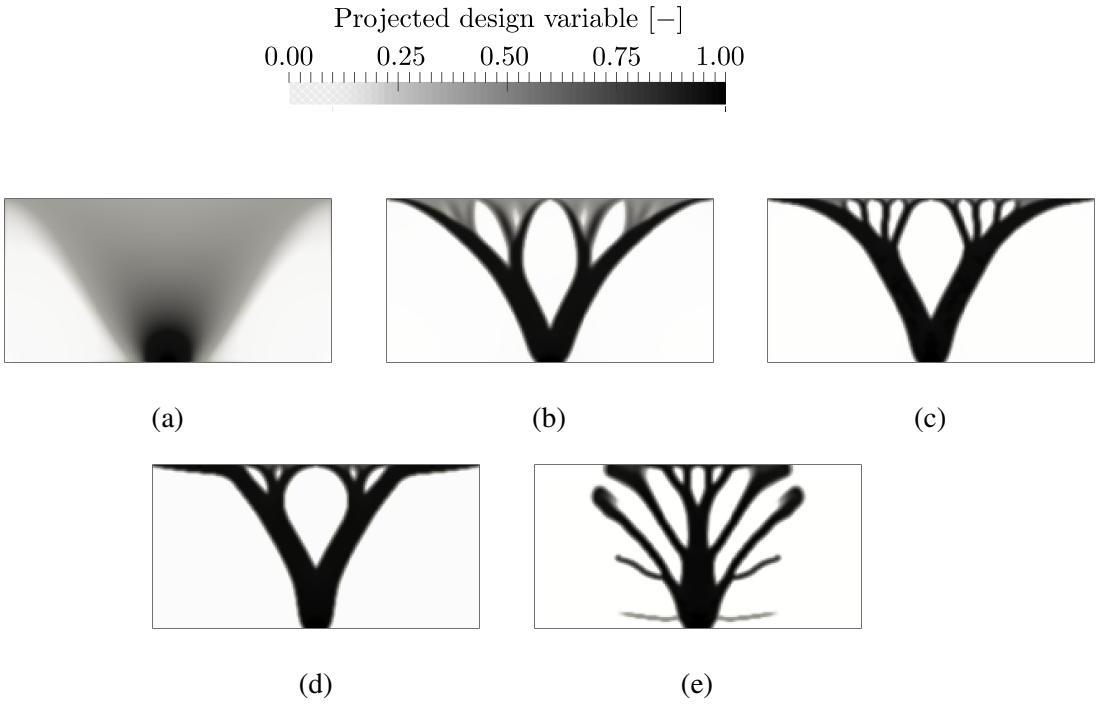

Fig. 2.10. The effect of the SIMP exponent, p, on the optimized designs. (a): $p = 1$, $z = 7.108e-3$; (b): $p = 2$, $z = 5.103e-3$; (c): $p = 3$, $z = 5.033e-3$; (d): $p = 5$, $z = 5.043e-3$; (e): $p = 10$, $z = 5.429e-3$;

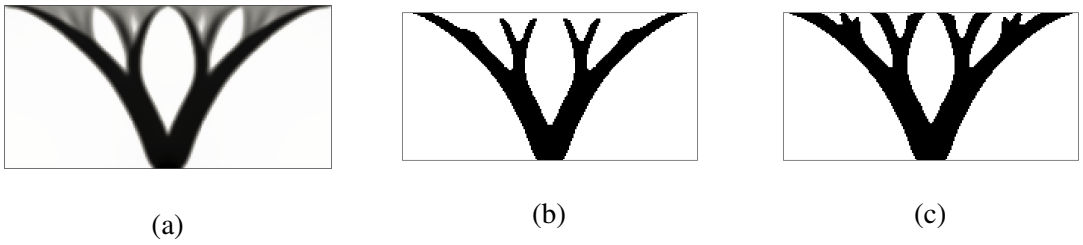

Fig. 2.11. Post-processing for performance comparison. (a): optimized design for $p = 2$; (b): projected optimized design with $\eta = 0.5$; (c): projected optimized design with $\eta = 0.375$

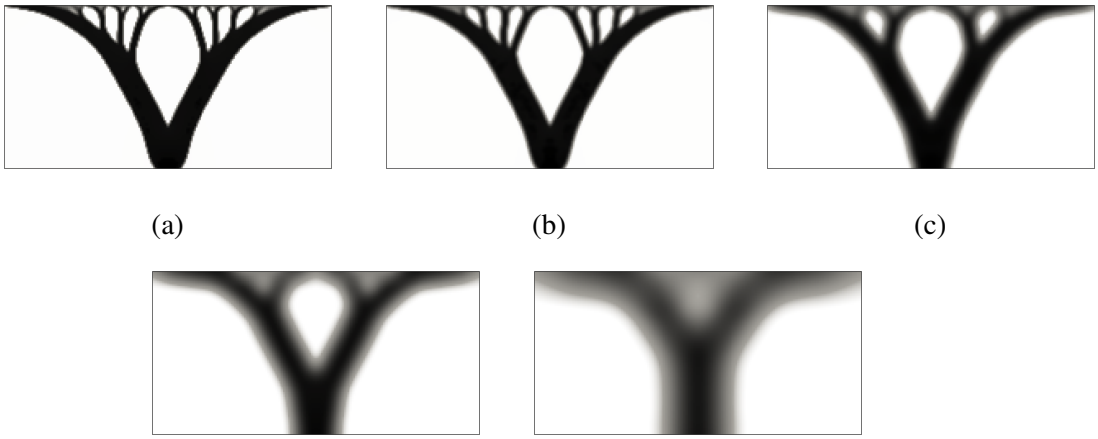

(a) (b) (c)

(d) (e)

Fig. 2.12. The effect of the density filter radius, r_f, on the optimized designs. (a): $r_f = 0.011$, $z = 5.032e-3$; (b): $r_f = 0.021$, $z = 5.033e-3$; (c): $r_f = 0.051$, $z = 5.041e-3$; (d): $r_f = 0.101$, $z = 5.075e-3$; (e): $r_f = 0.201$, $z = 5.147e-3$

The projection threshold is iteratively changed to $\eta = 0.375$ such that the volume fraction of the layout displayed in Figure 2.11(b) is 25.01 %. All the objective values reported in the figure captions are calculated on layouts obtained through this procedure. Using $p = 3$ allows the best performing layout to be obtained. Note that this value is generally recommended when using a SIMP interpolation [395]. Further increasing the penalization exponent is not beneficial for performance. A large performance reduction is observed for $p = 10$. Although beneficial for convergence to binary $\{0;\ 1\}$ layouts, raising the SIMP exponent increases the non-convexity of the optimization problem. As a consequence, the chances to get stuck into unsatisfactory local minima are higher when using a gradient-based optimizer such as GCMMA.

Figure 2.12 shows the optimized dissipator layouts obtained for different values of the filter radius, r_f. The filter blurs the interface between HCM and BM yielding a larger amount of "gray" material in the optimized layouts. This is an inherent effect of the filter operator and has nothing to do with penalization. Topology modifications are observed when the filter radius is raised over the default value of $r_f = 0.021$. The thin structural features connected to the top boundary disappear. This is a consequence of both the penalization and filtering: the designs evolve in such a way that the length of the "gray" interface is reduced. In this example, the filter radius has

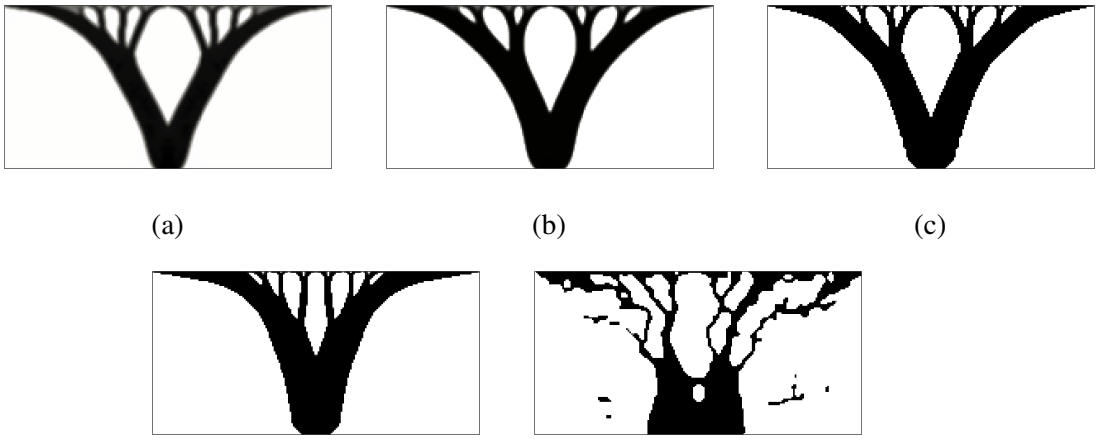

(a) (b) (c)

(d) (e)

Fig. 2.13. The effect of the projection steepness parameter, β, on the optimized designs. (a): $\beta = 1$, $z = 5.033e-3$; (b): $\beta = 5$, $z = 5.049e-3$; (c): $\beta = 30$, $z = 5.055e-3$; (d): $\beta = 100$, $z = 5.072e-3$; (e): $\beta = 200$, $z = 5.621e-3$

only a limited effect on the performance of the optimized layouts. However, in our experience, incautious combinations of r_f and p may result in trivial heat transfer structures with a small heat transfer area.

The fuzziness introduced by the filter operator can be cured by raising the projection parameter β such that the amount of "gray" material at the interface is reduced on the FE space. The optimized layouts obtained for different values of the steepness parameters are collected in Figure 2.13. To avoid the use of a continuation scheme for β, we adopt the asymptotes initialization strategy (2.41). The inspection of the design features close to the top boundary reveals that the amount of gray material is reduced when increasing β. This is desirable if the geometry needs to be manufactured as it eliminates the need for post-processing procedures. However, for all cases considered, we obtained a better performance by simply post-processing the final optimized design obtained with $\beta = 1$. The optimized objective value increases with β indicating that the chances of convergence to unsatisfactory local minima are higher. For $\beta = 200$ (Figure 2.13(e)), the optimization procedure leads to an unnatural layout responsible of large performance reductions as compared to our $\beta = 1$ reference design.

The effect of the projection threshold, η, on the optimized layouts is shown in Figure 2.14. Recall that for $\beta \to \infty$, setting $\eta = 0$ and $\eta = 1$ allows the minimum

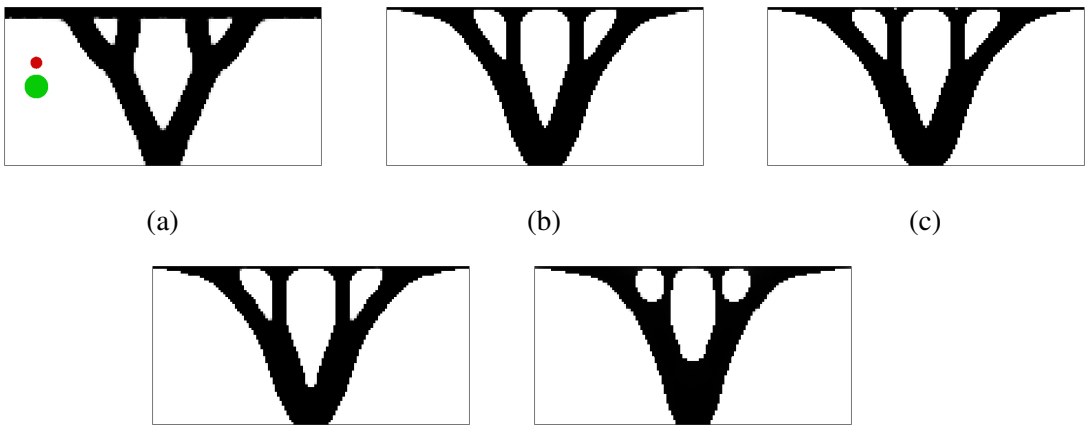

Fig. 2.14. The effect of the projection threshold, η, on the optimized designs. (a): $\eta = 0.00$, $z = 5.035e-3$; the green and red circles have diameters of $2r_f$ and r_f respectively; (b): $\eta = 0.25$, $z = 5.032e-3$; (c): $\eta = 0.50$, $z = 5.034e-3$;; (d): $\eta = 0.75$, $z = 5.036e-3$; (e): $\eta = 1.00$, $z = 5.133$

feature size of HCM and BM to be prescribed. To facilitate the visualization of this design capability, the optimized designs were obtained with $\beta = 120$ and $r_f = 0.075$. Also in this case the asymptotes position is initialized according to (2.41). The red and green circles displayed Figure 2.14(a) have diameters r_f and $2r_f$, respectively. In the layout optimized with $\eta = 0.00$, the thickness of the HCM connections is nearly constant within the design domain. A thinner horizontal HCM element is in contact with the top boundary. A closer analysis of the optimized layout suggests that the minimum feature size of HCM is $2r_f$ far from the boundaries and r_f close to the boundaries. This was anticipated with the 1D study presented in Section 2.4.2. In Figure 2.14(e) obtained with $\eta = 1.00$, we observe that the local curvature radius of the holes is always larger than $2r_f$ and that the shape of the smallest holes approximates the green circle. In our experience, the appearance of circular holes in optimized structures is frequent when a minimum feature size is prescribed on the BM. In designs optimized with $\eta = 0.25$, $\eta = 0.50$ and $\eta = 0.75$, we notice no connection between the size of the design features and the one of the filter. The layout optimized for $\eta = 0.25$ yields the best performance. However, only slight objective differences are predicted in the cases considered for $\eta < 1$. For $\eta = 1$, we obtain an optimized geometry that results in non-negligible performance reductions as compared to the alternatives.

2.6 Conclusions

This chapter reviewed the fundamentals of topology optimization as a practical design tool. After describing the design and optimization models that are used in the remainder of this thesis, we investigated the effect of some selected topology optimization parameters using a simple design optimization example. The results will help to justify the choices and to predict the effects of these numerical parameters when solving the energy problems considered in this thesis.

Chapter 3

Design of fins with a simplified phase change model

The utilization of PCMs for TES allows the construction of cheap and compact units, ideally suited to domestic space heating applications [296]. A schematic representation of the storage capacity for sensible and latent TES units is presented in Figure 3.1. When the temperature difference between the source providing thermal energy, T_{source}, and the sink retrieving thermal energy, T_{sink}, is sufficiently small, the PCM yields a higher amount of heat stored. This allows a reduction of the required storage volume and in turn decreases the cost of the installation. It is well known that the market uptake of LHTES units is hampered by the low thermal conductivity of the most popular PCMs, which slows the charge/discharge dynamics and limit the achievable power density. For this reason, the search of optimal high conducting structures for heat transfer enhancement in LHTES is an active research field in the heat transfer community. Most of the state-of-art design procedures start with the formulation of a design concept, which is then improved through modifications of a few design parameters. Different starting layouts most often lead to different optimized layouts as the geometry parametrization does not allow to morph continuously across design concepts. As a result, uncountable geometries have been proposed to answer a unique design question. This suggests that the literature lacks a thorough design optimization procedure for LHTES systems allowing dramatic design changes. This chapter demonstrates how topology optimization can be used to skip the design concept formulation step, to catch design trends using matchless design freedom and to answer practical design questions. We focus more

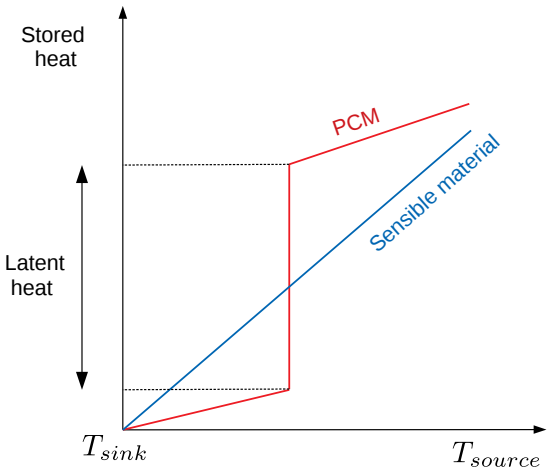

Fig. 3.1. Stored heat in sensible and latent TES units as a function of the temperature difference between the source and the sink

on design freedom rather than physics complexity. For this reason, phase change is accounted during the analysis through a simplified model that neglects natural convection. This assumption will be relaxed in Chapters 5 and 6. The plan of the chapter is as follows. In Section 3.1 we thoroughly review the most popular LHTES system configurations; Section 3.2 discusses the strategies for solving phase change problems through nonlinear diffusion and Section 3.3 describes in detail our numerical model and implementation and verifies the accuracy of the framework; Section 3.4 identifies alternative formulations of the design optimization problem and gives some algorithmic details regarding sensitivity analysis; finally, Section 3.5 presents design examples of practical interest and discusses design trends useful for technology practitioners.

Some of the contents of this chapter were published in International Journal of Heat and Mass Transfer **[J2]** and presented at the 4th International Conference on Computational Methods for Thermal Problems **[C4]**.

3.1 Review of state-of-the-art LHTES systems

In this section, we review the state-of-the-art LHTES system configurations, including the options for the container and the most popular heat transfer enhancement strategies.

Agyenim and co-authors [7] argued that two types of containers are currently considered for commercial LHTES installations, namely the rectangular and the cylindrical one. The latter is no-doubt the most popular due to the faster charge/discharge dynamics [509], reduced heat losses per unit of storage material and compatibility with piping materials of general engineering use. Three different configurations were investigated for the cylindrical layout including: (i) concentric tubes with Heat Transfer Fluid (HTF) in the internal pipe and PCM in the annulus, (ii) concentric tubes with PCM in the internal pipe and HTF in the annulus, (iii) shell-and-tube systems with HTF filling the pipes and PCM filling the shell. The study conducted by the authors of [121] demonstrates that Option (i) allows an increased performance by reducing the process time as compared to Option (ii). Also, Agyenim et al. [7] pointed out that the losses are reduced during charge as the supplied thermal power is used to melt the PCM. However, we observe that this does not hold true during discharge. Option (iii) is a convenient choice for medium-large installations. The experiments presented in [6] revealed that the multi-tube single-shell configuration favors natural convection, reducing the time required for melting as compared to Option (i). No substantial differences were reported concerning solidification because this process was mostly ruled by diffusion. A separate note is required to discuss Triplex Tube Heat eXchanger (TTHX), that seems to create high scientific interest nowadays. In his seminal paper [221], Jian proposed to adopt three concentric tubes and circulate HTF in both the internal pipe and the most external annulus with PCM filling the intermediate ring. Lately, different configurations were considered to such a detail that it is hard to identify differences between the published papers. Interestingly, most of this literature comes from the same research group. Only recently, other researches, e.g. [227, 21, 285], started considering this option. We believe that much more *independent* research is needed before TTHX can be considered as a reliable alternative to the ones discussed above.

Most of the PCMs of practical interest have low thermal conductivity. This limits the amount of energy that can be transferred between the HTF and PCM in time spans of interest for the applications. A notable exception is represented

by the metallic PCMs but their high melting temperature limits their utilization to Concentrating Solar Power (CSP) systems. For a comprehensive discussion on PCM thermo-physical properties, we refer the reader of this monograph to Chapter 6. In the past three decades, many researchers dedicated to the search of heat transfer enhancement techniques for LHTES systems. Research directions can be grouped in three categories:

- **Diffusion distance reduction**, where HCM structures of various shapes and configurations are embedded in the PCM such that the average diffusion distance within the PCM is reduced. This category includes extended surfaces, multiple and/or multi-pass HTF tubes, heat pipes and metal capsules.

  A comprehensive overview of extended surfaces is presented later in this section. The utilization of multiple HTF tubes is the most popular option for large installations as a unique shell needs to be fabricated. This yields costs savings as compared to multiple single-tube systems. Note that this layout corresponds to Option (iii) for cylindrical containers as discussed before. The enhancement effect is due to the increased heat transfer area between the HTF and PCM and the reduced average diffusion distance within PCM. Although this approach was first adopted as an *alternative* to the use of fins [6], recent studies [107, 239] considered the combination of the two enhancement approaches. We will deal with the design optimization for this combined option in Chapter 6 of this thesis. Multi-pass configurations such as the one reported by the authors of [222, 239] yield the same advantages listed for multi-tube systems. The difference is that a unique stream is circulated within the pipes. Hence, the effectiveness is reduced along the flow path due to a decreasing temperature difference between the HTF and PCM. Enhancement through heat pipes is a rather new concept for LHTESs and more research should be performed to assess the potential of this technology [215]. In the most popular configuration, heat pipes are positioned across the HTF tube such that the evaporator and condenser sections come in contact with either the HTF or PCM [377]. By increasing the length of the adiabatic section, designers can "lump" heat sinks/sources far apart from the HTF tube. The encapsulation of PCM within spherical metallic capsules reached maturity at the industrial level [296]. Besides heat transfer enhancement, the reasons for choosing encapsulation may also include chemical compatibility and thermal

and mechanical stability [239]. Depending on the capsule size, Khan et al. [239] distinguished among nano-encapsulation, micro-encapsulation and macro-encapsulation.

- **Effective conductivity increase**, where PCM is manipulated through multi-scale techniques such that its macroscopic thermal conductivity is improved. This category includes cellular metals, rings and brushes, Natural Expanded Graphite (NEG) composites and dispersed nanoparticles. A discussion on the state-of-the art solutions for cellular metals is left for Chapter 4.

  Rings are pieces of tubes that are commonly used in chemical engineering processes such as distillation due to their large surface area per volume. They were first adopted for LHTES enhancement by the authors of [430], showing comparable performance to longitudinal fins. Brushes are ordered arrangements of high conductivity carbon fibers that were first used as enhancement devices by Fukai et al. [151]. As shown by the same authors in [150], the fibers layout can be *engineered* around the tubes such that the effective conductivity of the resulting composite is increased with a minimal penalty on the storage capacity. A fast growing portion of the published literature concerns the use of high conducting nanoparticles dispersed in PCM. Most studies deal with powders containing aluminum, copper or carbon [215]. Recent researches focus particularly on nanotubes and nanowires for which some authors [449] reported improvements to the thermal conductivity up to 40 %. The ease in manufacturing and low cost [453] motivated the early interest in NEG-PCM composites for LHTES enhancement. A porosity of 10 % of the graphite matrix is recommended in [239] for best performances. From our review, it seems like the current manufacturing processes are able to control the obtained porosity with precision but the topology of the micro-layout can hardly be customized.

- **Others**, including the (few) methods that do not fit in any of the categories above such as the utilization of multiple PCMs and intermediate HTFs.

  Using multiple PCMs can alleviate the problem of heat transfer deterioration along the HTF path due to the reducing temperature difference between the HTF and PCM. For faster charge, PCMs should be arranged in a decreasing order of melting temperature such that a nearly constant temperature difference is maintained along the HTF pipe [329]. Since increasing melting temperatures

are desired for discharge, the flow direction should be reversed during this process [215]. Using an intermediate HTF was first proposed by Adinberg et al. [4] in their reflux storage for CSP applications. As with heat pipes, the operational principle relies on evaporation and condensation. However, here the region between the condenser and evaporator is non-adiabatic and filled with tubes embedded in PCM. Heat is stored and retrieved by means of the gravity-assisted motion of the vapors along the tubes.

Figure 3.2 summarizes the proposed classification of enhancement techniques. The strategies considered within this monograph are highlighted in red. Since Chapters 3, 5 and 6 deal with the design optimization of HCM fins, in the remainder of this section we present and discuss some of the most popular extended surface configurations. A similar description for cellular metals is left for Chapter 4. The search for the optimal shape of fins attracted large attention within the heat transfer community. As a consequence, the literature on this topic spans several decades. The following discussion skips the earliest developments and focuses on the most recent findings. An extensive review of this vast body of literature revealed that the investigated fin layouts are of five types: longitudinal, circular, Y-shaped or tree, pins and helical. A schematic representation of these layouts is shown in Figure 3.3.

Due to their easy design and fabrication, longitudinal fins represent the most popular extended surface geometry in the LHTES community, accounting for more than 60 % of the installations [2]. Focusing on shell-and-tube systems, Khan et al. [239] observed that an accurate design of longitudinal fins is crucial for the performance. Their study revealed that it is more convenient to increase the fin length rather than its thickness. The experiments presented in [347] reported that this fin configuration is more beneficial to solidification than to melting. Hosseini et al. [209] investigated both numerically and experimentally the effect of the fins height. They found that increasing the height leads to a more symmetric evolution of the melting front, yielding a better utilization of the stored energy. Solomon [401] observed that longitudinal fins suppress convection in the liquid PCM, therefore slowing the charge of the unit. For their free cooling application, they recommended to use fins occupying 60 % of the annular distance. Also Darzi et al. [108] found that longitudinal fins are highly effective for solidification but yield negligible contribution for melting in that natural convection is inhibited. For this reason, Beck et al. [45] recommended designs guaranteeing unrestricted natural convection

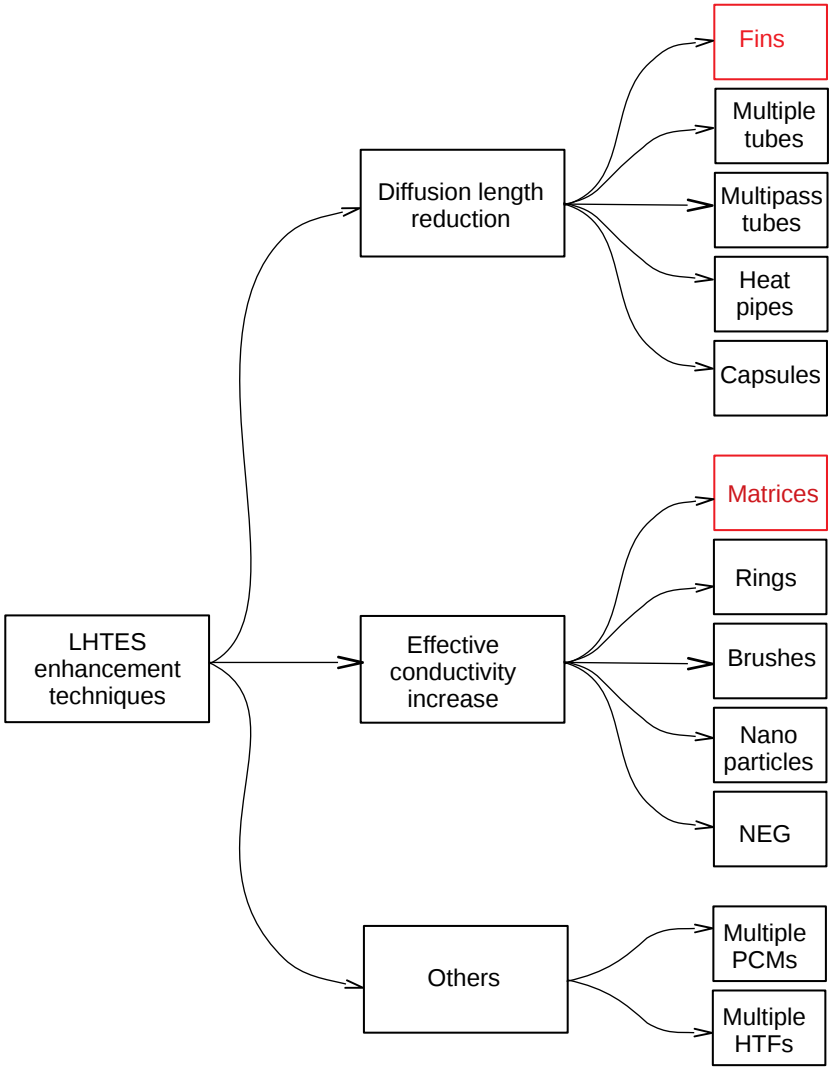

Fig. 3.2. Classification of heat transfer enhancement techniques for LHTES

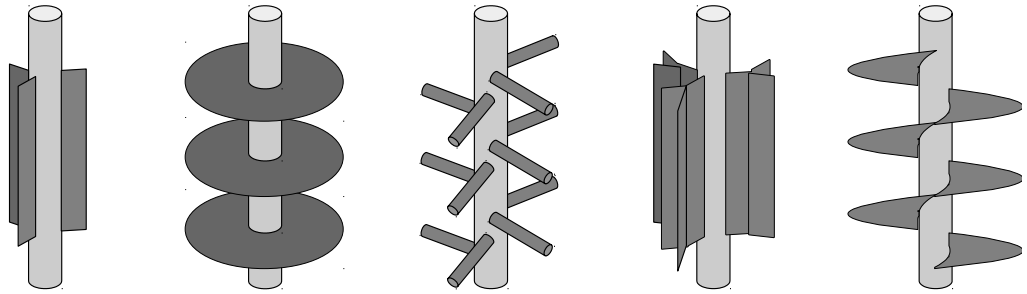

(a) (b) (c) (d) (e)

Fig. 3.3. Schematics of reviewed fin layouts. (a): longitudinal; (b): circular; (c): pins; (d): Y-shaped or tree; (e): helical

for improved melting rates. Building on these observations, Yuan et al. [483] and Kazemy et al. [235] recently found an optimal tilt angle of longitudinal fins that enhances convective transport. This research direction was anticipated by Liu and Groulx [271], who examined the effect of the fins orientation through experiments. They found that four diagonal fins yield reduced melting time as compared to two horizontal and two vertical fins. Negligible differences in performance were observed for solidification.

Circular fins were considered for heat transfer enhancement in LHTES units later than longitudinal fins. Back to 1992, Choi and Kim [88] observed that "Investigations of circular fins in cylindrical geometry are very few in number". The simple layout and consequent easy manufacturing motivated the development of this concept as demonstrated by the large number of studies that are being published these days. The experiments described in [325] showed that increasing the density of fins along the pipe is by far more beneficial than increasing the velocity of the HTF. Wang et al. [452] investigated the effect of the fin pitch, height and thickness. When using small inter-fin distances, they reported a larger effect of the fin height than thickness. The performance was found to be slightly sensitive to both the previous parameters when using high fin pitches. The authors of [480] studied how natural convection in vertical units is affected by the circular fins design. Based on their parametric study, they recommended a specific fin number, thickness and inter-fin distance such that the melting time is minimized. A similar trend concerning natural convection was noticed by Jmal and Baccar [222] for solidification in air-PCM units. Kuboth et al. [253] recently showed numerically that varying the fin density distribution along the

HTF pipe is beneficial for performance. They suggested to increase linearly the fin density from the inlet to the outlet using a growth factor of 10.

Pin fins geometries were first adopted as heat transfer enhancers in PCM for electronics cooling applications. The interested reader can consult [362] for a comprehensive review of heat sink geometries. In a recent review [2] on heat transfer enhancement in LHTES, this layout is only listed as a suitable alternative to plate fins for maximum heat dissipation in heat sinks and no reference to studies in the field of LHTES is given. This demonstrates that the investigations on this layout are in their early days. We found only two examples of applications to thermal storage units. Bruno et al. [417] claimed to be the first research group that considered external pins attached to the HTF pipes. Their work reported reduced performance as compared to the circular fins. A similar conclusion was later drawn by the authors of [48], where the pin fin effectiveness was calculated to be lower than that of the annular fins. It is curious that this geometry attracted such little attention among researchers, despite the large interest in the field of electronics cooling. We think that more research should be conducted to assess the real potential of this configuration. In both the studies analyzed, it is not clear whether the amount of HCM is kept constant when comparing the alternative configurations. In our opinion, this is a fundamental prerequisite to draw meaningful conclusions. Furthermore, in [417] natural convection is neglected. This factor can modify the outcome of the comparison since pins allows a nearly unrestricted motion of the buoyant eddies.

The need for performance improvement of longitudinal fins gave momentum to the development of Y-shaped or tree fins. Sciacovelli et al. [374] adopted a response surface optimization method to optimize the fin length and bifurcation angle. The authors found that the discharge efficiency can be increased by 24 % if optimal fins with two bifurcations are chosen. In a more recent development [375], the authors were able to obtain an optimized tilt angle along the longitudinal direction such that the solidification time is reduced. Lohrasbi et al. [278] adopted the same optimization approach of [374] to optimize V-shaped geometries where the bifurcation of the Y geometry is in contact with the HTF pipe. Recently, more "exotic" geometries have started to appear. For instance, the authors of [383] parametrized a fin geometry mimicking the crystal structure of a snowflake and reported significant performance improvements as compared to the conventional longitudinal fins. Note that similar structures were obtained by the Institute of Engineering Thermodynamics (DLR,

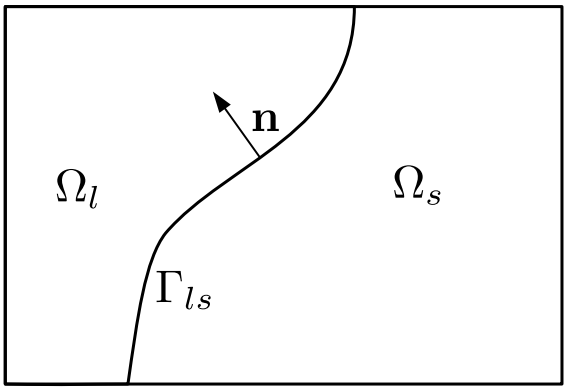

Fig. 3.4. Schematic of a generic solid-liquid phase change process

Germany) [257] and patented by Le Commissariat a l'energie atomique et aux energies alternatives (CEA, France) [320].

Another option that researchers have recently started to consider is represented by helical fins. The layout proposed by Kozak et al. [360] yielded an increased melting rate with respect to the conventional alternatives. Furthermore, it demonstrated practical advantages such as the prevention of voids in solidification, prevention of large pressures in melting and ease of maintenance. The same geometry was previously considered by the authors of [45]. Their numerical results suggested that the helical configuration is responsible for a small performance reduction as compared to the simple longitudinal fins.

3.2 Modeling diffusion-driven phase change

Here, we discuss the available computational strategies for computing the response of phase change systems through nonlinear diffusion. In particular, we focus on fixed-grid approaches such as the enthalpy, the apparent heat capacity and the source methods.

Melting or solidification of a pure material with a moving boundary separating the two phases is referred to as Stefan problem. A snapshot of a generic solid-liquid phase change process is presented in Figure 3.4. The liquid fills Ω_l while the solid fills Ω_s. The two phases are separated by an interface, Γ_{ls}. With negligible

advective transport and constant density and specific heat, the thermal response can be described by the following set of governing equations:

$$\rho_s c_{p_s} \frac{\partial T}{\partial t} = \frac{\partial}{\partial x_i}\left(k_{s_{ij}} \frac{\partial T}{\partial x_j}\right) \qquad \text{in } \Omega_s, \tag{3.1}$$

$$\rho_l c_{p_l} \frac{\partial T}{\partial t} = \frac{\partial}{\partial x_i}\left(k_{l_{ij}} \frac{\partial T}{\partial x_j}\right) \qquad \text{in } \Omega_l, \tag{3.2}$$

$$T = T_m \qquad \text{on } \Gamma_{ls}, \tag{3.3}$$

$$k_{s_{ij}} \frac{\partial T}{\partial x_j} n_i - k_{l_{ij}} \frac{\partial T}{\partial x_j} n_i = \rho_s \mathscr{L} v_{\Gamma_{ls}} n_i \qquad \text{on } \Gamma_{ls}, \tag{3.4}$$

where T is the temperature, ρ_s and ρ_l represent the solid and liquid densities, c_{p_s} and c_{p_l} represent the solid and liquid specific heats, $k_{s_{ij}}$ and $k_{l_{ij}}$ are the conductivity tensors of the solid and of the liquid, $\mathscr{L}$ is the latent heat per unit mass of the solid, n_i is the liquid-pointing normal of the interface and $v_{\Gamma_{ls}}$ is its propagation velocity. Equations (3.1) and (3.2) prescribe the diffusion heat transfer in the solid and liquid regions, respectively. Eq. (3.3) identifies the melting (solidification) front as the isotherm with $T = T_m$, with T_m being the melting temperature. Eq. (3.4), broadly referred to as the Stefan condition [440], is a differential heat balance on the moving interface.

Early interests in solving phase change problems date back to the end of the 19^{th} century, when Stefan found the analytical solution for a diffusive isothermal melting in a semi-infinite 1D medium with constant thermo-physical properties and under the "one-phase" assumption [211]. "One phase" refers to the fact that only a single phase is present since the initial temperature of the slab corresponds to the melting temperature [211]. In dimensionless settings, the velocity of the interface is uniquely determined by the Stefan number Ste:

$$Ste = \frac{c_p \left(T - T_m\right)}{\Delta h_{sl}}, \tag{3.5}$$

where c_p is the solid or liquid specific heat and Δh_{sl} is the specific enthalpy change for the phase transition. This original definition is clearly restricted to single-phase problems, but was later modified for more complicated processes. Stefan's work was extended by Neumann to two-phase melting problems [211], in which the initial temperature field is lower than the melting temperature.

The analytical solutions of the Stefan problem are limited to semi-infinite problems, constant thermo-physical properties and homogeneous initial conditions. Approximate analytical methods allowed a slight increase in the flexibility of the problem formulation. A notable example in this class is the heat balance method of Godman et al. [168]. In summary, it consists in choosing a suitable approximating function of the temperature complying with the boundary conditions (e.g. polynomials or trigonometric series), integrating in space to obtain an Ordinary Differential Equation (ODE) referred to as the heat-balance integral, and then solving the ODE in time. The authors adopted a thermal layer approach similar to the boundary layer in fluid mechanics that allowed the integration domain to be restricted. The assumption was motivated by the fact that a sudden temperature variation at a boundary "is not immediately felt through the slab" [168]. The approximate analytical methods allow more complex boundary conditions to be considered. However, the selection of the approximating function requires a special care and may be prohibitive in multi-dimensional problems.

The need for solutions of practical interest gave momentum to the development of numerical methods for phase change problems. Those can be subdivided in two broad categories, i.e. deforming grid and fixed grid methods. Fixed grid methods allow the solution of the Stefan problem on a (structured) spatial grid that does not conform with the solid-liquid interface. Enthalpy-based and immersed boundary techniques belong to this class. Since the numerical method adopted to produce the results presented in this monograph is a fixed grid method, further details are discussed in the following sections. The fundamental idea behind the deforming grid methods is to adapt the spatial or temporal grid dynamically in such a way that the mesh conforms with the regions occupied by the two phases. A rather straightforward route was followed by Gupta et al. [191], who kept a fixed spatial mesh and formulated a variable time-stepping strategy such that the boundary moves of one space mesh element during each time-step. However, it is hard to extend this method to multi-dimensional problems with complicated domains [211]. The alternative approach consists of a dynamic adaptation of the space grid. This approach was used primarily in the FEM community [440], see for instance [60, 283, 12, 485]. The node motion modifies the FEM formulation in that the basis function, N^h, are time-dependent:

$$T^h(\mathbf{x},T) = N_i^h(\mathbf{x},t)T_i(t), \tag{3.6}$$

where T^h denotes the approximated temperature field and the index i runs over the nodes of the FEM mesh. A standard FEM assembly can be adopted for the diffusion term in (3.1) and (3.2). However, the temporal accumulation term requires a special care. The time differentiation of (3.6) leads to [283]:

$$\frac{\partial T^h}{\partial t} = \frac{\partial N_i^h}{\partial t} T_i + N_i^h \frac{dT_i}{dt} = \mathbf{v}_m \cdot \nabla N_i^h T_i + N_i^h \frac{dT_i}{dt}, \tag{3.7}$$

where $\mathbf{v}_m$ is the mesh deformation velocity defined as:

$$\mathbf{v}_m = -\frac{d\mathbf{x}}{dt}, \tag{3.8}$$

with $\mathbf{x} = N_i^h \mathbf{x}_i$ being the position. Note that an additional *convective* term is present to account for the mesh motion. The problem is now analyzed through a local coordinate system implicitly attached to the mesh, which moves and deforms simultaneously with it. The solution of the resulting FEM model can be obtained provided that the deformation velocity is specified at each mesh node. At the boundary, we can make use of the Stefan condition (3.4). This (scalar) equation results in well-posed problem only in 1D. Multi-dimensionality demands for the specification of a deforming direction. Eq. (3.4) will then provide the magnitude of the deformation. There are a number of different ways to compute the deformation velocity of the internal nodes. Most of them are based on solving pseudo-elasticity equations with boundary conditions of the first kind. These are given by the computed deformation at the interface and the zero deformation at the Dirichlet boundary. This option can be fairly cheap since it is possible to partially re-utilize the diffusion matrix [440].

Although the deforming grid methods are generally regarded as the most accurate route, they also demand for a high computational cost [440]. Furthermore, the choice of the deformation direction is a crucial operation for the accuracy and stability of the method [440]. The analyst should select it according to the expected front propagation direction in such a way that grid distortions and highly skewed elements are avoided. Finally, the utilization of variable-grid methods may be challenging in problems with non-smooth solid-liquid interfaces or without a sharp phase change temperature [333]. In the remainder of this section, we focus on three fixed grid approaches: the enthalpy method, the apparent heat capacity method and the source method.

3.2.1 Enthalpy method

Most of the fixed grid methods rely on a single governing equation:

$$\frac{\partial h}{\partial t} = \frac{\partial}{\partial x_i}\left(k_{ij}\frac{\partial T}{\partial x_j}\right), \tag{3.9}$$

where h is the total enthalpy per unit volume defined as:

$$h = (1-f)\int_{T_{ref}}^{T} \rho c_{p_s} d\tau + f\left(\int_{T_{ref}}^{T} \rho c_{p_l} d\tau + \rho\mathscr{L}\right), \tag{3.10}$$

where T_{ref} is the reference temperature for the enthalpy calculation and $f \in [0,1]$ is the liquid fraction. When subcooling and phase separation are negligible, the liquid fraction is taken as a function of the temperature only [439]. However, it can be generalized to include the dependence on phenomenological quantities, such as the melting, solidification and nucleation rate. Note that Voller et al. [439] showed that it is possible to obtain (3.9) from the Stefan problem. Considering the presented formulation instead of the original Stefan problem yields several advantages. We converted a two-region problem into a single-region problem with a unique governing equation. Solving for Eq. (3.9) does not require the tracking of the melting front and implicitly satisfies the interface condition (3.4). The location of the interface is not a degree of freedom but it can be computed by post-processing the converged solution. This formulation can also naturally deal with phase change phenomena that do not result in a sharp interface. Recall that this point is a major limitation of deforming grid methods.

Eq. (3.9) can be readily solved using a fully explicit integration strategy if a suitable energy-enthalpy relation is defined. A popular approach [440] is to use h as a primary state variable and to update T at each time step based on the current enthalpy field. The explicit marching can then be summarized in two recursive steps:

1. Compute the temperature field and diffusive term at the current time step based on the current enthalpy field
2. Compute the enthalpy field at the next time iteration based on the diffusive term assembled in step (1)

The advantage of choosing the enthalpy as the primary state variable lies in the fact that $T(h)$ shows no jump discontinuities even in the case of isothermal phase change. The numerical experiments conducted by Voller [440] on a 1D example present evidence that this scheme results in oscillations of the temperature in time, whose magnitude increases for decreasing Stefan numbers. The author argued that the method is stable meaning that the amplitude of the oscillations does not grow with time. However, no formal proof was provided. Furthermore, the stability of numerical time integration methods generally concerns perturbations of the approximated set of *data* on which the differential problem depends. For parabolic problems, the time marching through θ-methods with $\theta < 0.5$ is conditionally stable, i.e. the time step cannot be chosen arbitrarily but it is bounded by stability requirements [342]. Implicit time-stepping techniques were adopted to obtain unconditional stability. In his review [439], Voller et al. discussed two implicit alternatives to the explicit marching: Gauss-Seidel and Newton methods. He later argued that, due to the large nonlinearity, "developing an appropriate solution that outperforms an explicit scheme is a numerical challenge".

3.2.2 Apparent heat capacity method

With the apparent heat capacity technique, phase change is modeled by increasing the specific heat of the PCM. With negligible convective transport, the governing equation reduces to a nonlinear Fourier equation:

$$c_a \frac{\partial T}{\partial t} = \frac{\partial}{x_i}\left(k_{ij}\frac{\partial T}{\partial x_j}\right), \tag{3.11}$$

where c_a is referred to as the apparent heat capacity. This term retains the nonlinearity brought by the liquid fraction, f, on the enthalpy-temperature relation (3.10). Dividing Eq. (3.9) with (3.11) yields:

$$c_a = \frac{\partial h}{\partial T}. \tag{3.12}$$

Note that Eq. (3.11) is formulated as a function of a single state field (temperature) and does not require the computation of auxiliary variables. The apparent heat capacity method can be easily incorporated into existing numerical codes. For this reason, the method encountered a widespread popularity in literature [11].

Obtaining the apparent heat capacity through analytical differentiation of the enthalpy-temperature relation can potentially yield numerical problems. First, $h(T)$ may contain jump discontinuities, e.g. in isothermal phase change, that are non-differentiable. A common approach to deal with isothermal phase change is to *smear* the discontinuity to allow for differentiability. For instance, considering a constant specific heat in each phase, a piece-wise relaxation can be written as:

$$h(T) = \begin{cases} c_{p_s}\left(T - T_{ref}\right) & T \leq T_m - \varepsilon_T \\ \int\limits_{T_{ref}}^{T} c_{p_{sl}}(T)d\tau + f(T)\mathscr{L} & T_m - \varepsilon_T < T \leq T_m + \varepsilon_T \\ c_{p_l}\left(T - T_{ref}\right) & T > T_m + \varepsilon_T \end{cases}, \tag{3.13}$$

where ε_T is the half-width of the phase transition temperature difference and $c_{p_{sl}}(T)$ is an intermediate temperature-dependent specific heat. Equation (3.13) is shown in the schematic of Figure 3.5(a). Note that only for pure substances and eutectic mixtures a melting temperature, T_m, can be defined precisely. For non-eutectic mixtures, there is no sharp melting temperature [296] and the formulation (3.13) retains physical significance. The intermediate specific heat, $c_{p_{sl}}$, is generally considered as a constant and set to $c_{p_{sl}} = 0.5(c_{p_s} + c_{p_l})$ [440] and the liquid fraction is taken as linear in the smeared region, $T_m - \varepsilon_T < T \leq T_m + \varepsilon_T$ [296]. With these assumptions, differentiating (3.13) through (3.12) yields [211]:

$$c_a = \begin{cases} c_{p_s} & T \leq T_m - \varepsilon_T \\ c_{p_{sl}} + \frac{1}{2\varepsilon_T}\mathscr{L} & T_m - \varepsilon_T < T \leq T_m + \varepsilon_T \\ c_{p_l} & T > T_m + \varepsilon_T \end{cases}, \tag{3.14}$$

A schematic representation of Equation (3.14) is given in Figure 3.5(b). A small ε_T results in large nonlinearities that may affect the convergence of the iterative solution procedure. More importantly, a too narrow c_a spike may lead to large inaccuracies. If special care is not taken in the selection of the time-marching scheme, there is a chance that a nodal position *skips* completely the capacity spike, meaning that the latent heat effect gets lost completely. To alleviate this problem, Comini et al. [100] suggested to employ a spatial averaging of c_a. Their formulation was later refined by

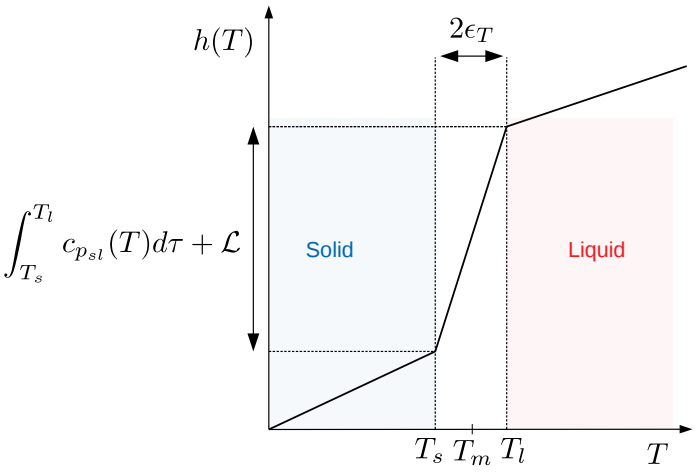

(a)

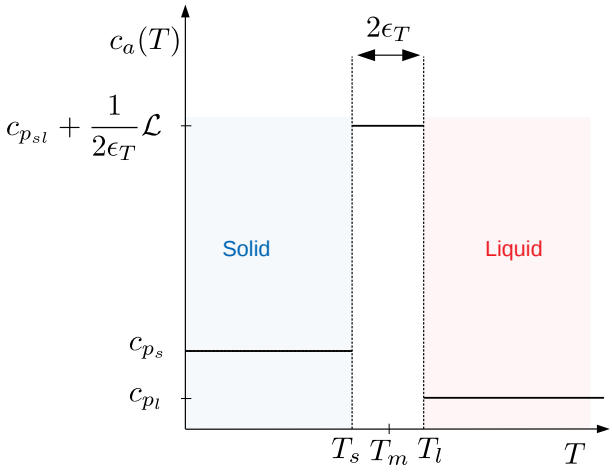

(b)

Fig. 3.5. (a): Piece-wise relaxation of the enthalpy-temperature relation; (b): apparent specific heat

Lemmon et al. [259] to yield:

$$c_a = \frac{\sum_i (\partial h)/(\partial x_i)^2}{\sum_i (\partial T)/(\partial x_i)^2}. \tag{3.15}$$

In a finite element framework, h can be evaluated using the same shape functions adopted to approximate the temperature [304]. A more physically-sound alternative [333] was proposed by Morgan et al. [304]. The authors adopted the following time-averaging:

$$c_a = \frac{h^{(k+1)} - h^{(k)}}{T^{(k+1)} - T^{(k)}}, \tag{3.16}$$

where the subscript k indexes the time iterations. Here, c_a is evaluated directly at the integration points [99]. Pham [335] proposed to reduce the inaccuracies due to the numerical integration by using a lumped capacitance. The masses are concentrated at the mesh nodes and the enthalpies are found directly from the nodal temperatures. This approach avoids the problem of numerical integration of the capacity term. Furthermore, evidence [333] was presented that the capacitance lumping extends the stability of linear time-dependent problems. However, Reference [333] reported that lumping can yield negative masses when using high order elements. Pham later claimed [334] that differences in the numerical results obtained with the consistent and lumped capacitance formulations are too small to be of practical importance.

3.2.3 Source method

The source method isolates the latent heat nonlinearity in a source term. This agrees with the intuition that a melting body behaves as a thermostat that retrieves energy from the system (negative source term), while a solidification body behaves as a thermostat that releases energy (positive source term) to the system. In the FEM literature, this method is also referred to as "fictitious heat flow" or "budget node" method [439, 357, 358]. With negligible convective transport, the governing equations reduces to:

$$\rho c_p \frac{\partial T}{\partial t} = \frac{\partial}{\partial x_i}\left(k_{ij}\frac{\partial T}{\partial x_j}\right) - \rho \mathscr{L}\frac{\partial f}{\partial t}, \tag{3.17}$$

where $c_p = (1-f)c_{p_s} + f c_{p_l}$. Note that in most materials, the c_p nonlinearity is much smaller than the one due to the phase transition. Hence, the former can be

safely ignored in some cases. Differently from the apparent heat capacity technique, this method does not require the artificial smearing of the melting temperature range. However, the liquid fraction field, f, needs to be computed at every time instant. Iterative methods similar to those used for the enthalpy method were developed in literature. A general implicit approach to solve the isothermal phase change at nonlinear iteration "k" consists of the following two steps:

1. Solve for T^{k+1} using f^k,
2. Update f^{k+1} such that the nodes undergoing phase change (identified by $0 < f^k < 1$) have a temperature of T_m.

The efficiency of the method is clearly determined by Step 2, which distinguishes among the approaches presented in [439, 357, 358]. The earliest source methods had robust but slow convergence [439]. Voller and Swaminathan [438] presented an improved iteration method with faster convergence in which the liquid fraction in step 1 is evaluated at iteration $(k+1)$ using a linearization of the source term in temperature. Advances of the source method in the finite element community concerned the computation of a quasi-consistent or fully consistent Jacobian for the utilization of quasi-Newton [102] or Newton methods [130]. In [130], the weak form of the governing equations had the following source term:

$$q_i = -\rho \mathscr{L} \int_{\Omega} N_i \frac{\partial f}{\partial t} d\mathbf{x}, \tag{3.18}$$

where N_i is the shape function centered in node i and $\mathbf{x} \in \mathbb{R}^{N_{dim}}$ with N_{dim} representing the number of spatial dimensions. Using a two-level differentiation formula to approximate the time derivative yields:

$$q_i = \frac{\rho \mathscr{L} \left(\int_{\Omega} N_i f^{(n+1)} d\mathbf{x} - \int_{\Omega} N_i f^{(n)} d\mathbf{x} \right)}{t^{(n+1)} - t^{(n)}}. \tag{3.19}$$

It can be demonstrated that it is possible to recover a somewhat similar approximation to the time-averaged apparent heat capacity proposed by Morgan et al. [304] (Eq. (3.16)). Considering the capacity lumping described in [335] in deriving (3.16), we

obtain:

$$\bar{c}_{a_i} = \mathscr{L} \int_{\Omega} N_i \frac{f^{(n+1)} - f^{(n)}}{T^{(n+1)} - T^{(n)}} d\mathbf{x}, \tag{3.20}$$

where $\bar{c}_{a_i}$ is a lumped capacity that fills the diagonal of the capacitance matrix at position (i,i). One could argue that the spatial variation of the temperature is small as compared to the one of the liquid fraction in elements undergoing phase change. This assumption allows considering the denominator as constant during the numerical integration and obtain an approximate apparent lumped capacity, $\hat{\bar{c}}_{a_i}$. If a two-level differentiation scheme is adopted for the temperature and neglecting the effect of the specific heat, we recover the following contribution to the residual:

$$\rho \hat{\bar{c}}_{a_i} \frac{T^{(n+1)} - T^{(n)}}{t^{(n+1)} - t^{(n)}} = \rho \mathscr{L} \frac{\int_{\Omega} N_i \left(f^{(n+1)} - f^{(n)} \right) d\mathbf{x}}{\cancel{T^{(n+1)} - T^{(n)}}} \frac{\cancel{T^{(n+1)} - T^{(n)}}}{t^{(n+1)} - t^{(n)}} = q_i. \tag{3.21}$$

In case of a sharp solid-liquid interface, the integration of (3.19) requires a discontinuous integration, whether Gauss quadrature with a large number of integration points [102] or exact analytical integration [130]. However, when the mushy regions span several elements, the conventional Gauss quadrature is expected to yield an acceptable accuracy.

3.3 Numerical model

In this section, we present the governing equations as well as our numerical model and solution strategy. As discussed in Section 3.1, the solidification dynamics is ruled mostly by diffusion while melting is largely affected by convection. For this reason, the simplified phase change model adopted here allows only discharge to be predicted with acceptable accuracy. The charge of the unit will be considered in Chapters 5 and 6.

Figure 3.6 presents a schematic of the physical problem considered on a quarter of the unit cross-section. The temperature, T_d, is prescribed at the internal boundary, Γ_d, to represent the contact with the tube containing the HTF while a homogeneous Neumann boundary condition is prescribed on Γ_{N_1} to describe an adiabatic boundary (external envelope) and on Γ_{N_2} to account for the angular periodicity.

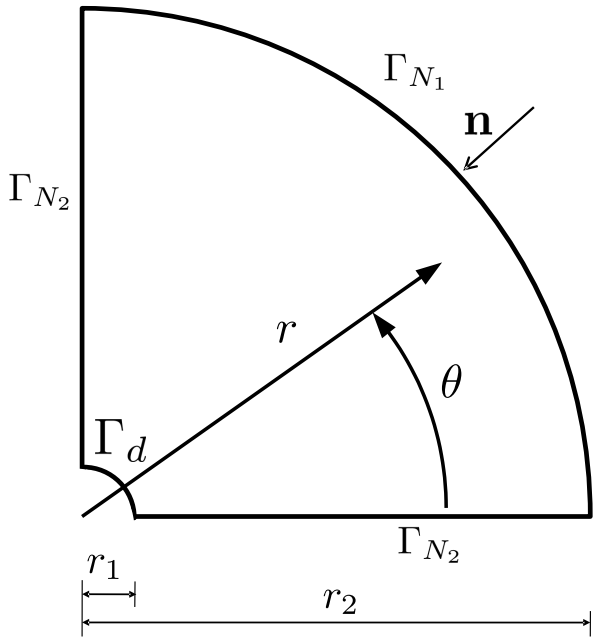

Fig. 3.6. Schematic of the ground domain considered with boundary conditions

We model diffusion phase change using the source method discussed in Section 3.2.3. To allow for greater generality of the results presented, we cast the governing equation in a dimensionless form, computed with reference to the thermo-physical properties of the PCM. We adopt the following dimensionless variables:

- dimensionless time (Fourier number)

$$t^* = \frac{\alpha_{PCM} t}{L^2} = Fo, \tag{3.22}$$

- dimensionless coordinate

$$x_i^* = \frac{x_i}{L}, \tag{3.23}$$

- dimensionless temperature

$$T^* = \frac{T - T_{min}}{T_{max} - T_{min}}, \tag{3.24}$$

- dimensionless latent heat (phase transition number)

$$\mathscr{L}^* = \frac{\mathscr{L}}{c_{p_{PCM}}(T_{max} - T_{min})} = \frac{1}{Ste}, \tag{3.25}$$

where L is the characteristic length, α_{PCM} is the thermal diffusivity of the PCM, Fo is the Fourier number, T_{max} and T_{min} are the maximum and minimum temperature of the entire process. The dimensionless variables are marked with an asterisk to distinguish them from their dimensional counterpart.

We consider temperature-independent thermo-physical properties, constant density, isotropic thermal conductivity and ignore the internal heat generation.

3.3.1 Governing equations

Substituting Eqs. (3.22) through (3.25) into Eq. (3.17) we obtain:

$$C(s)\frac{\partial T^*}{\partial t^*} = \frac{\partial}{\partial x_i^*}\left(K_{ij}(s)\frac{\partial T^*}{\partial x_j^*}\right) - \gamma(s)\mathscr{L}^*\frac{\partial f^*}{\partial t^*}, \tag{3.26}$$

where $C(s)$ is a design-dependent capacitance, $K_{ij}(s)$ is a design-dependent conductivity and $\gamma(s)$ is a design-dependent switch of the latent heat source term that activates it in the PCM portion of the domain and deactivates it in the HCM. The liquid fraction is here defined directly as a function of the dimensionless temperature $f^* = f(T^*)$. To allow for differentiability, the following logistic distribution function is used rather than a piece-wise formulation:

$$f^* = \frac{1}{1+\exp(-\xi_{log}(T^* - T_m^*))}, \tag{3.27}$$

where $\xi_{log} = 15$ is a constant that controls the steepness of the logistic curve and is dependent on the temperature range of the mushy zone. The material interpolation strategies should be formulated in such a way to recover consistent material properties in Ω_{HCM} and Ω_{PCM}, i.e.:

$$C = \begin{cases} \frac{(\rho c_p)_{HCM}}{(\rho c_p)_{PCM}} & in \quad \Omega_{HCM} \\ 1 & in \quad \Omega_{PCM} \end{cases}, \tag{3.28}$$

$$K_{ij} = \begin{cases} \frac{k_{HCM}}{k_{PCM}}\delta_{ij} & in \quad \Omega_{HCM} \\ \delta_{ij} & in \quad \Omega_{PCM} \end{cases}, \tag{3.29}$$

$$\gamma = \begin{cases} 0 & in \quad \Omega_{HCM} \\ 1 & in \quad \Omega_{PCM} \end{cases}, \tag{3.30}$$

where δ_{ij} is the Kronecker delta. The time-independent Dirichlet and Neumann boundary conditions are given by:

$$T^* = T_d^* \qquad on \quad \Gamma_d, \quad \forall t^*, \tag{3.31}$$

$$-K_{ij}\frac{\partial T^*}{\partial x_j^*}n_i = 0 \qquad on \quad \Gamma_{N_1} \cup \Gamma_{N_2}, \quad \forall t^*, \tag{3.32}$$

where n_i is the inward pointing normal on Ω_D. The space-independent initial conditions are:

$$T^* = T_I^* \qquad in \quad \Omega_{HCM} \cup \Omega_{PCM}, \quad \text{at } t^* = 0, \tag{3.33}$$

with T_I^* being the initial dimensionless temperature field.

3.3.2 Finite Element model

The weighted residual statement of (3.26) over the computational domain Ω can be written as:

$$\int_\Omega w^h \left(C(s)\frac{\partial T^*}{\partial t^*} - \frac{\partial}{\partial x_i^*}\left(K_{ij}(s)\frac{\partial T^*}{\partial x_j^*} \right) + \gamma(s)\mathscr{L}^*\frac{\partial f^*}{\partial t^*} \right) d\mathbf{x} = 0, \tag{3.34}$$

where w^h are admissible weighting functions defined later. Due to the presence of the second-order term, Eq. (3.34) can be further elaborated to obtain the weak form, with lower continuity requirements on the state field. The integration by parts of higher order derivatives (Green-Gauss theorem) leads to:

$$\int_\Omega w^h \left(C(s)\frac{\partial T^*}{\partial t^*} + \gamma(s)\mathscr{L}^*\frac{\partial f^*}{\partial t^*} \right) d\mathbf{x} + \int_\Omega \left(\frac{\partial w^h}{\partial x_i^*}\left(K_{ij}(s)\frac{\partial T^*}{\partial x_j^*} \right) \right) d\mathbf{x} + \int_{\Gamma_{N_1} \cup \Gamma_{N_2}} w^h q \, d\mathbf{x}' = 0, \tag{3.35}$$

where $\mathbf{x}' \in \mathbb{R}^{d-1}$ and $q = 0$ due to (3.32).

The dimensionless temperature is approximated by a suitable trial function T^{h^*}, which is selected from the following function space:

$$\mathscr{U}_T = \{T^{h^*} \in \mathscr{H}^1(\Omega);\ T^{h^*} = T_d^* \ \text{ on } \Gamma_d\}, \tag{3.36}$$

where $\mathscr{U}_T$ is a Hilbert space consisting of scalar functions with square integrable first derivatives. In a similar manner, the test function space is defined as:

$$\mathscr{V} = \{w^h \in \mathscr{H}^1(\Omega);\ w^h = 0 \ \text{ on } \Gamma_d\}. \tag{3.37}$$

Note that the only difference between the function spaces (3.37) and (3.36) is that the test functions should be zero on the boundary while the trial functions should satisfy the Dirichlet condition. This asymmetry can be cured by modifying the trial functions through the addition of lifting functions of the boundary datum [342]. The approximate temperature field can be written as a product of time-dependent nodal temperature values, T_i^*, and a set of spatially-varying shape functions, N_i. This split between spatial and temporal dependencies leads to:

$$T^*(\mathbf{x},t) \simeq T^{h^*}(\mathbf{x},t) = \sum_{i=1}^{N_n} T_i^*(t) N_i(\mathbf{x}), \tag{3.38}$$

where N_n corresponds to the number of nodes of the finite element mesh. Eq. (3.38) can be casted more conveniently in vector form:

$$T^{h^*} = \mathbf{N}^T \mathbf{T}^*, \tag{3.39}$$

where $\mathbf{N}$ denotes the column vector of the shape functions and $\mathbf{T}^*$ is the column vector of the dimensionless nodal temperatures. The asterisk indicating the dimensionless variables is dropped for brevity hereafter. All the shape functions considered in this monograph are Lagrange polynomials of order 1. As in the Galerkin method, we consider the test function as being equal to the shape functions, i.e. $w^h = N$. This is a natural choice when the test functions are seen as virtual variations of the dependent variable as in the Ritz method [350]. The substitution of (3.39) into (3.35) leads to the weak-form Galerkin model, which is conveniently given in matrix form as follows:

$$\mathbf{R}_{us} = \mathbf{C}\dot{\mathbf{T}} + \mathbf{K}\mathbf{T} + \dot{\mathbf{L}}(\mathbf{T}) = \mathbf{0}, \tag{3.40}$$

where $\mathbf{R}_{us}$ is the vector of unstabilized residuals, $\dot{()}$ indicates the time derivative, $\mathbf{C}$ is the capacitance matrix, $\mathbf{K}$ is the conductivity matrix and $\dot{\mathbf{L}}$ is the latent heat source term vector. Eq. (3.35) is referred to as semi-discrete weak form since the spatial components have been discretized but the temporal ones are still continuous. In the next section, we present methods for the time discretization that allows a fully discrete formulation to be obtained. The matrices and vectors appearing in (3.40) are defined as:

$$\mathbf{C} = \int_{\Omega} C\mathbf{N}\mathbf{N}^T d\mathbf{x}, \tag{3.41}$$

$$\mathbf{K} = \int_{\Omega} \frac{\partial \mathbf{N}}{\partial x_i} K_{ij} \frac{\partial \mathbf{N}^T}{\partial x_j} d\mathbf{x}, \tag{3.42}$$

$$\mathbf{L} = \int_{\Omega} \mathbf{N}\gamma\mathscr{L}f(\mathbf{N}^T\mathbf{T})d\mathbf{x}. \tag{3.43}$$

For stability reasons, the vector of unstabilized residuals, $\mathbf{R}_{us}$, is augmented with a stabilization contribution as follows:

$$\mathbf{R} = \mathbf{R}_{us} + \mathbf{R}_{GGLS} = \mathbf{0}, \tag{3.44}$$

where $\mathbf{R}$ is the vector of residuals and $\mathbf{R}_{GGLS}$ is a stabilization term that is described in the following section.

3.3.3 Stabilization

The finite element formulations based on the Galerkin method are known to produce spurious oscillations in problems affected by thermal boundary layers thinner than the element size [216]. The discretization cannot reproduce the true solution and satisfy the heat balance simultaneously. This situation generally occurs in problems with low diffusivity materials and small time-steps [195], creating regions with steep gradients referred to as thermal shocks [129]. Modeling of PCM belongs to this category. Small time-steps are required to resolve the fast transients at the beginning of the charge/discharge processes, especially when fluid flow is resolved in the liquid region (see Chapter 5). However, the low conductivity of PCMs prevents the thermal signal from traveling several elements. In purely diffusive problems, the thermal shocks have short-term effects that mildly affect the long-term predictions. However,

over/undershooting may influence substantially the flow field in problems driven by natural convection and invalidate long-term solutions. The picture is even worse when simulating PCMs, since the oscillations may lead to a premature or retarded phase transition.

A variety of different solutions were proposed in the finite element community to cure this problem. For instance, Fachinotti [129] adopted a diffusion-split method where the implicit diffusion term is artificially augmented to satisfy stability requirements and is balanced explicitly through a fictitious source term. Hachem et al. [195] locally enriched the Galerkin formulation using bubble functions, satisfying homogenous Dirichlet conditions on the element boundary. In the present monograph, we will use the Gradient Galerkin Least Squares (GGLS) stabilization strategy originally developed by Franca and Do Carmo [146], and later adopted by Ilinca et al. [216] for transient diffusion problems. The GGLS operator acts on the gradient of the strong form residuals as follows:

$$\mathbf{R}_{GGLS} = \sum_{e=1}^{N_e} \int_{\Omega_e} \frac{\partial \mathbf{N}}{\partial x_i} k \tau_{GGLS} \frac{\partial}{\partial x_i} \left(C(s) \frac{\partial T^{h^*}}{\partial t^*} - \cancelto{0}{\frac{\partial}{\partial x_i^*} \left(K_{ij}(s) \frac{\partial T^{h^*}}{\partial x_j^*} \right)} + \gamma(s) \mathscr{L}^* \frac{\partial f^*}{\partial t^*} \right) d\mathbf{x}, \tag{3.45}$$

where N_e is the number of elements and Ω_e is the element domain. The summation operator highlights that the stabilization is added only over the elements *interior*. Note that the second term in brackets vanishes for the linear shape functions adopted in this monograph. The stabilization term, τ_{GGLS}, is computed as follows [216]:

$$\tau_{GGLS} = \frac{h^2}{6k} \xi, \tag{3.46}$$

where [216]:

$$\xi = \frac{\cosh(\sqrt{6\alpha_{GGLS}}) + 2}{\cosh(\sqrt{6\alpha_{GGLS}}) - 1} - \frac{1}{\alpha_{GGLS}}, \tag{3.47}$$

$$\alpha_{GGLS} = \frac{\rho c_p}{\Delta t} \frac{h^2}{6k}, \tag{3.48}$$

with h being the element size. The parameter α_{GGLS} represents the ratio of the transient to diffusive contributions to the residuals. For dynamic problems dominated by the transient contribution, $\alpha_{GGLS} >> 1$ and $\xi \to 1$. In this situation, Ilinca and Hetu [216] showed that the contribution of the stabilization corresponds to the use

of an artificial conductivity defined as:

$$k_a = k\alpha_{GGLS}. \tag{3.49}$$

The smoothing effect of the GGLS stabilization is demonstrated for a 1D phase change problem similar to the one considered in the current chapter. We consider a finite slab of length $L = 1$, initially at temperature $T_I^* = 0.5$ and connected to a hot thermostat on the right side at temperature $T_r^* = 0.5$. The slab is filled with PCM, with melting temperature $T_m^* = 0$ and Stefan number $Ste = 0.1$. At $t^* > 0$, the left boundary is suddenly connected to a cold thermostat at temperature $T_l^* = -0.5$. Figure 3.7 shows the slab temperature at different time instants with and without the GGLS stabilization. The numerical results obtained without stabilization suffer from an unbounded solution. At $t^* = 1e-5$, the computed temperature at the third, fifth and sixth node is not bounded between the values of the adjacent nodes. On the other hand, the GGLS stabilization allows a physical solution to obtained. Figures 3.7(b) and (c) show that the time advancement gradually smooths both the undershoots and overshoots.

3.3.4 Temporal discretization

With the aim of converting the ODE obtained in (3.40) to a set of algebraic equations, a suitable temporal approximation scheme should be selected. In principle, one could treat time as an additional (spatial) coordinate and discretize it using the finite element procedure presented in the previous section. This requires the specification of both initial and final time conditions [117]. The common finite element practice adopts a finite difference approximation via the Θ-method. The time derivative of the unknown vector is approximated using a two-point finite difference as follows:

$$\dot{\mathbf{T}} = \frac{\mathbf{T}^{(n+1)} - \mathbf{T}^{(n)}}{\Delta t^{(n)}}. \tag{3.50}$$

A similar approximation can be adopted for the latent heat source term yielding:

$$\dot{\mathbf{L}} = \frac{\mathbf{L}^{(n+1)} - \mathbf{L}^{(n)}}{\Delta t^{(n)}}. \tag{3.51}$$

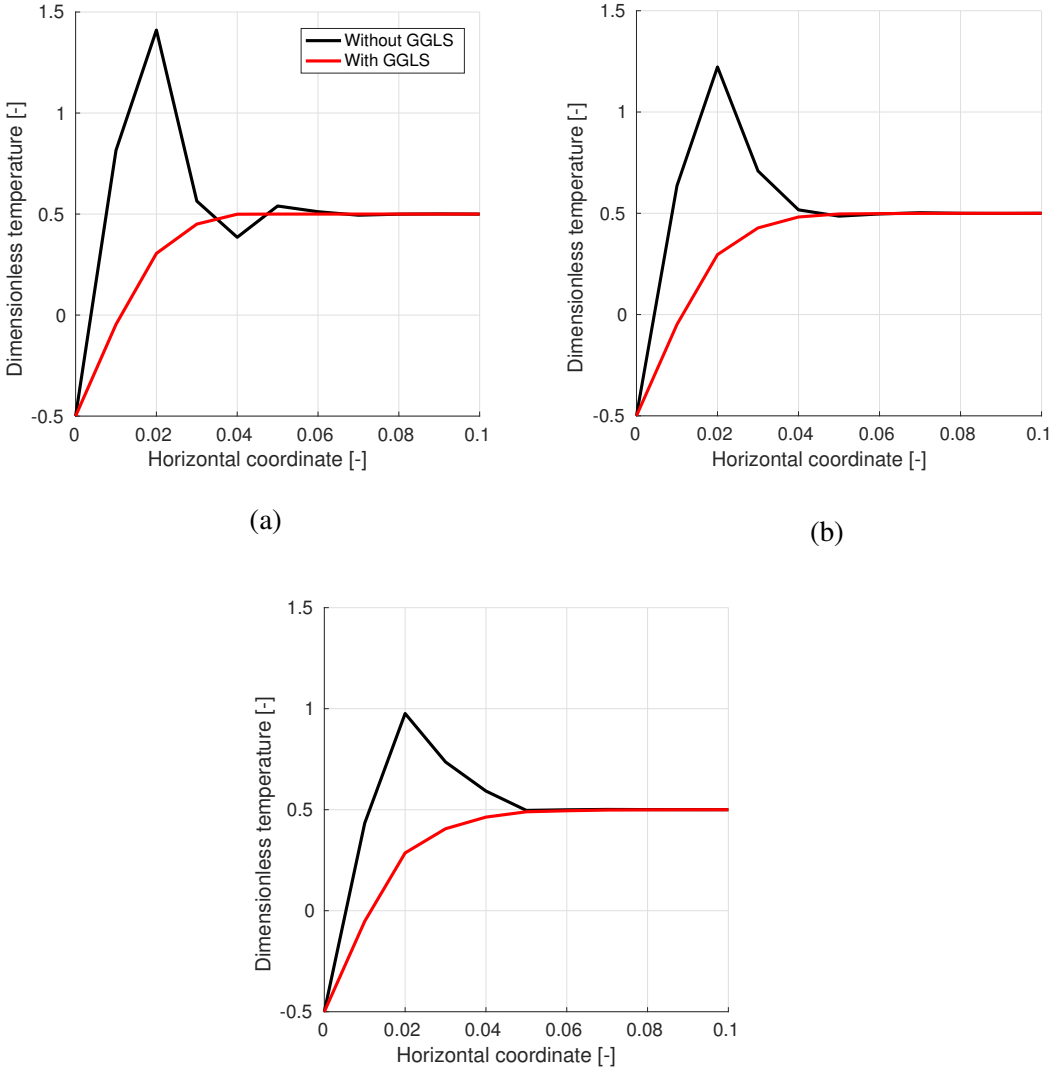

(a)

(b)

(c)

Fig. 3.7. Effect of the GGLS stabilization on over and under-shooting when advancing with small time steps. (a): $t^* = 1e-5$; (b): $t^* = 5e-5$; (c): $t^* = 1e-4$;

The static portion of the residuals is constructed using an intermediate temperature computed as:

$$\bar{\mathbf{T}} = \Theta \mathbf{T}^{(n+1)} + (1-\Theta) T^{(n)}. \tag{3.52}$$

The parameter Θ is a weighted average coefficient that defines wether the intermediate temperature is closer to $T^{(n+1)}$ or to $T^{(n)}$. Different values of Θ leads to different well-know time discretization schemes such as [350]:

- the explicit Euler scheme with $\Theta = 0$,
- the Crank-Nicolson scheme with $\Theta = 0.5$,
- the Galerkin scheme with $\Theta = 2/3$,
- the implicit Euler scheme with $\Theta = 1$.

For $\Theta \geq 0.5$, the time-marching is unconditionally stable [350]. This means that time restrictions are not required to make the integration stable, i.e. with an ultimately bounded error. In this thesis, we choose the implicit Euler scheme for its inherent robustness and stability properties [433]. This corresponds to a 1^{st} order Backward Differentiation Formula (BDF) scheme.

Using (3.50) through (3.52) in (3.40) with $\Theta = 1$ leads to the following (fully discrete) unstabilized residuals:

$$\mathbf{R}_{us}^{(n+1)} = \mathbf{C}\frac{\mathbf{T}^{(n+1)} - \mathbf{T}^{(n)}}{\Delta t^{(n)}} + \mathbf{K}\mathbf{T}^{(n+1)} + \frac{\mathbf{L}^{(n+1)}\left(\mathbf{T}^{(n+1)}\right) - \mathbf{L}^{(n)}\left(\mathbf{T}^{(n)}\right)}{\Delta t^{(n)}}. \tag{3.53}$$

Augmenting (3.53) with the fully discrete version of (3.45) gives the residuals at the time iteration (n+1), $\mathbf{R}^{(n+1)}$. At the time-step $n = 0$, these equations reduce to satisfy the initial conditions:

$$\mathbf{R}^{(0)} = \mathbf{T}^{(0)} - \mathbf{T}. \tag{3.54}$$

For every subsequent time-step when $n > 0$, we solve the nonlinear problem $\mathbf{R}^{(n+1)} = \mathbf{0}$ through the Newton method, as discussed in the following section.

To obtain the results presented in this chapter, we advance in time using a fixed time-step. A refined time-stepping strategy is proposed in 5.2.3 and used to produce all the results presented in Chapters 5 and 6.

3.3.5 Nonlinear solution

To solve the nonlinear systems of equations arising in (3.53), we adopt the Newton method for two main reasons. First, this method allows superior convergence properties than the simpler Picard iteration method [350]. It can be shown that the convergence is quadratic if the second and third derivatives of the residual have some specific properties [224]. Second, the discrete adjoint method for sensitivity analysis presented in Chapter 2 requires the computation of the Jacobian matrix. As the need for Jacobian assembling is a basic requirement of Netwon method, the same piece of code can then be used for both the forward and sensitivity analyses. Despite these advantages, the Newton method has a small radius of convergence, which may complicate the solution in case of strong nonlinearities and/or a bad initial guess of the solution vector. In transient problems, the time steps can be iteratively adapted to obtain Newton convergence. As a matter of fact, a pseudo-transient continuation (or pseudo time-stepping) [237] can be used with Newton method to obtain the solution of numerically challenging steady-state problems where no good approximation of the root is available.

To illustrate the Newton method, let us consider a generic iteration "k". We look for an iterative procedure resulting in a recursive relation of the form:

$$\mathbf{T}^{k+1} = \mathbf{T}^k + \alpha_r \Delta \mathbf{T}^k, \tag{3.55}$$

where $\Delta \mathbf{T}^k$ represents the update step, while α_r is referred to as under(over)-relaxation factor and will be discussed next. Expanding the residual vector (3.53) in a Taylor series leads to:

$$\mathbf{0} = \mathbf{R}(\mathbf{T}^k) + \left.\frac{\partial \mathbf{R}}{\partial \mathbf{T}}\right|_{\mathbf{T}^k} \Delta \mathbf{T}^k + \mathscr{O}(\Delta \mathbf{T})^2, \tag{3.56}$$

where the partial derivative of the residuals with respect to the state variables is the Jacobian matrix (or tangent matrix):

$$\mathbf{J} = \left.\frac{\partial \mathbf{R}}{\partial \mathbf{T}}\right|_{\mathbf{T}^k}. \tag{3.57}$$

Neglecting higher order terms, solving (3.56) for $\Delta\mathbf{T}^k$ and substituting in (3.55) leads to:

$$\mathbf{T}^{k+1} = \mathbf{T}^k - \alpha_r \mathbf{J}(\mathbf{T}^k)^{-1}\mathbf{R}(\mathbf{T}^k). \tag{3.58}$$

The iterative procedure is stopped when the following convergence criteria is satisfied:

$$\mathscr{F}(||\mathbf{R}(T^k)||) < \varepsilon_{nl}, \tag{3.59}$$

where ε_{nl} is a user-specified tolerance and $\mathscr{F}(||\mathbf{R}(T^k)||)$ is some measure of the residuals norm. In this thesis, we adopt the following:

$$\mathscr{F}(||\mathbf{R}(T^k)||) = \frac{||\mathbf{R}(T^k)||_2}{||\mathbf{R}(T^0)||_2}, \tag{3.60}$$

where $||\cdot||_2$ denotes the L_2 norm. Let us now consider the time iteration $(n+1)$, for which the Newton method is applied to compute $T^{(n+1)}$ and the previous state variables field $T^{(n)}$ is known. Considering the fully discrete residual formulation presented in (3.53), we can split the Jacobian as following:

$$\mathbf{J}^{(n+1)} = \mathbf{J}_s^{(n+1)} + \mathbf{J}_{dyn}^{(n+1)}, \tag{3.61}$$

where $\mathbf{J}_s^{(n+1)}$ and $\mathbf{J}_{dyn}^{(n+1)}$ are the static and dynamic Jacobians, respectively. Due to the absence of boundary fluxes, the former only contains the diffusion term:

$$\mathbf{J}_s^{(n+1)} = \mathbf{K}. \tag{3.62}$$

The dynamic Jacobian is defined as:

$$\mathbf{J}_{dyn}^{(n+1)} = \frac{\mathbf{C}}{\Delta t^{(n)}} + \frac{1}{\Delta t^{(n)}}\frac{\partial \mathbf{L}^{(n+1)}}{\partial \mathbf{T}^{(n+1)}} + \mathbf{J}_{GGLS}^{(n+1)}, \tag{3.63}$$

where $\mathbf{J}_{GGLS}$ is the Jacobian of the stabilization contribution. The second term accounts for the latent heat source. Recalling Eq. (3.43), using the Leibniz integration rule and the chain rule, we obtain:

$$\frac{\partial \mathbf{L}^{(n+1)}}{\partial \mathbf{T}^{(n+1)}} = \int_\Omega \mathbf{N}\mathbf{N}^T \gamma \mathscr{L} \frac{\partial f}{\partial T} d\mathbf{x}. \tag{3.64}$$

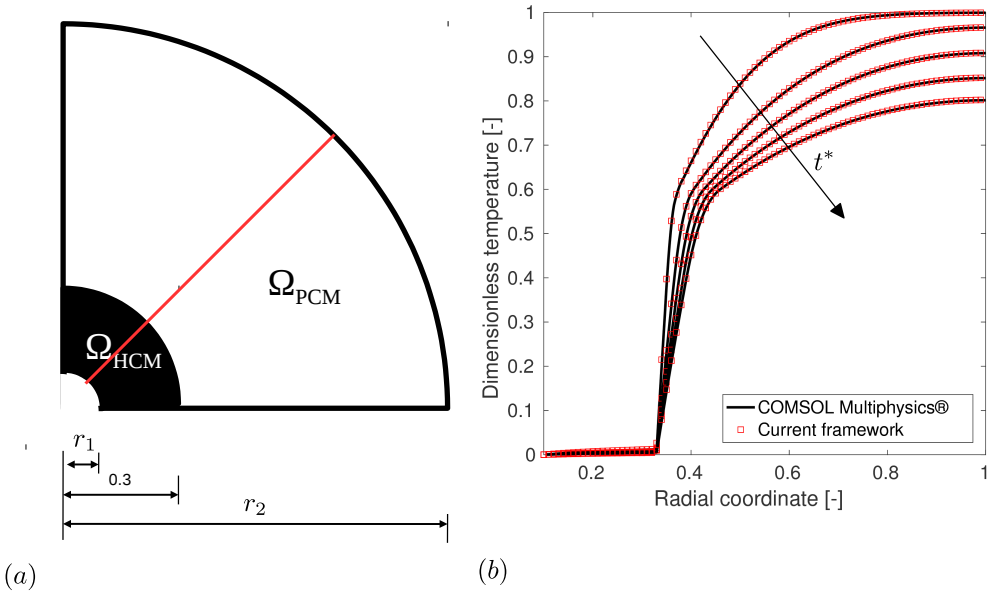

Fig. 3.8. Verification of accuracy of the computational model. (a): Schematic of the geometry considered; (b): comparison of the temperature profiles at $t^* = \{0.01;\ 0.05;\ 0.09;\ 0.13;\ 0.17\}$

In a similar manner, we elaborate the GGLS stabilization contribution (3.45) to obtain:

$$\mathbf{J}_{GGLS}^{(n+1)} = \sum_{e=1}^{N_e} \int_{\Omega} \frac{\partial \mathbf{N}}{\partial x_i} k \tau_{GGLS} \frac{\partial \mathbf{N}^T}{\partial x_i} \left(\frac{C(s)}{\Delta t} + \gamma(s) \mathscr{L} \frac{1}{\Delta t} \frac{\partial f}{\partial T} \right) d\mathbf{x}. \tag{3.65}$$

3.3.6 Model verification

The analysis framework presented in this section is verified on a reference problem against the results obtained with the finite element commercial package COMSOL Multiphysics [101]. We simulate the discharge of a storage unit with the geometry shown in Figure 3.8(a). The computational mesh is composed of 11970 quadrilateral bilinear elements with angular size $\Delta\theta = 1^\circ$ and radial size $\Delta r = r\Delta\theta$. A representation is given in Figure 3.9(a). We use the same materials adopted for the design optimization study reported in [374]. The relevant thermo-physical properties rewritten in non-dimensional form are presented in Table 3.1 while all the relevant analysis parameters are summarized in Table 3.2. Figure 3.8(b) shows the temperature profile along the red line highlighted in Figure 3.8(a) at different time instants, i.e.

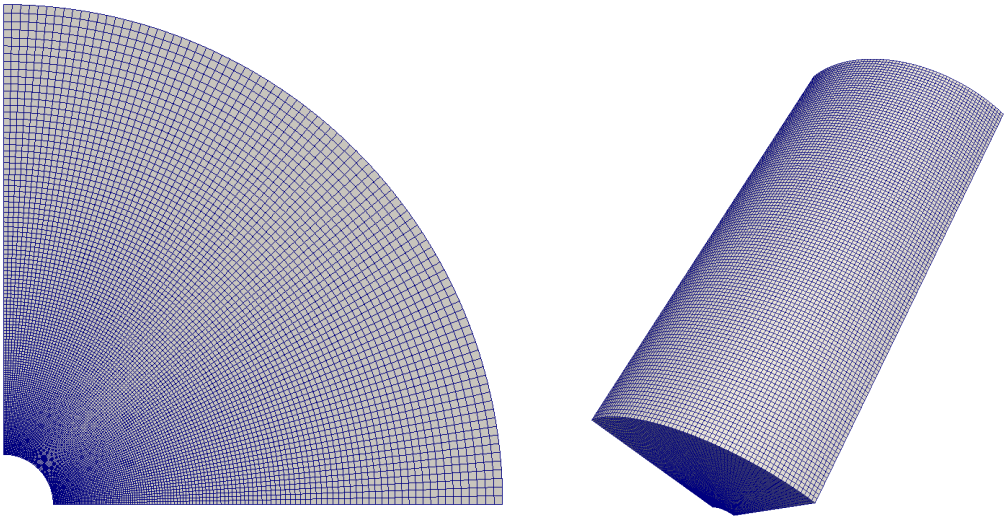

(a) (b)

Fig. 3.9. (a): 2D computational mesh; (b): 3D computational mesh

Table 3.1. Thermo-physical properties of materials in dimensionless settings

Description	Symbol	Value
Conductivity ratio	$\frac{k_{HCM}}{k_{PCM}}$	600
Capacitance ratio	$\frac{(\rho c_p)_{HCM}}{(\rho c_p)_{PCM}}$	1.6
Dimensionless Latent heat	$\mathscr{L}^*$	20
Dimensionless melting temperature	T_m^*	0.5

Table 3.2. Relevant analysis parameters

Description	Symbol	Value
Boundary heat flux	$\mathbf{q}_n$	$\mathbf{0}$
Imposed temperature	T_d^*	0
Initial temperature	T_I^*	1

$t^* = \{0.01;\ 0.05;\ 0.09;\ 0.13;\ 0.17\}$. We observe that the thermal response predicted by the current framework agrees well with the results obtained with COMSOL. The relative error L_2 norm is computed as 4.01×10^{-4} with a standard deviation of 1.66×10^{-4}. These results suggest that the presented model and its implementation are able to predict with sufficient accuracy the discharge of LHTES units in which the convective effects are negligible.

3.4 Design optimization problem

The design of efficient fins for solidification enhancement in LHTES requires that the geometry fulfills the following design criteria:

1. it allows the discharge of the maximum amount of energy in the least time, in order to utilize the full energy density potential of the unit,
2. it allows the retrieval of the energy at a constant rate, providing a steady power output.

In the following sections, we will present three alternative optimization problem formulations. The Energy Minization (EM) and the Time Minimization (TM) are two alternatives targeting design criterion (1). The Steadiness Maximization (SM) formulation is devised for the design criterion (2).

3.4.1 Energy Minimization

The EM problem formulation represents the following design question: *what is the optimal topology of HCM that allows discharging the maximum amount of energy from a given amount of PCM in a given time period?*

In mathematical terms this corresponds to:

$$\begin{aligned} \underset{\mathbf{s}}{\text{minimize}} \quad & z(\mathbf{T}^*(\mathbf{s}), \mathbf{s}) = E \quad at \quad t^* = t_f^* \\ \text{subject to} \quad & \int_{\Omega_D} \rho_s(s)\, d\mathbf{x} - \Phi \int_{\Omega_D} d\mathbf{x} \leq 0 \\ & \mathbf{s} \in \mathbf{S} = \left\{ \mathbb{R}^{N_s} \mid s_{min} \leq s_i \leq s_{max}, i = 1, ..., N_s \right\} \end{aligned} , \tag{3.66}$$

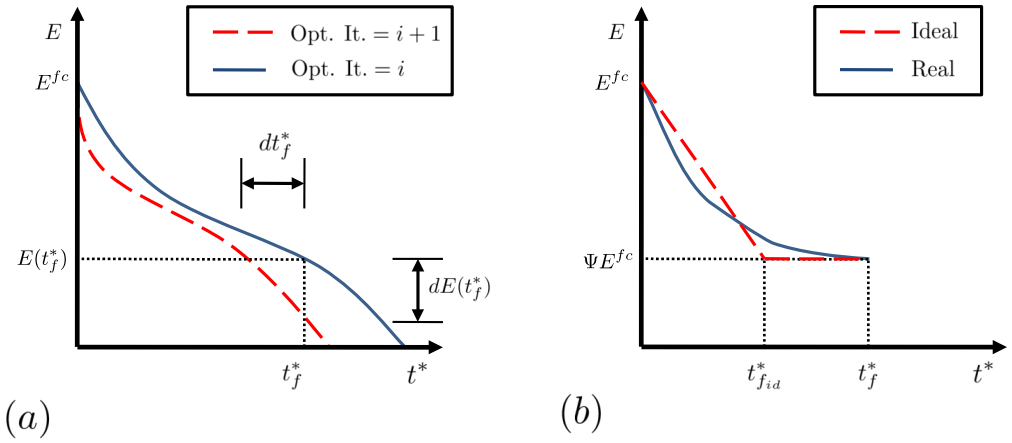

Fig. 3.10. Optimization problem formulations. (a): EM vs TM update; (b): ideal vs real energy history used for Steadiness Maximization

where $E = \int_{\Omega_D} (CT^* + \gamma f^* L^*)\ d\mathbf{x}$ is the dimensionless energy content of the unit, $\rho_s = \bar{s}$ is the projected design variable field corresponding to the normalized density of HCM, $\mathbf{s}$ is the vector of design variables, Φ the maximum volume fraction of HCM and N_s the number of design variables with upper and lower bounds denoted by s_{max} and s_{min}, respectively. The inequality constraint prevents the trivial solution of having the entire design domain filled with HCM.

Figure 3.10(a) shows the discharge at two generic design iterations, i and $i+1$. In the EM procedure, the final time t_f^* is fixed and $dE(t_f^*)$ represents the objective reduction achieved with the optimization iteration.

3.4.2 Time Minimization

The TM optimization problem formulation considers the following design question: *what is the optimal topology of HCM that allows discharging a given amount of*

energy from a given amount of PCM in the least time? This translates into:

$$\begin{aligned} \underset{\mathbf{s}}{\text{minimize}} \quad & z(\mathbf{T}^*(\mathbf{s}),\mathbf{s}) = t_f^* \\ \text{subject to} \quad & E - \Psi E^{fc} = 0 \quad at \quad t^* = t_f^* \\ & \int_{\Omega_D} \rho_s(s)\, d\mathbf{x} - \Phi \int_{\Omega_D} d\mathbf{x} \leq 0 \\ & \mathbf{s} \in \mathbf{S} = \left\{ \mathbb{R}^{N_s} \mid s_{min} \leq s_i \leq s_{max}, i = 1,...,N_s \right\} \end{aligned} \quad , \tag{3.67}$$

where Ψ is a specified target energy fraction and E^{fc} is the total dimensionless energy in the tank in the fully charged condition. Note that the optimizer does not *see* the final energy equality constraint. This is enforced implicitly during the analysis by iteratively halving the time-step until the constraint is satisfied within a user-specified error tolerance, ε_t. An improved strategy to control the time-stepping such that the condition is satisfied is presented in Section 5.2.3. Problem (3.67) is quite similar to (3.66) but presents the complication that the objective to be minimized is an independent variable. For this reason, we linearize the energy history around the final time, t_f^*, to obtain:

$$E(t^*) = E(t_f^*) + \left.\frac{dE}{dt^*}\right|_{t^*=t_f^*} \left(t^* - t_f^*\right) + O\left((t^* - t_f^*)^2\right). \tag{3.68}$$

Neglecting higher order terms, rearranging and differentiating leads to:

$$\frac{dt_f^*}{d\mathbf{s}} = \left(-\left.\frac{dE}{dt^*}\right|_{t^*=t_f^*} \right)^{-1} \frac{dE(t^*)}{d\mathbf{s}}, \tag{3.69}$$

where $dE(t_f^*)/ds = 0$ because $E(t_f^*)$ is a constant in the TM procedure. Note that the linearization allowed reformulating an independent variable as a function of a dependent variable, with respect to which design sensitivities can be computed. The objective gradients differ from the ones computed with the EM approach by a multiplication factor. Solving for (3.67) requires minimal code modifications with respect to (3.66).

A schematic representation of the TM procedure is also shown in Figure 3.10(b). Here the final energy E_f is fixed and dt_f^* represents the objective reduction achieved with the optimization iteration.

3.4.3 Steadiness Maximization

The SM formulation considers the following design question: *what is the optimal topology of HCM fins that maximizes the steadiness of the TES discharge?* Mathematically:

$$\begin{aligned}
\underset{\mathbf{s}}{\text{minimize}} \quad & z(\mathbf{T}^*(\mathbf{s}),\mathbf{s}) = \int_0^{\max\left(t_f^*,\, t_{f_{id}}^*\right)} \left(E(t^*) - E_{id}(t^*)\right)^2 dt^* \\
\text{subject to} \quad & E - \Psi E^{fc} = 0 \quad at \quad t^* = t_f^* \\
& \int_{\Omega_D} \rho_s(s)\, d\mathbf{x} - \Phi \int_{\Omega_D} d\mathbf{x} \leq 0 \\
& h_{t_f} = t_f^* - t_{f_{id}}^* \leq 0 \\
& \mathbf{s} \in \mathbf{S} = \left\{ \mathbb{R}^{N_s} \mid s_{min} \leq s_i \leq s_{max}, i = 1,...,N_s \right\}
\end{aligned} \quad , \tag{3.70}$$

where $E_{id}(t^*)$ is an ideal discharge history with the following form:

$$E_{id}(t^*) = \begin{cases} E^{fc} - \frac{E^{fc}(1-\Psi)}{t_{f_{id}}^*} t^* & \text{if } t^* \leq t_{f_{id}}^* \\ \Psi E^{fc} & \text{if } t^* > t_{f_{id}}^* \end{cases} , \tag{3.71}$$

where $t_{f_{id}}^*$ is an ideal discharge time. A representative sketch of the ideal discharge history is given in in Fig. 3.10(b). For $t^* \leq t_{fd}^*$ the energy history is linear, hence the power output is steady. This is the reason why we refer to this approach as *Steadiness* Maximization. The second inequality constraint, h_{t_f}, imposes a maximum limit on the discharge time and has the aim of providing control over this important design criterion to avoid undesirably lengthy discharge processes. The design sensitivities with respect to it are computed using the chain rule as follows:

$$\frac{dh_{t_f}}{d\mathbf{s}} = \frac{\partial h_{t_f}}{\partial t_f^*} \frac{dt_f^*}{d\mathbf{s}} \tag{3.72}$$

where the second multiplication term is obtained as detailed in (3.69). For the computation of z in the cases in which $t_f^* < t_{f_{id}}^*$, the real discharge history is taken as a constant $E(t^*) = \Psi E^{fc}$ in the range $t_f^* < t_f^* \leq t_{f_{id}}^*$. For $t_f^* > t_{f_{id}}^*$, the optimization problem is infeasible. However, the GCMMA or MMA routines do not guarantee a sequence of feasible solutions. The objective still needs to be computed in case of intermediate non-feasible steps. This is the reason for the second case of (3.71).

3.4.4 Material interpolation and regularization

As discussed in Section 2.4.1, topology optimization with density methods requires a smart interpolation strategy, driving the optimization process to binary $\{0;\ 1\}$ designs. A suitable interpolation function should be identified for each design-dependent term in the governing equation (3.26). For the numerical studies presented in this chapter, we adopt the classical SIMP approach (2.28). The conductivity, $K(s)$, is interpolated using a power-law exponent of 2. The capacitance, $C(s)$, and the latent heat switch, $\gamma(s)$, are interpolated linearly, so that no unnecessary nonlinearity is added to the problem. In preliminary numerical studies, we observed that penalizing the conductivity was sufficient to achieve a fair convergence to binary designs.

The regularization of the problem is here achieved through the linear filter presented in Eq. (2.37). To cure the fuzziness introduced by the filter operator we adopt the "tanh" projection operator (Eq. (2.40)). We set the projection threshold, η, to 0.5 and the projection steepness parameter, β, to 1. Note that this choice of parameters results in a mild projection that does not provide any feature size control.

3.4.5 Sensitivity analysis

The adjoint method presented in Section 2.3.2 is used to compute the optimization criteria gradients necessary to drive our gradient-based optimizer. For the sensitivity analysis of transient problems, Eq. (2.26) can be generalized as follows. Let us a consider a total residual vector, $\mathbf{R}_{tot}$, where the contributions of all the time steps taken from the time-solver are stacked sequentially:

$$\mathbf{R}_{tot} = [\mathbf{R}^{(0)^T},\ \mathbf{R}^{(1)^T}, ...,\ \mathbf{R}^{(N_t)^T}]^T, \tag{3.73}$$

where N_t is the total number of time steps. Proceeding in a similar manner for the generic state variable field $\mathbf{u}$:

$$\mathbf{u}_{tot} = [\mathbf{u}^{(0)^T},\ \mathbf{u}^{(1)^T}, ...,\ \mathbf{u}^{(N_t)^T}]^T. \tag{3.74}$$

Considering $\mathbf{u}_{tot}$ instead of $\mathbf{u}$ and $\mathbf{R}_{tot}$ instead of $\mathbf{R}$ and repeating the procedure described in Section 2.3.2 leads to the following adjoint system:

$$\left(\frac{\partial \mathbf{R}_{tot}}{\partial \mathbf{u}_{tot}}\right)^T \boldsymbol{\lambda}_{tot} = \frac{\partial q_j}{\partial \mathbf{u}_{tot}}, \tag{3.75}$$

where $\boldsymbol{\lambda}_{tot}$ is the stacked vector of adjoint variables:

$$\boldsymbol{\lambda}_{tot} = [\boldsymbol{\lambda}^{(0)^T}, \boldsymbol{\lambda}^{(1)^T}, ..., \boldsymbol{\lambda}^{(N_t)^T}]^T. \tag{3.76}$$

The partial derivative of the total residuals with respect to the vector of state variables is a matrix $(N_t \times N_u) \times (N_t \times N_u)$, where N_u is the number of total degrees of freedom. The sparsity pattern depends on the temporal discretization scheme adopted. For the two point scheme described in Section 3.3.4, it is a lower bidiagonal block matrix defined as:

$$\frac{\partial \mathbf{R}_{tot}^{(n)}}{\partial \mathbf{u}_{tot}^{(i)}} = \begin{cases} \mathbf{J}_{dyn}^{(n-1)} & \text{for } i = n-1 \\ \mathbf{J}^{(n)} & \text{for } i = n \\ \mathbf{0} & \text{otherwise} \end{cases}. \tag{3.77}$$

Due to (3.54), the differentiation with respect to the initial condition leads to:

$$\frac{\partial \mathbf{R}_{tot}^{(0)}}{\partial \mathbf{u}_{tot}^{(i)}} = \begin{cases} \mathbf{I} & \text{for } i = 0 \\ \mathbf{0} & \text{otherwise} \end{cases}. \tag{3.78}$$

Rewriting (3.75) in matrix form and using (3.77) and (3.78) results in:

$$\begin{bmatrix} \mathbf{I} & \mathbf{J}_{dyn}^{(0)^T} & & & \\ & \mathbf{J}^{(1)^T} & \mathbf{J}_{dyn}^{(1)^T} & & \\ & & \mathbf{J}^{(2)^T} & \ddots & \\ & & & \ddots & \mathbf{J}_{dyn}^{(N_t-1)^T} \\ & & & & \mathbf{J}^{(N_t)^T} \end{bmatrix} \begin{bmatrix} \boldsymbol{\lambda}^0 \\ \boldsymbol{\lambda}^1 \\ \vdots \\ \vdots \\ \boldsymbol{\lambda}^{N_t} \end{bmatrix} = \begin{bmatrix} (\partial q_j)/(\partial \mathbf{u}^{(0)}) \\ (\partial q_j)/(\partial \mathbf{u}^{(1)}) \\ \vdots \\ \vdots \\ (\partial q_j)/(\partial \mathbf{u}^{(N_t)}) \end{bmatrix}. \tag{3.79}$$

Since there is a single matrix block at the end of the diagonal, the final adjoint field $\boldsymbol{\lambda}^{N_t}$ can be computed promptly as:

$$\boldsymbol{\lambda}^{N_t} = \mathbf{J}^{(N_t)^{-T}} \frac{\partial q_j}{\partial \mathbf{u}^{(N_t)}}. \tag{3.80}$$

Equation (3.79) can be then solved by backward substitution. This corresponds to the following backward time integration:

$$\left(\mathbf{J}^{(n)}\right)^T \boldsymbol{\lambda}^{(n)} = \frac{\partial q_j}{\partial \mathbf{u}^{(n)}} - \mathbf{J}_{dyn}^{(n)^T} \boldsymbol{\lambda}^{(n+1)} \tag{3.81}$$

for $n = N_t - 1, \ldots, 0$. Finally, the discrete sensitivity field is calculated using the time-dependent version of Eq. (2.27):

$$\frac{dq_j}{d\mathbf{s}} = \frac{\partial q_j}{\partial \mathbf{s}} - \boldsymbol{\lambda}_{tot}^T \frac{\partial \mathbf{R}_{tot}}{\partial \mathbf{s}}. \tag{3.82}$$

The assembly of Eqs. (3.82) and (3.81) requires the forward solution of the state equations. For this reason, in this thesis the forward solutions are dumped on disk for every time-step of the analysis. The backward time integration proceeds using the same time-steps adopted during the forward analysis.

3.4.6 Verification of accuracy of sensitivity analysis

The accuracy of the sensitivity analysis framework described in the previous section is checked against the sensitivities with respect to the TM objective obtained through central finite differences:

$$\left(\frac{dz}{ds_i}\right)_{fd} = \frac{z(s_i + \varepsilon_{s_i}) - z(s_i - \varepsilon_{s_i}))}{2\varepsilon_{s_i}}, \tag{3.83}$$

where ε_{s_i} is the perturbation size. The deviation is quantified on 30 design variables through the L_2 norm of the relative error. Figure 3.11 shows the results obtained for different perturbation sizes on the initial design, corresponding to a homogeneous design variable field $s = \Phi$, and on the optimized nominal design presented in Section 3.5.1. The minimum error is achieved for a perturbation size of $\varepsilon_{s_i} = 10^{-3}$ for both the initial and final design. Reducing the perturbation size from $\varepsilon_{s_i} = 10^{-1}$ to $\varepsilon_{s_i} = 10^{-4}$, yields a decrease of the error. As expected for central finite differences [196], the rate of convergence is quadratic ($\sim \mathcal{O}(\varepsilon_{s_i}^2)$) with respect to the perturbation. For $\varepsilon_{s_i} < 10^{-4}$, the error increases again as cancellation dominates [196]. Overall, we observe an acceptable agreement between the analytical and finite difference sensitivities. This suggests the correctness of our analytical derivations and implementation.

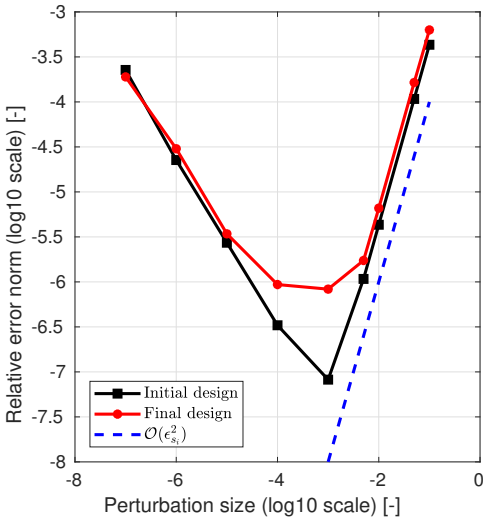

Fig. 3.11. Finite difference check of adjoint sensitivities on the initial and final optimized designs

3.5 Numerical results and design trends

In this section, we describe the numerical studies and discuss the results obtained. For all the results presenter hereafter, the thermo-physical properties and analysis parameters are the same introduced for the verification study presented in the previous section (see Tables 3.1 and 3.2). The design domain corresponds to the one depicted in Figure 3.6, which is discretized using the mesh adopted for the verification study in Section 3.3.6 and shown in Figure 3.9(a). For the 3D design optimization studies presented, the design domain corresponds to a linear out-of-plane extrusion of the 2D geometry, with adiabatic boundary conditions at the bottom and at the top. The height Z of the quarter hollow cylinder is set to 3. The mesh has characteristic dimensions $\Delta\theta = 1.38^\circ$, $\Delta r = 90$ and $\Delta z = 0.025$, yielding a total of 507000 hexahedral trilinear elements. A representation is shown in Figure 3.9(b). In all the numerical examples, the maximum volume fraction of HCM, Φ, is set to 10 %.

3.5.1 Nominal longitudinal design

Here, we illustrate how our topology optimization framework generates optimized fin designs for a reference case with a target energy fraction, Ψ, of 5 %. This will be referred to as nominal diffusion design.

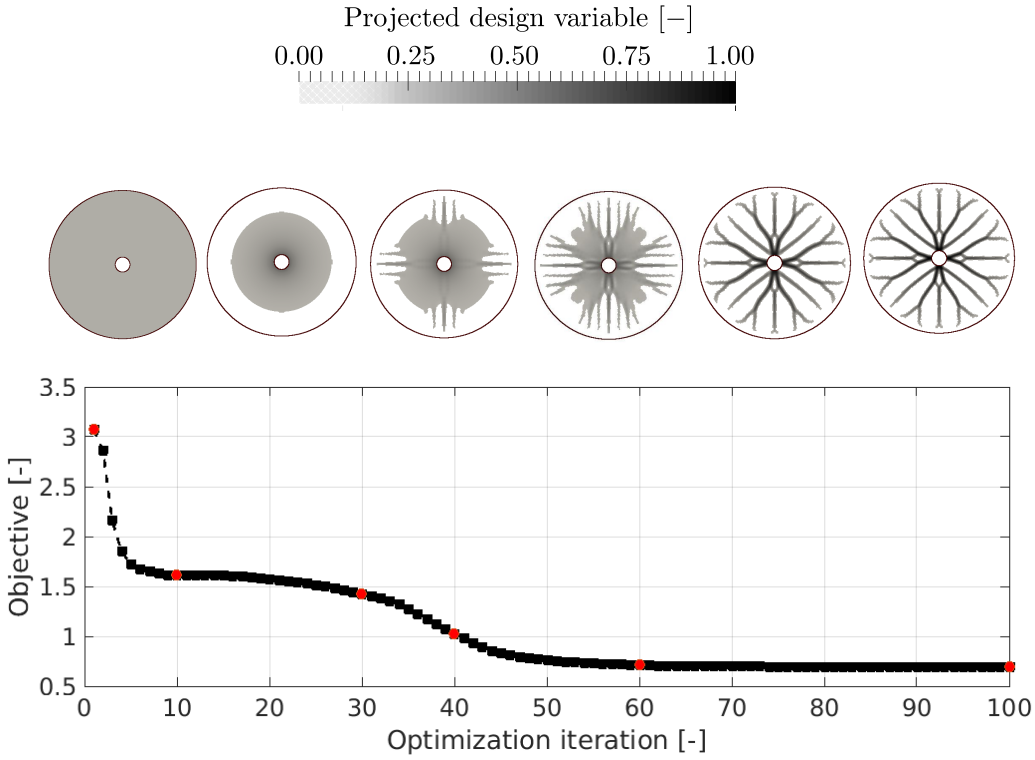

Fig. 3.12. Objective history along the optimization in nominal conditions. Snapshots of the design are shown at selected optimization iterations

The objective history obtained using the TM formulation along with snapshots of the design at selected iterations is depicted in Figure 3.12. All the designs presented in this chapter correspond to contour plots of the projected design variable field, where only regions with $\bar{s} \geq 0.1$ are shown. Also note that the same colorbar shown in Figure 3.12 is used for all the results. The initial design corresponds to a homogeneous material distribution $s = 0.1$ on the design domain Ω_D. During the first iterations, HCM concentrates in a region close to the internal tube, yielding a large reduction of the objective. Then, the convergence rate slows down until some conductive branches break the problem symmetry (iteration 30), which is when we observe the second quick objective drop. The final optimized design is obtained after 100 iterations. It shows a quasi-periodic pattern along the radial coordinate every $\Delta\theta = 45°$. Second-order branched structures alternate to unbranched fins. The fin tips are roughly equally spaced along the angular coordinate every 15°. Note that the convergence to binary designs could be improved by further raising the penalization

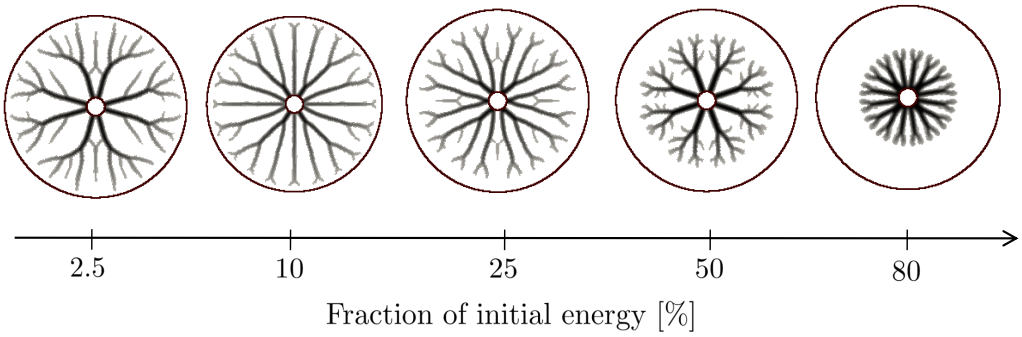

Fig. 3.13. Optimized designs obtained by sweeping the energy constraint

exponent in the conductivity interpolation using a continuation scheme. However, this degree of convergence was considered satisfactory for diffusive structures. A more aggressive penalization approach will be considered in Chapter 5, where the convergence to binary designs is of crucial importance for the correct prediction of the flow dynamics.

3.5.2 The trade-off between time and discharged energy

In this section, we explore the inherent trade-off between the discharge time, t_f^*, and the target energy fraction, Ψ. We solve the optimization problem using both the TM and the EM approach.

First, we solve the TM problem (3.67) setting the target energy fraction, Ψ, to 2.5 %, 5 %, 10 %, 25 %, 50 % and 80 %. The optimized designs obtained are depicted in Figure 3.13. Recall that the optimized design obtained for $\Psi = 5$ % corresponds to the nominal case that was presented in the previous section. As the target energy fraction, Ψ, increases, the characteristic length of the fins decreases to occupy a smaller region close to the internal tube leaving a hot external shell. Post-processing the designs optimized for $\Psi = \{80\,;50\,;25\}$ % reveals that the maximum length of the fins scales as $l_{max} \sim \sqrt{1-\Psi}$. This trend is not visible at smaller energy fractions. Once the fins achieve the length corresponding to the radius of the external envelope, the rate of the energy extraction is increased by moving HCM from the region close to the internal pipe to the region close to the external shell. In the optimized designs for $\Psi = 10$ % and $\Psi = 2.5$%, the internal tube is connected to fewer and thicker branches, which ramify at a wider angle.

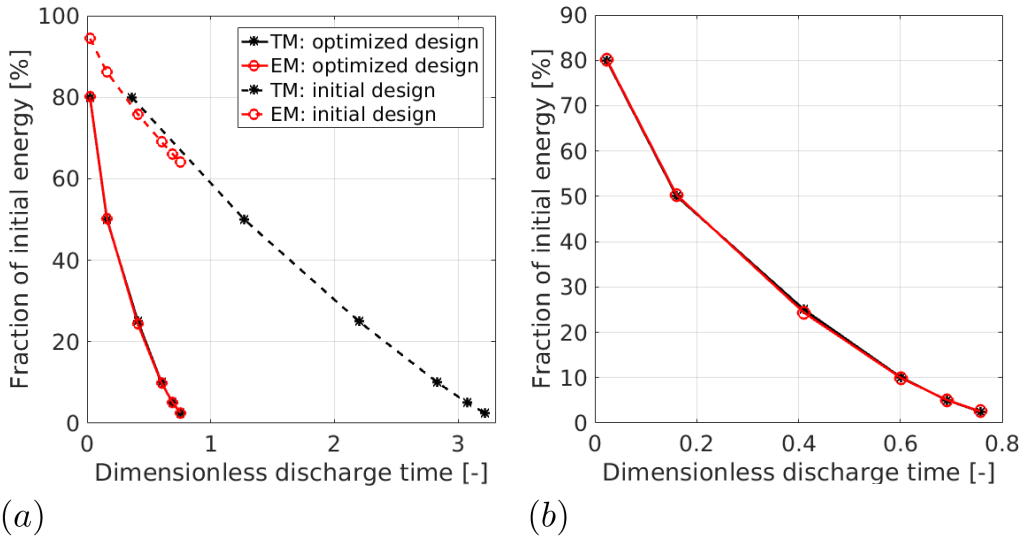

Fig. 3.14. (a): Convergence to Pareto front with the TM and with the EM procedure; (b): converged Pareto front

Then, the optimized final time obtained is set as a constraint for 6 optimization runs using the EM formulation (3.66). The initial and final performance curves in the objective space are shown in Fig. 3.14(a). The TM performance curve moves along the time axis (i.e. from right to left) during the optimization convergence. The EM performance curve moves along the energy axis (i.e. from top to bottom). The two approaches converge to the same Pareto front, that is presented in Figure 3.14(b). A closer inspection reveals that the maximum relative deviation between the two procedures is 2.75 %. This suggests that they can be used interchangeably to answer two alternative design questions. However, in early studies we observed that the EM formulation gives a poorer performance when setting a high final time. We conjecture that this behavior can arise as a result of badly scaled sensitivities due to a too *flat* energy history but we did not investigated this further. Also, we noticed that it might be challenging to set a reasonable final time as a constraint if the fin layout is unknown. The dynamics of the unit is largely influenced by the interpolation choice and changes dramatically during the optimization convergence.

To exclude the possibility of convergence to poor local minima, we now cross-check the performance of the TM designs with different residual energy targets Ψ. Each design optimized for a certain Ψ is expected to perform better than the other designs in that particular Ψ condition. For each optimized design, Figure

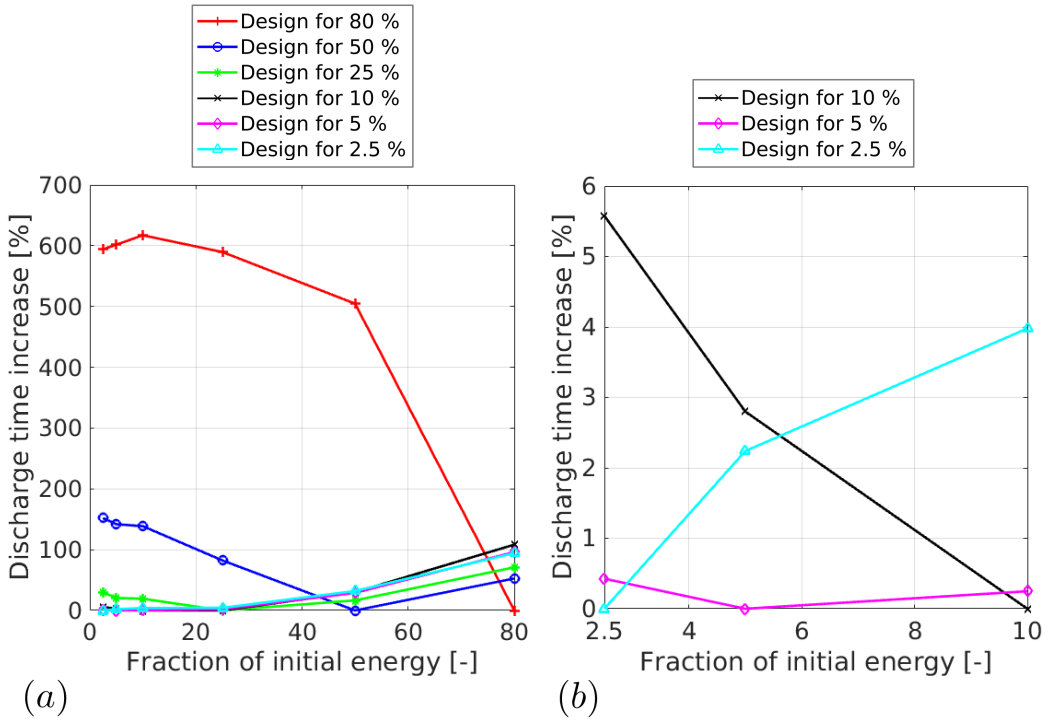

Fig. 3.15. Performance cross-check on the optimized designs. (a): Entire Ψ spectrum; (b): zoom over the low Ψ spectrum

3.15(a) plots the discharge time increase as compared to the optimized design for that particular Ψ. It can be seen that the optimized designs perform as expected. We note that either a badly designed or a badly utilized TES system can result in substantial performance reductions, highlighting the importance of an accurate prediction of the discharge dynamics during the design optimization process. For instance, if the design optimized for $\Psi = 80$ % is used to discharge the tank up to $\Psi = 10$ %, nearly a 600 % time increase is obtained as compared to what required by the design optimized for that situation. Taking a closer look at the low energy region (depicted in Fig. 3.15.(b)), which is the most meaningful for TES applications, we observe a much more robust performance, i.e. the designs look slightly sensitive to changes in Ψ. Our nominal design can be used for discharges down to $\Psi = 10$ % and $\Psi = 2.5$ % with less than 1 % performance reductions as compared to the structures optimized for those cases.

The results presented in this section demonstrate that topology optimization allows the tracking of precise design trends along a Pareto front final time - final

energy. The two design problem formulations give similar results but we reported superior performance of the TM procedure in some specific cases. We also observed that the proposed nominal design behaves robustly in the range of desired final energy values of interest for the development of practical LHTES systems.

3.5.3 Towards a constant power output

This numerical example aims at showing how topology optimization can address more complicated and interesting objectives for the design of LHTES units. Sensible storage systems where the same material is used as Heat Storage Medium (HSM) and HTF, e.g. domestic hot water storages, can deliver a high and constant thermal power. This last feature is desirable in many applications in which the unit is directly linked with downstream components such as refrigeration machines. In the LHTES systems considered in this chapter, heat travels by diffusion from the internal pipe to the PCM. As a result, the average temperature difference reduces exponentially in time, yielding a similar trend for the thermal power output. To manipulate the energy history and increase the steadiness of discharge, we adopt the optimization problem formulation (3.70).

To investigate how the ideal discharge time affects both the optimized designs and performance, we run four optimization cases with $t^*_{f_{id}} = \{1;\ 1.4;\ 1.8;\ 2.2\}$. The performance of the optimized designs is shown in Figure 3.16. In the range of values considered, we observe a trade-off between discharge time and steadiness. The objective drops from the initial value of 6.1 when $t^*_{f_{id}} = 1.0$ to the final value of 2.6 when when $t^*_{f_{id}} = 2.2$. On the right y-axis of Fig. 3.16, we plot an alternative metric to quantify steadiness: the dimensionless heat transfer drop. It is calculated as the difference between the initial and the final heat transfer rate as follows:

$$\Delta q = \int_{\Gamma_d} -k_{ij}\frac{\partial T^*}{\partial x_j}\bigg|_{t^*=0} n_i \, d\mathbf{x}' - \int_{\Gamma_d} -k_{ij}\frac{\partial T^*}{\partial x_j}\bigg|_{t^*=t^*_f} n_i \, d\mathbf{x}'. \tag{3.84}$$

We observe that this second steadiness measure shows a trend comparable to the one of the objective.

The optimized distribution of HCM for the four cases considered is shown in Figure 3.17. The "quick" design (i.e. $t^*_{f_{id}} = 1.0$) looks very similar to the optimized designs of the previous section for the low Ψ region. As the discharge time increases,

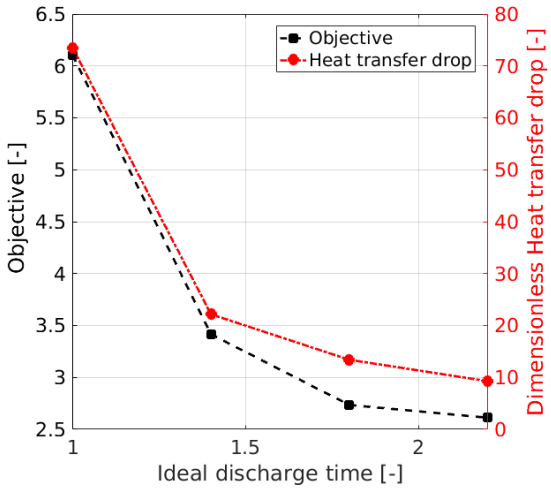

Fig. 3.16. Trade-off between discharge time and steadiness of discharge

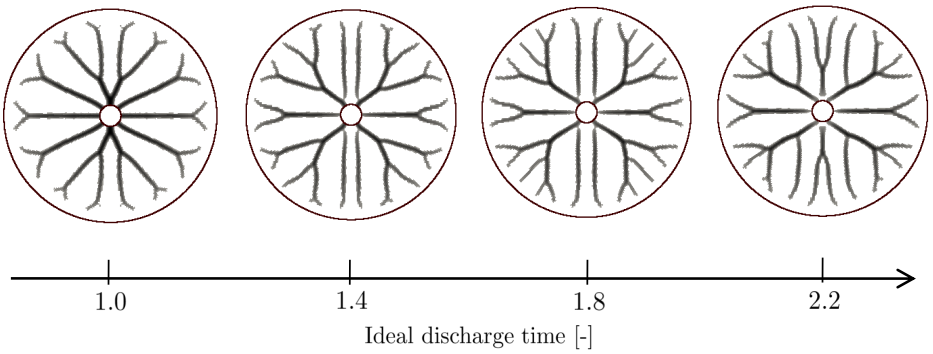

Fig. 3.17. Optimized designs obtained with the Steadiness Maximization approach for different values of the ideal discharge time

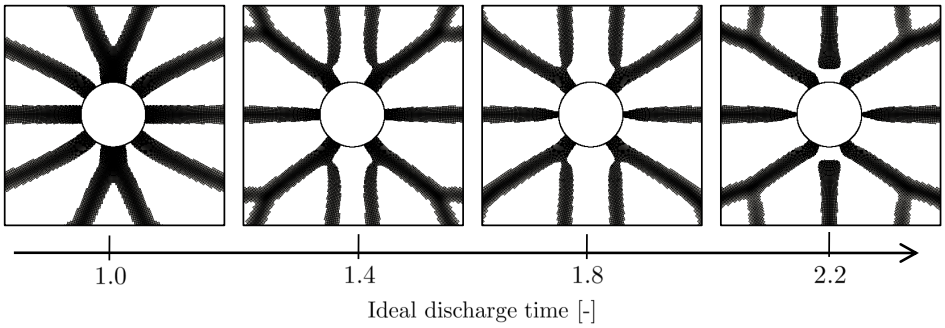

Fig. 3.18. Zoomed-in view of the region close to the internal tube.

more HCM is moved towards the external envelope through wide angle ramifications and secondary branches. In the "slow" designs (i.e. with $t^*_{f_{id}} = 1.8$ and $t^*_{f_{id}} = 2.2$), the fin base is not in contact with the internal tube and leaves a small PCM gap. For better visualization of the fin base disconnect, Figure 3.18 shows a zoomed-in view into the region close to the internal tube. This feature is effective in limiting the initial heat transfer rate but complicates the fabrication of the fin. Manufacturability is not considered in our optimization problem formulation and the practical realization of the device is beyond the scope of this chapter. However, the design trends obtained through this numerical study can still be useful to identify possible manufacturing strategies for steady power structures. For instance, a high porous metal matrix could be installed in the PCM gap to provide mechanical support to the fins. The discharge histories of the four optimized designs is shown in Figure 3.19. To enhance the readability, we plot on the x-axis the discharge time normalized with respect to the ideal discharge time $t^*_{f_{id}}$. As the final time constraint is relaxed, the real energy history gets closer to the ideal one. A large performance improvement is achievable if the discharge time is increased from 1.0 to 1.4. Even the optimized design for $t^*_{f_{id}} = 2.2$ does not perfectly match the desired discharge history.

To show that the fin disconnect increases the performance, we manually altered the design optimized for $t^*_{f_{id}} = 2.2$ (referred to as disconnected design) and filled the PCM gap with HCM to obtain the connected design shown in Figure 3.20(a), hereafter referred to as connected design 1. The energy histories for the two designs considered along with the ideal one are represented in Figure 3.20(b). The connected design 1 yields a reduction of the total time needed for discharge. However, the

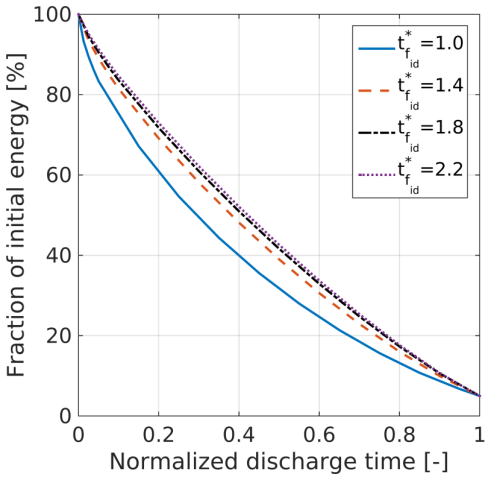

Fig. 3.19. Normalized energy history during the discharge for the 4 optimized designs

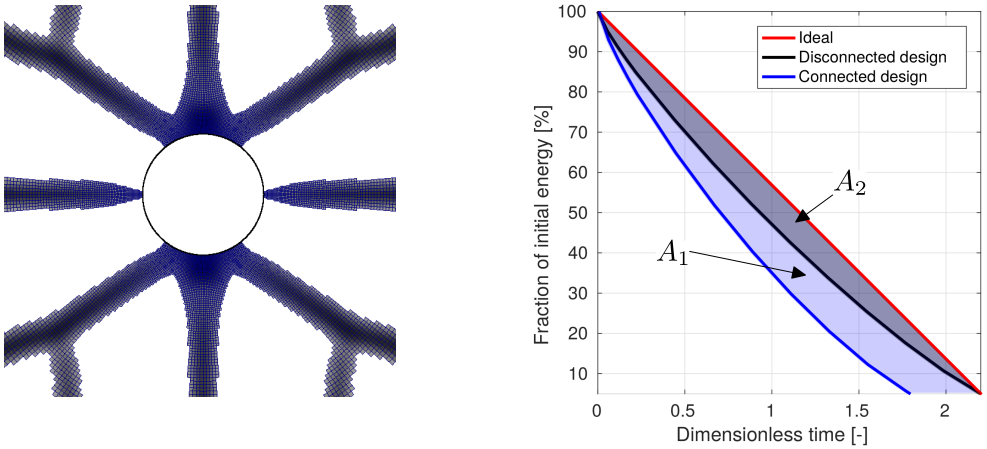

(a) (b)

Fig. 3.20. (a): Connected version of the disconnected optimized design obtained for $t^*_{f_{id}} = 2.2$; (b): comparison of the energy history during the discharge

Table 3.3. Comparison of the connected and disconnected designs

	Design		
Performance	Connected 1	Connected 2	Disconnected
Volume variation [%]	+ 1.710	- 0.001	0.000
Discharge time [-]	1.77	1.81	2.20
Objective [-]	14.63	14.21	2.68

disconnected design approximates better the ideal discharge curve. The area enclosed between the ideal discharge curve and the one of the disconnected design, i.e. A_1, is smaller than the area enclosed between the ideal discharge curve and the one of the connected design 1, i.e. $A_1 + A_2$. This demonstrates that a superior objective value is obtained with the disconnected design. Our manipulation of the design field to close the PCM gap resulted in a geometry for which the maximum volume fraction of HCM, Φ, is exceeded by 1.710 %. One may wonder whether this affects the outcome of the previous analysis. For this reason, we iteratively raised the projection threshold, η, in (2.40) to produce a third layout for which the amount of HCM differs from the maximum allowed by only - 0.001 %. This geometry is referred to as connected design 2. The objective value and the discharge time registered for the three cases are reported in Table 3.3. The results show that the connected designs result in similar performance and the amount of HCM slightly affects the achievable steadiness when all the fins are attached to the inner tube.

This example demonstrated that it is possible to manipulate the discharge history of the LHTES unit to obtain a steadier power output. The steadiness measure is improved through the use of a small PCM gap in contact with the HTF pipe that complicates manufacturing.

3.5.4 The effect of melting temperature and conductivity ratio

This section studies the effect of the PCM thermo-physical properties on both the optimized design and performance. To build physical intuition, we first consider a parametric analysis on the 1D problem presented in Figure 3.21. A bar composed of a matrix material, B, and an insert material, A, is initially at temperature $T_I^* = 1$, when suddenly comes in contact with a cold thermostat on the left boundary, Γ_d, at a temperature of $T_d^* = 0$. The right boundary, Γ_n, is insulated. We monitor how

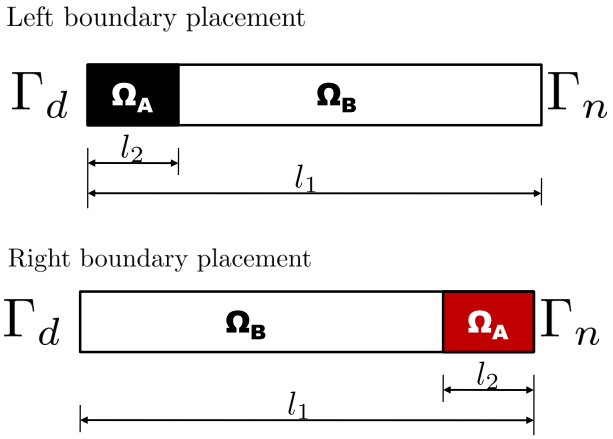

Fig. 3.21. Different setups used to investigate the effect of the melting temperature on the discharge dynamics

Table 3.4. Parameters values used for the 4 cases considered in the 1D example

	Parameter							
Case	K_A	C_A	$\mathscr{L}_A^*$	$T_{m_A}^*$	K_B	C_B	$\mathscr{L}_B^*$	$T_{m_B}^*$
1	sweeped	1	0	-	1	1	0	-
2	1	sweeped	0	-	1	1	0	-
3	1	0.66	0.66	sweeped	1	1	0	-
4	1	1	60	sweeped	1	31	0	-

different topology choices, i.e. the placement of the insert in contact with either the left or right boundary, and different material choices affect the discharge time. As for the nominal design, we consider $\Psi = 5$ %. The spatial discretization adopted consists of 500 linear Galerkin elements; the time integration is performed with a 1^{st} order BDF scheme with $\Delta t^* = 0.001$.

The material combinations investigated are summarized in Table 3.4. Cases 1 and 2 consider A and B as two sensible materials, with no nonlinearity. The former is intended to analyze the effect of the insert conductivity while the latter aims at investigating the effect of its specific heat. Cases 3 and 4 consider A as PCM and study the dynamics of nonlinear inserts embedded in a linear matrix for different melting temperatures. Case 3 analyzes a PCM with a small nonlinearity while Case 4 considers a PCM with a large nonlinearity. To allow for meaningful comparisons, materials A and B are taken with the same integral capacitance in the temperature

range $0 \leq T^* \leq 1$ such that :

$$\int_0^1 \left(C + \frac{\partial f^*}{\partial T^*} \mathscr{L}^* \right)_A dT^* = C_B. \tag{3.85}$$

The results of this parametric analysis are summarized in Figure 3.22. The ratios reported on the x-axis correspond to the properties of material A divided by the properties of material B. From the examination of Case 1 and Case 2, it can be concluded that:

- The conductivity of the insert plays a relevant role on the discharge dynamics only when it is in contact with the Dirichlet boundary, i.e. in the region characterized by high heat transfer.
- The specific heat of the insert influences remarkably the time required for the discharge only when in contact with the Neumann boundary, i.e. in the region characterized by low heat transfer.
- It is better to place high conductivity/high specific heat inserts close to the Dirichlet boundary and low conductivity/low specific heat inserts close to the Neumann boundary.

For Cases 3 and, 4 we observe the following:

- The melting temperature has some effects on the discharge time only if the insert is placed on the right boundary, i.e. the low heat transfer region.
- The melting temperature influences the optimal topology of the bar. Low melting temperature inserts are best placed close to the Neumann boundary while high melting temperature inserts should be positioned close to the Dirichlet boundary. For high melting temperatures, the insert quickly gets rid of the latent heat during the high heat flux period (i.e. at the beginning of the process) and for the remaining part of the process behaves as a low capacitance material, that is best placed close to the Neumann boundary. On the other hand, for low melting temperature inserts, the latent heat is withdrawn at the end of the process in a period characterized by low heat transfer regimes. In this latter case, it is better to choose the left boundary configuration, which makes the discharge time nearly insensitive to the insert capacitance.

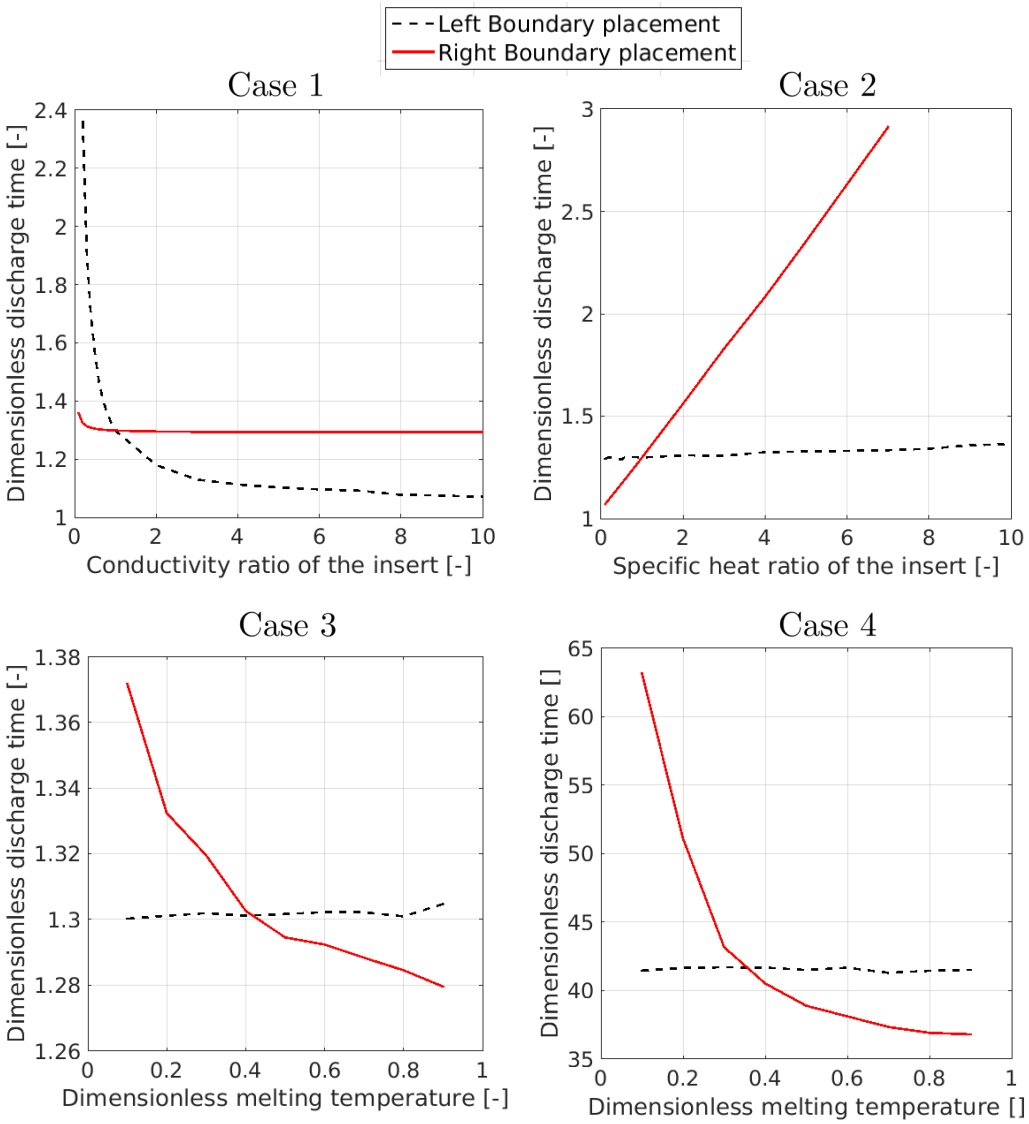

Fig. 3.22. Results of the 1D parametric analysis

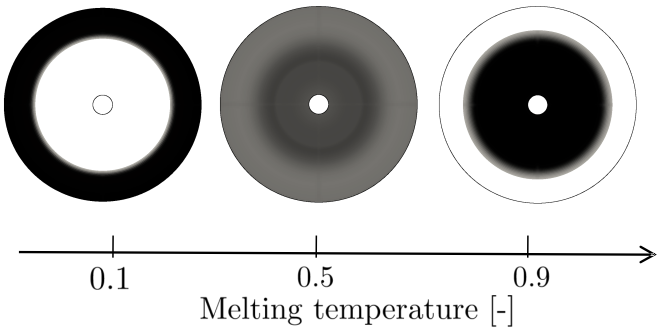

Fig. 3.23. Effect of the melting temperature on the final design. The full linear material is shown in black, the nonlinear material in white while intermediated phases are in gray

- The magnitude of this effect increases with the nonlinearity of the insert: a closer look at the y scale shows that the effect is negligible for Case 3 and becomes dominant for Case 4.

Now we use topology optimization to find the optimal topology of material A and B with the problem set-up considered in previous examples (Fig. 3.6). We choose the materials considered for Case 4. Note that only for this example, the volume fraction Φ is set to 0.5. Figure 3.23 shows the final designs obtained for 3 different melting temperatures, i.e. 0.1, 0.5 and 0.9. The linear material is shown in black, the nonlinear material in white while intermediate phases are in gray. For low melting temperatures, the nonlinear material is aggregated towards the internal tube; for high melting temperatures, it is confined on the external shell. The optimization with $T_m^* = 0.1$ and $T_m^* = 0.9$ converges well to $\{0;\ 1\}$ designs. On the other hand, the one with $T_m^* = 0.5$ has still a considerable amount of gray material. The results obtained with the 1D problem showed that at intermediate melting temperatures, $T_m^* \sim 0.5$, the latent heat slightly influences the optimal placement of the insert. Despite this different degree of convergence, the layout obtained with $T_m^* = 0.5$ confirms the findings of the 1D example: the optimized topology should be similar to the one obtained with $T_m^* = 0.9$, i.e. internal linear material/external nonlinear material.

To exclude the eventuality of convergence to unsatisfactory local minima, we perform a cross-check optimization run in which the optimized design for $T_m^* = 0.1$ is used as a starting solution to the problem with $T_m^* = 0.9$. The objective history along with snapshots of the designs at selected iterations is shown in Figure 3.24. Here,

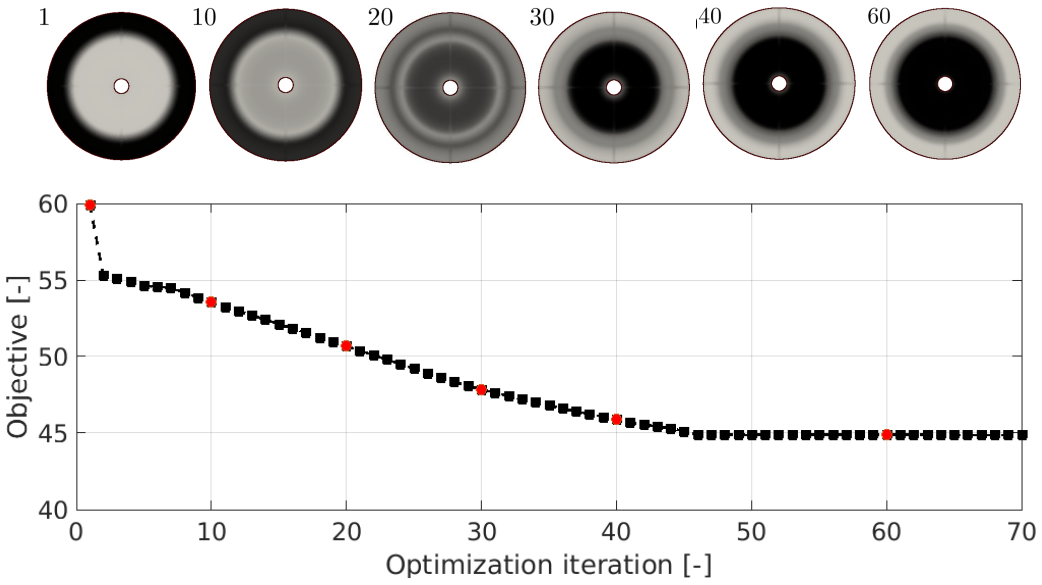

Fig. 3.24. Objective history along the optimization when the optimized design for $T_m^* = 0.1$ is used as initial guess in the optimization problem with $T_m^* = 0.9$

the layouts are not clipped at $\bar{s} = 0.1$ to facilitate the visualization of the evolution. We notice that it takes roughly 20 iterations to reverse the optimized design to a nearly homogeneous distribution. From this point onward, the topology evolves similarly to what we observed for the design at $T_m^* = 0.9$, where nonlinear material is progressively concentrated towards the external insulated boundary.

In this section, we demonstrated that the melting temperature can be responsible of topological changes for specific material choices. However, we noticed negligible effects for material properties in the range of interest for practical TES applications. This study also suggests that a topology optimization framework can be useful for the design of multi-PCM systems.

3.5.5 3D designs

In this section, we consider the design optimization of three-dimensional structures using the TM formulation.

The objective history and the design evolution along the optimization process for the 3D design with $\Psi = 5$ % is shown in Figure 3.25. The layouts shown corresponds to iso-surfaces of the design variable field at $s = 0.1$. The design is

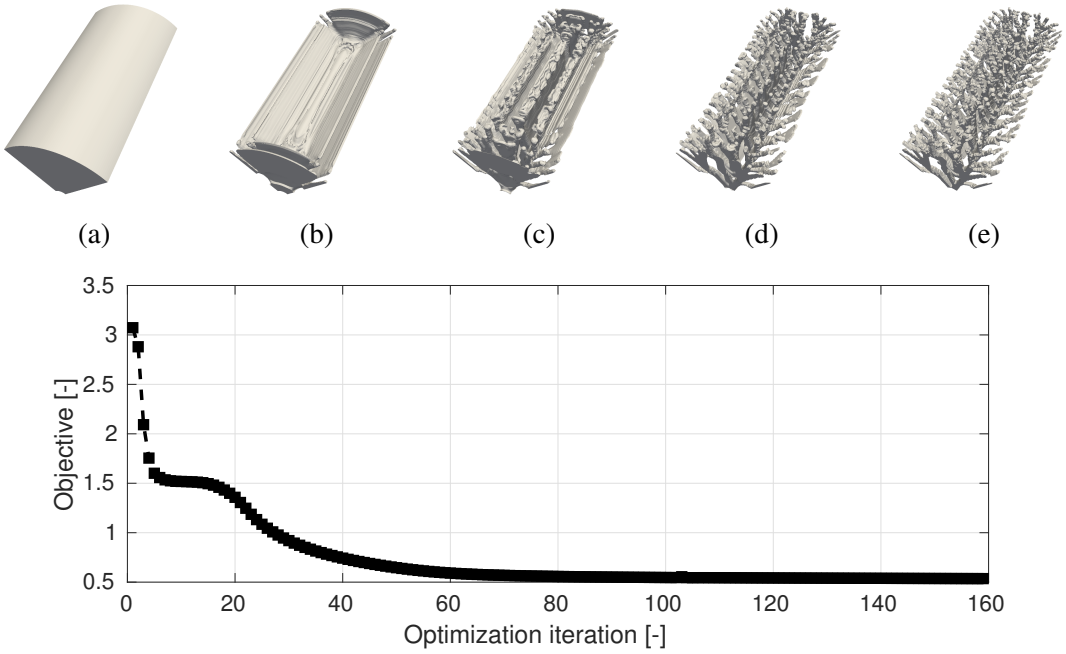

Fig. 3.25. Objective history and design evolution along the optimization process for the 3D design example with $\Psi = 5$ %. (a): Initial guess; (b): iteration 20; (c): iteration 40; (d): iteration 60; (e): iteration 100. The layouts shown corresponds to iso-surfaces of the design variable field at $s = 0.1$

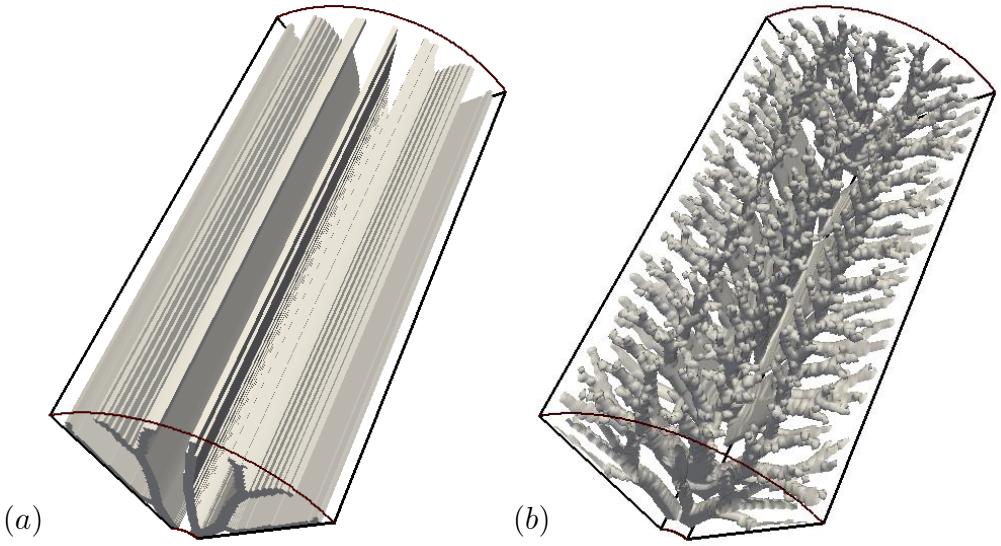

Fig. 3.26. Longitudinal 2D design obtained by extrusion (a) vs full 3D design (b)

initialized with a homogeneous design variable field as for all the 2D numerical examples. During the first 20 iterations, HCM concentrates along the top, bottom and symmetric boundaries and in a longitudinal region in contact with the HTF pipe. From Iteration 20 to Iteration 60, these regions gradually evolve into well defined HCM formations, yielding a large objective reduction. Then, these HCM features grow to extend further towards the external envelope as visible in the design at Iteration 100, resulting in only minor performance improvements.

The final 3D solution obtained after 160 design iterations is shown in Figure 3.26(b), which visualizes the main qualitative differences with the extruded 2D nominal layout (Figure 3.26(a)). The optimized geometry in 3D is an interesting mixture of some of the different fin concepts discussed in Section 3.1 such as longitudinal fins, circular fins, and pin fins. Similar to circular fins, our 3D geometry alternates cross-sections with large and small volume fractions of HCM, leaving some PCM gaps along the z axis. Furthermore, most cross sections with high HCM volume fraction show patterns similar to the 2D (longitudinal) design. Finally, the fin tips closely resemble the disordered geometries of pin fins, elongating freely in the three directions. These features yield a similar diffusion distance in all the directions, suggesting that the optimized structure also exploits the third dimension for heat transfer. To quantify the amount of heat transferred along the axial dimension, we

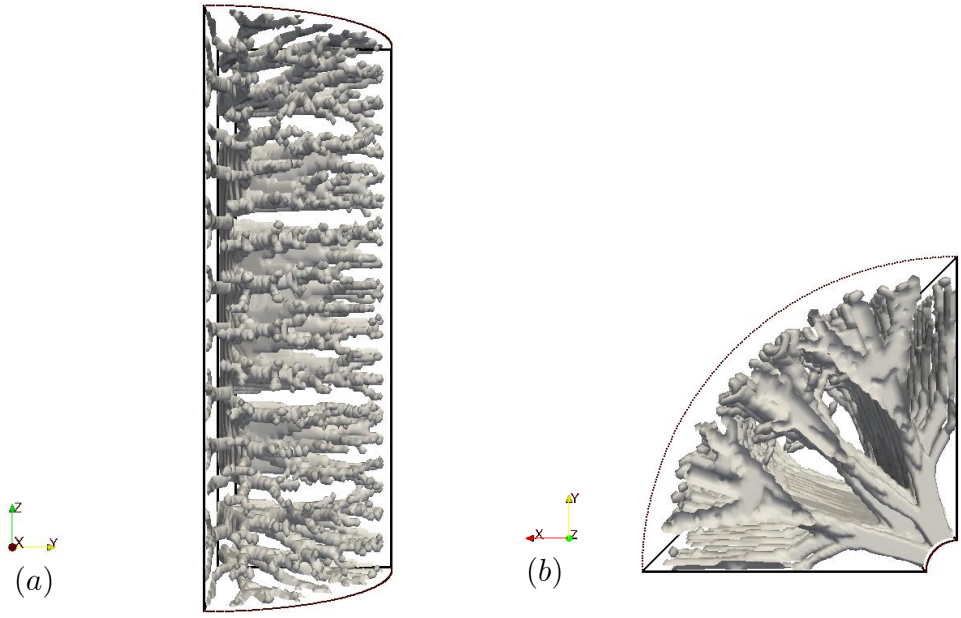

Fig. 3.27. Visualization of the optimized 3D design. (a): Top view; (b): front view

adopted the following measure:

$$\tilde{q}_z = \frac{||\bar{\nabla}_z T^*||_2}{||\bar{\nabla}_{x,y} T^*||_2}, \tag{3.86}$$

where $\bar{\nabla}$ denotes the time-averaged gradient. Note that for every extruded 2D design we have $\tilde{q}_z = 0$ %. For the nominal 3D design, we obtain $\tilde{q}_z = 153$ % meaning that a large portion of heat is transferred along the axial direction. The front and top views visible in Figure 3.27 display some additional details. As visible from the front view, the distribution of HCM concentrates more at the center than at the top and bottom boundaries. This agrees with the intuition that less HCM should be placed on the boundaries since less energy has to be extracted. Despite these boundary features, the design looks quasi-periodic along the z-axis. This suggests that structures with improved performance can be expected to be obtained through optimization studies that consider a shorter portion of the shell with a higher design resolution.

We revisit the energy versus time trade-off in 3D with 3 different values of the energy fraction, Ψ, i.e. 25 %, 10 % and 5 %. Figure 3.28(a) shows a comparison between the Pareto fronts for the 3D and the 2D cases. Exploiting the third dimension allows the Pareto front to be shifted towards smaller times. Figure 3.28(b) presents

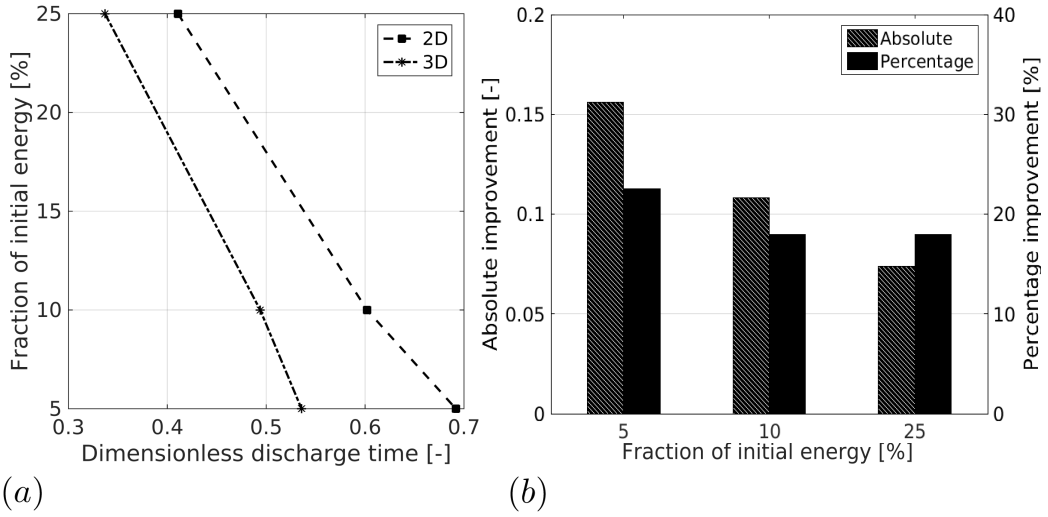

Fig. 3.28. Performance improvement obtained by considering a full 3D optimization. (a): Shift of the Pareto front; (b): summary of absolute and percentage improvements

the absolute and relative improvements achieved. We report an average discharge time reduction between 18.0 % and 22.6 % with respect to the corresponding 2D cases. In the range of values considered, the advantages of accounting for the third dimension in design studies increase for smaller desired energy fractions, Ψ.

This section highlighted the need for full 3D optimization strategies when designing TES systems with phase change. The optimized 3D designs not only show some unexpected features but also outperform the 2D alternatives by roughly 20 % due to the increased design freedom. We expect similar design trends in other volume-to-line/volume-to-area maximum access problems such as those investigated in [477].

3.6 Conclusions

In this chapter, we demonstrated the use of topology optimization for heat transfer enhancement in LHTES units. A graphical summary of the main application-oriented advances is presented in Figure 3.29. The design studies in two dimensions using the TM and the EM formulations converged on a smooth Pareto front residual energy/process time. The trade-off among these design criteria manifests with highly

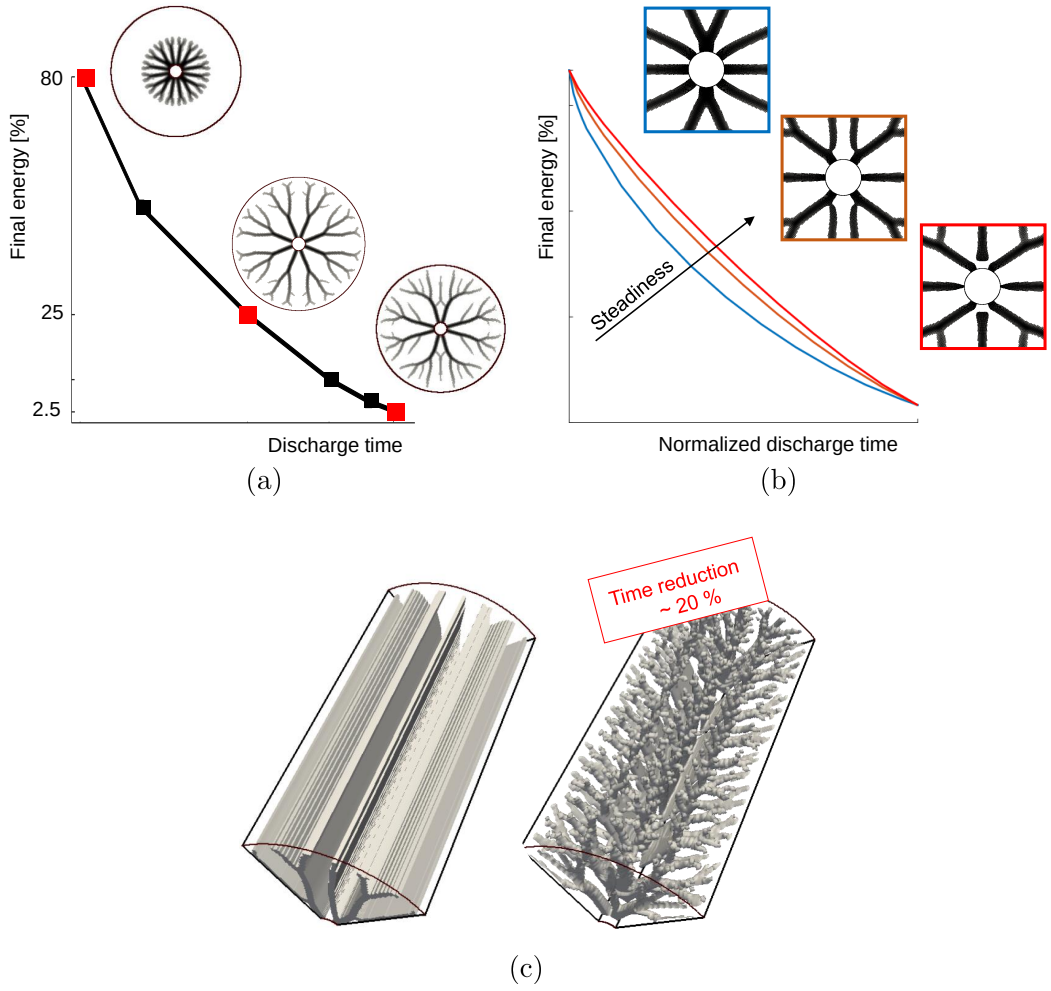

Fig. 3.29. Graphical summary of the main application-oriented advances of the chapter. (a): Design trend final energy/process time; (b): design features promoting the power output steadiness; (c): 2D vs 3D geometries

different layouts and performance (Figure 3.29(a)). By including a measure of power output steadiness in the objective, we obtained fin layouts that are disconnected from the HTF pipe (Figure 3.29(b)). A PCM gap smooths the initial heat transfer peak but complicates the manufacturing process. Our investigations on the effect of PCM properties on the optimized layouts revealed that the melting temperature can be responsible of topological changes. However, those are expected to be of practical interests only for design of multi-PCM systems. Finally, moving to a 3D design domain yielded unintuitive features that were not not apparent in reduced dimensionality (Figure 3.29(c)). The optimized layouts freely span the three dimensions such that strong heat transfer is recorded along the direction parallel to the HTF pipe. The increased design freedom led to an average 20 % reduction in the discharge time.

The results presented were obtained using the assumption of negligible convective transport. This assumption is relaxed in Chapter 5 and Chapter 6, in which natural convection is considered in the analysis.

Chapter 4

Design of multi-scale conducting structures

Engineered multi-scale structures offer exceptional design freedom. The material properties at the microscopic level can be finely controlled such that the the performance of devices is maximized for specific applications. Filling engineered multi-scale metal structures with PCMs leads to composites with spatially-varying conductivity and capacitance that could be used for thermal storage, temperature control and thermal management applications. Recent advances in Additive Manufacturing (AM) boosted a large research interest in multi-scale structures across various fields of engineering. However, important technological flaws of AM still hamper the practical applications. In this chapter, we propose a topology optimization framework to design assemblies of periodic cellular materials that can be fabricated by conventional manufacturing technologies. We demonstrate a multi-scale and multi-material framework in which the structure, the layout of the material subdomains and their micro-structures are optimized concurrently. To limit the geometrical complexity at the macroscopic scale and comply with manufacturing requirements, our design model uses level-sets parametrized by geometric primitives.

The outline of the chapter is as following. In Section 4.1, we review the state-of-the-art multi-scale heat transfer structures with a focus on the manufacturing technologies and applications to LHTES units. Section 4.2 presents both the theory and numerical model of our homogenization framework. The multi-scale and multi-material design methods are described in Section 4.3 and 4.4, respectively, while

the design models that use geometric primitives are discussed in 4.5. Section 4.6 presents and discusses the numerical results obtained for both a steady-state heat sink and an LHTES unit. Finally, Section 4.7 summarizes the main findings and identifies opportunities for future research.

Some of the contents of this chapter were presented at the 12th World Congress of Structural and Multidisciplinary Optimisation **[C1]** and are included in a paper draft in preparation for submission to Computer Methods in Applied Mechanics and Engineering ([**J6**]).

4.1 Review of multi-scale heat transfer structures

Cellular solids can be classified according to the topology of the unit cell composing their reticular structure. Stochastic foams cannot be characterized by a single cell and the topology cannot be controlled [443]. Due to the absent design possibilities, we refer to these geometries as non-engineered structures. Periodic structures are characterized by a unit cell that is repeated in either two directions (prismatic structures or Linear Cellular Alloys (LCA) [204]) or three directions (truss or lattice materials) [443]. Although manufacturing constraints are present, in this latter case the topology of the unit cell can be controlled to a certain extent. Recent advances in manufacturing have led to a new class of cellular solids where the topology of the reticular structure can be fully controlled with no need of periodicity. The topology of the cell can be tailored to location-specific requirements. These are generally referred to as architected cellular materials with ordered and location-specific structure [371]. Since the last two categories allow a precise design, we refer to both as engineered structures. Engineered and non-engineered multi-scale structures can be further divided into open-cell and closed-cell. Open-cell structures are composed of interconnected void regions, allowing a non-obstructed fluid flow [199]. Closed-cells structures are composed of separated enclosures.

The technologies available for impregnating PCM within open-cell structures are mature. The direct infiltration is a viable route but potentially yields a large amount of air bubbles trapped within the composites. According to the recent review of Zhang et al. [494], the most effective manufacturing method is the vacuum impregnation. The fabrication of PCM-metal composites using cellular structures with closed cells is also well-known. For instance, a possible approach is described

in [472], where the metal structure is slowly pressed into a mold occupied by the liquid PCM. A process similar to vacuum impregnation with no active mechanical agents was described in [264]. In the following sections, we will briefly review the manufacturing technologies and LHTES applications of multi-scale structures. Since the references mentioned above indicated that the fabrication methods of PCM-metal composites are well-established, we will focus only on the manufacturing technologies for empty cellular solids.

4.1.1 Non-engineered structures

Stochastic metal structures can be fabricated in a number of different ways. Banhart [40] divided the available processes in four categories depending on the state of matter of the metal during the fabrication. When using liquid metals, the most popular manufacturing processes include foaming by direct gas injection or insertion of a blowing agent, solid-gas eutectic solidification and investment casting [40]. Sintering is no doubt the most popular manufacturing process when using metals in the solid state. A large control over the pore size and distribution [301] can be achieved as compared to liquid-based metal processes and open-cell structures are generally obtained [403]. Finally, stochastic foams can be obtained by electro-deposition and vapor deposition when the metal is in ionic and gaseous state [40]. Also in this latter case, the manufacturing generally leads to open-cell structures [199]. Besides metals, another popular stochastic structure for heat transfer applications is Compressed Expanded Graphite (CEG). Natural graphite is first expanded by chemical and thermal treatment such that a 99.8 % porosity material is obtained [296]. Expanded graphite can then be mechanically compressed as desired to obtain high conducting matrices that are then impregnated with PCM. The large stochastic complexity of graphite matrix micro-structures in general leads to only moderate impregnation ratios ($\sim$ 80 % [296]).

Heat transfer enhancement in LHTES units using stochastic structures was an active research field in the past decades. Cabeza et al. [72] compared the performance of a commercial PCM-CEG composite to the one of stainless steel and copper pieces dispersions. Their experiments revealed the superiority of the CEG-PCM structure due to the presence of uninterrupted heat transfer paths. Mills et al. [300] also focused on CEG-PCM composites and reported an increase in the thermal conductivity from 20 to 130 times as compared to the pure PCM. Their results

presented evidence that the typical uni-axial compression leads to large thermal conductivity anisotropies. The anisotropy issue is not observed in metal foams due to the different fabrication processes involved. This may be considered an advantage with respect to CEG. Fleming et al. [140] investigated the use of a commercial aluminum foam for both melting and solidification of water. Their experimental results showed that the enhancement ranged from 100 % to 20 % for melting and solidification, respectively. This difference has to be attributed to the high thermal conductivity of the ice as compared to the liquid water. Tian and Cui [103] considered copper foams as a possible enhancement strategy. Their experiments revealed that the average heat transfer rate can be increased by 36 % during charge when compared to a case with pure PCM. The study of Zhou et al. [498] suggested that the utilization of metal foams may yield additional advantages. The authors observed a large reduction of the super-cooling effect in hydrate salts when embedded in metal stochastic structures. As early studies proved large benefits of multi-scale structures for LHTES units, researchers are now investigating the effect of some grade parameters such as the pore density (given in Pores Per Inch (PPI)) and porosity. The experiments performed by Atal et al. [36] had the aim of assessing the effect of the porosity of aluminum foams on the performance of an LHTES unit. They concluded that a lower porosity leads to a faster discharge and charge. This trend is particularly noticeable at small heat transfer rates. Zhu and co-authors [504] investigated the effect of the pore density of an aluminum foam for melting of PCM in a cavity. They found that a higher pore density leads to faster discharge dynamics due to the larger heat transfer area. The numerical results of Gao et al. [153] suggested that this trend can be questioned as natural convection is suppressed at high pore densities. The authors proposed an optimized structure with a porosity of 94 % and a pore density of 45 PPI. Recently, the trade-off between conductive and convective transport suggested an interesting novel design concept. Metallic structures can be placed only in areas interested by strong diffusion heat transfer in such a way to leave undisturbed flow in areas interested by strong convective heat transfer. This reduces the costs by limiting the amount of HCM used. Xu et al. [475] investigated this simple idea on a shell-and-tube LHTES unit. The authors proposed a system in which the metal foam fills partially the shell and optimized the filling height. In a subsequent study [474], more advanced configurations of the porous insert were investigated. A similar research [505] was conducted in the context of thermal management of electronics. The authors found through experiments

that a partial fill may yield substantial costs savings at the expense of negligible performance drops.

4.1.2 Engineered structures

A growing interest in engineered cellular structures is arising in recent years [199]. According to Tian et al. [420], periodic materials are superior to stochastic structures for heat transfer applications and there is a large room for design-related advances. Wadley [442] reviewed a wide range of fabrication processes for the mass production of periodic cellular metals. The conventional hexagonal honeycomb structures can be obtained by strip bonding of metal sheets and expansion [442]. The triangular and square honeycombs are easily fabricated by assembling slotted metal strips [442]. A wide variety of other topologies can be obtained by stacking corrugated metal sheets or by extrusion [442]. In this regard, a revolutionary manufacturing process was proposed in [91]. It consists of two steps. First, a metal oxide paste is extruded through a die. Then, the extruded medium is dried and reduced in hydrogen atmosphere so that the pure metal is recovered. A high flexibility in the distribution of the shapes and sizes of the unit cells is obtained. In the context of cellular metals with 3D periodicity, lattice micro-structures can be fabricated through investment casting, folding of perforated metal sheets, weaving and braiding of metal wires [442]. As noted by Williams et al. [462], these fabrication strategies have limited geometrical freedom for shaping the macro-structure. Although in some specific cases it is possible to customize its shape to a certain extent (e.g. by smartly cutting metal panels and sheets in honeycomb and corrugated structures), in general this can be done only by conventional subtractive manufacturing. Furthermore, all the manufacturing processes mentioned so far yield a unique micro-structure within the material. Periodicity is a fabrication requirement. Recent advances in manufacturing led to a relaxation of this periodicity constraint. Thanks to a layer-by-layer building process, AM allows a matchless geometric freedom: the topology of the cell can be varied at the macro-scale according to location-specific requirements. However, the adoption of metal-based AM is still hampered by its high costs, slow build rates, residual thermal stresses and poor finishing of parts [462]. For these reasons, Williams et al. [462] proposed to use metal oxide as a printed agent and then sinter it in a reducing atmosphere to obtain a pure metal. This approach has similarities with the extrusion process described in [91]. Mun et al. [305] used AM to fabricate

a sacrificial pattern that was then used for molding and casting. This method allows the clustering of patterns for mass production at the cost of unavoidable periodicity of the 3D-printed parts. A similar method to combine AM and investment casting was recently presented in [398]. In this case, the molds are directly printed without the need for a sacrificial pattern.

One of the first studies considering engineered periodic structures for heat transfer enhancement in LHTES units is the work of Hoogendoorn and Bart [208]. Motivated by the high cost of finned tubes, the authors tested conventional honeycomb layouts and aluminum thin strips. Their results revealed remarkable performance improvements as compared to pure PCM. A few years later, Bugaje [71] conducted some experiments to assess the performance of a star matrix obtained from expanded aluminum. The authors observed that the enhancement effect is comparable but slightly lower than the one of fins, due to the thermal contact resistance. Following the advancements claimed by these seminal works, Tong et al. [422] conducted a numerical study to asses the effect of convection in LHTES units filled by metal matrices. The authors obtained that convective effects modify the system dynamics in a significant manner only during melting. No noticeable effect was observed for solidification. An order of magnitude increase in thermal conductivity was later reported by Nayak et al. [309] with an aluminum matrix submerged into Eicosane. In both the previous studies, the authors made no assumptions on the cellular topology: the conductivity and permeability were obtained by semi-empirical equations for porous media, similar to those adopted for the modeling of stochastic structures. A specific cellular layout was investigated by Mesalhy et al. [299], who considered an orthogonal grid of circular fibers. The macroscopic conductivity was obtained analytically considering the micro-scale geometry. Their parametric study suggested that high porosities and high thermal conductivities are desirable features for large diffusion and convective transport in LHTES. Li and Wu [265] investigated a similar structure but considered HCM connections with rectangular cross-section. The authors introduced no scale separation and the conductivity was obtained by direct numerical simulation. This approach allowed studying the influence of the pore density on the performance. However, no analysis nor discussion on the effect of the cellular topology was presented. This topic was covered earlier by Fiedler et al. [139] and Tian et al. [420] in the context of heat transfer enhancement for electronics cooling. The authors investigated various cellular layouts and found that the geometry plays a significant role for performance.

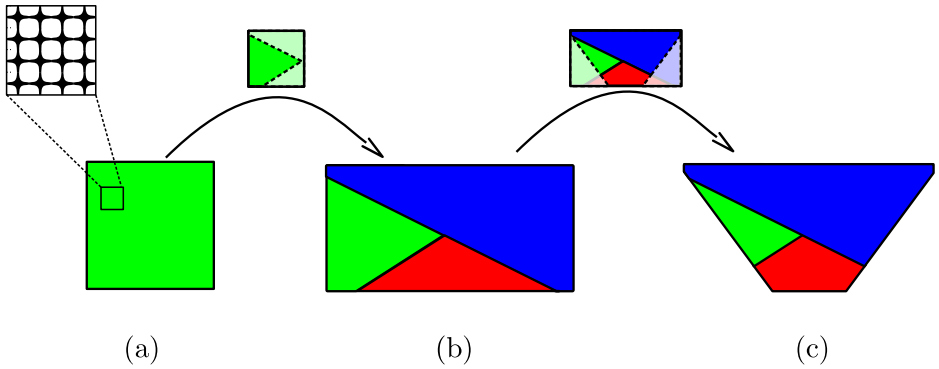

Fig. 4.1. Conceptual representation of the design model considered in this chapter. (a): Optimized periodic material; (b): optimized "machinable" assembly of periodic materials; (c): optimized "machinable" structure

4.1.3 Literature/technology gaps and design opportunities

From the literature and technology overview presented in the previous sections, we highlight three important facts:

1. A matchless control over the mechanical properties of devices is possible through architected materials with spatially-varying micro-structures [371]. However, the current mass-scale manufacturing technologies for multi-scale metal structures yield periodic cellular materials [91, 442, 305].

2. The macroscopic shape of the periodic structures fabricated by mass-production technologies can be customized only by conventional machining [462], demanding for design procedures with a tight control over their geometrical complexity.

3. The placement and macroscopic shape of multi-scale structures is crucial for some applications, e.g. LHTES units [475, 474, 505].

In this chapter, we propose a design framework that creates optimized heat transfer structures building on the previous observations. A conceptual representation is given in Figure 4.1 for the dissipator geometry considered in Chapter 2. Inspired by fact 1, we consider an assembly of a limited number of materials with local periodicity. Given fact 2, we parametrize each material subdomain such that "well-behaved" "machinable" shapes are obtained. We optimize all the micro-structures

of the periodic materials as well as their aggregation layout. As the conventional manufacturing technologies were demonstrated for a large number of microscopic layouts, we do not limit their geometrical complexity. Finally, considering facts 2 and 3, we optimize also the "external" layout of the assembly, i.e. the structure, using again a "machinable" parametrization. To our knowledge, a unique paper [261] dealt with multi-scale topology optimization with movable material subdomains. The authors of this recent valuable contribution used a discrete density-based description at the macro-scale, which does not address fact 2. Furthermore, their heuristic density threshold demands the optimization of micro-structures with predefined volume fractions, which are free to evolve in our framework.

4.2 Homogenization

Computing system responses in highly heterogeneous media is of interest in many fields of science and engineering. A direct numerical treatment is complicated by the fact that the size of the period of the micro-structure, Y, is generally order of magnitudes smaller than the size of the medium filling the macroscopic domain, Ω_D. Denoting by ε the ratio between the size of the period and the size of the medium, one could identify the following scaling behavior for the number of degrees-of-freedom to be solved for [18]:

$$N_{dof} \sim \frac{1}{\varepsilon^{N_{dim}}}. \tag{4.1}$$

Considering a typical multi-scale heat transfer structure (e.g. the 45 PPI foam proposed in [153]) filling a square cube with side length equal to 1 m, one obtains a scale ratio of $\varepsilon = 0.00085$. According to (4.1), the direct numerical solution of a multi-scale heat transfer problem in 3D involves a 1.6×10^9 increase in degrees of freedom as compared to the analysis conducted in Chapter 3. To overcome this difficulty, one can first consider a microscopic description of the problem and then formulate equivalent material models for the analysis at the macroscopic scale. There exist at least two approaches to achieve this goal. A typical route in engineering is the so-called Representative Volume Element (RVE) method. The analyst considers a microscopic problem on a period T of size $||Y|| \ll ||T|| \ll ||\Omega_D||$. Then, a constitutive behavior is reconstructed by averaging the responses to a well-chosen set of loads. As noted by Allaire [18], the averaged property may depend on the sample size, load values and boundary conditions. The second method is

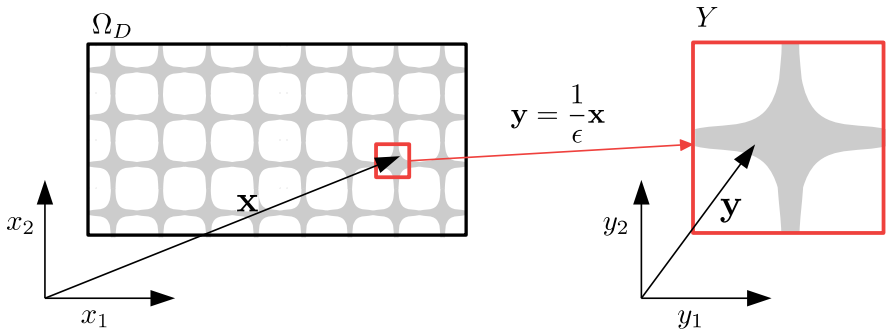

Fig. 4.2. Two-scale expansion in periodic medium

referred to as homogenization. Differently from the RVE approach, it has rigorous mathematical justifications. The homogenized properties are obtained from an asymptotic analysis on the characteristic inhomogeneity dimension, ε. This is the method of choice for the analysis of the multi-scale heat transfer structures adopted in this thesis. Figure 4.2 shows a representation of the scale separation for a periodic medium in 2D. We assign a coordinate system $\mathbf{x}$ in $\mathbb{R}^2$ to the macro-scale problem in Ω_D. The domain is composed by a set of periodic square cells with side length εY. Following standard conventions, we assign a local coordinate system $\mathbf{y} = \mathbf{x}/\varepsilon$ in $\mathbb{R}^2$ to each of the cells. The factor $1/\varepsilon$ can be regarded as a "zoom" operator that enlarges the size of the periodic cell such that it is comparable to the size of the medium at the macroscopic scale [202]. The periodicity assumption involves that the spatial variation of a generic physical property, e.g. the conductivity k, can be described as follows [202]:

$$k(\mathbf{x} + \mathbf{n}_Y \mathbf{Y} + \mathbf{y}) = k(\mathbf{y}), \tag{4.2}$$

where $\mathbf{n}_Y$ is a diagonal translation matrix whose non-zero components, n_{ii}, are arbitrary integers.

In the following section, we will briefly present the fundamentals of the homogenization method. For the sake of brevity, we will not provide mathematical proofs. We refer the interested reader to the large body of literature on the topic, for instance [364, 118, 90, 18].

4.2.1 Two-scale asymptotic expansion

The two-scale representation inspires an intuitive reflection. Any physical response will present slow variations in $\mathbf{x}$ and fast variations in $\mathbf{y}$. The key (heuristic) assumption of the homogenization method is to consider a response function of the form:

$$T(\mathbf{x}) \sim T_0(\mathbf{x},\mathbf{y}) + \varepsilon T_1(\mathbf{x},\mathbf{y}) + \varepsilon^2 T_2(\mathbf{x},\mathbf{y}) + \ldots + \varepsilon^\infty T_\infty(\mathbf{x},\mathbf{y}), \tag{4.3}$$

where each term T_i is a function of both scales $\mathbf{x}$ and $\mathbf{y}$ and Y-periodic in $\mathbf{y}$. For the following derivations, we can truncate the series at the second order. Eq. (4.3) is referred to as two-scale asymptotic expansion or ansatz. Hassani and Hinton [202] noted that this technique was already used in the theory of vibrations. Using the chain rule, we obtain the following derivation rule:

$$\frac{dT_i}{dx} = \frac{\partial T_i}{\partial x} + \frac{1}{\varepsilon}\frac{\partial T_i}{\partial y}. \tag{4.4}$$

Now consider a steady-state diffusion problem such as the one described by Eq. (2.44). Here, we do not make any assumption on the boundary conditions and on the conductivity tensor which is in general anisotropic. We obtain:

$$-\frac{\partial}{\partial x_i}\left(k_{ij}(\mathbf{y})\frac{\partial T}{\partial x_j}\right) = q_v. \tag{4.5}$$

Since the medium is assumed as periodic, the conductivity depends only upon the microscopic variable, $\mathbf{y}$ (Equation (4.2)). Casting the expansion (4.3) into (4.5) and differentiating using the rule (4.4) leads to the following cascade of equations [18]:

$$\begin{aligned}
&-\varepsilon^{-2}\left[\frac{\partial}{\partial y_i}\left(k_{ij}(\mathbf{y})\frac{\partial T_0(\mathbf{x},\mathbf{y})}{\partial y_j}\right)\right] \\
&-\varepsilon^{-1}\left[\frac{\partial}{\partial y_i}\left(k_{ij}(\mathbf{y})\left(\frac{\partial T_0(\mathbf{x},\mathbf{y})}{\partial x_j}+\frac{\partial T_1(\mathbf{x},\mathbf{y})}{\partial y_j}\right)\right)+\frac{\partial}{\partial x_i}\left(k_{ij}(\mathbf{y})\frac{\partial T_0(\mathbf{x},\mathbf{y})}{\partial y_j}\right)\right] \\
&-\varepsilon^{0}\left[\frac{\partial}{\partial x_i}\left(k_{ij}(\mathbf{y})\left(\frac{\partial T_0(\mathbf{x},\mathbf{y})}{\partial x_j}+\frac{\partial T_1(\mathbf{x},\mathbf{y})}{\partial y_j}\right)\right)+\frac{\partial}{\partial y_i}\left(k_{ij}(\mathbf{y})\left(\frac{\partial T_1(\mathbf{x},\mathbf{y})}{\partial x_j}+\frac{\partial T_2(\mathbf{x},\mathbf{y})}{\partial y_j}\right)\right)\right] \\
&= q_v.
\end{aligned} \tag{4.6}$$

Noting that a power series in ε (such as Eq. (4.3)) is zero for all ε if the coefficients are zero [18], we can solve (4.6) by considering separate equations for each power

of ε. Starting from ε^{-2}, we obtain:

$$\frac{\partial}{\partial y_i}\left(k_{ij}(\mathbf{y})\frac{\partial T_0(\mathbf{x},\mathbf{y})}{\partial y_j}\right)=0, \tag{4.7}$$

that is a periodic problem in the microscopic domain, Y. It can be shown that all the solutions to (4.7) differ by a lift function in $\mathbf{x}$. Hence, the important conclusion brought by (4.7) is that T_0 is independent of $\mathbf{y}$ so that we can write:

$$T_0(\mathbf{x},\mathbf{y})=T_0(\mathbf{x}). \tag{4.8}$$

Using (4.8), the second ε^{-1} term in Eq. (4.6) disappears. We obtain the following equation for ε^{-1}:

$$\frac{\partial}{\partial y_i}\left(k_{ij}(\mathbf{y})\left(\frac{\partial T_0(\mathbf{x})}{\partial x_j}+\frac{\partial T_1(\mathbf{x},\mathbf{y})}{\partial y_j}\right)\right)=0, \tag{4.9}$$

which gives a relationship between T_1 and T_0. Since T_1 is linear in the gradient of T_0 with respect to $\mathbf{x}$, without loss of generality it is possible to write:

$$T_1(\mathbf{x},\mathbf{y})=\omega^{(l)}(\mathbf{y})\frac{\partial T_0(\mathbf{x})}{\partial x_l}+\tilde{T}_1(\mathbf{x}), \tag{4.10}$$

which $\omega^{(l)}$ is a y-dependent linearity weight and $\tilde{T}_1$ is a constant in $\mathbf{y}$. The substitution of (4.10) into (4.9) leads to the following equation:

$$\frac{\partial}{\partial y_i}\left(k_{ij}(\mathbf{y})\left(\hat{e}_j^{(l)}+\frac{\partial \omega^{(l)}(\mathbf{y})}{\partial y_j}\right)\right)=0, \tag{4.11}$$

where $\hat{e}_j^{(l)}$ is a unit vector in the "l" direction. Here, $\omega^{(l)}$ represents the "local variation of temperature created by an average (or macroscopic) gradient", $\hat{e}_j^{(l)}$ [18]. Augmenting the homogenization equation (4.11) with periodic boundary conditions gives the so-called cell problem. The equation for ε^0 reads:

$$-\frac{\partial}{\partial x_i}\left(k_{ij}(\mathbf{y})\left(\frac{\partial T_0(\mathbf{x},\mathbf{y})}{\partial x_j}+\frac{\partial T_1(\mathbf{x},\mathbf{y})}{\partial y_j}\right)\right)-\frac{\partial}{\partial y_i}\left(k_{ij}(\mathbf{y})\left(\frac{\partial T_1(\mathbf{x},\mathbf{y})}{\partial x_j}+\frac{\partial T_2(\mathbf{x},\mathbf{y})}{\partial y_j}\right)\right)=q_v. \tag{4.12}$$

Integrating (4.12) over Y simplifies things a lot. This a consequence of a fact that is easy to verify [202]: the integral over the period of the derivative of a periodic function is zero. Hence the second term in (4.12) disappears when taking the integral. The substitution of (4.10) into (4.12) and integration leads to:

$$\frac{1}{||Y||}\int_Y \left[\frac{\partial}{\partial x_i}\left(k_{ij}(\mathbf{y})\left(\frac{\partial \omega^{(l)}}{\partial y_j}\frac{\partial T_0}{\partial x_l}+\frac{\partial T_0}{\partial x_j}\right)\right)+q_v\right] d\mathbf{y}=0, \tag{4.13}$$

which can be simplified by commuting the integral and differential operator and by rearranging the saturated indexes in the first term. These operations yield:

$$-\frac{\partial}{\partial x_i}\underbrace{\left[\frac{1}{||Y||}\int_Y \left(k_{il}(\mathbf{y})\frac{\partial \omega^{(j)}}{\partial y_l}+k_{ij}(\mathbf{y})\right) d\mathbf{y}\right]}_{k_{ij}^H}\frac{\partial T_0}{\partial x_j}=q_v, \tag{4.14}$$

where the term in bracket is the homogenized conductivity k_{ij}^H. Augmenting (4.14) with the macroscopic boundary conditions gives the so-called homogenized problem. The state field T_0 computed by solving (4.14) can be corrected using T_1 and T_2 to recover the oscillatory behavior. In this thesis, we neglect the correctors T_1 and T_2 in our homogenized solution. This approach is valid in the case of small ε values [18] as those of typical heat transfer structures. This assumption yields $T = T_0$.

The homogenization framework can be easily adapted to the simplified phase change model described in Chapter 3. One can modify the two-scale asymptotic expansion (4.3) to allow for time-dependence:

$$T(t,\mathbf{x}) \sim T_0(t,\mathbf{x},\mathbf{y})+\varepsilon T_1(t,\mathbf{x},\mathbf{y})+\varepsilon^2 T_2(t,\mathbf{x},\mathbf{y})+\ldots+\varepsilon^\infty T_\infty(t,\mathbf{x},\mathbf{y}). \tag{4.15}$$

The time dependence does not yield any contribution in Equations (4.7) and (4.9) as the chain rule (4.4) only contributes to the spatial derivatives without affecting the temporal derivatives. The cell problem is thus the same as the steady-state version (4.11). The homogenized macroscopic latent heat, $\mathscr{L}^H$, and specific heat, c_p^H, can be computed through a simple integral averaging [18]:

$$c_p^H = \frac{1}{||Y||}\int_Y c_p(\mathbf{y})\, d\mathbf{y}, \tag{4.16}$$

$$\mathscr{L}^H = \frac{1}{||Y||}\int_Y \mathscr{L}(\mathbf{y})\, d\mathbf{y}. \tag{4.17}$$

A similar conclusion could have reached by intuition. The capacitance of the medium is a *bulk* property: it is not affected by the topology of the micro-structure but only by the relative volume fractions of the material constituents.

4.2.2 Numerical solution of the cell problems

Solving the cell problems allows the components of the macroscopic conductivity to be computed. A pseudo-algorithm is composed of two steps:

1. Solve (4.11) for all the N_{dim} independent unit gradients to obtain the periodic responses, $\boldsymbol{\omega}^{(i)}$.

2. Post-process the periodic responses, $\boldsymbol{\omega}^{(i)}$, with the definition of the homogenized conductivity in (4.14) to compute all the components of the tensor. Due to the symmetry of the conductivity tensor, only 3 components are needed when $N_{dim} = 2$.

Only in a few cases this procedure can be done analytically, e.g for rank laminate composites [201]. For general microscopic structures, the homogenized properties can be obtained by numerical means. In this thesis we follow the FE route. Detailed derivations of FE formulations for (4.11) in the context of linear elasticity are presented in [173, 201] while a concise Matlab implementation is reported in [29]. The weighted integral statement of the cell equation (4.11) over Y is written as:

$$\int_Y w^h \left(\frac{\partial}{\partial y_i} \left(k_{ij}(\mathbf{y}) \left(\hat{e}_j^{(l)} + \frac{\partial \omega^{(l)}(\mathbf{y})}{\partial y_j} \right) \right) \right) d\mathbf{y} = 0, \tag{4.18}$$

where w^h represents an admissible weighting function. Integrating by parts and neglecting the boundary integrals due to the periodicity condition leads to the following weak form of the cell problem:

$$\int_Y \frac{\partial w^h}{\partial y_i} k_{ij} \frac{\partial \omega^{(l)}}{\partial y_j}\, d\mathbf{y} + \int_Y \frac{\partial w^h}{\partial y_i} k_{ij} \hat{e}_j^{(l)}\, d\mathbf{y} = 0. \tag{4.19}$$

The periodic response, $\omega^{(l)}$, is approximated by the trial function, $\omega^{(l)^h}$. The weighting and approximation functions are taken from the following function spaces:

$$\begin{aligned} \mathscr{U}_Y &= \{\omega^{(l)^h} \in \mathscr{H}^1(Y);\ \omega^{(l)^h} \text{ is Y-periodic on } \partial Y\}, \\ \mathscr{V}_Y &= \{w^h \in \mathscr{H}^1(Y);\ w^h = 0 \ \text{ on } \partial Y\}, \end{aligned} \tag{4.20}$$

where $\mathscr{U}_Y$ and $\mathscr{V}_Y$ are Hilbert spaces consisting of scalar functions with square integrable first derivatives. We write the approximate periodic response as a product between nodal values and spatially-varying shape functions as following:

$$\omega^{(l)}(\mathbf{y}) \simeq \omega^{(l)^h}(\mathbf{y}) = \sum_{i=1}^{N_n} N_i(\mathbf{y})\omega_i^{(l)} = \mathbf{N}^T \boldsymbol{\omega}^{(l)}, \tag{4.21}$$

where $\boldsymbol{\omega}^{(l)}$ denotes a column vector with nodal values of $\omega^{(l)}$. The test functions are taken equal to the shape functions as in the Galerkin method, i.e. $w^h = N$. With this assumption, the residuals, $\mathbf{R}_m^{(l)}$, of the weak-form Galerkin model for the cell equation read:

$$\mathbf{R}_m^{(l)} = \mathbf{K}_Y \boldsymbol{\omega}^{(l)} + \mathbf{e}^{(l)} = \mathbf{0}, \tag{4.22}$$

where $\mathbf{K}_Y$ has the same definition as in Eq. (3.42) but the integration is performed of Y rather than over Ω and the load vector $\mathbf{e}^{(l)}$ is defined as:

$$\mathbf{e}^{(l)} = \int_Y \frac{\partial \mathbf{N}}{\partial y_i} k_{ij} \hat{e}_j^{(l)}\, d\mathbf{y}. \tag{4.23}$$

Solving (4.22) is simple as it is a linear system. The unique care in the solution procedure should be taken to deal with the periodic boundary conditions. In this thesis, we adopt the method of Lagrange multipliers to enforce periodicity, using multi-freedom linear constraints. The vector of unknowns is augmented with the vector of Lagrange multipliers, one per each constraint. The microscopic conductivity matrix, $\mathbf{K}_Y$, is bordered to include the Lagrange multiplier contributions to the state equations and the equations stating the connectivity between the degrees of freedom. This method was preferred over a master-slave elimination because of the easier implementation within the presented numerical framework. However, this approach enlarges the dimensionality of the system matrix and its positive definiteness is lost. For these reasons, elimination methods are generally preferred for numerical homogenization as pointed out by the authors of [29].

4.2.3 Verification through forward homogenization

Here, we test the accuracy of the FE micro-scale analysis framework described in the previous section.

Perrins et al. [331] investigated hexagonal and square arrays of high conducting cylinders embedded in a low conducting matrix material. They used a method devised by Rayleigh [348] to compute the effective conductivity of the composite material. Their analysis yielded analytical results in the form of a series expansion. For square arrays, the conductivity expression obtained from the truncation of the expansion at the third order reads [331]:

$$k_{ii}^{H} = k_{ii_{BM}} \frac{1-2\Phi}{\sigma+\Phi-\frac{0.075422\Phi^{6}\sigma}{\sigma^{2}-1.060283\Phi^{12}}-\frac{0.000076\Phi^{12}}{\sigma}}, \tag{4.24}$$

where Φ is the volume fraction of the cylindrical inclusions and σ is a parameter defined as:

$$\sigma = \frac{1+\hat{k}}{1-\hat{k}}, \tag{4.25}$$

where $\hat{k}$ is the conductivity ratio between the HCM cylinders and the BM matrix. The considered microscopic layout yields an isotropic medium, hence $k_{11} = k_{22}$ and $k_{12} = k_{21} = 0$. We analyze a case with $\hat{k} = 10$ and $k_{ii_{BM}} = 1$ and compare the results obtained for different volume fractions, Φ, of the HCM. For this choice of $\hat{k}$, the analytical expression (4.24) retains a precision of the predictions to the fourth digit up to a maximum volume fraction of $\Phi = 0.4$ [331].

We solve the cell problem by FE analysis as described in the previous section. We consider a square microscopic domain, Y, with a side of length $L = 1$, which is discretized with quadrilateral bilinear elements. We use three alternative computational grids: a coarse mesh with 20×20 elements with characteristic size $h_y = 0.05$, an intermediate mesh with 50×50 elements with characteristic size $h_y = 0.02$ and a fine mesh with 100×100 elements with characteristic size $h_y = 0.01$. The cylinders are represented in the analysis through a density approach. Verifying the geometry representation model is also of interest here since this computational framework will be used for the multi-scale analysis and design through topology optimization. Each node falling within the radius of the inclusions is assigned a microscopic design variable of $s_m = 1$, representing the HCM. A value of $s_m = 0$ is assigned to the other nodes and represents the BM. The elemental densities are obtained by filtering the

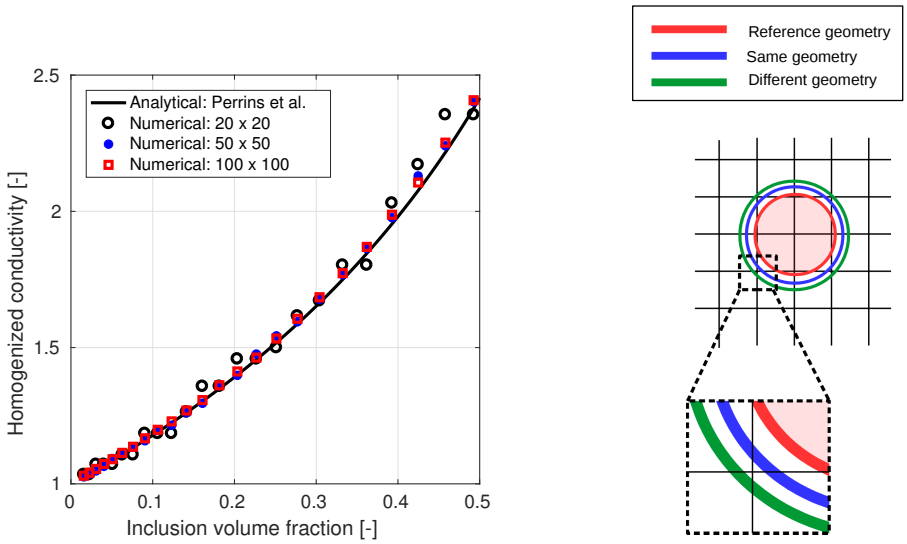

(a) (b)

Fig. 4.3. (a): Verification of the numerical homogenization framework through comparison with analytical predictions of Perrins et al. [331]; (b): discontinuity of the geometry representation with respect to the inclusion radius

nodal design variable field with (2.37) and projecting it using (2.40) with $\beta = 1000$. The filter radius is calculated such that elemental densities are simple average of the nodal design variable values. The steep projection applied helps to get rid of the "gray" material. In case it exists, the conductivity is interpolated linearly. Figure 4.3 presents the homogenized conductivity obtained using the three meshes and the one predicted using the analytical expression (4.24). The numerical curves approximate well the analytical one. The absolute relative mean error and its standard deviation are 0.022 and 0.044 for the coarse mesh, 0.009 and 0.012 for the intermediate mesh, 0.008 and 0.010 for the fine mesh. We notice that the accuracy of the prediction slightly deteriorates for high volume fractions. Furthermore a step-wise trend is visible for the coarse mesh curve. This is a result of the density-based geometry representation. As visible in Figure 4.3(b), the geometry changes are not continuous with respect to the radius of the inclusion. When the radius is increased from the red circle to the blue circle, no geometry changes are observed. The same number of nodes are contained within the circle. On the other hand, the geometry gets modified when increasing the radius of the inclusion to create the green circle. This phenomenon yields only minimal effects as the mesh is refined.

4.3 Multi-scale analysis and design

In this section, we present multi-scale analysis and design approaches using topology optimization. First, we introduce material design through inverse homogenization and verify the developed optimization capabilities using the array of cylinders considered in the previous section. Then, we present several multi-scale approaches with particular focus on the one adopted in this thesis.

4.3.1 Material design

Homogenization allows the computation of effective macroscopic properties when the periodic micro-structure is known. From early days in topology optimization, researchers focused on inverse homogenization. This optimization problem addresses the following design question: *what is the microscopic layout required to obtain a target macroscopic property?* This branch of research is also referred to as material design.

The first contribution to material design within the topology optimization community can be traced back to Sigmund [389]. The author formulated the problem as a weight minimization with equality constraints prescribing the values of the elasticity tensor components. His results demonstrated that extremal macroscopic physical properties can be obtained if the micro-structure is carefully controlled. In particular, materials with negative Poisson ratio were designed. This design framework was later used for bulk modulus maximization in three-phase composites [162] and for design of extremal (e.g. negative) thermal expansion [388] materials. In the field of heat transfer, several works dealt with the inverse homogenization of conductivity-like properties. Hyun and Torquato [214] explored the micro-structures filling the gap between the HS bounds. Similarly, Zhou and Li [503, 501] used topology optimization to find the micro-structures realizing the Milton-Kohn (MK) bounds considering general three-phase anisotropic composites. Two-phase and three-phase isotropic micro-structures lying on the theoretical bounds are found to conform to Vigdergauz-like [435] formations [74]. Following these early contributions, material design expanded rapidly to other fields such as the permeability maximization in fluidic systems [181], design of functionally-graded materials [502], multi-functional materials [112], and metamaterials [115]. A thorough review on the use of topology optimization for material design was recently published by

Cadman et al. [74]. According to the authors, two alternative optimization problem formulations gained popularity among researchers. The first formulation aims at obtaining extremal material properties. For instance, when seeking the composite with minimal macroscopic conductivity the objective can be stated as:

$$z(s_m) = \sum_{i=1}^{N_{dim}} \sum_{j=1}^{N_{dim}} k_{ij}^{H}(s_m), \tag{4.26}$$

The second formulation aims at obtaining a target value for each component of the conductivity tensor. In this case, the objective can be written using a quadratic measure of the deviation from the target:

$$z(s_m) = \sum_{i=1}^{N_{dim}} \sum_{j=1}^{N_{dim}} \left(k_{ij}^{H}(s_m) - k_{ij}^{H^*} \right)^2, \tag{4.27}$$

where $k_{ij}^{H^*}$ denotes the target conductivity tensor. Since material design will be a fundamental building block of our multi-scale framework, we perform a verification example. We consider the inverse version of the homogenization example of the previous section. By imposing the target isotropic conductivity and the volume fraction of the inclusion, we aim at recovering a square array of cylindrical inclusions as those investigated by Perrins et al. [331]. We consider the same design domain, Y, adopted for the forward example and discretize it using the 100×100 elements mesh. A design variable, s_m, is assigned to each node of the mesh. The density filter (2.37) with $r_{f_m} = 0.051$ and the projection operator (2.40) with $\beta_m = 1$ and $\eta_m = 0.5$ are used to obtain the microscopic physical design variables, ρ_{s_m}, defined at the element level. The objective is defined as in Eq. (4.27) using the conductivities calculated with Eq. (4.24) for a specified volume fraction, Φ, of HCM. The physical design variable, ρ_{s_m}, is used to interpolate the conductivity using a SIMP law (Equation (2.28)). The microscopic penalization exponent, p_m, is raised every 200 design iterations using the following continuation scheme $p_m = \{3;\ 5;\ 7\}$. As we wish to recover a precise target volume fraction, the standard linear volume constraint (2.29) is modified as follows:

$$\left(\int_Y \rho_{s_m} d\mathbf{y} - \Phi \int_Y d\mathbf{y} \right)^2 - \varepsilon_\Phi \leq 0, \tag{4.28}$$

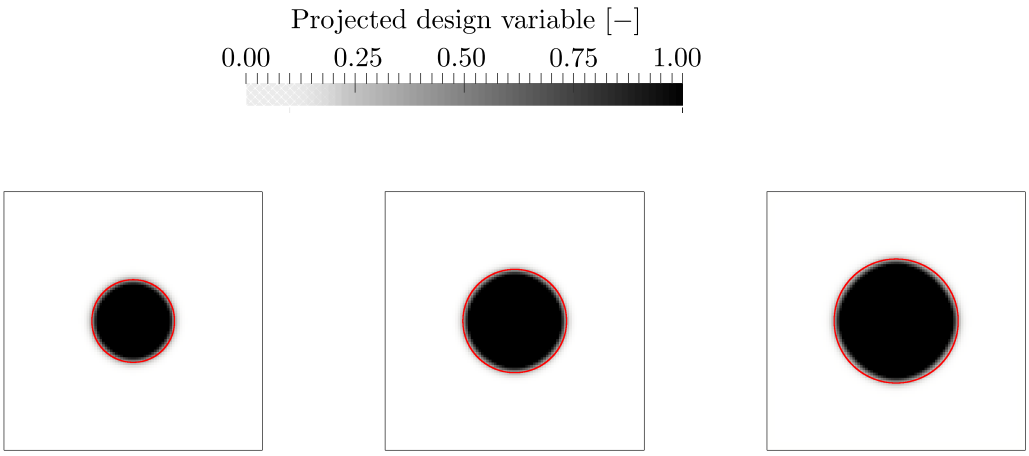

Fig. 4.4. Verification of the current framework through inverse homogenization with different volume fractions. (a): $\phi = 0.0804$; (b): $\phi = 0.1256$; (c): $\phi = 0.1809$. The red lines show the boundaries of the target HCM cylinders considered in Perrins et al. [331]

where ε_Φ is a small number here set to 1×10^{-4}. The micro-structure layout is evolved using GCMMA with the same parameters listed in Table 2.1. The objective and constraints sensitivities are calculated using the discrete adjoint method described in Section (2.3.2). Figure 4.4 presents the results obtained considering inclusions or radius $r = \{0.16;\ 0.20;\ 0.24\}$ corresponding to volume fractions of $\Phi = \{0.0804;\ 0.1256;\ 0.1809\}$. The red lines represent the boundary of the target cylindrical inclusions. The acceptable qualitative agreement suggests that our topology optimization framework for material design yields sufficiently accurate results to be integrated in a multi-scale design optimization framework.

4.3.2 Multi-scale design

Material design yields tailored micro-structures with desired macroscopic properties. However, their utilization in real macroscopic systems may be non-optimal due to the complexity and variety of boundary conditions and performance metrics. For this reason, the idea of integrating the design at both scales arises naturally. The

designers can modify the micro-structure to tailor effective properties in such a way that the performance of the macro-scale system is optimized.

The first contribution to multi-scale topology optimization is probably the hierarchical method of Rodrigues et al. [355]. For each element of the macroscopic FE mesh a micro-structure is optimized. Hence, in general this multi-scale approach yields N_e different micro-structures. The flow of computations is organized in two nested loops. At the macro-scale (the outer loop), the optimal distribution of material is sought to obtain maximum compliance under a volume constraint. At the micro-scale (the inner loop), the topology of the micro-structure is modified to yield local maximum strain energy. The micro-scale problems are also subject to a maximum volume constraint, fixed by the amount of material allocated in the macroscopic loop. This has clear similarities with the homogenization approach for topology optimization that was proposed by Bendsoe and Kikuchi [55] in the early days of the method. However, in that seminal work [55], the authors limited the design freedom at the micro-scale to the angle and size of the rectangular holes. On the other hand, in [355] full design freedom is allowed at the micro-scale through the use of a density-based geometry description. The hierarchical approach was later extended to the optimization of 3D structures [93] and utilized for a variety of applications such as bi-material laminated composite design [96] and bone remodelling [95]. In an interesting recent development, Coelho et al. [94] modified the original approach considering a limited number of subdomains with a unique micro-structure. This is in contrast with the "point-wise varying micro-structure" of the original method and represents a step towards the practical manufacturing. The authors acknowledged that "the optimal solution obtained will depend on the designer experience to define a proper domain subdivision". For this reason, they first conducted some preliminary multi-scale optimization runs using the original "point-wise" formulation; then, they analyzed the distribution of the composites and heuristically selected a suitable domain subdivision. A nonlinear version of the hierarchical method was recently presented in [308]. This paper introduced another modification to the original problem formulation. In this case, no macroscopic design variable enters the optimization routine. The material allocation at the macroscopic scale is entirely governed by the microscopic design variables.

Although the hierarchical approach demonstrated to be effective in many cases, the inner iteration loop modifies the micro-structures and in turn affects the macroscopic equilibrium. According to Xia and Breiktopf [469, 471], this "interface

nonlinearity" yields to divergence when used in BESO frameworks for topology optimization [212]. Hence, the authors adopted a FE^2 strategy [138], where the micro-scale design is treated as a generalized nonlinear behavior. The advantages of this approach include an easy extension to problems with constitutive nonlinearities at the micro-scale and a possible utilization of reduced order models, see e.g. [470]. Both the hierarchical and FE^2 methods described so far are based on a clear decoupling between the optimization processes at the microscopic and macroscopic scales. This allows a straightforward parallel implementation. However, the point-wise strain energy maximization approach within the inner loop can hardly be extended to problems beyond solid mechanics. Sivapuram et al. [397] recognized this difficulty and proposed a general decomposition strategy based on the objective and constraints linearization that is applicable to any design problem.

An alternative and rather "exotic" approach for multi-scale design is Free Material Optimization (FMO), which dates back to the contributions [352, 52]. It consists of solving design optimization problems at the two scales in a *sequential* manner [372]. The macro-scale problem is first solved using the constitutive properties as design variables, e.g. the components of the conductivity tensor. Then, several material design problems are solved to obtain the target properties. As noted by [397], a strong limitation of this approach is that it may be hard to set physics attainability constraints on constitutive tensors and conservative assumptions are required in most cases.

Instead of using homogenization to bridge the scales, Alexandersen and Lazarov [14, 15] used multi-scale FEM [119] for multi-scale design. Here, the structure is completely resolved and no scale separation is introduced. This approach yields three advantages: it takes into consideration the finite size of microscopic structures, which is important when ε is not particularly small; it allows boundary effects to be considered; it ensures the creation of fully connected microscopic structures. Following a similar research direction in which the structure is fully resolved, Wu and co-authors [468] recently considered the optimization of 3D-printed bone-like structures. The micro-structures arise from the imposition of a p-norm aggregation of *local* volume constraints, computed with a filtering procedure similar to (2.37). Reticular structures were obtained also in the case of aligned principal stress directions through the use of an anisotropic filter. Resolving the full structure yields discrete problems, involving a large number of degrees of freedom. In [14], the authors managed to limit the computational complexity by using the same spectral

preconditioner for several design iterations and by enforcing a periodicity condition on the micro-structures. Despite these advances, the extensions of the method to complex multi-physics problems, requiring nonlinear and/or transient analysis, is still considered a challenge.

Most of the multi-scale methods above can be seen as a "varying-gray" type of optimizations. A point-wise varying micro-structure is optimized. This questions the local periodicity assumption for homogenization and complicates manufacturing [94]. Motivated by this latter argument, Liu and Cheng [274] developed a multi-scale optimization procedure that considers a single periodic micro-structure within the macroscopic design domain, Ω_D. The placement of the periodic composite at the macroscopic level is also optimized, yielding a concurrent material and structure design optimization framework. Note that optimizing a unique material and seeking its optimal placement does not fit within the hierarchical framework. When a unique micro-structure is considered, the design changes at the macro-scale would be prevented. The method is based on two sets of design variables:

- $s_m \in [0,\ 1]$ governing the micro-structure topology in such a way that $\rho_{s_m}(s_m) = 1$ denotes material and $\rho_{s_m}(s_m) = 0$ denotes BM or void in the microscopic design domain, Y. The microscopic physical design variables, ρ_{s_m}, are used to interpolate the material properties when solving the cell problem (4.11) using a conventional SIMP procedure such as (Equation (2.28)):

$$k_{ij}^m(\rho_{s_m}) = k_{ij_{BM}} + (k_{ij_{HCM}} - k_{ij_{BM}})\rho_{s_m}^{p_m}, \tag{4.29}$$

  where k_{ij}^m is the value of conductivity adopted in the micro-scale problem. In the original paper [274], the authors adopted neither filtering nor projection at the micro-scale such that $\rho_{s_m} = s_m$.

- $s_M \in [0,\ 1]$ governing the macro-structure topology in such a way that $\rho_{s_{M_0}}(s_M) = 1$ denotes *composite* and $\rho_{s_{M_0}}(s_M) = 0$ denotes BM or void in the macroscopic design domain, Ω_D. The macroscopic physical design variables, $\rho_{s_{M_0}}$, are used to interpolate the homogenized material properties when solving the macroscopic problem. Considering the conductivity, we have:

$$k_{ij}(\rho_{s_{M_0}}, \rho_{s_m}) = k_{ij_{BM}} + (k_{ij}^H(\rho_{s_m}) - k_{ij_{BM}})\rho_{s_{M_0}}^{p_M}, \tag{4.30}$$

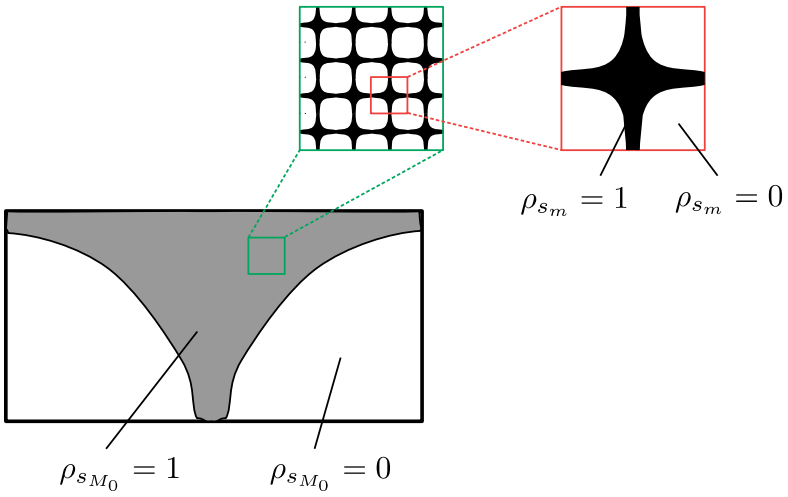

Fig. 4.5. Graphical representation of the PAMP multi-scale design model

where p_M is the macroscopic SIMP exponent; the homogenized conductivity, k_{ij}^H, depends on the microscopic design variables, ρ_{s_m}, through the utilization of (4.29) when solving the cell problem (4.11). The subscript "0" in $\rho_{s_{M_0}}$ denotes the density field of the structure and is used to distinguish it from other macroscopic density fields arising in our multi-material design optimization framework. In the original paper [274], the authors adopted neither filtering nor projection at the macro-scale such that $\rho_{s_{M_0}} = s_M$. Although Eq. (4.30) can be regarded as a SIMP procedure at the macro-scale, the homogenized properties are in general anisotropic. Hence, the authors [274] named the material law (4.30) as Porous Anisotropic Material with Penalization (PAMP) interpolation.

In contrast to the typical mono-scale topology optimization procedures where a "black-white" design is sought and to the previously described "varying-gray" multi-scale framework, this approach tries to obtain "gray-white" material configurations [274]. A graphical representation of the PAMP design model for the dissipator geometry considered in Chapter 2 is given in Figure 4.5. Both the set of design variables are updated following a one-shot procedure without inner optimization loops. The optimization problem can then be formulated without particular modifications with respect to the mono-scale case. A simple augmentation of the design variable set is required to include both s_m and s_M. In their seminal paper [274], Liu and Cheng constrained the local volume fraction of the composite to comply with practical

fabrication techniques. We did not find this fabrication requirement in the successive works of their research group. The examples of application of this method span different fields of engineering. For instance, Niu et al. [311] designed multi-scale structures for maximized dynamic performance, Guo et al. [190] considered compliance maximization under load uncertainties while in [113] the authors applied the PAMP optimization procedure to thermoelastic problems.

The ability to optimize a single microscopic structure and to find the optimized placement of this composite in the macroscopic domain is a unique feature of the PAMP framework. Due to the manufacturing requirements highlighted in Section 4.1, we build primarily on this approach to develop our multi-scale design framework. We extend the original method in two ways. First, instead of a unique micro-structure, we consider a fixed number of different micro-structures filling different subdomains. We control the geometry of the subdomains using a multi-material design framework (see Section 4.4). Second, we parametrize both the structure and the subdomains using geometric primitives to allow a higher control over the geometrical complexity (see Section 4.5). The layout of the structure is evolved using a structure level set field, $\phi_0(\mathbf{s}_M)$. This geometry description is then mapped to the elemental density field, $\rho_{s_{M_0}}$, as described in Section 4.4.1

4.4 Multi-material analysis and design

The advances in topology optimization towards multi-material devices proceeded in a number of different directions. Early developments along the density-based route can be found in [388], [162] and [386]. Using material design through inverse homogenization, the authors designed the micro-structure of a composite made of two materials and void. Their approach requires two density fields. A generic material property, $(\cdot)$, is interpolated as follows [388]:

$$(\cdot) = \rho_{s_{M_0}}^p \left((1 - \rho_{s_{M_1}}^p)(\cdot)_1 + \rho_{s_{M_1}}^p (\cdot)_2 \right). \tag{4.31}$$

In Eq. (4.31), $\rho_{s_{M_0}}$ is used to define the transition between the structure and void as done for single-material SIMP and is usually augmented with a $(\cdot)_{min}$ to prevent singularities in the solution of the physical problem. The second density variable can be seen as a mixture coefficient such that $\rho_{s_{M_1}} = 1$ denotes pure material 2 while

$\rho_{s_1} = 0$ denotes pure material 1. The material interpolation law (4.31) was later extended in [404] to allow an arbitrary number of material phases, N_m, through the introduction of $N_m - 1$ design variable fields. The generalization of (4.31) can be written as follows [404]:

$$(\cdot) = \rho^p_{s_{M_0}} \left(\sum_{j=1}^{N_m-1} \prod_{i=1}^{j-1} \rho^p_{s_{M_i}} \left(1 - \rho^p_{s_{M_j}}\right) (\cdot)_j + \prod_{i=1}^{N_m-1} \rho^p_{s_{M_i}} (\cdot)_{N_m} \right). \tag{4.32}$$

The authors noted that premature convergence to unsatisfactory local minima was likely with a high number of material phases. Hence, both a modified penalization strategy and an alternative weighting of the material properties were proposed. This framework is referred to as Discrete Material Optimization (DMO). Another approach that is worth of mention in the density direction is the one followed by Yin et al. [481]. The authors used an exponential peak function model to describe the transition between different materials. This allows the inclusion of any number of materials if the "width" of the material peaks is sufficiently small. The advantage of this method is that it requires the introduction of a single design variable field. However, to our knowledge this approach encountered limited popularity.

The earliest level-set treatments of multiple material phases built on the partitioning level-set scheme. This method was developed in [497] to simulate the behavior of bubbles and droplets in complex multi-phase flows. Each material domain, Ω_i, is parametrized by a unique level set field, ϕ_i, such that:

$$\Omega_i(\mathbf{x}) = \{\mathbf{x} \in \Omega : \phi_i(\mathbf{x}) > 0\}. \tag{4.33}$$

The computational domain, Ω, is partitioned in a family of N_m material domains $\{\Omega_1; \Omega_2; \ldots; \Omega_{N_m}\}$ such that:

$$\Omega = \bigcup_{i=1}^{N_m} \Omega_i, \quad \Omega_i \cap \Omega_j = \emptyset \qquad \text{for } i \neq j. \tag{4.34}$$

Using this approach requires $N_m - 1$ level-set fields since the BM or void is not parametrized explicitly. In design optimization studies, the number of design variables, N_s, scales linearly with the number of materials as in multi-material SIMP. Due to (4.33), this method requires no-overlap between the positive level-set regions. This should be enforced in the optimization process yielding $N_m - 2$ constraints

that may impact the regularity of the optimization problem and the computational complexity of its solution procedure. A similar drawback is shared by the piece-wise constant level-set model used in [266, 414, 282]. Although this approach has the advantage of using a unique LSF, the material overlaps should be impeded explicitly in the optimization process. Wang and Wang [451] presented a multi-material topology optimization method in which the level-sets do not directly represent the material domains. This decoupling strategy allows the overlap of the positive level-set regions, eliminating the need for non-overlap constraints. The interface between all the materials, Γ_m, is obtained from the union of all the level-set zero contours:

$$\Gamma_m = \bigcup_{i=1}^{N_m} \Gamma_i, \quad \Gamma_i(\mathbf{x}') = \{\mathbf{x}' : \phi_i(\mathbf{x}) = 0\}. \tag{4.35}$$

The material domains are then identified by all the regions bordered by Γ_m. This means that the intersections of the positive level-set regions now represent additional material domains. Collecting all the level-set functions in a unique vector $\boldsymbol{\phi} = [\phi_1,\ \phi_2,\ \ldots,\ \phi_{N_m-1}]^T$, this material parametrization concept can be expressed in vector form:

$$\Omega_i(\mathbf{x}) = \{\mathbf{x} \in \Omega : \mathbf{H}(\boldsymbol{\phi}) = \mathbf{v}_i\}, \tag{4.36}$$

where $\boldsymbol{v}_i$ is a constant vector with components $v_{ij} \in \{0;\ 1\}$ and $\mathbf{H}$ is a vector Heaviside function. Since the authors took inspiration from a level-set framework [434] developed for image processing, this multi-material treatment is commonly referred to as "color" level-set. This approach yields $N_m = 2^{N_\phi}$ material domains with N_ϕ being the number of level-sets. The color level-set method was applied successfully to several optimization problems, ranging from stress-based design [189] to heat transfer [506] and metamaterial design [458].

Although this improved scaling behavior of N_ϕ with respect to N_m significantly decreases the computational complexity, such a high number of material domains may be undesirable. For instance, if one wishes to optimize the configuration of five materials, three level-sets are needed and three redundant material phases are created. A suitable rule should be identified to treat them in the analysis. For this reason, Wang et al. [457] reverted to a linear N_ϕ- N_m scaling. The material domains

are identified through the following rule:

$$\Omega_i(\mathbf{x}) = \begin{cases} \{\mathbf{x} \in \Omega_D : \phi_i(\mathbf{x}) < 0\} & \text{for } i = 1 \\ \{\mathbf{x} \in \Omega_D : \phi_j(\mathbf{x}) > 0,\ \phi_i(\mathbf{x}) < 0\} & \text{for } i = 2,\ \ldots,\ N_m - 1,\ \ j = 1,\ \ldots,\ i-1 \\ \{\mathbf{x} \in \Omega_D : \phi_j(\mathbf{x}) > 0\} & \text{for } i = N_m,\ \ j = 1,\ \ldots,\ N_m - 1 \end{cases}. \tag{4.37}$$

With this approach, $N_\phi = N_m - 1$ level-sets are required to describe the arrangement of N_m materials and no redundant material regions are created. Differently from the partitioning level-set scheme [497], here the overlap between the positive level-set regions is allowed without leading to the overlap between material domains. A generic property, $(\cdot)$, can be computed using:

$$(\cdot) = \sum_{j=1}^{N_m-1} \prod_{i=1}^{j-1} H(\phi_i)\left(1 - H(\phi_j)\right)(\cdot)_j + \prod_{i=1}^{N_m-1} H(\phi_i)(\cdot)_{N_m}. \tag{4.38}$$

It is useful to define N_m material indicator fields, χ_i, similar to the density variables adopted for single-material density-based procedures. In our convention $\chi_i(\mathbf{x}) = 1$ if $\mathbf{x}$ lies within Ω_i and $\chi_i(\mathbf{x}) = 0$ otherwise. The material indicator field is defined as follows:

$$\chi_i = \begin{cases} \prod_{j=1}^{i-1} H(\phi_j)\left(1 - H(\phi_i)\right) & \text{for } i = 1,\ \ldots,\ N_m - 1 \\ \prod_{j=1}^{N_m-1} H(\phi_j) & \text{for } i = N_m \end{cases}. \tag{4.39}$$

Using this definition, Eq. (4.38) can be simplified into:

$$(\cdot) = \sum_{i=1}^{N_m} \chi_i (\cdot)_i. \tag{4.40}$$

Since this is the multi-material model of choice in this thesis, we further illustrate the method with a simple conceptual example. Consider the structure represented in Figure 4.6, which is enclosed by the design domain boundary, Γ_D, and composed of three different materials, i.e. Ω_1, Ω_2 and Ω_3. Two LSFs (ϕ_1 and ϕ_2) are needed to describe this material configuration. The three material domains are defined as follows:

$$\begin{aligned} \Omega_1(\mathbf{x}) &= \{\mathbf{x} \in \Omega_D : \phi_1(\mathbf{x}) < 0\}, \\ \Omega_2(\mathbf{x}) &= \{\mathbf{x} \in \Omega_D : \phi_1(\mathbf{x}) > 0, \phi_2(\mathbf{x}) < 0\}, \\ \Omega_3(\mathbf{x}) &= \{\mathbf{x} \in \Omega_D : \phi_1(\mathbf{x}) > 0, \phi_2(\mathbf{x}) > 0\}. \end{aligned} \tag{4.41}$$

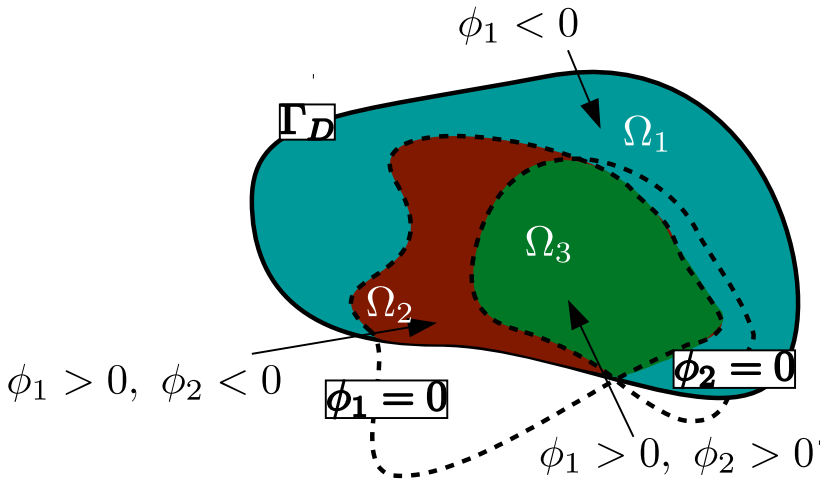

Fig. 4.6. Schematic of the multi-material level-set model adopted in this thesis (Wang et al. [457])

Using (4.39), the material indicator functions for this case are computed as:

$$\begin{aligned} \chi_1 &= 1 - H(\phi_1), \\ \chi_2 &= H(\phi_1)\,(1 - H(\phi_2))\,, \\ \chi_3 &= H(\phi_1)H(\phi_2). \end{aligned} \tag{4.42}$$

As noted by the authors of [457], the explicit expression (4.38) facilitates the sensitivity analysis. We add that another key advantage of (4.38) is that it allows a straightforward integration with density-based analysis models. Although this approach has several similarities with the multi-material density-based mixture model (4.31), a level-set description is here utilized. When using level-sets parametrized by geometric primitives, we can benefit of an easier control on the geometrical complexity of the material domains. This allows obtaining "well-behaved" "machinable" shapes as those required by the conventional fabrication methods of multi-scale structures (see Section 4.1). Further details on the geometric primitive design framework will be given in the Section 4.5.

4.4.1 Density-based mapping of level-sets

In this chapter, we account for the level-set geometry description in the analysis model by using a density-based procedure that allows an easy integration with the macroscopic analysis framework described in Chapter 3. LSFs are first mapped into the $[0,\ 1]$ interval through the use of a trigonometric smoothed Heaviside projection $\tilde{H}$ (Eq. (2.3)). Then, an elemental density is assigned to each FE of the mesh through a direct point-wise mapping based on the position of each element centroid (Eq. (2.4)). At the end of this procedure, the level-set field, ϕ_i, is converted to a density field:

$$\rho_{s_{M_i}} = \tilde{H}(\phi_i) \qquad \text{for } i = 0,\ \ldots,\ N_m - 1, \tag{4.43}$$

where for $i = 0$ we obtain the density-based mapping of the structural level-set field adopted in the PAMP interpolation (Eq. (4.30)). The density fields obtained for $i > 0$ cannot be used directly as material indicator functions to weight the material properties. Substituting (4.43) into (4.39) leads to the following relation between the material indicators and densities:

$$\chi_i = \begin{cases} \prod_{j=1}^{i-1} \rho_{s_{M_j}} \left(1 - \rho_{s_{M_i}}\right) & \text{for } i = 1,\ \ldots,\ N_m - 1 \\ \prod_{j=1}^{N_m - 1} \rho_{s_{M_j}} & \text{for } i = N_m \end{cases}. \tag{4.44}$$

The comparison of Eq. (4.44) with Eq. (4.32) shows that the obtained analysis model corresponds to a generalized SIMP strategy with $p = 1$ and $\rho_{s_{M_0}} = 1$. The utilization of a smoothed Heaviside function yields regions with intermediate density within the design domain. This shares some similarities with the inherent fuzziness at the interfaces when using the density filter (2.37). Note that by modifying the Heaviside smoothing half-bandwidth, ξ, we do not have the direct control on the size of the smearing on the design domain. This depends also on the local gradient of the LSF at the interface. When the level-sets are parametrized by nodal design variables, some regularization techniques may be required to control the gradients near the interface [427]. Otherwise the blurred region may extend dramatically where the gradients are flat, leading to an anisotropic bias during design optimization procedures. Using level-sets parametrized by geometric primitives allows LSF gradients to be obtained analytically. A possible strategy is to rescale ξ based on local gradient information. Since the macro-shapes adopted in this chapter are reasonably "well-behaved" and ξ is computed such that the intermediate densities span over a few elements, we

used a fixed ξ and did not observe any anisotropic effect on both the analysis and design optimization. Furthermore, since intermediate density values are unavoidable, we do not adopt any SIMP-like penalization here. In preliminary optimization runs, we noted that penalizing the intermediate densities may yield the undesirable effect that the length of the material interfaces is minimized, leading to poorly performing configurations. The inaccuracies in the analysis due to intermediate non-physical material may affect the outcome of the optimization. For this reason, some tuning was necessary to select the value of the "smearing" parameter, ξ, in (2.3). The optimized designs are then analyzed using $\xi = 0$ to make sure the layouts perform as expected. Alternatively, one could project the density fields using (2.40) and slowly raise the projection steepness parameter, β, along the optimization. Further developments of this option are left for future studies.

As in Chapter 3, three material properties need to be interpolated at the macro-scale, i.e. the conductivity ratio, K, the capacitance ratio, C, and the latent heat switch, γ. Due to the multi-scale optimization framework described in Section 4.3, the conductivity at the macro-scale is in general anisotropic. Hence, each component of the conductivity tensor, K_{lm}, should be interpolated separately. We use the multi-material formulation (4.38) to obtain the composite properties and the PAMP interpolation (4.30) to switch between the composite and the BM. With this approach, the conductivity ratio, K_{lm}, is expressed as:

$$K_{lm}(\mathbf{s}) = \left(1 - \rho_{s_{M_0}}\right) + \rho_{s_{M_0}} \sum_{i=1}^{N_m} \chi_i(\mathbf{s}_M) K^H_{lm_i}(\mathbf{s}_m), \tag{4.45}$$

where the vector of microscopic and macroscopic design variables are stacked in $\mathbf{s} = [\mathbf{s}_m^T \ \mathbf{s}_M^T]^T$. In design studies in which we do not consider the design optimization of the structure, we set $\phi_0 > 0$ so that we obtain $\rho_{s_{M_0}} = 1$ everywhere in Ω_D. Note that for $\rho_{s_{M_0}} = 0$ we obtain $K_{lm}(\mathbf{s}) = 1$ corresponding to the conductivity of pure PCM in our dimensionless settings. For the purpose of computing the linear volume constraint (2.29), it is useful to introduce a normalized density of HCM at the macro-scale, corresponding to the ρ_s used in Chapter 3. To avoid confusion with the other density-like variables, we will refer to this quantity as local volume fraction with Φ_{loc}. This can be obtained as a generic property through weighting of the material

indicator functions and the structural density field :

$$\Phi_{loc}(\mathbf{s}) = \rho_{s_{M_0}} \sum_{i=1}^{N_m} \chi_i(\mathbf{s}_M)\Phi_{m_i}(\mathbf{s}_m), \tag{4.46}$$

where Φ_{mi} denotes the *microscopic* volume fraction of the HCM for each material:

$$\Phi_{m_i} = \frac{\int_Y \rho_{s_m} d\mathbf{y}}{\int_Y d\mathbf{y}}. \tag{4.47}$$

The first term in (4.45) is not considered in (4.46) since $\Phi_{loc} = 0$ in pure PCM regions. As discussed in Section 4.2, the latent heat and capacity contributions do not depend upon the microscopic layout. We can formulate their interpolation by exploiting the definition (4.46). The latent heat switch is computed as:

$$\gamma(\mathbf{s}) = 1 - \Phi_{loc}(\mathbf{s}), \tag{4.48}$$

while the capacitance contribution is computed as:

$$C(\mathbf{s}) = 1 + \left(\frac{(\rho c_p)_{HCM}}{(\rho c_p)_{PCM}} - 1 \right) \Phi_{loc}(\mathbf{s}). \tag{4.49}$$

4.4.2 Superposition of interfaces

Here, we present and discuss a possible issue which may arise during the superposition of the interfaces using a density-based mapping of the multi-material framework (4.37). With this goal, we consider a simple 1D example.

Figure 4.7(a) shows a schematic representation of the example. A bar with length $L = 1$ is composed of three materials, occupying Ω_1, Ω_2 and Ω_3. The material interfaces are positioned such that there is no overlap and a minimum thickness of the material patches is guaranteed. In this example, we consider $l_{\Gamma_{23}} = 0.3$ and $l_{\Gamma_{12}} = 0.1$. This geometry can be represented by using two level-set fields such as ϕ_1 and ϕ_2 depicted in Figure 4.7. After discretizing the bar with 100 equal-length FEs, we map the level-set fields on the piece-wise constant density fields, $\rho_{s_{M_1}}$ and $\rho_{s_{M_2}}$, based on the position of the element centroids. For this operation, we adopt the smoothed Heaviside (2.3) using a smoothing half-bandwidth of $\xi = 0.2$. This is a rather large half-bandwidth but serves for the purpose of enlarging the interface

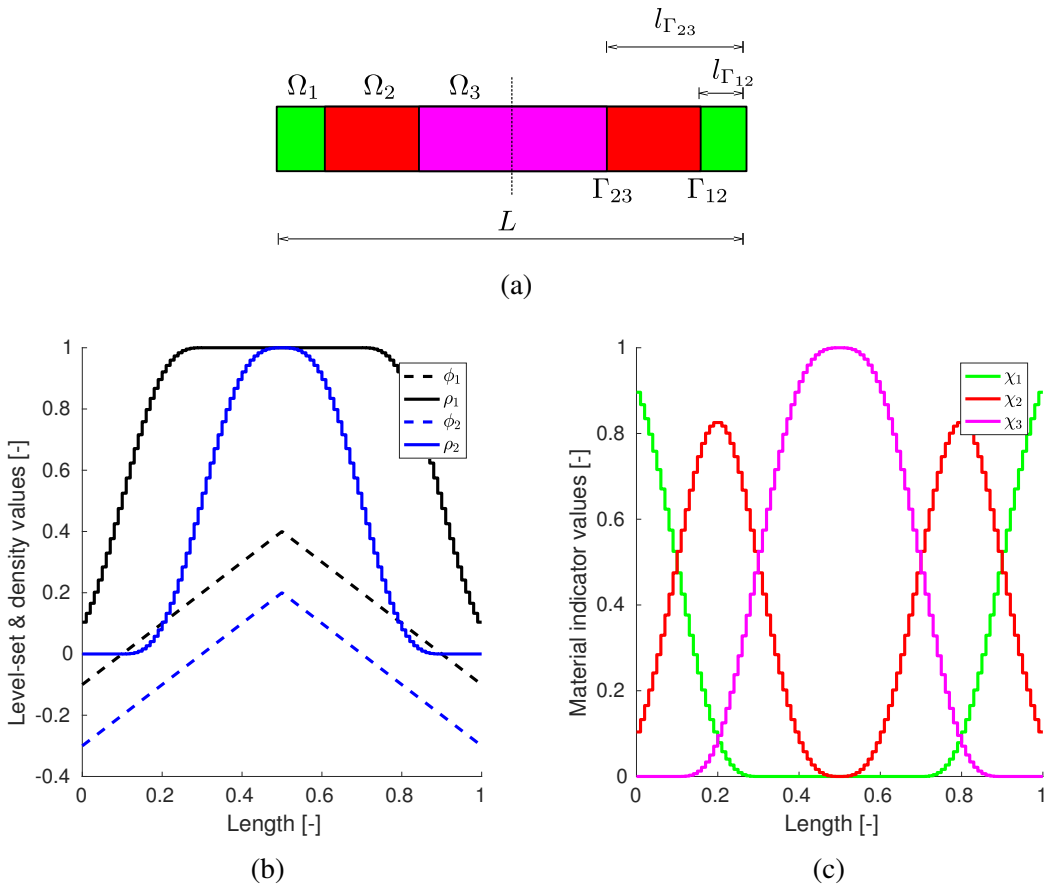

Fig. 4.7. (a): Multi-material bar configuration yielding no particular accuracy issues; (b): level-set description and density-based mapping; (c): material indicator fields

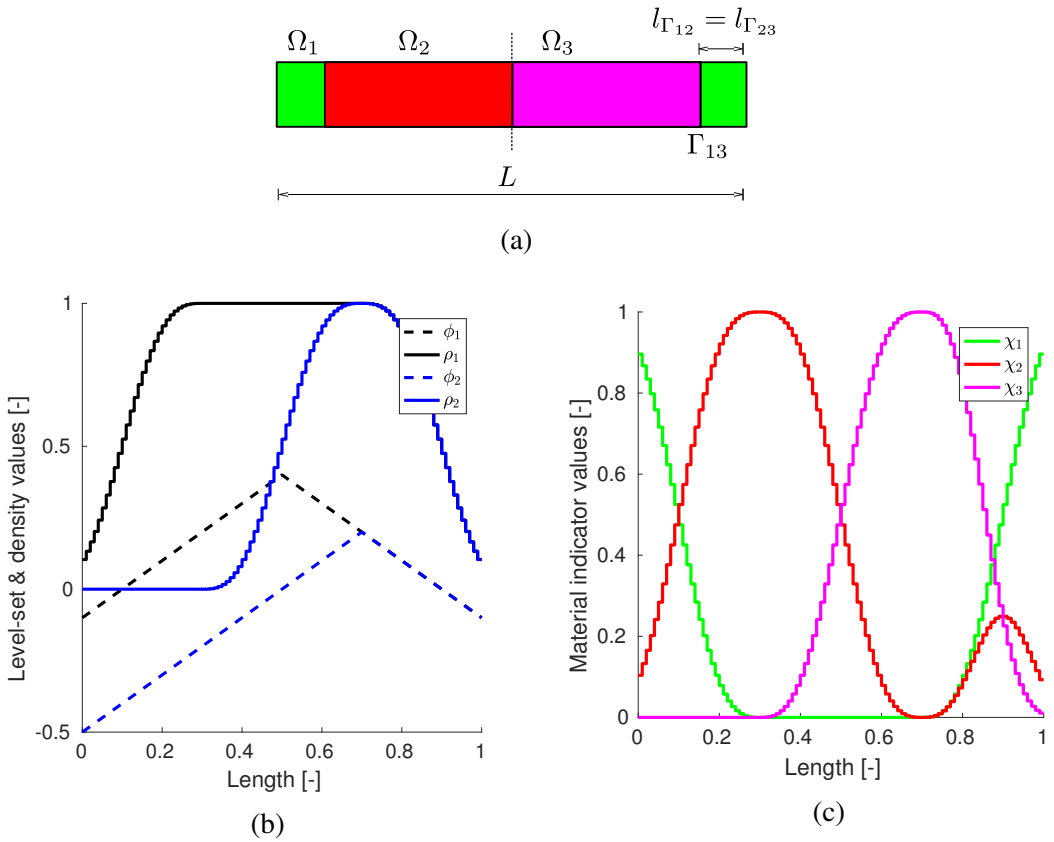

Fig. 4.8. (a): Multi-material bar configuration yielding accuracy problems at the interface; (b): level-set description and density-based mapping; (c): material indicator fields

smearing and magnifying its effect. The material indicator fields are computed from the density fields according to (4.44). The results are shown in Fig. 4.7(c). Although the smearing will affect the outcome of the prediction, this material configuration is not responsible for particular accuracy problems. Each material indicator, χ_i, is higher then zero only in the regions close to each Ω_i patch.

Let us now consider a different material placement such as the one presented in Figure 4.8(a). The material domain Ω_3 is now shifted along the x-axis such that the interfaces Γ_{12} and Γ_{23} are coincident and a material interface Γ_{13} is created. A possible level-set multi-material description and the corresponding element-wise constant density-based mapping is represented in Figure 4.8(b). The material indicators obtained from the utilization of (4.44) are shown in Figure 4.8(c). Although the material 2 is not connected to the interface Γ_{13}, its material indicator field, χ_2,

experiences a peak there. This may modify considerably the material property fields and consequently the numerical predictions. Furthermore, it is expected that the optimization framework will try to leverage this flaw by creating and smartly placing the unphysical overlapping interfaces within the design domain. It is possible to reduce the peak width by acting on ξ. However, since this problem is inherent in the density-based version of the multi-material description (4.37), it is not possible to reduce the peak magnitude. Due to the highlighted computational inaccuracy, the smoothing half-bandwidth, ξ, should be chosen carefully in multi-material design studies. Furthermore, we always analyze the optimized designs using $\xi = 0$ to make sure that layouts perform as expected.

4.5 Geometric primitives design model

In many cases of practical interest, it is desirable to obtain optimized layouts with specific geometric requirements. According to the review on the manufacturing options presented in Section 4.1, designers often wish to obtain cellular periodic structures and assemblies of structures featuring "well-behaved" "machinable" shapes with a limited geometrical complexity. Another example is the case in which a truss-like structure should be manufactured by assembling a number of available bars and one aims at obtaining optimized geometries with straight members. The ground structure approach adopted in truss optimization allows a straightforward treatment of this requirement. However, this capability is lost when moving to a continuum setting. In typical nodal or elemental density-based topology optimization procedures, it is hard to accommodate the geometric constraints. This issue motivated the development of topology optimization using geometric primitives. The first work in this research direction was conducted by Norato et al. [315]. The authors used fixed-width fixed-thickness rectangular bars parametrized by the bar end-points. The geometry in the design space, where the bars are defined, is mapped on the analysis space through the concept of geometric projection [314]. The elemental density is defined as a measure of the intersection between the structural member and the filter kernel:

$$\rho_{s_{M_0}}(\mathbf{x}) = \frac{||N^e \cup \Omega_s||}{||N^e||}, \tag{4.50}$$

where Ω_s indicates the region occupied by the structure. Under the assumption that the structural member boundary is straight in the intersected region, the elemental

density can be obtained analytically using a signed distance function of the element centroid from the collection of bars. A Kreisselmeier Steinhauser (KS) function [251] was used to aggregate the distance functions computed with respect to multiple structural members. This framework was later extended to 3D problems [494], where optimized plate structures are sought, and to stress-based topology optimization [493]. In [494], the authors introduced an additional sizing variable for each plate to allow the optimizer for removal of the structural members. This was penalized using a RAMP interpolation. Furthermore, an additional design variable field was introduced to allow arbitrary-shaped holes and non-rectangular boundaries. Differently from the initial idea presented in [315], in both [494] and [496] the authors smoothly aggregated the density fields resulting from the different structural members rather than aggregating the distance functions. They used a KS function in [496] and a p-norm function in [494].

Other works using geometric primitives in topology optimization originated with the primary aim of establishing a direct link between the geometry models used in topology optimization and in Computer Aided Design (CAD) systems. In [188], the authors referred to this approach as Moving Morphable Component (MMC) and described it as an "adaptive ground structure approach" for topology optimization. The layout was described using the level-set approach. The structural LSF, ϕ_0, was obtained as follows:

$$\phi_0(\mathbf{x}) = \max_i \left(\phi_{p_i}(\mathbf{x})\right), \tag{4.51}$$

where ϕ_{p_i} denotes the level-set field of each moving component. This corresponds to a union operator on the structural members. Note that the authors did not assign a sizing variable to each structural member as done in [494]. They noted that the removal of geometric primitives is possible through a complete overlap of the moving components. The LSF of each member, ϕ_{p_i}, was defined using superellipses parametrized by 5 design variables. This framework was later extended by the same authors [187] to components with variable thickness and curved skeletons using a simple coordinate transformation. This allows the parametrization of components with complex shapes. Both contributions [188] and [187] employed an XFEM analysis framework. Motivated by the need for increased computational efficiency, in [495] the authors demonstrated topology optimization with geometric primitives using the Ersatz material approach. A polynomially smoothed Heaviside function was used to map the level-set field on the $[0,\ 1]$ interval. Then, the elemental density

was obtained as average of the structural LSF at the element nodes. Using the Ersatz material approach, Zhang et al. [495] formulated an hybrid density/level-set approach for the optimization of structures with embedded components. The latter were described by geometric primitives. In a later development, the authors [493] showed that the MMC design model allows geometric complexity to be controlled with ease through the use of a component indicator function that depends explicitly on the design variables. More recently, Sharma [381] developed an XFEM-based design framework using geometric primitives. The author extended the approach to 3D linear elastic problems and thermo-elasticity. Furthermore, he introduced an anisotropic filtering scheme that yields smooth boundaries with no undesirable mass losses.

4.5.1 Structure and materials parametrization

In this chapter, we adopt a geometric primitives design model based on level-sets as done in [188]. The structural components and material domains are described by combinations of rectangles, squares, ellipses or circles. We will refer to any of these as patch. The level-set field of a patch, ϕ_{p_i}, is defined using the level-set function of a superellipse in $\mathbb{R}_{\geq 0}$. In 2D, we have:

$$\phi_{p_i}(\mathbf{x}^\star) = 1 - \left(\left(\frac{x_1^\star}{a} \right)^{p_c} + \left(\frac{x_2^\star}{b} \right)^{p_c} \right)^{\frac{1}{p_c}}, \tag{4.52}$$

where the generalization of norm allows the degree of "cuboidness" of the component to be tuned by modifying the norm exponent p_c, $a > 0$ is the half-length, $b > 0$ is the half-width and $\mathbf{x}^\star$ denotes the local coordinate system of the patch. The transformation from the Cartesian coordinates to the local coordinates is obtained using:

$$\begin{bmatrix} x_1^\star \\ x_2^\star \end{bmatrix} = \begin{bmatrix} \cos\theta & \sin\theta \\ -\sin\theta & \cos\theta \end{bmatrix} \begin{bmatrix} x_1 - x_1^c \\ x_2 - x_2^c \end{bmatrix}, \tag{4.53}$$

where x_1^c and x_2^c are the coordinates of the patch center. Note that the sign choice in (4.52) is motivated by the need to comply with the standard level-set parametrization (2.2), where the structure fills the positive level-set region. The level-set field can be evolved by acting on 5 design variables, i.e. $\{a,\ b,\ \theta,\ x_1^c,\ x_2^c\}$. Hence, the patch can stretch, elongate, rotate and move within the design domain.

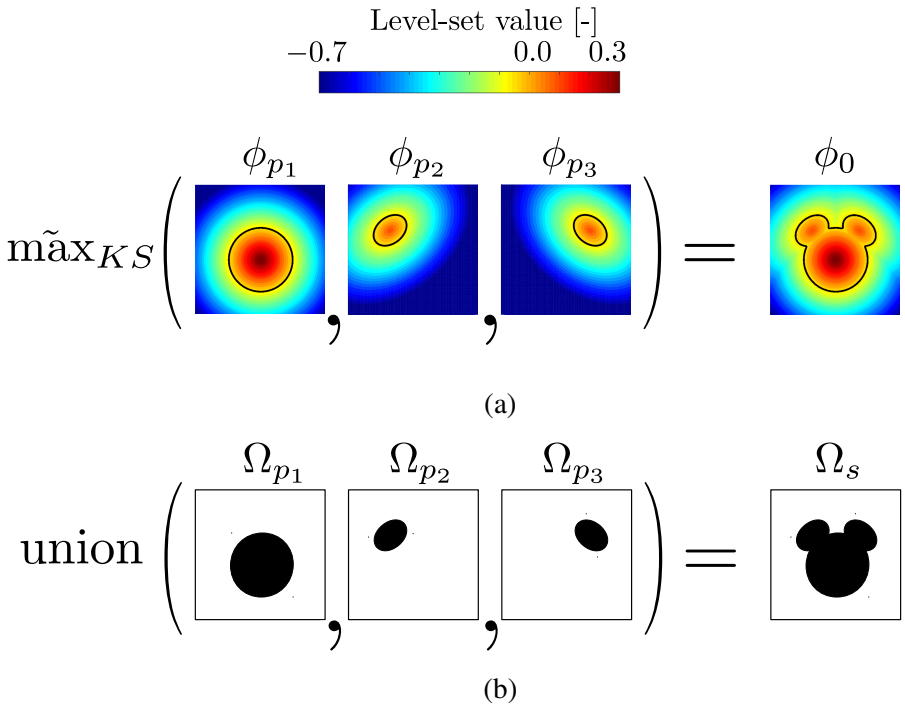

Fig. 4.9. (a): Smooth maximum function of level-set fields; (b): smooth union of geometric primitive components into a structure

We combine multiple geometric primitives through a smooth union. This is defined by a differentiable maximum operator on LSFs. We use the KS maximum approximation [251]. The resulting LSF is obtained as:

$$\phi = \tilde{\max}_{KS}\phi_i = \frac{1}{\beta_{KS}} \ln\left(\sum_{i=1}^{N_p} \exp\left(\beta_{KS}\phi_{p_i}\right)\right), \tag{4.54}$$

where N_p is the number of patches and β_{KS} is a parameter controlling the smoothness of the approximation. We set this parameter to 20 in this thesis. The union of a sufficient number of primitive components results in non-trivial geometries and allows a reasonable design freedom in most cases. Eq. (4.54) provides an upper bound to the hard maximum function and converges to it for $\beta_{KS} \to \infty$ [431]. The obtained level-set field in Eq. (4.54) can be directly used as the structural level-set, ϕ_0. As the smoothed union of morphable components is one of the basic building blocks of this chapter, a representative schematic is shown in Figure 4.9. Say one wishes to describe a Mickey mouse structure by using only patch level-set functions. Equations (4.52) and (4.53) can be used to obtain the LSFs representing the face

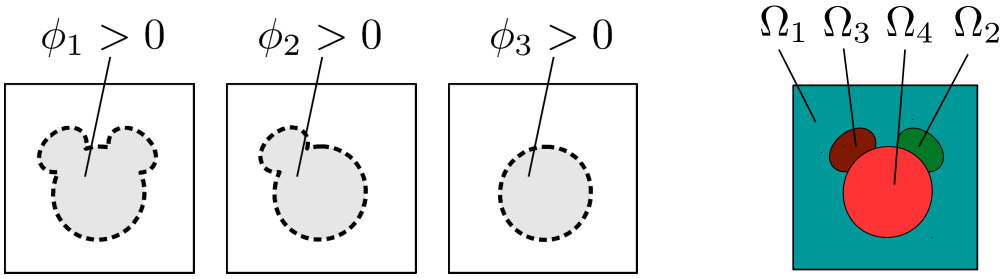

(a) (b)

Fig. 4.10. Parametrization of the multi-material Mickey mouse by using material domains shaped as geometric primitives. (a): level-sets definition using patches; (b): resulting multi-material configuration

(ϕ_{p_1}), the left ear (ϕ_{p_2}) and the right ear (ϕ_{p_3}). Using the KS operator yields the LSF, ϕ_0, shown in Fig. 4.9. Each of the patch level-sets, ϕ_{p_i}, defines a structural member filling Ω_{p_i}. Using the KS maximum approximation corresponds to a smooth (i.e. differentiable) union of the structural members as shown in Figure (4.9)(b), yielding a structure that fills Ω_s.

Using the operator (4.54), it is possible to define the material domains using geometric primitives to obtain "well-behaved" shapes. Referring to the multi-material framework (4.37), we define the level-sets as following:

$$\phi_i = \tilde{\max}_{KS} \phi_{p_j} \qquad \text{for } j = 1,\ 2,\ \ldots, N_m - i. \tag{4.55}$$

In words, the number of patches aggregated by the KS decreases when the level-set index increases. To visualize the procedure, consider a multi-material version of the Mickey mouse example. For simplicity, here the structural level-set, ϕ_0, does not play any role, i.e. consider $\phi_0 = 1$ everywhere. Using (4.55), we can write:

$$\begin{aligned} \phi_1 &= \tilde{\max}_{KS}\left(\phi_{p_1}, \phi_{p_2}, \phi_{p_3}\right), \\ \phi_2 &= \tilde{\max}_{KS}\left(\phi_{p_1}, \phi_{p_2}\right), \\ \phi_3 &= \tilde{\max}_{KS}\left(\phi_{p_1}\right). \end{aligned} \tag{4.56}$$

These level-sets are represented in 4.10 (a). When using level-sets (4.56) in (4.37), we recover the material configuration depicted in Figure 4.10(b).

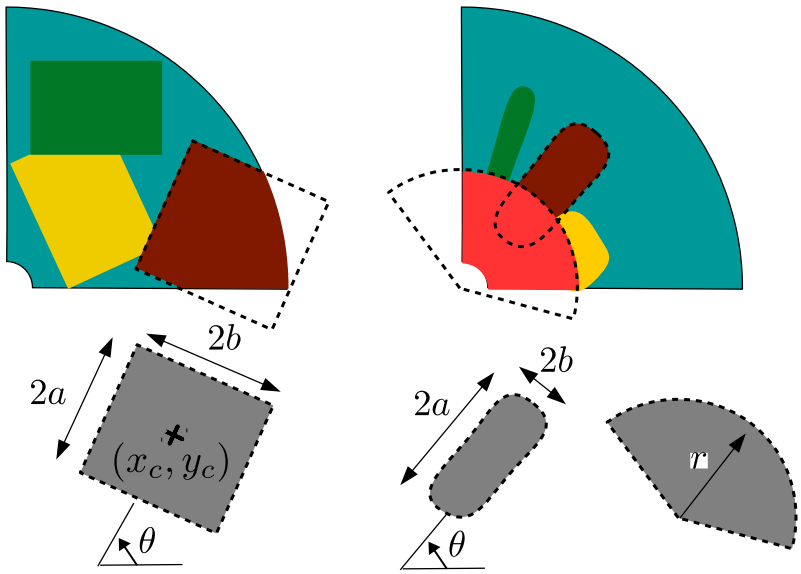

(a) (b)

Fig. 4.11. Parametrization of the material domains with representation of the design variables. (a): Floating patches; (b): finger agglomerate

4.5.2 Multi-material and structure configurations

In this chapter, we will consider a number of predefined configurations when optimizing the material domains and the macroscopic structure. The first one is obtained by simply filling the design domain with a varying number of patches, between 3 and 5, resulting in 4 and 6 materials, respectively. This configuration will be used uniquely for the material domains parametrization. Figure 4.11(a) highlights the design variables and shows a possible arrangement of the four materials obtained by considering three rectangular patches as geometric primitives. In the patches-type of configuration, we have $N_{s_M} = 5N_\phi$ macroscopic design variables. For the sake of the material domains parametrization, we will also consider a particular agglomerate of patches that takes inspiration from the petal configuration of Coffin and Maute [97] . A circle ($p_c = 2$) is centered at $x_1^c = 0$, $x_2^c = 0$. Since the rotation does not modify the layout, its unique design variable is the radius $r_s = a = b$. Some patches

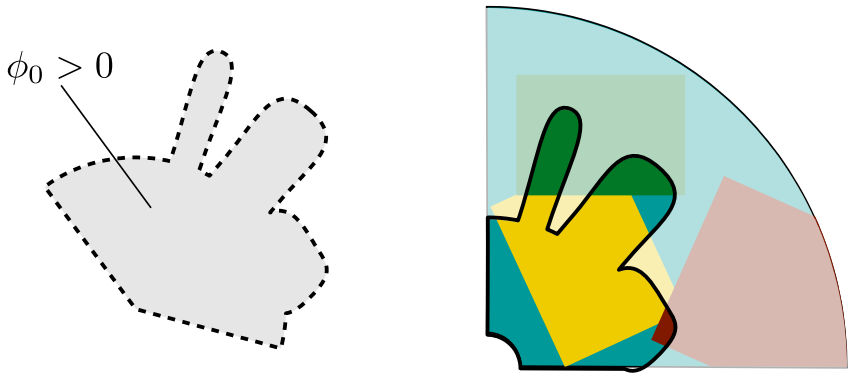

(a) (b)

Fig. 4.12. Concurrent structure and material parametrization. (a): Structure finger design; (b): structure finger design with patches background

are attached to the circle in such a way that their center coordinates are described by:

$$\begin{aligned} x_1^c &= r_s \cos\theta, \\ x_2^c &= r_s \sin\theta. \end{aligned} \tag{4.57}$$

Hence each of the attached patch is controlled by three design variables resulting in a total of $N_{s_M} = 1 + 3(N_\phi - 1)$ macroscopic design variables. We will refer to this particular arrangement as "finger" design. Figure 4.11 (b) shows a multi-material description obtained by using the finger-type of arrangement of geometric primitives.

Using both the PAMP-type interpolation (4.30) and the multi-material framework (4.37) allows the decoupling of the structure and material parameterizations. In design optimization studies considering also the optimization of the structure, we will consider a finger-type of agglomerate for the ϕ_0 definition. For the parametrization of material domains, we will consider a patches-type of arrangement. This yields a finger-like structure with patches background such as the one depicted in Figure (4.12). The opaque regions in Fig (4.12)(b) indicate pure BM.

4.6 Numerical results and design trends

In this section, we present and discuss the numerical results obtained with our multi-scale and multi-material design optimization framework based on geometric

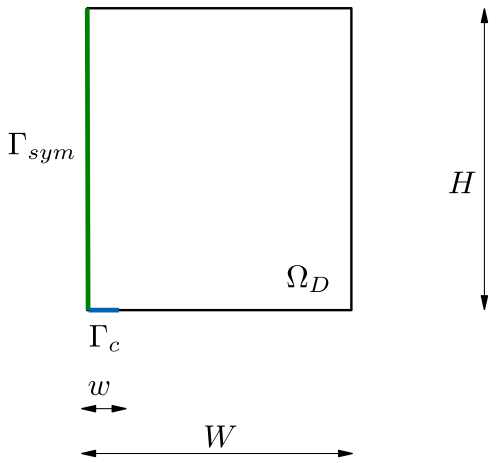

Fig. 4.13. Schematic of the steady-state diffusion heat sink design optimization problem

primitives. First, we test the design capabilities on a simple numerical example. Then, we provide the optimized multi-scale layouts for heat transfer enhancement in LHTES units.

4.6.1 Steady-state diffusion heat sink

For the sake of demonstrating the optimization framework described in this chapter, we consider an example with reduced physics complexity: a heat sink governed by steady-state diffusion (Eq. (2.44)). A schematic of the design and computational domain, Ω_D, is presented in Figure 4.13. A rectangle with dimensions $W = 3.5$ and $H = 4$ is loaded by a homogeneous heat generation $q_v = 400$. A cold temperature $T = 0$ is prescribed on the boundary Γ_c that is $w = 0.1$ wide. Symmetry is enforced on Γ_{sym}. All the remaining boundaries are adiabatic. We aim at finding the optimal multi-scale layout of HCM within Ω_D such that the spatial integral of the temperature

is minimized. This corresponds to the following optimization problem:

$$\begin{aligned} &\underset{\mathbf{s}}{\text{minimize}} && \int_{\Omega_D} T\, d\mathbf{x} \\ &\text{subject to} && \int_{\Omega_D} \Phi_{loc}\, d\mathbf{x} - V^* \leq 0 \\ & && \mathbf{s} = [\mathbf{s}_m^T,\ \mathbf{s}_M^T]^T \in \mathbf{S} = \left\{ \mathbb{R}^{N_s} \mid s_{min_i} \leq s_i \leq s_{max_i}, i = 1, ..., N_s \right\} \end{aligned} \quad , \tag{4.58}$$

where s_{min_i} and s_{max_i} denote the minimum and maximum values of the design variable, s_i. The maximum volume of HCM is set to 20 % of the total. The macroscopic design domain is discretized with 5600 bilinear quadrilateral elements with characteristic size $h = 0.05$. The microscopic design and computational domain is the one considered in Sections 4.2.3 and 4.3.1 for the verification of the forward and inverse homogenization frameworks. We use the 50×50 discretization with 2500 bilinear quadrilateral elements. The thermal conductivity of HCM and BM is set to 600 and 1 respectively. The optimization problems are solved using GCMMA. As compared to the set-up summarized in Table 2.1, we modified the relative step-size and the upper asymptote adaptivity to $\Delta s = 0.01$ and $\alpha_+ = 1.1$.

Smoothed union of geometric primitives

The ability of aggregating geometric primitives through a smooth union operator is a basic building block of our design framework. Here, we demonstrate this capability on a mono-scale design example. We optimize the structure (by evolving ϕ_0) of a single fully solid material, i.e. the micro-layout is described by $s_m = 1$ everywhere in Y.

We start by considering the finger parametrization introduced in Section 4.5.2 for defining ϕ_0. The complete list of design variable bounds and parameters for this geometry description is presented in Table 4.1 The magnitude of the Heaviside smearing largely affects the design sensitivities. The value reported in Table 4.1 was selected after preliminary finite difference checks on the initial guess. Note that this choice is problem-dependent and is not constant for all the problems considered in this chapter. Furthermore, ξ modifies the amount of non-physical intermediate material in the design domain. To allow for meaningful performance comparisons, all the optimized objective values reported in this chapter are obtained using $\xi = 0$.

Table 4.1. Finger design parameterization bounds and parameters for the heat sink example

Description	Symbol	Value
Minimum circle radius	r_{min}	1e-4
Maximum circle radius	r_{max}	4
Minimum finger half-width	a_{min}	0.4
Maximum finger half-width	a_{max}	4
Minimum finger half-height	b_{min}	0.4
Maximum finger half-height	b_{max}	4
Minimum finger tilt	θ_{min}	0
Maximum finger tilt	θ_{max}	$\pi/2$
"Cuboidness" parameter	p_c	2
Heaviside half band-width	ξ	0.1

The evolution of the design along the optimization process is shown in Figure 4.14 for both a one-finger and a three-finger parametrization. The designs are evolved using 4 and 10 macroscopic design variables, respectively. The objective and volume constraint histories are shown in Figure 4.15. The objective is normalized with the initial value of the one-finger example, $z_0 = 15933$. This normalization parameter will be adopted for all the objective values presented for the heat sink example. The constraint is normalized with respect to the maximum volume, V^*. The starting guesses are shown in Figure 4.14(a). As visible from the constraint value presented in Figure 4.15(b), the initial one-finger layout uses less HCM than V^*. Instead, the three-finger layout uses more HCM than allowed. In 7-8 optimization iterations, the amount of HCM in the design domain changes until it hits the maximum bound. This yields a constant decrease and increase of the objective for the one-finger and for the three-finger design. No substantial layout modifications are observed in this initial part of the optimization process. In Figure 4.14(b), the designs look simply a "rescaled" version of the initial guess. From iteration 10 to iteration 60 (Figure 4.14(d)), the geometries are modified substantially. The fingers rotate such that their tips point towards the angles of the design domain. These modifications yield a large performance increase: the objective is reduced by 43.1 % and 59.3 % in the one-finger and three-finger case. A further slight reduction is observed from iteration 60 to iteration 100. In Figure 4.14(e), the fingers look stretched along the chosen direction and the internal circle looks moderately grown. We notice negligible layout and performance changes in the last 20 iterations. The final normalized objectives

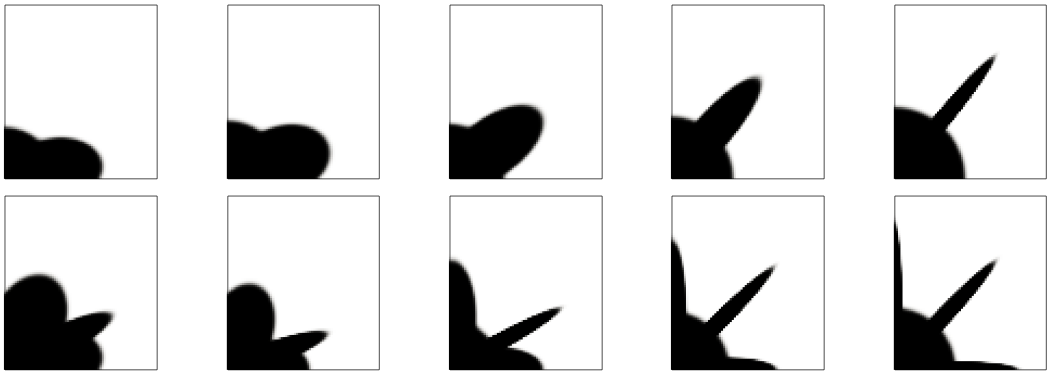

(a) (b) (c) (d) (e)

Fig. 4.14. Design evolution along the optimization process for the one-finger and three-finger examples. (a): Iteration 0; (b): iteration 10; (c): iteration 30; (d): iteration 60; (e): iteration 100

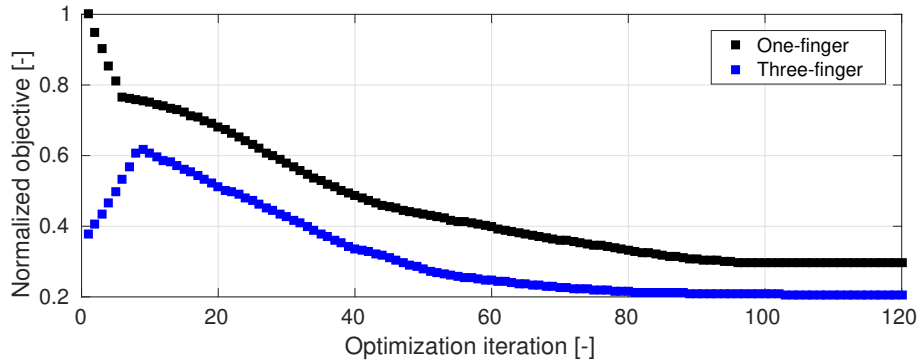

(a)

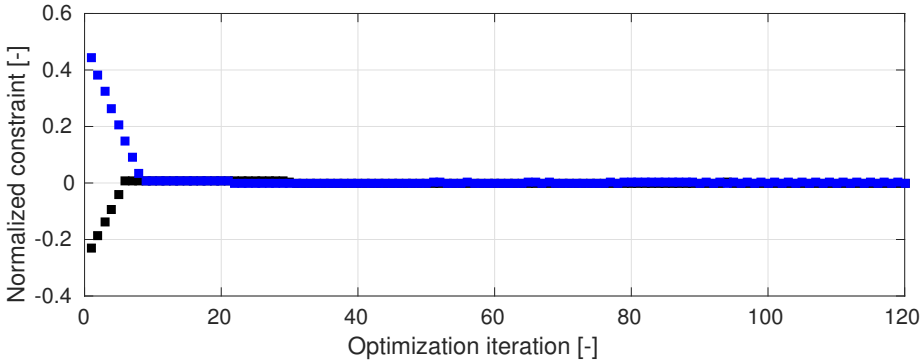

(b)

Fig. 4.15. Normalized objective (a) and volume constraint (b) histories along the optimization process for the finger design examples

Table 4.2. Patches design parameterization bounds and parameters for the heat sink example

Description	Symbol	Value
Minimum patch half-width	a_{min}	0.2
Maximum patch half-width	a_{max}	2
Minimum patch half-height	b_{min}	0.2
Maximum patch half-height	b_{max}	2
Minimum x coordinate center	$x_{c_{min}}$	0
Maximum x coordinate center	$x_{c_{min}}$	3.5
Minimum y coordinate center	$y_{c_{min}}$	0
Maximum y coordinate center	$y_{c_{min}}$	4
Minimum finger tilt	θ_{min}	0
Maximum finger tilt	θ_{max}	$\pi/2$
"Cuboidness" parameter	p_c	2
Heaviside half band-width	ξ	0.1

are 0.296 for the one-finger layout and 0.205 for the three-finger layout. More design freedom leads to a superior performance. Similar optimization solutions are obtained for different initial guesses. However, we observed that all the geometric primitives should be "visible" in the initial guess, meaning that a complete overlap between fingers should be avoided. When an overlap occurs or a geometric primitive exits the design domain completely, there is no chance to recover it. The objective and constraint gradients with respect to the design variables through which it is parametrized are zero.

To test the patches parametrization discussed in Section 4.5.2, we consider a design example using a smoothed union of five patches. The layout is evolved using 25 design variables. The bounds and relevant parameters for this configuration are reported in Table 4.2. In this design example, oscillations in the objective history were observed after 20-30 iterations. For this reason, the maximum number of inner iterations N_{in} of GCMMA was increased from the reference value of 2 (see Table 2.1) to 3. The snapshots of the design at selected optimization iterations along with the objective history are presented in Figure 4.16. The initial guess corresponds to 5 circles of equal area positioned as displayed in Figure 4.16(a). This configuration yields poor performance as no HCM is in contact with Γ_c. One of the circular patch quickly migrates towards the cold boundary as visible in Figure 4.16(b). Once the contact is established, the remaining patches start stretching and orientating in a such

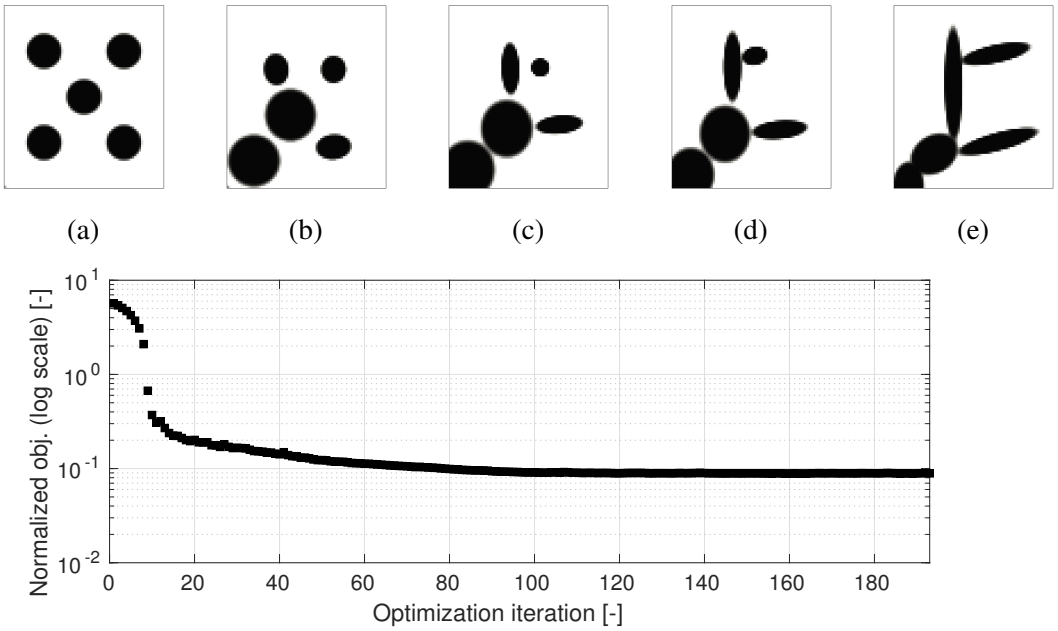

Fig. 4.16. Patches design example. Snapshots of layout at iteration 0 (a), iteration 10 (b), iteration 60 (c), iteration 100 (d) and iteration 193 (e). (f): Objective history along the optimization process

a way that a tree-like heat transfer structure is created (Figure 4.16(d)). Only minor layout and performance modifications are observed from this point to convergence, which is reached after 193 design iterations. The optimized layout is shown in Figure 4.16(e). Due to its larger design freedom, this geometry yields a higher performance than the finger layouts. The calculated normalized objective is 0.0878.

This section demonstrated the use of the KS maximum function to aggregate structural members defined using geometric primitives. The layouts converge to "machinable" structures that are controlled by a limited number of design variables.

Optimizing the micro-structure

Here, we describe the results obtained when optimizing the microscopic layout of the steady-state heat sink device. We consider a micro-scale problem with a single material component, i.e. a unique topology of the microscopic layout is optimized. No design freedom at the macroscopic level on the shape of the material domains and structure is considered, i.e. $\phi_0 > 0$ and $\phi_1 < 0$ everywhere in Ω_D. The microscopic geometry is parametrized using nodal design variables, s_m, that are converted into elemental densities, ρ_{s_m}, using the filtering and projection approach presented in Chapter 2. The filter radius is set to $r_{f_m} = 0.051$. The microscopic SIMP exponent, p_m, and projection steepness parameter, β_m, are slowly raised using the following continuation scheme:

$$\begin{aligned} p_m &= \{1;\ 2;\ 3;\ 3;\ 5\}, \\ \beta_m &= \{1;\ 1;\ 1;\ 4;\ 8\}. \end{aligned} \tag{4.59}$$

The projection threshold is hold constant at $\eta_m = 0.5$. In our implementation, the filter is non-periodic and truncated at the boundary. This ensures the evolution of the micro-scale geometry also when the layout is initialized with a homogeneous design variable field, s_m. In this case, the homogenized properties and volume constraint sensitivities with respect to the design variables located in the middle of the design domain differ from those located close to the boundaries. This is not the case when a periodic filter is adopted. For this reason, other authors initialized the micro-layouts with either a random design variable field [28] or a specific initial configuration [82]. The first step does not yield penalization when considering the linear volume constraint of Eq. (4.58). Although in this design example a non-penalized step could be avoided, in our experience this is essential in the multi-material design examples considered next. It serves for the purpose of redistributing HCM among

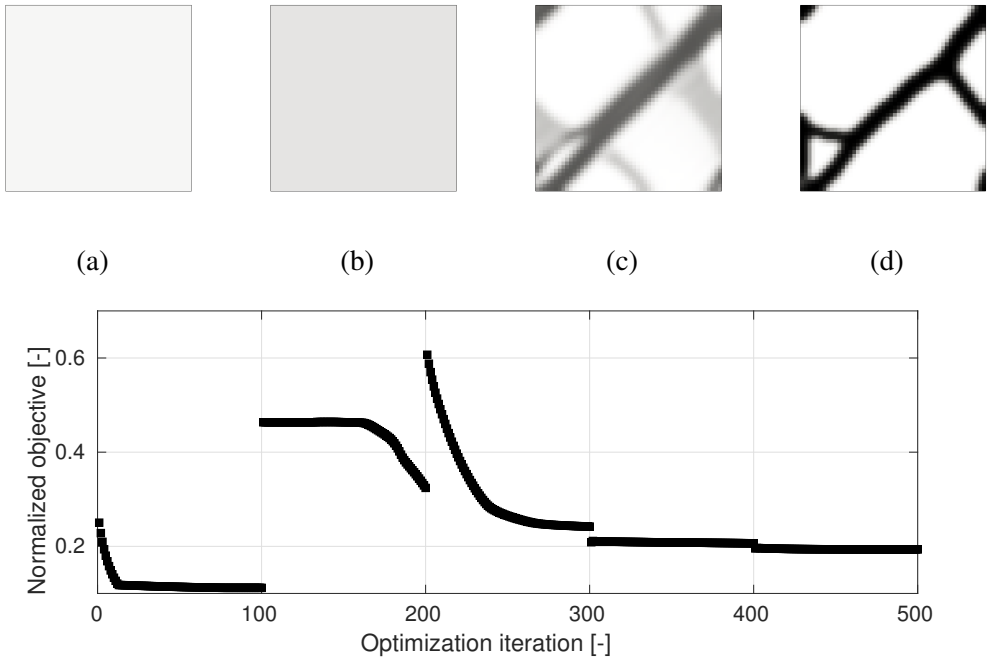

Fig. 4.17. Objective history with microscopic layout at selected iterations. (a): Iteration 0; (b): iteration 100; (c): iteration 200; (d): iteration 300

materials domains. A premature convergence to poor local minima micro-layouts was observed otherwise. The transition between continuation steps is performed every 100 iterations. The convergence of the optimization process is verified only after the completion of the final step. The normalized objective history alongside with the evolution of the microscopic layout is presented in figure 4.17. The initial guess corresponds to a homogeneous microscopic design variable field $s_m = 0.1$. During the first continuation step, HCM is homogeneously aggregated within the periodic domain to reach to maximum HCM volume. This is responsible for a moderate objective reduction. We notice no progress towards a binary $\{0;\ 1\}$ geometry. A layout starts appearing during the second continuation step, since the intermediate design variables are penalized more strongly. A clear pattern is observed at iteration 200 (Figure 4.17(c)). However, large areas with intermediate "gray" material are still present. Those disappear nearly completely at the end of the third continuation step as visible in Figure 4.17(d). However, the layout boundaries are still blurred by the filter. To improve the accuracy of the numerical homogenization predictions, the steepness of the projection is increased in the last two continuation steps. This yields negligible layout and performance modifications. The final optimized layout

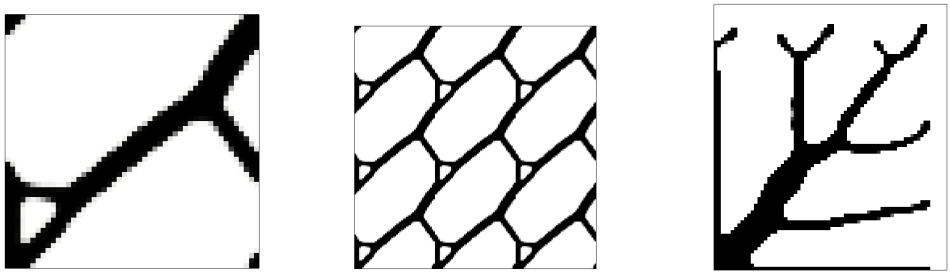

Fig. 4.18. (a): Optimized microscopic layout; (b): composite visualization using a grid of 3×3 periods; (c): optimized fin layout

is shown in Figure 4.18(a). The normalized objective achievable with this geometry is 0.193. To test the effectiveness of the initialization, we conduct an optimization example with a pseudo-random initial distribution $s = 0.2 + 10^{-3}\mathscr{T}$, where $\mathscr{T}$ is a random operator returning values in the range $[-0.5,\ 0.5]$. We obtain a layout that performs 2.898 % worse than the one represented in Figure 4.18(a). In the remainder of the chapter, we will always display a grid of 3×3 periods as the one depicted in Figure 4.18(b). This visualization allows the HCM connectivity between contiguous periodic cells to be visualized.

Although this optimization required for multi-scale analysis, the design variables are defined only at the microscopic level. When density-like design variables are defined only at the macroscopic level with no freedom on the material layout, one recovers a fin layout optimization framework similar to the one considered in Chapter 3. To asses the advantage of switching to a multi-scale design optimization procedure, we compute a reference fin layout. Also in this case, we consider a three-field density strategy. The macroscopic SIMP exponent p_M and projection steepness parameter β_M are varied following the continuation strategy (4.59). The macroscopic density filter has radius $r_{f_M} = 0.25$. The final optimized design is shown in Figure 4.18(c). The computed normalized objective for this case is 0.061. This result suggests that fins are more effective heat transfer enhancers than engineered cellular structures with a periodic and unique micro-structure.

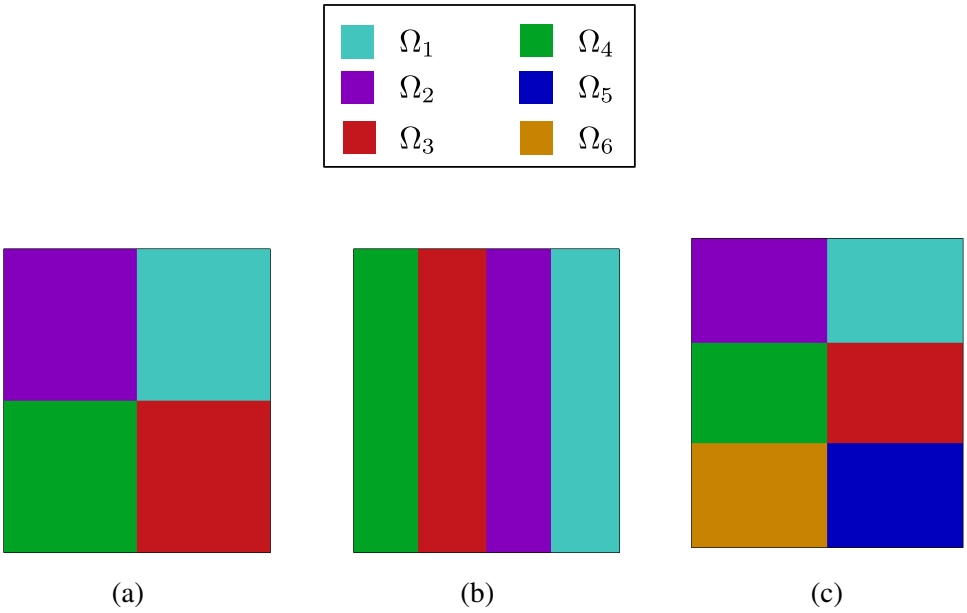

Fig. 4.19. (a): Materials configuration for the 2×2 grid example; (b): materials configuration for the vertical stack example; (c): materials configuration for the 3×2 grid example

Adding more materials

In this section, we consider the optimization of multiple material micro-structures. As in the previous section, we allow no design freedom at the macro-scale: the material domains are fixed and their shape is not optimized. The structure level set, ϕ_0, is positive everywhere in Ω_D. We focus on three alternative configurations, depicted in Figure 4.19. The first configuration (Figure 4.19(a)) consists of four material domains ordered in a 2×2 grid. The second configuration (Figure 4.19(b)) consists of four materials domains ordered in a vertical stack. The last configuration (Figure 4.19(c)) consists of six materials domains ordered in a 3×2 grid.

Figure 4.20 shows the evolution of the microscopic layouts for the 2×2 grid configuration during the optimization convergence. The normalized objective histories for all the configurations are shown in Figure 4.21. In all the design studies, the microscopic design variable field is initialized as a homogeneous distribution $s_m = 0.2$ within Y. During the first 100 iterations, HCM is redistributed efficiently among the material domains, concentrating in those that are in contact with Γ_c. We observe no formation of microscopic features since the intermediate design vari-

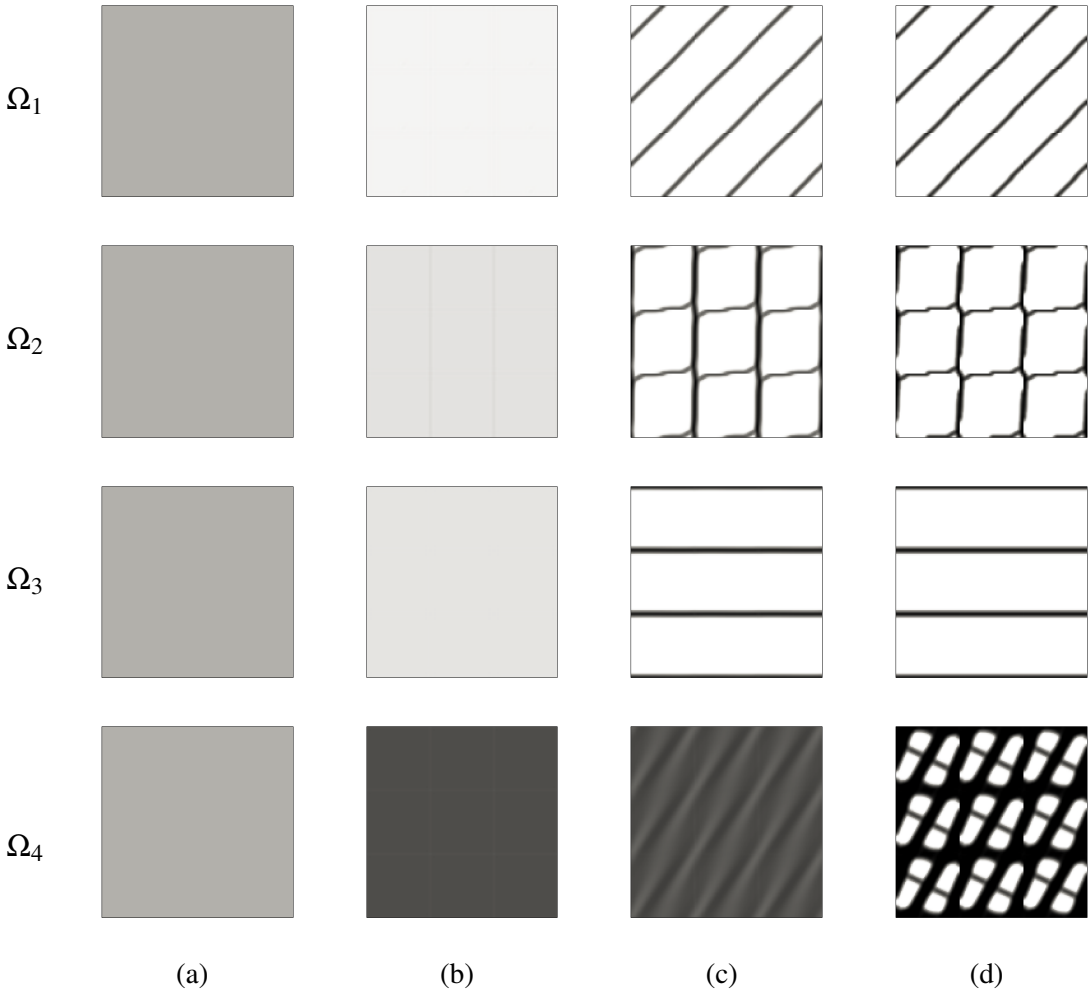

Fig. 4.20. Microscopic layouts evolution of the 2×2 grid configuration at selected iterations. (a): Iteration 0; (b): iteration 100; (c): iteration 200; (d): iteration 300

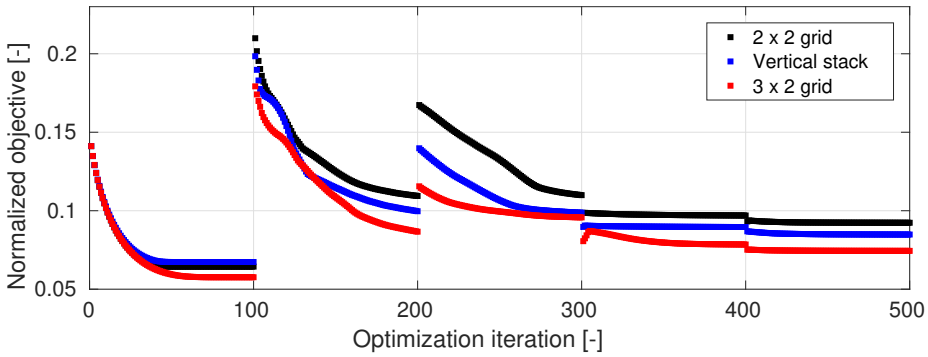

Fig. 4.21. Normalized objective histories along the optimization process for the three material configurations

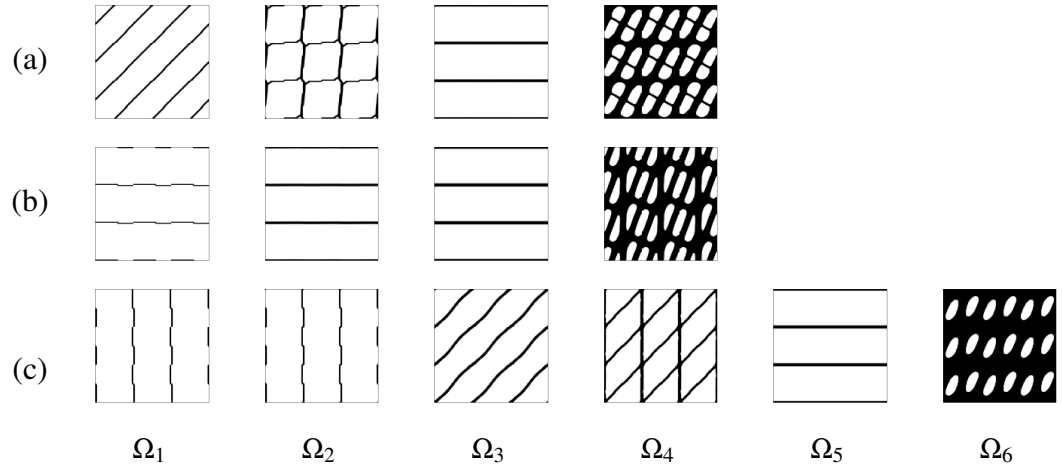

Fig. 4.22. Optimized microscopic layouts for the 2×2 grid configuration (a), for the vertical stack configuration (b) and for the 3×2 grid configuration (b)

able values are non-penalized during the first continuation step. During the second continuation step, a large objective reduction is achieved through the formation of well-defined micro-structures in Ω_1, Ω_2 and Ω_3. At iteration 200, large regions with "gray" material are still present in the microscopic layout of the material occupying Ω_4. Those disappear nearly completely during the third continuation step due to a larger penalization effect. At the beginning of the fourth continuation step, the objective of the 3×2 grid configuration grows. The increase of the projection steepness parameter results in a volume constraint violation and a few optimization iterations are needed to recover a design set within the feasible region.

The optimized microscopic layouts for all the configurations are shown in Figure 4.22. The microscopic layouts of the 2×2 grid configuration in Ω_4 and Ω_3 closely resemble the ones of the 3×2 grid configuration in Ω_6 and Ω_5. However, some microscopic layout differences are noticeable in the top portion of the design domain. The utilization of more material domains allows a reduction of the normalized objective by 19.3 %, from 0.092 of the 2×2 grid configuration to 0.074 of the 3×2 grid configuration. Comparing the performance of the 2×2 grid configuration with the one of the vertical stack configuration prompts additional reflections. Both these designs use the same number of materials. However, arranging the materials in a stack yields 8.0 % better performance than using a 2×2 grid. This suggests that assuming a priori the materials arrangement is crucial for the performance of

the optimized layouts. For this reason, in the next section we will avoid making this assumption.

Note that all the optimized objective values obtained in this section are higher than the one of the reference fins design. The best performing configuration (the 3×2 grid of materials) results in a 21.3 % larger objective. This suggests that a multi-scale design optimization framework considering fixed material domains may not yield any performance improvement as compared to a mono-scale analysis and design strategy.

Moving the material domains

In this section, we increase the design freedom of our framework by considering the optimization of material domains. The grid-like arrangements considered in the previous section are now able to morph during the optimization. We consider the multi-material patches configuration described in Section 4.5.2 with three and five floating patches. The macroscopic design variable bounds and parameters are all equal to those presented in Table 4.2 except for the "cuboidness" parameter which is here set to $p_c = 10$ and the Heaviside smoothing bandwidth here set to $\xi = 0.05$. A reduction of ξ was necessary to limit the inaccuracies related to the superposition of interfaces, as discussed in 4.4.2. This value was selected by trial-and-error on preliminary optimization runs. No design freedom is considered as regards to the structure, hence $\phi_0 > 0$ everywhere within Ω_D.

Figure 4.23 presents the evolution of the material indicator fields and microscopic designs during the optimization process for the three patches configuration. The material level-sets are evolved using 15 macroscopic design variables. The objective history is displayed in Figure 4.24. Since the material domains are accounted for in the analysis model through a density-based representation, the material boundaries are fuzzy in the analysis. Hence, we adopt a visualization in which the opacity varies linearly with the magnitude of each material indicator field, χ_i. The same visualization strategy will be used for all the movable material examples presented in the remainder of the chapter. Recall that all the optimized objective values listed are obtained with $\xi = 0$ such that the fuzziness effect does not affect the final performance comparisons. The initial guess on the macroscopic design variables is formulated such that a 2×2 grid of material domains is obtained, as in one of the fixed domain examples of the previous section. The initial microscopic layout

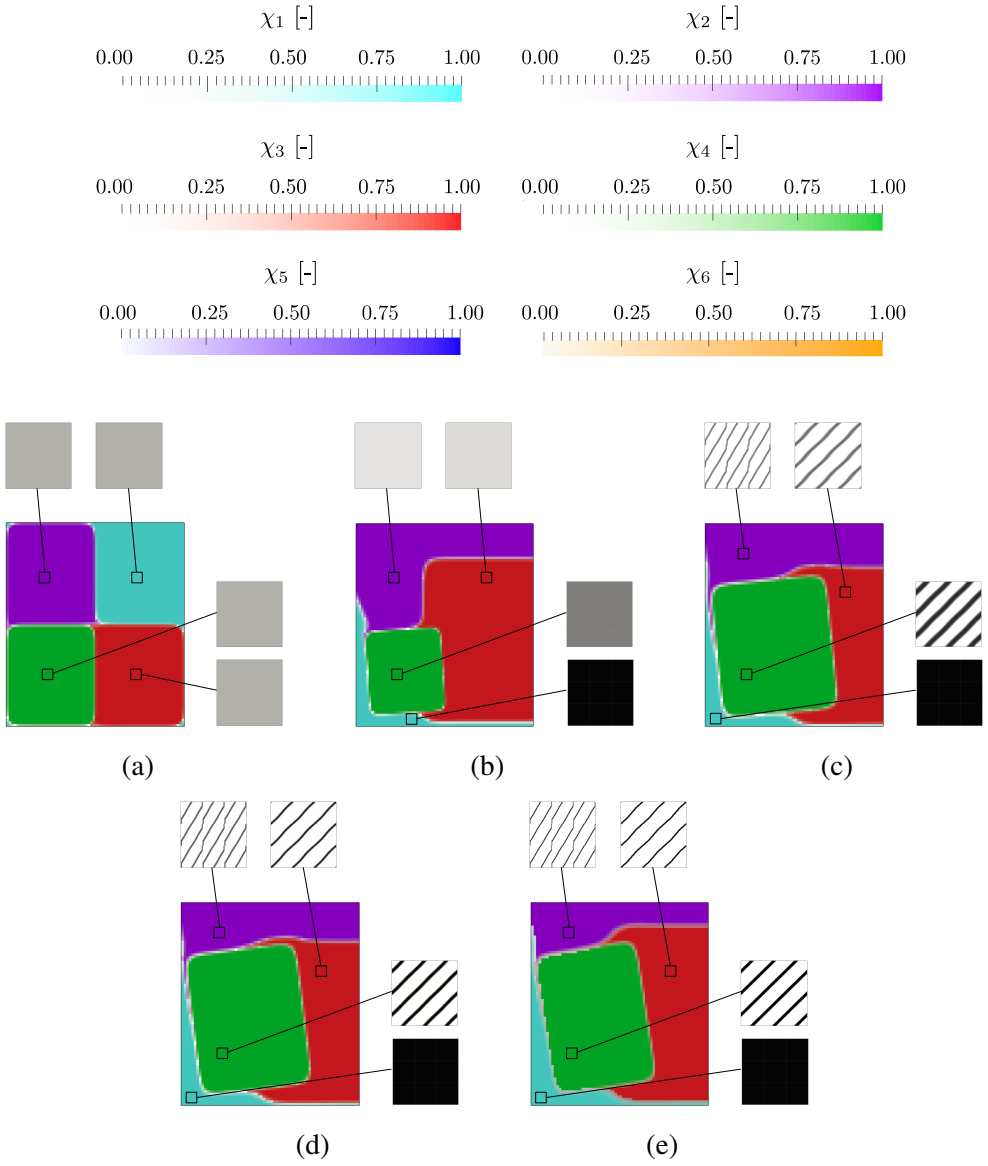

Fig. 4.23. Evolution of the microscopic and macroscopic layouts for the three movable patches example at selected iterations. (a): Iteration 0; (b): iteration 100; (c): iteration 200; (d): iteration 300; (e): iteration 500

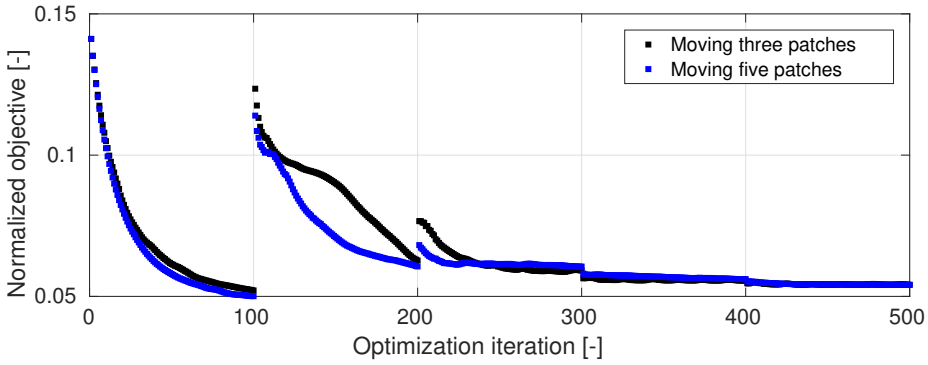

Fig. 4.24. Normalized objective histories along the optimization process when using movable material domains

is a homogeneous $s_m = 0.2$ field in Y. During the first continuation step, HCM is just redistributed among material domains with no formation of binary $\{0;\ 1\}$ design features. The green material detaches from Γ_c and starts floating. This creates a thin Ω_1 region in contact with the bottom and left boundaries of the design domain. Here, HCM is rapidly concentrated such that a homogeneous $\rho_{s_m} = 1$ field is obtained within Y. This yields a larger objective reduction as compared to the first continuation step of the fixed 2×2 grid configuration. From iteration 100 to iteration 200, noticeable design modifications are observed at both the macroscopic and microscopic level. The microscopic layouts evolve into black-and white patterns. The green floating domain grows and moves such that the shape of Ω_1 changes slightly while Ω_2 and Ω_4 are confined at the top and right boundaries, respectively. Also during this step, the objective is reduced to a greater extent as compared to the fixed material case. Only minor layout and performance variations are observed during the last 300 iterations of the optimization process. The final optimized design shown in 4.24(e) consists of two thin fully solid regions (i.e. fins) elongating on the top and left boundaries and three multi-scale structures with diagonal HCM stripes. The local volume fraction of the micro-structures, ϕ_{loc}, reduces when moving away from Γ_c. The normalized objective value of the optimized configuration analyzed with $\xi = 0$ is 0.055, corresponding to a 9.5 % objective reduction as compared to the fins of Figure 4.18(c). This indicates that a multi-scale design optimization framework may be convenient when the material domains are able to morph.

To analyze the effect of additional design freedom obtained through the introduction of more moving materials, we consider a morphable version of the 3×2

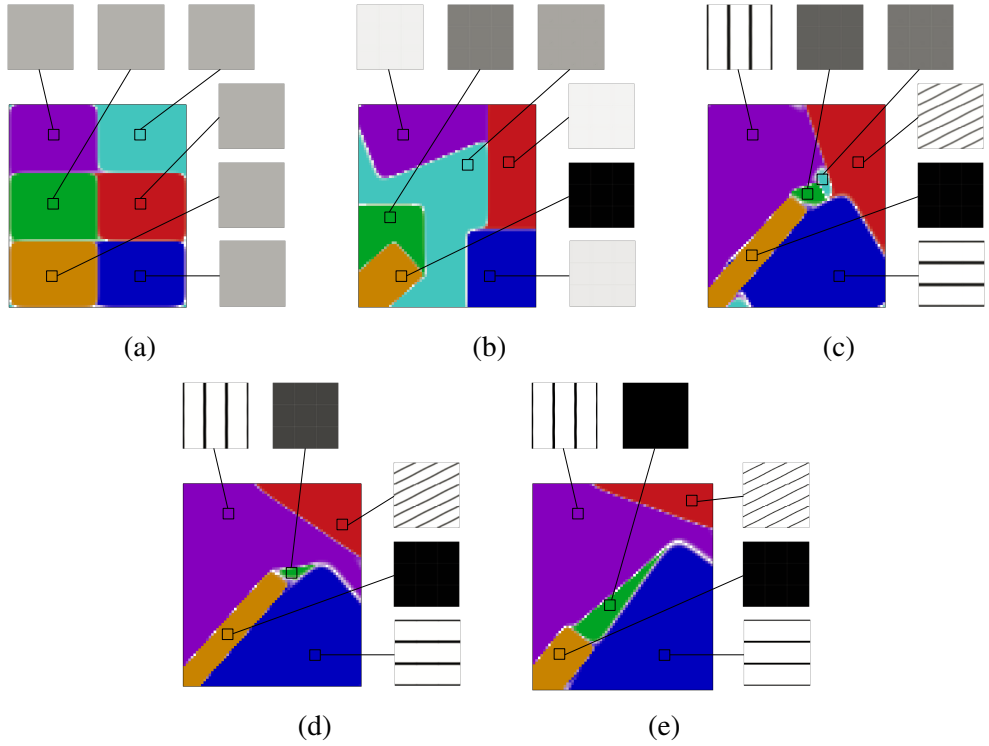

Fig. 4.25. Evolution of the microscopic and macroscopic layouts for the five movable patches example at selected iterations. (a): Iteration 0; (b): iteration 100; (c): iteration 200; (d): iteration 300; (e): iteration 500

grid configuration discussed in the previous section. This is obtained by using 5 patches that are evolved with 25 macroscopic design variables. Figure 4.25 presents the evolution of the macroscopic and microscopic layouts at selected optimization iterations. The objective history is plotted in Figure 4.24 together with the three moving patches example. The initial guess consists of a 3×2 grid of material domains with a homogeneous $s_m = 0.2$ microscopic design variable field. During the first continuation step, the redistribution of HCM largely relies on the motion of the material domains. Ω_2, Ω_3 and Ω_5 migrate close to the right and top boundaries and a small ϕ_{loc} is attributed to these materials. More HCM is allocated in Ω_4 and Ω_6, which are positioned close to Γ_c. The central region is occupied by Ω_1, with an intermediate ρ_{s_m} layout. The material domains evolve rapidly also in the second continuation step. Ω_6 grows towards the center of Ω_D to form a diagonal fin that separates the design domain in three well-distinct regions occupied by Ω_2, Ω_3 and Ω_5. The remaining materials (Ω_4 and Ω_1) occupy a small portion of the design domain and their microscopic layout is still homogeneous. Ω_1 disappears from the

design domain during the third continuation step. The disappearance of materials is allowed in our design optimization framework. To avoid this event, we also performed some numerical experiments with a minimum material volume constraint but we obtained nearly unaltered performance of the optimized configurations. The microscopic layout of Ω_4 starts converging to a binary geometry during the last 200 iterations, when this material domain evolves into a triangular region of pure HCM. The final layout (Figure 4.25) consists of a diagonal fin surrounded by laminates with horizontal, vertical and diagonal HCM stripes. The optimized objective of this layout is 0.052, yielding only a 5.4 % improvement as compared to the three morphable patches layout. Since Ω_6 and Ω_4 have the same micro-structure, we observe that a similar layout could be obtained also in the previous experiment using only four materials. This suggests that the optimized configurations are at best local minima. Although we found that using a large number of materials helps to prevent the convergence to trivial solutions, we always rely on physical intuition to critically assess the optimized designs.

Optimizing the structure on the foreground

In this section, we analyze the effect of using a structure level-set, ϕ_0, to control explicitly the external shape of the assembly of materials. The structure level-set is defined as a finger-type of agglomerate of geometric primitives (see Section 4.5.2) with three fingers. The design variable bounds and parameters for this agglomerate are set as in Table 4.1 except for $p_c = 10$ and $\xi = 0.05$. The material domains are controlled using three patches with the same bounds and parameters as in the previous section. The macroscopic layout is evolved using 25 design variables as for the five movable patches example.

Figure 4.26 shows the evolution of both the microscopic and macroscopic layouts along the optimization process. The normalized objective history is displayed in Figure 4.27. To start from an unbiased layout, the initial material configuration is chosen in such a way that all the material domains lie within the finger-type structure. During the first continuation step, the external structure grows to occupy nearly the entire design domain. Also in this case, the material domains are arranged in regions of increasing distance from Γ_c, such that the HCM can be efficiently redistributed. Only minor modifications (mainly at the macroscopic level) are observed during the second continuation step. Ω_4 grows substantially during the third continuation step

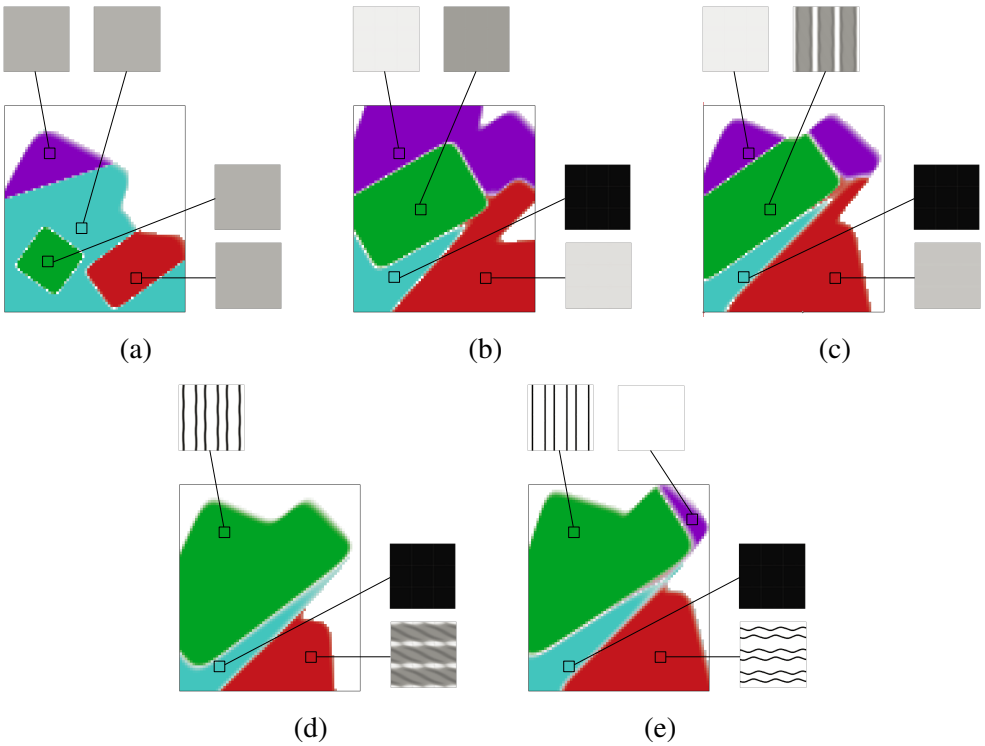

Fig. 4.26. Optimized microscopic and macroscopic layouts at selected iterations when optimizing the structure on the foreground. (a): Iteration 0; (b): iteration 100; (c): iteration 200; (d): iteration 300; (e): iteration 500

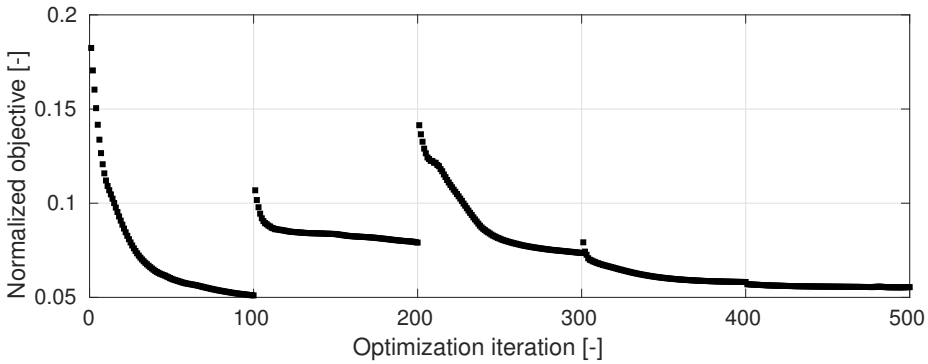

Fig. 4.27. Normalized objective histories along the optimization process when optimizing the structure on the foreground

Table 4.3. Comparison of the performance when using the wave-like and the rank-1 laminate (straight) micro-structures

	Micro-structure	
Performance	Wavy	Straight
k_{11}^H [-]	6.0728e+01	6.1661e+01
k_{22}^H [-]	1.2354e+00	1.1124e+00
k_{12}^H [-]	-1.4648e-03	0.0000e+00
Normalized objective [-]	0.052636	0.053196

such that Ω_2 is lost from the structure. The convergence to binary $\{0;\ 1\}$ microscopic layouts is slower in this design example. A well-defined geometry for Ω_3 is obtained only during the last 200 iterations. The material domain Ω_2 reappears during these last continuation steps with no HCM in its micro-structure such that the shape of the external assembly is further modified. The reappearance of material domains is possible in our multi-material design optimization framework. The final layout consists of a triangular fin oriented along the design domain diagonal surrounded by two matrices with straight vertical and wave-like horizontal HCM stripes. In the optimized configuration, the finger-like structure does not occupy the entire design domain. The normalized objective value for this design case is 0.054, corresponding to an intermediate performance between the three and the five moving patches design examples considered in the previous section.

Finally, to test the effectiveness of the wave-like micro-structure in Ω_3, we consider a possible alternative. This consists of a rank-1 laminate with the straight conducting paths aligned in the y_1 direction and the same volume fraction of the wave-like material. The homogenized material properties of this micro-structure are obtained analytically following [477]. All the micro-structures are analyzed using $\beta = 1000$ to avoid the possibility of bias due to intermediate microscopic density values. The homogenized properties and the performance of the two structures are summarized in Table 4.3. The results show that there are minor but non-negligible differences between the two alternative materials. The wave-like material allows a higher k_{22}^H to be achieved at the cost of a reduction in k_{11}^H. Overall, using a rank-1 laminate with horizontal HCM stripes leads to a 1.06 % worse performance of the macro-structure.

Table 4.4. Patches design parameterization bounds and parameters for the LHTES example

Description	Symbol	Value
Minimum patch half-width	a_{min}	0.1
Maximum patch half-width	a_{max}	1
Minimum patch half-height	b_{min}	0.1
Maximum patch half-height	b_{max}	1
Minimum x coordinate center	$x_{c_{min}}$	0
Maximum x coordinate center	$x_{c_{min}}$	1
Minimum y coordinate center	$y_{c_{min}}$	0
Maximum y coordinate center	$y_{c_{min}}$	1
Minimum finger tilt	θ_{min}	0
Maximum finger tilt	θ_{max}	$\pi/2$
"Cuboidness" parameter	p_c	10
Heaviside half band-width	ξ	0.05

4.6.2 Design of multi-scale structures for LHTES units

In this section, we use our multi-scale multi-material optimization framework to design practical conducting structures for LHTES units. Phase change is modeled through the purely diffusive physical model introduced in Chapter 3 and described by the governing PDE (3.26). We focus on the discharge of the unit, modeled by setting $T_I^* = 1$ and $T_d^* = 0$. The time stepping is stopped when the energy in the tank drops below 5 % of the total energy capacity. The macroscopic governing equations are discretized in space and time using the FE framework adopted in Chapter 3. The microscopic homogenization equations are solved with the FE framework described in Section 4.2 using the 20×20 elements mesh with 400 bilinear quadrilateral elements. We aim at minimizing the time required for the complete discharge of the unit. Hence, we adopt the optimization problem formulation (3.67). The thermo-physical properties of the material constituents were listed in Table 3.1. Differently from Chapter 3, here we consider a maximum volume fraction Φ of 20 %. The macroscopic layouts are controlled using the parametrization options presented in Section 4.5.2. The design variable bounds and parameters for the patches and for the finger agglomerate are given in Tables 4.4 and 4.5. The SIMP penalization exponents, p_m and p_M, and the projection steepness parameter, β_m, are slowly raised during the optimization process following the continuation scheme (4.59).

Table 4.5. Finger design parameterization bounds and parameters for the LHTES example

Description	Symbol	Value
Minimum circle radius	r_{min}	1e-4
Maximum circle radius	r_{max}	1
Minimum finger half-width	a_{min}	0.1
Maximum finger half-width	a_{max}	1
Minimum finger half-height	b_{min}	0.1
Maximum finger half-height	b_{max}	1
Minimum finger tilt	θ_{min}	0
Maximum finger tilt	θ_{max}	$\pi/2$
"Cuboidness" parameter	p_c	10
Heaviside half band-width	ξ	0.05

To assess the advantage of switching to a multi-scale multi-material design optimization framework, we will compare the performance of the optimized layouts with the two reference heat transfer structures depicted in Figure 4.28. The first one (Figure 4.28(a)) is a fin layout obtained considering no design freedom at the microscopic level. This geometry is computed using the optimization framework presented in Chapter 3. All the black portions of the design domain denote pure HCM while the white portions denote pure PCM. The design differs with respect to those analyzed in the previous chapter uniquely due to the modified maximum volume fraction and continuation scheme on the penalization and projection parameters. Using this geometry allows the unit to be discharged in $t^* = 0.272$. Hereafter, we will refer to this quantity as the reference discharge time, t^*_{ref}. The second geometry is a single-material multi-scale structure filling the entire shell. Using this optimized structure yields the complete discharge of the tank in $t^* = 0.447$, corresponding to a 64.3 % increase with respect to the fins. This result suggests that filling the unit with a unique periodic cellular structure, although optimized at the microscopic level, may not be a convenient choice for heat transfer enhancement in LHTES units.

Adding more materials

Here, we relax the single material assumption and consider two alternative arrangements of periodic structures in the LHTES unit. The material domains are fixed and the HCM structure fills the entire shell.

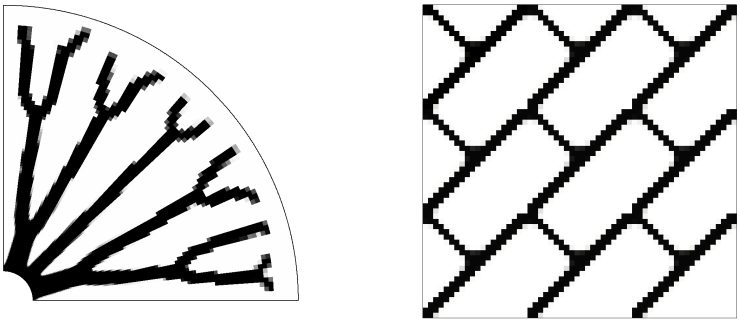

(a) (b)

Fig. 4.28. Reference mono-scale optimized designs. (a): Macroscopic layout of fins; (b): microscopic layout of single-material metal matrix

Similarly to one of the alternatives considered in the heat sink numerical example, the first material configuration consists of a 2×2 grid of material domains. This configuration along with all the optimized micro-structures is represented in Figure 4.29(a). A reticular geometry occupies Ω_4, which is contact with the HTF pipe. Micro-structures with vertical, diagonal and horizontal HCM stripes evolve in Ω_2, Ω_1, and Ω_3, respectively. A smaller local volume fraction, Φ_{loc}, is obtained within these regions. This agrees with intuition: smaller connections are required in the regions far from the internal pipe since less heat is transferred there during the entire process. The second material configuration (Figure 4.29(b)) consists of five rings. The material interfaces are placed at $r^* = \{0.2;\ 0.4;\ 0.6;\ 0.8\}$. Inspired by the famous Russian baby-dolls, we will refer to this layout as Matryoshka circles configuration. The optimized microscopic layouts consist of four reticular geometries with varying local volume fraction. The amount of HCM reduces when moving away from the Dirichlet boundary. Only diagonal HCM laminates emerge from the optimization process in Ω_1, which is the furthest the HTF pipe.

Figure 4.30 compares the energy history during the discharge of these units with the one of the topology-optimized fins. The performances obtained with the multi-material configurations are comparable to the one of the fins. The Matryoshka option requires a 0.9 % longer time than the fin geometry for a complete discharge. On the other hand, using the 2×2 grid configuration allows the discharge time to be decreased by 3.3 %. A closer inspection of the energy curves reveals that the discharge rate of the grid configuration is slightly slower at the beginning of the

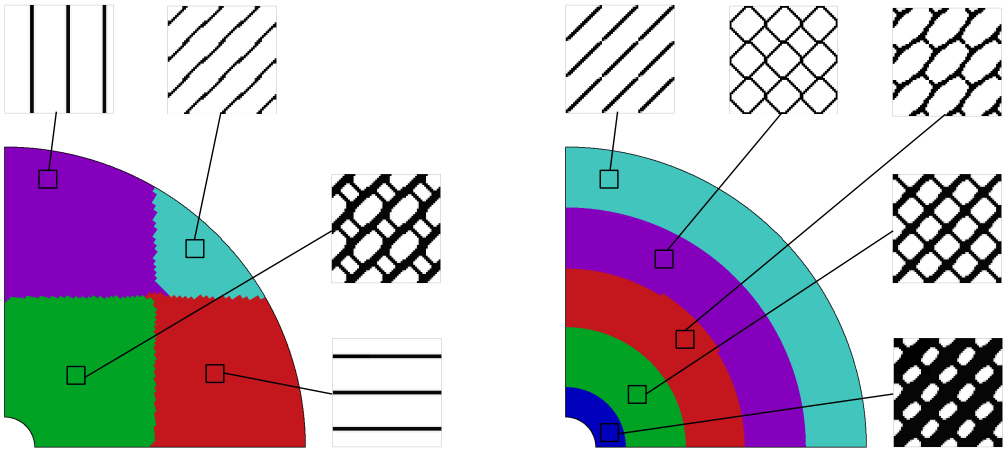

(a) (b)

Fig. 4.29. Optimized microscopic layouts for two fixed materials configurations. (a): 2×2 grid; (b): Matryoshka circles

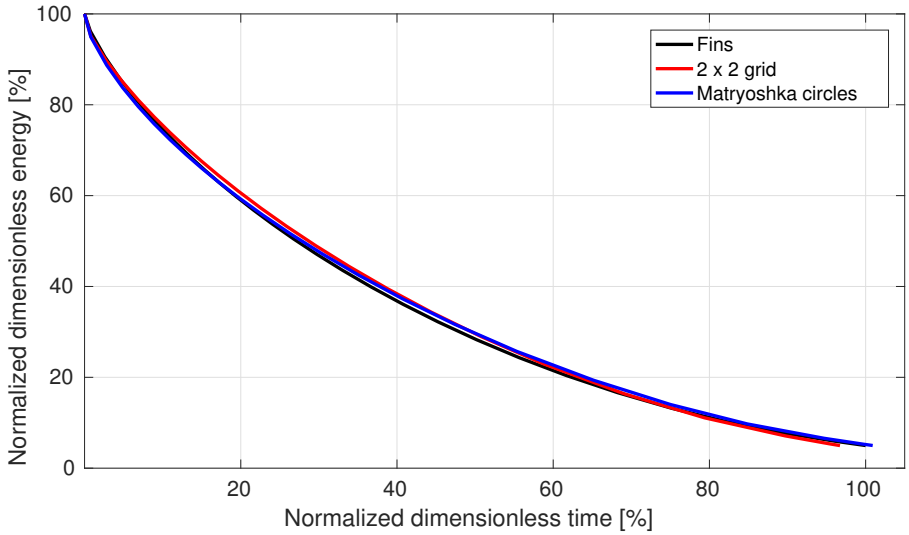

Fig. 4.30. Normalized energy histories of the optimized fins and multi-scale structures with fixed material configurations

process. To gain further insights behind these performance differences, it is useful to study the liquid fraction evolution presented in Figure 4.31. The snapshots are taken at 20 %, 40 %, 60 % and 80 % of the reference discharge time. When using the topology-optimized fins, the solidification front advances rapidly following the fin geometry. At $t^* = 0.4\, t^*_{ref}$, the mushy PCM occupies uniquely the fins interstices and a thin region in contact with the external envelope. Since most of the heat propagates radially, the solidification from at the end of the process approximates well the shell geometry. Different discharge dynamics are observed for the multi-material layouts. In the grid configuration, solidification proceeds slowly at the beginning of the process. At $t^* = 0.2\, t^*_{ref}$, the amount of solidified material is less than the alternatives. However, when the solidification front reaches Ω_2 and Ω_3, it rapidly expands in the vertical and horizontal direction. This explains the limited heat transfer drop registered for this structure. At $t^* = 0.6\, t^*_{ref}$, only the mushy region occupying Ω_1 needs to be cooled away. Solidification in the Matryoshka configuration evolves in a different manner. Since at fixed r^* the micro-structure cannot change with the angular position, the solidification front cannot evolve radially. Propagation along the $\theta = \pi/4$ direction is faster than along the $\theta = 0$ and $\theta = \pi/2$ directions. Hence, the mushy PCM tends to be accumulated at the corners of the design domain. This explains the limited heat transfer rate at the end of the discharge process.

Moving the material domains and the structure

The differences in performance between the alternative material configurations considered in the previous section suggest that improvements of those layouts are possible by adding design freedom at the macroscopic level. We consider three alternative options for the macroscopic parametrization. The first one consists of three floating patches (Section 4.5.2). The initial guess corresponds to a 2×2 grid as in the fixed layout of the previous Section. Figure 4.32(a) shows the optimized microscopic and macroscopic layouts for this design case. Similarly to what obtained in the heat sink design example, pure HCM concentrates close to the bottom and left boundaries to form two thin fins. The material domain Ω_4 floats within the design domain and is occupied by a metal matrix with thick diagonal HCM stripes. This material domain is bordered by low volume fraction structures with thin HCM stripes. The second parametrization of material domains consists of a finger-type of agglomerate with three fingers (see Section 4.5.2). The optimized layout (Figure

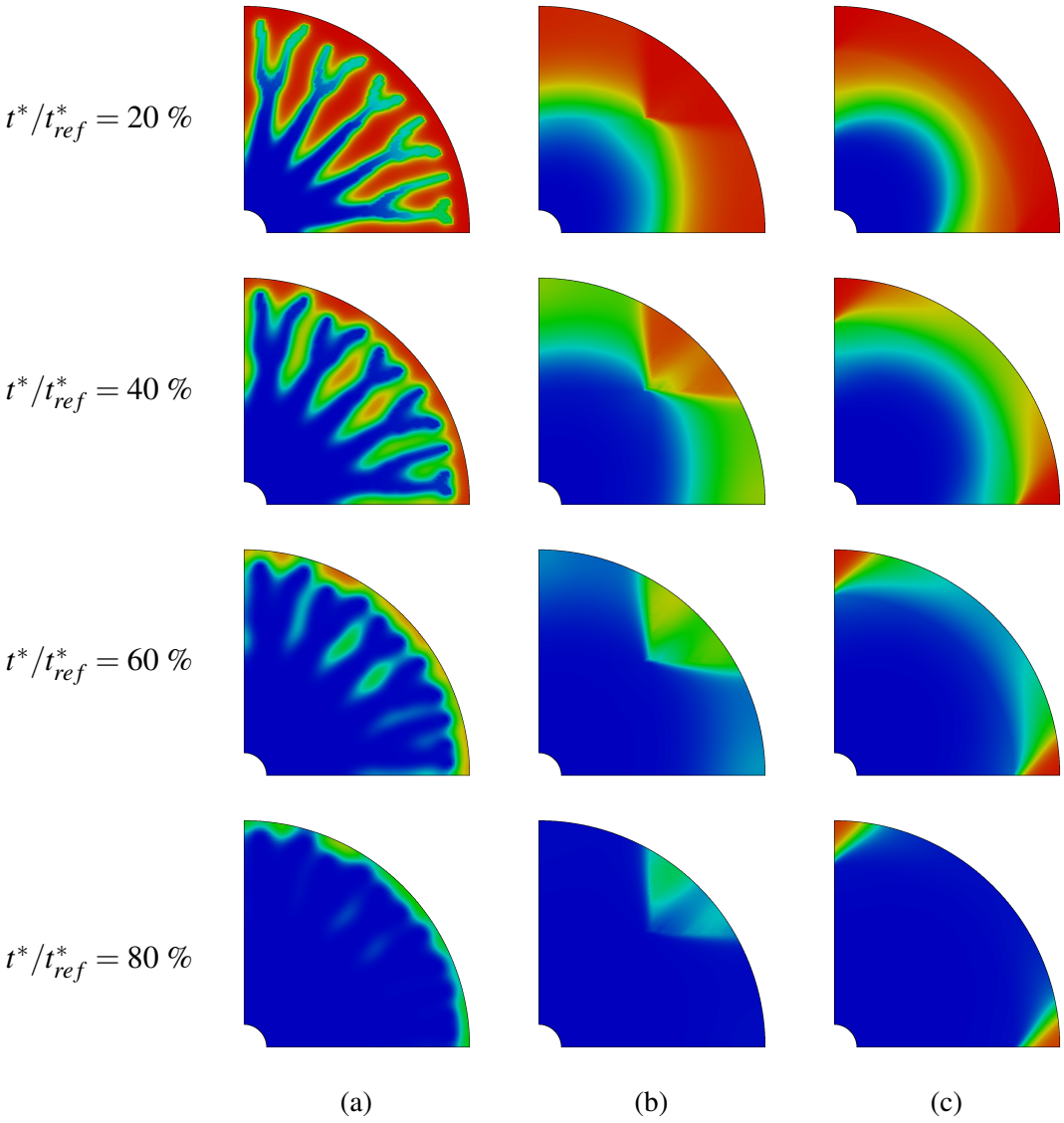

Fig. 4.31. Liquid fraction evolution of the optimized fin design and fixed material configurations. (a): Fins; (b): 2×2 grid; (c): Matryoshka circles

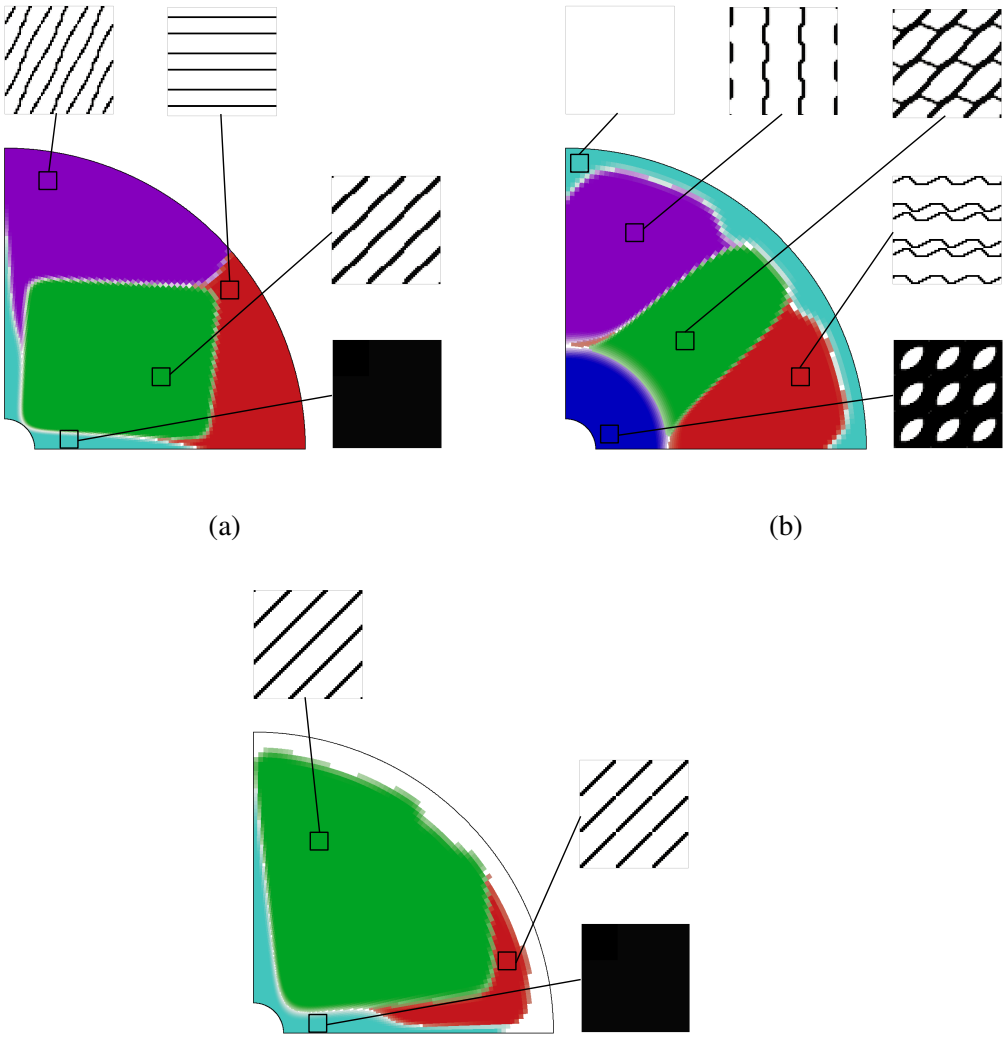

(a) (b)

(c)

Fig. 4.32. Optimized macroscopic and microscopic layouts for three moving metal matrices configurations. (a): Three patches; (b): three fingers; (c): finger structure with patches background

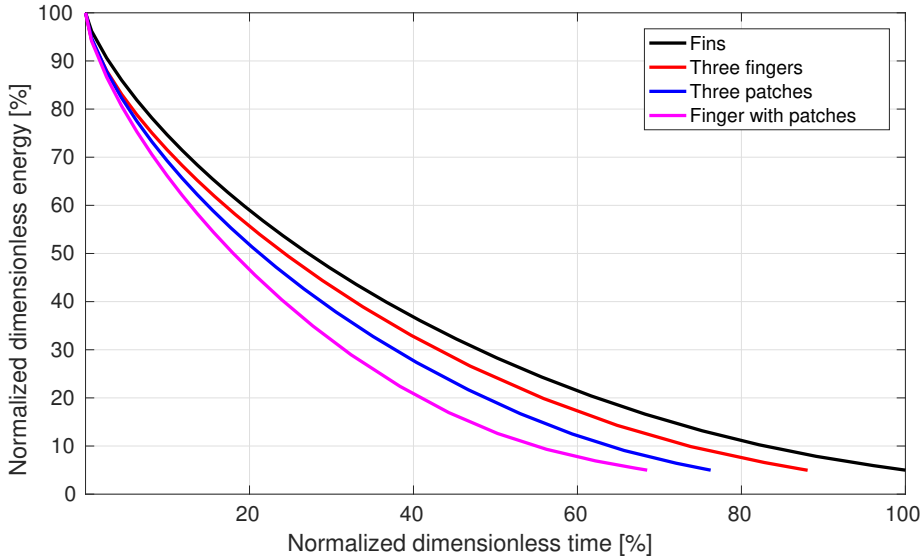

Fig. 4.33. Normalized energy histories of the optimized fin design and moving material configurations

4.32(b)) is composed by an inner ring with a large volume fraction material. The fingers are approximately equally spaced along the angular direction. The diagonal finger is filled with a thick HCM reticular geometry. The materials occupying the other fingers are composed by wave-like vertical and horizontal HCM stripes. The material domain Ω_1 occupies a thin region close to the external envelope and is made of full PCM. The last option we considered is obtained by adopting different parameterizations for the structure and material domains. The structure level-set, ϕ_0, is defined as the finger-type of agglomerate of geometric primitives. The material domains are controlled by three patches. Figure 4.32(c) shows the optimized layouts for this case. As for the moving patches configuration, two fins are created aligned along the $\theta = 0$ and $\theta = \pi/2$ directions. The remainder of the structure is composed only by two materials, as Ω_2 disappears during the optimization process. Nearly the same micro-structure is obtained in Ω_3 and Ω_4 such that this region can be considered as occupied by a unique material. The structure layout approximates a circle with a radius slightly smaller than the shell.

The energy histories during a complete discharge process for these three designs are compared to the one of the topology-optimized fins in Figure 4.33. All the alternatives yield performance improvements with respect to the fins. The discharge time is reduced by 11.9 %, 23.7 % and 31.5 % when using the material finger layout,

the material patches layout and the finger structure with material patches layout. A similar trend would be obtained also for partial discharges. The gaps in performance build gradually in time. Differently from what obtained for the heat sink example, the choice on the macroscopic parametrization strongly affects the performance.

The liquid fraction evolution for all the layouts considered is presented in Figure 4.34. Note that the snapshots at $t^* = 0.8\ t^*_{ref}$ for the patches and finger-plus-patches configurations are not shown since the discharge is already completed. As compared to what observed in the previous section, the solidification fronts propagate more concentrically with the internal pipe. This is well visible at $t^* = 0.6\ t^*_{ref}$. For all the designs, the mushy regions are well distributed close to the shell and corners of the design domain. Different discharge dynamics are observed for $t^* < 0.6\ t^*_{ref}$. In the three patches layout and in the finger-plus-patches layout, the solidification propagates rapidly following the two fins and resulting in a nearly triangular solidified region at $t^* = 0.2\ t^*_{ref}$. Then, in the patches design, solid PCM is rapidly created in Ω_4 morphing the solidification front towards the center. In the fingers-plus-patches configuration, the front advances along the diagonal direction until it reaches the border of the structure. The gap between the structure and the shell is then cooled slowly due to the absence of HCM. In the finger configuration, the solidification front first advances towards the center of the design domain following the central finger Ω_4. Then, the heat is transfered in the $\theta = 0$ and $\theta = \pi/2$ directions by exploiting the particular micro-structures of the side fingers. Also for this case, a large portion of time at the end of the process is used to cool the pure PCM gap close to the external shell.

4.7 Conclusions

In this chapter, we developed a multi-scale multi-material optimization framework to obtain "machinable" assemblies of periodic heat transfer structures. We first demonstrated the approach on a steady-state heat sink example. Then, we applied the method for the practical design of geometries for heat transfer enhancement in LHTES units. A graphical summary of the main application-oriented advances for LHTES units obtained in the chapter is presented in Figure 4.35. The optimization results suggest that optimizing a single periodic structure yields a reduced performance as compared to topology-optimized fin layouts. Improvements are possible

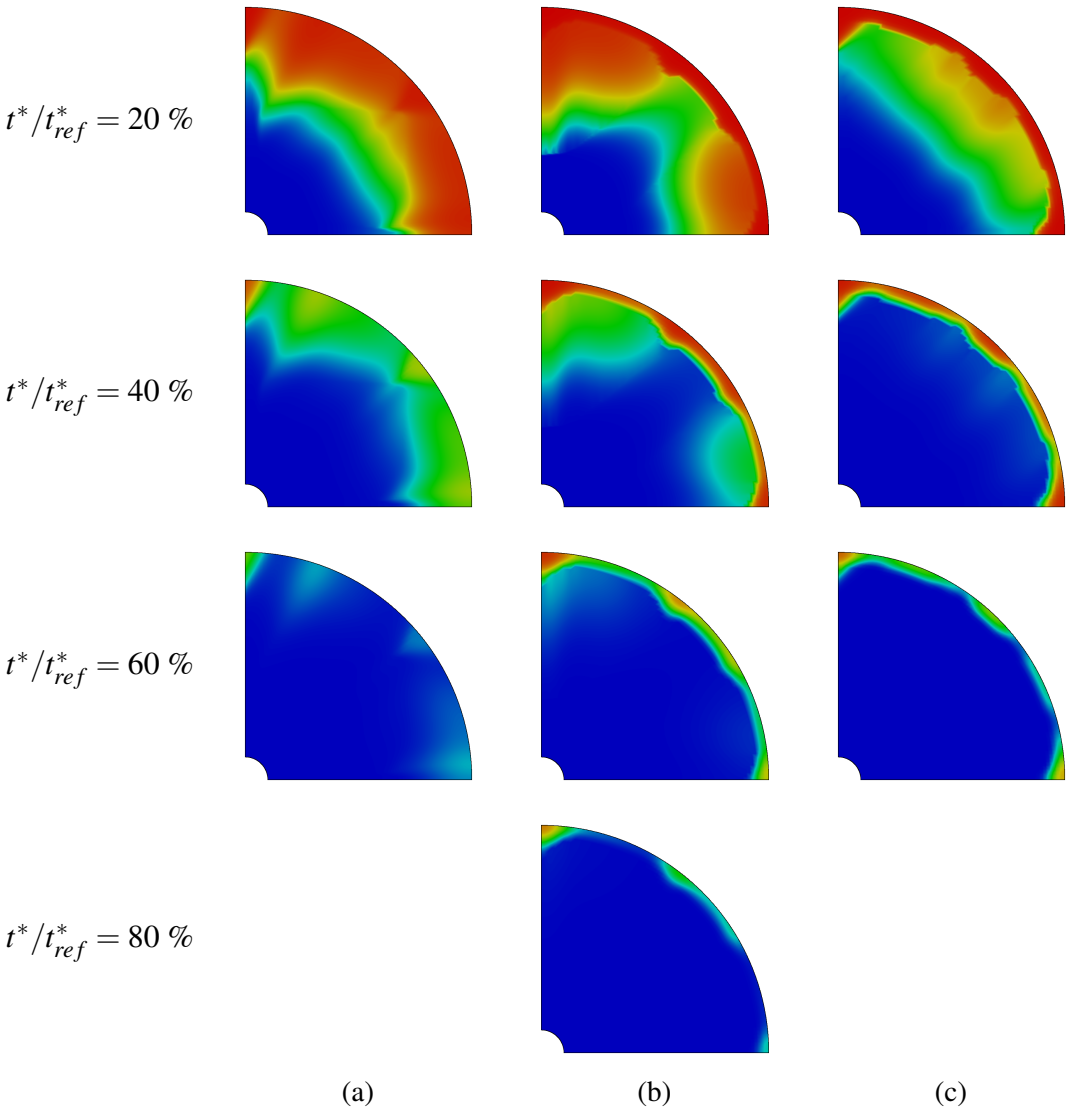

Fig. 4.34. Liquid fraction evolution of the optimized fin design and fixed material configurations. (a): Three patches; (b): three fingers; (c): finger structure with patches background

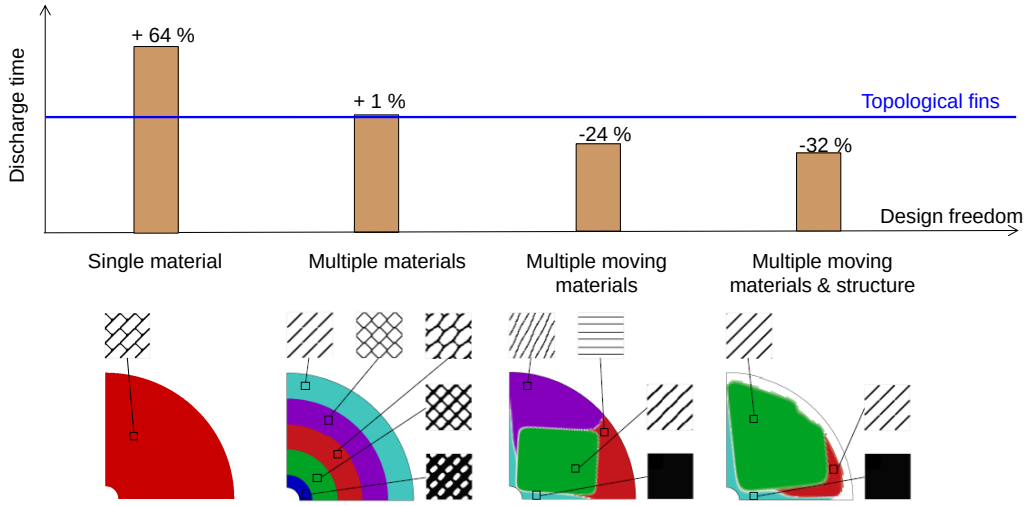

Fig. 4.35. Graphical summary of the main application-oriented advances of the chapter

by optimizing multiple structures within the design domain instead of a single one. Whether this strategy fills completely the gap in performance is problem-dependent. In the LHTES study, the discharge times of our fixed multi-material assemblies were comparable to the one of fins. However, in the heat sink study, our best configuration resulted in a 21.3 % larger objective. The choice of the aggregation layout of the structure relies on the designer experience. Different assumptions lead to large differences in performance. For this reason, we optimized both the microstructures and the aggregation layout of the periodic materials. This was achieved by using geometric primitive level-sets so that reasonably "well-behaved" shapes of the material domains are obtained. The resulting optimized configurations are superior to the topology-optimized fins for both the design studies. We obtained a maximum reduction of the objective of 14.8 % and 23.7 % for the heat sink and for the LHTES unit, respectively. Inspired by the concurrent structure and material PAMP design approach, we then extended the optimization framework to allow a decoupled parametrization of the material domains and structure, both controlled by geometric primitive level-sets. Although this strategy did not yield benefits in the heat sink study, we obtained large gains in the LHTES unit. The optimized structure has low geometrical complexity and allows the discharge time to be reduced by 31.5 % as compared to the topology-optimized fins.

Chapter 5

Exploiting convective transport

Chapters 3 and 4 relied on a simplified phase change model. Considering only diffusion for design optimization studies is questionable. The convective effects and fin layout are tightly connected and it is hard to assess whether convection can be neglected if the design is unknown. Some recent design studies [46, 109, 436] investigated the effect of specific layout features on convective transport. Different conclusions were drawn for melting and solidification, suggesting that different layouts may be required to enhance the two processes. In this chapter, we aim at exploring how the optimized layouts are affected by fluid flow and identifying what makes the structures optimized for melting different from those optimized for solidification. The remainder of this chapter is organized as follows: in Section 5.1 we review possible methods for modeling convection in the liquid PCM; in Section 5.2, we present, verify and validate our finite element numerical model and implementation; Section 5.3 introduces the material interpolation strategies for conjugate heat transfer and Section 5.4 discusses some issues that one may encounter when choosing suitable continuation strategies to design devices relying on natural or forced convection; finally, in Section 5.5 we examine and compare the topology-optimized designs for melting and solidification and we present a possible approach to reduce the layout complexity in the spirit of an easier manufacturing.

Some of the contents of this chapter were published in Applied Energy **[J1]** and presented at the 2017 ASME Summer Heat Transfer Conference **[C2]**.

5.1 Modeling convection/diffusion phase change

In most of the phase change phenomena of practical interest, the fluid motion yields a non-negligible contribution to the thermal response and has to be taken into consideration in the analysis. Hence, the diffusive Stefan problem presented in Section 3.2 needs to be modified accordingly. Considering a laminar incompressible viscous flow, the Stefan problem is augmented with the Navier-Stokes equations in the liquid domain, Ω_l, as follows:

$$\frac{\partial v_i}{\partial x_i} = 0 \qquad \text{in } \Omega_l, \tag{5.1}$$

$$\rho_l \frac{\partial v_i}{\partial t} + \rho_l v_j \frac{\partial v_i}{\partial x_j} = \frac{\partial \sigma_{ij}}{\partial x_j} + F_i \qquad \text{in } \Omega_l, \tag{5.2}$$

where v_i is the velocity, F_i is a momentum source term, and σ_{ij} is the viscous stress tensor. Equation (5.1) acts as a kinematic constraint in prescribing a divergence-free flow. Equation (5.2) is the balance of momentum along the direction "i". The constitutive equation for viscous, isotropic, incompressible fluids allows the stress tensor to be written as [349]:

$$\sigma_{ij} = -p\delta_{ij} + \mu_l \left(\frac{\partial v_j}{\partial x_i} + \frac{\partial v_i}{\partial x_j} \right), \tag{5.3}$$

where μ_l is the dynamic viscosity of the liquid PCM. In isothermal melting or solidification, the fluid-dynamic response can be computed considering a no-slip condition $v_i = 0$ at the (sharp) solid-liquid interface. The energy equation in the melt (Eq. (3.2)) needs to be modified to include a convective contribution:

$$\rho c_{p_l} \frac{\partial T}{\partial t} + \rho c_{p_l} v_i \frac{\partial T}{\partial x_i} = \frac{\partial}{\partial x_i} \left(k_{l_{ij}} \frac{\partial T}{\partial x_j} \right) \qquad \text{in } \Omega_l. \tag{5.4}$$

In Chapter 3, we discussed the numerical advantages of using a fixed grid method instead of solving the full Stefan problem using a variable grid that conforms with the interface. With a fixed grid approach, there is no need to satisfy the interface conditions at the solid-liquid front [76]. Furthermore, the general fixed grid formulation needs only minimal modifications for non-isothermal phase change where a mushy region is present, as in metal alloys and organic PCMs. The extension of the fixed-grid approaches presented in Chapter 3 for the transient nonlinear

diffusion equation demands a proper modification of the momentum equation in such a way that: (i) the velocities, and consequently the advective energy transport, are zero in the solid region, (ii) the full set of Navier-Stokes equations (Equations (5.1) and (5.2)) are recovered in liquid region, (iii) the dynamics in the mushy zone is predicted accurately.

After the early developments of numerical methods for convection-diffusion phase change, Voller et al. [437] identified three possible ways to modify the momentum equation:

(1) switch-off techniques,

(2) variable viscosity,

(3) porosity.

The approach (1) as described by Morgan [303] is the most straightforward. The nodal velocities are constrained to zero when the nodal temperature drops below the liquidus temperature. Instead of using the liquidus temperature to identify the non-convective regions, Voller et al. [437] generalized the formulation by using a threshold liquid fraction. The author of [303] acknowledged that the approach is less accurate than the alternatives (2) or (3). However, he advocated that it is simpler to implement in explicit schemes. The inaccuracies of simple switch-off techniques were later investigated by other authors, for instance Ma and Zhang [284]. It was argued by these authors that the approach (1) is a simple numerical artifact and has no physical significance. On the other hand, the approaches (2) and (3) are suitable to model phase change with specific melting and solidification dynamics. Those are discussed in more details in the following sections.

5.1.1 Variable viscosity method

This modeling strategy can be adopted for amorphous materials such as waxes or glasses [441]. In this case, the solid is dispersed in melt pool such that both the solid and liquid move at the same velocity. The viscosity of the mixture increases from small values (PCM behaving like a fluid) to large values (PCM behaving like a solid) during the transition from liquid to solid [321].

The first work adopting this approach is the one of Gartling [155], who used a temperature-dependent viscosity interpolating an arbitrary large value (representing the solid viscosity) and the liquid viscosity. Voller et al. [437] and then Cao and Faghri [76] later proposed:

$$\mu = \mu_l + B(1-f), \tag{5.5}$$

where μ is the effective viscosity and $B \to \infty$ is a large constant. The authors argued that using a latent heat (or liquid fraction) formulation such as (5.5) might be more convenient since isothermal phase change may be treated with equal ease. Another approach is the one proposed in [56] where the effective viscosity is written using the harmonic mean:

$$\mu = \frac{\mu_l}{f}, \tag{5.6}$$

whose denominator needs to be modified for practical implementation to allow for a minimum value such that the divisions by zero are avoided. The interpolations (5.5) and (5.6) were compared in [437]. The arithmetic formulation was found to lead to faster solidification as compared to the harmonic one.

5.1.2 Porosity method

This model is applicable when the solid PCM is separated from the melt [441] and is not moving. Here, the mushy region is composed of columnar dendritic structures with the base attached to solidified PCM and with the tip submerged in the melt pool. As noted by Mehrabian and co-authors [297], this is a multi-scale type of problem. The typical spacing of dendrite arms is three orders of magnitude lower than the width of the mushy zone. Reference [297] is one of the first works proposing a Darcy flow model to predict the interdendritic flow [43]. Ganesan and Porier [152] later extended the porous media formulation by using a volume-averaging approach. They obtained [47, 57]:

$$\rho_l \frac{\partial \tilde{v}_i}{\partial t} + \rho_l \tilde{v}_j \frac{\partial \tilde{v}_i}{\partial x_j} = -\frac{\partial p}{\partial x_i} + \frac{1}{f}\frac{\partial}{\partial x_j}\left(\mu_l f\left(\frac{\partial \tilde{v}_i}{\partial x_j} + \frac{\partial \tilde{v}_j}{\partial x_i}\right)\right) \underbrace{-f\frac{\mu_l}{\kappa}\tilde{v}_i}_{F_{i_{pm}}}, \tag{5.7}$$

where κ is the permeability and $\tilde{v}_i$ is the interdendritic velocity which is related to the superficial (volume-averaged) velocity, v_i, through the Dupuit-Forchheimer

relationship [310]:

$$\tilde{v}_i = \frac{v_i}{\varepsilon_p}, \tag{5.8}$$

where ε_p is the porosity of the medium. Note that in the mushy zone we can write $\varepsilon_p = f$. The inclusion of the advective transport in the momentum equation for flows in porous media led to some controversies in the engineering community. For instance, Nield and Bejan [310] observed that this term is generally small and can be safely neglected in numerical computations. Also, the authors argued that the transient term can be dropped since it decays very rapidly [310]. However, Gartling advocated that this is a reasonable approximation when porosity patterns with *evolutionary* features are considered. The Darcy's law allows the flow to be reproduced faithfully at the dendrite base, where the porosity approaches zero. However, when moving to the dendrite tip, the full Navier-Stokes equations need to be recovered [154]. It is customary to group the last term of Eq. (5.7) in a porous medium momentum sink, $F_{i_{pm}}$, that can be formulated directly as a function of the liquid fraction, f. For (nearly) isothermal phase-change a linear relation was proposed in [437] as:

$$F_{i_{pm}} = -A_{m_l}(1-f)v_i, \tag{5.9}$$

where A_{m_l} is a large constant. Eq. (5.9) has the advantage of yielding a limited nonlinearity as compared to various alternative formulations [64]. A more popular approach consists in using a momentum sink inspired by the Kozeny-Carman equation [64]:

$$F_{i_{pm}} = -A_{m_{KC}} \frac{(1-f)^2}{f^3 + \varepsilon_m} v_i, \tag{5.10}$$

where $A_{m_{KC}}$ is referred to as the mushy constant whose value depends mainly on the morphology of the solid formations and ε_m is a small value to avoid the divisions by zero. Eq. (5.10) was derived for packed beds of solid particles invested by a Darcy flow [78]. In this case, the constant $A_{m_{CK}}$ takes the form [310]:

$$A_{m_{KC}} = \frac{D_h^2}{180}, \tag{5.11}$$

where D_h is the average hydraulic diameter of the particles obtained by probabilistic sampling. The numerical value at the denominator was obtained through a best-fit on experimental results [310]. The experimental evidence presented in [339] recommended the Kozeny-Carman approach as the best choice for large liquid

fractions. Furthermore, this approach has the advantage of having a clear physical rationale that motivates its formulation. For this reason, this is the most widespread approach in the literature nowadays, see for instance [473, 260, 220]. However, the choice of the mushy constant, $A_{m_{KC}}$, introduces some arbitrariness that may invalidate the advantage of using a physical-based model. Voller et al. [437], Shmueli et al. [385] and later Kumar and Krishna [255] observed that the value of the mushy constant largely affects the thermal and fluid-dynamic response of PCM systems.

Substituting (5.8) into Eq. (5.7) leads to an equation for the superficial velocity:

$$\frac{\rho_l}{f}\frac{\partial v_i}{\partial t}+\frac{\rho_l}{f^2}v_j\frac{\partial v_i}{\partial x_j}=-\frac{\partial p}{\partial x_i}+\frac{1}{f}\frac{\partial}{\partial x_j}\left(\mu_l\left(\frac{\partial v_i}{\partial x_j}+\frac{\partial v_j}{\partial x_i}\right)\right)+F_{i_{pm}}. \tag{5.12}$$

The comparison of (5.12) with (5.2) shows that the advective, the diffusive and the transient term needs to be modified to account for the varying liquid fraction in the mushy region. However, Voller et al. [64] argued that the porosity sink "will dominate over the transient, convective, and diffusive components" leading to the original Kozeny-Carman equation [78]. Hence, authors simply adopted [437, 64, 441]:

$$\rho\frac{\partial v_i}{\partial t}+\rho v_j\frac{\partial v_i}{\partial x_j}=-\frac{\partial p}{\partial x_i}+\frac{\partial}{\partial x_j}\left(\mu\left(\frac{\partial v_i}{\partial x_j}+\frac{\partial v_j}{\partial x_i}\right)\right)+F_{i_{pm}}, \tag{5.13}$$

with the momentum sink defined as in (5.10). Although the validity of the previous assumption can be questioned (we found no quantitative assessment in this direction), Eq. (5.13) represents a standard formulation in the phase change literature of today. In most studies, see for instance [385, 30, 230, 3], a fitting of the mushy constant A_m with experimental results was done considering (5.13). For this reason, this is the reference momentum equation for PCMs used throughout this monograph.

5.2 Numerical model

In this chapter, the design and computational domains need to be modified from the ones presented in Chapter 3. Due to the effect of natural convection, the symmetry along the $y = 0$ axis of the cross-section no longer applies. Figure 5.1 shows a schematic of the design domain Ω_D considered hereafter. It consists of a reflection along the $y = 0$ axis of the design domain considered for the diffusive designs (Figure 3.6).

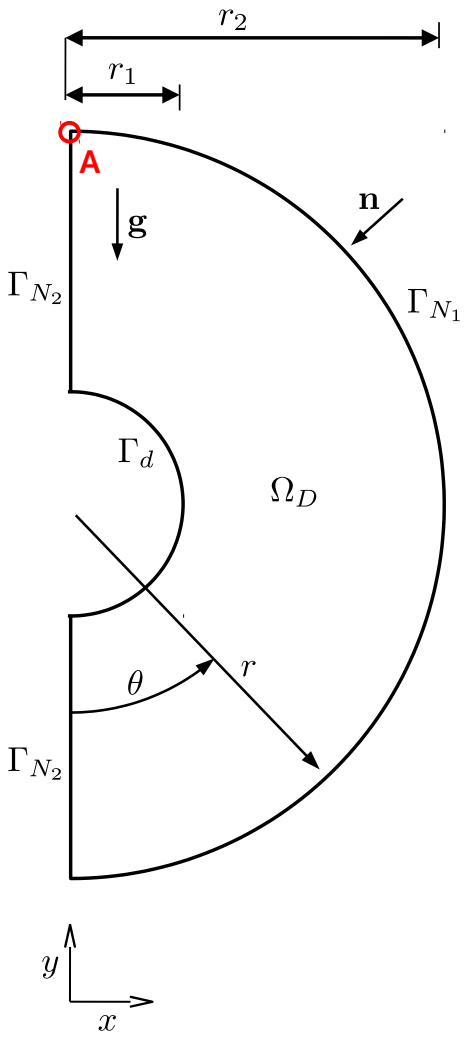

Fig. 5.1. Design and computational domain

Similarly to what we did in Section 3.3, here we rework the governing equations to obtain a dimensionless setting. The dimensionless time, length and temperature are equal to the ones adopted for the diffusion model (Eqs. (3.22) (3.23) and (3.24), respectively). Considering fluid flow requires the introduction of:

- the dimensionless velocity
$$v_i^* = v_i/U, \tag{5.14}$$
where U is a reference velocity,
- the dimensionless pressure
$$p^* = p/(\rho_0 U^2). \tag{5.15}$$
where ρ_0 is a reference density.

Recall that all the dimensionless quantities are marked with an asterisk. The reference velocity is taken as the diffusion velocity, U, of the PCM calculated as:

$$U = \frac{\alpha_{t_{PCM}}}{L}, \tag{5.16}$$

where $\alpha_{t_{PCM}}$ is the thermal diffusivity of the PCM. The reference density, ρ_0, is taken as the average PCM density. The governing equations presented in 3.3.1 are augmented with the continuity and momentum equations formulated using the standard porosity model (Eq. (5.13)). Under the assumption of constant fluid properties, incompressible flow and negligible viscous dissipation we have:

$$\frac{\partial v_i^*}{\partial x_i^*} = 0, \tag{5.17}$$

$$\frac{\partial v_i^*}{\partial t^*} + v_j^* \frac{\partial v_i^*}{\partial x_j^*} = -\frac{\partial p_i^*}{\partial x_i^*} + Pr \frac{\partial}{\partial x_j} \left(\frac{\partial v_i^*}{\partial x_j^*} + \frac{\partial v_j^*}{\partial x_i^*} \right) + F_{nc_i}^* + F_{b_i}^*(s) + F_{pm_i}^*, \tag{5.18}$$

where Pr is the Prandtl number, $F_{nc_i}^*$ is a volumetric term accounting for temperature-induced buoyancy forces and $F_{b_i}^*(s)$ is a design-dependent momentum source term that will be discussed later. For incompressible non-isothermal flows with small density variations, $\Delta\rho$, as compared to the reference density, ρ_0, natural convection can be accounted by considering the density variations only in the buoyancy term as

follows [350]:

$$\rho g_i = \rho_0 g_i + \Delta\rho g_i \sim \rho_0 g_i + \rho_0 \beta_T (T - T_0) g_i, \tag{5.19}$$

where β_T is the coefficient of thermal expansion and T_0 a reference temperature. Equation (5.19) is generally referred to as Boussinesq approximation and it is of common use in the Computational Fluid-Dynamics (CFD) community. The constant term, $\rho_0 g_i$, can be absorbed into the pressure term to obtain a total pressure accounting for the gravitational head [13]. Hence, using the dimensionless variables previously introduced we obtain:

$$F^*_{nc_i} = -Ra\ Pr\ e^g_i T^*, \tag{5.20}$$

where e^g_i is the unit vector in the direction of gravity and Ra is the Rayleigh number.

As discussed in the previous section, the porosity term, $F^*_{pm_i}$, ensures that the velocities are zero in the solid PCM region and that accurate predictions are obtained in the mushy region. The dimensionless version of (5.10) is written as:

$$F^*_{pm_i} = -\frac{A_{m_{CK}}}{\rho_0 U/L} \frac{(1-f)^2}{f^3 + \varepsilon_m} v^*_i, \tag{5.21}$$

where the constants are set as $\varepsilon_m = 10^{-3}$ and $A_{mushy} = 10^8$ kg/(m^3 s) according to [385].

The energy equation (3.26) is modified through the addition of convective transport:

$$\frac{\partial T^*}{\partial t^*} + v^*_j \left(1 + \gamma(s)\mathscr{L}^* \frac{\partial f}{\partial T^*}\right) \frac{\partial T^*}{\partial x^*_j} = \frac{\partial}{\partial x^*_j}\left(K_{ij}(s) \frac{\partial T^*}{\partial x^*_i}\right) - \gamma(s)\mathscr{L}^* \frac{\partial f^*}{\partial t^*}. \tag{5.22}$$

The term in brackets on the left-hand side accounts for the convective energy transport in the form of both sensible and latent heat. Note that the latter is modeled with an apparent heat capacity formulation (Section 3.2.2).

Moving to the boundary conditions, we prescribe an adiabatic boundary on the external shell Γ_{N_1} and a symmetry boundary condition on Γ_{N_2} such that:

$$-K_{ij} \frac{\partial T^*}{\partial x^*_j} n_i = 0 \qquad on \quad \Gamma_{N_1} \cup \Gamma_{N_2}, \quad \forall t^*. \tag{5.23}$$

The temperature is fixed at the internal boundary, Γ_d, to represent the contact with the tube containing the HTF. Mathematically:

$$T^* = T_d^* \qquad on \quad \Gamma_d, \quad \forall t^*, \tag{5.24}$$

where T_d^* is the dimensionless temperature of the HTF pipe, which takes different values for charge and discharge. The interaction with the external shell and pipe boundaries is modeled using a no-slip condition. Due to symmetry, only non-penetration is prescribed on the boundary running along the y-axis. Mathematically:

$$v_i^* = \mathbf{0} \qquad on \quad \Gamma_d \cup \Gamma_{N_1}, \quad \forall t^*, \tag{5.25}$$

$$v_i^* n_i = 0 \qquad on \quad \Gamma_{N_2}, \quad \forall t^*. \tag{5.26}$$

To obtain a well-posed incompressible Navier-Stokes problem in the enclosure, the pressure $p^* = 0$ is specified at point A (Fig. 5.1). This choice does not modify the thermal and fluid-dynamic responses. The initial conditions are:

$$\begin{aligned} &T^* = T_I^* \quad in \quad \Omega_D, \quad \text{at } t^* = 0, \\ &v_i^* = \mathbf{0} \quad in \quad \Omega_D, \quad \text{at } t^* = 0, \\ &p^* = 0 \quad in \quad \Omega_D, \quad \text{at } t^* = 0. \end{aligned} \tag{5.27}$$

5.2.1 Finite Element model

Equations (5.17), (5.18) and (5.22) are discretized in space using a mixed finite element model. Denoting by R_c, $\mathbf{R}_m$, R_{en} the residuals of the strong form of the continuity, momentum and energy equation respectively, the weighted integral statement over the computational domain, Ω, is written as:

$$\int_\Omega \eta^h R_c \, d\mathbf{x} = 0, \tag{5.28}$$

$$\int_\Omega \xi_i^h R_{m_i} \, d\mathbf{x} = 0, \tag{5.29}$$

$$\int_\Omega w^h R_{en} \, d\mathbf{x} = 0, \tag{5.30}$$

where η^h and ξ_i^h are the weight functions of the continuity and momentum equations. Integration by parts of the viscous term in Eq. (5.29) and of the diffusive term in Eq. (5.30) allows the weak forms of the governing equations to be obtained.

The approximation and weighting functions for the temperature field were defined in (3.36) and (3.37). The pressure and velocity fields are approximated using p^h and $\mathbf{v}^h$ taken from the following function spaces:

$$\begin{aligned} \mathscr{U}_p &= \{p^h \in \mathscr{H}^1(\Omega);\ p^h = p_d^*\ \text{ on } \Gamma_{d_p}\}, \\ \mathbf{U} &= \{\mathbf{v}^h \in \mathscr{H}^1(\Omega);\ \mathbf{v}^h = \mathbf{v}_d^*\ \text{ on } \Gamma_{d_v}\}, \end{aligned} \tag{5.31}$$

where Γ_{d_p} and Γ_{d_v} denotes generic Dirichlet boundaries for the pressures and velocities, respectively, and $\mathscr{U}_p$ and $\mathbf{U}$ are Hilbert spaces consisting of scalar functions and vector functions with square integrable first derivatives. Through the modification of the Dirichlet boundary restrictions in (5.31), we obtain the weighting function spaces as:

$$\begin{aligned} \mathscr{V}_p &= \{\eta^h \in \mathscr{H}^1(\Omega);\ \eta^h = 0\ \text{ on } \Gamma_{d_p}\}, \\ \mathbf{V} &= \{\boldsymbol{\xi}^h \in \mathscr{H}^1(\Omega);\ \boldsymbol{\xi}^h = \mathbf{0}\ \text{ on } \Gamma_{d_v}\}, \end{aligned} \tag{5.32}$$

In Eq. (3.38), we showed how to write a spatial-temporal split to obtain the approximate temperature field. Further, using the Galerkin method, the temperature shape functions, N, were chosen equal to the weight functions, w^h. Following a similar route for the pressure and velocities leads to:

$$p^h(\mathbf{x},t) = \sum_{j=1}^{N_n} p_j^*(t)\eta_j(\mathbf{x}) = \boldsymbol{\eta}^{h^T}\mathbf{p}^*, \tag{5.33}$$

$$v_i^h(\mathbf{x},t) = \sum_{j=1}^{N_n} v_{i_j}^*(t)\xi_j(\mathbf{x}) = \boldsymbol{\xi}^{h^T}\mathbf{v}_i^*, \tag{5.34}$$

where p_j^* and $v_{i_j}^*$ are time-dependent nodal pressure and velocity values and $\mathbf{p}^*$ and $\mathbf{v}_i^*$ represent their collection in column vectors. In (5.34), we took the same approximating function, ξ_j, for all the velocity components. The asterisk indicating the dimensionless variables is dropped for brevity hereafter. Recalling (5.20), p_j^* and $\mathbf{p}^*$ represent the total pressure including the gravitational head. Substituting (3.38), (5.33) and (5.34) in the weak form of the governing equations leads to the following

unstabilized Galerkin model of the Navier-Stokes equations in matrix form [350]:

$$\mathbf{R}_{us,c} = \mathbf{Q}_j^T \mathbf{v}_j = \mathbf{0}, \tag{5.35}$$

$$\mathbf{R}_{us,m_i} = \mathbf{M}\dot{\mathbf{v}}_i + \mathbf{A}_m \mathbf{v}_i + \mathbf{D}_{ij}\mathbf{v}_j - \mathbf{Q}_i \mathbf{p} - \mathbf{F}_i = \mathbf{0}, \tag{5.36}$$

where:

$$\mathbf{Q}_j = \int_\Omega \frac{\partial \boldsymbol{\xi}^h}{\partial x_j} \eta^h d\mathbf{x}, \tag{5.37}$$

$$\mathbf{M}_j = \int_\Omega \boldsymbol{\xi}^h \boldsymbol{\xi}^{h^T} d\mathbf{x}, \tag{5.38}$$

$$\mathbf{A}_m = \int_\Omega \boldsymbol{\xi}^h (\boldsymbol{\xi}^{h^T} \mathbf{v}_j) \frac{\partial \boldsymbol{\xi}^{h^T}}{\partial x_j} d\mathbf{x}, \tag{5.39}$$

$$\mathbf{D}_{ij} = \begin{cases} \int_\Omega Pr \left(2 \frac{\partial \boldsymbol{\xi}^h}{\partial x_i} \frac{\partial \boldsymbol{\xi}^{h^T}}{\partial x_i} + \frac{\partial \boldsymbol{\xi}^h}{\partial x_l} \frac{\partial \boldsymbol{\xi}^{h^T}}{\partial x_l} \right) d\mathbf{x} & \text{for } j = i, l \neq i \\ \int_\Omega Pr \left(\frac{\partial \boldsymbol{\xi}^h}{\partial x_i} \frac{\partial \boldsymbol{\xi}^{h^T}}{\partial x_j} \right) d\mathbf{x} & \text{for } j \neq i \end{cases}, \tag{5.40}$$

$$\mathbf{F}_i = \int_\Omega \boldsymbol{\xi}^h \left(F_{nc_i} + F_{b_i}(s) + F_{pm_i} \right) d\mathbf{x} + \int_{\Gamma_N} \boldsymbol{\xi}^h f_i \, d\mathbf{x}', \tag{5.41}$$

with f_i being the traction on Γ_N. The energy equation presented in (3.40) is modified through the addition of a convective term as following:

$$\mathbf{R}_{us,e} = \mathbf{C}\dot{\mathbf{T}} + \mathbf{A}_T \mathbf{T} + \mathbf{K}\mathbf{T} + \dot{\mathbf{L}} + \mathbf{q} = \mathbf{0}, \tag{5.42}$$

where:

$$\mathbf{A}_T = \int_\Omega \mathbf{N} \left(1 + \gamma \mathscr{L} \frac{\partial f}{\partial T} \right) (\boldsymbol{\xi}^{h^T} \mathbf{v}_j) \frac{\partial \mathbf{N}}{\partial x_j} d\mathbf{x}. \tag{5.43}$$

To avoid numerical instabilities, the discrete residuals are augmented with stabilization terms as follows:

$$\mathbf{R}_c = \mathbf{R}_{us,c} + \mathbf{R}_{c_{PSPG}}, \tag{5.44}$$

$$\mathbf{R}_{m_i} = \mathbf{R}_{us,m_i} + \mathbf{R}_{m_{i_{SUPG}}}, \tag{5.45}$$

$$\mathbf{R}_e = \mathbf{R}_{us,e} + \mathbf{R}_{e_{SUPG}} + \mathbf{R}_{e_{GGLS}}, \tag{5.46}$$

where $\mathbf{R}_{c_{PSPG}}$, $\mathbf{R}_{m_{i_{SUPG}}}$ and $\mathbf{R}_{e_{SUPG}}$ are detailed in the following section, while $\mathbf{R}_{e_{GGLS}}$ is the GGLS stabilization contribution to the residuals. A discussion on the GGLS stabilization was given in Section 3.3.3, which includes the main motivations for its use when modeling phase change systems and a numerical example showing its effectiveness. The definition given in (3.45) for $\mathbf{R}_{e_{GGLS}}$ is here augmented with the following advective contribution:

$$\mathbf{R}_{GGLS_A} = \sum_{e=1}^{N_e} \int_{\Omega_e} \frac{\partial \mathbf{N}}{\partial x_i} k \tau_{GGLS} \frac{\partial}{\partial x_i} \left(v_j^h \left(1 + \gamma \mathscr{L} \frac{\partial f}{\partial T} \right) \frac{\partial T^h}{\partial x_j} \right) d\mathbf{x}. \tag{5.47}$$

5.2.2 Stabilization

The treatment of incompressible flows with finite element results in two different types of instabilities [419]. First, the advective transport of both momentum and energy for a high Peclet number, Pe, leads to oscillations in the predicted velocity and temperature fields. This situation occurs in convection-dominated transport when the downstream boundary conditions force rapid solution variations. Second, the equal order interpolation for the velocities and pressure fails to satisfy the Babuska-Brezzi condition, yielding instabilities in the pressure field. The pressure field singularity exhibits as a checkerboard pattern with tight oscillations between positive and negative values.

This first problem is well known also in the finite difference and finite volume community [67]. The instabilities were observed to arise for $Pe > 2$ when the convective flux is approximated by central differences [433]. A simple upwinding along with more complicated hybrid schemes were proposed to solve the problem. The underlying idea is to substitute the downstream node contribution to the advective flux with the one of the current node. Intuitively, the convective fluxes are calculated as if the transported field is shifted by one nodal position. This procedure lowers the accuracy of the convection term approximation to the first order and the truncation error to the second order. For this reason, the discretization error introduced by the upwinding procedures (but not only) is commonly referred to as numerical diffusion. It can be shown that the sum of a diffusion term with an artificial diffusivity $\tilde{k} = vh/2$ and a convective term approximated by central differences results in the upwind scheme [67]. Since the 1D Galerkin finite element method with piece-wise linear shape functions yields the central difference approximation, the early developments

in the finite element community tried to leverage the finite difference advancements. According to Brooks and Hughes [67], three main paths were followed: artificial diffusion, smart quadrature and Petrov-Galerkin weighting. The latter has the advantage of yielding a consistent formulation. However, the extension to multi-dimensional problems revealed a cross-wind diffusion that affects the solution accuracy also in the direction normal to the flow propagation. Following the anisotropic artificial diffusion idea developed in [238], Brooks and Hughes [67] proposed a Petrov-Galerkin formulation with the following weighting function:

$$\tilde{N} = N + \tilde{N}, \tag{5.48}$$

where N is the Galerkin shape function and $\tilde{N}$ is a perturbation defined as:

$$\tilde{N} = \frac{\tilde{k}}{||\mathbf{v}||_2} \hat{v}_j \frac{\partial N}{\partial x_j} = \tau_{SUPG} v_j \frac{\partial N}{\partial x_j}, \tag{5.49}$$

where $\hat{v}_j$ is a normalized velocity component and τ_{SUPG} is a stabilizing term later introduced by [418, 419]. Weighting the convective component with a perturbation of the type $\tilde{N}$ is equal to a weak diffusion term with artificial diffusivity [67]:

$$\tilde{k}_{ij} = \tilde{k} \hat{v}_i \hat{v}_j. \tag{5.50}$$

Using the weight function (5.49) for the energy equation and a similar $\tilde{\xi}$ for the momentum equation, we obtain the following Streamline Upwind Petrov-Galerkin (SUPG) contribution to the residuals:

$$\mathbf{R}_{m_{i_{SUPG}}} = \sum_{e=1}^{N_e} \int_{\Omega_e} \tau_{SUPG} (\boldsymbol{\xi}^{h^T} \mathbf{v}_j) \frac{\partial \boldsymbol{\xi}^h}{\partial x_j} R^h_{m_i} d\mathbf{x}, \tag{5.51}$$

$$\mathbf{R}_{en_{SUPG}} = \sum_{e=1}^{N_e} \int_{\Omega_e} \tau_{SUPG} (\mathbf{N}^T \mathbf{v}_j) \frac{\partial \mathbf{N}}{\partial x_j} R^h_{en} d\mathbf{x}, \tag{5.52}$$

where $R^h_{m_i}$ and R^h_{en} represent the residual of the strong form of the momentum and energy equation calculated using the trial functions presented in the previous section.

Adopting Petrov-Galerkin formulations to improve stability with no compromise over consistency is the general idea that drove also the development of Pressure Stabilized Petrov-Galerkin (PSPG) method. In an original paper on incompressible Stokes flow [213], Hughes et al. developed a formulation able to circumvent the

Babuska-Brezzi condition, removing all the restrictions on the shape functions choice. Their error analysis led to the following perturbation function:

$$\tilde{\xi} = \tau_{PSPG} \frac{1}{\rho} \frac{\partial \boldsymbol{\eta}^h}{\partial x_i}, \tag{5.53}$$

which yields the following contribution to the residuals of the continuity equation:

$$\mathbf{R}_{c_{PSPG}} = \sum_{e=1}^{N_e} \int_{\Omega_e} \tau_{PSPG} \frac{1}{\rho} \frac{\partial \boldsymbol{\eta}^h}{\partial x_i} R^h_{m_i} d\mathbf{x}. \tag{5.54}$$

5.2.3 Adaptive time-stepping

The residuals of the semi-discrete momentum and energy equations are discretized in time adopting a backward Euler scheme as described in Section 3.3.4. Differently from what presented in Chapter 3, here the time-step size is changed using an adaptive scheme. Extremely small time-steps are required to resolve the flow at the initial instants of the process. Using a fixed time-stepping strategy would result in prohibitively slow analyses. Adaptive time-stepping allows to take bigger steps when the flow is developed. In addition, using adaptive time-stepping allows the local control of the truncation error introduced by (3.50). The numerical methods for time-step control developed in three main directions [425]:

- error estimates of the local truncation error based on a comparative error analysis of two integration methods with similar order [170, 156],
- heuristics based on the physical insights of the analyst on the problem [463, 223],
- control theory methods such as the Proportional Integral Derivative (PID) control [192, 399].

In this monograph, we adopt the approach suggested in [156] for its ease of implementation and proved accuracy for phase change problems. The adapted time-step $(\Delta t^*)^{(n+1)}_{ad}$ is controlled as follows:

$$(\Delta t^*)^{(n+1)}_{ad} = (\Delta t^*)^{(n)} \left(a \frac{\delta_t}{d^{(n+1)}} \right)^b, \tag{5.55}$$

where $a = 2$ and $b = 1/2$ for first order-schemes [156]. The parameter δ_t is a user-specified error tolerance and $d^{(n+1)}$ is a local estimate of the truncation error defined as:

$$d^{(n+1)} = \left(\frac{1}{N_d \max(\mathbf{u})^2} \sum_{i=1}^{N_d} (u_i^{(n+1)} - u_{i_p}^{(n+1)})^2 \right)^{1/2}, \tag{5.56}$$

where N_d is the number of degrees of freedom, $u_i^{(n+1)}$ is the solution computed through the implicit Euler scheme and $u_{i_p}^{(n+1)}$ is the degree of freedom computed with the following extrapolation:

$$\mathbf{u}_p^{(n+1)} = \mathbf{u}^{(n)} + \Delta t^{*(n)} \dot{\mathbf{u}}^{(n)}. \tag{5.57}$$

Note that $\mathbf{u}$ collects all the degrees of freedom in a unique vector by stacking the dimensionless pressures, velocities and temperatures as follows:

$$\mathbf{u} = \begin{bmatrix} \mathbf{p} \\ \mathbf{v} \\ \mathbf{T} \end{bmatrix}, \tag{5.58}$$

where in two dimensions we have:

$$\mathbf{v} = \begin{bmatrix} \mathbf{v}_1 \\ \mathbf{v}_2 \end{bmatrix}. \tag{5.59}$$

In our implementation, we prescribe a maximum ratio between the consecutive time-steps as well as a minimum and a maximum absolute time-step. To enforce the final time constraint of (3.67), we refined the approach presented in Chapter 3. At each time step, we estimate the remaining process time $(\Delta t^*)_{extr}^{(n+1)}$ based on a linear extrapolation of the energy history:

$$(\Delta t^*)_{extr}^{(n+1)} = (\Delta t^*)^{(n)} \frac{\Psi E^{fc} - E^{(n+1)}}{E^{(n+1)} - E^{(n)}}. \tag{5.60}$$

The fraction on the right-hand side is positive for both the charge and discharge processes due to the monotonicity of the energy history. The time-step $(n+1)$ is then chosen as:

$$(\Delta t^*)^{(n+1)} = \min \left((\Delta t^*)_{ad}^{(n+1)}, (\Delta t^*)_{extr}^{(n+1)} \right). \tag{5.61}$$

The time solver is stopped when the the final time constraint of (3.67) is satisfied within a specified relative tolerance, ε_t.

5.2.4 Nonlinear solution

The nonlinear system of equations arising from the spatial and temporal discretization presented above are solved with the Newton method as done for the diffusive systems. Following the procedure presented in 3.61, we split the Jacobian in a static and in a dynamic contribution, $\mathbf{J}_s$ and $\mathbf{J}_{dyn}$. This operation simplifies the sensitivity analysis of the transient problems as presented in Section 3.4.5. After stacking the momentum residuals as we did in 5.59 for the velocities:

$$\mathbf{R}_m = \begin{bmatrix} \mathbf{R}_{m_1} \\ \mathbf{R}_{m_2} \end{bmatrix}, \tag{5.62}$$

the static Jacobian of the mixed finite element model can be written in block form as:

$$\mathbf{J}_s = \begin{bmatrix} \mathbf{J}_{cp,s} & \mathbf{J}_{cv,s} & \mathbf{0} \\ \mathbf{J}_{mp,s} & \mathbf{J}_{mv,s} & \mathbf{J}_{mT,s} \\ \mathbf{0} & \mathbf{J}_{ev,s} & \mathbf{J}_{eT,s} \end{bmatrix}, \tag{5.63}$$

where:

$$\mathbf{J}_{cp,s} = \frac{\partial \mathbf{R}_{c,PSPG}}{\partial \mathbf{p}}, \tag{5.64}$$

$$\mathbf{J}_{cv,s} = \begin{bmatrix} \mathbf{Q}_1^T & \mathbf{Q}_2^T \end{bmatrix} + \frac{\partial \mathbf{R}_{c,PSPG}}{\partial \mathbf{v}}, \tag{5.65}$$

$$\mathbf{J}_{mp,s} = -\begin{bmatrix} \mathbf{Q}_1 & \mathbf{Q}_2 \end{bmatrix}^T + \frac{\partial \mathbf{R}_{m,SUPG}}{\partial \mathbf{p}}, \tag{5.66}$$

$$\mathbf{J}_{mv,s} = \mathrm{diag}\left(\mathbf{A}_m, \mathbf{A}_m\right) + \frac{\partial \mathbf{A}_m}{\partial \mathbf{v}}\mathbf{v} + \mathbf{D} + \frac{\partial \mathbf{R}_{m,SUPG}}{\partial \mathbf{v}}, \tag{5.67}$$

$$\mathbf{J}_{mT,s} = -\begin{bmatrix} \frac{\partial F_{nc_1}}{\partial \mathbf{T}} & \frac{\partial F_{nc_2}}{\partial \mathbf{T}} \end{bmatrix}^T + \frac{\partial \mathbf{R}_{m,SUPG}}{\partial \mathbf{T}}, \tag{5.68}$$

$$\mathbf{J}_{ev,s} = \frac{\partial \mathbf{A}_T}{\partial \mathbf{v}}\mathbf{T} + \frac{\partial \mathbf{R}_{e,SUPG}}{\partial \mathbf{v}}, \tag{5.69}$$

$$\mathbf{J}_{eT,s} = \mathbf{A}_T + \mathbf{K} + \frac{\partial \mathbf{R}_{e,SUPG}}{\partial \mathbf{T}}. \tag{5.70}$$

The dynamic contribution to Jacobian has the following form:

$$\mathbf{J}_{dyn} = \begin{bmatrix} \mathbf{0} & \mathbf{J}_{cv,dyn} & \mathbf{0} \\ \mathbf{0} & \mathbf{J}_{mv,dyn} & \mathbf{0} \\ \mathbf{0} & \mathbf{0} & \mathbf{J}_{eT,dyn} \end{bmatrix}, \tag{5.71}$$

where:

$$\mathbf{J}_{cp,dyn} = \frac{1}{\Delta t^{(n)}} \frac{\partial \mathbf{R}_{c,PSPG}}{\partial \dot{\mathbf{v}}}, \tag{5.72}$$

$$\mathbf{J}_{mv,dyn} = \frac{1}{\Delta t^{(n)}} \left(\text{diag}\left(\mathbf{M}, \mathbf{M}\right) + \frac{\partial \mathbf{R}_{m,SUPG}}{\partial \dot{\mathbf{v}}} \right), \tag{5.73}$$

$$\mathbf{J}_{eT,dyn} = \frac{1}{\Delta t^{(n)}} \left(\mathbf{C} + \frac{\partial \mathbf{L}}{\partial \mathbf{T}} + \frac{\partial \mathbf{R}_{e,SUPG}}{\partial \dot{\mathbf{T}}} + \frac{\partial \mathbf{R}_{e,SUPG}}{\partial \dot{\mathbf{L}}} \frac{\partial \mathbf{L}}{\partial \mathbf{T}} + \frac{\partial \mathbf{R}_{e,GGLS}}{\partial \dot{\mathbf{T}}} + \frac{\partial \mathbf{R}_{e,GGLS}}{\partial \dot{\mathbf{L}}} \frac{\partial \mathbf{L}}{\partial \mathbf{T}} \right). \tag{5.74}$$

Note that in this monograph we utilize a fully consistent Jacobian that includes the derivative of the stabilization parameters τ_{SUPG}, τ_{PSPG} and τ_{GGLS}.

5.2.5 Verification and validation

To check the accuracy of the presented framework in predicting the response of the convective systems, we proceed in three steps. First, we compare our predictions with benchmark numerical solutions for steady-state natural convection in a square cavity. Then, we demonstrate our model for phase change problems by comparing our predictions with experimental results for melting in a rectangular cavity. Last, we test the accuracy in the shell-and-tube unit considered in this chapter. With this aim, we compare our results with those obtained with COMSOL Multiphysics [101] since no benchmark numerical solution nor experimental study is available considering a setup similar to the one that we adopt.

The thermally-driven cavity problem is a classical benchmark numerical example first proposed by De Vahl Davis [110]. The results obtained by various research groups were collected in [111]. A square cavity with adiabatic top and bottom boundaries is differentially heated such that the left and right boundaries are kept at $T^* = 1$ and $T^* = 0$. No-slip and no-penetration are imposed at all the walls. Our predictions for $Ra = \{10^5;\ 10^6\}$ are compared to those obtained by Mayne et al. [295], Wan et al. [104] and to the ones obtained with COMSOL Multiphysics. The results shown in Figure 5.2 indicate an acceptable qualitative agreement of our

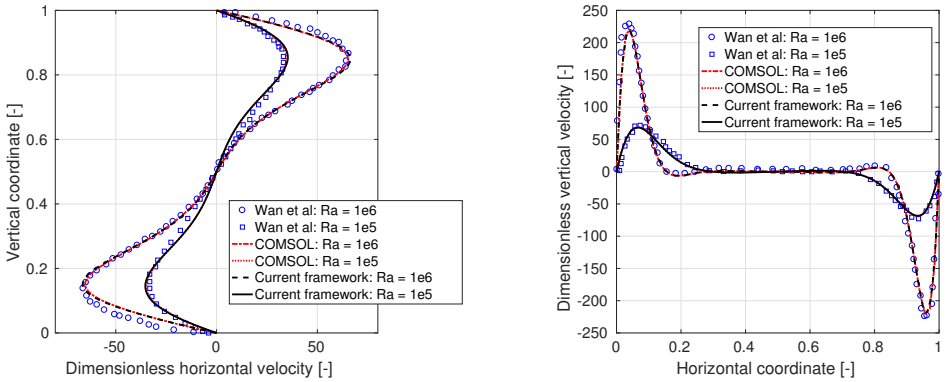

(a)

(b)

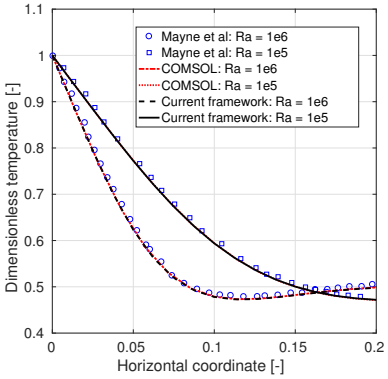

(c)

Fig. 5.2. Differentially heated cavity test. (a): Horizontal velocity at mid-width; (b): vertical velocity at mid-height; (c): temperature at mid-height

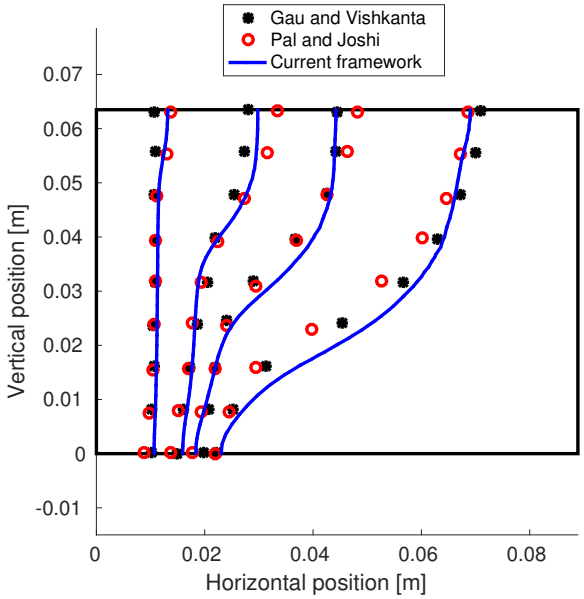

Fig. 5.3. Validation of the presented framework through comparisons with experimental results on melting of gallium in a square cavity

framework with the previous literature studies. Our predictions on the maximum horizontal velocity at mid-width and maximum vertical velocity at mid-height have a maximum deviation of 0.7 % from the benchmarks. The horizontal velocity plot reported in Figure 5.2(a) highlights an increase of the boundary layer predicted by our framework. However, our results are in good agreement with those obtained through COMSOL. The temperature profiles at mid-height also agree well with those reported in [295]. The deviation of the maximum Nusselt number along the left boundary is computed as 1.1 %. Note that the setup presented in [295] considers $T^* = 0.5$ and $T^* = -0.5$ for the hot and cold boundaries. Hence, the temperature field obtained by those authors was lifted for the sake of comparisons.

The melting of gallium in a rectangular cavity with vertical walls was investigated experimentally by Gau and Vishkanta [157]. The left and right wall are kept at $T = 311.15$ K and $T = 301.3$ K, respectively. The top and bottom boundaries are insulated. The initial temperature of the enclosure is set to $T = 301.3$ K. Figure 5.3 shows a comparison of the melting front evolution between the numerical prediction of our framework, the experimental results of Gau and Vishkanta [157] and the numerical results of Pal and Joshi [324]. Visible discrepancies are observed only in the central part of the melting front as this is the region interested by the highest

Table 5.1. Comparison of the accuracy of the current framework with the one of Pal and Joshy [324]

	Numerical framework	
Error	Current	Pal and Joshy [324]
Absolute mean [m]	0.0015	0.0017
Absolute max [m]	0.0058	0.0053

Table 5.2. Properties of the PCM considered

Description	Symbol	Value
Dimensionless latent heat	$\mathscr{L}^*$	20
Dimensionless melting temperature	T_m^*	0.5
Rayleigh number	Ra	10^5
Prandtl number	Pr	30

convective transport due to the moderate velocities and large enthalpy gradients close to the the interface. Small velocity and temperature differences can lead to large deviations. The error can be attributed to our artificial smearing of the liquid fraction (Eq. (3.27)) that has no physical rationale when modeling pure substances with isothermal phase change. The deviation could be reduced by calibrating ξ_{log} and $A_{m_{CK}}$ to the experimental data [385, 240, 30]. Table 5.1 shows a comparison of the accuracy of the current framework with the one of Pal and Joshy [324]. The error is computed in terms of the melt front position along the horizontal direction at a specified height. To compare points at different heights, both the numerical curves are interpolated linearly. The results show that the accuracy of the presented numerical framework is similar to the reference numerical study of Pal and Joshy [324]. For this reason, we consider our model reliable enough to predict the phase change phenomenon.

We now verify our phase change model in the shell-and-tube geometry. We consider the same PCM used in Chapter 3. The thermo-physical properties are summarized in Table 5.2. The outer and inner shell radius are set to $r_2 = 1$ and $r_1 = 0.3$ respectively. We perform a mesh convergence study, comparing three different meshes with characteristic sizes $\Delta\theta = \{\pi/45;\ \pi/90;\ \pi/180\}$ to a reference mesh with $\Delta\theta = \pi/360$. The radial element size is calculated as $\Delta r = r\Delta\theta$. The charge time deviations computed with respect to the reference mesh are summarized

Table 5.3. Mesh convergence verification. The deviation is calculated with respect to a reference case with $\Delta\theta = \pi/360$

Mesh size $\Delta\theta$ [-]	Deviation [%]
$\pi/45$	5.24
$\pi/90$	1.01
$\pi/180$	0.48

Table 5.4. Time-stepping verification. The deviation is calculated with respect to a reference case with $\delta_t = 0.005$

Integration tolerance δ_t [-]	Deviation [%]
0.04	3.74
0.02	1.38
0.01	0.21

in Table 5.3. A mesh with characteristic size $\Delta\theta = \pi/180$ with 12851 quadrilateral elements is chosen to produce all the results presented in this chapter as it ensures a limited deviation from the reference mesh. To verify the independence of the results from the time-stepping strategy, we run four analyses with different values of the integration tolerance, δ_t. The charge times obtained with $\delta_t = \{0.04;\ 0.02;\ 0.01\}$ are compared to that of a reference case with $\delta_t = 0.005$. Adopting an integration tolerance of $\delta_t = 0.01$ yields only a 0.21 % deviation from the reference case and is found sufficient to ensure the time-step independence of the results. A summary of this verification analysis is presented in Table 5.4. The evolution of the iso-temperature contour at $T^* = 0.5$ obtained with $\delta_t = 0.01$ and with $\Delta\theta = \pi/180$ is shown in Figure 5.4 alongside with the results obtained with COMSOL Multiphysics [101]. The qualitative agreement suggests that our modeling framework is able to predict with fidelity the thermal and fluid-dynamic response in shell-and-tube LHTES units.

5.3 Design optimization problem

In this chapter and in the next one, the optimization problem is formulated using the TM approach presented in Chapter 3. The flow of computations for the transient sensitivity analysis using the adjoint method are the same described in Section

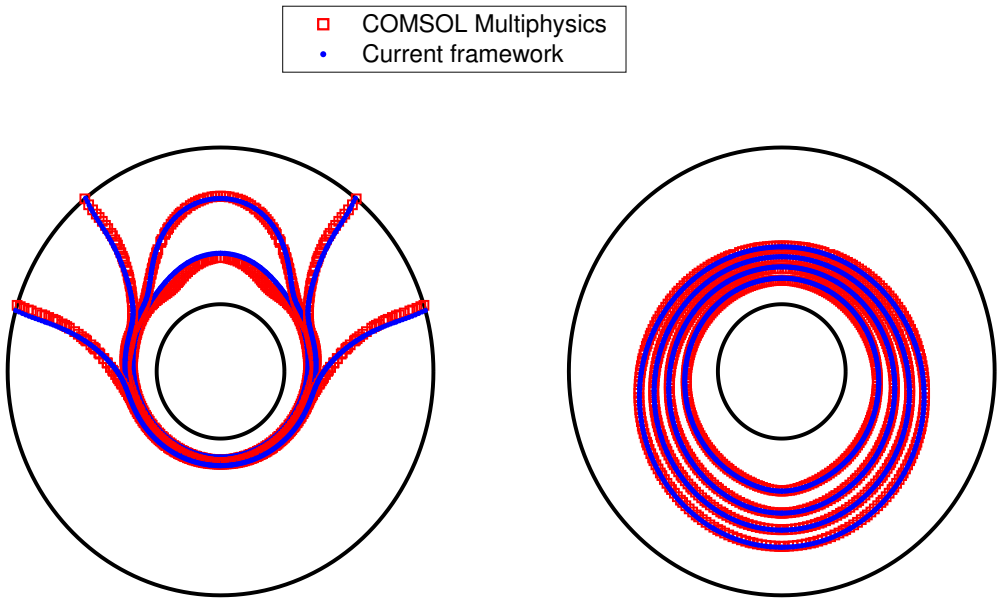

(a) (b)

Fig. 5.4. Accuracy test of the current framework against COMSOL Multiphysics. Comparison of the $T^* = 0.5$ iso-temperature contour at $t^* = \{1;2;3,4\}$ for both melting (a) and solidification (b)

3.4. The material interpolation and regularization strategies require some additional discussion, which is reported in the next sections.

5.3.1 Material interpolation

Although the concept of material interpolation is general in the field of topology optimization, fluid mechanics requires a specific interpolation strategy that differs from the one discussed in Section 3.4. The identification of the material property to interpolate is non-trivial. The seminal paper of Borrvall and Petersson [63] borrowed some concepts from lubrication theory. They considered a 3D flow confined between parallel plates where the characteristic size of the plates, L, was order of magnitudes larger than the channel separation distance, h. Due to slowly varying h and laminar flow, the velocity field was assumed parallel to the plates with a Poiseuille velocity profile in the direction orthogonal to the parallel plates. The analysis space was then reduced from 3D to 2D, considering the plane at half separation distance. The out-of-plane viscous effects were taken into account in the momentum equation through an absorption term [322]:

$$F_{pois_i} = -12\frac{\mu}{h^2}v_i, \tag{5.75}$$

that can be obtained from the integration of the Cauchy stress tensor along the out-of-plane direction. The plates distance, h, was used as piece-wise constant physical design variable. This seminal study [63] focused on Stokes flow, i.e. with no advective momentum transport. Arguing that most flows of engineering interest result in Reynolds numbers $Re >> 1$, Gersborg-Hansen et al. [158] later extended the method to practical Navier-Stokes problems. The authors also noted that augmenting the Stokes model through a sink term of the form (5.75) corresponds to a Brinkman-like model for flow in porous media with inverse permeability, α_b, defined as:

$$\alpha_b = 12\frac{\mu}{h^2}. \tag{5.76}$$

This observation led to research directions that progressively abandoned the original parallel plates idea. In the lubrication-derived approaches presented above, a minimum bound on the inverse permeability α_b arises naturally from the definition of a

maximum channel depth, h_{max}:

$$\alpha_{b_{min}} = 12\frac{\mu}{h_{max}^2}. \tag{5.77}$$

Olesen et al. [322] first considered the minimum inverse permeability as $\alpha_{b_{min}} = 0$. Evgragov [127] later rigorously proved that the inclusion of zero and infinite permeability results in a well-posed problem when considering dissipation minimization with Stokes flow. However, he argued that this does not hold in general for other flow conditions and/or objective functionals. In Ref. [126], the same author demonstrated that ill-posed problems are generated when considering Navier-Stokes equations, since the design-to-flow mapping is not continuous. Evgragov [126] proposed to solve this issue by filtering and using a slightly compressible formulation. Another step towards the abandonment of the original lubrication approach was the optimization of 3D Stokes flow devices, first considered by Aage et al. [1]. Recall that the lubrication approximation leads to a reduced dimensionality of the analysis and optimization. We notice that in principle augmenting the momentum equations with a Brinkman sink shares the criticalities listed in Section 5.1.2 for the porosity method for phase change. However, this approach works well in practice and encountered broad acceptance in the community. It was applied to Navier-Stokes equations in both two [290, 13] and three dimensions [27, 16]. A complementary material interpolation approach was followed by Guest and Prevost [180], who improved the original Brinkman sink formulation with a Stokes-Darcy interpolation. This is useful when optimizing devices with permeable solid materials. Furthermore, the analysis with intermediate design variable values retains a physical interpretation. Despite these advantages, the method did not encounter broad acceptance and applications were mostly limited to multi-scale design of porous structures, where the permeability tensor in the Darcy equation is obtained by homogenization procedures similar to those described in Chapter 4, see for instance [179, 182].

The choice of the α_b-s dependence was less debated. In [63], the authors noted that a linear interpolation leads to a severe penalization of intermediate "gray" designs, yielding convergence to local minima. However, only a linear interpolation was found to guarantee the convergence to binary $\{0,1\}$ layouts [63]. Hence, most researchers adopted a continuation approach where a convex interpolation is slowly morphed into a linear one. The choice of the continuation strategy is somewhat heuristic and highly problem-dependent. In our experience, defining a proper con-

tinuation strategy in conjugate heat transfer problems can be tricky. Some possible issues are discussed in detail in Section 5.4.

In this monograph, we adopt the classical Brinkman sink approach. In our dimensionless framework we have:

$$F^*_{b_i}(s) = -\alpha^*_b(s)v^*_i, \tag{5.78}$$

where the property α^*_b physically corresponds to:

$$\alpha^*_b = \frac{Pr}{Da}, \tag{5.79}$$

where Da is the Darcy number. Due to physics similarities, we adopt the interpolation strategy proposed by Alexandersen et al. [13, 16] for natural convection problems:

$$\alpha^*_b(\bar{s}) = \alpha^*_{max}\frac{1-\bar{s}}{1+q_\alpha\bar{s}}, \tag{5.80}$$

where q_α is a convexity factor used to control the shape of the interpolation function at intermediate values of $\bar{s}$, and α^*_{max} is a large value approximating ∞. Note that a nil Brinkman sink is obtained for $\bar{s} = 1$. In our implementation, $\bar{s} = 1$ denotes full PCM while $\bar{s} = 0$ denotes full HCM. This agrees with [13, 16] but is opposite to the density parameterization adopted in Chapters 3 ad 4. To maintain consistency with [13, 16], the design-dependent conductance $K(\bar{s})$ is written using the following RAMP-like interpolation:

$$K(\bar{s}) = \frac{\bar{s}(C_k(1+q_f-1)+1)}{C_k(1+q_f\bar{s})}, \tag{5.81}$$

where q_f is a convexity factor and $C_k = \alpha_{t_{PCM}}/\alpha_{t_{HCM}}$ is the diffusivity ratio between the PCM and HCM. The latent heat factor, $\gamma(\bar{s})$, is interpolated linearly, i.e. using a SIMP approach with exponent $p = 1$.

5.3.2 Regularization

Early contributions [63] in the field of fluid topology optimization already reported that regularization is non-necessary for minimum dissipation (or minimum pressure drop) problems. This well agrees with the intuition that a minimum dissipation

problem can be thought as a compliance maximization [180]. In our experience, convective heat transfer problems for maximum thermal dissipation suffer from the same lack-of-solution illness found for the compliance minimization of structures. Hence, we adopt the three-field regularization strategy presented in Section 3.4.

5.4 Continuation strategies in conjugate heat transfer

As discussed in Chapter 2 of this monograph, a popular (and heuristic) strategy to obtain convergence to binary $\{0;\ 1\}$ designs whilst avoiding unsatisfactory local minima is to slowly ramp the penalization parameters and solve one optimization problem per each continuation step. The optimized layout at each step is used as initial guess for the next step. Although this demonstrated to be effective in many problems of practical interest, selecting a proper continuation strategy in multi-physics problem can be a non-trivial task. The physical design variables should be always penalized such that the physics complexity is maintained in its entirety. The results presented in this chapter and in Chapter 6 are obtained by raising the convexity parameter, q_f, (Eq. (5.81)) along with the projection parameter, β, in three steps as follows:

$$\begin{aligned} &\beta \in \{1;2;4\}, \\ &q_f \in \{1;10;10^2\}. \end{aligned} \tag{5.82}$$

The remaining material interpolation parameters of (5.80) are held constant at $q_\alpha = 10$ and $\alpha_{max} = 10^7$. This strategy revealed to be able to avoid unsatisfactory local minima in preliminary numerical tests that we conducted for both solidification and melting enhancement.

The remainder of this section aims at showing and investigating possible issues that may arise in coupled fluid-dynamic and heat transfer problems for an improper selection of the continuation strategy. We limit the physics complexity for an easier intuition. Hence, both the phase change and temporal dynamics are not considered. We focus on two design examples: a natural convection heat sink and a forced convection heat sink. Both the optimization problems are solved with the numerical implementation framework presented in this chapter.

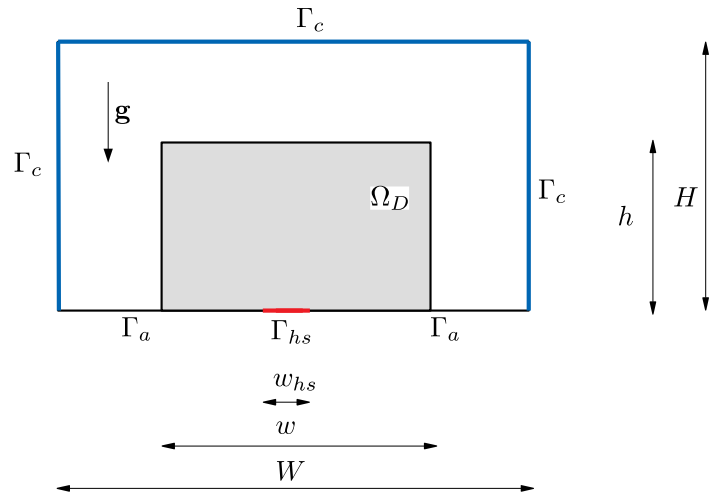

Fig. 5.5. Schematic of the natural convection heat sink design optimization problem

5.4.1 Natural convection heat sink

Topology optimization of heat sinks cooled by natural convection was first studied by Alexandersen et al. [13, 16]. Here, we adopt design and computational domains similar to the ones described in their seminal 2D paper [13]. Figure 5.5 presents a schematic of the problem considered. Two rectangle with dimensions $W = 7$, $w = 4$, $H = 4$ and $h = 2$ are heated on Γ_{hs} having width $w_{hs} = 0.2$ with an inward heat flux, $q^* = 90$. A cold temperature $T^* = 0$ is set on the three boundaries denoted with Γ_c. The two bottom boundaries indicated with Γ_a are adiabatic. No-slip and non-penetration are prescribed on all the boundaries. We aim at finding the optimal layout of HCM within the design domain, Ω_D, such that the temperature on the heated boundary is minimized. Hence, the optimization problem can be written as:

$$\begin{aligned} \underset{\mathbf{s}}{\text{minimize}} \quad & z = \int_{\Gamma_{hs}} T^* \, d\mathbf{x}' \\ \text{subject to} \quad & \int_{\Omega_D} (1-\bar{s}) \, d\mathbf{x} - \Phi \int_{\Omega_D} d\mathbf{x} \leq 0 \\ & \mathbf{s} \in \mathbf{S} = \left\{ \mathbb{R}^{N_s} \mid s_{min} \leq s_i \leq s_{max}, i = 1, ..., N_s \right\} \end{aligned} \quad , \tag{5.83}$$

where the design domain volume fraction, Φ, is set to 50 %. The portion of computational domain outside the design domain $\Omega \setminus \Omega_D$ is set to full fluid. The problem governing equations can be obtained through a slight modification of the more gen-

eral framework we considered for phase change problems with natural convection. The state-dependent Kozeny-Carman sink, $F^*_{pm_i}$, appearing in the momentum equation (Eq. (5.18)) is here set to 0. The phase transition contribution in (5.22) are neglected by setting $\mathscr{L}^* = 0$. The Prandtl number is set to unity while the diffusivity ratio between fluid and solid, C_k, is set to 1 %. We discretize the domain with quadrilateral bilinear element with characteristic size $\delta x = 0.025$ resulting in 180964 degrees of freedom.

To understand how the physics at the initial optimization iteration is affected by the choice of the penalization parameters we proceed as follows. First, we set a homogeneous design variable distribution $s = 1 - \Phi$ everywhere in the design domain, Ω_D, that corresponds to our usual initial guess for topology optimization. Then, we run a set of 40 analysis considering all the combinations of the penalization parameters varied as follows:

$$\begin{aligned} q_\alpha &= \{1e0;\ 1e1;\ 1e2;\ 1e3;\ 1e4;\ 1e5;\ 1e6;\ 1e7\} \\ q_f &= \{1e0;\ 1e1;\ 1e2;\ 1e3;\ 1e4\} \end{aligned} . \tag{5.84}$$

Last, we compute an indicator function quantifying the amount of heat transferred by convection with respect to the total within the design domain:

$$\hat{q}_{conv} = \frac{\int\limits_{\Omega_D} ||v_i^* T^*||_2 d\mathbf{x}}{\int\limits_{\Omega_D} \left|\left| K_{ij} \frac{\partial T^*}{\partial x_j^*} \right|\right|_2 d\mathbf{x} + \int\limits_{\Omega_D} ||v_i^* T^*||_2 d\mathbf{x}} . \tag{5.85}$$

The convection indicator $\hat{q}_{conv} \in [0,1]$ so that 0 denotes a purely conductive contribution and 1 denotes a purely convective contribution. The computed $\hat{q}_{conv}$ distribution for different Rayleigh numbers is presented in Figure 5.6. White iso-contours are plotted for $\hat{q}_{conv} = \{0.05;\ 0.95\}$ such that is possible to identify three different regions. The red region is dominated by convection, the blue region is dominated by conduction. A balance between alternative heat transfer mechanisms is observed only for the region enclosed by the iso-contours. When the Rayleigh number is increased, the iso-contours are shifted to the left such that the the size of the convection region grows while the one of the conduction region diminishes.

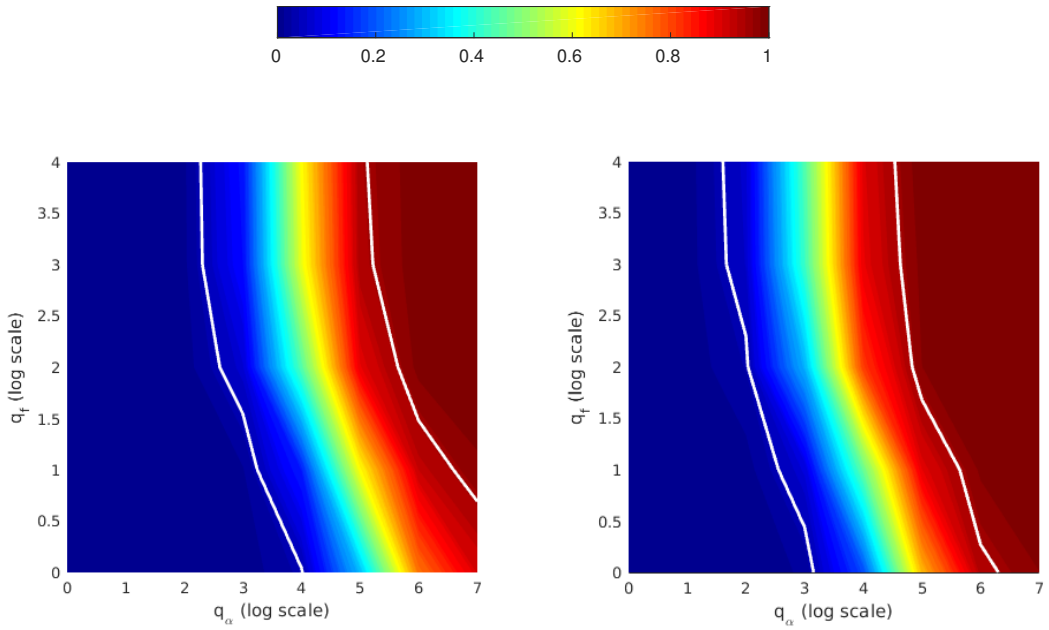

(a) (b)

Fig. 5.6. Convective transport indicator, $\hat{q}_{conv}$, distribution for different Rayleigh numbers. (a): $Ra = 1280$; (b): $Ra = 6400$. The white iso-contours are plotted for $\hat{q}_{conv} = \{0.05;\ 0.95\}$

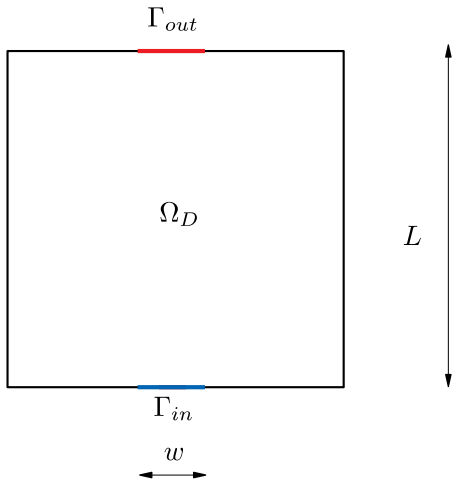

Fig. 5.7. Schematic of the forced convection heat sink design optimization problem

5.4.2 Forced convection heat sink

Topology optimization of heat sinks cooled by forced convection was considered in a few more studies than those considering natural convection heat sinks, see for instance [248, 290, 317]. A schematic of the design example considered here is presented in Figure 5.7. We consider square design and computational domains with dimensions $L = 0.11$ and $w = 0.02$ and a volumetric heat generation $q_v^* = 5.56e4$. A cooling fluid flows from the inlet, Γ_{in}, to the outlet, Γ_{out}. We prescribe vanishing normal and tangential stresses at the outlet $\sigma_{ij}n_j = \mathbf{0}$. At the inlet we set both a vanishing tangential velocity $v_i^* t_i = 0$ with t_i being the unit tangent vector and a normal stress $n_i\sigma_{ij}n_j = p_{in}^*$. No-slip and non-penetration are set on the remaining boundaries. A cold temperature $T^* = 0$ is prescribed at the inlet and a fully developed condition with vanishing temperature gradients in the normal direction is prescribed at the outlet. The remaining boundaries are adiabatic. We aim at finding the optimal layout of HCM such that the integral temperature is minimized. The optimization

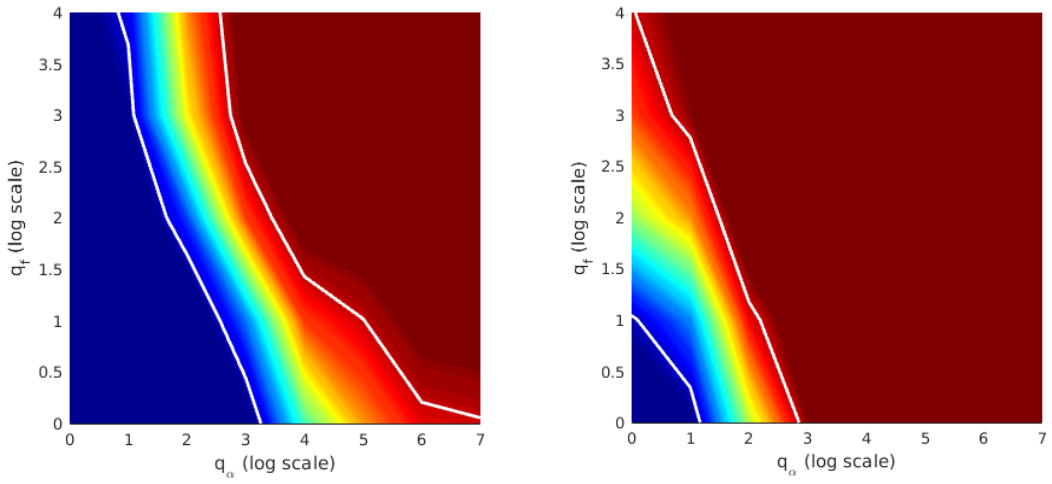

(a) (b)

Fig. 5.8. Convective transport indicator $\hat{q}_{conv}$ distribution for different inlet pressures. (a): $p^*_{in} = 0.1$; (b): $p^*_{in} = 10$. White iso-contours are plotted for $\hat{q}_{conv} = \{0.05;\ 0.95\}$

problem reads:

$$\begin{aligned} \underset{\mathbf{s}}{\text{minimize}} \quad & z = \int_{\Omega_D} T^* \, d\mathbf{x} \\ \text{subject to} \quad & \left(\frac{\int_{\Omega_D} (1 - \bar{s}) \, d\mathbf{x}}{\Phi \int_{\Omega_D} d\mathbf{x}} - 1 \right)^2 - \varepsilon_V^2 \leq 0 \\ & \mathbf{s} \in \mathbf{S} = \left\{ \mathbb{R}^{N_s} \mid s_{min} \leq s_i \leq s_{max}, i = 1, ..., N_s \right\} \end{aligned} \quad , \tag{5.86}$$

where the volume constraint is here written as a weak equality constraint such that the amount of HCM differs from the maximum allowed at worst by a small number, $\varepsilon_V = 1e-4$. This was necessary to avoid trivial solutions with no HCM within the design domain, which we observed arising in few optimization cases. Natural convection is not considered in this study, hence we set $Ra = 0$. The computational domain is discretized using bilinear quadrilateral elements with characteristic size $\delta x = 7.3e-4$ yielding a total of 92412 degrees of freedom. Figure 5.8 displays the distribution of the convection indicator, $\hat{q}_{conv}$, obtained by sweeping q_α and q_f as described in the previous section. Also in this case, a negligible convective transport is observed at small values of q_f- q_α while heat transfer is dominated by convection at high values. Raising the inlet pressure has similar effects to an increased Rayleigh number for the natural convection example.

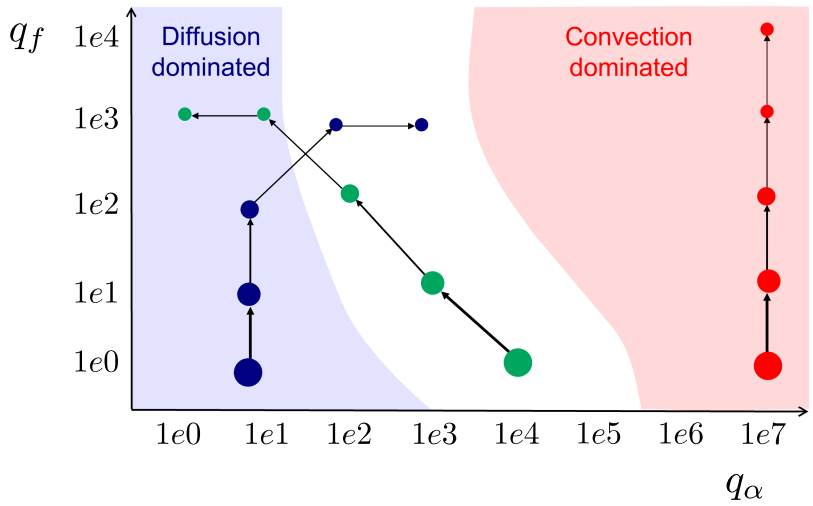

Fig. 5.9. Representation of alternative continuation trajectories

5.4.3 Possible continuation strategies

Through inductive reasoning, we can generalize the results described in the previous sections and obtain the simplified schematic presented in Figure 5.9. For intermediate design variable values, large q_α and q_f lead to an excessive penalization of conductive heat transfer such that convection is the leading heat transfer mechanism. On the other hand, small q_α and q_f values penalize convective transport too strongly such that diffusion dominates. To understand what kind of physics is "felt" by the "gray" regions during the optimization convergence, it is useful to plot the continuation trajectories on this q_α-q_f representative space. We consider three possible continuation alternatives:

- **Continuation strategy (i)** (indicated in red) is obtained from [13]. It consists of the following steps:

$$\begin{aligned} q_f &= \{1e0;\ 1e1;\ 1e2;\ 1e3;\ 1e4\}, \\ q_\alpha &= \{1e7;\ 1e7;\ 1e7;\ 1e7;\ 1e7\}. \end{aligned} \tag{5.87}$$

  As this trajectory lies in the convective region, this strategy is likely to privilege convective structures.

- **Continuation strategy (ii)** (indicated in blue) is a modified version of the one presented in [16]. The penalization parameters are raised as follows:

$$\begin{aligned} q_f &= \{0.881;\ 8.81;\ 88.1;\ 881;\ 881\}, \\ q_\alpha &= \{8;\ 8;\ 8;\ 98;\ 998\}. \end{aligned} \tag{5.88}$$

  As the early continuation steps of this trajectory are positioned in the diffusive region, this strategy is likely to privilege diffusive structures.

- **Continuation strategy (iii)** (indicated in green) is an alternative to the previous ones that aims at approximating the shape of the transition region such that both the heat transfer mechanisms are present along the optimization process. It consists of the following steps:

$$\begin{aligned} q_f &= \{1e0;\ 1e1;\ 1e2;\ 1e3;\ 1e4\}, \\ q_\alpha &= \{1e4;\ 1e3;\ 1e2;\ 1e1;\ 1e0\}. \end{aligned} \tag{5.89}$$

For all the cases, we consider a fixed $\alpha_{max} = 1e7$ as in [13]. Note that in [16], the authors ramp also this parameter along the optimization process. The effect of this parameter is considered separately in Section 5.4.5. Upon marching along each continuation trajectory, the amount of gray material reduces. Due to the strong non-convexity of the optimization problem, the geometry evolves into a particular local minimum during the earliest continuation steps, and hardly escapes from it during the following continuation steps. The radius of the circles in Figure 5.9 represents qualitatively the ability of each continuation step to morph the design into an effective structure.

5.4.4 Comparison of performance

Figure 5.10 collects the optimized designs obtained with the three continuation strategies for the natural convection example. Continuation strategy (i) yields optimized layouts that differ significantly from those obtained with the alternative trajectories. The HCM aggregates in the center of the design domain in a branched triangular structure. For higher Rayleigh numbers, some solid material is left at the top corners of the design domain. Although the suspended solid material is not physically realistic, our density-based topology optimization framework allows this

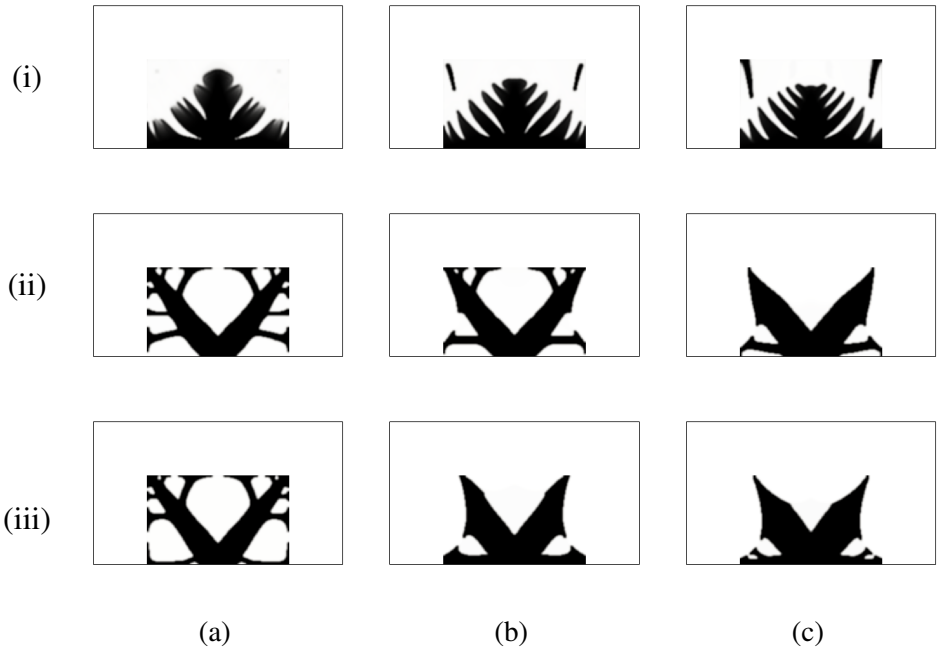

Fig. 5.10. Optimized designs obtained with the three continuation strategies in the natural convection example at different Rayleigh numbers. (a): $Ra = 1280$; (b): $Ra = 3200$; (c): $Ra = 6400$

type of solution. The disconnected HCM yields a negligible contribution to the heat dissipation through diffusion. This suggests that the floating features arise to manipulate the flow such that high velocity streams come in contact with the triangular structure. Continuation strategies (ii) and (iii) result in similar optimized structures. Noticeable differences are visible at the intermediate Rayleigh number, for which Continuation strategy (ii) presents diffusive-like branches at the top of the design domain that are not observed in the optimized structure obtained with Continuation strategy (iii). To cross-check the performance of the optimized structures presented in Figure 5.10, the final design variable field is projected with a step Heaviside function centered in $\bar{s} = 0.5$ such that pure HCM is obtained for $\bar{s} \geq 0.5$ and pure fluid is recovered for $\bar{s} < 0.5$. This ensures that the interpolation parameters have no effect on the analysis. The performance of these modified layouts is reported in Table 5.5. Continuation strategy (iii) yields always a reduced objective as compared to the alternatives. Continuation strategy (ii) results in similar performance at low Rayleigh numbers. Continuation strategy (i) is always the worst-performing choice in the range of values considered.

Table 5.5. Optimized objective in the natural convection example with the three different continuation strategies

	Rayleigh number		
Continuation strategy	1280	3200	6400
(i)	6.48	6.11	5.55
(ii)	5.75	5.61	5.33
(iii)	5.72	5.37	4.39

Table 5.6. Optimized objective (x 10^2) in the forced convection example with the three different continuation strategies

	Inlet pressure		
Continuation strategy	0.1	5	10
(i)	6.73	0.84	0.42
(ii)	2.75	1.53	1.02
(iii)	6.72	0.64	0.39

The optimized layouts obtained with the three continuation strategies in the forced convection example are reported in Figure 5.11. Continuation strategy (ii) leads to optimized designs that suppress fluid flow. The HCM is concentrated close to the cold inlet so that the domain can be cooled by diffusion. At higher p_{in}^*, similar solutions are observed but the convergence to binary $\{0;\ 1\}$ designs is poor. This suggests that moving to a high q_α at late continuation steps may be unsatisfactory for some problems. Continuation strategies (i) and (iii) result in similar layouts. A flow channel departing from the inlet bifurcates in a number of different paths. With Continuation scheme (iii), the channels are concentrated towards the outlet and the structure relies on HCM to cool the bottom corners of the design domain. At high pressures, Continuations strategy (i) leads to a geometry that is nearly symmetric with respect to the x-axis. This suggests that the diffusive transport is slightly exploited. The Heaviside projection is again adopted to post-process the optimized layouts before a cross-check analysis. The performance of the projected layouts is summarized in Table 5.6. At $p_{in}^* = 0.1$, Continuation strategy (ii) leads to the best-performing design. When the fluid motion driving force is too small, a diffusive structure connected to the inlet is convenient even if the flow is completely suppressed. Continuation schemes (i) and (iii) did not reveal this

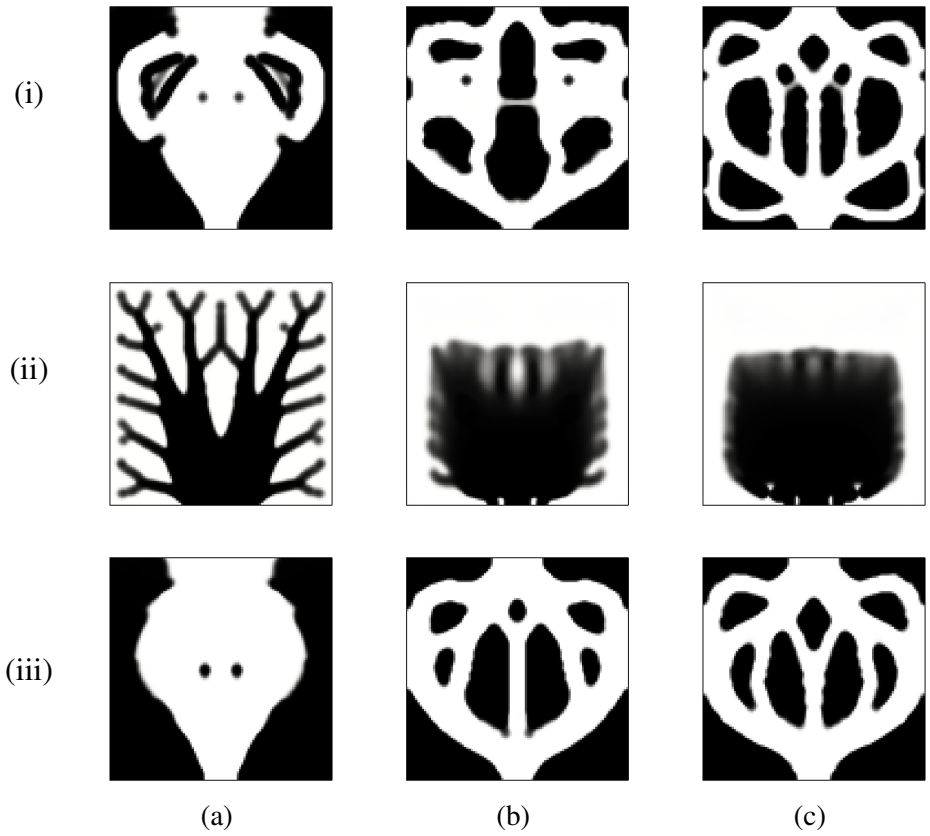

Fig. 5.11. Optimized designs obtained with the three continuation strategies in the forced convection example at different inlet pressures. (a): $p^*_{in} = 0.1$; (b): $p^*_{in} = 5$; (c): $p^*_{in} = 10$

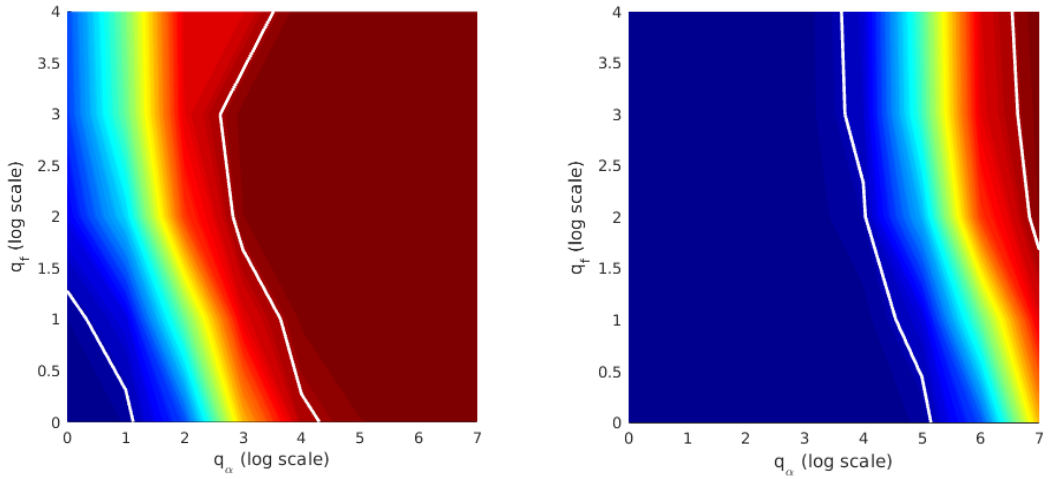

(a) (b)

Fig. 5.12. Effect of the maximum Brinkman constant on $\hat{q}_{conv}$. (a): $\alpha_{max} = 1e5$; (b): $\alpha_{max} = 1e9$

optimized solution as the convective transport contribution was overestimated at early design iterations. At higher inlet pressures, exploiting the flow for cooling the domain becomes important. At $p^*_{in} = 5$ and $p^*_{in} = 10$, Continuation scheme (iii) yields superior performance than the alternatives.

The results presented in this section demonstrate that the continuation trajectories on the interpolation parameters are of primary importance in coupled flow and heat transfer problems. Improper choices may lead to unsatisfactory local minima that do not exploit sufficiently either convective or diffusive heat transfer.

5.4.5 On the effect of the maximum Brinkman constant

In this section, we investigate the effect of the maximum Brinkman constant, α_{max}. For brevity, the results are presented only for the natural convection example. Similar trends were observed for the forced convection example.

The computed maps of the convection indicator, $\hat{q}_{conv}$, at $Ra = 100$ for different values of $\alpha_{max} = \{1e5;\ 1e9\}$ are presented in Figure 5.12. Recall that the results for $\alpha_{max} = 1e7$ were presented in Figure 5.6(b). Raising the maximum Brinkman constant shifts the iso-contours to the right and enlarges the size of the diffusion-

(a) (b) (c)

Fig. 5.13. Effect of the maximum Brinkman constant on the optimized designs of the natural convection example at $Ra = 100$ obtained with Continuation strategy (iii); (a): $\alpha_{max} = 1e5$; (b): $\alpha_{max} = 1e7$; (c): $\alpha_{max} = 1e9$

Table 5.7. Optimized objective obtained using Continuation strategy (iii) in the natural convection example with the three different values of α_{max}

α_{max}	Objective [-]
1e5	6.02
1e7	4.47
1e9	5.51

dominated region. The convection in the "gray" regions of the design domain is penalized more strongly with $\alpha_{max} = 1e9$. The optimized layouts obtained through Continuation strategy (iii) with different values of α_{max} are presented in Figure 5.13. The optimized geometry obtained at small α_{max} resembles the triangular structures observed in Figure 5.10 for Continuation strategy (i). Recall that the latter trajectory is likely to lie on a q_α-q_f region dominated by convection. This favors the generation of features that exploit convective heat transport. When α_{max} is raised, the optimized structure evolves progressively into more conductive-like layouts. Figure 5.13(c) has similarities with the designs presented in Figure 5.10 for Continuation scheme (ii), whose trajectory lies in the diffusion region. To cross-check the performance of the different designs, the design variable field is projected as done in the previous sections. Differently from the convexity parameters q_f and q_α, the value of α_{max} modifies also the response of the pure black-white designs. All the projected designs are thus analyzed with $\alpha_{max} = 1e9$ such that the fluid flow is maximally penalized in the solid regions. The optimized objective function values for the different cases are reported in Table 5.7. The optimized layout obtained by setting $\alpha_{max} = 1e7$ during

the optimization is largely superior to the alternatives. This suggests that the choice of this parameter requires special care.

5.5 Numerical results and design trends

Here, we present and discuss the numerical studies conducted for both melting and solidification enhancement in single-tube LHTES units. First, we compute a reference design obtained neglecting fluid flow. This geometry is compared with the convective layouts optimized for fastest melting and solidification. After the verification of the identified design trends with body-fitted analyses, we compare the performance of the optimized geometries with a longitudinal layout; then, we present a method to reduce the complexity of the topology-optimized designs for easier manufacturing and we test it on a real application.

The thermo-physical properties of PCM and the domain dimensions were introduced in Section 5.2.5. As in the forced and natural convection heat sink studies, we set the diffusivity ratio between PCM and HCM, C_k, to 1 %.

5.5.1 Diffusion design

In this section, we compute a reference solution where fluid flow is neglected. This is referred to as diffusive design hereafter. Similar optimization studies were considered in Chapter 3. However, the design interpolation strategies adopted here differ: a higher penalization of the intermediate design variables is desirable to ensure the convergence to binary $\{0;\ 1\}$ designs. This is essential for the correct flow prediction when natural convection is considered. Furthermore, also the design domain was modified. We consider a charge process, which is reproduced with a hot Dirichlet condition $T_d^* = 1$ and a cold initial temperature field $T_I^* = 0$. The charge is considered complete when the energy level in the tank reaches 95 % of the total capacity. Due to the absence of convective effects, we obtained the same optimized design when considering a discharge process from 100 % down to 5 % of the total capacity.

The objective history, normalized with respect to the initial value, along with the design at selected iterations is shown in Figure 5.14. The initial design correspond to a homogeneous distribution $\bar{s} = 0.9$. In Figure 5.14, the designs corresponds

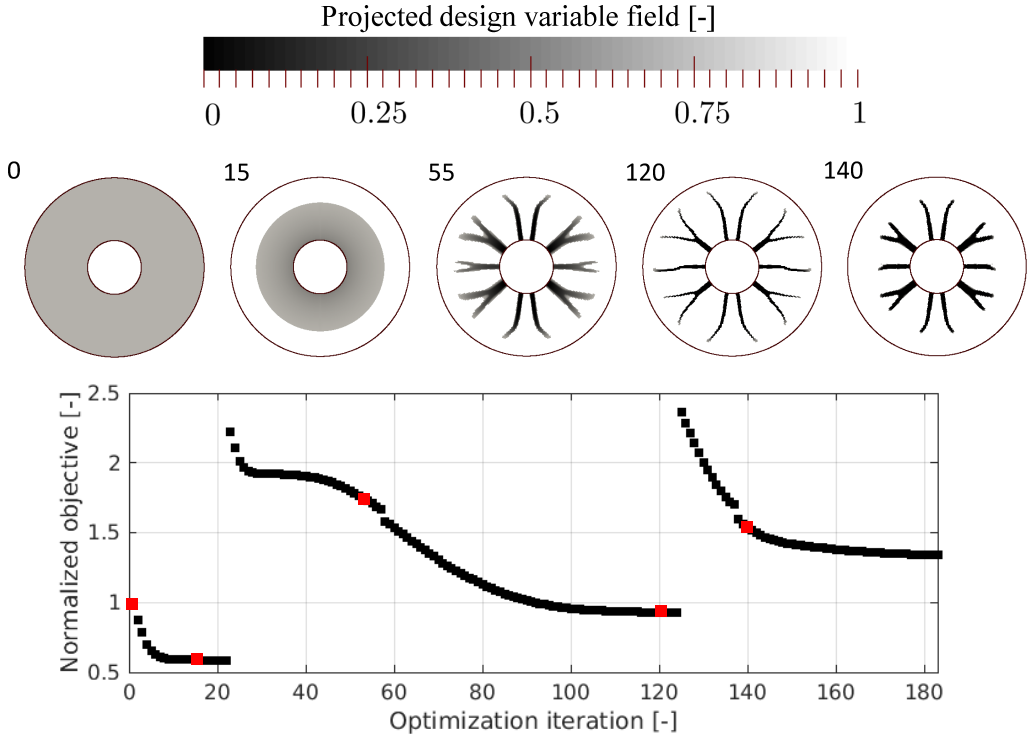

Fig. 5.14. Normalized objective history during the optimization of the diffusive design. The design evolution is shown at selected iterations. The jumps in the objective correspond to the updates of the continuation scheme

to contour plots of the projected design variable field thresholded at $\bar{s} = 0.9$. The evolution of the objective shows three well-distinct stages, which correspond to the continuation scheme steps described in 5.4. In the first step, HCM concentrates in a region close to the internal tube and converges after 22 iterations. The second continuation step, which penalizes the intermediate design variables more strongly, triggers a ramification (iteration 55) and converges to a structure with extremely thin design features (iteration 120). During the third continuation step, those small design details characterized by intermediate design variables disappear so that shorter and thicker fins are created. Note the three continuation steps are necessary to achieve a satisfactory convergence to binary $\{0;\ 1\}$ designs. Despite a lower objective function, the converged designs after the first and the second continuation step present large non-physical "gray" regions. To quantify whether an optimized design converged to a discrete solution, we adopt a measure of non-discreteness similar to the one proposed by Sigmund [392]:

$$M_{nd} = \frac{\int_{\Omega_D} 4\bar{s}(1-\bar{s})\, dV}{\int_{\Omega_D} dV}, \tag{5.90}$$

which intuitively represents the area fraction of the design domain in which the projected design variable has not fully converged to either 0 or 1. When there are no regions with intermediate design variables, M_{nd} is 0 %. If $\bar{s} = 0.5$ everywhere, we would obtain $M_{nd} = 100$ %. The final optimized design obtained thresholding the projected design variable field at $\bar{s} = 0.5$ is shown in Figure 5.16(a). The calculated measure of non-discreteness M_{nd} for this layout is 1.44 %. Figure 5.15 shows how the optimized geometry depends on the threshold choice. The layout obtained thresholding the design variable field at $\bar{s} = 0.9$ (Figure 5.15(a)) slightly differs from the one obtained with a threshold of $\bar{s} = 0.1$ (Figure 5.15(b)). This test qualitatively confirms that the amount of intermediate gray material is limited. The optimized design is nearly symmetric with respect to the x-axis and shows quasi-periodicity along the angular direction with period $\Delta\theta = \pi/2$. The structure shows both longitudinal fins and Y-shaped (tree-like) fins around the HTF tube. The formers are used extensively for heat transfer enhancement in LHTES, as discussed in Chapter 3 of this monograph. Similarly to what obtained in Chapter 3, the branched fins are alternated to non-branched ones.

This section presented the optimization of a fin layout without considering natural convection during the analysis. This geometry will be used in the following sections

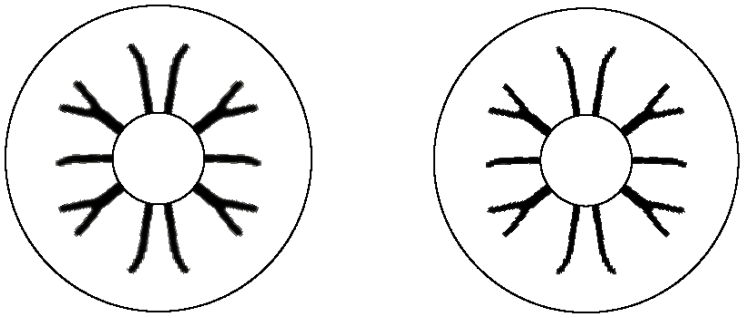

Fig. 5.15. (a): Final layout obtained for the diffusive design thresholded at $\bar{s} = 0.9$; (b): final layout obtained for the diffusive design thresholded at $\bar{s} = 0.1$

to benchmark the designs optimized considering fluid flow. Our diffusion geometry presents similar features to those obtained in Chapter 3 of this monograph.

5.5.2 Melting design

In this section, we consider a melting process, i.e. the charge of a LHTES unit. In this study, natural convection is considered. Referring to the boundary and initial conditions discussed in (5.24) and (5.27), to mimic melting we consider a hot Dirichlet condition $T_d^* = 1$ and a cold initial temperature field $T_I^* = 0$. Similarly to the diffusive design, the charge is considered complete when the energy level in the tank reaches 95 % of the total capacity. The optimized design obtained for melting is shown in Figure 5.16(b). In this case, we obtain a measure of non-discreteness M_{nd} of 1.19 %. The melting design is profoundly different from the one obtained in Section 5.5.1: the HCM concentrates in the bottom part of the storage unit to form a conductive-like structure that occupies the shell sector parameterized by $-\pi/3 < \theta < \pi/3$. The top portion of the shell is slightly occupied by HCM to leave room for fluid flow. To highlight the main layout differences between the two cases, Figure 5.16(c) presents a superposition of the optimized designs for diffusion and melting. The design here is represented by the contour of the projected design variable at $\bar{s} = 0.5$. We observe three main features:

(i) the top portion of the unit shows only two short fins which are slightly offset from the radial direction;

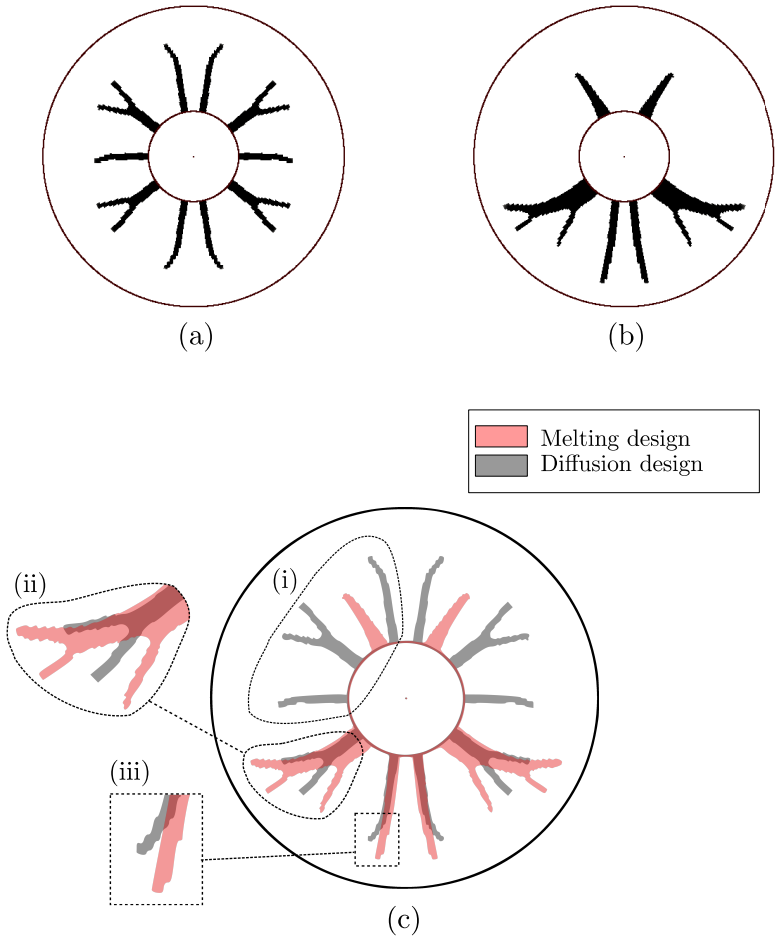

Fig. 5.16. (a): Final layout obtained for the diffusive design; (b): final layout obtained for the melting design; (c) superposition of the two designs with zoom-in of the most relevant differences. The designs displayed were obtained by thresholding the projected design variable field at $\bar{s} = 0.5$

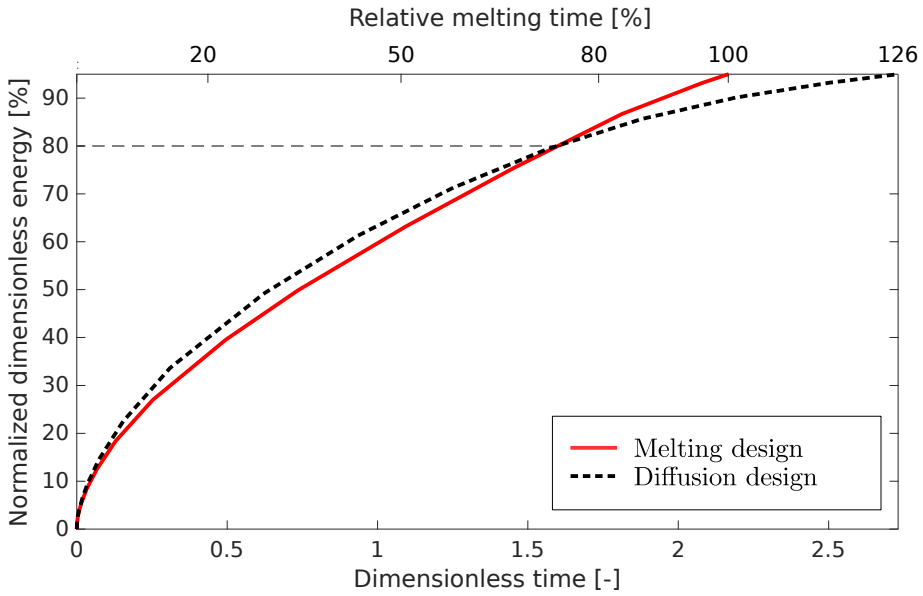

Fig. 5.17. Energy histories of the melting and diffusive designs during a melting test

(ii) two large and thick branches are visible at $\theta = -\pi/3$ and $\theta = \pi/3$ with second-order bifurcations. These fins extend ~ 37.8 % more in the radial direction than those obtained in the diffusive design;

(iii) two thin branches elongates towards the bottom of the shell. These structural components are ~ 19.6 % longer that the diffusive fins obtained at the same angular position.

The radial position of the two thick branches described in (ii) recalls the results obtained in [452]. The authors observed that this particular configuration enhances heat transfer through convective transport. However, differently from our configuration, their design does not show any fin in the upper part of the unit and has a unique longitudinal fin elongating towards the bottom.

The normalized energy histories of the diffusive and melting designs are compared in a melting test. Here, both the layouts are analyzed for a charge of the unit including fluid flow. The results are plotted in Figure 5.17. Initially, the melting design shows a slower charge rate than the diffusive design. This is due to the fact that diffusion is the dominant heat transfer mechanism during the initial portion of the process. However, the heat transfer rate of the diffusive design slows down

whereas the melting design maintains a fairly constant charge rate by exploiting the onset of natural convection. If the desired degree of charge of the storage units, Ψ_c, is above 80.2 %, the convective design is the best-performing choice. This limit is specific to the particular design domain and material properties considered here. For the nominal charge case in which $\Psi_c = 95$ %, we obtain that the diffusive geometry demands 25.9 % more time than the melting design to complete the charge process. Note that the particular choice of Ψ_c corresponds to an ideal utilization of the unit. Partial charge-discharge cycles may occur in real systems. Figure (5.18) shows the liquid fraction evolution at selected time instants of the melting test, corresponding to 20 %, 50 %, 80 % and 100 % of the total charge time of the melting design, $t^*_{f_m}$. At $t^* = 0.2\, t^*_{f_m}$, the liquid layer is thin and natural convection does not yield noticeable modifications of the melting front. During this initial stage of the process, the diffusive structure is more effective: thinner branches lead to more heat transfer area as compared to the convective layout. As the fluid layer widens, natural convection starts to modify the shape of the melting front ($t^* = 0.5\, t^*_{f_m}$) and becomes dominant at $t^* = 0.8\, t^*_{f_m}$. The short fins of the melting design redirect the upward-moving fluid layer in such a way that the liquid PCM quickly fills the upper portion of the tank. The convective stream hardly reaches the region below the pipe, which is heated by long diffusive-like branches. The diffusive design can hardly get rid of the mushy region at the bottom of the tank. To better visualize the main heat transfer mechanisms, the magnitude of the average convective heat transfer rate, $\bar{q}_{v_i}$, and of the conductive heat transfer rate, $\bar{q}_{k_i}$, are depicted in Figure 5.19. These quantities are calculated as:

$$\bar{q}_{v_i} = \frac{\int_0^{t^*_f} \left(v^*_i (T^* + \gamma f^* \mathscr{L}^*) \right) dt^*}{t^*_f}, \tag{5.91}$$

$$\bar{q}_{k_i} = \frac{\int_0^{t^*_f} \left(- K_{ij} \frac{\partial T^*}{\partial x^*_j} \right) dt^*}{t^*_f}, \tag{5.92}$$

where t^*_f indicates the final time of the process of interest, set to $t^*_{f_m}$ here as we are dealing with melting. The melting design largely utilizes the top fins and a portion of the pipe surface to enhance the convective heat transfer. This is confirmed by considering the conductive heat transfer plot which shows a large conductive contribution in the same region. A wide eddy maintains a high temperature gradient at the interface: hot fluid is rapidly transported away leaving room for cold fluid coming from the outer part of the shell. This mechanism can be better observed

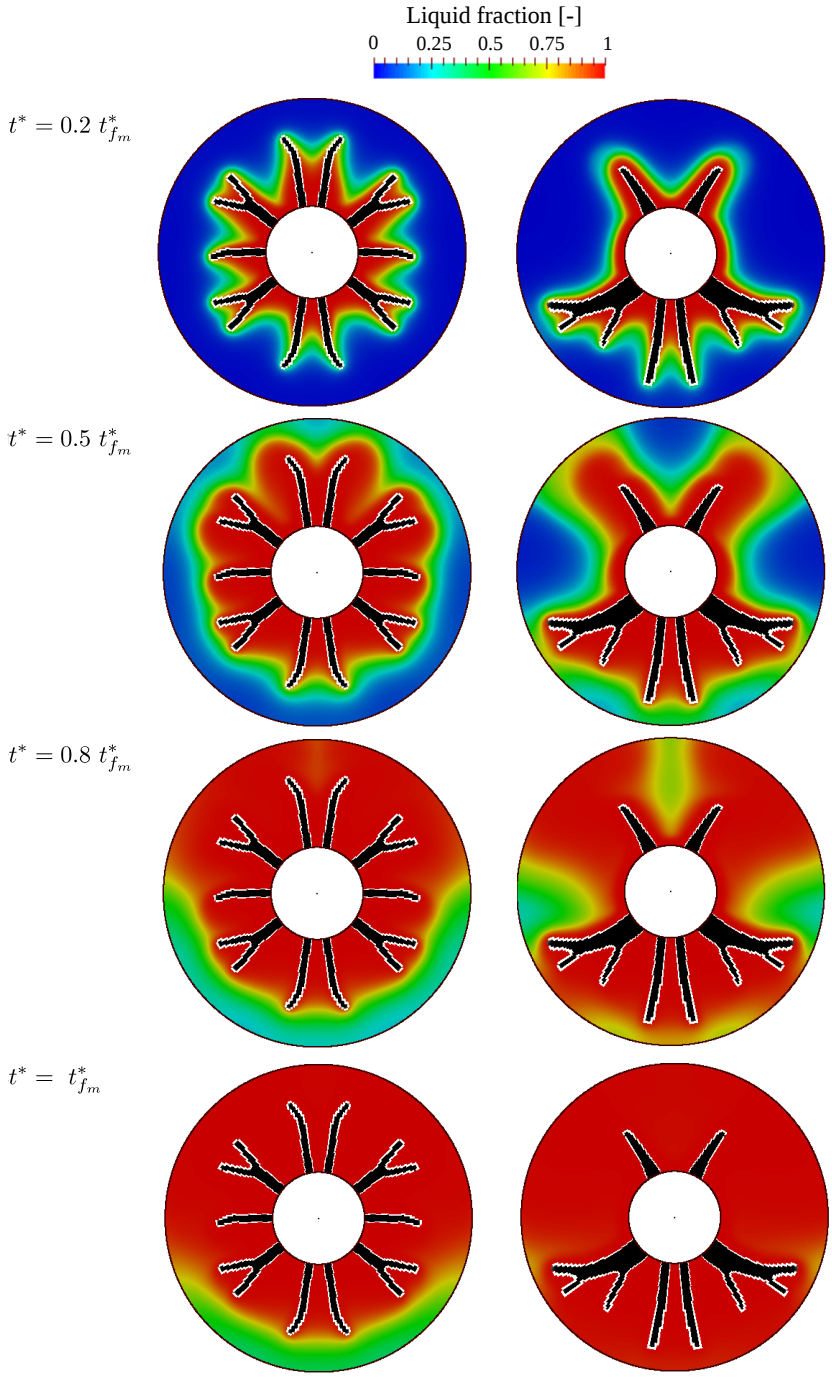

Fig. 5.18. Liquid fractions at selected time instants during melting. The left column shows the diffusive design while the right column shows the melting design

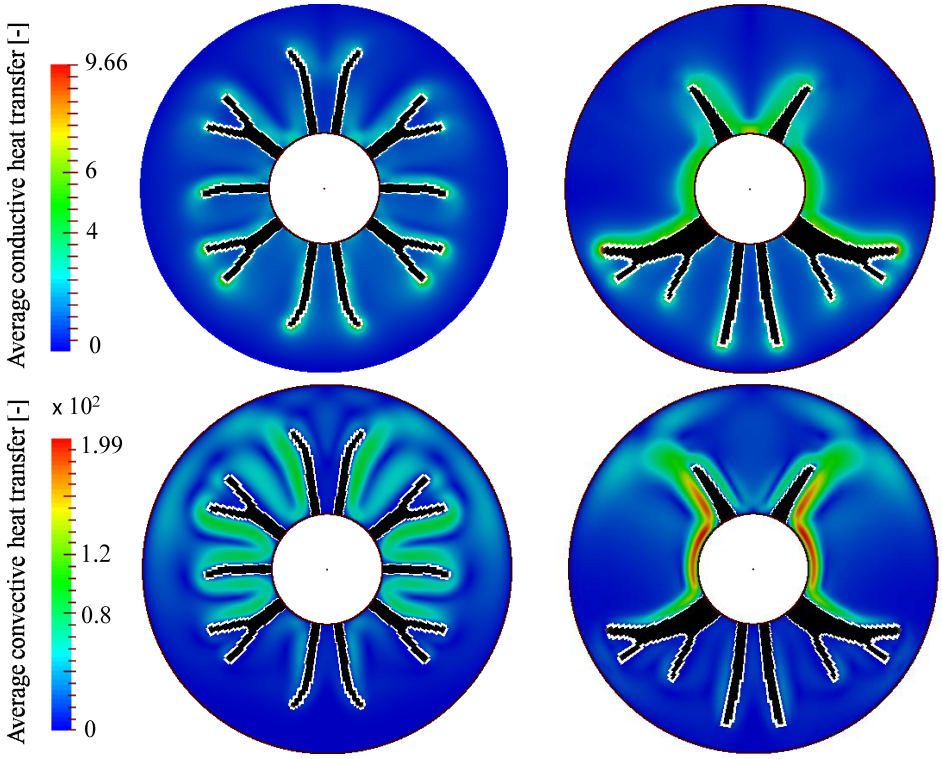

Fig. 5.19. Average conductive and convective heat transfer rate during melting. The left column shows the diffusive design while the right column shows the melting design

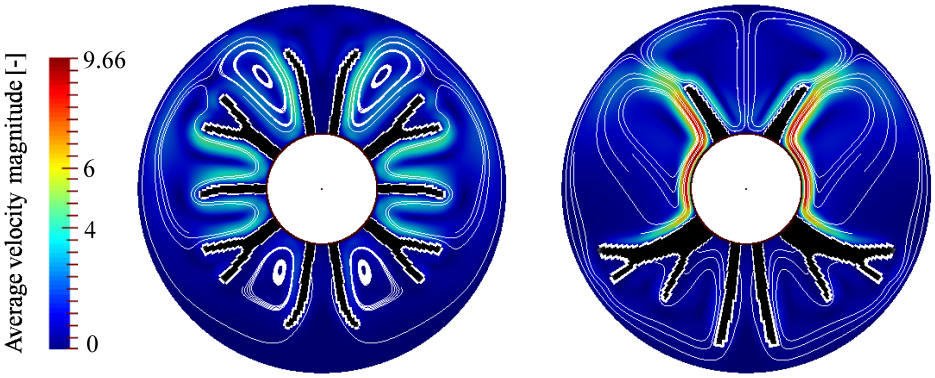

Fig. 5.20. Average velocity magnitude with streamlines during melting. The left column shows the diffusive design while the right column shows the melting design

in Figure 5.20, where we show the average velocity magnitude alongside with streamlines. From a careful examination of the velocity plot, it is clear that the fins positioned above the pipe have the function of redirecting the flow towards the external shell. In the region below the pipe, convection is negligible and heat is transferred mainly by conduction. The ramification patterns of the diffusive design inhibit the formation of large convective eddies. The conductive heat transfer plot of the diffusive design shows a high average heat transfer rate at the fin tips indicating that conduction takes place mainly in the radial direction.

This numerical study presents evidence that melting can be enhanced remarkably through convective transport if the fins are designed with specific features, such as short baffles in the top portion of the unit and a big diffusive structure at the bottom.

5.5.3 Solidification design

Here, we consider a solidification process corresponding to the discharge of the LHTES unit. Also in this numerical example, we account for fluid flow. Solidification is modeled by considering a cold internal tube $T_d^* = 0$ (Eq. (5.24)) and a hot initial temperature field $T_I^* = 1$ (Eq. (5.27)). The discharge is considered complete when the energy level in the tank reaches 5 % of the total capacity. The optimized design obtained for solidification is shown in Figure 5.21(b). The calculated measure of non-discreteness M_{nd} for this layout is 1.37 %. The optimized diffusive design is shown again in Figure 5.21(a) to facilitate the comparisons. To highlight the main

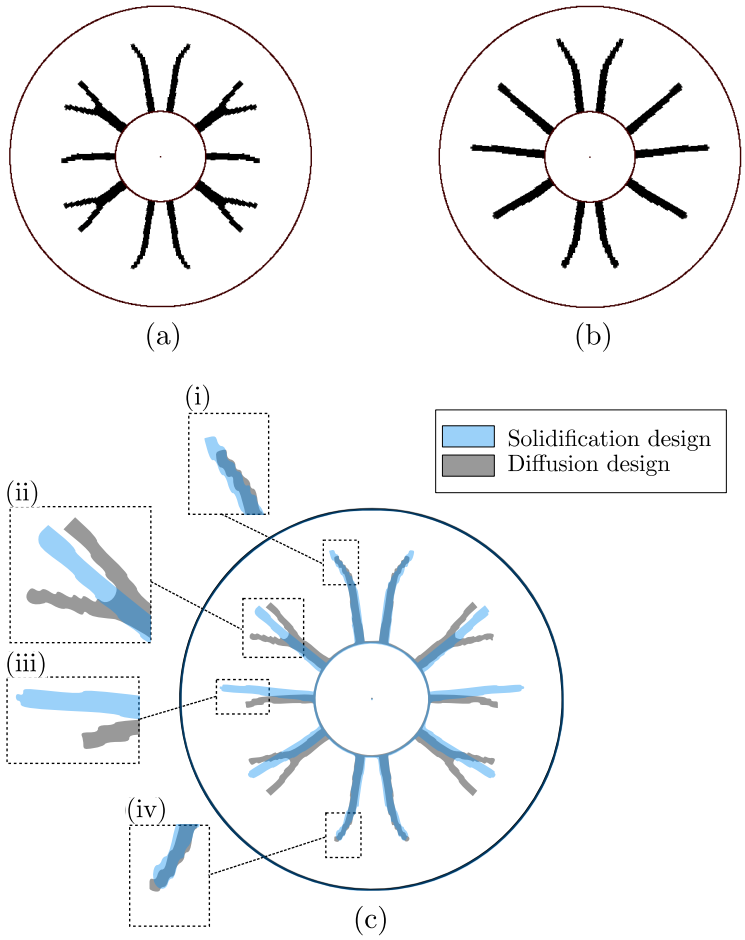

Fig. 5.21. (a): Final layout obtained for the diffusive design; (b): final layout obtained for the solidification design; (c) superposition of the two designs with zoom-in of the most relevant differences. The designs displayed were obtained by thresholding the projected design variable field at $\bar{s} = 0.5$

layout differences between the two cases, Figure 5.21(c) shows a superposition of the optimized designs represented by the projected design variable field contoured at $\bar{s} = 0.5$. The solidification design closely resembles the one obtained considering only diffusion. However, accounting for natural convection in the analysis results in four small modifications:

(i) the branches elongating towards the top of the shell are ~ 9.3 % longer than those of the diffusive design;

(ii) the bifurcations of the intermediate branches are not visible;

(iii) the horizontal branches are ~ 43.7 % longer than than those of the diffusive design;

(iv) the branches elongating towards the bottom of the shell are ~ 3.2 % shorter than those of the diffusive design.

The aspects (i) and (iv) result in a higher concentration of HCM in the upper half the shell. This feature agrees with the intuition that a larger heat transfer area should be utilized in the regions where the solidification front lags behind. The obtained design is similar to the many longitudinal fin layouts utilized in literature and presented in Chapter 3. However, to our best knowledge no previous study in literature considered a varying fin length along the angular position in the shell, as we obtained thanks to features (i), (iii), (iv). The normalized energy histories of the diffusive and solidification designs during the discharge of the unit are shown in Figure 5.22. The solidification design outperforms the diffusive design for any choice of the discharge fraction, Ψ_d. The energy histories are very close to each other until $t^* \sim 0.45$, when they start to diverge. From this point onward, the temporal gap between the two curves increases gradually in time. Overall, the diffusive design demands 11.1 % more time than the solidification design to discharge the unit. The liquid fraction evolution for the solidification test is shown in Figure 5.23 at 20 %, 50 %, 80 % and 100 % of the discharge time of the solidification design, $t^*_{f_s}$. The shape of the solidification front has negligible differences for $t^* = 0.2\, t^*_{f_s}$ and $t^* = 0.5\, t^*_{f_s}$. The snapshots taken at $t^* = 0.8\, t^*_{f_s}$ and $t^* = t^*_{f_s}$ show that the solidification design allows maintaining the solidus line nearly concentric with the internal tube thanks to the longer fins located above the pipe. In the meantime, the solidification front of the diffusive design starts drifting downward. This asymmetry with respect to

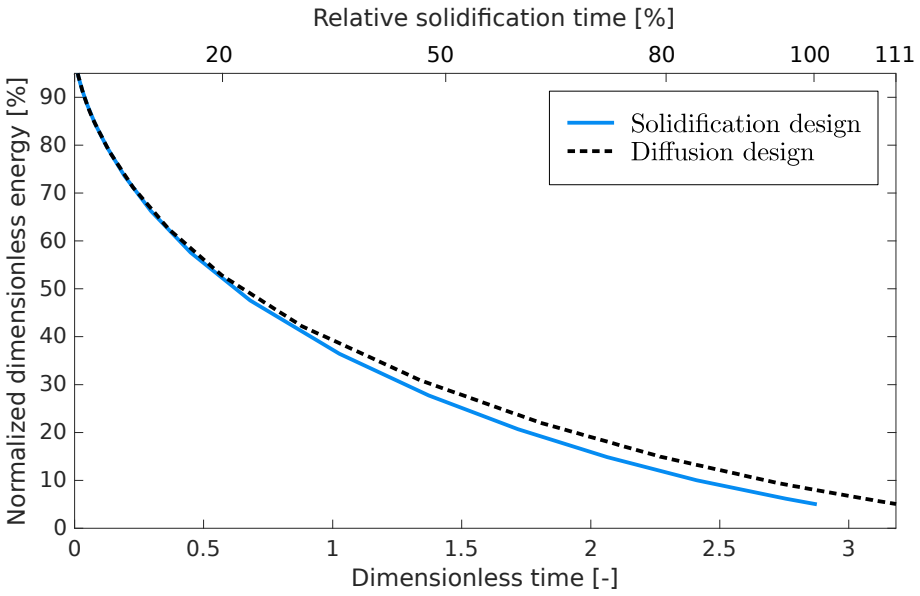

Fig. 5.22. Energy histories of the solidification and diffusive designs during a solidification test

the x-axis is responsible for the increased discharge time: the "left-over" mushy region at the top of the shell has to be cooled away for the discharge completion. Further insights can be gained by considering the average heat transfer rates in Figure 5.24, obtained from Eqs. (5.91) and (5.92) with $t_f^* = t_{f_s}^*$. The conductive portion in the diffusive design is concentrated at the fin tips similarly to what we observed for the same geometry in the melting test. On the other hand, the solidification design transports a non-negligible amount of conductive heat transfer along the fin sides. This indicates that the solidification layout results in a more homogeneous heat transfer distribution and a better utilization of the fin material. In this case, the flow can penetrate close to the internal tube. The ramification patterns visible in the diffusive design inhibit this mechanism, suppressing natural convection. From the examination of the streamlines shown in Figure 5.25, we notice that the diffusion geometry confines the fluid outside of the finned region. This creates a tall and thin eddy with a high downward velocity which contributes to the asymmetry of the solidus line discussed before. Conversely, the downward velocity in the solidification design is limited because of the presence of the small interstitial eddies and the longer horizontal fins. Figure 5.25 also shows that the velocities involved in solidification

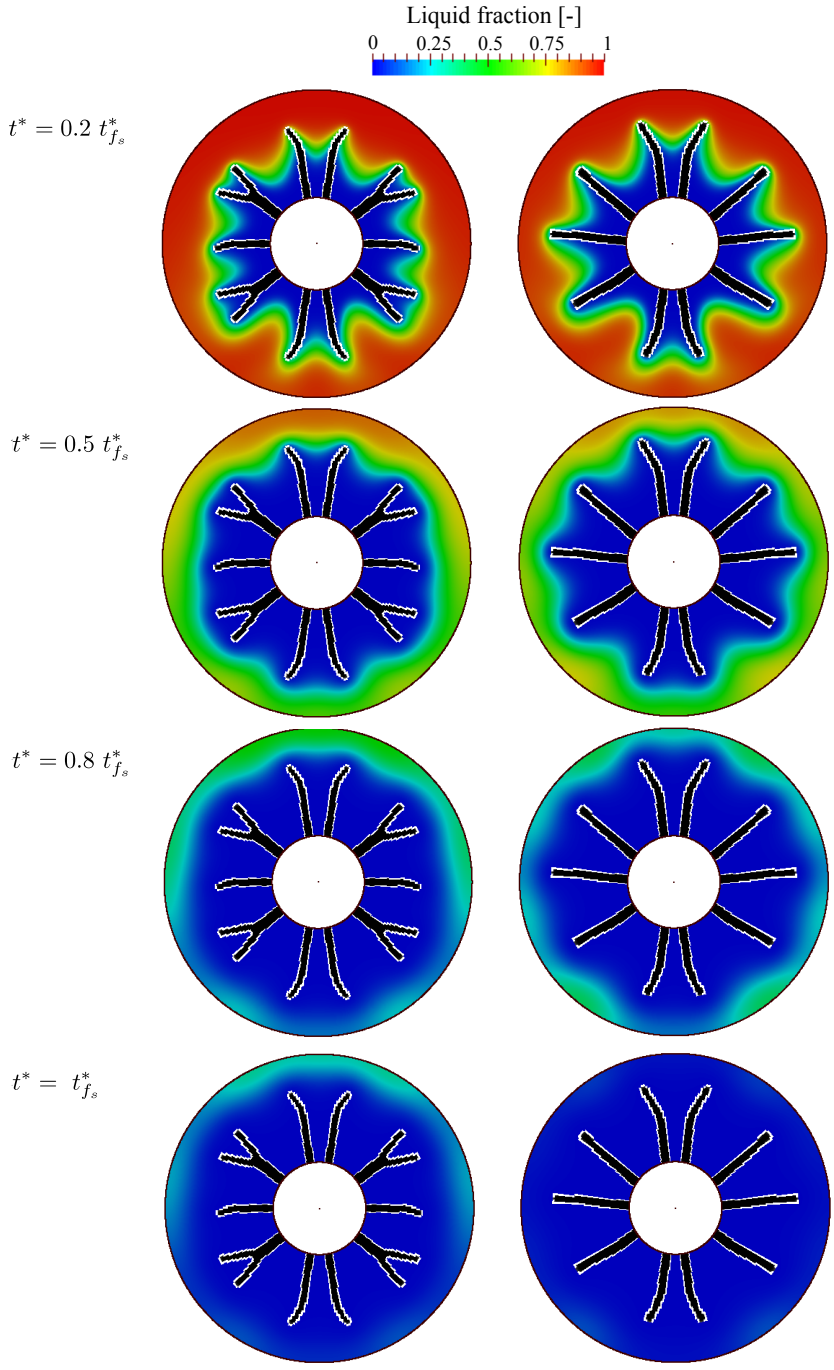

Fig. 5.23. Liquid fractions at selected time instants during solidification. The left column shows the diffusive design while the right column shows the solidification design

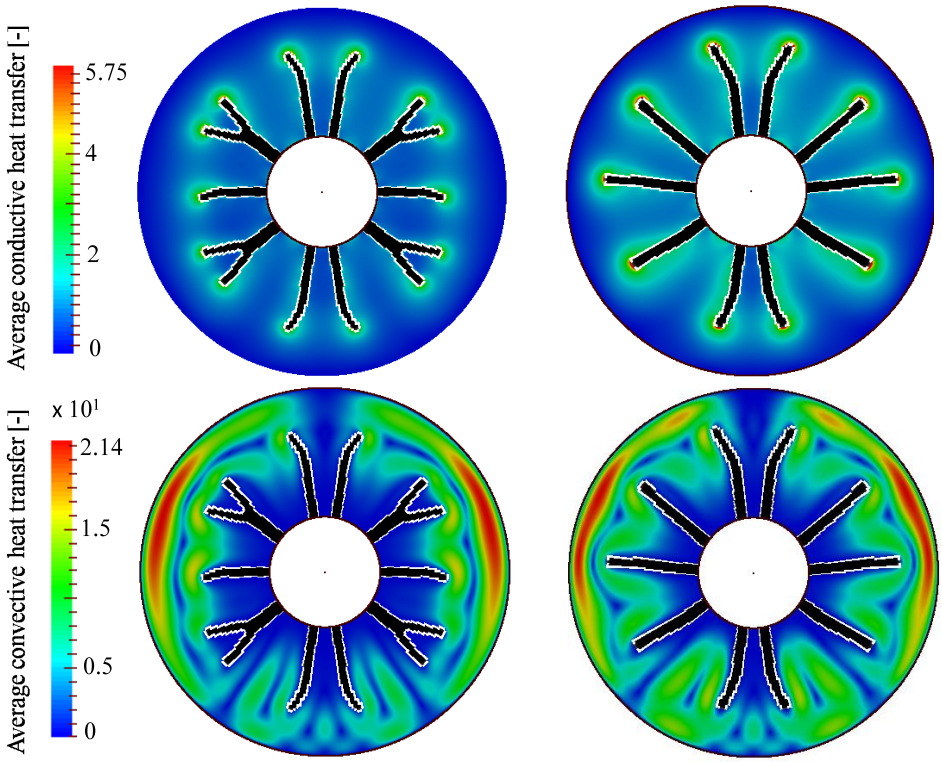

Fig. 5.24. Average conductive and convective heat transfer rate during solidification. The left column shows the diffusive design while the right column shows the solidification design

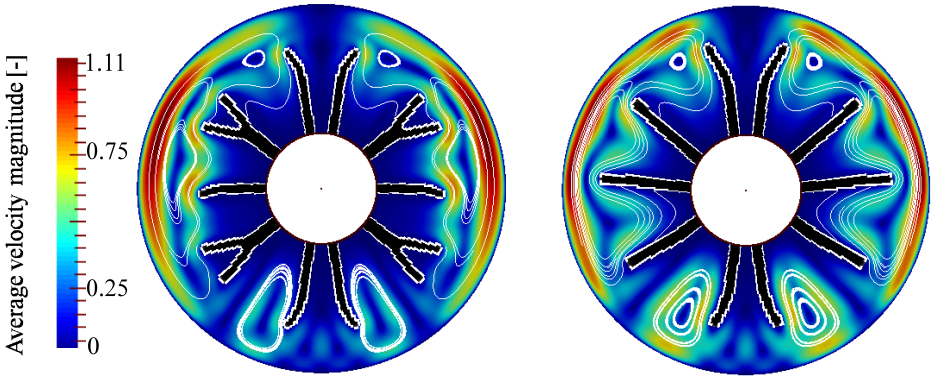

Fig. 5.25. Average velocity magnitude with streamlines during solidification. The left column shows the diffusive design while the right column shows the solidification design

Table 5.8. Charge time computed with a high-fidelity framework in COMSOL Multyphysics

	Performance		
Design	Ch. time [-]	TopOpt dev. [%]	TopOpt dev. ($\beta = 1000$) [%]
Thresh. melting	1.72	+ 25.58	+ 7.76
Thresh. diffusive	2.13	+ 27.67	+ 5.44

are significantly lower than those involved in melting (Fig. 5.20). This limits the average heat transfer rate and results in a long time required for the discharge as compared to the charge of the LHTES unit.

5.5.4 Verification of density-based physical model

This section questions the accuracy of the density-based physical model in predicting the thermal and flow responses of our optimized LHTES units. We compare the predictions of a density-based description to those of a body-fitted grid that allows an explicit tracking of the materials interface. This a-posteriori cross-check is important for two main reasons. First, the material interpolation strategy used in density-based topology optimization does not allow to enforce no-slip conditions at the walls and may result in unphysical fluid-dynamic response that can alter both the optimization results and the identified design trends. Second, selecting a proper threshold for converting a continuous density map to a sharp layout is crucial for manufacturing and needs to be verified.

For the body-fitted studies, we consider two computational domains separated by an interface that conforms to the $\bar{s} = 0.5$ iso-contour of the optimized design variable field. These domains are then meshed using high resolution body-fitted grids with 38976 and 32617 free quadrangular elements for the melting and diffusive designs, respectively. A graphical representation of the meshed PCM domain in the melting design is reported in Figure 5.26 along with a zoomed-in view that allows the resolution at the boundary to be appreciated. The charge times obtained with this high-fidelity framework are reported in Table 5.8. The results indicate that the our density-based topology optimization framework predicts roughly a 26 % higher charge time as compared to the high-fidelity framework. Figure 5.27 reports the dimensionless diffusivity field along the red line depicted in Figure 5.26.

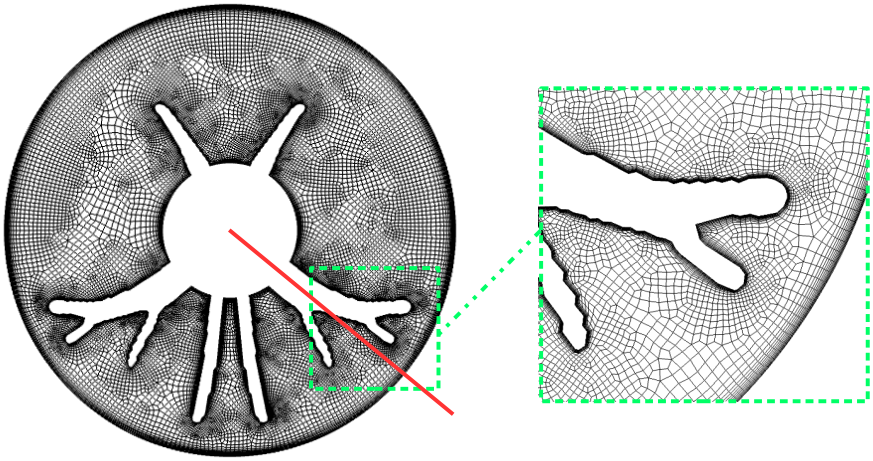

Fig. 5.26. Meshed PCM domain of the post-processed melting design using a high resolution body-fitted mesh in COMSOL

Table 5.9. Discharge time computed with a high-fidelity framework in COMSOL Multyphysics

	Performance		
Design	Disch. time [-]	TopOpt dev. [%]	TopOpt dev. ($\beta = 1000$) [%]
Thres. solidification	2.22	+ 29.28	+ 3.42
Thres. diffusive	2.49	+ 27.71	+ 2.37

The thresholding process eliminates the regions filled with intermediate density, resulting in a higher average diffusivity. To investigate the effect of the non-physical intermediate material on the performance, we analyze the topology-optimized layouts using a large steepness parameter of the projection (2.40), $\beta = 1000$. As summarized in Table 5.8, this procedure strongly reduces the computed deviation with respect to the high-fidelity framework. This suggests that the artificial manipulation of the fluid boundary layer due to the raster geometry representation yields a moderate error. The same computations are repeated for the solidification design, leading to the results reported in Table 5.9. In this case, the deviation is higher and smaller when the designs are analyzed using the reference and the large β, respectively. This is due to the leading role of conductive transport as compared to convective transport in solidification. Hence, the deviations computed with the reference β depend largely on the presence of the intermediate non-physical material. The flow prediction is

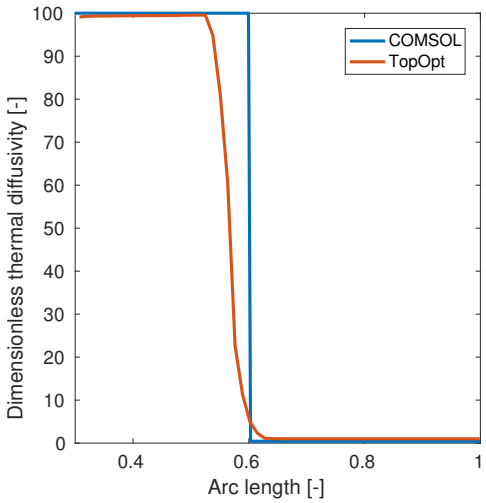

Fig. 5.27. Dimensionless thermal diffusivity along the red line indicated in Figure 5.26

slightly affected by the raster geometry representation due to the small velocities involved.

Instead of raising the projection steepness parameters, β, the performance differences between the body-fitted and density-based analysis models could be decreased also by reducing the radius of the density filter (2.37). However, in our framework it is not possible to eliminate completely the fuzziness of the geometry representation by acting on r_f. As we adopt nodal design variables, a minimum filter size is required to ensure that an element-wise constant filtered density, $\tilde{s}$, is assigned to each element of the FE mesh.

From the analysis presented in this section, it can be concluded that our topology optimization framework is able to capture with sufficient accuracy the main physical phenomena so that the design trends are preserved and the final manufactured fin layouts perform as expected.

5.5.5 Comparison with longitudinal fins

To further question the effectiveness of our optimized layouts, we use the body-fitted high-fidelity simulation framework discussed in the previous section to compare the performance of our optimized geometries with a conventional longitudinal layout

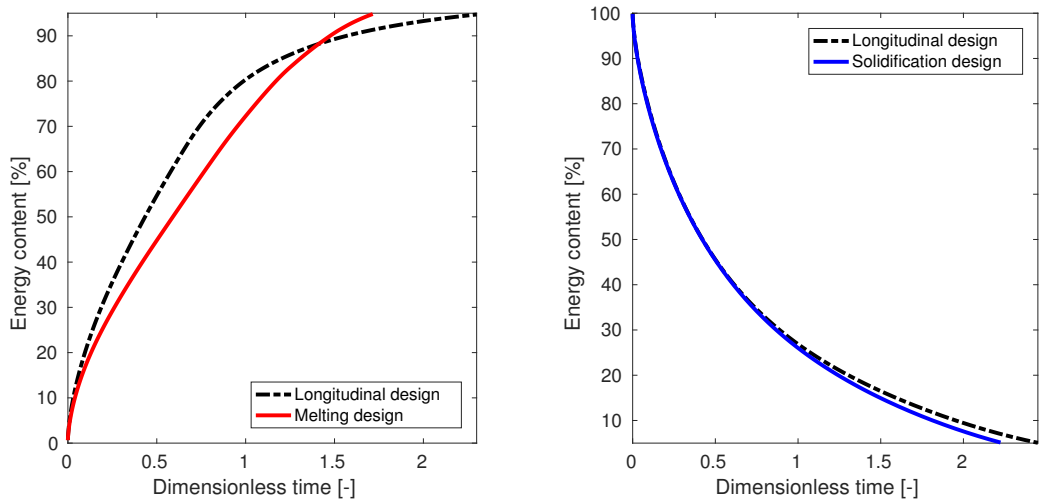

(a) (b)

Fig. 5.28. High-fidelity comparison of energy histories between the topology-optimized and longitudinal geometries. (a): Charge; (b): discharge

(Figure 5.30(b)). The latter is composed of 10 fixed-length fins equally spaced along the angular direction. The fin length is computed as the average of those obtained for a solidification layout with reduced geometric complexity (Figure 5.30(a)), that will be discussed in Section 5.5.6. The energy histories during melting and solidification are shown in Figure 5.28. Our optimized layouts yield a reduction of 25.7 % and 9.1 % of the charge and discharge time as compared to the conventional geometry. We observe trends similar to the ones discussed when analyzing and comparing the performance of the convective geometries to the one of the diffusive geometry. In melting, the longitudinal fins yield a quick charge during the initial part of the process. When the energy content reaches roughly 80 % of the total capacity, the heat transfer rate drops dramatically. This is because the mushy region at the bottom of the shell is slowly melted away, similarly to what we observed for the diffusive design in Figure 5.18. The topology-optimized design allows a much steadier power output to be maintained by exploiting the onset of convective transport. For this reason, it yields a quicker charge for $\Psi_c > 88.7$ %. On the other hand, the solidification design is superior to the longitudinal geometry for any choice of the target energy fraction, Ψ_d.

These results demonstrate that the topology-optimized designs yield substantial advantages as compared to the popular longitudinal layout. One could argue that per-

formance gains are not enough to justify the increased manufacturing complexity. In the next section, we will show a possible method to reduce the geometric complexity without modifying the most relevant features of the optimized layouts.

5.5.6 Reduction of geometric complexity for a real application

In this section, we propose a method to reduce the geometric complexity of the optimized designs in the spirit of easier manufacturing. We test the reduced geometries in a real-world application: a small-scale storage unit for DHNs. Due to the high compactness of the LHTES, the unit can be installed at each thermal user location in parallel to the building heat exchanger. We assume that the building is heated by a low-temperature system. This allows the placement of the unit and heat exchanger on the return line of the primary network, typically at 70 °C. We consider this value as the Dirichlet boundary condition during charge. On the other hand, the HTF temperature during discharge (and thus the Dirichlet boundary) is set to 20 °C, corresponding to the temperature of the secondary network at the startup. The material properties and the shell dimensions are the same used for the design study presented in [375]. The radius of the HTF tube is here set to $r_1 = 0.0165$ m to keep consistency with the dimensions adopted in this chapter. Three designs are analyzed: the optimized layout obtained with our topology optimization framework, a modified version with reduced complexity that allows easier manufacturing and the classical design with longitudinal fins. All the analyses are conducted using the high-fidelity body-fitted framework adopted in the previous sections.

Figure 5.29 shows the procedure followed to reduce the complexity of the topology-optimized layout. First, the optimized geometry (thresholded at $\bar{s} = 0.5$) is interpolated over a 300 $\times$ 300 grid (Figure 5.29(a)). Then, a binary skeleton (Figure 5.29(b)) is obtained through sequential thinning [340, 353]. The branch junctions, bifurcations and extrema are then manually identified and linked with line segments to obtain a straight skeleton (Fig. 5.29(c)). Finally, a uniform fin thickness is calculated such that the HCM volume fraction is equal to the one of the original design. The computed reduced layout is depicted in Figure 5.29(d). The reduced layout obtained for the solidification case is depicted in Figure 5.30 alongside with the benchmark longitudinal layout. Note that the designs shown in 5.30(a) and 5.30(b) differ in terms of length and tilt angle of the fins. Figure 5.31 shows the performance of the analyzed geometries over a full charge and discharge.

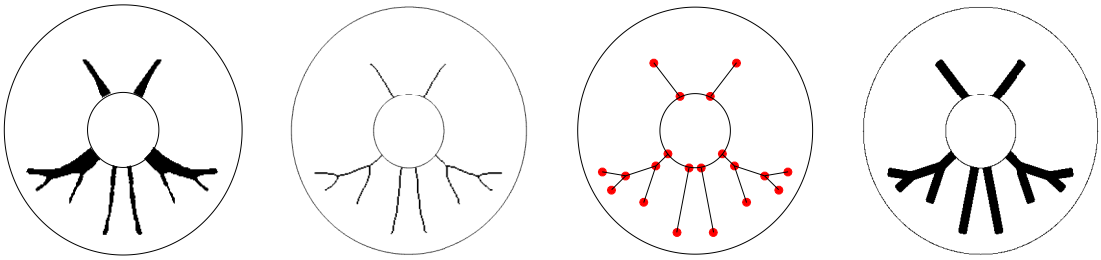

(a) (b) (c) (d)

Fig. 5.29. Reduction of complexity of the topological melting design for easier manufacturing. (a): 300 $\times$ 300 pixelated geometry; (b): skeletonized geometry; (c): straight skeletonized geometry; (d): final reduced geometry

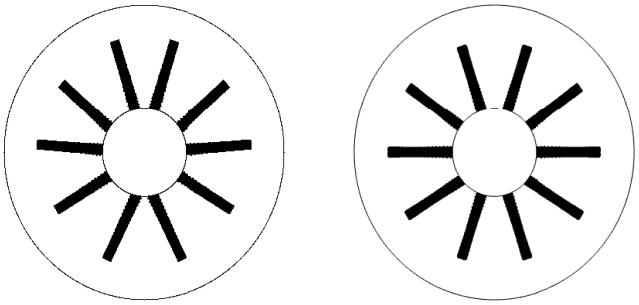

(a) (b)

Fig. 5.30. (a): Reduced topological solidification geometry; (b): reference longitudinal geometry

When using the topology-optimized design, the charge of the unit can be completed in 3076 s corresponding to a 37.3 % reduction of the discharge time as compared to the unit equipped with the classical longitudinal fins. The simplification of the geometry complexity presented in Figure 5.29 results in a layout that increases the discharge time by 256 s, corresponding to a 8.23 % performance reduction. However, the reduced geometry still yields a 32.3 % enhancement as compared to the longitudinal one. Note that the use of longitudinal fins again yields a higher charge rate at the beginning of the process. When tested during a discharge case (Figure 5.31(b)), the performance differences are less evident. The topology-optimized design and its version with reduced complexity yield a 15.2 % and a 7.3 % reduction in the discharge time as compared to the classical geometry. Although limited in magnitude, the improvement achieved through the utilization of the design with reduced geometric complexity highlights the importance of a variable length and angular distance of the fins.

This section demonstrated a possible approach to reduce the geometric complexity of topology-optimized results, facilitating manufacturing. This strategy allows the main topology features to be preserved and was found to yield remarkable advantages with respect to the classical longitudinal fins for both charge and discharge of a real-world LHTES unit.

5.6 Conclusions

In this chapter, we extended the design and analysis framework developed in Chapter 3 to account for natural convection in the liquid PCM. We first presented some issues that may arise in density-based topology optimization for conjugate heat transfer problems. Our simplified numerical examples demonstrated that an improper selection of the continuation trajectory on the penalization parameters may lead to unsatisfactory configurations, which do not exploit sufficiently either the convective or diffusive heat transfer. Then, we searched for heat transfer structures exploiting convective transport for fastest melting and solidification in LHTES units.

A graphical summary of the main application-oriented advances is presented in Figure 5.32. The results suggest that neglecting fluid flow in design optimization studies leads to suboptimal configurations and proved that the heat transfer structures optimized for melting are in general different from those optimized for solidification.

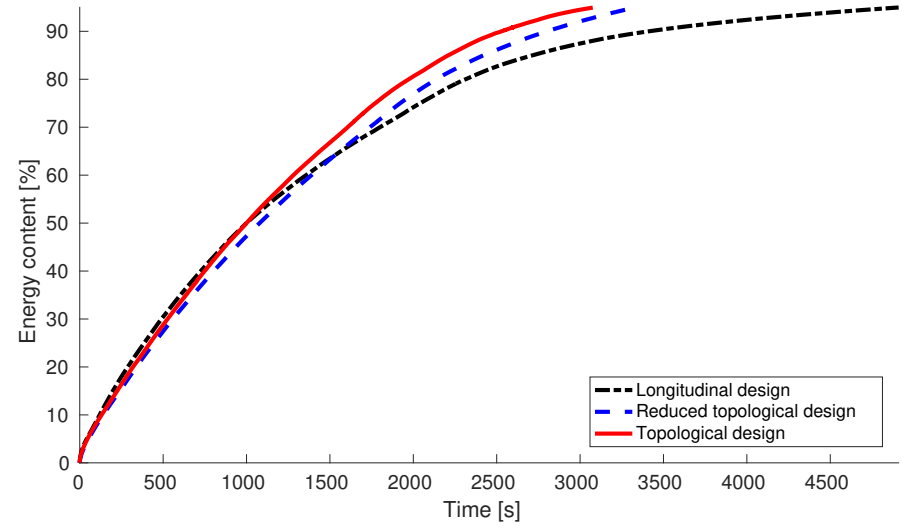

(a)

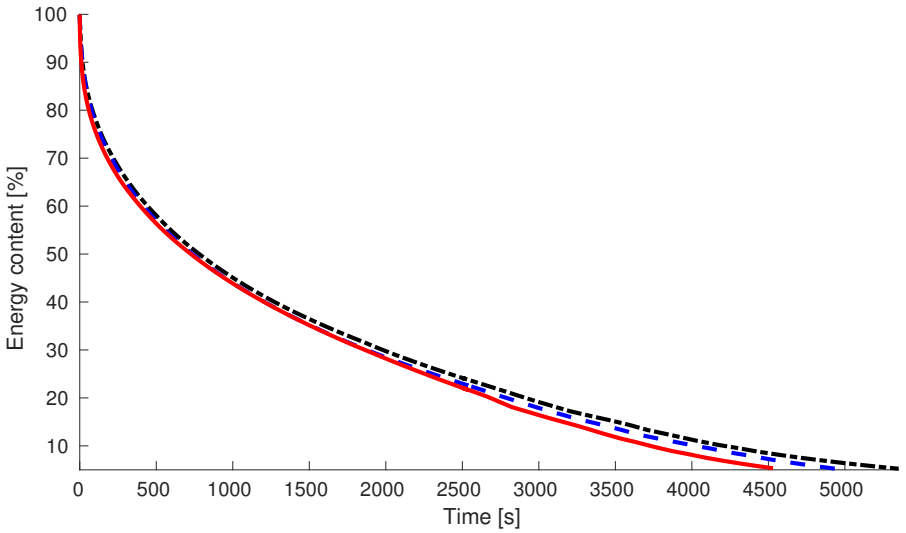

(b)

Fig. 5.31. Energy histories during charge (a) and discharge (b) of a real-world LHTES unit

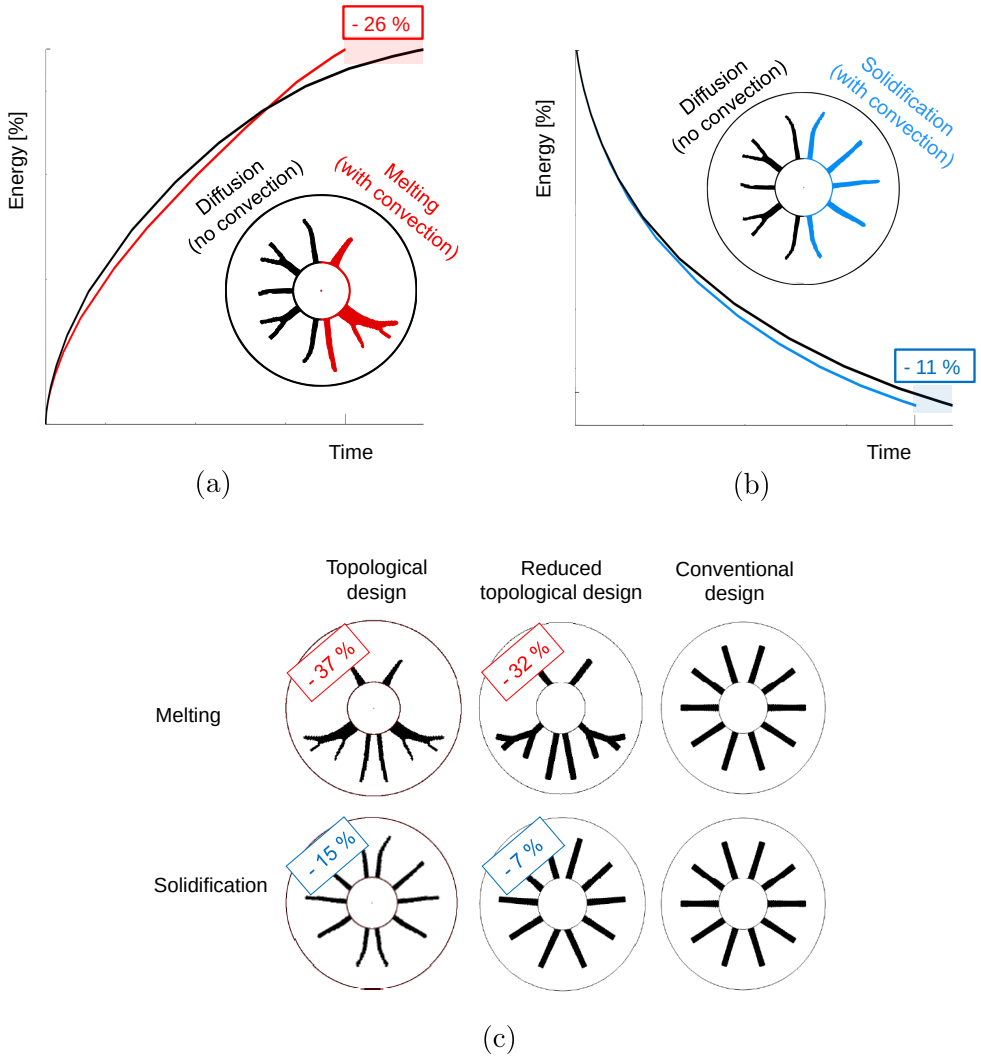

Fig. 5.32. Graphical summary of the main application-oriented advances of the chapter. (a): Effect of natural convection on the optimized design and performance for melting enhancement; (b): effect of natural convection on the optimized design and performance for solidification enhancement; (c): layout and performance comparison of simplified topological geometries for easier manufacturing

A fast melting requires a nearly empty top of the shell such that sufficient room is left for the upward fluid motion (Figure 5.32(a)). The diffusive fins concentrate in the bottom portion of the unit. Using this layout allows the discharge time to be reduced by nearly 26 % as compared to a benchmark design obtained considering only diffusion. On the other hand, the geometry optimized for solidification presents minor modifications with respect to the diffusive layout (Figure 5.32(b)). In this case, considering natural convection in the analysis yields a layout responsible of an 11 % reduction in the discharge time. These design trends are not affected by our density-based physical model, as verified through analyses with body-fitted grids conforming to computational domains obtained from the thresholded optimized design variable field. This high-fidelity framework was then used to compare the topology-optimized geometries against a conventional longitudinal layout. The results indicate that large performance enhancements for both charge and discharge can be obtained through topology optimization. Last, we presented a method for post-processing the optimized layouts into easily manufacturable geometries that conserve the main topology features (Figure 5.32(c)). As compared to the benchmark longitudinal layout, the obtained geometries yield a considerable reduction in the time required for the complete charge and discharge of a storage unit for district heating applications.

In this chapter, we focused on single-tube configurations that are popular in lab-scale or small-scale facilities. However, most of the commercial installations consist of multiple tubes immersed in a unique shell. The extension of these results to multi-tube systems through a circular periodicity assumption is complicated by the anisotropy of convective transport. For this reason, the design optimization of multi-tube units merits an ad-hoc treatment and will be discussed in Chapter 6.

Chapter 6

Design of practical multi-tube units

The shell-and-tube units with multiple tubes distinguish from the other LHTES configurations for their high compactness, large heat transfer area and easy integration with multiple hydraulic loops, preventing the mixing between HTFs. However, a limited body of literature is devoted to the search of the optimal heat transfer structures in this configuration. A popular approach to analyze and optimize multi-tube systems consists in simulating a single tube under the assumption of periodicity, see for instance [256, 219, 218, 250, 42, 480]. Representing multiple tubes by a collection of many single tubes surrounded by PCM rings only approximates the shell area and does not account for boundary effects [50]. Natural convection further questions the periodicity assumption. Agyenim et al. [7] found experimentally that the horizontal multi-tube systems develop multiple convective cells with a complicated interaction. Similar observations were drawn by the authors of [186] and [120], who proposed specific features to exploit convective transport in this configuration. Bridging the gap with the practical technology development of these units require more precise insights on specific design issues. Four fundamental questions remain unanswered:

(i) For which range of material properties do convective features matter?

(ii) How does the periodicity assumption affect the optimized layouts and performance?

(iii) Do systems with separate hydraulic loop require for ad-hoc geometries?

(iv) How are design and performance affected by the HCM and PCM choice?

This chapter aims at shedding light on these practical design issues.

The outline of the chapter is as follows: in Section 6.1 we review the most popular materials used as HCMs and PCMs in LHTES units; Section 6.2 presents and verifies numerically a heuristic approach able to answer question (i); finally, Section 6.3 answers questions (ii) through (iv) with specific numerical examples.

6.1 Overview of materials in LHTES units

When selecting a PCM for a particular application, a number of physical, technical and economic requirements can be identified [296]. Physical criteria are used for a primary selection. The ideal PCM features:

- a phase change temperature matching the application of interest;
- a high phase change enthalpy per unit volume, leading to a high energy density;
- a high thermal conductivity, allowing the charge and discharge of the unit in time spans matching the applications requirements;
- no phase separation, leading to reversible cycles with no performance degradation;
- little subcooling, yielding charge/discharge cycles over a small temperature range.

Technical requirements mainly concern the chemical properties of the PCM [39], which should be chemically stable, compatible with the construction material to avoid corrosion, non-toxic and non-flammable. Economic requirements deal with the availability of storage material at low cost.

A storage material satisfying all these requirements has yet to be found. It is possible however to categorize PCMs in such a way that classes with similar physical and technical properties are identified. A possible classification strategy is depicted in Figure 6.1. This option based on the chemical properties is rather popular in the literature, see for instance [499, 402]. PCMs are subdivided into organic, inorganic and eutectic mixtures. Organic PCMs can be further classified into paraffins, fatty acids, alcohols and glycols. Inorganics include salts, salt hydrates and metallic

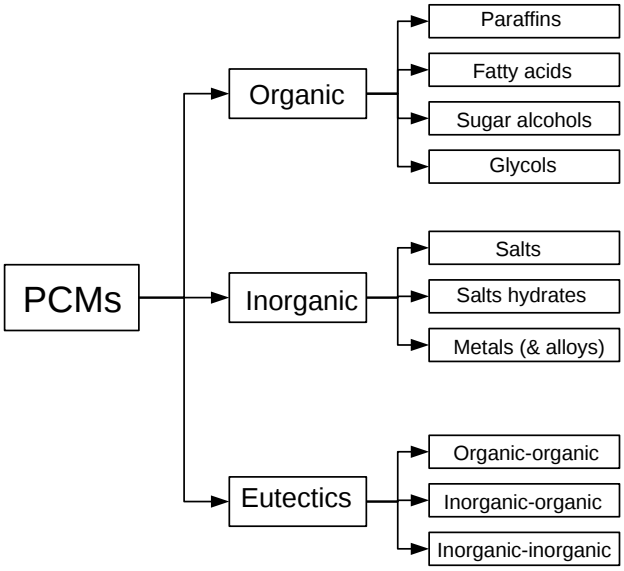

Fig. 6.1. Classification of PCMs based on chemical properties

alloys. Eutectics are mixtures of different constituents and can be organic-organic, organic-inorganic and inorganic-inorganic. In the following sections, we review the most important organic and inorganic PCMs.

The melting temperature and the enthalpy of phase change are not independent. Richardson first observed that melting and solidification yield a fixed entropy change in conductor materials [296]. Considering an isothermal phase transition of a closed thermodynamic system with negligible volume changes and gravitational forces we can write [131, 296]:

$$\Delta S = \frac{\Delta H}{T_m} = \text{constant}, \tag{6.1}$$

where S is the entropy, H is the enthalpy and T_m is the melting temperature. Richardson's rule is restricted to metallic materials and the validity for other substances is often questioned. However, Figure 6.2 shows that a rough correlation between melting temperature and specific enthalpy of phase change is present. The storage materials with high melting temperature such as salts feature a high energy density. PCMs with low melting temperature are able to store a limited amount of latent heat during the phase transition. Table 6.1 reports typical energy density ranges of PCM along with those of popular sensible TES alternatives. For a reference temperature

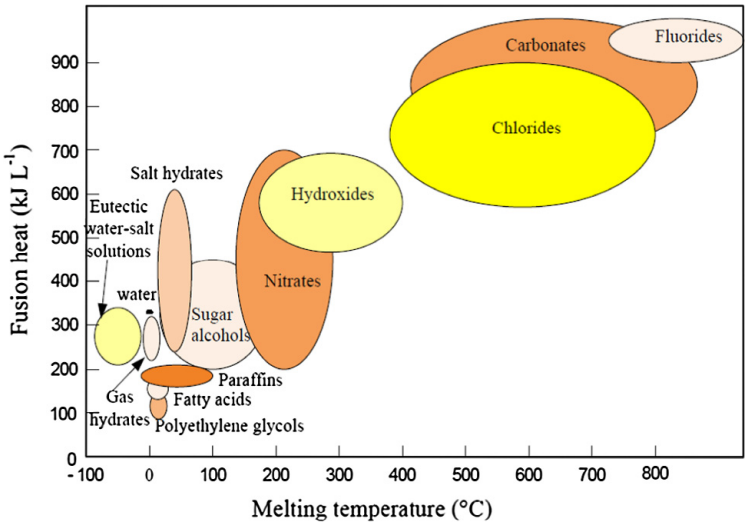

Fig. 6.2. Melting temperatures and enthalpies of different classes of PCMs [492]

difference of 20 $^{\circ}C$, exploiting phase change allows reducing the storage unit size of a water tank by at least a factor of 2. Agyenim [7] proposed a classification of PCMs based on their melting temperature, arguing that this criterion is directly linked to the applications. The storage materials with low melting temperatures, i.e. $T_m \leq 65$ $^{\circ}$C, can be used for domestic heating and cooling, storage of off-peak electricity and integration in building materials. This category includes water, water-salt solutions, and all the organic PCMs. Due to the wide variety of possible applications, this temperature range is the one that was investigated the most [7]. The materials melting at intermediate temperatures (80 $^{\circ}C \leq T_m \leq 120$ $^{\circ}C$), such as some paraffins, sugar alcohols and some salt hydrates are adopted for storage on the evaporator side of LiBr-H_2O absorption cooling systems or for storage in large district heating networks [98]. The materials with high melting temperature ($T_m > 150$ $^{\circ}C$) can be used in storage units connected to CSP plants or industrial waste-heat recovery systems [77]. This temperature range includes salts, salt eutectics and metals.

6.1.1 Organic PCM

Organic PCMs include alcanes, fatty acids, glycols, alcohols and esters. To date, alcanes (i.e. paraffins) are by far the preferred option at the commercial level [7]. This material class covers a wide melting temperature range. They are hydrocarbons with general formula $C_nH_{(2n+2)}$ with C being a carbon atom and H a hydrogen

Table 6.1. Energy density ranges of the most popular storage materials

Material	Energy density $[MJ/m^3]$	Reference	Notes
Sensible			
Water	84	[296]	$\Delta T = 20\ ^\circ C$
Rocks	50	[296]	$\Delta T = 20\ ^\circ C$
Organic oils	30-33	[23]	$\Delta T = 20\ ^\circ C$
Salts	39-75	[23]	$\Delta T = 20\ ^\circ C$
PCM			
Paraffins	169-204	[23]	
Salt hydrates	263-548	[23]	
Salts	631-1584	[23]	
Water	360	[296]	

atom. The melting temperature raises with increasing length of the molecular chain such that $T_m \sim \ln(n)$. In practical applications, only materials with $n > 14$ are used. Paraffins have large enthalpy of fusion with respect to mass and can fully solidify with practically no subcooling. They are also well resistant to phase separation. However, their thermal conductivity rarely exceeds 0.2 W/(m K). Furthermore, their low density results in small volumetric energy densities as compared to alternative PCMs with similar melting temperatures, such as salt hydrates. They are little reactive at nominal operating temperatures and compatible with metallic materials. At high temperatures, i.e. $T > 200\ ^\circ C$, they become chemically unstable: the short chain molecules break and evaporate yielding flammable mixtures.

Fatty acids respond to the general formula $CH_3C_nH_{2n}COOH$. As compared to alcanes, one end of the paraffinic chain is substituted by a carboxyl group. These PCMs have thermo-physical properties similar to those of paraffins [296]. Several eutectic mixtures of fatty acids were experimented [484]. Eutetics generally decrease the phase change temperature of pure acids with negligible modifications of the enthalpy of phase change. A similar effect can be obtained through the esterification reaction. Researchers mainly chose stearic acid and palmitic acid to obtain esters with low melting temperature and high enthalpy of phase change. Some scholars [368, 366, 367] reported only moderate thermal degradation after repeated cycling. However, the authors of [484] argued that thermal stability of these storage materials is strongly affected by the presence of impurities.

Sugar alcohols belong to a material class that has received little attention by researchers so far [23]. They are hydrogenated carbohydrate with general formula $CH_2OH[CH(OH)]_nCH_2OH$ [296]. Their melting temperature ranges from 90 ° C to 200 ° C making them good candidates for intermediate temperature applications. Their high density and specific enthalpy of phase change results in high latent heat per unit volume as compared to alternative organic PCMs. However, they require subcooling for complete solidification. Furthermore, recent experimental results [400] demonstrated that some sugar alcohols, e.g. galacticol, feature a poor stability to thermal cycling. This suggests that much more research needs to be conducted before this class of material can be used in real-world thermal storage applications.

In the category of glycols, Polyethylene glycol (PEG) is the most popular material for thermal energy storage with phase change. It is a polymer composed of a long dymetyhil ether chain, resulting in the general formula $C_{2n}H_{4n+2}O_{n+1}$ [296]. PEG comes in various grades, i.e. from PEG400 to PEG10000, depending on its molecular weight. Both the melting temperature and enthalpy increase with the length of the molecular chains. PEGs have high chemical and thermal stability as demonstrated in several experimental studies [336, 382].

6.1.2 Inorganic PCM

Inorganic PCMs include salt hydrates, salts, metals and metal alloys. They generally have higher volumetric energy density than organic materials due to their higher density [499]. However, they often require subcooling and some inorganic PCMs may lead to severe corrosion of the container material [296].

Salt hydrates are inorganic salts containing a large amount of crystallized water. They have a highly stable crystal structure that results in higher melting temperatures than water [296]: they melt in the range $30\ ^\circ C < T_m < 50\ ^\circ C$ [23]. Some relevant technical impediments prevented their widespread adoption for storage purposes. First, phase separation is observed since all salt hydrates consist of several components. This in turn affects the cycling stability. For this reason, gelling or thickening agents to hinder sedimentation were considered [336]. Subcooling can also be a major problem. Mehling and Cabeza [296] reported subcoolings as large as 80 °C for some materials. Furthermore, high corrosion rates were observed for a few salt

hydrates when in contact with metals such as copper, aluminum and brass [73, 307]. This restricts the spectrum of usable HCMs for heat transfer enhancement purposes.

Salts melt at temperatures higher than 150 ° C. They are considered as suitable candidates for high temperature applications such as CSP [275]. The thermo-physical properties vary substantially among nitrates, carbonates, hydroxides and clorides. Zalba et al. [486] observed that only a few pure inorganic salts posses a high latent heat of fusion. For this reason, double and ternary eutectic compositions were largely investigated. In general, they feature a moderate thermal conductivity, limited subcooling and high chemical and thermal stabilities [296]. However compatibility problems of some salts with some common HCMs were reported [275, 384].

Metal and metal alloys were limited in applications for their high density, which complicates the design of containers. However, their melting enthalpy per unit volume is comparable to the one of salts [77] for similar ranges of melting temperatures. The high conductivity of metals yields fast charge and discharge kinetics with no need for heat transfer enhancement systems. The authors of [486] reported that the selection of metallic materials for storage purposes is complicated by the lack of a comprehensive database able to solve some major discrepancies in thermo-physical data obtained in the previous researches.

6.1.3 High conducting materials

The most common HCM options for extended surfaces in LHTES are aluminum, graphite, copper and steel [405, 275, 77, 23]. The selection of the extended surface material is a crucial step for obtaining cost-effective installations. However, it is hard to extract fundamental selection guidelines from the available LHTES literature. According to Ibrahim et al. [215], the relevant selection criteria are the thermal conductivity, density, corrosion potential and cost. Steel is often excluded as enhancement material due to its high density and low thermal conductivity. However, finned steel tubes are standard components in heat transfer equipment [405] and thus they can represent an option in practice. For instance, finned steel tubes were used recently in CSP [287] and refrigeration [163] applications. Copper is the second most conductive metal after silver [75]. Hence, it is commonly considered as one of the most effective enhancers. Examples of recent studies considering copper fins are [306, 235]. However, we observe that its large density leads to bulky and

Table 6.2. Thermo-physical properties and cost of most popular HCMs

	Material			
Property	Graphite foil	Aluminum	Stainless steel	Copper
Thermal conductivity [W/(m K)]	150	200	20	350
Specific heat [kJ/(kg K)]	0.7	0.9	0.5	0.4
Density [kg/m^3]	1000	2700	7800	8880
Diffusivity [m^2/s] (x10^6)	214.29	82.31	5.13	99.43
Cost per unit volume [k$/m^3]	10	7	20	40
Cost per unit mass [k$/kg]	10	2.59	2.56	4.54

expensive installations. Furthermore, compatibility issues with fatty acids were reported in [136]. Graphite and aluminum feature high conductivity, low density and cost. For these reasons, they represent the most widespread options for heat transfer enhancement in LHTES as demonstrated by the large number of studies recently published, e.g. [380, 132, 487, 23]. Both graphite and aluminum yield no galvanic corrosion when in contact with galvanized steel [275], a common material choice for the HTF pipes. Graphite is preferred for high temperature applications [77] as it does not get corroded by nitrates and nitrites. Below 330 °C, also aluminum fins can be used since no long-term degradation was observed when in contact with those salts [405]. The thermo-physical properties of these materials along with their estimated cost per unit volume as obtained from [405] are summarized in Table 6.2.

The volumetric cost carries large uncertainty. It depends on the vendor pricing scheme, on the quantity of the material purchased and on the specific industrial process with which it was treated. In most cases, the cost is not publicly available but it is a result of private trading. Since this parameter is of crucial importance for some of the results presented in this chapter, we collected a number of alternative references. To allow meaningful comparisons over data corresponding to different years, all the values are normalized with respect to the volumetric price of aluminum. As motivated in [75], the price fluctuations in time are rapid but the price ratios among different materials tend to vary slowly. The work of Steinmann et al. [405] was the only one we found listing the cost values for graphite foils. Table 6.3 summarizes the outcome of this literature review. The results suggest that we can set the costs of HCM as those reported in [405] with sufficient confidence.

Table 6.3. Review on the volumetric cost of HCMs. The reported values are normalized with respect to the cost of aluminum

	Material			
Reference	Graphite foil	Aluminum	Stainless steel	Copper
[44]	-	1	3.61	4.88
[35]	-	1	-	3.84
[226]	-	1	3.14	10.81
[75]	-	1	1.96	3.55
[405]	1.42	1	2.85	5.71

6.2 A heuristic method to anticipate design trends

In some recent studies [436, 109, 46], specific layout features of extended surfaces were proposed to enhance convective transport. Given the large differences in material properties highlighted in the previous section, it is hard to extrapolate some design guidelines valid for general LHTES units. It is desirable for designers to estimate in advance whether these details are important or negligible for performance. In the latter case, convection could be safely ignored during the design optimization procedure. In this section, we first propose and then verify a heuristic method able to provide rule-of-thumb indications.

6.2.1 The method of intersection of asymptotes

We are interested in anticipating for which combinations of material properties the optimized design transitions from conduction-dominated to convection-dominated structures. We found that the PCM-to-HCM diffusivity ratio, C_k, has the largest effect on the optimized layouts. Some preliminary numerical studies showed that the transition covers a small range of C_k values. To identify this range, we look for the intersection of two extrema conditions, as shown in the schematics presented in Figure 6.3. For $C_k \to 0$, the extended surface has the potential for a dramatic enhancement through conductive transport. Hence, we conjecture that the optimal HCM structure suppresses convective flows in order to create highly branched layouts, favoring diffusion. If this is true, convection yields such a limited contribution to performance that fluid flow can be neglected. We call this condition the diffusion-dominant asymptote. For $C_k \to \infty$, the fins limit the conductive heat transfer rate due to the low diffusivity

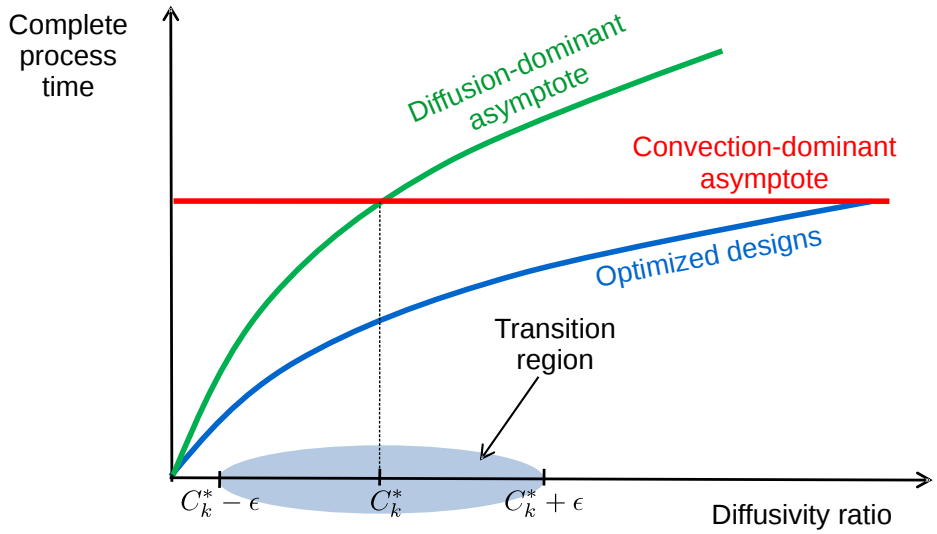

Fig. 6.3. Schematic of the intersection of asymptotes method used to identify the transition region from conductive-like designs to convective-like designs

of the HCM and impede the creation of beneficial convective currents. Hence, we speculate that no HCM is present in the optimal configuration such that convective transport is maximally exploited. We will refer to this condition as convection-dominant asymptote. The choice of the HCM affects only the performance of the diffusion-dominant asymptote: the time required for a complete charge/discharge varies roughly as $\sim \sqrt{C_k}$. The performance of the convection-dominant asymptote is constant with respect to C_k and depends exclusively on the Rayleigh number, Ra, of the liquid PCM: a higher Ra yields a quicker process completion. The performance curve of the optimal HCM structures lies always below the asymptotes because fins can exploit both conduction and convection. For $C_k \to 0$, the curve of the optimal designs tends to the diffusion-dominant asymptote, while it tends to the convection-dominant asymptote for $C_k \to \infty$. The optimal structure continuously evolves from a highly branched configuration to a virgin design domain (i.e. no HCM present). We believe that the most visible design changes can be expected for $C_k \sim C_k^*$, where C_k^* indicates the abscissa corresponding to the intersection of the two asymptotes. We refer to the C_k range parametrized with $C_k^* - \varepsilon_k < C_k < C_k^* + \varepsilon_k$ as the transition region.

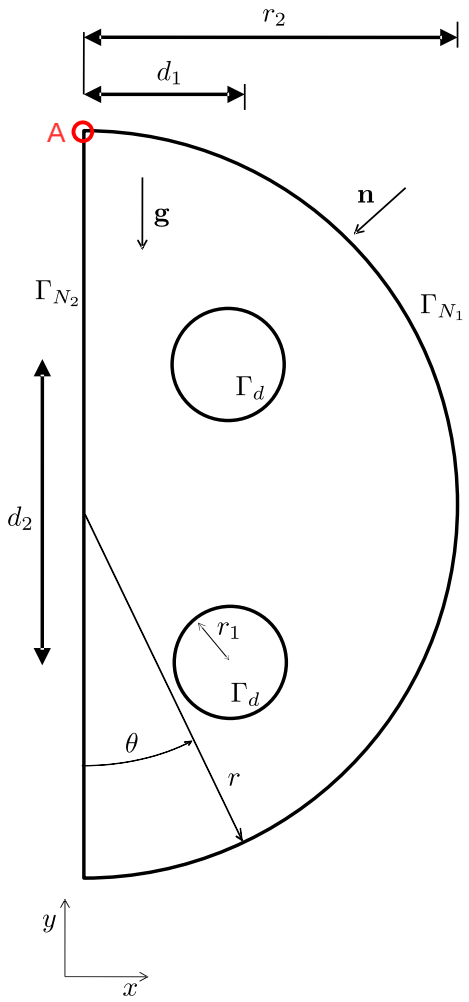

Fig. 6.4. Schematic of the design domain considered in this chapter

6.2.2 Verification

Here, we verify numerically the method of intersection of asymptotes presented in the previous section. We consider both charge (melting) and discharge (solidification) including fluid flow in the analysis. To mimic melting, we consider a hot Dirichlet condition $T_d^* = 1$ and a cold initial temperature field $T_I^* = 0$. On the other hand, solidification is reproduced with $T_d^* = 0$ and $T_I^* = 1$. The charge and discharge are considered complete when the energy level in the tank reaches 95 % and 5 % of the total capacity, respectively. A schematic of the multi-tube design and computational domains is given in Figure 6.4. We adopt the same governing equations, boundary

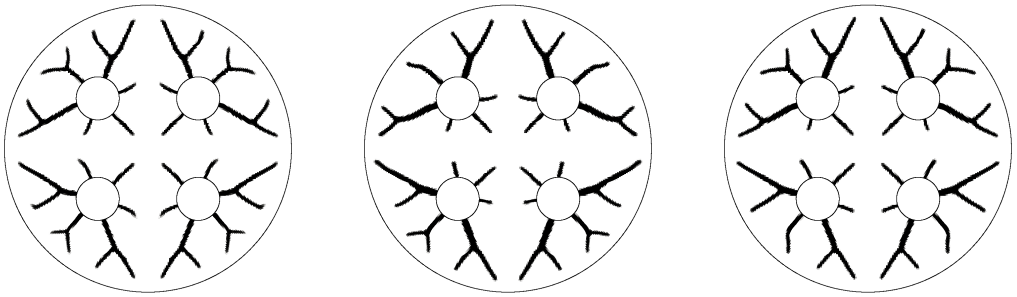

(a) (b) (c)

Fig. 6.5. (a) Optimized diffusive design used to compute the diffusion asymptote; (b): melting design optimized for $C_k = 0.2$ %; (c): solidification design optimized for $C_k = 0.2$ %

conditions and numerical model presented for the single tube geometry in Chapter 5. The design domain has dimensions $r_1 = 0.125$, $r_2 = 1$, $d_1 = 0.35$ and $d_2 = 0.7$. We use a free-quadrangular mesh with 15932 quadrilateral bilinear elements with characteristic size $h = 0.01$.

The calculated asymptotic graphs for melting and solidification are given in Figure 6.6. The diffusion-dominant asymptote was obtained by mapping the performance of a reference diffusive layout (Figure 6.5(a)) for different values of C_k in the range $0.1\ \% \leq C_k \leq 20\ \%$. This geometry was obtained considering $C_k = 0.1$ % and without accounting for convection in the analysis. The convection-dominant asymptote corresponds to the charge/discharge time of a storage unit without fins. In the melting case, the two asymptotes intersect at $C_k^* \sim 3.5$ %. The performance curve of the optimized designs is computed by running four optimization cases with $C_k = \{0.2;\ 1.0;\ 2.0;\ 5.0\}$ %. The transition region is investigated by studying the design differences between the layouts optimized for $C_k = 2$ % and $C_k = 5$ %. In the solidification case, no intersection was observed in the range of values considered. Nevertheless, a similar analysis is performed to cross-check whether noticeable design features are created or destroyed far from the intersection of the asymptotes. From the examination of Figure 6.6, it is possible to obtain some preliminary insights into the design trends. We notice that the optimized designs curve in melting moves rapidly away from the diffusion-dominant asymptote. This indicates that the optimized design is quickly morphing from a diffusive to a convective structure. This trend is less evident in solidification indicating that smaller design changes can be expected. The performance of the designs optimized for $C_k = 0.2$ % in both melting

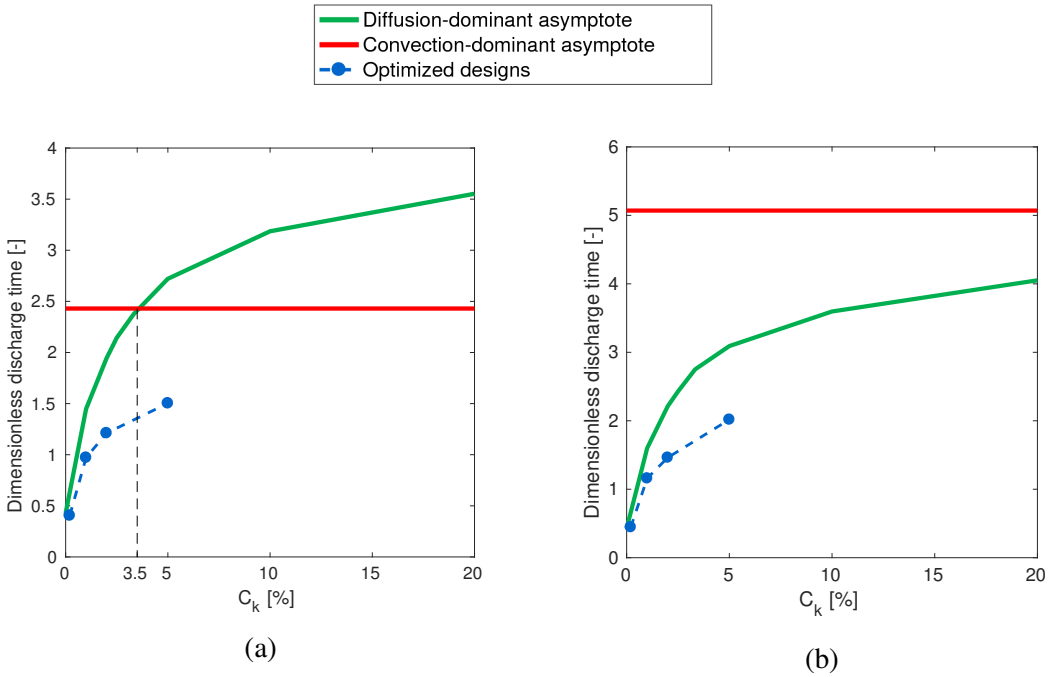

Fig. 6.6. Intersection of asymptotes for melting (a) and solidification (b) in multi-tube storage units

and solidification is nearly coincident with the diffusion asymptote, anticipating large similarities in the layouts. This is confirmed by the optimized geometries shown in Figure 6.5(b) and 6.5(c).

Figure 6.7 shows three optimized designs obtained in the melting case for $C_k \geq 1$ %. Design (b) closely resembles design (a) exception made for a few details. The fins become thicker and shorter due to the decreased diffusivity of the HCM. Design (c) shows some fundamental design differences with respect to the previous cases. The HCM fins surrounding the top tubes are now short structures with a completely changed orientation. No HCM element elongates towards the top region of the external shell. Large and thick fins stem from the bottom pipes towards the lower portion of the unit. The optimized designs obtained in solidification are presented in Figure 6.8. Designs (a) and (b) for solidification enhancement are qualitatively similar. Design (c) presents thicker finning elements but no substantial modifications of the fins orientation are observed.

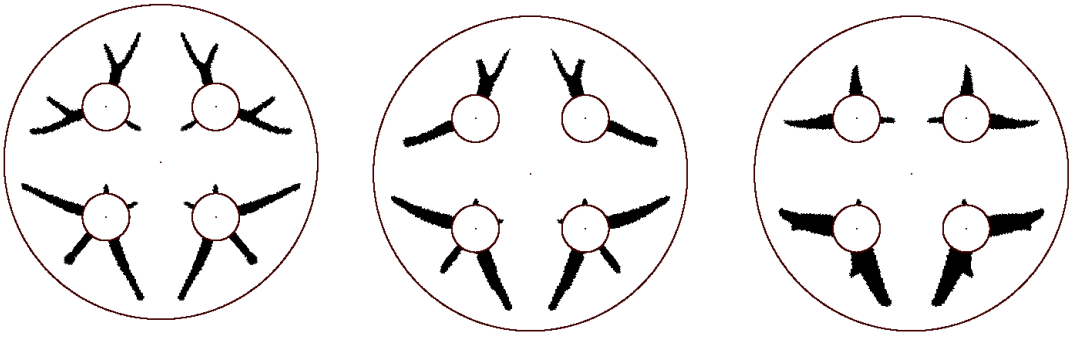

(a) (b) (c)

Fig. 6.7. Optimized designs for melting in the multi-tube storage unit. (a): Optimized design for $C_k = 1$ %, (b): optimized design for $C_k = 2$ %, (c): optimized design for $C_k = 5$ %

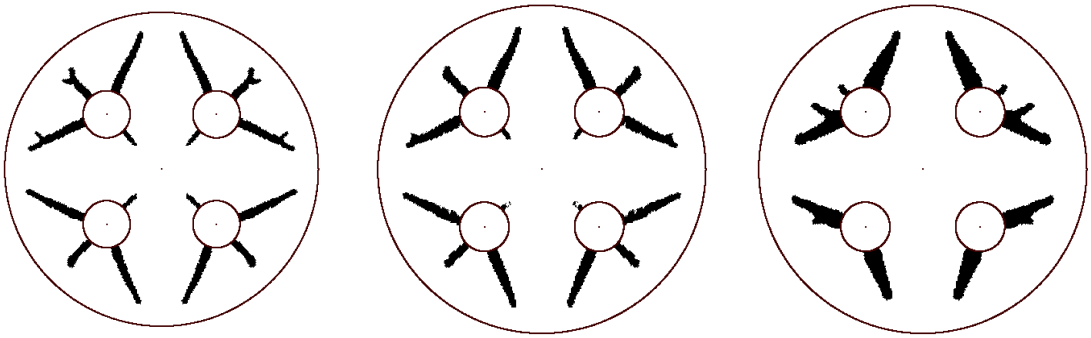

(a) (b) (c)

Fig. 6.8. Optimized designs for solidification in the multi-tube storage unit. (a): Optimized design for $C_k = 1$ %, (b): optimized design for $C_k = 2$ %, (c): optimized design for $C_k = 5$ %

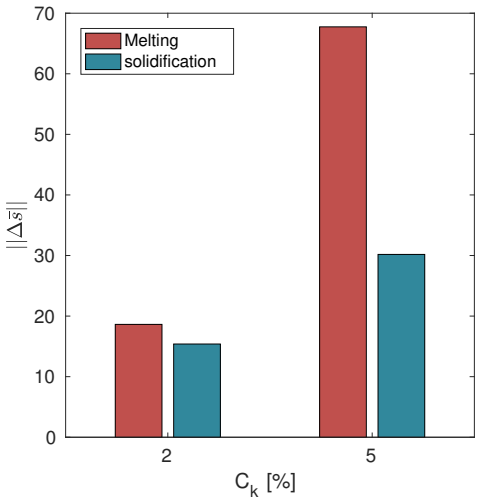

Fig. 6.9. Global of measure of design changes compared to the reference optimized design with $C_k = 1$ %

To quantify the observed design changes, we consider the following global criterion:

$$||\Delta\bar{s}|| = \frac{\int_{\Omega_D} \max\left(\bar{s} - \bar{s}_{ref}, 0\right) d\mathbf{x}}{\Phi \int_{\Omega_D} d\mathbf{x}}, \tag{6.2}$$

which expresses how much HCM in the reference layout parametrized by $\bar{s}_{ref}$ is substituted by PCM in the optimized layout parametrized by $\bar{s}$. Recall that $\bar{s} = 0$ denotes pure HCM and $\bar{s} = 1$ denotes pure PCM as discussed in Section 5.3.1. We consider as reference designs the ones optimized for $C_k = 1$ %, i.e. design (a) in Figure 6.7 for melting and design (a) in Figure 6.8 for solidification. The values of $||\Delta\bar{s}||$ calculated for the layouts optimized for $C_k = 2$ % and $C_k = 5$ % are shown in Figure 6.9. Both designs optimized for $C_k = 2$ % are very similar to their reference layouts: the design changes amount to 18.63 % and 15.39 % for melting and solidification, respectively. The melting design, which is close to the asymptote intersection, morphs of an additional 49.12 % when moving to the case with $C_k = 5\%$. On the other hand, only an additional 14.79 % of design modifications are calculated for the solidification case.

The liquid fraction evolution along the charge history is represented in Figure 6.10. For a meaningful comparison, the snapshots are taken at 20 %, 50 % and 80 % of their final charge time, t_c^*. Note that t_c^* is different for each of the geometries analyzed. The shape of the melting front highlights that the designs exploit different

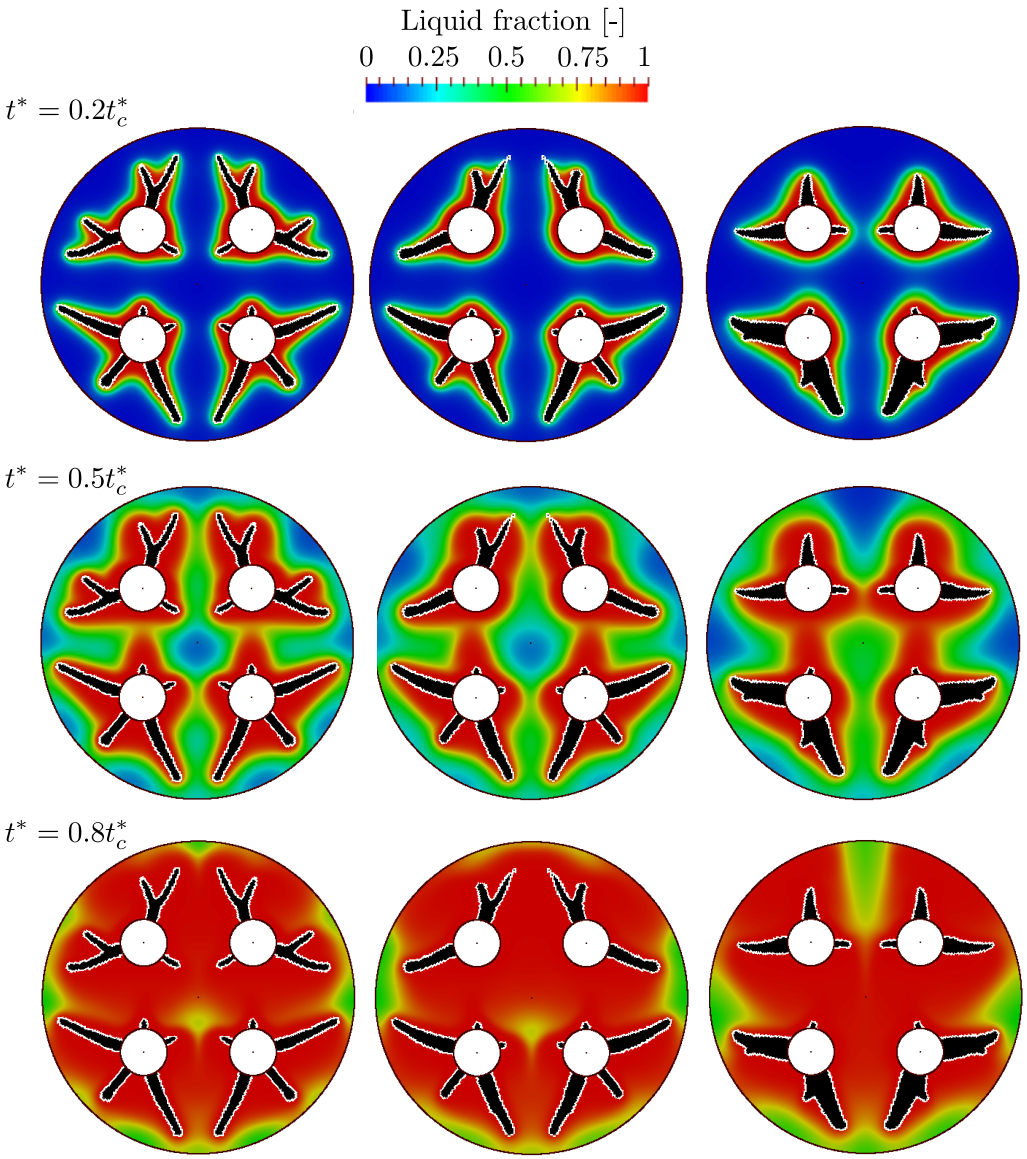

Fig. 6.10. Liquid fractions during melting at selected fraction of the final charge time, t_c^*, of each case. Referring to Figure 6.7, the left column shows design (a), the intermediate column shows the design (b), the right column shows design (c)

strategies to fill the storage unit with liquid PCM. At 20 % of the process, no relevant differences are visible. At 50 %, we notice that some liquid PCM starts dripping upward from the bottom tube and merges with the melted region surrounding the top tubes. Designs (a) and (b) are slower than (c) in this merging process. At 80 % of the charge process, the melting front surrounding the structures (a) and (b) is fairly concentric with the external shell. Design (c) shows a strongly advected liquidus profile. The orientation of the fins relative to the position of the mushy PCM at $t^* = 0.8\ t_c^*$ suggests the dominant heat transfer mechanism of the remaining part of the process. For all the mushy areas visible in designs (a) and (b), it is possible to identify a fin elongating towards them. On the other hand, the mushy PCM located in the upper region of design (c) is not pointed by any fin. This indicates that the latter structure relies on natural convection of the liquid PCM to complete the charge process. The analysis of the liquid fraction evolution during solidification does not provide meaningful insights. We observe negligible differences in the solidification front shape across the three designs.

This study demonstrated the utilization of the method of the intersection of asymptotes to identify the transition region from conductive-like to convective-like designs. This approach helps to identify the ranges of material properties for which neglecting fluid flow in the analysis would slightly impact on the outcome of the optimization.

6.3 Numerical results and design trends

In this section, we describe the numerical examples and study the results obtained for the practical design of multi-tube LHTES units. First, we question the periodicity assumption and assess its impact on the outcome of design studies. Then, we optimize a HCM structure for units with separate hydraulic loops. Last, we solve the problem of choosing the best enhancer material under a fixed investment cost constraint. The numerical model, material properties and design optimization problem are equal to those adopted in Chapter 5. The design domain and its dimensions were presented in Section 6.2. The HTF pipe placement adopted in Section 6.2.2 is here slightly modified to obtain four circular quasi-periodic regions, needed for the first numerical study. Hence, we set $d_1 = 0.414$ and $d_2 = 0.828$ such that the pipes are concentric with the circles inscribed in each of the quarters of the cross-section.

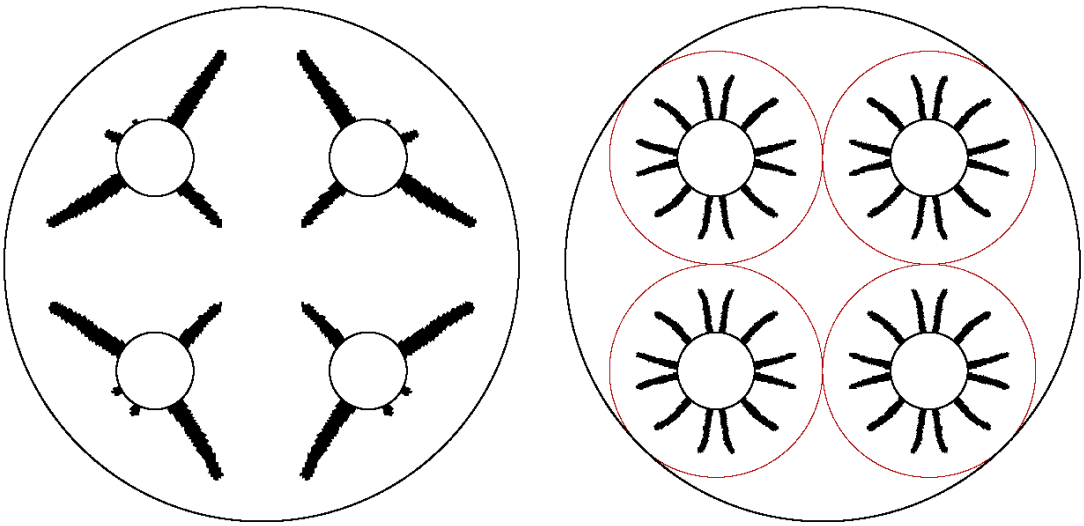

(a) (b)

Fig. 6.11. Optimized designs obtained without (a) and with (b) the circular periodicity assumption. Each of the red circles in (b) indicate the periodic region considered

6.3.1 The effect of the periodicity assumption

In this section, we optimize and analyze both a multi-tube and a periodic single-tube geometry to investigate the effectiveness of the periodicity assumption. Fluid flow is neglected such that the design differences are uniquely due to boundary effects. For this reason, the gravitational source term in Eq. (5.18) is ignored in the analysis. We focus on a discharge case, which is considered complete when the energy level in the tank reaches 5 % of the total energy capacity. Solidification is reproduced by considering a cold internal tube $T_d^* = 0$ (Eq. (5.24)) and a hot initial temperature field $T_I^* = 1$ (Eq. (5.27)). Due to the absence of fluid flow, the same optimized structure would be obtained considering a charge process with a target energy level of 95 %.

The optimized layout obtained considering the entire geometry is compared to the one obtained considering a circular periodicity assumption in Figure 6.11. The layout optimized without periodicity presents 3 large and 2 small fins around each tube which vary in length and tilt angle. The geometry is nearly symmetric with respect to the x-axis which is in agreement with the isotropy of the conductive heat transfer and the symmetry of the domain and boundary conditions. The layout optimized considering a circular quasi-periodic region presents significant differences. Each

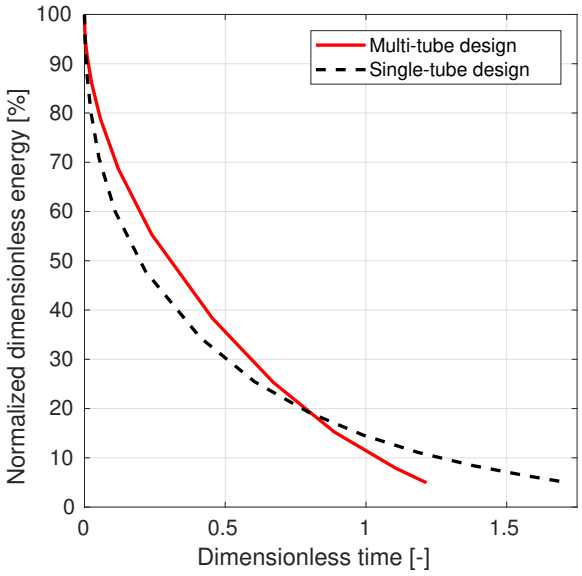

Fig. 6.12. Energy histories during a discharge process for the full multi-tube and for the periodic single-tube layouts

tube is surrounded by 12 fins without bifurcations elongating in the radial direction. The higher number of fins yields a higher heat transfer area than the multi-tube design. Figure 6.12 reports the energy history of the two designs during the discharge process. The design obtained considering the full multi-tube geometry reaches the desired energy level in 29.7 % less time than the layout obtained from the single-tube periodic geometry. However, the latter would yield a faster discharge for partial processes down to 18.8 % of the total energy capacity. The examination of the liquid fraction evolution reported in Figure 6.13 allows this trend to be interpreted. At the beginning of the process ($t^* = 0.24$ and $t^* = 0.60$), the solidification rate is higher for the single-tube design due to a higher concentration of HCM close to the HTF pipes and a larger heat transfer area. The solidification fronts advance following concentric circles that quickly reach the external shell and merge with those of the other tubes. This results in a drop of the discharge rate: only sensible heat can be transferred along the directions in which the solidification fronts merge or hit the shell. At $t^* = 1.21$, four residual mushy regions are visible close to the shell at $\theta = \{0;\ \pi/2;\ \pi;\ 3\pi/2\}$. The solidification fronts in the multi-tube design propagates with shapes that well approximates a quarter of the shell. No merging

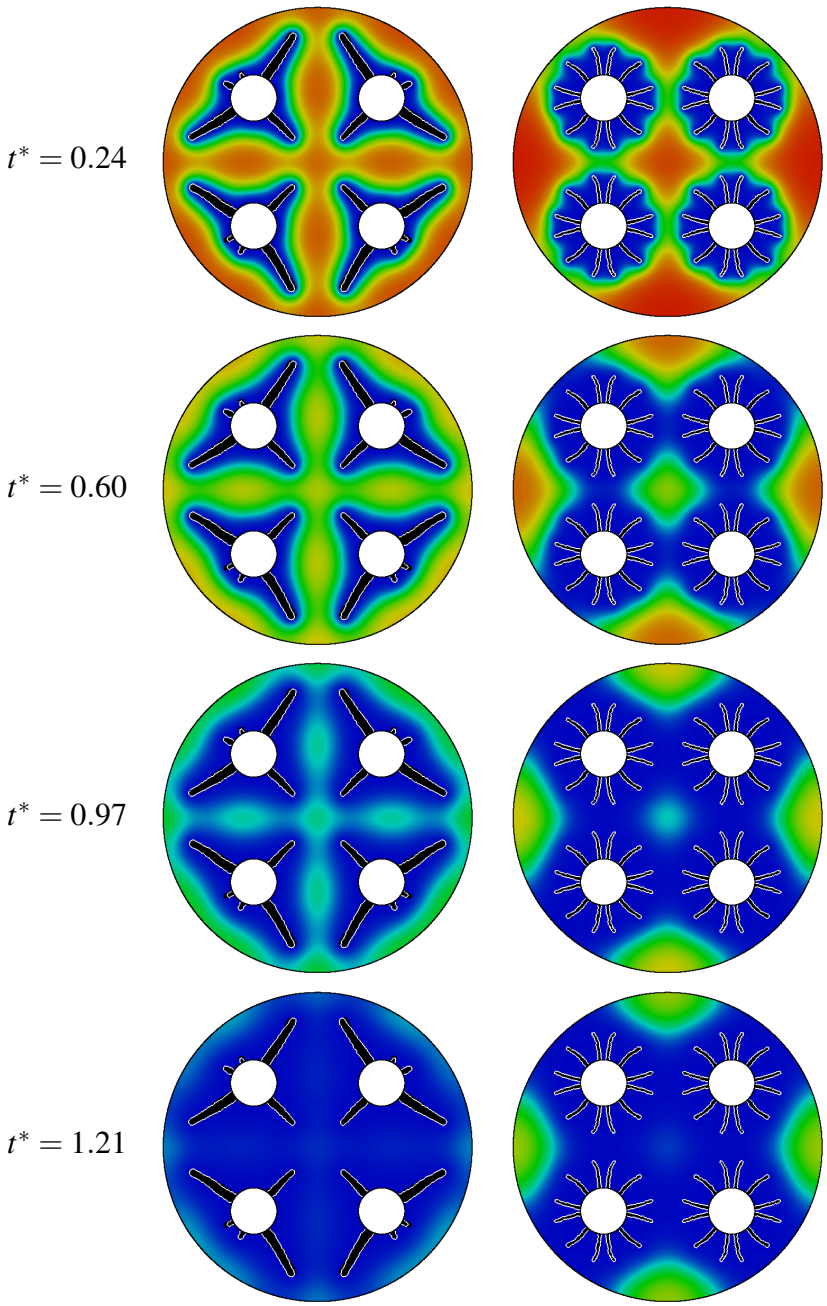

Fig. 6.13. Liquid fractions during the discharge at selected time instants. The left column shows the full multi-tube design, the right column shows the design obtained exploiting the circular periodicity assumption

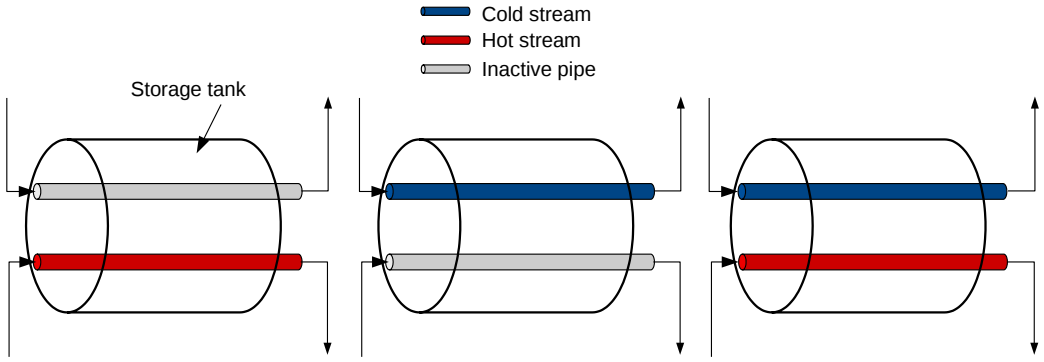

Fig. 6.14. Schematic representation of a multi-tube system with separate loops during charge (left), discharge (center) and simultaneous charge and discharge (right)

between the solidification fronts of different tubes is observed for $t^* < 0.97$ and a high heat transfer rate is maintained for the whole duration of the discharge process.

The results described in this section demonstrated that representing multi-tube units with a single periodic cell in general leads to suboptimal designs due to boundary effects.

6.3.2 Design of unit with separate hydraulic loops

This section deals with the optimization of multi-tubes units with two separate loops for the HTFs such as the system considered by Allouche et al. [20]. The separation of the HTFs yields various advantages such as the simpler mechanical system design, operation without contact/contamination between the two HTFs [279, 467], possibility of simultaneous charge and discharge [312] and operation with different operating pressures. The latter is a practical design requirement for the integration of LHTES units in DH systems. A schematic representation of the separate loops concept is given in Figure 6.14. We consider a charge followed by a discharge with target energy fractions of 95 % and 5 %, respectively. The objective is to minimize the total time, given as the sum of the duration of the two processes. We constrain the design variable field in such a way that a HCM layer of thickness $\delta r = 0.02$ covers the HTF pipes. This is necessary to correctly model heat conduction in the pipe-covering material during the periods of inactivity. The optimized design is represented in Figure 6.15(a). This layout shows no ramification

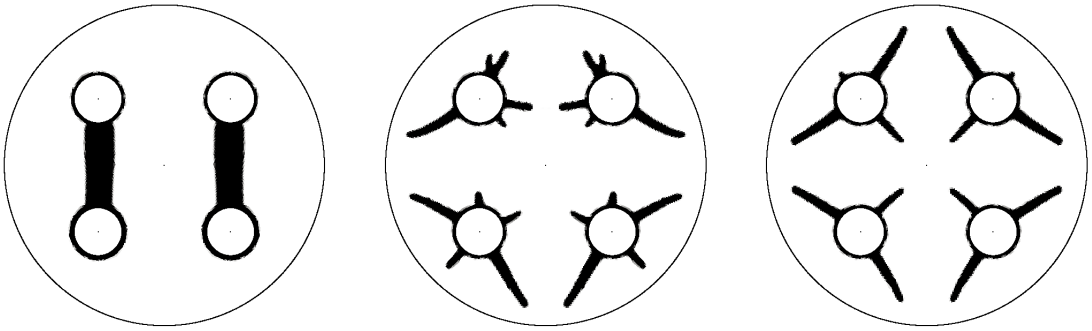

(a) (b) (c)

Fig. 6.15. (a): Optimized design of a unit with separate hydraulic loops; (b): optimized design of a single-loop unit for fastest charge; (c): optimized design of a single loop unit for fastest discharge

pattern on the surface of the pipes. A single thick HCM path is created to connect the top pipes with the bottom pipes. This feature allows the effective utilization of all the HCM in the tank: the links ensure that no isolated HCM regions are created and that the pipe-covering material is utilized during both charge and discharge. A closer examination reveals that additional HCM is aggregated around the bottom pipes, while the top ones have the prescribed minimum thickness value. This indicates that the bottom region of the unit is more critical for performance. The geometries shown in Figure 6.15(b) and 6.15(c) are single-loop designs optimized for fastest charge and discharge, respectively. Figure 6.16 shows the energy histories obtained with the three layouts. Design (b) and (c) require 171.3 % and 150.6 % more time than design (a) to complete the cycle. The most critical process is discharge, accounting for 71.4 % and 72.0 % of the total delay accumulated. The charge of design (a) is slower than the ones of the other geometries for $t^* < 0.742$. The heat transfer rate of designs (b) and (c) suddenly decreases when the unit has been charged up to roughly 70 % of the total capacity. A look at the liquid fraction evolution presented in Figure 6.17 helps to interpret this event. The large heat transfer area of designs (b) and (c) allows a quick melting of the bottom region of the shell. At $t^* = 0.74$, the energy content of the tank is approximately 40 % of the fully charged condition. However, the liquid PCM is distributed unevenly and a large portion of the solid PCM is located far away from the heated pipe. On the other hand, the melting front of design (a) is shifted upward at the beginning of the process thanks to the HCM path linking the top and the bottom pipes. From this point onward, the liquid is rapidly advected towards the

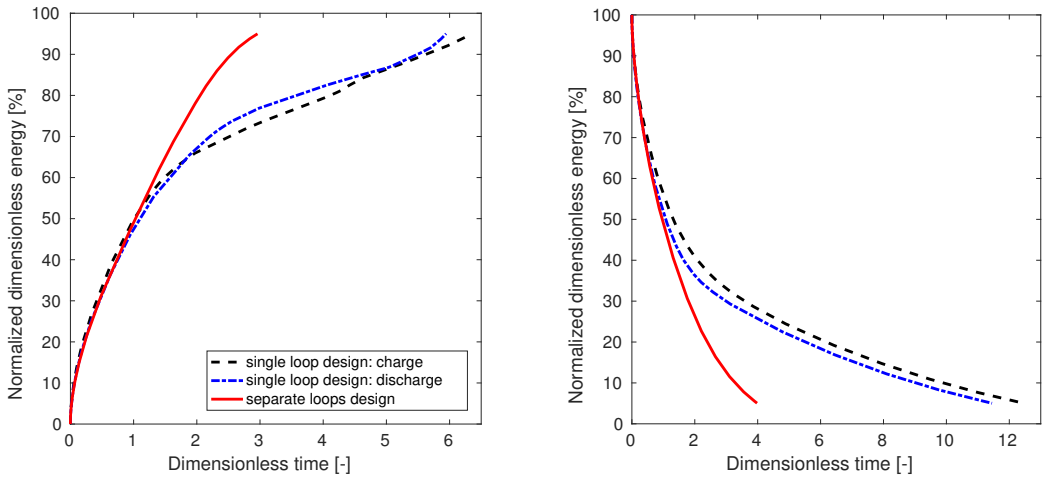

(a) (b)

Fig. 6.16. (a): Energy history during the charge process; (b): energy history during the discharge process

top so that at $t^* = 1.48$ the energy level of the tank reaches 63 % of the fully charged condition. Roughly the same amount of time is required to feed the tank with the remaining 32 % of energy: the absence of conductive fins makes it hard to melt away the mushy area in the lower region of the tank.

The energy histories during the solidification process (Figure 6.16(b)) are very similar for the three designs when $t^* < 1.304$. Also in this case, layouts (b) and (c) experience a sudden heat transfer drop. The reason for this behavior is visible in Figure 6.18. By comparing the liquid fraction distribution of designs (b) and (c) at $t^* = 0.99$ and $t^* = 1.99$, we notice that a fast energy retrieval is achievable at the beginning of the process through the solidification of the upper part of the shell. When the top half is fully solidified, the fins attached to the top tube lose their functionality and the solidification of the lower portion of the tank fully relies on diffusion through the solid PCM. The absence of branched structures in design (a) suggests that, also in this case, the process is ruled by diffusion through the PCM. However, at $t^* = 1.99$, it is clear that the average diffusion length that has to be traveled by the solidification front is shorter for design (a). The solidus line propagates in a nearly concentric way with respect to the external shell. Note that the higher performance gap between single-loop and separate loop layouts during

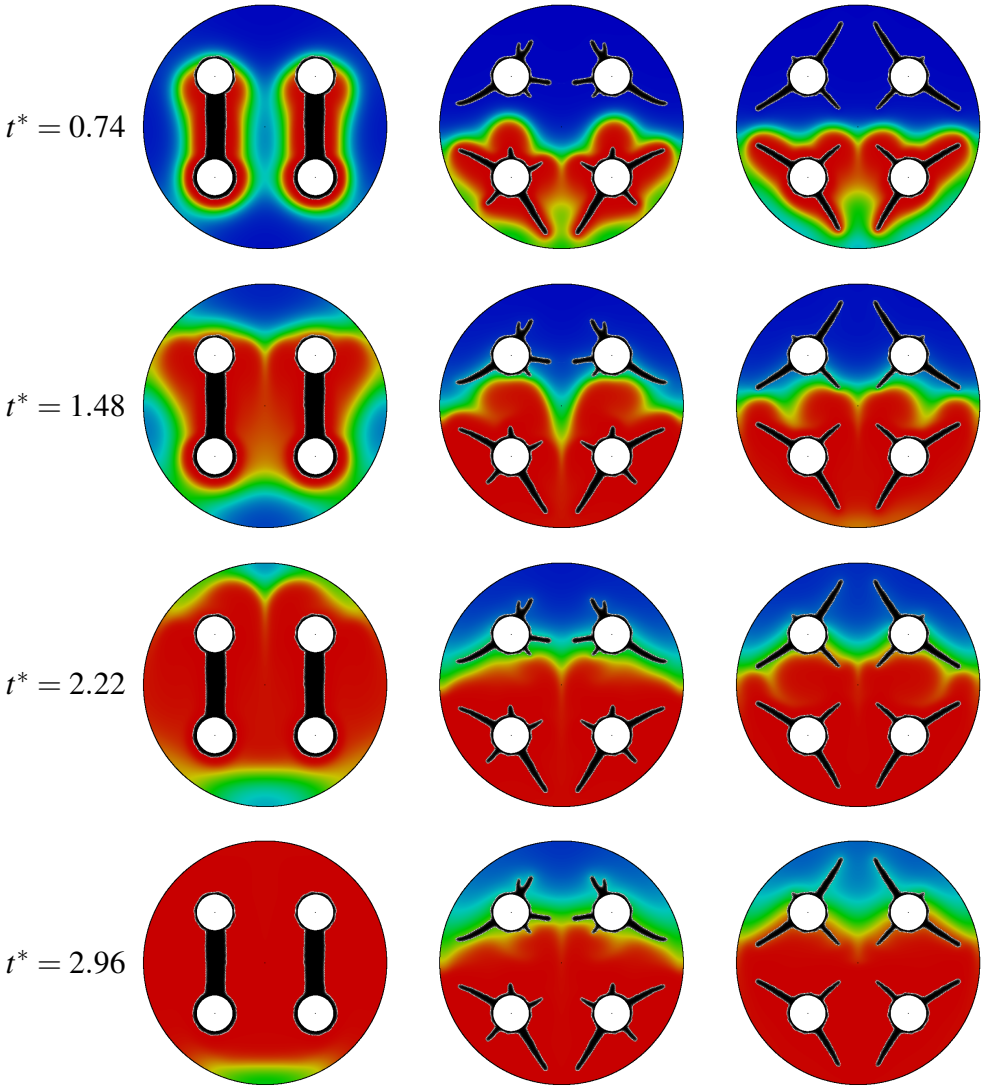

Fig. 6.17. Liquid fractions at selected time instants during melting. The left column shows design (a), the center column shows design (b) and the right column shows design (c)

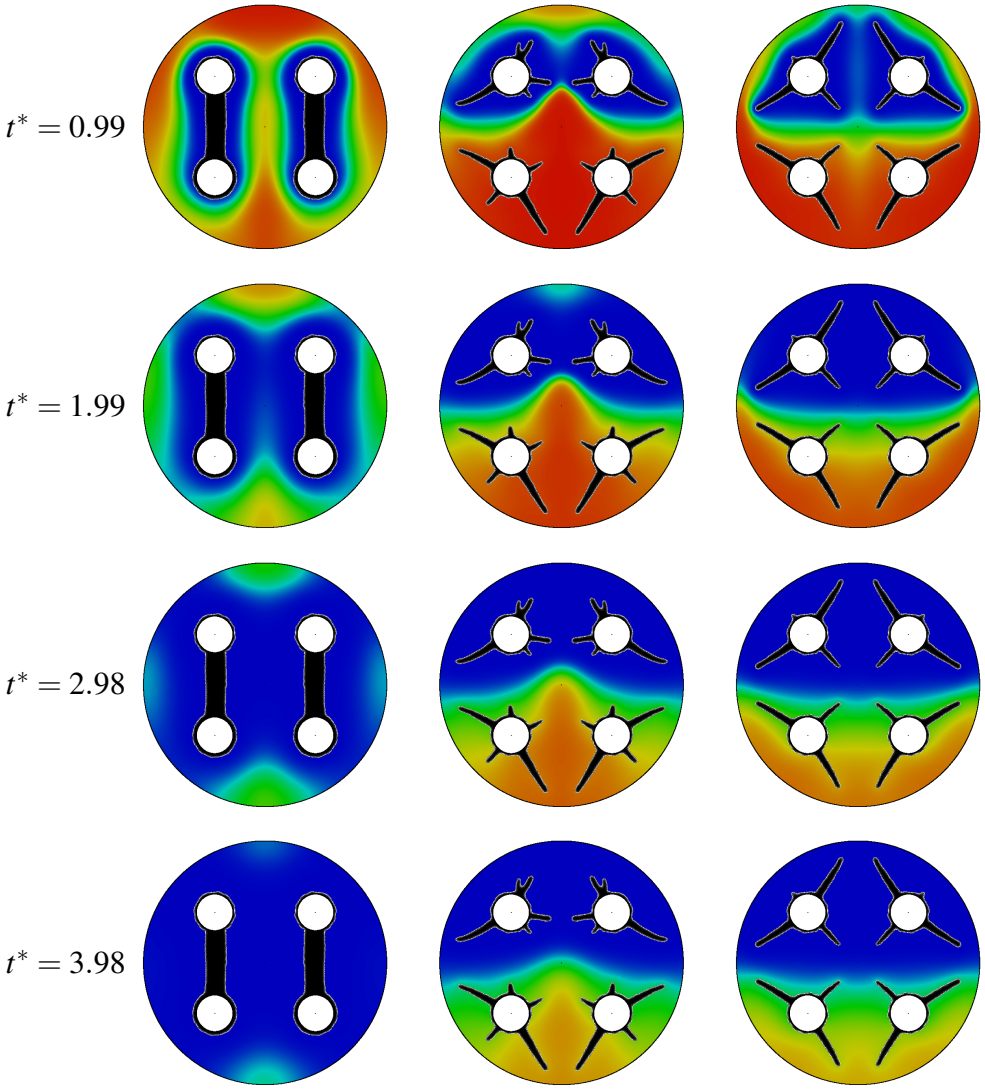

Fig. 6.18. Liquid fractions at selected time instants during solidification. The left column shows design (a), the center column shows design (b) and the right column shows design (c)

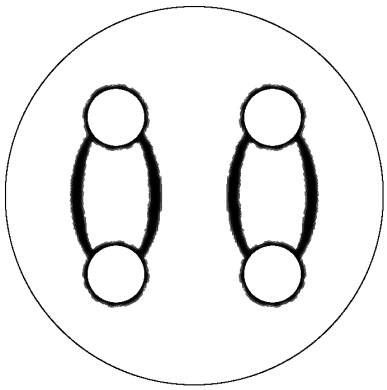

Fig. 6.19. Alternative geometry with double HCM connections between HTF pipes

Table 6.4. Performance of the alternative layout

	Performance	
Process	Process time [-]	Deviation from topological design [%]
Charge	3.31	+ 12.99
Discharge	3.91	- 1.38
Charge-discharge	7.22	+ 4.18

discharge is due to negligible convective transport. The upward fluid motion helps to heat the top portion of the shell during the charge of the unit.

The examination of the optimized layout raised some doubts over the validity of the numerical results: why a single and thick HCM connection? Why not increasing the interface for higher heat transfer rate? To answer these questions and make sure the optimized layout is not a poorly performing local minimum, we benchmarked it with the geometry presented in Figure 6.19, which consists of four curved HCM connections between the top and the bottom pipes. The performance of this configuration is summarized in Table 6.4. The alternative layout yields a moderate increase of the charge time, while discharge is slightly quicker. Overall, the completion of the charge-discharge cycle requires 4.18 % more time than the topology-optimized layout. To understand the physical reasons behind this performance gap, it is useful to study the average velocity magnitude field shown in Figure 6.20. For both melting and solidification, the topology-optimized design yields stronger convective currents that expedite energy transport in the shell. On the other hand, the layout of the alternative geometry suppresses fluid motion in the areas enclosed by HCM and

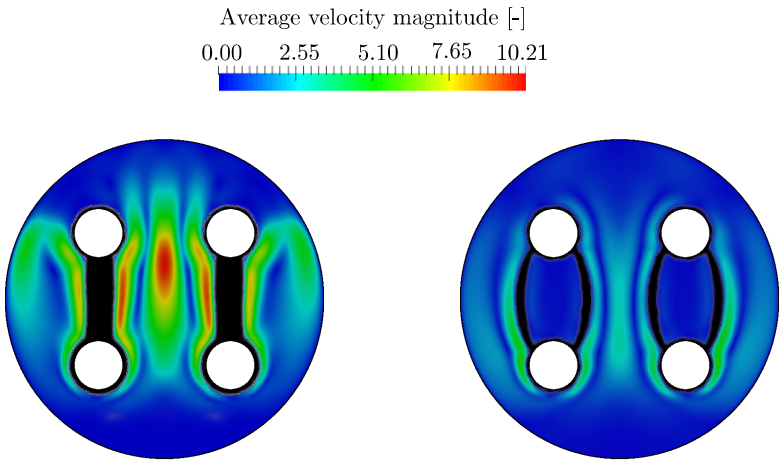

(a)

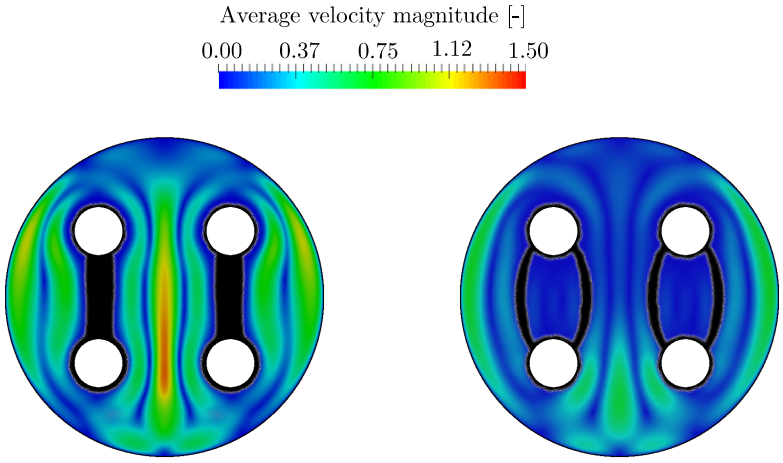

(b)

Fig. 6.20. Average velocity magnitude of the two geometries during melting (a) and solidification (b)

prevents the formation of tall eddies. Weak convective streams concentrate in a region close to the HCM structure. Velocity differences are large for charge: the maximum average velocity is 10.02 for the topology-optimized design and 4.76 for the proposed alternative. This suggests that the reduction of convective transport is the main responsible for the longer charge time of the alternative geometry. On the other hand, we observe small velocity differences for discharge. As discussed in Chapter 5, convection contributes marginally to the discharge dynamics, which is mostly ruled by diffusion. Hence, the reduction of convective transport of the alternative geometry is more than compensated by the increase of diffusion due to the larger heat transfer area. This explains why the alternative geometry leads to a quicker discharge completion.

The numerical study described in this section presented the design optimization of units with two separate hydraulic loops for the HTFs. The optimized structure is extremely different from those optimized for single-loop units. Finned tubes optimized for enhanced melting and solidification in single-loop units are found to be efficient only in the initial part of the charge and discharge processes.

6.3.3 The effect of the HCM-PCM couple choice

In this section, we investigate how the optimized layouts and performance are affected by the choice of materials to be used as PCM and HCM. We test both the charge and discharge of the multi-tube unit. For charge, we consider $T_d^* = 1$ and $T_I^* = 0$ while we set $T_d^* = 0$ and $T_I^* = 1$ for discharge. The time-stepping in the two processes is stopped when 95 % of a reference energy capacity (discussed below) is charged and discharged, respectively.

We consider three alternative PCMs targeting different applications. PCM-11 is a salt hydrate with low melting temperature and moderate thermal conductivity which has been considered in [417] for refrigeration systems. The Solar Salt (SS) is a binary eutectic salt ($NaNO_3$–KNO_3 60–40 % wt.) with average melting temperature of 230 °C that is used in many CSP systems, see e.g. [145, 338]. RT100 is a paraffin wax that was considered in [98] for mid-temperature applications such as district heating. The thermo-physical properties of these materials are summarized in Table 6.5. The conductivity, density and specific heat have been averaged between those of the solid and liquid phase. For all the materials, we consider a mushy temperature

Table 6.5. Thermo-physical properties of the considered PCMs

	Material		
Property	PCM-11	SS	RT100
Melting temperature [°C]	-11	230	100
Latent heat [kJ/kg]	250	110	140
Thermal conductivity [W/(mK)]	1.25	0.5	0.2
Specific heat [kJ/(kg K)]	2.5	1.6	2
Density [kg/m^3]	1130	2000	800
Reference	[417]	[145]	[98]

difference of 5 ° C between pure solid and liquid and calculate ξ_{log} in Equation (3.27) accordingly. For the purpose of converting the problem to dimensionless settings, we consider $T_{max} = T_m + 10$, $T_{min} = T_m - 10$ and $L = 0.05$ m. Only the authors of [145] reported the dynamic viscosity and thermal expansion coefficient of their PCM. We could not find these properties for RT100 and PCM-11 elsewhere in the reviewed literature. For this reason, we adopt a unique value of thermal expansion coefficient for all the PCMs as $\beta = 3.2e-4$ 1/K, which corresponds to the one adopted in [145]. Similarly, we set a unique dynamic viscosity to $\mu = 5.6e-3$ Pa·s, which corresponds to the viscosity of SS at its melting temperature computed using the property equation listed in [145]. We investigate four different HCMs: aluminum, graphite, stainless steel and copper. The thermo-physical properties and cost were presented earlier in Table 6.2. For meaningful comparisons from a practical perspective, we consider a fixed investment on fin materials. Hence, we set a different maximum volume fraction for each HCM such that $\Phi = \{0.10;\ 0.07;\ 0.035;\ 0.0175\}$ for aluminum, graphite, steel and copper respectively. Different volume fractions of HCM lead to varying energy storage capacities of the unit complicating comparisons. During the analysis, we consider a fixed amount of energy to be charged/discharged from the unit, i.e. 95 % of a reference storage capacity, E_{ref}. This is taken as the capacity of the aluminum configuration with $\Phi = 0.10$. When comparing performances, we will refer to a multi-objective space energy density versus process time. Note that the energy density is not accounted for in the optimization problem formulation, which corresponds to the TM procedure (3.67). This performance criterion is computed considering the volume of PCM in the optimized structure. The cost of the PCM is not considered in this analysis as the focus here is on the cost of the enhancement

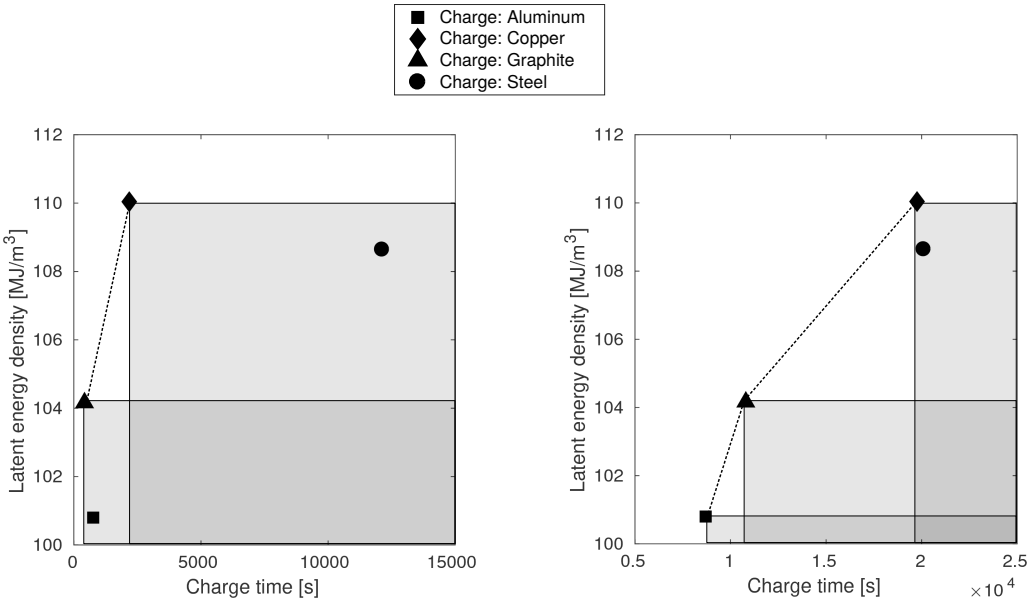

(a) (b)

Fig. 6.21. Charge time of a RT100 unit with different HCMs. (a): Using unphysical material properties obtained through the rule of mixtures; (b): using optimized heat transfer structures obtained through topology optimization. The regions of dominated materials are highlighted with gray boxes

device. However, for an average cost of PCM of 1 \$/kg as indicated in [23], only minimal changes in the prescribed volume fractions would be needed.

Before extending the analysis to other PCMs, we focus on finding the best HCMs for melting enhancement of a unit with RT100. As a rough preliminary step for material selection, we perform a set of 4 analyses considering volume-averaged material properties between HCM and PCM using the rule of mixtures:

$$\bar{(\cdot)} = (\cdot)_{HCM}\Phi + (\cdot)_{PCM}(1-\Phi), \tag{6.3}$$

where $(\cdot)$ denotes a generic material property and $\bar{(\cdot)}$ represents its volume-averaged value. All the analyses are performed with $\alpha_{max} = 0$ such that the unpenalized momentum equation is recovered. Although this correspond to an unphysical homogeneous and liquid material, we are interested in testing the ability of this simplification to provide material selection guidelines. The performance of our four HCM-RT100 homogeneous mixtures in the energy density versus charge time space is reported in Figure 6.21(a). Graphite and copper lie on a material Pareto front, meaning that

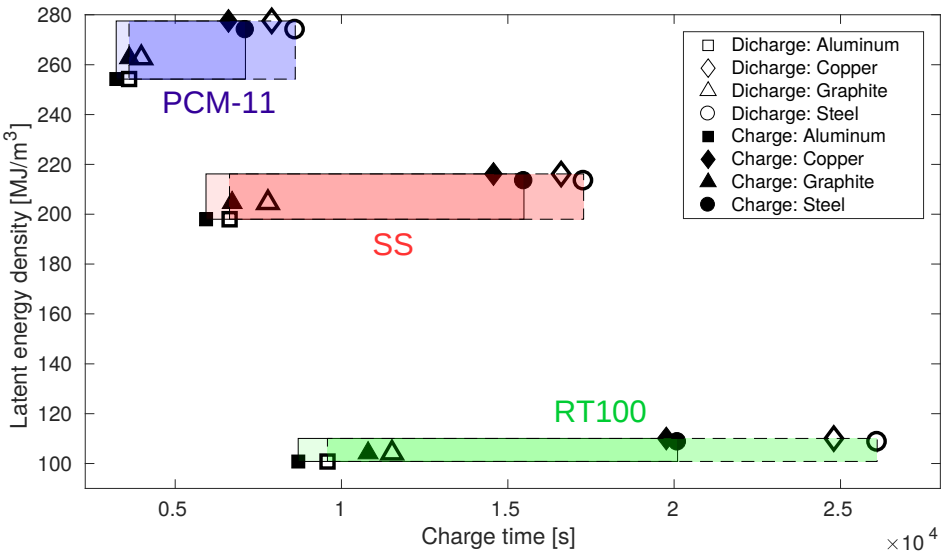

Fig. 6.22. Charge and discharge times in the optimized configurations for different HCM-PCM possible couplings

they are better than the alternatives with respect to at least one of the objectives. Aluminum and steel are dominated materials as the computed objective is worse than graphite or copper with respect to both objectives. Hence, the results obtained with this preliminary analysis lead to the conclusion that both aluminum and steel are not cost-effective options for melting enhancement of RT100. To check the validity of assumption 6.3, we now optimize fin layouts using topology optimization. The performance of the optimized layouts is reported in Figure 6.21(b). The stainless steel geometry is dominated by the copper one in agreement with what we found in the previous analysis. However, the optimized heat transfer structure using aluminum now lies on the Pareto front with graphite and copper. This presents evidence that the HCM cannot be chosen a-priori using averaged material properties if the fin layout is unknown.

The performance of the topology-optimized heat transfer structures with different HCMs and PCMs for both charge and discharge is summarized in Figure 6.22. For each PCM and for each process, we draw the rectangle with minimum area that encloses the computed values. This procedure highlights the ranges of energy density and process time of the optimized configurations. Note that the charge and discharge using the same PCM-HCM couple have nearly coincident energy densities since the

same maximum volume fraction, Φ, is set when optimizing the two processes. We observe the same trend identified for the structures enhancing melting of RT100 for all the PCMs analyzed in both charge and discharge. Aluminum, copper and graphite are cost-effective material choices while steel is a dominated material. Charge is always faster than discharge due to the stronger convective motion. The benefits due to convection are larger for the structures of copper and steel, for which melting is 17 % faster than solidification on average. An average of 9 % improvement for convective motion is computed for aluminum and graphite. Choosing a suitable HCM seems to be more important for solidification than for melting. The discharge using the optimized aluminum structures yields an average of 66 % time reduction with respect to the steel structures. On the other hand, when using aluminum instead of steel for charge, an average process time reduction of 53 % is computed. The high latent heat and thermal conductivity of PCM-11 leads to LHTES units with larger energy density and faster process dynamics than those with SS and RT100. For this material, the trade-off between energy density and process dynamics can be of interest to designers: the energy density of the unit can be increased by 23.30 MJ/m^3 if charge and discharge are allowed to be 0.95 and 1.19 hours longer. Considering this trade-off for RT100 is of minor importance: using copper instead of aluminum allows the energy density to be increased by only 9.24 MJ/m^3 but requires 3.05 and 4.22 hours more for the charge and discharge completion.

The layouts optimized for heat transfer enhancement in RT100, SS and PCM-11 are shown in Figures 6.23, 6.24, 6.25 respectively. All the aluminum structures are qualitatively similar. The HTF pipes are surrounded by four fins with varying length and tilt angle. We notice only minimal differences when comparing these layouts to those we obtained in Section 6.3.1 without considering natural convection in the analysis. This suggests that diffusion is the dominant heat transfer mechanism. The diffusivity ratio C_k ranges from 0.15 % to 0.54 % for the different PCMs and is far from the transition value of 3.5 % calculated in Section 6.2.2 for a case with the same volume fraction of HCM. The absence of convective features makes the layouts optimized for melting similar to those optimized for solidification. Analogous trends are observed for the graphite geometries, which look like thinned versions of the aluminum designs. The low volume fraction of the copper structures limits the complexity of the design evolution so that the resulting layouts consist of two short fins attached to the HTF pipes. The fins elongating towards the bottom of the shell are generally longer than those directed towards the top for discharge and

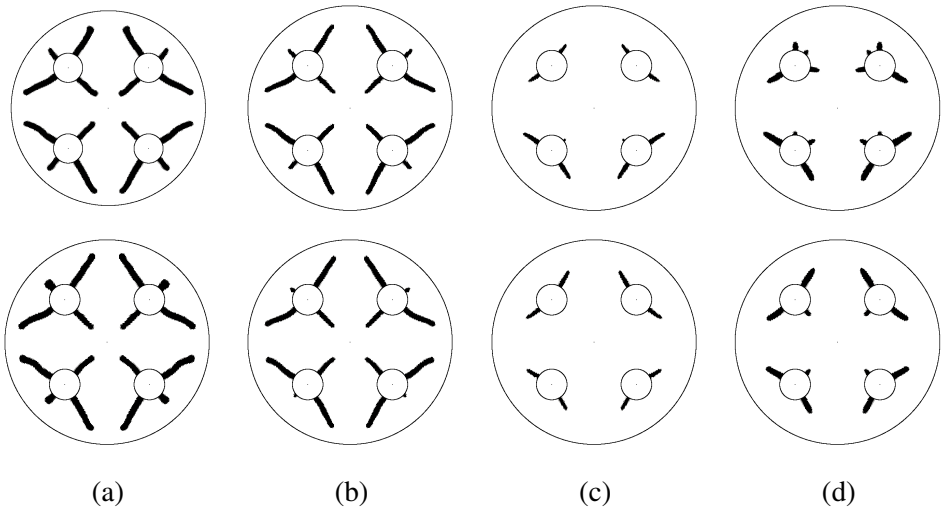

Fig. 6.23. Optimized designs for charge (top) and discharge (bottom) with paraffin RT100 as PCM. (a): Aluminum; (b): graphite; (c): copper; (d): steel

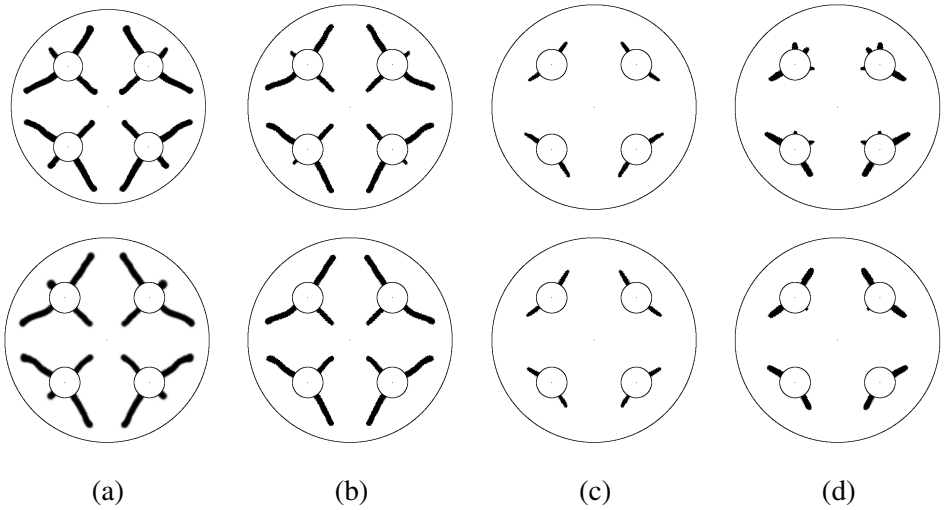

Fig. 6.24. Optimized designs for charge (top) and discharge (bottom) with SS as PCM. (a): Aluminum; (b): graphite; (c): copper; (d): steel

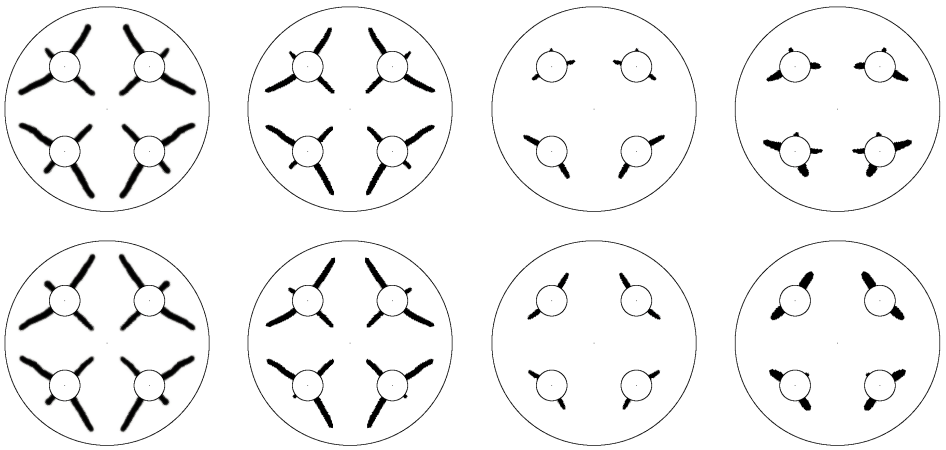

(a) (b) (c) (d)

Fig. 6.25. Optimized designs for charge (top) and discharge (bottom) with PCM-11 as PCM. (a): Aluminum; (b): graphite; (c): copper; (d): steel

shorter for charge. The fins orientation around the top tubes is comparable in RT100 ($C_k = 0.12$ %) and SS ($C_k = 0.15$ %) but changes completely when considering PCM-11 ($C_k = 0.44$ %). A similar modification of the tilt angle of the fins was observed across the transition region identified in Section 6.2.2. This suggests that the volume fraction of HCM modifies the position of the transition region along the C_k axis of Figure 6.3. Reducing the amount of conducting material yields limited possibilities of performance improvements through diffusion. Hence, exploiting convective transport with ad-hoc design features can be convenient even at low diffusivity ratios. The optimized layouts using steel as HCM present short and thick structures. For melting of all the PCMs considered, the fins orientation around the top tubes is similar to the one of Figure 6.7(c). This indicates that convection plays a major role here due the large diffusivity ratios (2.45 % $\leq C_k \leq$ 8.69 %).

To produce all the designs presented, we adopted a constant filter size, r_f despite different maximum volume fractions, Φ, are prescribed for different materials. This may overly penalize the designs with a small volume fraction, by preventing the formation of thin conducting members. A reduction of the filter size below the value adopted in this chapter requires the utilization of a FE mesh with a higher resolution. In fact, r_f was selected such that all the elements span at least a nodal design variable and an element-wise constant filtered density, $\tilde{s}$, can be obtained. On the other hand, there exist reasons for using a constant filter size. For instance, if the

fins are fabricated through the same manufacturing process, it would be desirable to obtain designs with an equal minimum feature size. Recall that in Section 2.4.2 we showed how it is possible to prescribe a minimum feature size (corresponding to $2r_f$ in regions sufficiently far from the boundaries of the design domain) by using the projection (2.40) with $\eta = 0$.

The results presented in this section showed that choosing a-priori the HCM for heat transfer enhancement in LHTES may be ineffective if the fins layout is unknown. Our forward analysis with volume-averaged material properties leads to the conclusion that both aluminum and steel are not cost-effective materials. When considering optimized structures instead, aluminum lies on a energy density versus process time Pareto front along with graphite and copper. Furthermore, we found that the optimized layouts made of graphite and aluminum are slightly sensitive to the choice of the PCM and process to be enhanced due to a high volume fraction of HCM and a low diffusivity ratio as compared to copper and steel.

6.4 Conclusions

In this chapter, topology optimization was used to answer four practical design questions that still hamper the large-scale technology development of multi-tube LHTES units. A graphical summary of the main application-oriented advances is presented in Figure 6.26. We proposed a heuristic approach able to give rule-of-thumb indications on the range of material properties for which convective features matter for performance. The topology optimization results confirmed the anticipated design trends. The results of our first numerical study suggested that representing multi-tube units with a collection of circular quasi-periodic cells generally leads to suboptimal configurations (Figure 6.26(a)). A premature merging of the phase front was observed along specific directions, yielding a quick heat transfer rate drop. The second study demonstrated that designing heat transfer structures for units with separate hydraulic loops demands for ad-hoc optimization (Figure 5.32(b)). The optimized layout consists of a thick HCM path linking the top to the bottom pipes, which ensures a full utilization of the HCM during both the charge and discharge. This design yields a dramatic acceleration of the complete charge-discharge cycle when compared to geometries optimized for the operation with a unique hydraulic loop. Our design optimization study under cost constraints revealed that aluminum,

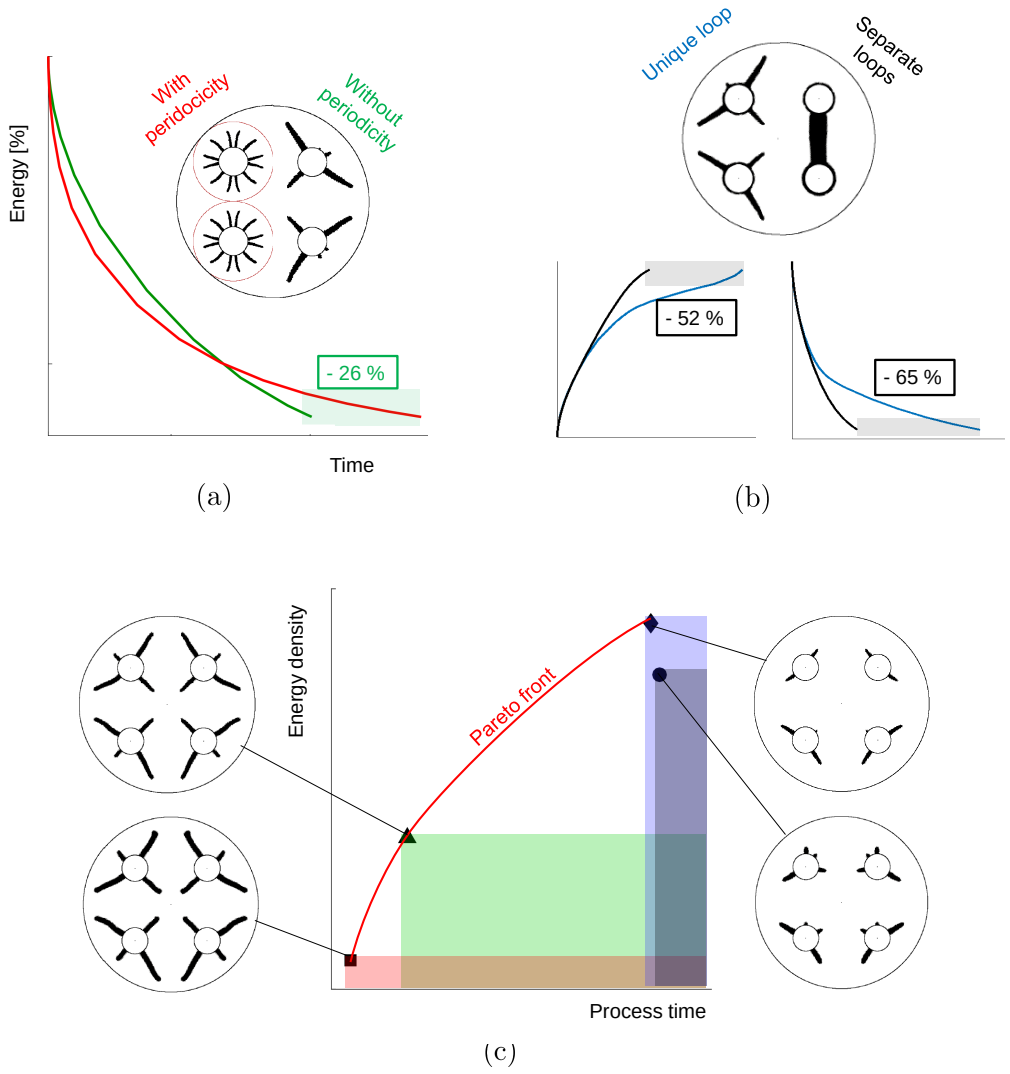

Fig. 6.26. Graphical summary of the main application-oriented advances of the chapter. (a): Effect of the periodicity assumption on optimized design and performance; (b): layout and performance comparison of geometries optimized for alternative hydraulic loop configurations; (c): design trend energy density/process time for different HCM choices

graphite and copper lie on a Pareto front energy density versus process time but steel was never found to be a cost-effective option (Figure 5.32(c)). The optimized geometries with graphite and aluminum look slightly affected by the type of PCM, suggesting that a modular fin layout may be efficient for practical installations.

Chapter 7

Design and control of resilient district heating networks

The large scale utilization of the locally available heat sources makes DH a rational and efficient domestic heating option. This technology was coupled successfully to high efficiency Combined Heat and Power (CHP) plants [447, 147], energy-intensive industries [263, 373] and renewable generation plants such as solar [464], biomass [426] and geothermal systems [476]. However, the fluid distribution networks are critical infrastructures. Small perturbations can rapidly propagate and lead to service failures. In this chapter, we use numerical optimization to improve the resilience of a DHN. The resilience denotes the ability of a system to absorb perturbations and quickly recover its functionality with a limited impact on the service quality. We demonstrate both a robust design and a centralized control optimization framework. Although control problems hardly fit within the context of this thesis, our optimization model is constructed using mathematical tools of popular use in topology optimization. The plan of the chapter is as follows. In Section 7.1, we introduce a quantitative notion of resilience and we review the state-of-the-art approaches for resilience improvements through design and control. In Section 7.2, we describe the governing equations and numerical model used to compute the fluid-dynamic and thermal responses of DHNs. In Section 7.3 and 7.4, we first introduce the optimization models adopted for robust design and centralized control; then, we present and discuss the results obtained for a real case-study. Finally, the main findings are summarized in Section 7.5.

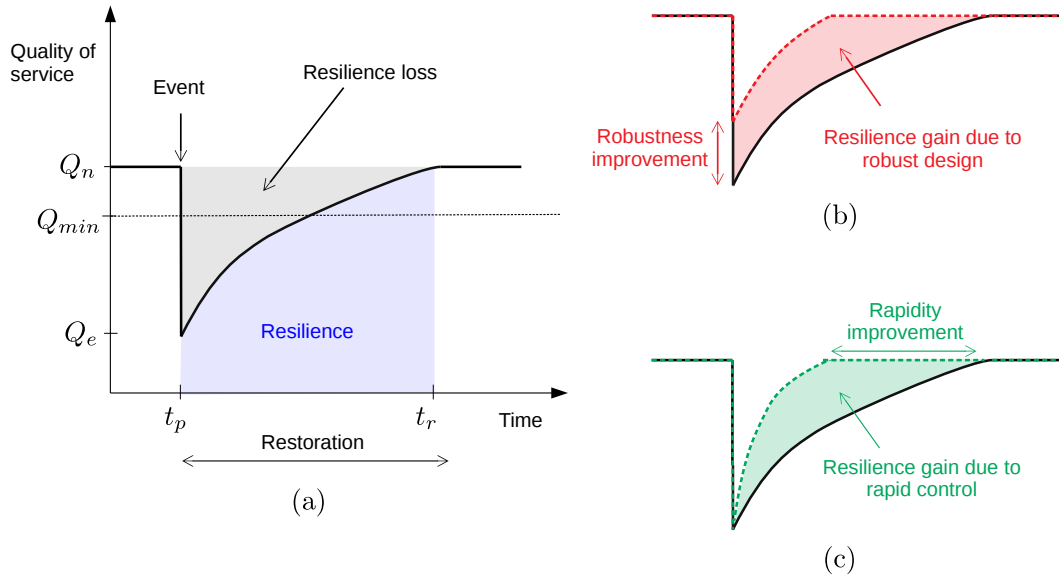

Fig. 7.1. (a): Resilience of infrastructures; (b): resilience gain through robust design; (c): resilience gain through rapid control

Some of the contents of this chapter were published in Energy [**J3**] and in Journal of Energy Resource Technology [**J4**] and presented at the ASME 2016 International Mechanical Engineering Congress and Exposition [**C3**] and at the 29th International Conference on Efficiency, Cost, Optimisation, Simulation and Environmental Impact of Energy Systems [**C5**].

7.1 Towards resilient district heating networks

In the civil engineering community, Bruneau et al. [68] proposed a clear quantitative metric to assess the resilience of infrastructures to seismic events. Figure 7.1(a) shows a representative schematic of the authors idea. Let us represent the performance of a system using a quality of service versus time plot. At time t_p, the system is suddenly perturbed by an event that decreases its functionality from Q_n to Q_e. Then, efforts are taken to improve the level of service until the nominal conditions are re-established at time t_r. The time period $t_r - t_p$ is referred to as the restoration phase. Bruneau and co-authors [68] quantified the resilience as the blue area shown in Figure 7.1(a). The resilience loss indicated in gray is commonly named "resilience triangle "[37, 354, 210]. A resilient system shows three fundamental features:

(a) Reduced probability that its functionality drops below acceptable limits, e.g. Q_{min} in Figure 7.1(a). We will refer to this concept as reliability.

(b) Reduced impact of perturbation events, i.e. $Q_n - Q_e$ in Figure 7.1(a). We will refer to this concept as robustness.

(c) Reduced time span of the restoration phase, i.e. $t_r - t_p$ in Figure 7.1(a). We will refer to this concept as rapidity.

Note that the previous definitions are not universal. The distinction between reliability, robustness and resilience is quite confused in the literature; often these terms are used interchangeably, see e.g. [169]. In this chapter, we will consider explicitly aspects (b) and (c) of the resilience in DHNs. The robustness is improved through design optimization, by modifying the topology of existing networks so that external perturbations are maximally absorbed. The rapidity is improved through control optimization, to quickly recover an acceptable level of service after disruptive events. The possible resilience improvements due to a robust design and rapid control are shown conceptually in Figure 7.1(b) and (c). In the next sections, we review the most widespread approaches and identify research opportunities for the resilient design and control of fluid distribution systems.

7.1.1 Improving resilience through design

Here, we consider the literature advancements for the resilient design of fluid distribution infrastructures. From the previous definition, robustness and reliability improvements are strictly connected. Although in this chapter we will focus only on the robustness aspect of resilience, the reliability design approaches are also briefly presented. In rare cases a Water Distribution Network (WDN) or a DHN can be designed from scratch. For this reason, most of the scholars interest lies in the improvement of the existing installations through the creation of loops. According to Todini [421], looped topologies yield redundancy and allow local failures to be overcome.

Reliability refers to the probability that the system "remains functional" [183]. In the context of WDNs and DHNs, the *functionality* includes both the demand satisfaction in terms of flows to be supplied and the range of pressures and temperatures at which these flows are provided [423]. Due to the stochastic nature of this

metric, a direct quantification of reliability involves the probabilistic mapping and integration of the failure region, which can be achieved with sampling approaches such as Monte Carlo method [66] or using first and second-order approximations of the failure surface [423]. Alternatively, researchers considered a variety of different deterministic measures of reliability. For instance, Farmani et al. [133] proposed a reliability indicator based on the minimum surplus pressure head. Based on concepts borrowed by information theory, Tanyimboh et al. [415, 416] introduced the notion of entropy for fluid networks. Although these ideas gained popularity in the civil engineering community, whether these deterministic measures are capable of accounting properly for the reliability strongly relies on the designer experience; it is hard to extend the proposed methods and findings to a wide range of systems.

Robustness refers to the ability of the system to reduce the impact of "disturbances, e.g. fluctuations of design parameters or noise" [166]. Gohler et al. [193] recently published an extensive review on the robustness metrics for engineering design. The authors identified four different categories:

- sensitivity metrics, quantifying robustness as a measure of the performance criteria gradients to noise factors;
- feasible space metrics, quantifying robustness as the size of the feasible set of an optimization problem with a minimum performance constraint;
- expectancy and dispersion metrics, quantifying robustness as a combination of statistical moments on performance criteria;
- probability of functional compliance metrics, quantifying robustness as the probability that the performance criteria are within acceptable limits.

The quantification of robustness using the last two categories was considered by many authors in the field of WDNs. For instance, Kapelan [233] and Babayan [38] defined robustness as the probability to satisfy a minimum pressure constraint in every node of the network. A hybrid approach between the two categories was proposed by Giustolisi et al. [166], who introduced a robustness indicator based on the distance between the expectancy of a performance criterion and a threshold value; the authors quantified this distance using the number of multiples of the standard deviation. Inspired by the classical robustness idea of Taguchi [413], Jung et al. [228] quantified robustness using a coefficient of variation, computed as the ratio of

the nodal pressure standard deviation to its average value. Within these robustness categories, it is possible to include also the scenario-based approaches. For instance, Cunha et al. [105] and later Marques et al. [291] approximated the expectancy of their performance criterion using a weighted sum with addends calculated in different scenarios; the sum weights were set equal to the scenarios probabilities. This method was extended also to the calculation of the standard deviations in [232]. All the previous approaches share common features with the reliability-based optimization methods in that they require some form of characterization of the input uncertainty, whether stochastic variable bounds or Probability Density Functions (PDFs) or both. Gathering correct statistics for the noise factors of fluid distribution networks is not trivial. As noted by Jung et al. [228], the probability distributions of the most common noise factors are in general not known and the literature lacks of an extensive database. Assumptions may have large impact on the optimization results. Under this perspective, the sensitivity metrics are of great interest. The robustness quantification is fully deterministic, reducing the risk of an optimization bias due to the use of incorrect statistics. Despite its wide acceptance across various engineering fields ranging from Micro-Electro-Mechanical Systems (MEMSs) [198] to electromagnetics [243] and geotechnical design [167], we found no design optimization study using sensitivity metrics in the WDN and DHN communities.

Concerning the choice of the optimization algorithm, most of the reviewed literature adopted heuristic or meta-heuristic global-search optimizers. Genetic Algorithm (GA) in both its original form or in slightly modified versions is no doubt the most popular choice [133, 233, 38, 166, 232, 228]. Other meta-heuristic algorithms that were considered for the optimization of fluid networks include (but are not limited to) Simulated Annealing (SA) [105, 291, 341], Scatter Search (ScS) [269] and Particle Swarm (PS) [408]. If properly used, these techniques guarantee a thorough exploration of the design space but require many system solutions per design variable, leading to a critical curse of dimensionality [86]. The optimization of large and complex DHNs with dynamic operation might be hardly tractable. Furthermore, using sampling approaches to compute statistics on the performance criteria further increases the computational burden. Banos et al. [41] acknowledged that most of the researchers focused on small benchmark examples (e.g. the Anytown WDN) and only a few applications considered real-world installations. Among the reviewed papers, the one with largest design space [232] counts 85 design variables.

This gives little hope to the use of practical optimization algorithms able to account for both uncertainty and transient operation in real-world DHNs. For instance, the Turin DHN counts more than 50000 pipe segments. The optimal design through more efficient NLP algorithms was considered in the earliest developments of the design methods for WDNs, such as in [149] and [429]. To our knowledge, only two researches formulated the design of flow networks using a topology optimization framework. Inspired by advances in truss structure optimization, Klarbring et al. [246] adopted the ground structure approach to design flow networks with minimal dissipation. The ground structure approach consists in selecting a large number of potential pipe connections, whose capacity is altered by the design variables during the optimization. Capacities hitting or approaching zero corresponds to topology changes. Differently from the optimization problem in structural mechanics and even for a simple Hagen-Poiseulle flow model, the fluid-dynamic response is nonlinear with respect to the capacity variables (e.g. cross-sectional area or diameter of the pipes) leading to non-convexity of the optimization problem. Arguing that in fluid networks "we cannot loose convexity any longer", Evgragov [128] later considered also the positions of the network nodes as design variables; the optimized layouts were superior to those obtained using the classical ground structure approach with fixed nodes. The gradient-based route was quickly abandoned for WDN design due to both its continuous nature (that requires a post-processing of the optimization results to obtain commercial diameters) and its convergence to local optima [125]. However, these methods allow a convenient scalability. If design sensitivities can be obtained cheaply, e.g. through the adjoint method, the computational complexity is slightly affected by the dimensionality of the design space. Back to 2003, Klarbring [246] presented a flow network design example with 3206 design variables.

This literature review can be summarized with three facts:

1. The detailed probabilistic characterization of the uncertainties in fluid networks is cumbersome in most cases and may greatly affect the optimization results.

2. The robust design based on sensitivity metrics is accepted in various engineering fields but was not considered for both WDNs and DHNs.

3. The heuristic and meta-heuristic optimization algorithms are popular for WDN design but their application to large real-world systems is hampered by their poor scaling properties.

In this chapter, we introduce a computational design approach for DHNs based on the previous facts. Given the facts 1 and 2, we design robustness using a sensitivity metric that does require the characterization of the noise uncertainty. Given fact 3, we formulate the design problem using topology optimization and update the network layout with a gradient-based optimizer. The objective and constraint gradients are computed by the discrete adjoint approach, which is computationally cheap and nearly insensitive to the design space dimension.

7.1.2 Increasing resilience through control

Here, we discuss the advancements in WDNs and DHNs control and identify the most promising approaches for resilience improvements. Controlling DHNs based on distributed meter readings and providing a customizable service in real-time are considered primary requirements for the energy grids of the future [281, 424]. Control can increase the rapidity of the infrastructures and is particularly important in the case of accidents. In this situation, the service should be restored as quickly as possible with a minimal impact on the customers comfort. Finding the optimal operation strategy for these systems is a time-consuming and non-trivial problem. The real-world installations often count several thousand users and multiple generation plants that are connected through complex fluid networks. The accurate prediction of the fluid-dynamic and thermal responses demands the utilization of complex simulation tools. The non-convexity of the optimization problems requires global-search algorithms. Furthermore, the large number of moving and dissipative components (i.e. valves and pumps) results in optimization problems with a high-dimensional control space. The literature in the context of WDNs and DHNs control can be divided into scheduling and real-time control.

Scheduling involves the day-ahead planning of devices (e.g. pumps) operation to minimize specific performance criteria, e.g. the energy consumption or operational cost [61]. Most frequently, the planning problems do not account for feedbacks from the data acquisition systems. Due to the "day-ahead" type of deadline, the execution time is rarely a strict constraint. Nevertheless, for the reasons discussed previously, scholars developed methods to reduce the computational complexity of the hydraulic and thermal analyses. Artificial Neural Network (ANN) surrogate models met large acceptance among researchers. Broad et al. [65] demonstrated the use of GA and ANN for pump scheduling in WDNs. A similar framework was

later considered by Behandish et al. [49], who optimized the operation of both the pumps and storage tanks. Within the context of DHNs, Guelpa et al. [175] demonstrated the coupling of GA with Proper Orthogonal Decomposition (POD) analysis. Following a parallel research direction, other authors adopted meta-heuristic techniques with improved convergence rate in order to retain the full complexity of the analysis model. Examples include Ant Colony Optimization (ACO) [280], Limited Discrepancy Search (LDS) [159] and PS [407]. Other scholars proposed to couple heuristic and deterministic algorithms. For instance, Giacomello et al. [161] developed a hybrid scheme for pump scheduling by combining the Greedy algorithm with standard Linear Programming (LP) routines.

The execution time is a primary constraint in real-time applications. A control law needs to be obtained on-the-fly based on information gathered through the data acquisition systems. The most typical real-time control strategies in WDNs and DHNs aims at reducing the pumping power [456], leakages [465], operational costs [165, 432] or emissions [365]. Due to the similarities in the nature of the optimization problem, the analysis and optimization approaches developed for scheduling were considered also for real-time control. Rao et al. [346] used the ANN-GA approach to optimize both the pumps statuses and valve openings using a 24 hours predictive framework. Kang [231] tackled a similar problem by modifying GA with a "warm" initialization of the population that partially reuses the previous optimization solutions. Differently from the context of planning, the optimization runs are performed after each sampling action of the metering facilities. As noted by the authors of [286] and [465], despite efforts towards a greater computational efficiency, the previous approaches hardly meet the strict time requirements of real-time control and are limited to small-scale applications. For this reason, the deterministic approaches are preferred. Examples of real-time control of WDNs using LP and NLP algorithms can be traced back to [326] and [80]. After the seminal work of Sandou et al. [365], the number of studies focusing on real-time control of DHNs grew fast over the last years. For instance, Wang et al. [456] used the Generalized Reduced Gradient (GRG) algorithm for optimization of both the pumps frequencies and valve openings in a medium-size DHNs. Giraud et al. [165] adopted a Model Predictive Control (MPC) framework based on Mixed Integer Linear Programming (MILP) to minimize the operational costs through the regulation of the heat generators, supply temperatures and pressures. A similar route was followed by Verrilli et al. [432], who considered also the regulation of the thermal energy storages and user thermal

loads. In rapidly-evolving systems, the utilization of standard MPC algorithms may lead to inaccuracies. The control law is optimized based on outdated information [171]. Hence it might be of more interest to obtain an approximate solution using the most up-to-date information [171]. Building on advances in control theory [116], a recent contribution [344] developed a method for real-time control using Sequential Convex Programming (SCP) and the Real Time Iteration (RTI) method. Instead of solving the optimization problem to full accuracy using fixed problem data, these are updated at each optimization iteration using the feedback from the metering devices. This method allows the straight-forward integration with the data acquisition systems with little limitations on the minimum sampling frequency. This possibility was considered in [466] and [465] in the context of WDNs.

Despite these valuable contributions, most of the commercial DH infrastructures are still controlled using a decentralized strategy. Each thermal user can regulate the flow based on its degree of discomfort. As a consequence, the failure events may yield a large reduction in the service quality for some users; the restoration rapidity is constrained by the time required to substitute the failed part. Hence, centralized control strategies for increased resilience are urgently needed. To our knowledge, no research considered control optimization under this perspective. In this chapter, we propose a control strategy of DHNs after failure events that aims at filling this literature gap. To cope with the strict execution time requirements, the optimization is conducted using MMA, which shares similarities with the SCP routines considered in [466]. The gradients of the objective and constraints with respect to the control variables are computed using the discrete adjoint method, which permits the scalability to real-world problems. Although we conduct only numerical experiments, our approach is designed to fit within an RTI framework. RTI can be of great interest for control during failure events, when the dynamics of the system is so fast that a full MPC procedure may be too slow to react to disturbances.

7.2 Modeling fluid distribution networks

In this section, we present a modeling framework for computing the fluid-dynamic and thermal responses of fluid distribution networks. We first simplify the governing equations to derive integral 1D formulations. Then, we construct a numerical model using a graph representation of the network.

7.2.1 Integral form of governing equations

We assume a steady-state and incompressible flow with isotropic and constant fluid properties and negligible viscous dissipation. The Navier-Stokes and energy equations can be written as in (5.1), (5.2) and (5.4). Assuming that the flow velocity and diffusion fluxes are aligned with the pipe direction, we can rework the governing equations in 1D considering:

$$\begin{aligned} v_i &= 0 && \text{for } i = 2,\ 3, \\ \frac{\partial}{\partial x_i} &= 0 && \text{for } i = 2,\ 3. \end{aligned} \tag{7.1}$$

Using the simplifications (7.1) and writing the stress tensor following the constitutive law (5.3), the governing equations can be stated as:

$$\rho \frac{\partial v_1}{\partial x_1} + \dot{m}_{ext} = 0, \tag{7.2}$$

$$\rho \underbrace{\frac{\partial v_1}{\partial t}}_{\text{(i)}} + \underbrace{v_1 \frac{\partial v_1}{\partial x_1}}_{\text{(ii)}} = -\frac{\partial P}{\partial x_1} + \underbrace{2\mu \frac{\partial v_1}{\partial x_1}}_{\text{(iii)}} - F_{loc} - F_{\perp}, \tag{7.3}$$

$$\underbrace{\rho c_p \frac{\partial T}{\partial t}}_{\text{(i)}} + \rho c_p v_1 \frac{\partial T}{\partial x_1} + \dot{m}_{ext} c_p T = \underbrace{k \frac{\partial^2 T}{\partial x_1^2}}_{\text{(ii)}} - q_{\perp}, \tag{7.4}$$

where $\dot{m}_{ext}$ and F_{loc} are mass and momentum sinks and P denotes the total pressure that includes the effect of gravity. The fluid-dynamic response in fluid networks governed by incompressible flow is in general much faster than the time frames of interest to the analyst. Hence, we neglect the transient term (i) in the momentum equation. We also consider two simplifications for the energy equation. First, as the convective energy transport is dominant, we neglect term (ii). Second, we consider only the steady-state version of (7.4) and neglect term (i). This assumption can be justified in small distribution networks as small water volumes are involved. We will relax this assumption when considering large networks in future studies. The momentum and energy sinks indicated with the subscript "$\perp$" account for the effect of the orthogonal contributions to the momentum and energy diffusion, which cannot

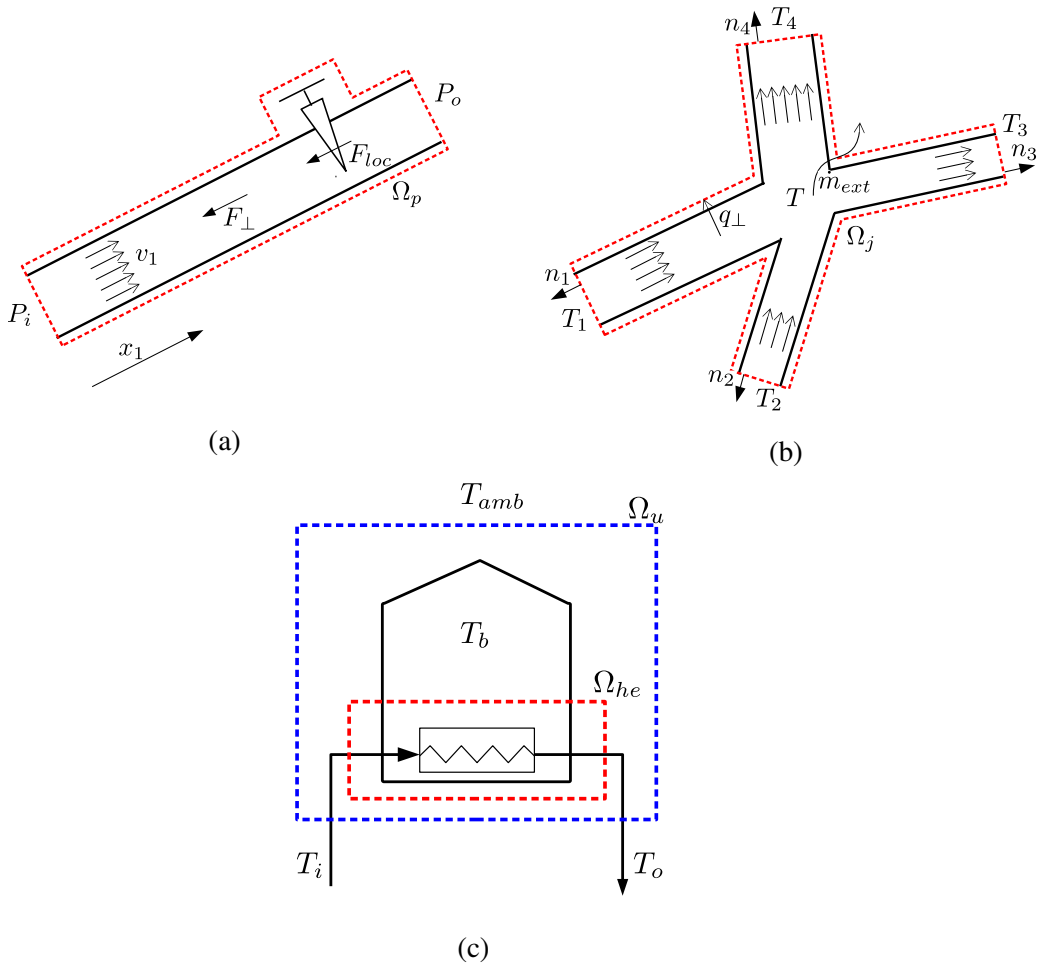

Fig. 7.2. Control volumes considered to obtain the integral form of the governing equations. (a): Pipe; (b): junction or bifurcation; (c): building and heat exchanger

be written explicitly in a 1D setting:

$$F_\perp = -\left(1-\delta_{1j}\right)\frac{\partial \sigma_{1j}}{\partial x_j}, \tag{7.5}$$

$$q_\perp = -\left(1-\delta_{1j}\right)k\frac{\partial^2 T}{\partial x_j^2}. \tag{7.6}$$

We now rework the simplified 1D governing equations in an integral form. Let us consider a pipe filling Ω_p with constant cross-section and no mass sinks as the one depicted in Figure 7.2(a). Terms (ii) and (iii) in Eq. (7.3) disappear due to the

continuity constraint (7.2). The integration over Ω_p leads to:

$$P_o - P_i = -\Delta p_{\perp} - \Delta p_{loc}, \tag{7.7}$$

where both the terms on the RHS are modeled using semi-empirical equations of standard engineering practice [25]:

$$\Delta p_{\perp} = \frac{1}{2} f_{\perp} \frac{L}{D} \rho v_1^2, \tag{7.8}$$

$$\Delta p_{loc} = \frac{1}{2} \beta_{loc} \rho v_1^2, \tag{7.9}$$

where $f_{\perp}$ is the Darcy-Weisbach friction factor, D is the diameter of the pipe, L is the length of the pipe and β_{loc} is the local pressure drop coefficient accounting for the effect of valves, bends and tees. Note that the phenomenological equations (7.8) and (7.9) allow both the laminar and turbulent flows in pipes to be considered with ease. The continuity equation (7.2) can be integrated over a control volume, Ω_j, (Figure 7.2(b)) enclosing a junction and half of the connected pipes. We obtain:

$$\sum_{i=1}^{N_p} G_i n_i + G_{ext} = 0, \tag{7.10}$$

where G_{ext} is an extracted mass flow rate at the junction, N_p is the number of pipes of the junction, n_i is the outward pointing normal of pipe "i" and G_i is its mass flow rate:

$$G_i = (\rho v S)_i, \tag{7.11}$$

with S being the pipe cross section. Under this convention, the mass flow rates exiting the control volume are positive and those entering the control volume are negative. Integrating the energy equation (7.4) over Ω_j leads to:

$$\sum_{i=1}^{N_p} c_p G_i T_i n_i + c_p G_{ext} T = -Q_{\perp}, \tag{7.12}$$

where T_i is the temperature of pipe "i" at the boundary of the control volume, T is the temperature of the junction where the mass flow rate extraction takes place, and $Q_{\perp}$ is the total energy loss due to the orthogonal temperature gradients. The latter is

formulated using the following heat transfer correlation:

$$Q_{\perp} = \frac{1}{2}\sum_{i=1}^{N_p} \pi D_i L_i U_{dg} \left(\bar{T} - T_g\right), \tag{7.13}$$

where $\bar{T}$ is the mean integral temperature of the control volume that we set equal to the one of the junction T, U_{dg} is the global heat transfer coefficient between the pipe and the ground and T_g is the ground temperature.

The thermal response of each thermal user is computed using a steady-state lumped-parameter approach that accounts for heat transfer across the heat exchanger, heat transfer in the building delivery system and thermal losses. The static assumption is valid for no external temperature variations and for fast control actions. Due to the large building capacitance, weak thermal transients would be observed during the controlled period. An integral energy balance across Ω_u (Figure 7.2(c)) reads:

$$G_b c_p (T_i - T_o) = K_V V (T_b - T_{amb}), \tag{7.14}$$

where G_b is the mass flow rate extracted at the building substation, T_i and T_o are the water inlet and outlet temperatures of the heat exchanger, V is the building volume, K_V is the volumetric heat loss coefficient, T_b is the building temperature and T_{amb} is the external ambient temperature. Eq. (7.14) introduces two additional unknowns, T_o and T_b. The temperature T_i can be obtained from (7.12). As a closure equation, we consider the following thermal balance across a control volume enclosing the heat exchanger, Ω_{he}:

$$G_b c_p (T_i - T_o) = (UA)\left(\frac{T_i + T_o}{2} - T_b\right), \tag{7.15}$$

where (UA) is the global transmittance of the heat exchanger and of the heat delivery system of the building. Its value for each of the building of the network is obtained through fitting on experimental data. Note that instead of using a standard logarithmic formulation, we linearize the characteristic temperature difference in (7.15) to benefit from linearity.

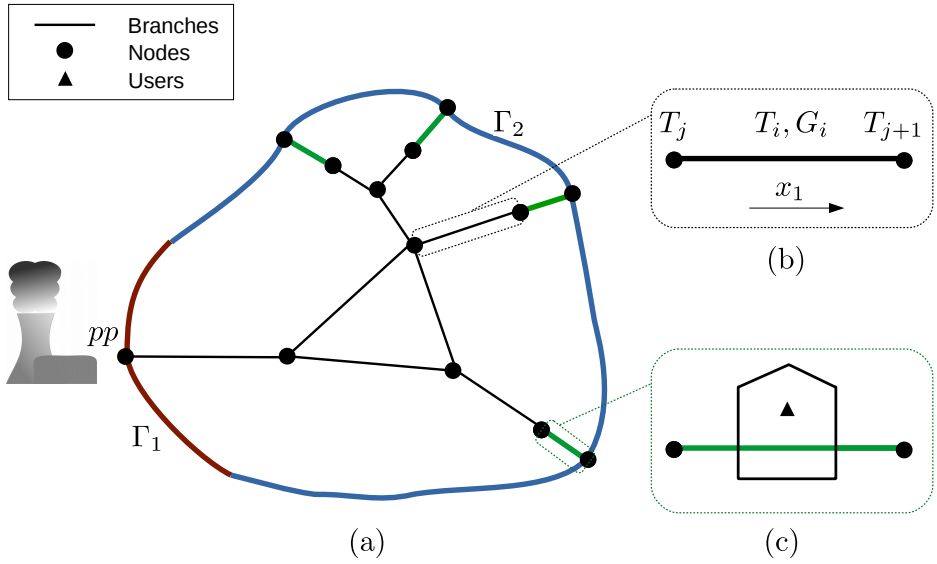

Fig. 7.3. Schematics of the graph representation of the fluid network

7.2.2 Numerical model

The entire network is modeled using a graph representation [59], which is shown schematically in Figure 7.3(a). The branches correspond to the pipe sections enclosed by either junctions are bifurcations, represented as nodes. In the supply line of DHNs, water is injected at the power plant and extracted at the user nodes. The green branches (Figure 7.3(c)) are numerical artifacts that serve for the purpose of calculating the thermal response of the users, as described in the previous section. The degrees of freedom to be solved for include three state variables: the mass flow rates, **G**, which are assigned to the branches, the total pressures, **P**, which are assigned to the nodes and the temperatures, **T**, which are assigned to the nodes and users. The network topology is uniquely represented by the incidence matrix $\mathbf{A} : \mathbb{R}^{N_b} \rightarrow \mathbb{R}^{N_n}$, with N_b being the number of branches and N_n being the number of nodes. Denoting with $\boldsymbol{Z} = \{\zeta_1, \zeta_2, ..., \zeta_{N_b}\}$ the set branches and $\boldsymbol{\Upsilon} = \{\upsilon_1, \upsilon_2, ..., \upsilon_{N_n}\}$ the set of nodes, the incidence matrix, **A**, is defined as following:

$$A_{ij} = \begin{cases} +1 & \text{if } \upsilon_i \text{ is the inlet node of branch } \zeta_j \\ -1 & \text{if } \upsilon_i \text{ is the outlet node of branch } \zeta_j \\ 0 & \text{otherwise} \end{cases}. \tag{7.16}$$

Using (7.16), the integral form of the continuity equation (7.10) can be casted in the following form:

$$\mathbf{R}_c = \mathbf{A}\mathbf{G} + \mathbf{G}_{ext} = \mathbf{0}, \tag{7.17}$$

where $\mathbf{R}_c$ is the vector of residuals of the continuity equation and $\mathbf{G}_{ext}$ is a vector collecting the nodal mass flow rate extractions. The integral form of the momentum equation (7.7) is written in matrix form as:

$$\mathbf{R}_m = \mathbf{B}\mathbf{G} - \mathbf{A}^T\mathbf{P} = \mathbf{0}, \tag{7.18}$$

where $\mathbf{R}_m$ is the vector of residuals of the momentum equation and $\mathbf{B}$ is a diagonal nonlinear operator, containing the fluid-dynamic resistance of each branch of the network formulated using (7.8) and (7.9):

$$B_{ii}(G_i) = \left(\frac{G\left(\frac{f_\perp}{D}L + \beta_{loc}\right)}{2\rho S^2} \right)_i. \tag{7.19}$$

The advective term of the integral form of the energy equations (7.12) contains the temperatures of the cross-sections located at the branch half lengths. Due to our graph-based representation, these are not degrees of freedom. Hence, the advective transport needs to be reformulated as a function of the nodal temperature values. As discussed in Section 5.2.2, instabilities arise in convection-dominated flows when the advective flux is approximated by central finite differences. For this reason, we use the upwind scheme [137] that guarantees unconditional boundedness [433]. Considering the generic branch shown in Figure 7.3(b), the temperature T_i in (7.12) is written as:

$$T_i = \frac{1}{G_i}\left(\max\left(G_i, 0\right) T_j - \min\left(G_i, 0\right) T_{j+1}\right). \tag{7.20}$$

Using (7.13) and (7.20), the integral form of the energy equation (7.12) and the building integral balances (7.14) and (7.15) can be written in matrix form as:

$$\mathbf{R}_e = \mathbf{C}\mathbf{T} - \mathbf{q} = \mathbf{0}, \tag{7.21}$$

where $\mathbf{R}_e$ is the vector of residuals of the energy equation, $\mathbf{C}$ is the conductance matrix and $\mathbf{q}$ is the heat load vector, containing all the constant terms of the heat losses in (7.13) and (7.14). The discretized governing equations are solved considering two sets of boundary conditions. For the design studies, the mass flow rates extracted

by the users are known. These values can be obtained from Eq. (7.14) by setting T_b equal to the desired temperature level and $T_i - T_o$ equal to a desired value of temperature drop. With reference to Figure 7.3(a), we have:

$$\begin{aligned} G_{ext_i} &= G_{b_i} \qquad \text{if } \mathbf{x}_i \in \Gamma_2, \\ P_i &= P_{pp} \qquad \text{if } \mathbf{x}_i \in \Gamma_1, \end{aligned} \tag{7.22}$$

where G_{b_i} is the mass flow rate requested by building "i" and P_{pp} is the design pressure level at the power plant node highlighted in Figure 7.3(a). For the control studies, the outlet mass flow rate is unknown as it depends on the valve openings at the users substations. Hence, we prescribe an outlet pressure condition and an inlet flow rate condition. Mathematically:

$$\begin{aligned} G_{ext_i} &= -G_{pp} \qquad \text{if } \mathbf{x}_i \in \Gamma_1, \\ P_i &= P_{out} \qquad \text{if } \mathbf{x}_i \in \Gamma_2, \end{aligned} \tag{7.23}$$

where G_{pp} is the injected mass flow rate at the power plant and P_{out} is the outlet pressure. To compute the thermal response, we prescribe the inlet temperature as follows:

$$T_i = T_{pp} \qquad \text{if } \mathbf{x}_i \in \Gamma_1, \tag{7.24}$$

where T_{pp} is the water temperature at the power plant node.

The fluid-dynamic problem is solved through the SIMPLE algorithm [327] to deal with the pressure-velocity coupling. At each SIMPLE iteration, the momentum equation is solved through a damped fixed-point iteration method. Numerical experiments showed that setting the damping parameter to 0.8 yields an acceptable trade-off between convergence stability and computational cost. The outer iterations are stopped when the L_2 norm of the relative residuals drops below $1e-9$. The presented analysis framework was verified and then validated with the experimental results obtained from the Turin district heating network, see [175, 174].

7.3 Robust design

In this section, we present and demonstrate our robust design framework for improved resilience of fluid distribution networks. We first describe the adopted design

and optimization models and introduce an alternative formulation for benchmark purposes. Then, we present the results obtained for several numerical examples conducted on a portion of the Turin DHN. Here, we do not account for the thermal response of the system in our optimization problem. Hence, we do not solve (7.21) for **T** during the analysis.

7.3.1 Design and optimization models

Following [246, 128], the topology of the network is here parameterized using the ground structure approach [54]. We start by populating the network with a large set of additional connections between the nodes as potential or vanishing branches. These are identified by enumeration of all the possible looping paths on the available road-ways. The network layout is controlled by acting on the pipe diameters as follows:

$$D_i(s_i) = D_{min} + (D_{max} - D_{min})\, s_i, \tag{7.25}$$

where $0 \leq \mathbf{s} \leq 1$ is a vector of design variables, D_{max} and D_{min} represent the maximum and minimum diameters, respectively. To describe topological changes, it is essential to allow for $D_{min} = 0$. However, this leads to non-solvable state equations. Hence, we consider the so-called ε-perturbation of the original optimization problem by setting a small and strictly positive bound on the pipe diameter, $D_{min} = \varepsilon$. Here, we assume that the ε-perturbed problem converges to the original problem for $\varepsilon \to 0$. Formal proofs of convergence for pressure loss minimization in networks governed by the Hagen-Poiseuille flow are discussed in [246] and [128].

In robust district heating networks, the level of service should be slightly affected by random perturbations such as fouling, chemicals deposition or leakages. We quantify the level of service with the minimum pressure in the supply network, $\min \mathbf{P}$. The random noise is modeled considering arbitrary variations of the local pressure drop coefficient, β_{loc}. We aim at maximizing the following measure of robustness:

$$z = \sum_{i=1}^{N_b} z_{loc_i} = \sum_{i=1}^{N_b} \hat{L}_i \underbrace{\frac{d\left(\min(\mathbf{P})\right)}{d\beta_{loc_i}}}_{\text{(I)}}, \tag{7.26}$$

where $\hat{L}_i$ is the normalized branch length and z_{loc_i} is the contribution of the branch "i" to the objective, hereafter referred to as local robustness. Multiplying the noise

sensitivities (term (I)) with $\hat{L}_i$ accounts for the fact that the magnitude and probability of the fluid-dynamic noise are generally proportional to the branch length. Note that our objective (7.26) is a fully deterministic sensitivity metric. Hence, it does not rely on statistical moments of the system response, as discussed in Section 7.1.1. We expect an agreement with conventional robust or reliability-based design approaches, dealing with uniformly-distributed and tightly-bounded stochastic variables with a linear objective-noise relation. To allow for differentiability, the hard minimum function in (7.26) is approximated using the generalized p-mean:

$$\min \mathbf{P} \simeq \tilde{\min}_{\text{pm}} \mathbf{P} = \left(\frac{1}{N_n} \sum_{i=1}^{N_n} P_i^{p_r} \right)^{\frac{1}{p_r}}, \tag{7.27}$$

where the exponent, p_r, is set to -10. The approximation (7.27) provides an upper bound to the hard minimum function and converges to it for $p_r \to -\infty$. The robustness measure (7.26) involves the sum over the gradient components of a criterion computed with respect to N_b variables. As N_b is in general high, we compute the noise sensitivities (term (I) in (7.26)) using the discrete adjoint method presented in Section 2.3.2 for the computation of design sensitivities. Substituting the design variables, $\mathbf{s}$, with the noise variables, $\boldsymbol{\beta}_{loc}$, and stacking the continuity and momentum state variables and residuals in the vectors $\mathbf{u} = [\mathbf{P}^T, \mathbf{G}^T]^T$ and $\mathbf{R} = [\mathbf{R}_c^T, \mathbf{R}_m^T]^T$, the noise sensitivities can be written as follows:

$$\frac{d\left(\tilde{\min}_{\text{pm}}(\mathbf{P})\right)}{d\boldsymbol{\beta}_{loc}} = \frac{\partial\left(\tilde{\min}_{\text{pm}}(\mathbf{P})\right)}{\partial\boldsymbol{\beta}_{loc}} - \boldsymbol{\lambda}_1^T \frac{\partial \mathbf{R}}{\partial \boldsymbol{\beta}_{loc}}, \tag{7.28}$$

where the first term on the RHS vanishes due to a nil explicit dependence and $\boldsymbol{\lambda}_1$ is a vector of adjoint variables computed by solving the following adjoint equation:

$$\mathbf{R}_\lambda = \left(\frac{\partial \mathbf{R}}{\partial \mathbf{u}} \right)^T \boldsymbol{\lambda}_1 - \frac{\partial\left(\tilde{\min}_{\text{pm}}(\mathbf{P})\right)}{\partial \mathbf{u}} = \mathbf{0}, \tag{7.29}$$

where $\mathbf{R}_\lambda$ is the vector of residuals of the adjoint equation.

Instead of the standard linear volume constraint adopted in topology optimization, we consider the following investment cost constraint:

$$\sum_{i=1}^{N_s} c_i(s_i) L_i - C^* \leq 0, \tag{7.30}$$

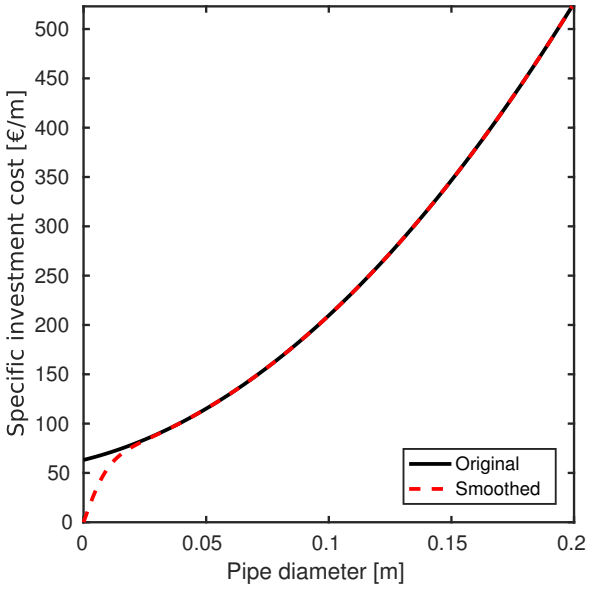

Fig. 7.4. Original and smoothed cost function

where C^* is the maximum bound on the investment and c_i is a specific cost per unit length of the pipe. We obtain this quantity through a quadratic fit to real market data. The computed formulation reads:

$$c_i = a_0 + a_1 D_i + a_2 D_i^2, \tag{7.31}$$

with $a_0 = 63$ €/m, $a_1 = 614$ €/m^2 and $a_2 = 8505$ €/m^3. Due to the fixed costs, a_0, Eq. (7.31) returns an investment higher than zero even for a pipe with a nil diameter. Hence, we modify the cost function so that $c_i \to 0$ when $D_i \to 0$. This is achieved by substituting a_0 in (7.31) with the following smoothed term:

$$\tilde{a_0} = a_0 \left(\frac{2}{1 + \exp\left(-\xi_{log} D_i\right)} - 1 \right), \tag{7.32}$$

where $\xi_{log} = 212$ is the quasi-variance of the logistic function set in order to recover 99 % of the fixed term, a_0, for $D = 25$ mm. This value is generally considered a lower limit due to manufacturing considerations. The smoothed cost function and its original version are represented in Figure 7.4. To sum up, the robustness

maximization problem is formulated as:

$$\mathscr{P}_{rob}: \begin{cases} \max\limits_{\mathbf{s}} & \sum\limits_{i=1}^{N_b} \dfrac{d(\tilde{\min}_{\text{pm}}\mathbf{P})}{d\beta_{loc_i}} \hat{L}_i \\ \text{s.t.} & \sum\limits_{i=1}^{N_s} c_i(s_i)L_i - C^* \leq 0 \\ & \mathbf{s} \in \mathbf{S} = \left\{ \mathbb{R}^{N_s} \mid 0 \leq s_i \leq 1, i = 1, ..., N_s \right\} \end{cases} . \tag{7.33}$$

To test the effectiveness of our robustness measure (7.26), we consider also a non-robust design case. The objective to be maximized is the smooth minimum pressure of the supply line. The alternative optimization problem reads:

$$\mathscr{P}_{P_{min}}: \begin{cases} \max\limits_{\mathbf{s}} & \tilde{\min}_{\text{pm}}\mathbf{P} \\ \text{s.t.} & \sum\limits_{i=1}^{N_s} c_i(s_i)L_i - C^* \leq 0 \\ & \mathbf{s} \in \mathbf{S} = \left\{ \mathbb{R}^{N_s} \mid 0 \leq s_i \leq 1, i = 1, ..., N_s \right\} \end{cases} . \tag{7.34}$$

The problem (7.34) corresponds to a minimization of the fluid-dynamic resistance of the network.

The design sensitivities with respect to the investment constraint are readily obtained since Eq. (7.30) is not state-dependent. Computing design sensitivities with respect to the objective (7.28) involves an additional adjoint equation. We can consider the standard formulation presented in Section 2.3.2 by constructing new augmented vectors of the state variables and residuals $\tilde{\mathbf{u}} = [\mathbf{P}^T, \mathbf{G}^T, \boldsymbol{\lambda}_1^T]^T$ and $\tilde{\mathbf{R}} = [\mathbf{R}_c^T, \mathbf{R}_m^T, \mathbf{R}_\lambda^T]^T$. The objective sensitivities can then be obtained from:

$$\frac{dz}{d\mathbf{s}} = \frac{\partial z}{\partial \mathbf{s}} - \boldsymbol{\lambda}_2^T \frac{\partial \tilde{\mathbf{R}}}{\partial \mathbf{s}}, \tag{7.35}$$

where the vector of adjoint variables $\boldsymbol{\lambda}_2$ is computed by solving the linear system:

$$\frac{\partial \tilde{\mathbf{R}}}{\partial \tilde{\mathbf{u}}} \boldsymbol{\lambda}_2 = \frac{\partial z}{\partial \tilde{\mathbf{u}}}. \tag{7.36}$$

The design sensitivities with respect to the alternative objective adopted in Problem (7.34) are obtained using the formulation discussed in Section 2.3.2 with

$\mathbf{u} = [\mathbf{P}^T,\ \mathbf{G}^T]^T$ and $\mathbf{R} = [\mathbf{R}_c^T,\ \mathbf{R}_m^T]^T$, as done to compute the robustness measure (7.26).

7.3.2 Numerical results and design trends

In this section, we present the optimized layouts and discuss the performance and design trends obtained through our robust design framework. First, we analyze the convergence of a reference design case. Then, we study how the optimized layouts and performance are affected by the allocated investment. Last, we benchmark the results of our framework with those obtained by solving the non-robust design optimization problem (7.34). The optimization problems are solved using MMA. As compared to Table 2.1, we modify the upper asymptote adaptivity $\alpha_+ = 1.2$ and the step-size $\Delta s = 0.01$. N_{in} and ρ_c^{min} are GCMMA-specific parameters and are not needed here.

The Turin DHN counts around 6500 buildings connected for a total thermal request of 1.3 GW in design conditions. The system is composed of a transportation and 182 distribution networks. The transportation network connects the thermal plants to each distribution network, which in turn supplies the heat to the users located in the vicinity of the connecting node. In this chapter, we focus on a medium-size distribution network that delivers thermal energy to 110 buildings. A representation is given in Figure 7.5. This subnetwork consists of 231 branches and is designed to satisfy a total thermal request of 17.6 MW. It is connected to the main transportation network in two points, which are labeled as "Inlet 1" and "Inlet 2" in Figure 7.5(b). In this design example, we consider the system as being alimented from Inlet 2. This configuration yields the most severe pressure drops and the effect of random noise can largely affect the level of service of the most remote users. The branches present in the current configuration and the potential looping paths of the ground structure are highlighted in Figure 7.5(b). The failure branches are considered only for control optimization and are treated as normal connections in this section. All the users are connected simultaneously and retrieve the thermal power corresponding to their design thermal load. The extracted mass flow rate at each building substation, $G_{ext_i} = G_{b_i}$, is computed from Eq. (7.14), considering constant values for the design outdoor temperature, T_{amb}, the design indoor temperature, T_b, and the temperature drop across the heat exchanger, $T_i - T_o$. The values of the most relevant parameters and properties are summarized in Table 7.1.

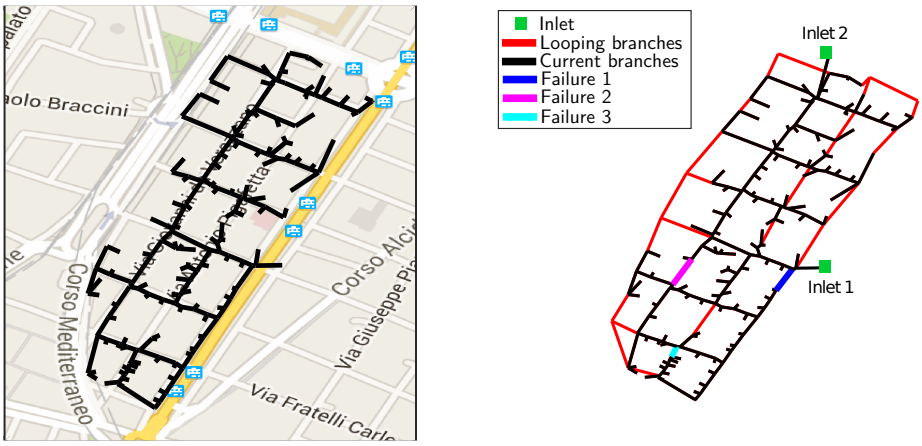

(a) (b)

Fig. 7.5. Overview of the subnetwork considered. (a): Representation on the Turin city map; (b): looping branches and failures considered in this chapter

Table 7.1. Parameters and properties for robust design

Description	Symbol	Value	Unit
Inlet total pressure	P_{pp}	6.5	bar
Design outdoor temperature	T_{amb}	265.15	K
Design indoor temperature	T_b	293.15	K
Temperature drop across heat exchanger	$T_i - T_o$	50	K
Dacy-Weisbach friction factor	f	0.014	-
Water density	ρ	1000	kg/m^3
Maximum diameter	D_{max}	0.25	m
Minimum diameter	D_{min}	0.001	m

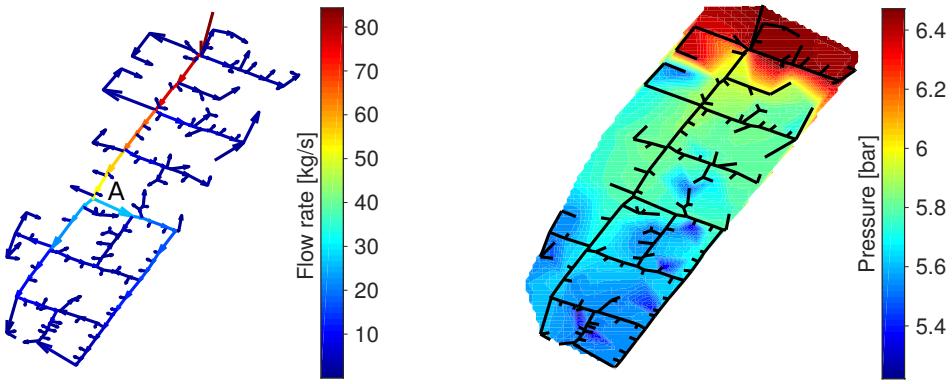

Fig. 7.6. Fluid-dynamic response in design conditions. (a): Mass flow rates; (b): pressures

Figure 7.6 shows the system response of the current network, in which no looping branches are present. A total mass flow rate of 84.3 kg/s at 6.5 bar is injected from inlet 2. In the northern portion of the network, the flow propagates mainly along a unique path since no loops are present. This yields large pressure drops. A total mass flow rate of 51.8 kg/s at 5.87 bar reaches node A (Figure 7.6(a)), where it is divided in two roughly equal streams. Due to the presence of loops, the pressure drops are limited in the southern portion of the network. Local minima of the pressure field are observed in correspondence of some users, due to a bad sizing of the pipes in their substations. This suggests that the maximum fluid-dynamic resistance can hardly be reduced by the construction of looping branches. The computed minimum pressure for this design case is 5.182 bar, corresponding to a maximum pressure drop from the power plant node of 1.318 bar along the supply line. The computed robustness measure amounts to -0.089 bar. To gain a physical understanding behind this value, consider the following β_{loc_i} perturbation field:

$$\delta\beta_{loc_i} = f_{\beta_{loc}}\hat{L}_i, \tag{7.37}$$

where $f_{\beta_{loc}}$ is a constant multiplication factor. If the minimum pressure is linear in $\delta\beta_{loc_i}$, for every unit increase of $f_{\beta_{loc}}$ the minimum pressure is reduced by 0.096 bar. Hence, the pressure drop along the supply line is doubled for $f_{\beta_{loc}} \geq 1.318/0.089 = 14.809$.

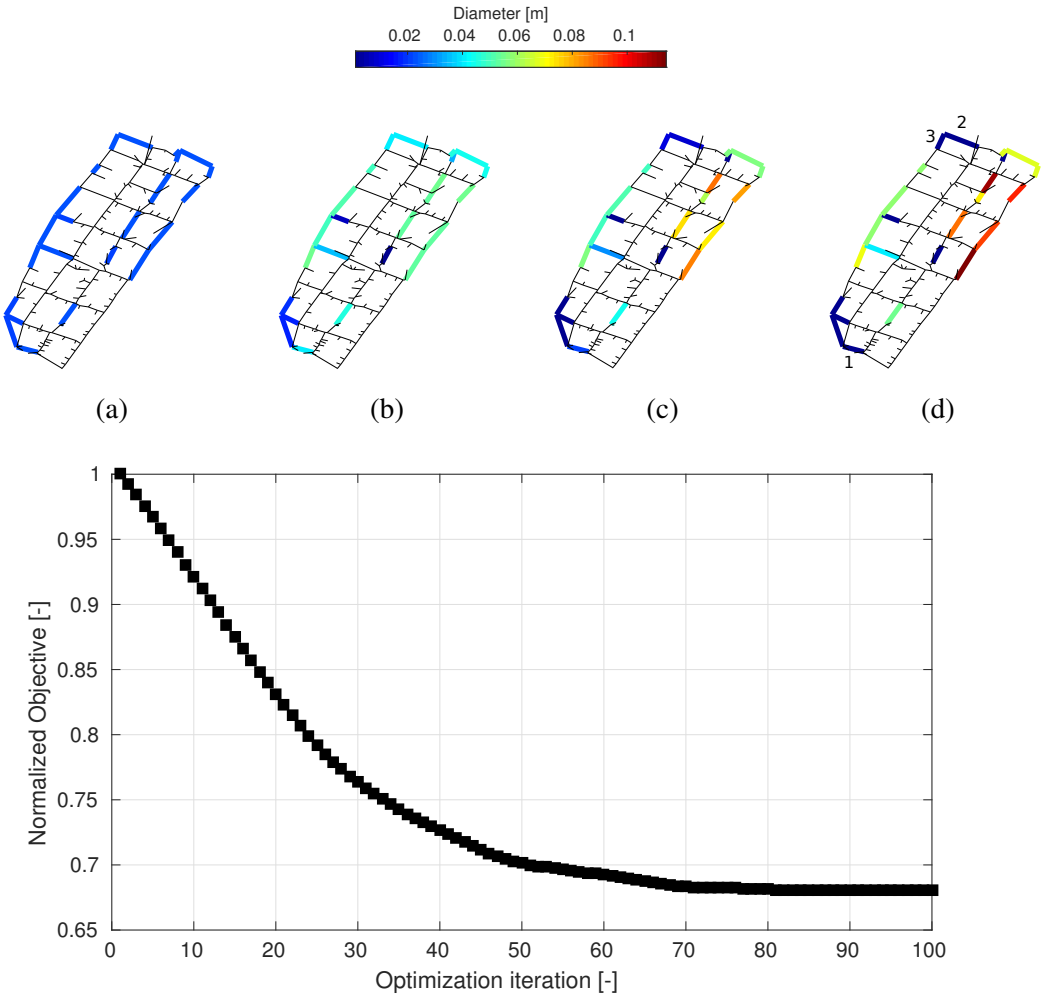

Fig. 7.7. Normalized objective history during the optimization of the nominal case. The design evolution is shown at selected optimization iterations. (a): Iteration 0; (b): iteration 30; (c): iteration 60; (d): iteration 100

Let us now consider a nominal robust design case with a reference investment of 200 k€. Figure 7.7 shows the objective history alongside with snapshots of the network layout at selected design iterations. The objective is normalized with respect to its initial value. The design is initialized by setting a constant diameter to all the branches of the ground structure, calculated in such a way that the investment cost (7.30) hits the maximum bound C^*. In this case, we computed an initial diameter of $D = 0.0122$ m. This initialization strategy is adopted for all the results presented in this section. During the first 30 iterations, large robustness improvements ($\sim$- 30 %) are obtained by increasing the size of most of the branches in the northern portion

of the network. Two pipes in the central region hit the minimum diameter bound. Most of the grown connections in the top region feature a similar diameter value at iteration 30. Differences start to emerge during the following 30 iterations. These changes are responsible for another 7.1 % reduction in the objective. At iteration 60, few preferred flow paths can be identified. Only minor objective improvements (-1.2 %) are registered during the last 40 iterations. However, we notice significant layout modifications as the diameters of Branches 1, 2 and 3 (Figure 7.7(d)) are reduced to the minimum value. The saved investment is reallocated nearly homogeneously among the looping branches of the northern portion of the network. Negligible objective improvements and layout modifications are observed after 100 iterations. If the optimized design is thresholded at $D_{th} = D_{min} + 0.0001$ m, the final layout counts 15 branches out of the possible 24.

Now we investigate the trade-off between investment and robustness. The maximum investment bound, C^*, is increased in 16 steps from 20 k€ to 1000 k€. For each case, an optimization run is performed. To analyze how the topology of the network evolves during the sweep, for each branch of the ground structure we compute the minimum investment at which it is visible in the optimized configuration. Formally, we define this quantity as follows:

$$C^*_{min_i} = \min\{C^* \in \mathbb{R}_{>0} : D^*_i(C^*) \geq D_{th}\}, \tag{7.38}$$

where D^*_i is the optimized value of diameter "i". This figure of merit is shown in 7.8. At low investments ($C^* \leq 60$ k€), four looping branches (4, 5, 6 and 7) are created close to the inlet. A long additional path composed of Branches 8, 9 and 10 appears on the optimized layouts for 60 k€ $< C^* \leq 100$ k€. Then, the connectivity on the eastern side is modified through the addition of three alternative paths (11, 12 and 13) in the range of investments 100 k€ $< C^* \leq 200$ k€. For 200 k€ $< C^* \leq 400$ k€, few other connections are created. No topology modifications are observed for $C^* > 400$ k€. Branch 14 is never convenient for $C^* \leq 1000$ k€. The robustness and cost are antagonist in the range of values considered. The optimized objective and the maximum investment lie on the Pareto front shown in Figure 7.9. According to the previous observations, we can divide the front in two regions:

(i) The region of *topology modifications* ($C^* \leq 400$ k€), where the Pareto front is steep and large robustness improvements are achievable at limited costs: a 400 k€ investment yields a 38.8 % increase in the objective.

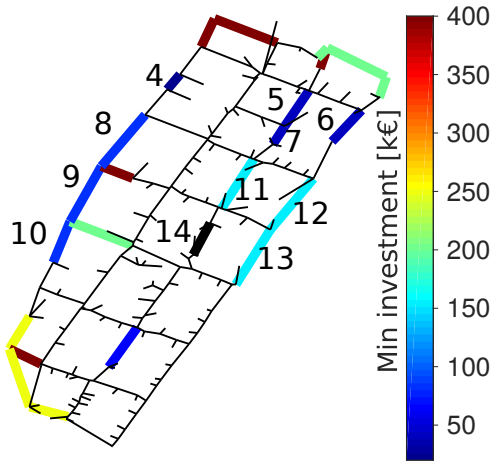

Fig. 7.8. Minimum investment $C^*_{min_i}$ required for the existence of each branch in the optimized configuration

(ii) The region of *non-topology modifications* ($C^* > 400$ k€), where the design ground field is nearly saturated. This region corresponds to the flat portion of the Pareto front. Here, only marginal robustness improvements are possible: a 600 k€ growth of the investment yields only a 1.1 % increase in robustness.

The optimized layouts obtained with $C^* = \{20;\ 200;\ 400;\ 1000\}$ k€ are shown in Figure 7.9(a), (b), (c) and (d), respectively. For the minimum investment case, the optimized layout consists of a unique short looping branch with $D = 0.066$ m. In all the remaining branches in the ground structure, we obtain $D < D_{th}$. Despite the limited investment and minor design modifications, this layout yields an increase of our robustness measure of 5.42 % as compared to the network in use today. Large differences in both the layout and performance are visible if the investment is raised up to nominal value of 200 k€. The optimized layout counts 14 additional looping branches. The connectivity is further modified when doubling the investment up to 400 k€. For this optimized layout, 8 other connections are visible and only Branch 14 has a diameter smaller than D_{th}. The size of the remaining branches grows homogeneously such that this layout looks a rescaled version of the design case optimized for $C^* = 200$ k€. For higher investments the topology of the network does not change anymore. With $C = 1000$ k€, most of the design variables corresponding to the pipes located in the eastern side of the network hit the maximum bound.

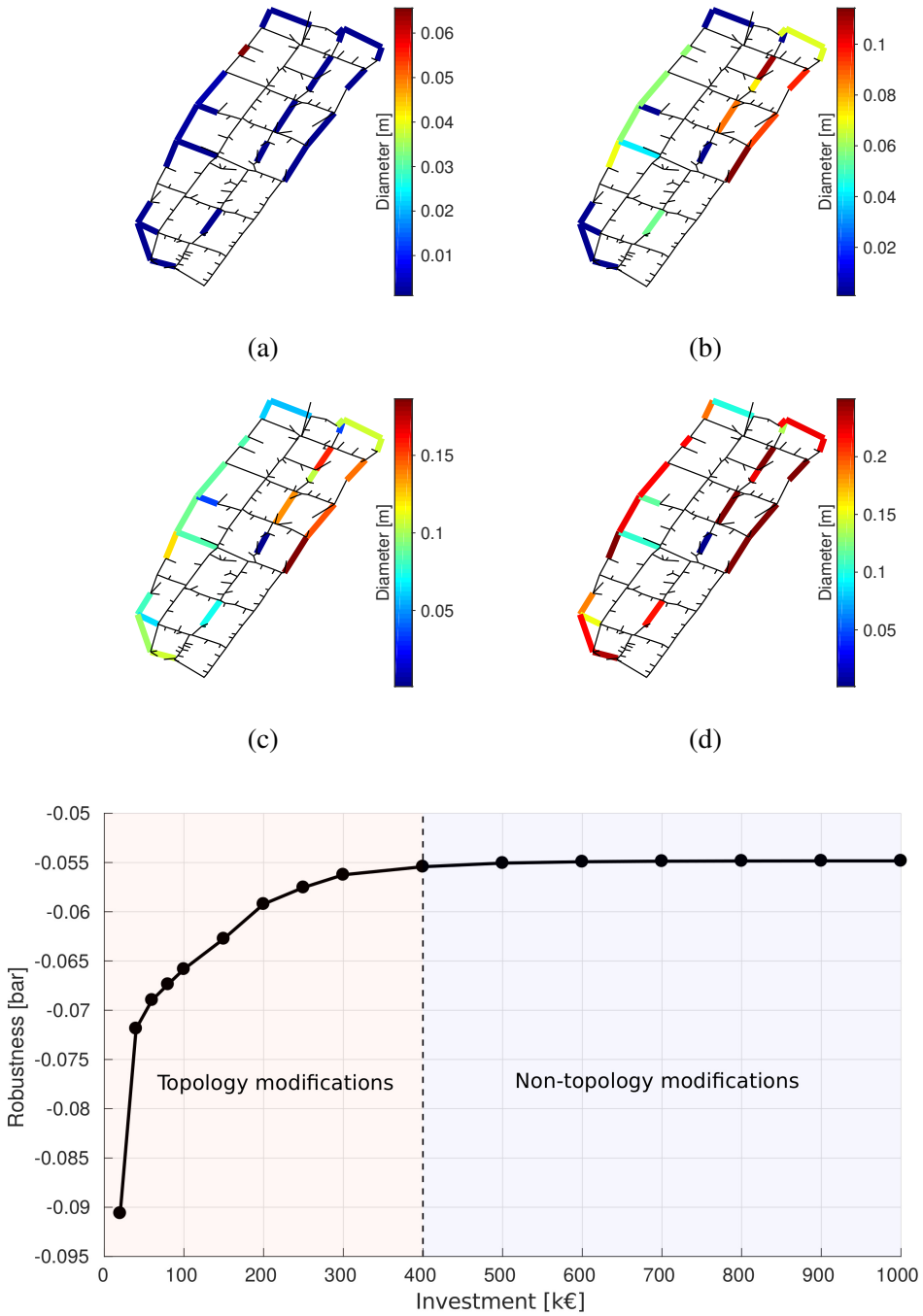

Fig. 7.9. Pareto front with selected optimized layouts. (a): 20 k€ ; (b): 200 k€ ; (c): 400 k€ ; (d): 1000 k€

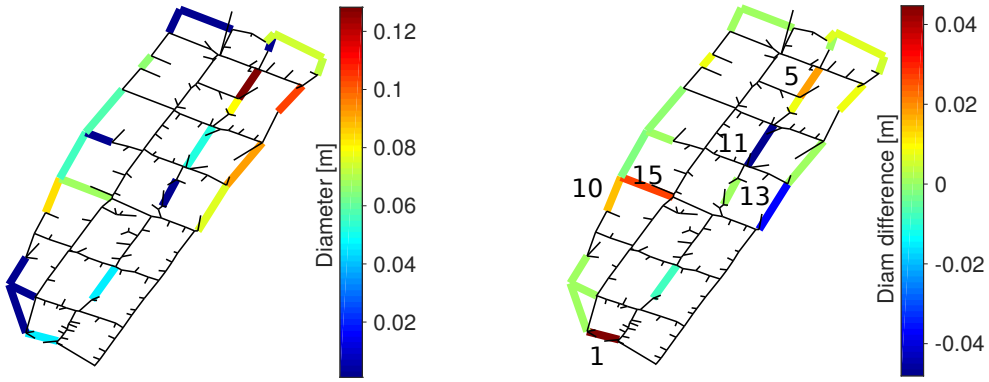

(a) (b)

Fig. 7.10. (a): Optimized layout when solving $\mathscr{P}_{P_{min}}$ with $C^* = 200$ k€; (b): difference between the solutions to $\mathscr{P}_{P_{min}}$ and $\mathscr{P}_{rob}$

Now we benchmark our robust design framework with both the optimized layout and performance obtained from a minimum pressure maximization design example. The optimization problem is formulated as in (7.34). The maximum investment is set to $C^* = 200$ k€ as for the nominal case. Figure 7.10(a) shows the optimized layout for this case. Figure 7.10(b) highlights the difference between the solutions to the problems $\mathscr{P}_{P_{min}}$ and $\mathscr{P}_{rob}$. The optimized network topologies are different. When maximizing the minimum pressure, Branch 1 has an optimized diameter of $D_1 = 0.048$ m. However, the diameter of this pipe degenerated to the minimum bound in our robust design framework. Furthermore, the diameters of Branches 10, 15 and 5 are increased by 0.017 m, 0.034 m and 0.018 m as compared to the solution of $\mathscr{P}_{rob}$. The cost of these modifications is covered by reducing the size of Branches 11 and 13. Slight modifications are observed for the remaining pipes. The smooth minimum pressures, $\tilde{\min}_{\text{pm}}\mathbf{P}$, strict minimum pressures, $\min\mathbf{P}$, and robustness measures calculated for both the solutions are compared in Table 7.2. Although solving $\mathscr{P}_{P_{min}}$ yields an increase of the smooth minimum pressure with respect to the robust design, the strict minimum pressure is lower. The overall differences are below 0.5 % for both the strict minimum pressure and its smooth approximation. The performance differences are non-negligible as regards to our robustness measure: the solution of $\mathscr{P}_{rob}$ allows an increase of 4.8 % as compared to the solution of $\mathscr{P}_{P_{min}}$.

Table 7.2. Performance of the solutions to $\mathscr{P}_{rob}$ and $\mathscr{P}_{P_{min}}$

	Design	
Performance	Robust	Min pressure
Smooth minimum pressure [bar]	5.9718	5.9936
Strict minimum pressure [bar]	5.4381	5.4365
Robustness [bar]	-0.0592	- 0.0622

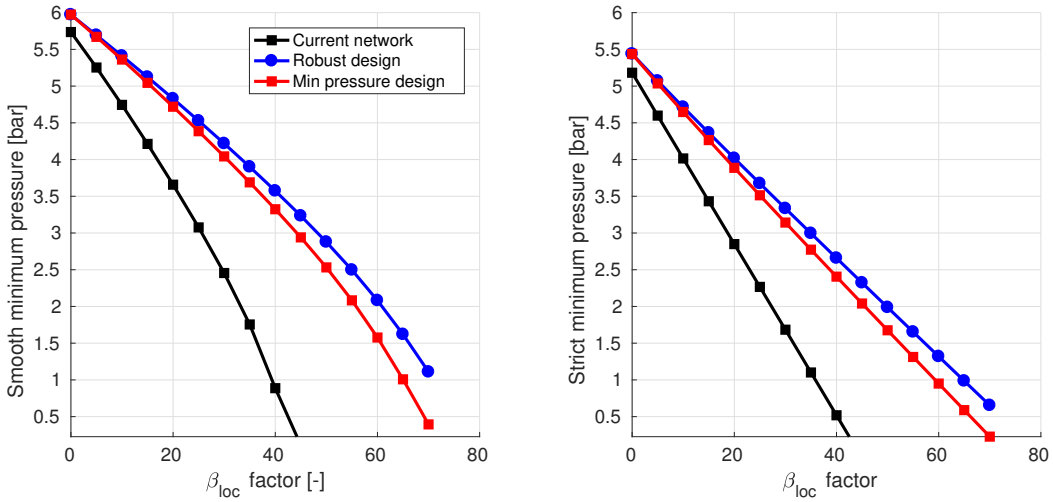

(a) (b)

Fig. 7.11. Response of the solutions to $\mathscr{P}_{rob}$, $\mathscr{P}_{P_{\min}}$ and current network to fluid-dynamic disturbances. (a): Smooth minimum pressure, $\tilde{\min}_{\text{pm}}\mathbf{P}$; (b): strict minimum pressure, $\min\mathbf{P}$

To investigate how these solutions respond to fluid-dynamic noise, we analyze the optimized designs in perturbed conditions. The local loss coefficients of the pipes are increased as follows:

$$\tilde{\beta}_{loc_i} = \beta_{loc_i} + \delta\beta_{loc_i}, \tag{7.39}$$

where $\tilde{\beta}_{loc_i}$ is the perturbed local loss coefficient of pipe "i" and $\delta\beta_{loc_i}$ is the perturbation defined according to (7.37). The multiplication factor, $f_{\beta_{loc}}$, is raised in 15 steps from 0 to 70. The results of this study are summarized in Figure (7.11), where we show also the performance of the network in use nowadays. Both the design formulations yields consistent improvements to the current situation. The differences between the solutions to $\mathscr{P}_{rob}$ and $\mathscr{P}_{P_{\min}}$ are limited for small disturbances. How-

ever, the gap between the two pressure curves increases gradually with $f_{\beta_{loc}}$. For a multiplication factor of 70, considering our robustness measure yields an increase in the smooth and strict minimum pressures of 164 % and 195 %, respectively. Note that in all cases, the strict minimum pressure scales roughly linearly with $f_{\beta_{loc}}$. This suggests that a probabilistic characterization of noise, e.g. obtaining stochastic bounds to maximize the feasible set or obtaining PDFs to minimize variance [193], may yield limited differences in this design example.

7.4 Centralized control

This section focuses on resilience improvements of DHNs through a centralized control during failure events. We first define the control variables, objective function and constraints of our framework. Then, we present a benchmark control strategy inspired by the typical habits in use nowadays. Last, we present the results obtained for several numerical experiments conducted on the same portion of the Turin DHN considered in the previous section.

7.4.1 Control and optimization models

Most of the control actions in a DHN are taken at each user location. The flow within the building heat exchanger can be adjusted through the manipulation of a valve. Our centralized control strategy aims at optimizing the set-up of all the user valves in the network. The vector of control variables, $\mathbf{s}$, is used to interpolate the local loss coefficient of the user control valves as follows:

$$\beta_{loc_i}(s_i) = \beta_{loc_{min}} + (\beta_{loc_{max}} - \beta_{loc_{min}})s_i \qquad i = 1, \ldots, N_s - 1, \tag{7.40}$$

where $\beta_{loc_{min}}$ and $\beta_{loc_{max}}$ are the minimum and maximum local pressure drop coefficients and N_s is the number of control variables. The flow can be prevented only for $\beta_{loc} \to \infty$ which leads to ill-conditioning of the state equations. Due to our steady-state assumption, valve closures are not of interest here as a nil flow would result in a nil thermal power transferred to the building connected. The modification of the control valves affects the equivalent fluid-dynamic resistance of the network. Setting a fixed inlet mass flow rate may yield a head drop higher than the one that

can be sustained by the circulation pump. The fluid-dynamic equilibrium between the network and the pump is obtained by modifying the inlet mass flow rate, G_{in}, during the optimization process, in such a way to meet a pumping constraint. The physical design variables set (7.40) is augmented with:

$$G_{in}(s_{N_s}) = G_{in}^{(0)}(\chi_{max} - \chi_{min})s_{N_s}, \tag{7.41}$$

where χ_{min} and χ_{max} are the minimum and maximum mass flow rates normalized with respect to the design value, $G_{in}^{(0)}$.

When controlling DHNs after a mechanical failure event, the primary concern is to guarantee the thermal comfort to *all* the connected users, so that the quality of service is maintained above acceptable limits. We formulate the optimization problem as a minimization of the discomfort of the most critical users. We quantify the thermal discomfort, γ_i, of user "i" as follows:

$$\gamma_i = \left(\frac{\Phi_i - \Phi_{sp_i}}{\Phi_{sp_i}} \right)^2, \tag{7.42}$$

where Φ_i is the real thermal power delivered to the user and Φ_{sp_i} is the ideal value, which would be required to obtain the internal set-point temperature, T_{sp}. This quantity is calculated as:

$$\Phi_{sp_i} = K_V V_i (T_{sp} - T_{amb}). \tag{7.43}$$

The term in brackets in Equation (7.42) represents the thermal power deficit or surplus in relative terms. We will refer to this quantity as thermal mismatch, $\|\Delta\Phi_i\|$, hereafter. The quadratic formulation (7.42) equally accounts for both the over-heating and under-heating. The thermal discomfort of the most critical users is obtained through a smooth maximum approximation using the p-mean formulation as in (7.27). The objective is written as:

$$z = \tilde{\max}_{\text{pm}} \boldsymbol{\gamma} = \left(\frac{1}{N_{bg}} \sum_{i=1}^{N_{bg}} \gamma_i^{p_\gamma} \right)^{\frac{1}{p_\gamma}}, \tag{7.44}$$

where N_{bg} is the number of buildings and p_γ is the p-mean exponent. Eq. (7.44) provides a lower bound to the hard maximum function and converges to it in the

limit of $p_\gamma \to \infty$ [431]. The optimization problem is augmented with a pressure head constraint to enforce the fluid-dynamic equilibrium with the circulation pump. Mathematically:

$$(\Delta P_{PH} - \Delta P_{max})^2 - \varepsilon_p^2 \leq 0. \tag{7.45}$$

Using the constraint (7.45) results in a weakly-imposed fluid-dynamic equilibrium, such that in the worst case the maximum pressure drop registered in the network $\Delta P_{max} = \max(\mathbf{P}) - \min(\mathbf{P})$ differs from the pump pressure head, ΔP_{PH}, by a small number, ε_p. To sum up, the optimization problem is formulated as:

$$\mathscr{P}_{\text{LMD}} : \begin{cases} \min\limits_{\mathbf{s}} & \tilde{\max}_{\text{pm}} \boldsymbol{\gamma} \\ \text{s.t.} & (\Delta P_{PH} - \Delta P_{max})^2 - \varepsilon_p^2 \leq 0 \\ & \mathbf{s} \in \mathbf{S} = \left\{ \mathbb{R}^{N_s} \mid 0 \leq s_i \leq 1, i = 1, ..., N_s \right\} \end{cases} . \tag{7.46}$$

As solving Problem (7.46) corresponds to minimizing the maximum discomfort, we will refer to this control strategy as Least Maximum Discomfort (LMD) Control. The objective and constraint gradients with respect to the control variables, $\mathbf{s}$, are computed with the discrete adjoint method described in Section 2.3.2. To this aim, the continuity, momentum and energy state variables and residuals are stacked in the vectors $\mathbf{u} = [\mathbf{P}^T, \mathbf{G}^T, \mathbf{T}^T]^T$ and $\mathbf{R} = [\mathbf{R}_c^T, \mathbf{R}_m^T, \mathbf{R}_e^T]^T$.

In order to permit useful comparisons, we benchmark our centralized control strategy with an alternative approach inspired by the current habits. This is labeled as Conventional Control or C-Control in short. The decisions are taken from each individual user based on the local degree of discomfort. There is an intrinsic hierarchy in the control possibilities. The control actions of the over-heated buildings are generally successful (a valve can always be *closed more* as long as $\beta_{loc} \leq \beta_{loc_{max}}$). The control actions of the under-heated buildings are limited by fluid-dynamic constraints: even if the user valves are completely open, the incoming mass flow rate may be inadequate to meet the thermal requirements. For this reason, we handle the over-heated and under-heated buildings separately. For over-heated buildings, we consider a criterion similar to (7.44):

$$\tilde{\max}_{\text{pm}} \gamma_k, \tag{7.47}$$

but here the index "k" spans only those buildings in which:

$$\Phi_k - \Phi_{sp_k} \geq 0. \tag{7.48}$$

The corresponding control variables are updated with MMA, using the gradients with respect to the criterion (7.47) and to the constraint (7.45). The control variables corresponding to the under-heated buildings are updated using a heuristic recursive relation of the form:

$$s_l^{(i+1)} = \max\left(s_{min}, s_l^{(i)} - f_s s_l^{(0)}\right), \tag{7.49}$$

where $s_l^{(0)}$ is the control variable value at iteration 0, $s_l^{(i)}$ is its value at the optimization iteration "i" and f_s is a constant multiplication factor here set to 0.2. The index l runs over those buildings in which:

$$\Phi_l - \Phi_{sp_l} < 0. \tag{7.50}$$

We stop the iterative procedure when the norm of the control variables change drops below $1e-5$ and the pumping constraint (7.45) is satisfied. This scheme revealed to be effective in the numerical examples described in the next section. Oscillations of the criterion (7.47) and pumping constraint (7.45) are severe only during the initial iterations, when the heuristic update (7.49) is dominant.

7.4.2 Numerical results and control trends

This section presents and discusses the performance of our centralized control framework in handling failure events. We focus on the same subnetwork considered for the robust design (Figure 7.5). The values of the most relevant parameters and properties are listed in Table 7.3. The failures are simulated by prescribing the maximum local loss coefficient, $\beta_{loc_{max}}$, to three selected branches, highlighted in Figure 7.5(b). We first shed light on the LMD-Control procedure focusing on a reference case with Inlet 1 and Failure 1, which is the combination with the largest influence on the system performance. Then, we assess the effect of the available pressure head for different failures and inlet positions. Last, we study how the malfunctions in the main transportation network can be managed through a centralized control of the considered distribution network. All the optimization

Table 7.3. Parameters and properties for the centralized control

Description	Symbol	Value	Unit
Relative outlet total pressure	P_{out}	0	Pa
Inlet temperature	T_{pp}	363.15	K
Dacy-Weisbach friction factor	f	0.014	-
Water density	ρ	1000	kg/m^3
Water specific heat	c_p	4186	J/(kg K)
Volumetric heat transfer coefficient	K	0.9	W/(m^3 K)
Set-point internal temperature	T_{sp}	293.15	K
Design outdoor temperature	T_{amb}	265.15	K
Minimum local pressure drop coefficient	$\beta_{loc_{min}}$	0	-
Maximum local pressure drop coefficient	$\beta_{loc_{max}}$	1e7	-
Minimum relative inlet mass flow rate	χ_{min}	0.5	-
Maximum relative inlet mass flow rate	χ_{max}	1.5	-

problems are solved using MMA. Compared to the parameters set-up discussed in the previous section, to produce the following results we set the constraint penalty as $c_1 = 10000$. Recall that $\mathscr{P}_{LMD}$ (7.46) includes an inequality constraint (7.45) that weakly enforces the fluid-dynamic equilibrium between the network and the circulation pump. Since we devised our control framework to fit within an RTI system, we would like to obtain a sequence of feasible solutions along the optimization process. In preliminary numerical studies, we observed that using the reference constraint penalty, $c_1 = 1000$, was leading to constraint violations of unacceptable magnitude along the optimization history. Raising c_1 to 10000 fixed the issue.

The objective history for the reference failure case is shown in Figure 7.12. The objective values are normalized with respect to the initial value, $z^{(0)}$. Convergence is reached in 134 control iterations and required a total computational time of only 246.89 s on an old machine equipped with two Intel i7-870 Quad-Core processors. This suggests that the developed framework is ideal for the integration within an RTI control system. We study only the first 100 iterations as minimal objective and thermal mismatch changes are observed after. The objective history is smooth and the improvements are quick. The maximum discomfort measure drops by more than 60 % in the first 20 iterations and it takes 80 more iterations to obtain an additional 20 % reduction. The initial discomfort field peaks in those regions that are located right downstream the malfunction. The thermal mismatch of this group of users is rapidly increased by redirecting some of the mass flow rate of the neighbors. This

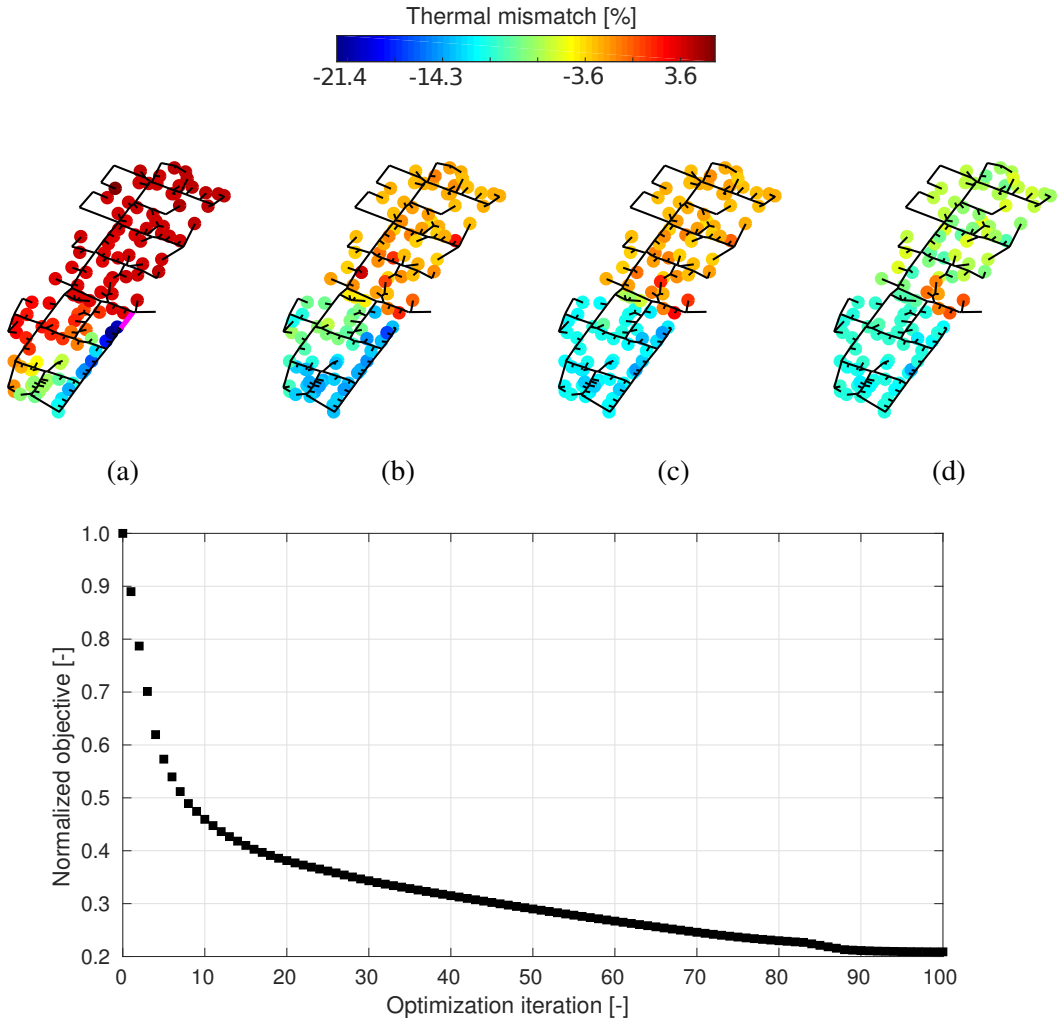

Fig. 7.12. Normalized objective history during the optimization of the reference failure case. The thermal mismatch field is shown at selected optimization iterations. (a): Iteration 0; (b): iteration 20; (c): iteration 50; (d): iteration 100

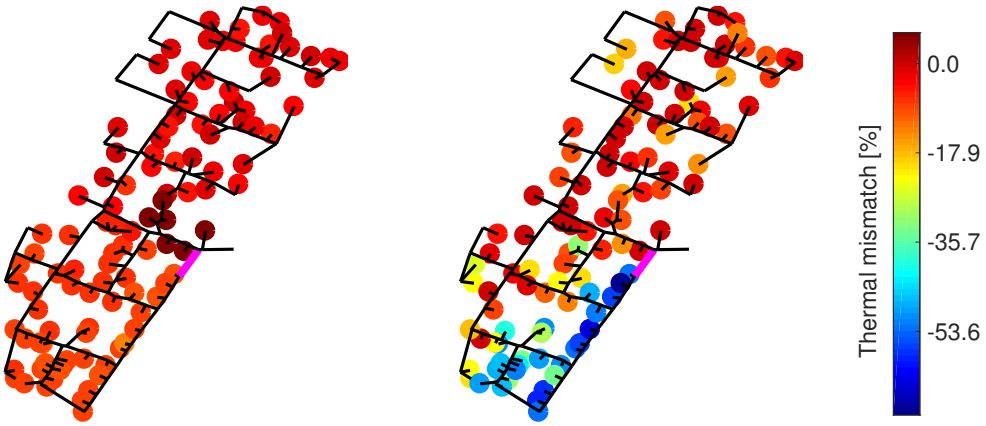

(a) (b)

Fig. 7.13. Final thermal mismatch field. (a): LMD-Control; (b): C-Control

smoothing process progressively enlarges the area with a negative thermal mismatch, which reaches the northern portion of the network after 20 iterations. At this point, it is still possible to clearly distinguish among three different zones: a cold zone (blue), an intermediate zone (green) and a warm zone (orange). The former two appear mixed together after 50 and 100 iterations. Figure 7.13 shows a comparison of the final thermal mismatch distributions obtained with the LMD-Control and C-Control. Our centralized control strategy results in a nearly homogeneous thermal mismatch field. On the other hand, the conventional operation strategy yields strong discomfort peaks. The users located right downstream the broken pipe feel the highest thermal discomfort. The head availabilities for these buildings are too low to provide mass flow rates able to satisfy their thermal requirements. Overall, the utilization of the LMD-Control yields a reduction in the global measure of discomfort of 96 % as compared to C-Control.

Now we investigate how the inlet pressure head affects the performance of both the control strategies. The pumping head, ΔP_{PH}, in (7.45) is increased in 6 steps of 14 % over the design value. For each case, an optimization run is performed. Figure 7.14 shows the evolution of the thermal mismatch distribution for $\Delta P_{PH} = \{100;\ 142;\ 184\}$ %. The snapshots are taken after 20, 50 and 100 iterations. Similar improvements are achieved within the first 20 iterations: the thermal mismatch peaks are smoothed over the whole south-east portion of the network. From iteration 20 to iteration 50, this "cold wave" expands to occupy

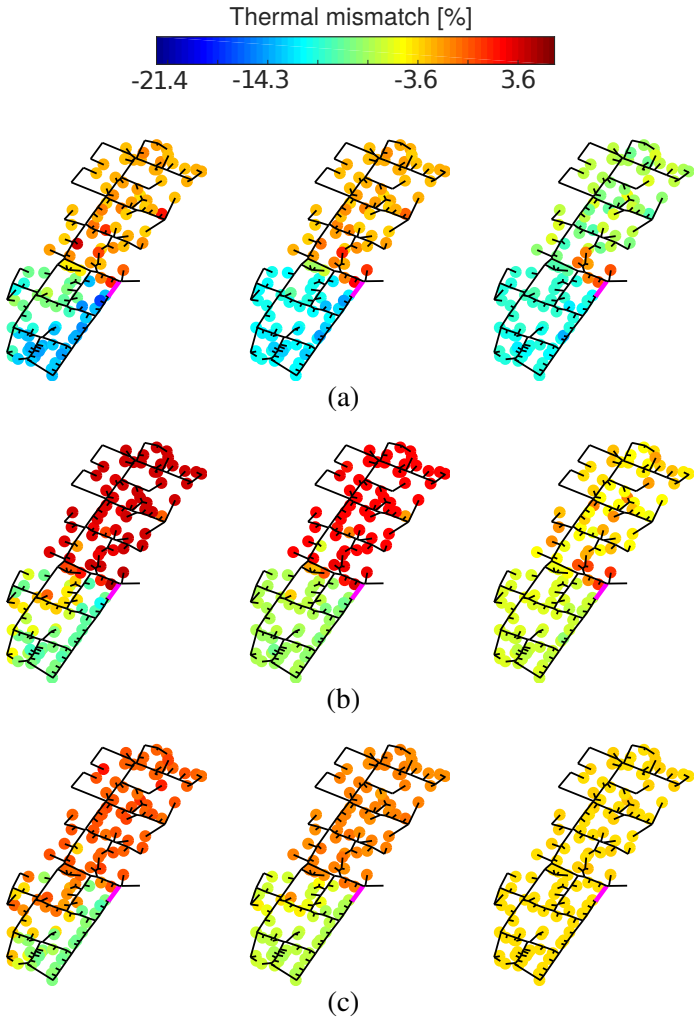

Fig. 7.14. Evolution of the thermal mismatch distribution for $\Delta P_{PH} = 100$ % (a), $\Delta P_{PH} = 142$ % (b), $\Delta P_{PH} = 184$ % (c). The snapshots are taken at iteration 20, iteration 50 and iteration 100

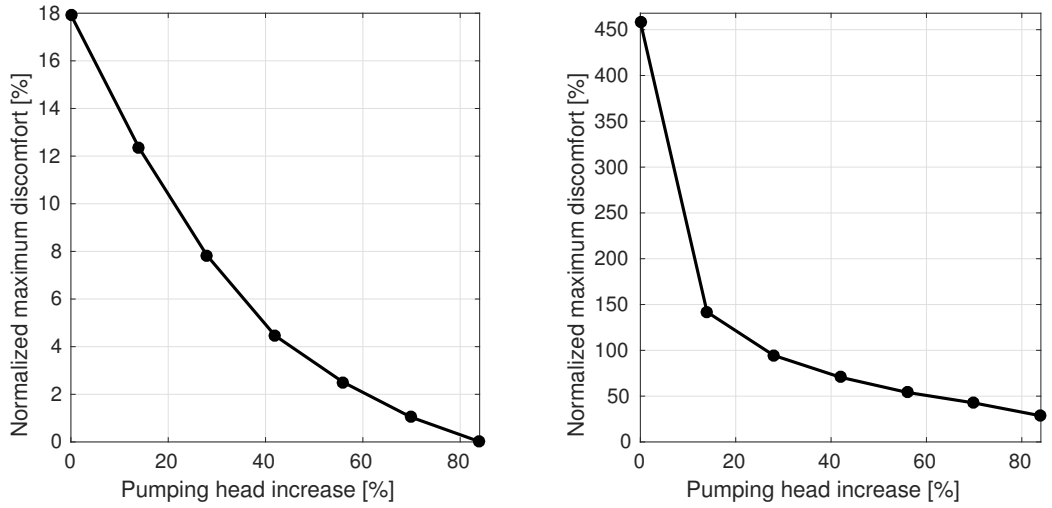

(a) (b)

Fig. 7.15. Effect of the inlet pressure head on the control strategy performance. (a): LMD-Control. (b): C-Control

the whole southern portion, while the northern one looks still warm. Substantial differences among the three cases are visible after iteration 50. At this stage, the over-heated buildings contribute meaningfully to the objective and the optimizer tries to blend the hot and the cold regions in a unique homogeneous field. The success of this last step largely depends upon the value of ΔP_{PH}. The final normalized objective values obtained for the LMD-Control and the C-Control are reported in Figure 7.15. Increasing ΔP_{PH} yields moderate effects on the performance of our centralized control strategy. It is possible to decrease the normalized objective from 18.0 % to 0.2 % with an 84 % increase in the pressure head. On the other hand, Figure 7.15(b) indicates that a growth of the inlet pressure head is crucial when using the conventional operation strategy. For all the values of ΔP_{PH} considered, the conventional strategy yields inferior performance with respect to the worst-performing case of our centralized strategy. This suggests that a centralized control strategy may be a valid alternative to the installation of a backup pumping system at the inlet of the distribution networks.

To generalize the previous observations, we study the influence of the location of the inlet and failure. With reference to Figure 7.5(b), the numerical experiments are first repeated considering Failure 2 and Failure 3. We study the subnetwork when alimented from Inlet 1. Figure 7.16(a) shows the outcome of this analysis. The trend

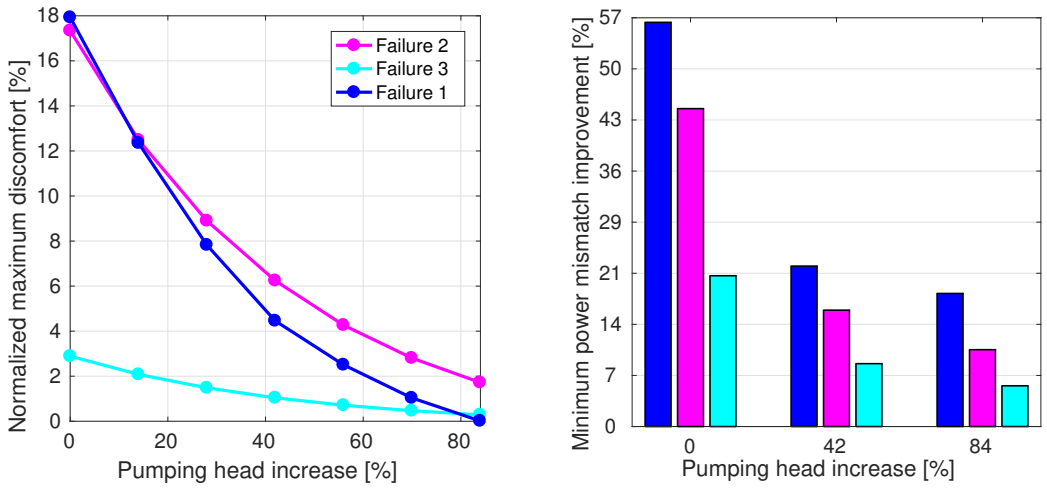

(a) (b)

Fig. 7.16. (a): Effect of the inlet pressure head on the control strategy performance for different failure locations; (b): summary of the performance improvements achievable with the LMD-Control compared to the C-Control for different failure locations

for Failure 1 was already presented in Figure 7.15 and is reported here to facilitate the comparisons. The three curves drop at different rates, indicating that the location of the failure modifies the effect of the available pressure head on the discomfort peaks. With no additional pressure head, Failure 1 yields the highest maximum thermal discomfort. However, this case results in the best performance for $\Delta P_{PH} = 184$ %. Figure 7.16(b) summarizes the improvements in the minimum thermal mismatch (i.e. the discomfort of the most under-heated user) obtained with respect to the C-Control. In all the cases considered, the performance gap between the control strategies drops quadratically when the pressure head is increased. The effect of the inlet location is shown in Figure 7.17. To obtain these results, we considered Failure 1 as in the reference configuration. The two curves exhibit a nearly constant spacing along the y axis and drop at the same rate. This suggests that the inlet position does not modify the effect of the available pressure head on the discomfort peaks. The improvements obtained with the LMD-Control with respect to the C-Control are summarized in Figure 7.17(b). With no additional pressure head, the gains are higher with Inlet 1 than with Inlet 2. The improvements obtained with Inlet 1 and Inlet 2 scale linearly and quadratically with ΔP_{PH}, respectively. As a consequence, for $\Delta P_{PH} = 184$ %, the LMD-Control yields larger benefits when water is injected at Inlet 2. These results

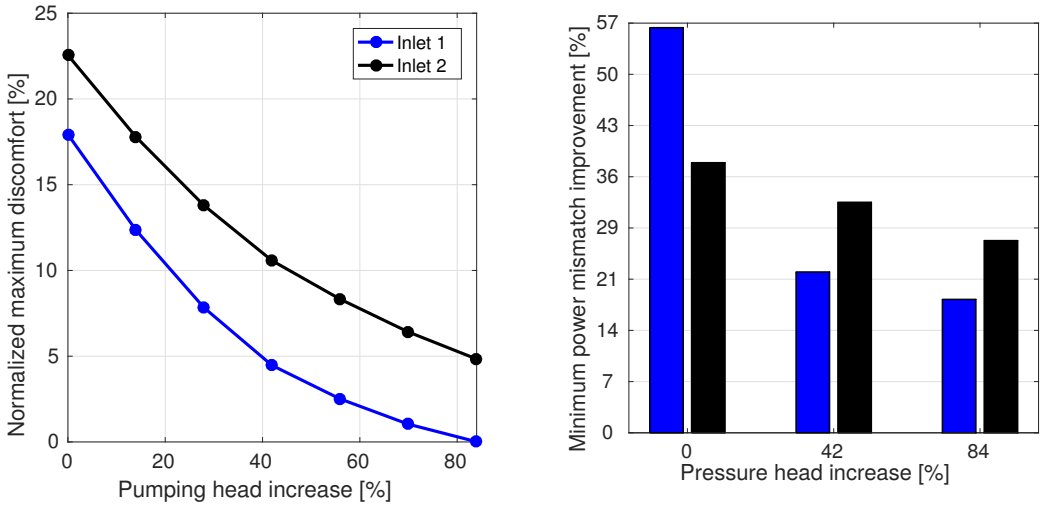

(a) (b)

Fig. 7.17. (a): Effect of the inlet pressure head on the control strategy performance for different inlet locations; (b): summary of the performance improvements achievable with the LMD-Control compared to the C-Control for different inlet locations

present evidence that the benefits of a backup pumping system depends largely on the location of the failures and slightly on the inlet position. However, the improvements of our control strategy with respect to the one in use today are observed to be more affected by the position of the inlet than by the location of the failure.

Here, we test the ability of our centralized control strategy to handle failures in the main supply line (transportation network) rather than in the controlled subnetwork. The mainly supply line of the Turin DHN is represented in Figure 7.18(a). The graph representation of this system counts 1373 nodes and 1389 branches. Hot water is injected in six different positions highlighted with green indicators. Those correspond to the location of the CHP plants, boilers and storage tanks. We consider two malfunctions, labeled as Failure 4 and Failure 5. In both cases, the location of the most critical distribution network, i.e. the one with the lowest available pressure head, corresponds to the one indicated in Figure 7.18(a). For simplicity, we assume that this critical subnetwork has the same topology and design specifications of the one considered for the previous analyses. Water is injected in this distribution network through Inlet 1, as in the reference case. The fluid-dynamic equilibrium lies at the intersection between the characteristic curves of the transportation and distribution networks. These curves are shown in Figure 7.18(b). All the values are normalized

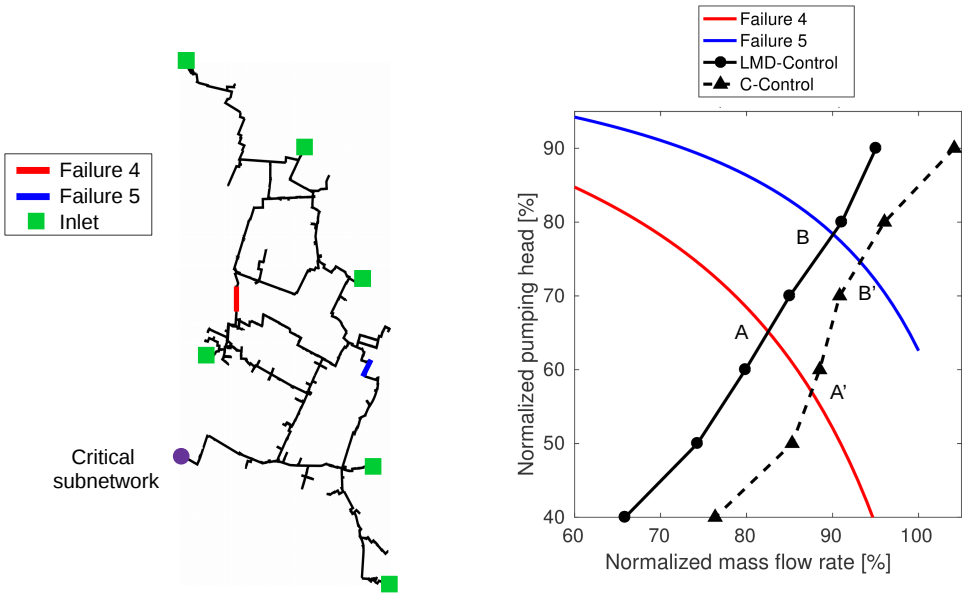

(a) (b)

Fig. 7.18. (a): Overview of the transportation network; (b): intersection of the main network characteristic curves with the subnetwork characteristic curves

with respect to the nominal operating conditions. The subnetwork control curves are obtained by sweeping the pressure head, ΔP_{PH}, in the nonlinear constraint (7.45) from 40 % to 90 % of the design value in steps of 10 %. The LMD-Control curve of the subnetwork intersects the main network characteristic curves in Point A and B. Failure 4 has larger impact than Failure 5 on the fluid-dynamic response. In this case, the system can be operated with 65.1 % of the design pressure head and 82.5 % of the design inlet mass flow rate. Point B locates at 78.3 % and 90.0 % of the design pressure head and inlet mass flow rate, respectively. When the subnetwork is operated through the C-Control, the fluid dynamic equilibrium moves to Point A' and B', with higher inlet mass flow rate and lower available pressure head with respect to A and B. Figure 7.19 shows the thermal mismatch field $\|\Delta\Phi\|$ in Points A, B, A' and B'. To obtain these results, we performed four additional optimization runs in which the maximum pressure head, ΔP_{PH}, was set according to the interpolated pressure head of the four points. The optimized inlet mass flow rates present negligible differences from the ones predicted through the piece-wise linear trend shown in Figure 7.18(b). For both Failure 4 and Failure 5, the LMD-Control yields a nearly "flat" thermal mismatch field. In Points A and B, all the network users are equally under-heated

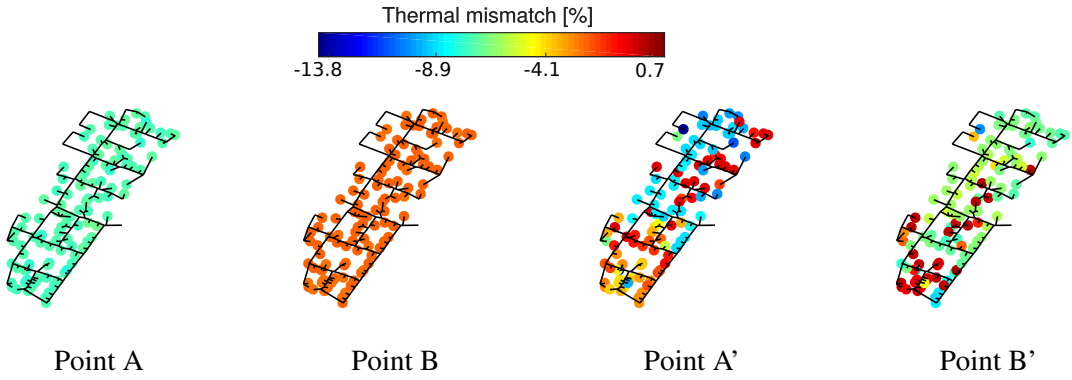

Fig. 7.19. Final thermal mismatch field $\|\Delta\Phi\|$ for failures in the main network

Table 7.4. Smooth maximum discomfort z ($\times 10^2$) [-] obtained for failures in the main network

	Control strategy	
Failure	LMD	Conventional
4	0.49	1.28
5	0.16	0.57

by roughly 7 % and 4 % so that the discomfort peaks are avoided. Operating the network with the C-Control (Points A' and B') results in a strong thermal imbalance. The users located in the northern portion of the system are more under-heated as compared to those located in the southern portion. This can be explained by the absence of loops in the northern portion, yielding a higher fluid-dynamic resistance. Despite this general trend, the thermal mismatch distribution is highly oscillating and presents multiple local minima and maxima. Whether a building thermal request is satisfied depends on both the available and nominal pressure heads at each user substation. The latter can vary substantially due to practical installation requirements. Table 7.4 summarizes the normalized maximum discomfort in the 4 points analyzed. Compared to the conventional operation strategy is use today, the LMD-Control allows our global discomfort measure to be reduced by roughly 62 % and 72 % in the two failure cases considered. These results suggest that a partial centralization of the control system may yield benefits also when mechanical failures are not located in the controlled area.

7.5 Conclusions

In this chapter, we demonstrated a robust design and a centralized control framework for increased resilience of DHNs. Robustness was defined using a sensitivity metric that does not require any probabilistic characterization of the noise uncertainty. The design problem was formulated using the ground structure approach for topology optimization where realistic looping paths are selected as potential or vanishing connections. Control aimed at minimizing a differentiable global measure of discomfort after a pipe breakage event. The optimization problem was solved using popular mathematical tools for topology optimization: MMA and discrete adjoint sensitivities. Both the design and control frameworks were tested on a limited portion of the Turin district heating network.

The most relevant application-oriented advances of this chapter are presented in Figure 7.20. The robust design results (Figure 7.20(a)) indicate that our sensitivity metric for robustness quantification well measures the ability to absorb fluid-dynamic perturbations. When analyzed considering a distributed fluid-dynamic noise, the layout optimized with our framework is superior to the one computed using a minimum pressure maximization formulation. Robustness and investment were found to be antagonist in the range of values considered. Large robustness improvements (+ 38.8 %) with a limited investment (400 k€) are possible through topology modifications of the network. Oversizing the pipes with no change of the connectivity leads to only minor benefits. The outcomes of our control numerical examples (Figure 7.20(b)) show that the proposed framework allow mechanical failures to be quickly handled with little impact on the level of service. The steep discomfort peaks that naturally arise when taking non-centralized control actions are eliminated. In the nominal conditions, the utilization of our centralized control framework yields a reduction in the global measure of discomfort of 96 % as compared to the control strategy in use today. Furthermore, we obtained improvements to the thermal deficit of the most critical user between 5.89 % and 56.38 % in all the failure cases analyzed. The inlet pressure head weakly affects the achievable performance. This suggests that adopting a centralized real-time control system may yield considerable investment savings on pumping equipment. Furthermore, a partially centralized system was found to be beneficial also when failures are not located in the controlled portion of the network.

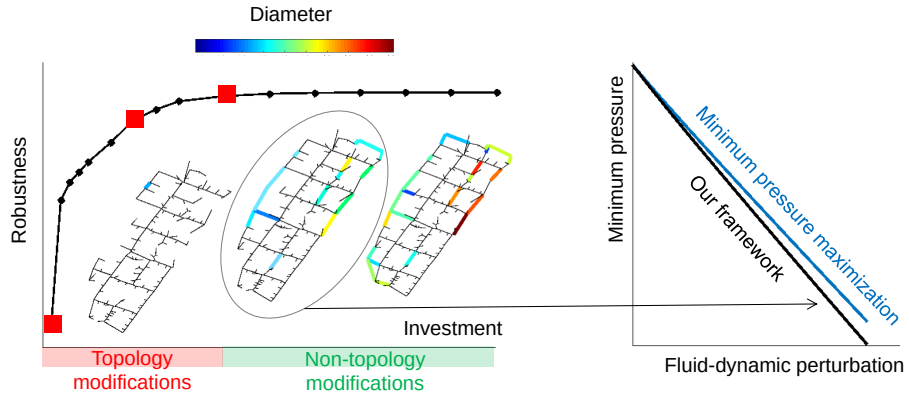

(a)

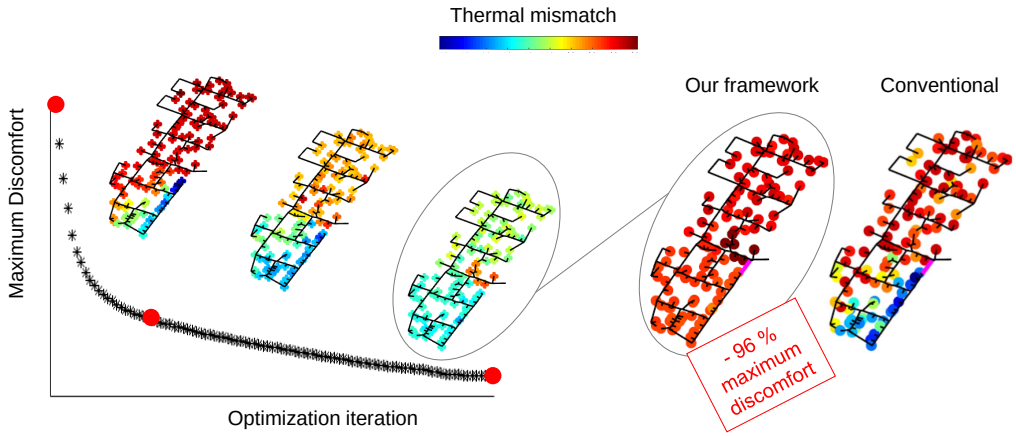

(b)

Fig. 7.20. Graphical summary of the main application-oriented advances obtained in this chapter using: (a) our robust design framework; (b) our centralized control framework

Chapter 8

Design of flow fields in PEM fuel cells

PEMFCs are electrochemical devices used to directly convert the chemical energy of hydrogen into electricity [79]. They represent an efficient power generation solution for both stationary and moving power systems such as automotive, aerospace and marine vehicles [461, 87, 9] because of their high power density, low operating temperature, low weight and fast startups [254, 461]. However, their limited durability and high cost are major obstacles to achieve a large scale commercialization [460]. The search for improved flow field geometries, yielding enhanced performance at reduced costs, is a long-standing problem in the fuel cell community. However, as observed for fins geometries in Chapter 3, most of the current literature deals with improvements to specific design concepts that are heuristically proposed following personal insights or intuition. The presence of a multitude of different solutions suggests that the choice of the design concept is crucial for the final geometry. Hence, also in this field, there is a urgent need for a thorough and affordable design optimization route, allowing dramatic design changes. In this chapter, we develop and demonstrate a topology optimization framework for the design of flow fields in PEMFCs. To our best knowledge, a unique study [242] dealt with topology optimization of fuel cells. This valuable contribution relies on overly simplified electrochemical and mass transport models and does not consider all the optimization criteria of practical interest for the development of these energy devices. Furthermore, the paper suffers from a limited resolution and convergence to well-defined manufacturable layouts. These shortcomings motivate the work presented hereafter.

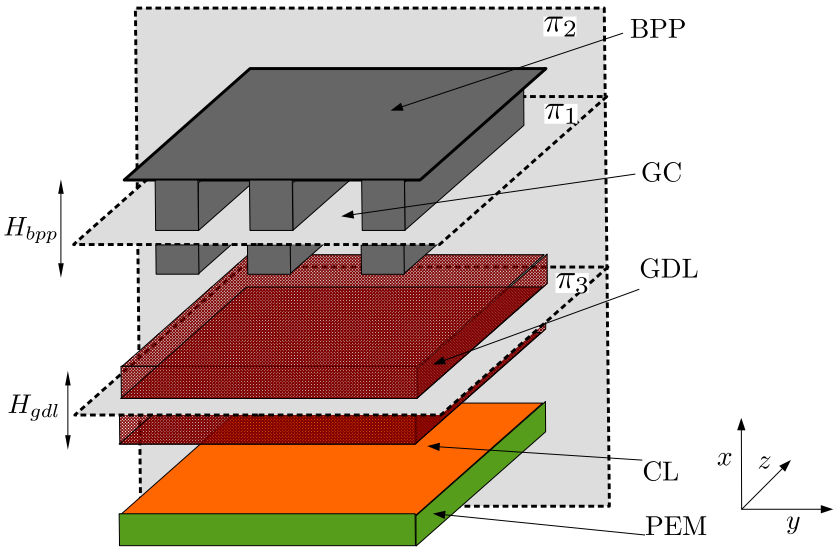

Fig. 8.1. Representative exploded view of the cathodic section of a PEM fuel cell

The plan of the chapter is as follows. In Section 8.1, we review the most popular technological solutions and identify room for improvements to the geometric design of PEMFCs. In Section 8.2, we describe a method capable of reducing the problem dimensionality and present the governing equations and numerical model used to predict gas dynamics, transport of chemical species and electrochemistry. Section 8.3 introduces the optimization framework focusing on the objective, constraints and material interpolation strategies. In Section 8.4, we calibrate and verify our 2D analysis framework and present numerical results and design trends. Finally, Section 8.5 summarizes the main contributions of the chapter.

Some of the contents of this chapter were presented at the 18$^{\text{th}}$ U.S. National Congress for Theoretical and Applied Mechanics ([**C6**]) and included in a paper draft that was submitted for publication in Applied Energy ([**J5**]).

8.1 Overview of geometric design in PEMFCs

A schematic exploded view of the cathode of a typical PEMFC is shown in Figure 8.1. It is composed of three stacked layers: a BPP, a Gas Diffusion Layer (GDL), and a Catalyst Layer (CL). The CL is positioned at the interface between the membrane and the GDL and is responsible for the recombination of oxygen with protons

through electrochemical reactions and mass transfer phenomena. The delicate catalyst structure is protected by the porous GDL, which provides a path for the reactants from the BPP to the CL and allows the transport of the electrons needed for the electrochemical reactions. The BPP serves as an electronic interconnection between adjacent cells and feeds the reactants to the electrode. A cross-section on a horizontal plane, e.g. π_1, reveals the presence of both solid and empty regions. The former are referred to as ribs and are generally made of graphite. The latter correspond to the channels in which the reactants flow. If a sufficient pressure differential is available, the gas is allowed to flow under the ribs (moving on a vertical plane, e.g. π_2) and reach the contiguous channel. The BPP is a crucial component, playing four major roles [32]:

(i) It should **distribute the reactants homogeneously** over the active sites. The poor distribution of the reactants may be a consequence of an uneven flow resistance of the channels caused by either a bad mechanical design or water accumulation and fouling [289]. Nonuniform electrochemical reactions affect water management [450] and yield water content and temperature inhomogeneities, leading to hygro-thermal stresses [10]. Delamination between the GDL and the membrane [318] may occur at early stages of the operating life, impacting on the durability.

(ii) It should guarantee a **high power generation at minimal pressure drop** from the inlet to the outlet. Large pressure drops may require a non-negligible parasitic power to drive external blowers. Furthermore, cross-leakages of reactants, mechanical stresses and reversible voltage losses may also arise as a consequence of excessive pressure drops [450, 268].

(iii) It should guarantee an **effective water management**; performance drops are observed due to both dehydration and flooding. Dehydration refers to the water depletion in the membrane and yields a reduced ionic conductivity and risk of de-adhesion [84]. Flooding refers to the liquid water accumulation in both the channels and GDL, which is manly due to a high rate of condensation [289, 207]. In PEMFC, the phenomenon is critical at the cathode, where vapor is produced due to the Oxygen Reduction Reaction (ORR) [9]. This leads to the deterioration of the oxygen transport over the reactive sites and in turn affects the performance. Flooding is seldom an issue in high temperature

PEMFCs due to the increased vapor saturation pressure [83]. However, in these systems different membranes are required to avoid dehydration [83].

(iv) It should provide a **low electrical resistance and high mechanical stability** by creating a sufficient contact area between the BPP and GDL [258].

In summary, the geometry of the BPP grooves affects the transport of both the reactants and electrons, reaction rate, pressure drop and water management [9]. These factors greatly influence the fuel cell performance [249]. Kahraman and Orhan [229] estimated that crafted designs can yield improvements to the power density as high as 50 %. For this reason, a vast body of literature investigated the effect of various geometrical features of the BPP. Researches towards enhancement techniques can be grouped in three categories: design of the channels and ribs, utilization of obstacles and design of the flow fields.

The design of the channels and ribs was tackled at different levels of complexity, ranging from the definition of the widths and depths to the shape optimization of the channel cross sections and utilization of tapered conduits. The former was generally considered using a channel-to-rib width ratio:

$$\tilde{W} = \frac{W_{ch}}{W_{rib}}, \tag{8.1}$$

where W_{ch} and W_{rib} represent the widths of the channels and ribs, respectively. Kumar and Reddy [254] were among the first to investigate systematically the effect of $\tilde{W}$ on performance. Their results indicate that there might be an optimum value of $\tilde{W}$ close to 3. The authors did not model the transport of electrons and their layout may result in a high electrical contact resistance. In this regard, the experiments conducted by Yoon et al. [482] suggest that mass transport has larger impact on performance than electric conduction. The authors considered layouts with $0.33 \leq \tilde{W} \leq 2$ and found that thinner ribs always lead to a higher power generation. Later, the numerical study by Ahmed and Sung [8] led to different conclusions. Their results indicate that at high current densities, large performance degradations can be expected for $\tilde{W} \geq 1.4$ due to the increased ohmic losses. Many other studies were later conducted to assess the effect of this parameter on performance, see e.g. [241, 445, 488]. Although the specific "optimized "values are of little interest due to the high variability of the test conditions, most of the findings suggest that increasing $\tilde{W}$ in general leads to a higher ohmic resistance and pressure drop, enhanced reactant distribution and

improved water management. As observed by Manso et al. [289], only a limited number of studies focused on the effect of the channel depth, H_{ch}. Afshari et al. [5] reported increased current densities for smaller depths and suggested to adopt 1 mm deep channels. The authors noted that a moderate increase of the pressure drop at reduced depths is unavoidable but slightly affects the net performance of the system. A recent numerical and experimental study reported in [445] revealed that reduced channel depths and thinner ribs are always beneficial for water management. At low operating voltages, these features prevent the accumulation of water in the GDL through strong under-rib convection. At high operating voltages, water plugs in the channels are eliminated thanks to large streamwise pressure gradients. All the studies discussed so far considered channels with rectangular cross-sections. Many scholars dedicated to the search of alternative channel configurations such as hemispherical, triangular, trapezoidal and stepped cross sections. Ferng and Su [135] observed that designing a proper channel cross-section is crucial for parallel flow fields but yields minor effects in serpentine layouts. The authors of [254] suggested to use triangular and hemispherical channels to obtain the most effective mass distribution over the active sites but did not discuss any issue related to water management. Later, the experiments conducted by Owejan et al. [323] revealed that the shape of the channel cross-section has large effects on the two-phase flow dynamics. Differently from rectangular channels, triangular ones were found to confine the accumulation of water at the channel angles in contact with GDL, yielding a little impact on the reactant distribution. Similar effects were reported in [148] for highly humidified streams in trapezoidal channels. However, the authors noted that some issues related to the membrane dehydration may arise when using dry streams due to an excessive water removal. Zeng et al. [489] used GA to conduct a formal shape optimization of trapezoidal channels by varying the width of the bottom and top edges. Their optimized layout features a edge ratio of 1.45 and yields an increase of 8.09 % in the output power compared to rectangular channels. Recently, Paulino et al. [328] compared numerically rectangular, trapezoidal and stepped channels. The authors confirmed the findings of Freire et al. [148] in regard to water management. However, they pointed out that rectangular cross-sections guarantee an improved electric performance and might be beneficial to intermittent applications, for which water management issues do not appear. The findings of the previous researches highlighted that water management and in turn reactant distribution are critical in the regions of the cell located close to the outlet section. There, the high water content

due to the upstream electrochemical reactions may quickly lead to flooding. The regions connected to the inlet are rarely responsible for performance drops. Building on these observations, many authors in the last decade focused on the design of tapered channels, i.e. with a varying cross-section along the path from the inlet to the outlet. The concept was first investigated numerically by Yan et al. [478] and Liu et al. [272]. The authors reported performance improvements for both width tapering, i.e. channel width increasing along the streamline direction, and height tapering, i.e. channel height decreasing along the streamline direction. Liu et al [272] pointed out that the advantages due to tapering are most visible at high current densities and that the pressure losses are in generally negligible as compared to the gains in power generation. Similar conclusions can be drawn from the experiments reported recently in [444]. The tests conducted at low air humidity revealed a negligible influence of tapering, suggesting that water management is the primary performance benefit of this enhancement technique. Wang et al. [454] optimized the height of the channels of a serpentine configuration using 5 design variables. Their optimized geometry is composed of 3 tapered channels and a divergent channel connected to the outlet. According to the authors, the convergent portions of the flow field improve the advective transport of the reactants within the GDL. The divergent portion serves for the purpose of minimizing the reactant cross-leakages to the outlet. The authors reported an 11.9 % increase to the power generation as compared to a conventional non-tapered configuration. Fontana et al. [144] later considered a single convergent channel with constant inclination. Their results show that an inclination of 0.75° leads to a 9.5 % increase in the power generation but requires a 350 % higher pressure at the inlet. More recently, Mancusi et al. [288] reported interesting insights on two-phase flow in tapered channels. The authors observed a transition from a slug flow regime to a film flow regime at large tapering angles, which may lead to a performance degradation due to the reduced oxygen transport. This suggests that in general it is possible to identify an optimal tapering angle. The main findings of the reviewed literature dealing with the design of the channels and ribs in PEMFCs are summarized in Table 8.1.

Differently from tapering, blockages (also referred to as baffles or indentations) are sudden variations of the channel cross-section, leading to partial or complete flow obstructions. The proposal of these geometrical features for PEMFC performance enhancement builds on advancements in the field of convective heat transfer [206]. The increased advective transport along the x direction (Figure 8.1) improves water

Table 8.1. Summary of the reviewed literature on the channels and ribs design in PEMFCs

Parameter	Findings	References
Width ratio $\tilde{W}$	• improved reactants distribution for higher $\tilde{W}$; • larger ohmic losses for higher $\tilde{W}$.	[254, 482, 8, 241, 445, 488]
Height H_{ch}	• improved water management for smaller H_{ch}; • moderate increase of pressure drop for smaller H_{ch}.	[34, 445]
Shape	• best reactants distribution with triangular and hemispherical channels; • best water management with triangular channels; • minimal ohmic losses with rectangular channels.	[254, 135, 323, 148, 489, 328]
Tapering	• improved water management with both width and height tapering; • creation of water films impacting water management at large tapering angles.	[478, 272, 454, 144, 288, 444]

management, thermal management and the homogeneity of the reactants distribution [207]. However, this comes at the expense of increased pressure drops [160, 330]. This concept was early examined in the seminal paper of Liu et al. [273]. The authors observed that the insertion of partial blockages is beneficial in particular at low operating potentials. At high voltages, local current density reductions in the regions located downstream the baffle may decrease the performance. The authors of [206] studied how the performance is affected by the blockage ratio, defined as the ratio of the obstructed to the total cross-sectional area of the channel. Their results show that a 100 % blockage leads to a higher performance despite requiring a higher fan power. Perng and co-authors [330] explicitly considered the effect of blockages on pressure drop and searched for the optimal shape of trapezoidal baffles. The authors reported that indentations with sides tilted by $\pi/3$ with respect to the flow direction leads to a 90 % power increase as compared to a conventional non-blocked design. Similarly, Ghanbarian et al. [160] compared the effects of alternative indentation profiles. Their results indicate that a trapezoidal dent profile yields the highest increase in the net power output as compared to a reference non-dented channel. Rather than focusing on the geometry of a single indentation, Heidary et

Table 8.2. Summary of the reviewed literature on the blockages design in PEMFCs

Parameter	Findings	References
Blockage ratio	complete blockage is always superior to partial.	[206]
Shape	highest increase in power output with trapezoidal profiles.	[330, 160]
Distribution	under-rib transport enhanced with staggered arrangement	[206, 207]

al. [206, 207] studied how to distribute blockages in the flow field. Their numerical and experimental results suggest that a staggered arrangement may be superior to the most popular inline arrangement as both under-rib and under-block convection are exploited. The inline arrangement of blockages leads to a negligible under-rib transport due to the small pressure differentials among parallel channels. The main findings of the reviewed literature dealing with the design of blockages in PEMFCs are summarized in Table 8.2.

The search for the optimal flow field layout for PEMFCs is a long-standing engineering challenge. The topology of the channels mainly affects the reactant distribution, pressure drop and water management. The reviewed works presented in the remainder of this section did not reveal a substantial influence on the electrical resistance and mechanical stability as a minimum rib width is generally ensured. For high temperature systems, the minimization of the pressure drop and the homogeneous mass transfer to the active sites are the primary design criteria since water management is rarely an issue [491]. The variety of the heuristic solutions available and the amount of seemingly unconnected published literature on the topic makes this field quite similar to the design of heat transfer surfaces in the LHTES units discussed in Section 3.1. The reviewed geometries can be roughly grouped in five categories: serpentine, parallel, interdigitated, mesh and bio-inspired. Some representative schematics are shown in Figure 8.2. The serpentine layout (Figure 8.2(a)) is no doubt the most popular solution among practitioners [268]. In this design, water is forced through a unique channel that connects the inlet to the outlet, using a tortuous path that covers the entire active surface. Water clogging is rarely a problem and occurs mainly in U-bends at high current densities. The results presented by Wang et al. [455] indicate that this layout is particularly convenient for scale-up to

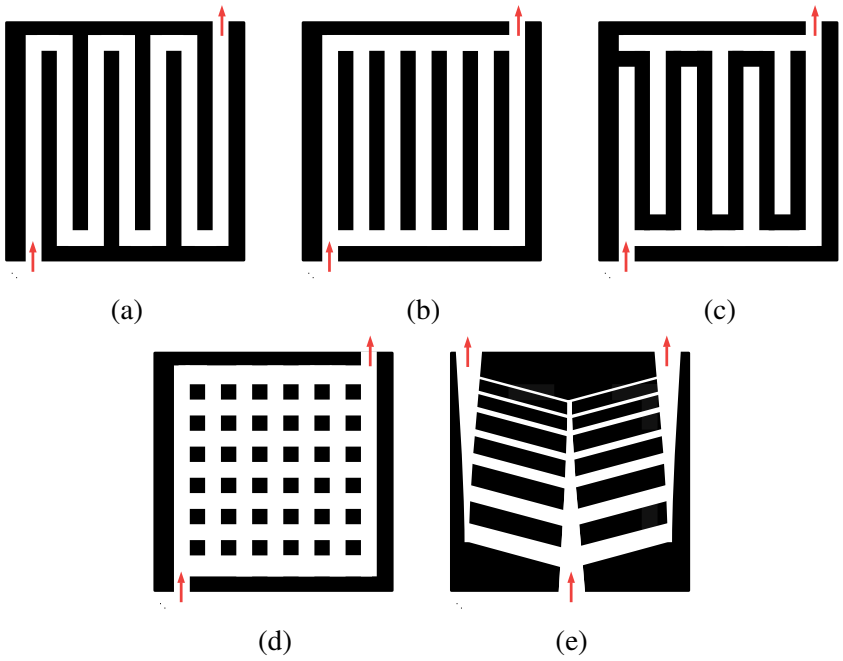

Fig. 8.2. Schematics of the most popular flow field geometries. The channels are indicated in white, the ribs are indicated in black; (a): serpentine; (b): parallel; (c): interdigitated; (d): mesh; (e): bio-inspired

commercial installations. An increase of the active area leads to a larger under-rib transport as a result of the higher pressure differential among contiguous channels. However, the recent experimental results of Chen et al. [85] suggests that this trend cannot be extrapolated in general as there should be an optimal pressure difference among contiguous channels for maximal power generation. The advantages of this configuration come at the expense of large pressure drops. Furthermore, Kahraman and Orhan [229] observed that the current density distribution may be critical due to a premature reactant depletion. To cure the issues of the reference design concept, research and technology developed in a number of different directions. A rather popular option is to use a multi-serpentine configuration in which the gas flows in a number of parallel serpentine-like paths [229]. An interesting alternative is the one proposed by Monsaf et al. [302], who used a concentric spiral layout, yielding increased mass transfer at reduced pressure drops. Alizadeh et al. [17] proposed a cascade layout, where three serpentine channels with different geometrical parameters are concatenated from the inlet to the outlet. In [234], an improved water removal was observed with the addition of porous carbon pins attached to the rib surfaces. Singdeo et al. [396] adopted a "compensated" arrangement, yielding a more uniform

reactant concentration in the central region of the cell for higher durability. Other authors, e.g. those of [376], reported an increased power density for serpentine wavy channels with sinuisodal width or convergent-divergent sections [89].

The parallel flow field layout (Figure 8.2(b)) consists of a number of straight channels aligned to the cell edges, connecting an inlet header to an outlet header. This solution guarantees a minimal pressure drop but is largely susceptible to performance degradations due to flooding [267]. As a result of an uneven flow distribution, water tends to accumulate in paths with smaller velocities, leading quickly to the formation of large stagnant areas [262]. The negligible pressure differentials among contiguous channels yields a limited under-rib transport [234]. The results of Taccani and Zuliani [412] for a high temperature PEMFC suggest that flooding might not be the only issue responsible for performance drops. The authors conjectured that the ineffective distribution of the reactants is mostly due to the creation of preferential flow paths. Furthermore, Wang et al. [455] noticed that water management degrades rapidly when the active area is increased, questioning the effectiveness of this layout for practical scale-up. The authors focusing on improvements to the parallel flow field concept are fewer in number than those that considered improved serpentine layouts [268]. Johnson et al. [225] proposed to use alternating convergent and divergent channels so that larger pressure differentials are created to boost under-rib convection. Ramos-Alvarado et al. [345] designed a parallel distributor with multiple stages of bifurcations leading to an improved power generation and reduced pressure drops. Similarly, Lim et al. [268] reported improved performance with multiple stages of distribution and Wang et al. [459] proposed to use small sub-channels connecting parallel paths. In the view of the authors, this strategy improves the water removal. Water management improvements in parallel flow fields were also considered by Imbrioscia et al. [217], who designed crafted baffles to limit water clogging and enhance the reactants distribution. Recently, Ashrafi et al. [34] showed that it is possible to eliminate the water plugs by a proper definition of the inclination angle of the channels.

Interdigitated flow fields (Figure 8.2(c)) can be seen as a modified version of the parallel layout with dead-end channels, where blockages are positioned close to the outlet and inlet headers in a staggered fashion. Recall that the blockages do not impede the flow completely. Due to the presence of the GDL underneath, the top horizontal header and the connected channels can be reached by under-rib motion of the reactants [267]. This mass transport mechanism prevents water flooding at

high current densities and yields a homogeneous reactants distribution [229]. The linear region of the polarization curve is extended so that mass transfer deterioration occurs at high current densities as compared to parallel and serpentine layouts [262]. However, a price should be paid in terms of large pressure drops and possible long-term damage of the GDL [229]. The research and technology improvements for interdigitated flow fields deal mainly with positioning and sizing of the blocking ribs. The most relevant strategies were already reviewed in this section when discussing the use of blockages for performance enhancement in PEMFC, see for instance [206, 207]. Note that due to layout similarities, these novel geometries are referred to as "modified parallel" or "modified interdigitated" with seemingly no distinction in literature.

The mesh flow field layouts (also referred to as grid or pin flow fields) (Figure 8.2(d)) consists of a regular grid of pins protruding from the BPP that creates an intricate groove of flow patterns when in contact with the GDL. Arvay et al. [32] argued that mesh layouts can be considered as a special case of parallel layouts in which the effect of water clogging is reduced without creating additional pressure drops. However, the creation of preferential flow paths quickly leads to a poor reactant distribution and water removal [229]. Furthermore, since in most cases PEMFCs are operated in laminar flow regimes, stable recirculation zones appear downstream each pin, creating regions with large reactant depletion [262]. Wang [450] observed that the ineffective distribution of the reactants "is not inherent but is a poor design." The authors [448] suggested to use different channel widths in the streamline and crosswind directions so that the flooded regions can be easily bypassed and large pressure differentials are created to remove the water plugs. Guo et al. [184] optimized the channel widths in a pin-type flow field adopting a network model similar to the one presented in Chapter 7. Their optimized design solved issues related to the poor distribution of the reactants and dramatically improved the performance of the reference mesh geometry. Lobato et al. [276, 277] pointed out that pin-type flow fields may be convenient for a high temperature PEMFC, where water management is not an issue. Their numerical and experimental analysis revealed that the polarization performance of pin-type flow fields is close to that of a serpentine flow field with slight drops at high current densities. The authors noted that current density and temperature inhomogeneities are diminished, promoting the durability of the cell [277].

Recently, nature-inspired flow field designs started mimicking some flow distribution systems that are found in nature such as lungs [247] and leaves [359, 106]. Roshandel et al. [359] were among the first to investigate the nature-inspired route for the design of BPPs in PEMFCs. The authors compared a leaf-like design to a lung-like design, reporting a higher performance for the first option. Later, Roshandel et al. [359] conducted a numerical study on a similar leaf geometry and revealed an increase to the power density of 56 % and 26 % with respect to parallel and serpentine layouts. Also Ruan et al. [361] proposed a "bio-mimetic" flow field that builds on observations of leaves flow patterns. A simplified version of their layout is presented in Figure 8.2(e). The diameters of the channels were selected according to the Murray's law. Their numerical experiments predicted an improved current density, pressure drop and thermal and water management as compared to serpentine and parallel layouts. The authors of [106] adopted a formal statistical framework to analyze the flow distribution patterns in leaves and compared a single-bifurcation layout with a double-bifurcation layout. Their results indicate that using two bifurcations yields a more uniform reactants distribution and in turn improves performance. However, the authors gave no indication on water management or pressure drop issues. A different bio-inspired configuration mimicking leaf veins was tested in [185] through numerical and experimental means. The results revealed a 25 % improvement to the power density with respect to a parallel layout. However, the pressure drop was increased by a factor of 20. The authors compared a fixed-width channel layout with a varying-width alternative obtained from the Murray's law and found that thickness plays only a minor role. Another leaf-like geometry was recently tested experimentally by Saripella et al. [369]. The authors reported that the interdigitated nature of their option leads to an effective water removal and a high under-rib transport as compared to a conventional single serpentine design. Arvay et al. [33] considered several pitchfork-like designs with branching patterns derived from the Murray's law. Their numerical results show that an increase of the number of branches leads to smaller pressure drops with little influence on the generated power. All their designs were found superior to conventional parallel and serpentine alternatives.

To sum up, the main features of the flow fields reviewed in this section are collected in Table 8.3.

Table 8.3. Summary of the main features of the reviewed flow fields for PEMFCs

Geometry	Features
Serpentine	• reduced formation of water clogs; • chance of premature reactant depletion; • large pressure drop.
Parallel	• performance degradation due to flooding; • uneven reactants distribution; • small pressure drop.
Interdigitated	• flooding prevented; • homogeneous reactants distribution; • highest pressure drop.
Mesh	• reduced consequences of flooding; • poorest reactants distribution; • minimal pressure drop.
Bio-inspired	• many heuristic alternatives; • generally improved water management and reactants distribution; • leaf-like options superior to lungs-like ones.

8.2 Physical model

Here, we give an overview of the theoretical and computational tools developed to compute the fluid-dynamic and electrochemical response of the system. First, we introduce the approach we used to reduce the analysis of a three-dimensional problem in 2D. Then, we present the governing equations that rule mass transport and electrochemistry along with the suitable boundary conditions. Last, we introduce the spatial discretization and numerical solution methods that we adopted.

8.2.1 Depth-averaging

In this chapter, we consider only the cathodic portion of the cell, which is the one showing the highest performance limitations [81]. We aim at finding an optimized layout of rectangular gas channels of height H_{bpp} in the BPP. Due to its computational complexity, topology optimization greatly benefits from analyses in reduced dimensionality. However, choosing a representative plane is not a trivial problem since the 3D transport effects are non-negligible. Considering a plane that crosses the GDL (such as π_3 in Figure 8.1) does not allow the effect of the flow field geometry to be considered. Choosing plane π_1 (Figure 8.1) would result in an inaccurate fluid response, as visible in Figure 8.3(a). The impermeable graphite ribs filling Ω_{rib} would suppress the flow across contiguous channels. However, as shown in Figure 8.3(c), mass transport across contiguous channels in 3D is possible thanks to the under-rib flow. For this reason, we use an averaging procedure that is inspired by [205]. Figure 8.3(c) shows a schematic representation of the process. We consider two RVEs stretched along the z direction so that they span the entire depth of the GDL and BPP. One comprises the channel and GDL, the other comprises the rib and GDL. We aim at obtaining two equivalent two-dimensional porous media, yielding the same transport response of the 3D system. This reduces to the calculation of the equivalent porosity $\bar{\varepsilon}_p$, permeability $\bar{\kappa}$ and species diffusivity $\bar{D}$. Similarly to homogenization (see Section 4.2), a formal averaging requires that the size of the RVE, T, is much smaller than the size of the macroscopic domain, Ω_D. This condition does not hold here as the depth of our RVEs corresponds to the macroscopic dimension. For this reason, in this chapter we follow a heuristic and simplified treatment following the conventional engineering practices. This approach will be verified in Section 8.4.1. For stratified media with the main transport direction aligned with the strata, we can

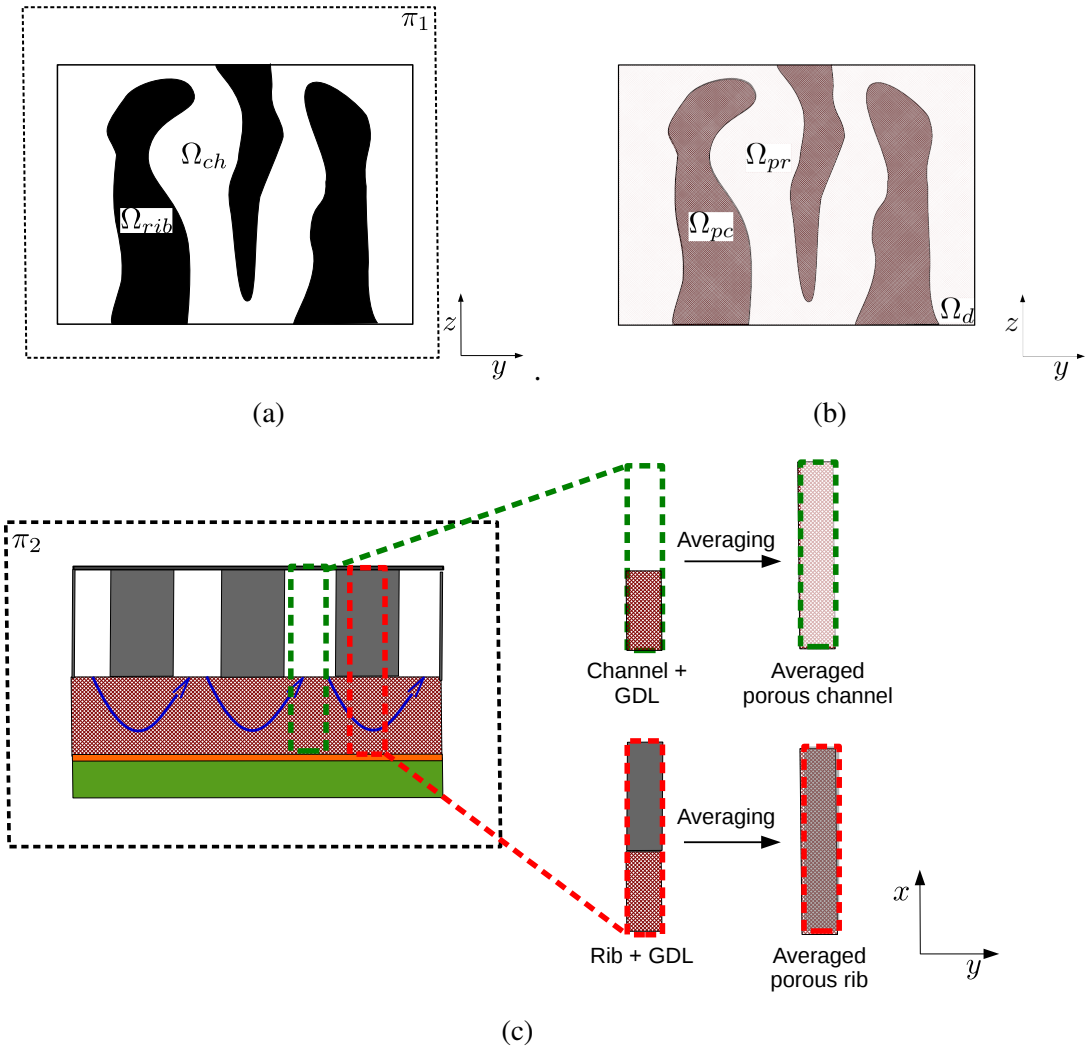

Fig. 8.3. (a): 2D plane leading to incorrect transport predictions; (b): final analysis and design domain; (c): averaging procedure

consider a simple depth-weighted mean of the transport properties [351] $\bar{\kappa}$ and $\bar{D}$. As the porosity is a bulk property (recall the discussion for c_p and $\mathscr{L}$ homogenization in Section 4.2), the same approach can be followed for the calculation of $\bar{\varepsilon}_p$. Hence, for all the properties we write:

$$\bar{(\cdot)} = \frac{(\cdot)_{gdl} H_{gdl} + (\cdot)_{bpp} H_{bpp}}{H_{bpp} + H_{gdl}}, \tag{8.2}$$

where $\bar{(\cdot)}$ indicates a generic averaged property for each of the equivalent porous media, H denotes the depth along the x direction and the subscripts "bpp" and "gdl" denote the BPP and the GDL, respectively. The property of the BPP, $(\cdot)_{bpp}$, can correspond to the one of the channels, $(\cdot)_{ch}$, or the one of the rib, $(\cdot)_{rib}$. In the former case we obtain an averaged property corresponding to a "porous channel", $\bar{(\cdot)}_{pc}$; in the latter case, we obtain an averaged property corresponding to a "porous rib", $\bar{(\cdot)}_{pr}$. This procedure leads to the computational and design domain depicted in Figure 8.3(b). It is subdivided into two non-overlapping sub-domains, Ω_{pc} and Ω_{pr}, such that $\Omega_D = \Omega_{pc} \cup \Omega_{pr}$, where Ω_{pc} and Ω_{pr} refer to the portions of the design domain occupied by the "porous channel" and the "porous rib", respectively.

8.2.2 Governing equations

The governing equations for the flow and transport in porous media can be derived from a formal averaging of the conservation laws over a RVE, with size much larger than the pore scale and much smaller than the characteristic dimensions of the flow. Due to the presence of the solid phase, a distinction should be made between two types of flow velocities. Averaging over a RVE that includes only the fluid phase leads to the intrinsic velocity $\tilde{v}_i$. Averaging over a RVE that includes both the fluid and solid phases leads to the superficial velocity v_i. The ratio between these quantities is given by the porosity of the medium ε_p using the Dupuit-Forchheimer equation (5.8). Considering a constant porosity and a steady-state incompressible flow, the continuity equation in porous media can be written directly as a function of the superficial velocity:

$$\frac{\partial v_i}{\partial x_i} = 0, \tag{8.3}$$

The momentum equation considered for the liquid PCM (5.7) can be reworked into:

$$\frac{1}{\varepsilon_p(s)^2}\left(\rho v_j \frac{\partial v_i}{\partial x_j}\right) = -\frac{\partial p}{\partial x_i} + \frac{1}{\varepsilon_p(s)}\left(\frac{\partial}{\partial x_j}\left(\mu\left(\frac{\partial v_i}{\partial x_j}+\frac{\partial v_j}{\partial x_i}\right)\right)\right) + F_{pois_i} + F_{b_i}(s) = 0, \tag{8.4}$$

where F_{pois} is a momentum sink accounting for the out-of-plane velocity gradients (Equation (5.75)) and $F_{b_i}(s)$ is the design-dependent portion of the Brinkmann sink (Equation (5.78)). Both terms were introduced in Section 5.3.1 when presenting alternative material interpolation strategies for fluid topology optimization. Equation (8.4) can be derived by restricting the averaging over the fluid portion of the RVE. Note that the porosity of the medium $\varepsilon_p(s)$ is a design-dependent property. The material interpolation strategies are discussed in Section 8.3.2. The transport of the chemical species in the cell is modeled through an advection-diffusion-reaction equation:

$$H_{tot}\rho v_i \frac{\partial \omega_k}{\partial x_i} = H_{tot}\frac{\partial j_{k_i}(s)}{\partial x_i} + R_k, \tag{8.5}$$

where ω_k is the mass fraction of the k^{th} chemical species, $j_{k_i}(s)$ is a design-dependent diffusive flux, $H_{tot} = H_{ch} + H_{bpp}$ is the depth of the electrode and R_k is the rate of the species generation due to electrochemical reactions. Eq. (8.5) is obtained considering a RVE that includes both the solid and fluid phase. Diffusion is modeled through a mixture-averaged formulation:

$$j_{k_i}(s) = \rho f_D(s) D_k^m \frac{\partial \omega_k}{\partial x_i} + \rho \omega_k f_D(s) D_k^m \frac{1}{M^m}\frac{\partial M^m}{\partial x_i}, \tag{8.6}$$

where $f_D(s)$ is a design-dependent diffusivity correction, M^m is the average molar mass, and D_k^m is calculated using the mixture-averaged diffusion model given by the Wilke relation [236]:

$$D_k^m = \frac{1-\omega_k}{\sum\limits_{\substack{k=1\\k\neq j}}^{n_s}\frac{\omega_k}{D_{kj}}}, \tag{8.7}$$

where n_s is the number of chemical species involved and D_{kj} represents the Maxwell-Stefan diffusivity tensor. The mixture-averaged diffusion model yields computational savings as compared to the full Maxwell-Stefan formulation in that the diffusion fluxes are explicitly dependent on the species gradients. Although Krishna and Wesselingh [252] pointed out that Eq. (8.7) can be used only in case of stagnant

non-transferring mixtures, it is rather popular in the fuel cell community [143]. The results presented in [270] suggest that the choice of the diffusion model for the analysis of the PEMFC cathode yields negligible perturbations to the response predictions. Anyway, we will test the validity of this assumption in Section 8.4.1. We solve Eq. (8.6) for $n_s - 1$ species. The mass fraction of the remaining chemical species is obtained using:

$$\omega_{n_s} = 1 - \sum_{i=1}^{n_s-1} \omega_i. \tag{8.8}$$

The reaction term in Eq. (8.5) is written as:

$$R_k = \frac{M_k \nu_k i_{loc}}{n_e F}, \tag{8.9}$$

where M_k is the molar mass, ν_k is the stoichiometric coefficient of the reaction, n_e is the number of participating electrons, and F is the Faraday constant. The local current density, i_{loc}, is calculated through the Butler-Volmer equation [81]:

$$i_{loc} = i_0 \frac{C_{O_2}}{C_{O_{2_{\text{ref}}}}} \left(\exp\left(\frac{\alpha_C}{R_g T} F \eta_c \right) - \exp\left(-\frac{1-\alpha_C}{R_g T} F \eta_c \right) \right), \tag{8.10}$$

where α_C is the cathodic charge transfer coefficients, T is the temperature, R_g is the ideal gas constant, C_{O_2} is the oxygen molar concentration and $C_{O_{2_{\text{ref}}}}$ its reference value, i_0 is the exchange current density referred to the area of the PEM, and η_c is the cathode overpotential. Predicting the electrochemical response by (8.10) carries the assumption that the concentration of protons, electrons and water does not limit the reaction rate [319]. The cathode overpotential is calculated as follows [258]:

$$\eta_c = V_{OC} - V_{cell} - R_o i_{loc}, \tag{8.11}$$

where V_{cell} is the prescribed operating voltage of the cell, V_{OC} is the open-circuit voltage and R_o is the Ohmic resistance accounting for charge transport through the membrane and both the electrodes. The relevant physical parameters and properties are listed in Table 8.4. The boundary conditions and characteristic dimensions of the considered domain are summarized in Figure 8.4. We prescribe a fully developed flow at Γ_{out} and a symmetry boundary condition along Γ_{sym} such that:

$$-\frac{\partial \omega_k}{\partial x_i} n_i = 0 \qquad \text{on} \quad \Gamma_{out} \cup \Gamma_{sym}, \tag{8.12}$$

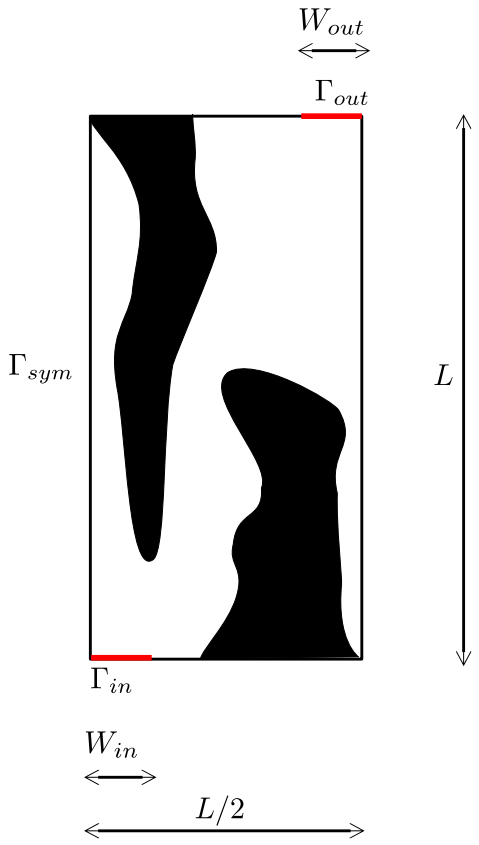

Fig. 8.4. Design domain and boundary conditions

Table 8.4. Relevant physical parameters and properties

Description	Symbol	Value	Unit
number of chemical species	n_s	3	–
number of participating electrons	n_e	4	–
molar mass H_2O	M_{H_2O}	18	g/mol
molar mass N_2	M_{N_2}	28	g/mol
molar mass O_2	M_{O_2}	32	g/mol
stoichiometric coefficient H_2O	ν_{H_2O}	2	–
stoichiometric coefficient N_2	ν_{N_2}	0	–
stoichiometric coefficient O_2	ν_{O_2}	-1	–
universal gas constant	R_g	8.3144	J/mol K
Faraday constant	F	96485.3	C/mol

where n is the outward-pointing normal. The chemical composition of the mixture at the inlet section is known such that:

$$\omega_k = \omega_{k_{in}} \qquad \text{on} \quad \Gamma_{in}, \tag{8.13}$$

where $\omega_{k_{in}}$ is the prescribed mass fraction at the inlet. A no-slip condition is prescribed on the sealing gasket wall. Due to symmetry, only non-penetration is prescribed along the symmetry axis such that:

$$v_i = \mathbf{0} \qquad \text{on} \quad \Gamma_{sg}, \tag{8.14}$$

$$v_i n_i = 0 \qquad \text{on} \quad \Gamma_{sym}, \tag{8.15}$$

where $\Gamma_{sg} = \Gamma_{tot} / (\Gamma_{sym} \cup \Gamma_{in} \cup \Gamma_{out})$ with Γ_{tot} representing all the boundaries of the design domain. For our design optimization studies, a normal stress condition augmented with a nil tangential velocity condition is prescribed at the inlet as follows:

$$n_i \sigma_{ij} n_j = F_{in} \qquad \text{on} \quad \Gamma_{in}, \tag{8.16}$$

$$v_i t_i = 0 \qquad \text{on} \quad \Gamma_{in}, \tag{8.17}$$

where t_i is a unit vector tangent to the boundary. Note that Eq. (8.16) well approximates an inlet pressure condition for low-viscosity fluids. For our calibration and verification studies, we consider also an alternative inlet condition with fixed flow

rate:

$$v_i n_i = \frac{V_{in}}{H_{tot} W_{ch}} \qquad \text{on} \quad \Gamma_{in}, \tag{8.18}$$

where V_{in} is the inlet volumetric flow rate. The condition (8.18) is augmented with the nil tangential velocity constraint (8.17). Vanishing normal and tangential stresses are prescribed at the outlet such that:

$$\sigma_{ij} n_j = \mathbf{0} \qquad \text{on} \quad \Gamma_{out}. \tag{8.19}$$

8.2.3 Finite element model

Equations (8.3), (8.4) and (8.6) are discretized in space using a mixed finite element model. Following the procedure described in Sections 3.3.2 and 5.2.1, the weak form of the governing equations is obtained by multiplying the residual of the strong form with a set of admissible test functions and integrating over the domain. The approximation and weighting functions for pressure and velocities were defined in (5.31) and (5.32). The approximation and weighting functions for transport of chemical species, ω_k, are defined in a similar way to what we have done for energy transport in (3.36) and (3.37):

$$\mathscr{U}_\omega = \{\omega_k^h \in \mathscr{H}^1(\Omega);\ \omega_k^h = \omega_{k_{in}}^h \text{ on } \Gamma_{in}\}, \tag{8.20}$$

$$\mathscr{V} = \{w^h \in \mathscr{H}^1(\Omega);\ w^h = 0 \ \text{ on } \Gamma_{in}\}, \tag{8.21}$$

where ω_k^h represents the approximate mass fraction field, and w^h is the weighting function of the advection-diffusion-reaction equation (8.6). The function spaces $\mathscr{U}_\omega$ and $\mathscr{V}$ are Hilbert spaces consisting of scalar functions with square integrable first derivatives. We write all the unknown fields as a product of spatially varying shape functions and nodal values. For pressure and velocities we use (5.33) and (5.34) and neglect time-dependence. For the mass fractions, we write:

$$\omega_k^h(\mathbf{x}) = \sum_{i=1}^{N_n} \omega_{k_i} N_i(\mathbf{x}) = \mathbf{N}^T \boldsymbol{\omega}_k, \tag{8.22}$$

where $\boldsymbol{\omega}_k$ is the column vector of nodal mass fraction values of the chemical species "k". The weight functions are chosen equal to the shape functions as in the Galerkin method. With these assumptions, we recover the unstabilized Galerkin model of

the Navier-Stokes equations presented in (5.35) and (5.36) with $\mathbf{M}_j = \mathbf{0}$ and where the definition of $\mathbf{A}_m$, $\mathbf{D}_{ij}$ and F_i is modified as follows to account for flow in porous media:

$$\mathbf{A}_m = \int_\Omega \frac{\rho}{\varepsilon_p^2} \boldsymbol{\xi}^h (\boldsymbol{\xi}^{h^T} \mathbf{v}_j) \frac{\partial \boldsymbol{\xi}^{h^T}}{\partial x_j} d\mathbf{x}, \tag{8.23}$$

$$\mathbf{D}_{ij} = \begin{cases} \int_\Omega \frac{\mu}{\varepsilon_p} \left(2 \frac{\partial \boldsymbol{\xi}^h}{\partial x_i} \frac{\partial \boldsymbol{\xi}^{h^T}}{\partial x_i} + \frac{\partial \boldsymbol{\xi}^h}{\partial x_l} \frac{\partial \boldsymbol{\xi}^{h^T}}{\partial x_l} \right) d\mathbf{x} & \text{for } j = i, l \neq i \\ \int_\Omega \frac{\mu}{\varepsilon_p} \left(\frac{\partial \boldsymbol{\xi}^h}{\partial x_i} \frac{\partial \boldsymbol{\xi}^{h^T}}{\partial x_j} \right) d\mathbf{x} & \text{for } j \neq i \end{cases}, \tag{8.24}$$

$$\mathbf{F}_i = \int_\Omega \boldsymbol{\xi}^h \left(F_{pois_i} + F_{b_i} \right) d\mathbf{x} + \int_{\Gamma_N} \boldsymbol{\xi}^h f_i d\mathbf{x}'. \tag{8.25}$$

Considering nil boundary diffusion fluxes as motivated in the previous section, the residual vector of the unstabilized Galerkin model of the advection-diffusion-reaction equation (8.6) is written as following:

$$\mathbf{R}_{\omega_{us}} = \mathbf{A}_\omega \boldsymbol{\omega}_k + \mathbf{K}_{kl} \boldsymbol{\omega}_l - \mathbf{R}_k = \mathbf{0}, \tag{8.26}$$

where:

$$\mathbf{A}_\omega = \int_\Omega H_{tot} \rho \mathbf{N} (\boldsymbol{\xi}^{h^T} \mathbf{v}_j) \frac{\partial \mathbf{N}}{\partial x_j} d\mathbf{x}, \tag{8.27}$$

$$\mathbf{K}_{kl} = \begin{cases} \int_\Omega H_{tot} \rho f_D D_k^m \left(1 + \frac{1}{M^n} \frac{\partial M^n}{\partial \omega_l} \right) \frac{\partial \mathbf{N}}{\partial x_i} \frac{\partial \mathbf{N}^T}{\partial x_i} d\mathbf{x} & \text{for } l = k \\ \int_\Omega H_{tot} \rho f_D D_k^m \frac{1}{M^n} \frac{\partial M^n}{\partial \omega_l} \frac{\partial \mathbf{N}}{\partial x_i} \frac{\partial \mathbf{N}^T}{\partial x_i} d\mathbf{x} & \text{for } l \neq k \end{cases}, \tag{8.28}$$

$$\mathbf{R}_k = \int_\Omega \mathbf{N} R_k \, d\mathbf{x}. \tag{8.29}$$

We use four-node quadrilateral finite elements to discretize the computational domain. The velocity, pressure and mass fractions are approximated by bilinear equal-order interpolations. As discussed in Section 5.2.2, using equal-order approximation functions for the velocity and pressure does not satisfy the Babuska-Brezzi condition and leads to spurious oscillations in the pressure field [213]. Furthermore, high Peclet numbers and sharp crosswind gradients may result in overshoots and undershoots in the concentration field, leading to an non-physical response [419]. To prevent these numerical instabilities, the residuals of the weak form of the governing equations

are augmented with consistent stabilization terms corresponding to Galerkin Least Squares (GLS) [203] and Cross-Wind Diffusion (CWD) [92]. Since in this chapter we adopt a commercial code [101] for the analyses, we will not discuss further details about the stabilization approaches. The nonlinear system of equations are solved with a damped Newton's method with damping coefficient set to 0.7. The discretized nonlinear problem is considered converged if the absolute residual norm drops below 10^{-7}. The linear systems of equations arising at each Newton's iteration are solved with the MUltifrontal Massively Parallel sparse direct Solver (MUMPS) [26].

8.3 Design optimization problem

In this section, we introduce the optimization problem formulation adopted for the design of the PEMFC flow fields. First, we define and discuss the objective and constraints. Then, we present our strategy to interpolate the material properties between the values obtained through our depth-averaging procedure (8.2). Last, we give details related to the numerical solution.

8.3.1 Objectives and constraints

We aim at distributing the reactant over the active sites in such a way that the most homogeneous current density field is created and the highest power generation is obtained at limited pressure drop. As discussed in Section 8.1, a non-uniform current density distribution is responsible for thermal stresses of the membrane, leading to both performance and material degradation [289, 32]. We consider two optimization criteria: the standard deviation, $\theta_{i_{loc}}$, of the current density distribution and the power output of the cell. We formulate the multi-objective optimization problem using a penalty method as follows:

$$\begin{aligned} \underset{\mathbf{s}}{\text{minimize}} \quad & \frac{w_\theta}{\theta^0_{i_{loc}}}\theta_{i_{loc}} - \frac{w_{\bar{W}}}{\bar{W}^0}\int_{\Omega_D} V_{cell} i_{loc}\, d\mathbf{x} \\ \text{subject to} \quad & \int_{\Omega_D} \rho_s\, d\mathbf{x} \leq V^* \\ & \mathbf{s} \in \mathbf{S} = \left\{ \mathbb{R}^{N_s} \mid s_{min} \leq s_i \leq s_{max},\ i = 1,\dots,N_s \right\} \end{aligned} \quad , \tag{8.30}$$

where $\rho_s = \bar{s}$ is the projected elemental design variable that is obtained from the nodal abstract design variable field, $\mathbf{s}$, using the linear filtering (2.37) and the exponential projection (2.38) [176], w_θ is the weighting factor for the standard deviation of the current density, $\theta^0_{i_{loc}}$ is the initial standard deviation of the current density, $w_{\bar{W}}$ is the weighting factor for the generated power, and $\bar{W}^0$ is the initial measure of the generated power. Note that the maximization of power requires a negative sign for the second term of the objective. The volume constraint prescribes that the total volume occupied by the "porous channels" (Figure 8.3(c)) is less than a prescribed value, V^*. The design sensitivities are computed using the discrete adjoint method presented in Section 2.3.2.

8.3.2 Material interpolation

A continuous transition from the "porous rib" to the "porous channel" (Figure 8.3(c)) is allowed using the physical design variable, ρ_s. We consider the "porous channel" and the "porous rib" as represented by $\rho_s = 1$ and $\rho_s = 0$, respectively. The Brinkman constant, α_b, is interpolated using (5.80) [13, 16]. Differently from the problems considered in Chapter 5, here α_{max} has a clear physical meaning. It serves for the purpose of recovering a porous media flow in the "porous rib" portion of the design domain. It is calculated as following:

$$\alpha_{max} = \bar{\alpha}_{b_{pr}} = \frac{\mu}{\bar{\kappa}_{pr}}, \tag{8.31}$$

where $\bar{\kappa}_{pr}$ is the equivalent permeability of the "porous rib" calculated using (8.2). Since $\bar{\kappa}_{pc} = \infty$, we would recover $\alpha_b = \bar{\alpha}_{b_{pc}} = 0$ in the "porous channel" and there is no need to account for a α_{min}. The design-dependent diffusivity correction, f_D, is interpolated using the SIMP law:

$$f_D(\rho_s) = \bar{f}_{D_{pr}} + (\bar{f}_{D_{pc}} - \bar{f}_{D_{pr}})\rho_s^p, \tag{8.32}$$

where p is the SIMP exponent, $\bar{f}_{D_{pr}}$ is the diffusivity correction factor of the "porous rib" and $\bar{f}_{D_{pc}}$ is the diffusivity correction factor of the "porous channel". These quantities are computed using the averaging law (8.2). The diffusivity factor in the GDL, $f_{D_{gdl}}$, is obtained from its porosity through the Bruggeman approximation

[81]:

$$f_{D_{gdl}} = \varepsilon_{p_{gdl}}^{3/2}. \tag{8.33}$$

The porosity is interpolated linearly as follows:

$$\varepsilon_p(\rho_s) = \bar{\varepsilon}_{p_{pr}} + (\bar{\varepsilon}_{p_{pc}} - \bar{\varepsilon}_{p_{pr}})\rho_s, \tag{8.34}$$

where $\bar{\varepsilon}_{p_{pr}}$ and $\bar{\varepsilon}_{p_{pc}}$ are the equivalent porosities of the "porous rib" and of the "porous channel" calculated using (8.2).

8.3.3 Numerical implementation

The optimization problems presented in this chapter are solved using GCMMA. As compared to Table 2.1, we modify the relative step-size to $\Delta s = 0.01$. To discourage oscillatory behaviors for a large curvature of the regularization, β, the position of the initial asymptotes is modified using the formulation proposed by [178]. A continuation on the convexity factors, q_α and p, is used to ensure a smooth evolution of the design and a stable convergence to satisfactory solutions. These parameters are modified during the optimization convergence as follows:

$$\begin{aligned} p &= \{1;\ 2;\ 3;\ 5\}, \\ q_\alpha &= \{10^4; 10^3; 10^2; 10^1\}. \end{aligned} \tag{8.35}$$

The projection steepness parameter is kept constant at $\beta = 50$. The transition to the next continuation step is performed every 60 iterations. The optimization procedure ends when all the continuation steps are completed. The convergence of the optimization process is verified after the final step. The optimization problem investigated in this chapter has similarities with the forced convection design example described in Section 5.4.2. The continuation trajectories should be chosen carefully to avoid a strong imbalance between convective and diffusive transport at all continuation steps. For inlet pressures higher than $F_{in} > 4$ Pa, we observed that strategy (8.35) leads to oscillations in the objective history; for $F_{in} > 20$ Pa we also obtained unsatisfactory local minima. Skipping the first continuation step fixed the issue, yielding both a stable convergence and solutions with superior performance. For this reason, for all design studies with $F_{in} > 4$ Pa, only the last three continuation steps are considered.

Table 8.5. Material properties and model parameters adopted from [197]

Description	Symbol	Value	Unit
membrane length	L	2.236×10^{-2}	m
channel width	W_{ch}	1.8×10^{-3}	m
channel depth	H_{ch}	1.8×10^{-3}	m
GDL depth	H_{gdl}	0.2×10^{-3}	m
open-circuit voltage	V_{OC}	1.22	V
ohmic resistance	R_o	7×10^{-5}	$\Omega \cdot \mathrm{m}^2$
cell temperature	T	343.15	K
oxygen reference concentration	$C_{O_{2_{\mathrm{ref}}}}$	30	$\mathrm{mol}/\mathrm{m}^3$
inlet flow rate	V_{in}	2×10^{-6}	m^3/s
cathodic transfer coefficient	α_c	0.5	–
porosity of the GDL	ε_{GDL}	0.8	–
inlet water mass fraction	ω_{H_2O}	0.1	–
inlet oxygen mass fraction	ω_{O_2}	0.9	–
dynamic viscosity	μ	2.07×10^{-5}	$\mathrm{Pa} \cdot \mathrm{s}$
oxygen diffusivity in water	D_{O_2,H_2O}	5.88×10^{-5}	m^2/s

8.4 Numerical results and design trends

In this section, we present and discuss the numerical results and design trends obtained. First, we calibrate a 3D physical model to a real system and verify the accuracy of our depth-averaging procedure by comparing 2D and 3D predictions. Then, we consider a reference design case with $F_{in} = 5$ Pa and compare its performance with conventional flow field layouts. Last, we investigate the effect of the inlet pressure and current standard deviation weight on the optimized designs and performance.

8.4.1 Calibration and verification of the analysis model

For calibration and verification purposes, we consider the high temperature PEMFC system investigated by [197]. It consists of the serpentine flow field with seven channels schematically shown in Figure 8.5. The relevant parameters and properties are summarized in Table 8.5. The system is alimented by a mixture of oxygen and water using a fixed flow rate. Hence, we set $n_s = 2$ and the velocity inlet boundary condition according to (8.18). Also, it is not possible to exploit symmetry in this numerical

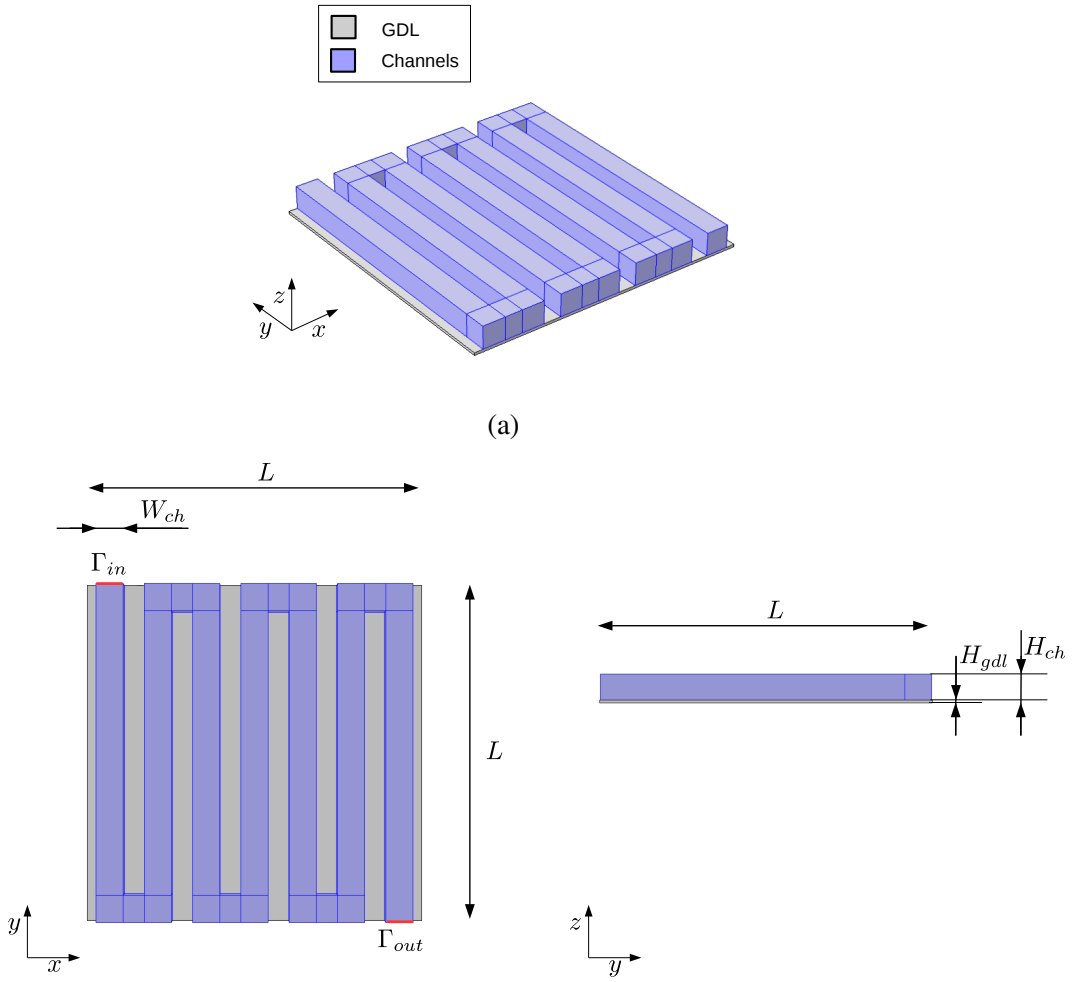

Fig. 8.5. Schematic representation of the 3D numerical study conducted for calibration and verification purposes. (a): 3D view; (b): top view; (c): side view

Table 8.6. Mesh convergence verification. The deviation is calculated with respect to a reference case with $\Delta h = 1.8$ mm

Mesh size Δh [mm]	2D deviation [%]	3D deviation [%]
7.2	5.68	4.50
4.5	1.97	0.74
2.7	0.64	0.27

example, i.e. $\Gamma_{sym} = \emptyset$. We developed both a full 3D model and a reduced 2D model with properties computed through the averaging procedure described in Section 8.2.1. The 3D and 2D computational domains are meshed using free tetrahedral and free quadrilateral elements with characteristic size $\Delta h = 2.7$ mm. This value is selected after a convergence study on the outlet oxygen flow rate obtained with $V_{cell} = 0.4$ V by comparing the predictions against those computed on a reference mesh with $\Delta h = 1.8$ mm. The results are summarized in Table 8.6. For the 3D numerical study, the mesh characteristic size in the GDL is computed as $\Delta h_{gdl} = \max\left(\Delta h/25,\ H_{gdl}\right)$. In [197], the electrochemistry at the anode was modeled using the Butler-Volmer equation and at cathode using a simplified Tafel equation [319]. To calibrate the model, the authors fitted the exchange current density to their experimental results. As our framework does not consider electrochemistry at the anode, we re-calibrate the exchange current density to their numerical results using a least-square fitting. For this process, we neglect the effect of the reactants concentration in (8.10). The computed value is $i_0 = 0.17$ A/m^2. The polarization curves obtained using a full 3D and our reduced 2D analysis frameworks are compared to the numerical and experimental results of [197] in Figure 8.6. This trend is obtained by sweeping the operating voltage of the cell, V_{cell}, in 10 steps from 0.2 V to 0.9 V and computing the average current density over the active area. Our 3D framework yields a mean relative deviation from the experimental and numerical results of 11.53 % and 3.03 %, respectively. Most of the error is computed for $V_{cell} \geq 0.7$ V, which is far from the practical operating conditions of the cell targeting a peak power generation ($V_{cell} \sim$ 0.4 V). For $0.3\ V \leq V_{cell} \leq 0.5\ V$, we observe a satisfactory match between our 3D model and the numerical and experimental results of [197]. This indicates that our calibrated model is able to predict the electrochemical response of a real cell with sufficient accuracy in practical operating conditions. The polarization curve obtained using the 2D model closely approximates the one obtained in 3D. Although at low operating voltages we observe a slight overestimation of the generated current, we

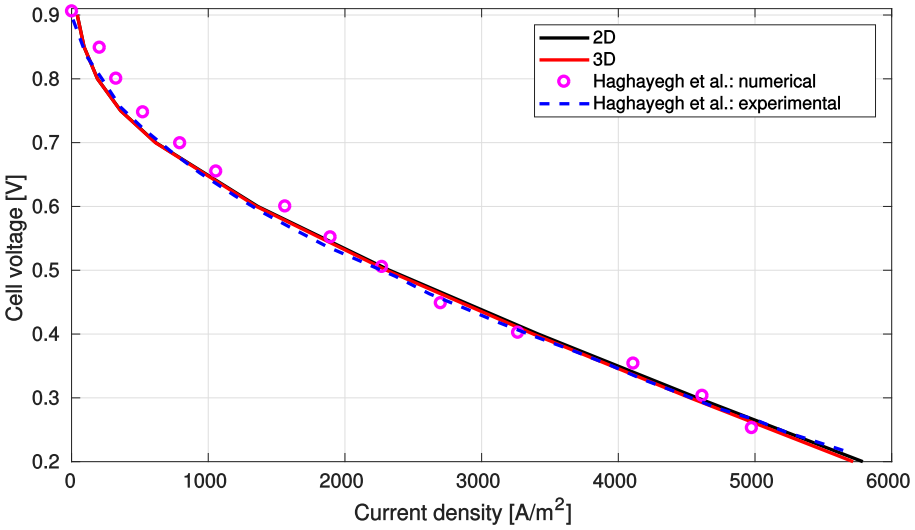

Fig. 8.6. Polarization curves obtained with the 2D and 3D models versus the experimental and numerical results of [197]

report a mean relative deviation of 0.65 %. This suggests that the oxygen distribution fields computed through the 2D and the 3D frameworks are comparable.

The most relevant state variable fields obtained using the 2D and 3D frameworks are qualitatively compared in Figure 8.7, for $V_{cell} = 0.4$ V. In 3D, we show the response distribution over two planes. In the portion of the domain occupied by the ribs, we consider plane π_3 (Figure 8.1) located at half-depth of the GDL. In the portion of the domain occupied by the channels, we consider plane π_1 located at half-depth of the BPP (Figure 8.1). The oxygen mass fraction field (Figure 8.7(a)) computed with the two frameworks is qualitatively similar. The oxygen concentrates mainly along the channels. Local minima are observed in correspondence of the ribs since the limited convection and diffusion leads to a higher reactant depletion. The 3D model predicts a minimum oxygen fraction on π_3 of 0.72 in a GDL region close to the outlet. Due to our depth-averaging procedure, this value is overestimated in the 2D model, leading to a higher current density generation. This mild trend is observable also in the polarization curve presented in Figure 8.6. The velocity fields are compared in Figure 8.7(b). The predictions of our 2D framework qualitatively match those of the 3D model. The ratio between maximum velocities in 2D and 3D is 67.9 %, approximating the theoretical ratio of average-to-maximum velocity in plane Poiseuille flow of 66.6 %. Note that the 3D framework predicts velocity

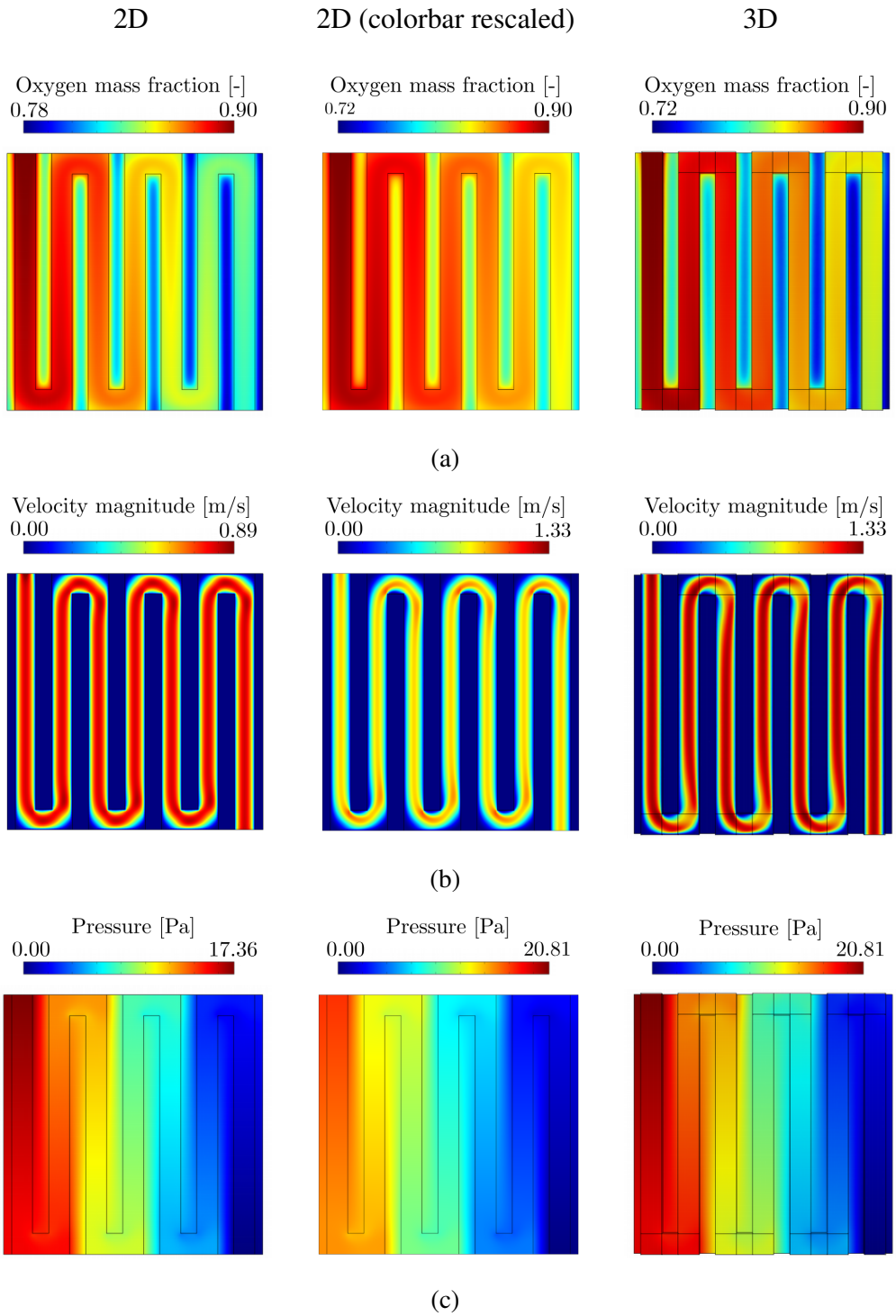

Fig. 8.7. Comparison of 2D and 3D responses. (a): Oxygen mass fraction field; (b): velocity field; (c): pressure field

reductions after U-bends that are not captured in 2D. Similar trends in 2D and 3D are observed also for the pressure field shown in Figure 8.7(c). The pressure diminishes gradually along the path from the inlet to the outlet. However, our 2D framework underestimates the pressure drop by 16.5 %. To assess how this difference can affect our fluid-dynamic predictions, we compute the characteristic curve of the cell by sweeping the inlet flow rate V_{in} from 10 % to 150 % of the reference case. The results are shown in Figure 8.8. The 3D model returns a super-linear pressure drop to flow rate relation. This trend is not reproducible in 2D under plane Poiseuille assumptions. We obtain a nearly linear relation using our 2D model. As the flow is laminar in the range of values considered ($8.7 \leq Re \leq 130.5$), we conjecture that the super-linear drag is connected to geometry features that invalidate the fully-developed flow assumption, such as U-bends. Recall that we observed sudden velocity reductions in Figure 8.7(c). To confirm this speculation, we compute the pressure drop over a single channel (the one connected to the inlet) and multiply the result by the number of channels to allow for comparisons. The 3D single-channel pressure drops closely match the 2D predictions. A high-fidelity 2D modeling of the 3D dynamics in serpentine flow fields would require the introduction of a quadratic Forchheimer drag term in correspondence of U-bends, e.g. in the regions highlighted in Figure 8.8(c). There, the momentum equation (8.4) can be augmented with the following sink [310]:

$$F_{fc_i} = -\rho \alpha_{fc} |v_i| v_i, \tag{8.36}$$

where α_{fc} is a multiplicative constant that can be calibrated by trial and error. Figure 8.8(b) shows that the 2D predictions approximate better the 3D ones as α_{fc_i} is increased. A value of $\alpha_{fc} = 500$ allows the super-linear drag effects to be reproduced with a high degree of accuracy. However, this value is highly geometry-dependent and hardly fits within an inverse design framework. For this reason, we neglect super-linear drag in our analysis model. We observe that a similar issue may arise in other 2D fluid topology optimization frameworks.

Figure 8.9 presents a comparison between the results obtained using a mixture-averaged and a full Maxwell-Stefan diffusion model. For this study, we adopt our 2D framework and we consider the cathode as alimented by air such that multi-component diffusion effects arise. The inlet mass fraction of the chemical species are set as $\omega_{H_2O} = 0.023$, $\omega_{O_2} = 0.228$ and $\omega_{N_2} = 0.749$ in agreement with [363]. The polarization curves (Figure 8.9(a)) match well. The mixture-averaged framework gives a mean relative deviation of 0.02 %. This indicates that the oxygen distribution

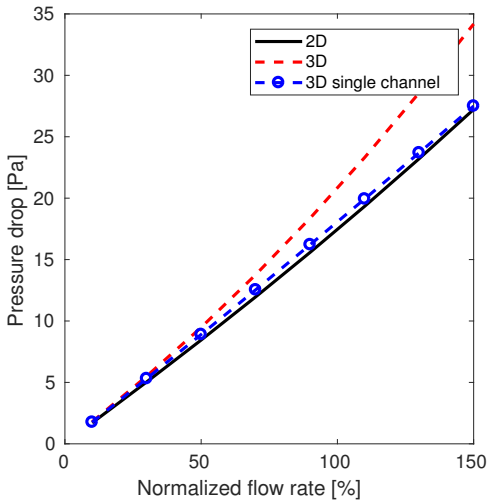

(a)

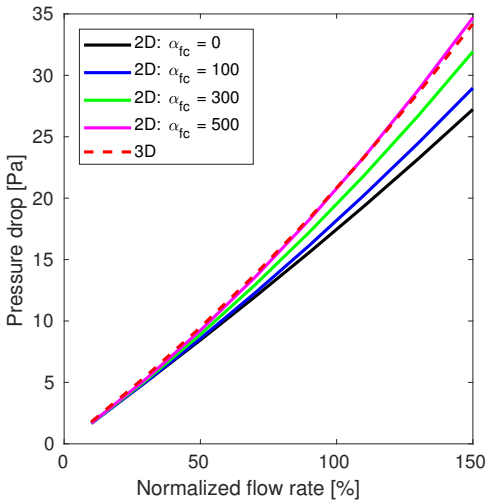

(b)

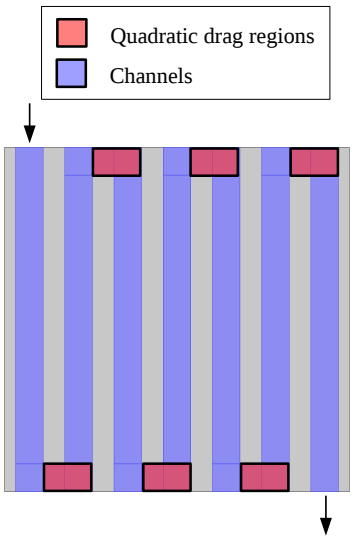

(c)

Fig. 8.8. Comparison of pressure drop using the 2D and 3D models. (a): reduction of 3D effects by the analysis of a single channel in 3D; (b): introduction of a quadratic Forchheimer drag term in 2D to account for 3D effects; (c): regions of the 2D geometry interested by quadratic drag

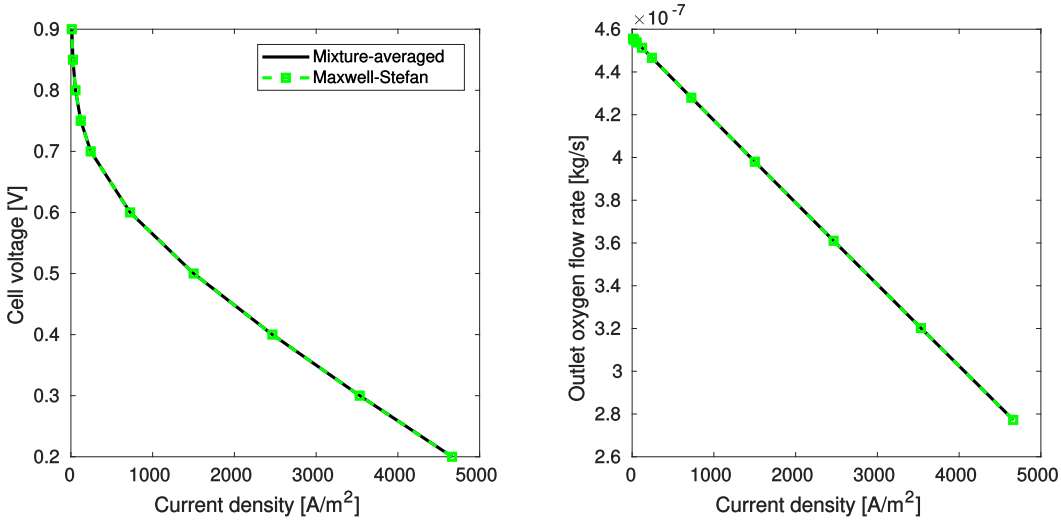

(a) (b)

Fig. 8.9. Comparison of responses using the mixture-averaged and Maxwell-Stefan diffusion models. (a): Polarization curve; (b): outlet oxygen mass flow rate

is slightly affected by the choice of the diffusion model. Kee et al. [236] observed that the mixture-averaged route may lead to species non-conservation. Figure 8.9(b) shows the outlet oxygen flow rate as a function of the current density generation for the two diffusion models. The results suggest that mass non-conservation is not an issue when modeling the cathode of a PEM fuel cell through a mixture-averaged diffusion model. The mean relative deviation is below 0.01 %.

8.4.2 Reference design

In this section, we present the design optimization results obtained for a reference case with $F_{in} = 5$ Pa and compare its performance with conventional flow field layouts. Here, we aim at maximizing only the generated power. Hence, we set $w_\theta = 0.00$ and $w_{\bar{W}} = 1.00$ in Eq. (8.30). The design and computational domain corresponds to the one shown in Figure 8.4 with $W_{in} = W_{out} = 1.20$ mm and $L = 22.36$ mm as in the previous section. The maximum volume of "porous channel" material, V^*, is set to 50 % of the total. The filtered elemental design variable field, $\tilde{s}$, is computed from the nodal design variable field, s, using a filter radius of $r_f = 0.35$ mm. The material properties are the same adopted for the verification study presented in Section 8.4.1. However, the channel and GDL depths are modified

to produce all the topology optimization results. Since our analysis framework does not account for either flooding or dehydration, there is a chance that the optimized designs will not perform as expected. As highlighted in Section 8.1, there is evidence that adopting small channel depths simplifies water management regardless of the flow field layout [5, 445]. For this reason, we choose the configuration adopted in [363], where $H_{gdl} = 0.38$ mm and $H_{ch} = 1.00$ mm. Note that water management is seldom an issue at higher temperatures [83]. Hence, the design results and trends presented hereafter apply to high temperature PEMFCs with little risk of bias due to our physics reduction.

The objective history along with snapshots of the projected design variable field at selected iterations is shown in Figure 8.10. For all the designs presented in this chapter, we will adopt the colorbar presented in Figure 8.10. The jumps in the objective history correspond to the transitions between the continuation steps. The initial design (Figure 8.10(a)) corresponds to a homogeneous projected design variable field at $\rho_s = 0.5$. Within the first continuation step, the "porous rib" material is retrieved from the regions close to the inlet and outlets and aggregated in two central areas. Four wide "porous channels" start to appear at iteration 20 (Figure 8.10(b)), which then evolve into Y-shaped connections at iteration 60 (Figure 8.10(c)). Some regions with intermediate ρ_s values are still present at the end of the first continuation step due to the moderate penalization of both the diffusive and advective transport. At iteration 100, as shown in Figure 8.10(d), the design converges to a binary $\{0;\ 1\}$ layout since a stronger penalization is applied on the intermediate ρ_s values. From this point onward, limited objective and layout modifications are observed. The final optimized design after 180 iterations is shown in Figure 8.11(a). This geometry shows features pertaining to different design concepts presented in Section 8.1. As in the parallel configuration, our optimized layout presents inlet and outlet headers that are connected by a number of alternative paths. The intricate groove of the flow channels somehow recalls the layout of the mesh flow fields. Furthermore, the width tapering of the main vertical channels and the inclination angle of the diagonal connections make it similar to the bio-inspired geometry proposed by [361] and schematically shown in Figure 8.2(e). For this design optimization case, the need for the last continuation step could be questioned. However, this last step is essential to ensure convergence to binary $\{0;\ 1\}$ designs at higher F_{in} values, as considered in the next section.

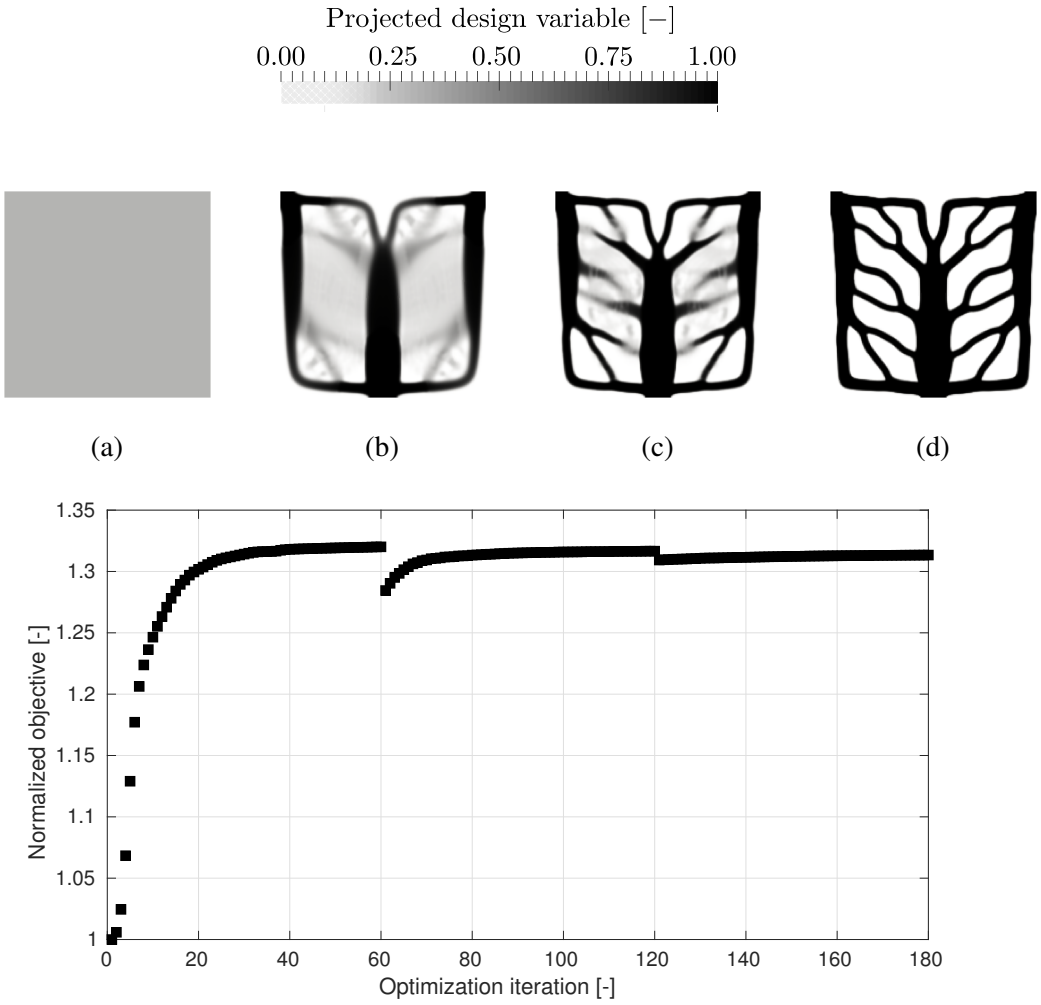

Fig. 8.10. Objective history during the optimization process with design snapshots taken at selected iterations. (a): initial guess; (b): iteration 20; (c): iteration 60; (d): iteration 100

Table 8.7. Average current density [A/m^2] for the three layouts

topology-optimized	parallel	serpentine
2785	2635	1120

Figure 8.11 shows a comparison of our optimized design with conventional flow channel layouts. Benchmark parallel and serpentine flow field layouts are displayed in Figures 8.11(d) and 8.11(g). For these geometries, the width of the channels, W_{ch}, is calculated so that the volume constraint in (8.30) is satisfied. The width of the inlet and outlets sections should be equal in all the layouts to allow for meaningful comparisons. Since $W_{ch} < W_{in}$ and $W_{ch} < W_{out}$, in the serpentine layout we created small convergent and divergent sections of length W_{ch} at the inlet and outlets, respectively. The average current density obtained with the three designs is summarized in Table 8.7. The topology-optimized design yields superior performance resulting in a 5.7 % and a 248.6 % increase in the average current density as compared to the parallel and serpentine designs, respectively. The velocity magnitude and the oxygen mass fraction field displayed in Figure 8.11 help to identify the physical reasons behind these performance differences. The average gas velocity in the serpentine layout is much smaller as compared to the other two alternatives. This is due to a higher average fluid-dynamic resistance of the paths linking the inlet to the outlets. Hence, the small amount of oxygen entering the cell is promptly depleted in a region close to the inlet, resulting in a negligible amount of power generation in the remainder of the cell. A premature reactant depletion in single serpentine flow fields was also observed in [229]. In agreement with the considerations of Taccani et al. [412], Figure 8.11(e) suggests that the reactants are distributed ineffectively when using a parallel flow field. The uneven fluid-dynamic resistance among the parallel paths yields regions with large oxygen depletion so that the minimum oxygen mass fraction is 11.07 %. The flow distribution is more efficient when using our topology-optimized design. The oxygen propagates in the cell following tree-like paths that closely resemble the diffusive patterns of topology-optimized fins for LHTES units presented in Chapter 3. This distribution strategy helps to avoid local minima of the reactant mass fraction field. The minimum oxygen mass fraction computed for the topology-optimized layout is 15.34 %.

To make sure that the design trends identified are not affected by our depth-averaging procedure, we analyze the alternative geometries in 3D. The 3D version

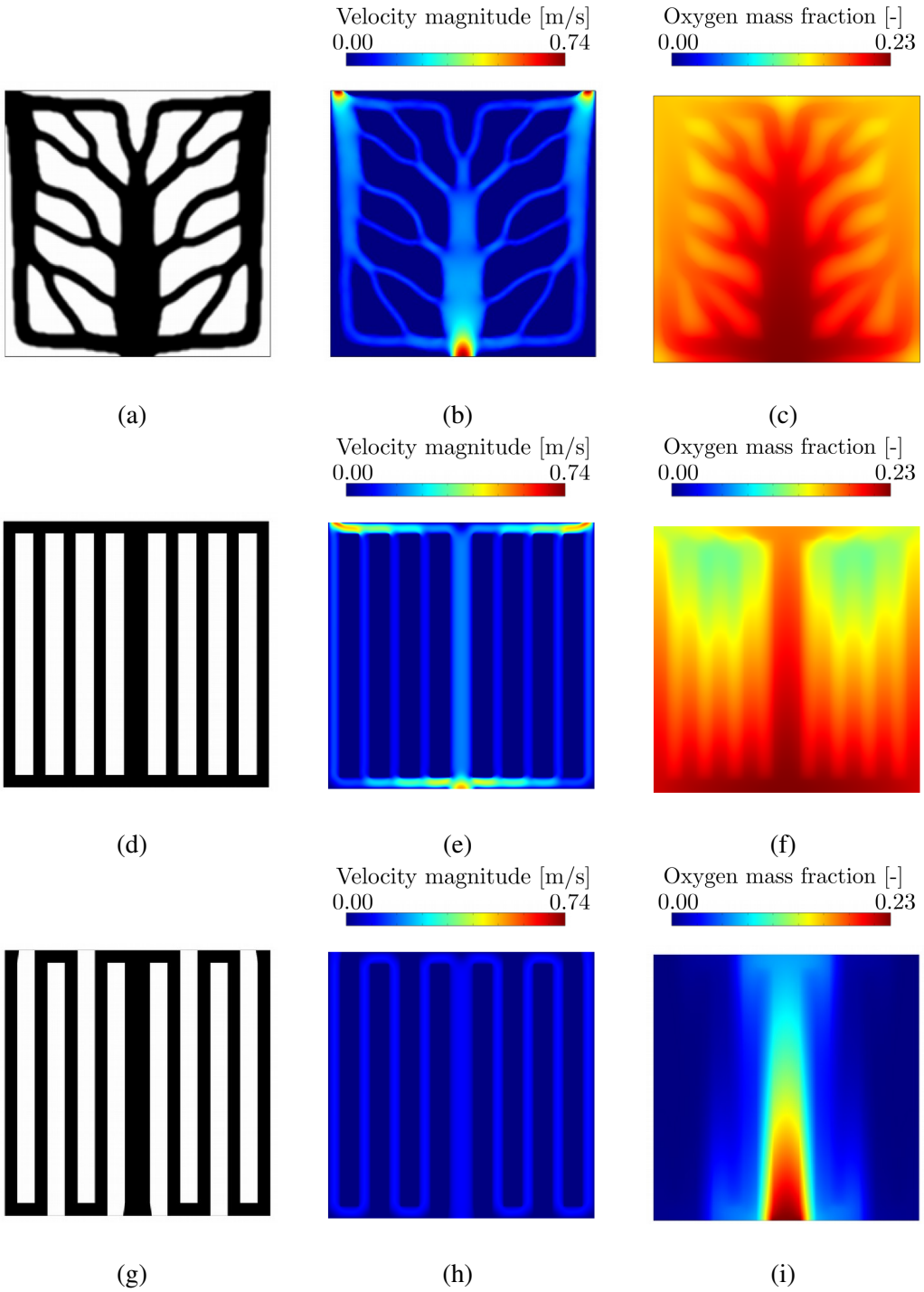

Fig. 8.11. Performance comparison with conventional flow field layouts for $F_{in} = 5$ Pa. Topology-optimized design (a) with its velocity field (b) and oxygen mass fraction (c). Parallel layout (d) with its velocity field (e) and oxygen mass fraction (f). Serpentine layout (g) with its velocity field (h) and oxygen mass fraction (i)

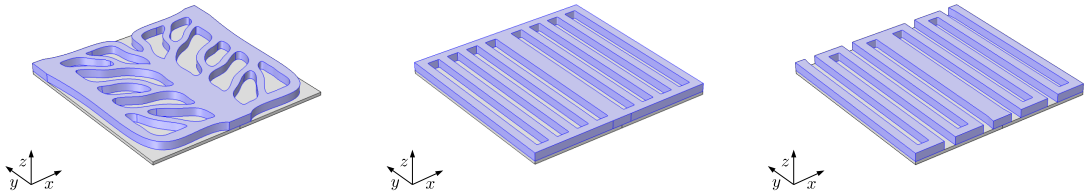

(a) (b) (c)

Fig. 8.12. 3D versions of the topology-optimized (a), parallel (b) and serpentine (c) designs

Table 8.8. Performance of the the 3D versions of the three layouts

	Design		
Performance	topology-optimized	parallel	serpentine
Average current density [A/m^2]	2770	2661	1034
2D deviation [%]	- 0.54	+ 0.97	- 7.68

of the topology-optimized layout is obtained using channel walls described by the $\rho_s = 0.5$ iso-countour. Views of the computed geometry and the 3D versions of the parallel and serpentine layouts are shown in Figure 8.12. The three geometries are analyzed using high-resolution body-fitted meshes with 444113, 431012, 468174 tetrahedral elements, respectively. The average current densities computed in 3D are summarized in Table 8.8. The results show a satisfactory match between the 2D and 3D predictions for the topology-optimized and parallel design. A larger discrepancy is computed for the serpentine layout due to the presence of quadratic drag effects in correspondence of U-bends that are not captured in 2D (see Section 8.4.1).

The results obtained in the presented numerical example showed that topology optimization allows optimized flow paths in PEMFC to be obtained without the need for a close-to-optimal design to start with. The layout computed for a reference pressure drop of $F_{in} = 5$ Pa is superior in terms of power generation to conventional alternatives like the serpentine and parallel configurations. Furthermore, the 3D results confirmed the design trends identified in 2D, suggesting that the depth-averaging procedure described in Section 8.2.1 is a reliable approach for topology optimization of electrochemical devices.

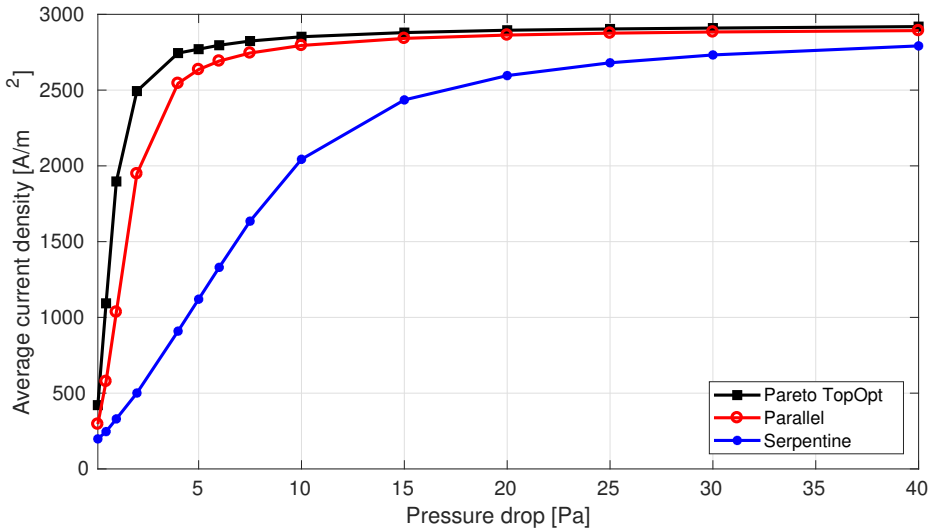

Fig. 8.13. Pareto front current density versus pressure drop

8.4.3 The trade-off between pressure drop and power generation

In this section, we analyze how the optimized designs and power output are affected by the choice of the inlet pressure, F_{in}. The model parameters and physical properties are unchanged with respect to the reference design.

We consider 14 different values of the inlet pressure in the range 0.1 Pa $\leq F_{in} \leq$ 40 Pa. Only minor design and performance differences are observed for $F_{in} >$ 40 Pa. For each case, a topology optimization run is performed. To benchmark the effectiveness of our topology optimization framework, the serpentine and parallel geometries are analyzed in the same conditions. The computed average current density is shown in Figure 8.13. In the range of values considered, a reduction in pressure drop can be obtained only at the expense of less power generation. Hence, these two performance criteria are antagonist and the curve of the optimized values in Figure 8.13 is an approximation of the multi-objective Pareto front. The layouts obtained with our optimization framework are always superior to the conventional alternatives. Improvements are large at low inlet pressures. The average current density of the topology-optimized layout at $F_{in} = 1$ Pa is 83.21 % and 574.8 % higher than the one obtained using the parallel and the serpentine flow fields, respectively. This gap reduces for higher F_{in} so that the performance enhancement of the topology-

optimized layout is only 0.89 % and 4.55 % at $F_{in} = 40$ Pa. This suggests that the topology of the flow distributor slightly affects the performance at high inlet pressures. The optimized layouts obtained at selected Pareto points are displayed in Figure 8.14. When a higher inlet pressure is available, the geometry evolves more freely resulting in unintuitive layouts. The number of connections increases and the width of the channels decreases creating more and more complicated geometries. The design optimized for $F_{in} = 40$ Pa shows similarities with the mesh design concept (Figure 8.2)(d). To quantify the design modifications along the Pareto front, we study the evolution of two performance metrics. The first one is the number of internal holes, N_h, in the layout (filled by "porous rib" material) representing the complexity of the flow channel topology. The values obtained for the different inlet pressures are presented in the bar chart of Figure 8.15(a). The number of internal holes, N_h, increases fast at low inlet pressures and levels-off at $F_{in} = 25$ Pa. From this point onward, no topology modifications are observed. The second performance metric is a perimeter measure, Γ_p, based on the total variation of the projected design variable field [395]:

$$\Gamma_p = \int_\Omega ||\nabla \rho_s||_2 \, d\mathbf{x}, \tag{8.37}$$

where $||\cdot||_2$ indicates the L_2 norm. The influence of the inlet pressure on the perimeter measure of the optimized designs is shown in Figure 8.15(b). The perimeter length increases monotonically in the range of values considered. At low inlet pressures, i.e. $F_{in} \ll 25$ Pa corresponding to the region of topological changes, a fast growth of the perimeter measure is observed. For higher inlet pressure values, i.e. $F_{in} > 25$ Pa, Γ_p is increased moderately as the perimeter modifications are obtained exclusively through a higher arc-to-chord ratio of the connections, resulting in a higher tortuosity of the channels.

To investigate how the optimized layouts perform when operated far from their reference pressure drop conditions, we consider the designs optimized for $F_{in} = \{0.1;\ 2.0;\ 5.0;\ 10.0;\ 40.0\}$ Pa. For each geometry, we run five analyses corresponding to different pressure drops, i.e. $F_{in} = \{0.1;\ 2.0;\ 5.0;\ 10.0;\ 40.0\}$ Pa. This cross-check also helps to exclude the possibility of convergence to unsatisfactory local minima. The outcome of this investigation is summarized in Figure 8.16. The results show that each layout performs better than the alternatives in the condition in which it is optimized for. Furthermore, it shows that the geometries optimized for $F_{in} = 2.0$ Pa and $F_{in} = 5.0$ Pa are slightly sensitive to changes in the operating inlet

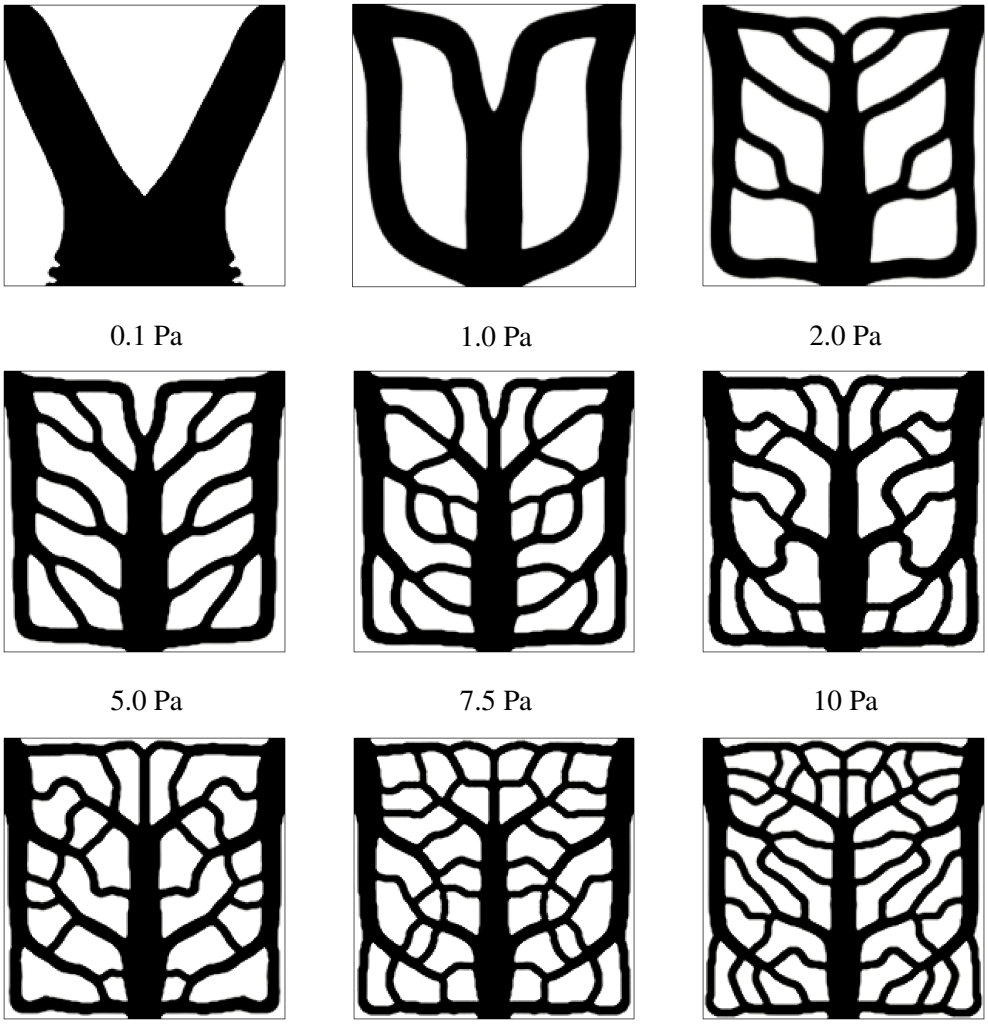

Fig. 8.14. Optimized designs obtained for different values of the imposed pressure drop, F_{in}

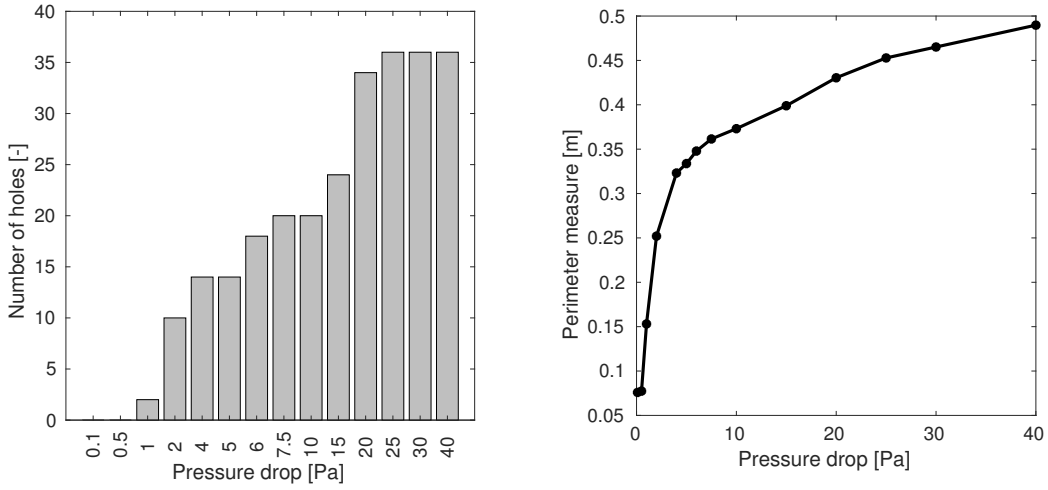

(a) (b)

Fig. 8.15. (a): Effect of the inlet pressure on the number of internal holes of the optimized layouts; (b): effect of the inlet pressure on the perimeter measure, Γ_p, of the optimized layouts

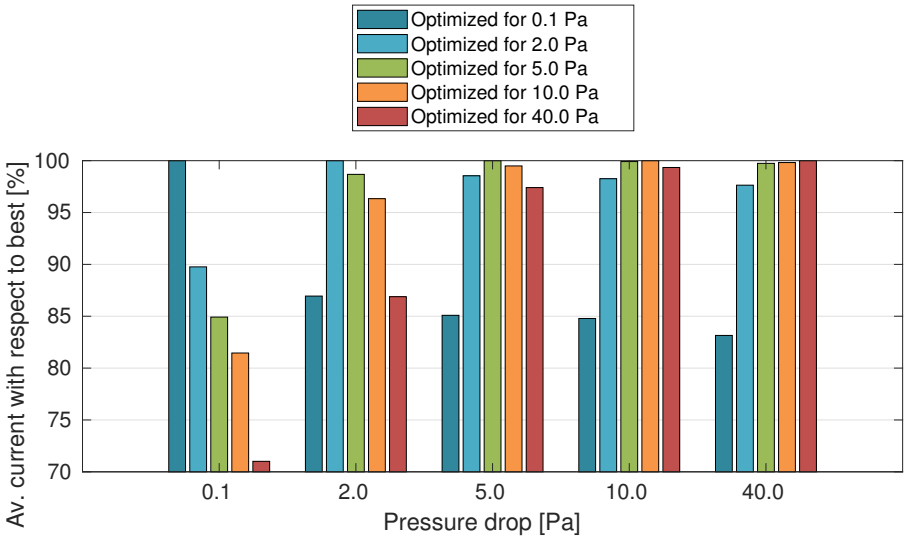

Fig. 8.16. Performance of the optimized layouts when operated far from their reference pressure drop conditions

pressure. The average current density drop in the cases analyzed is only 3.15 % and 3.34 %, respectively. On the other hand, the geometries optimized for $F_{in} = 0.1$ Pa and $F_{in} = 5.0$ Pa yield large performance reductions when operated far from their reference pressure drop condition.

This design study showed that the inlet pressure modifies consistently both the optimized designs and performance. At low inlet pressures, the topology complexity and power generation of the optimized designs increase fast. In this case, topology optimization yields layouts responsible of large improvements as compared to conventional flow fields. At high inlet pressures, the performance is slightly affected by the layout of the gas distributors. The geometry changes are only due to tortuosity modifications of the channels, yielding minor power generation enhancements.

8.4.4 Increasing the homogeneity of the current density distribution

In this section, we study the design trends obtained using the full penalty method, i.e. $w_\theta \neq 0.00$ and $w_{\bar{W}} \neq 0.00$. The optimization problem (8.30) is solved for five values of the current standard deviation weight in the range $0.25 \leq w_\theta \leq 7.50$. Minor design and performance differences are observed for $w_\theta > 7.50$. We consider the reference inlet pressure case, i.e. $F_{in} = 5$ Pa and a fixed value of the power generation weight $w_{\bar{W}} = 1.00$. The model parameters and material properties are unchanged with respect to the reference design. The optimized designs are shown in Figure 8.17 along with the reference design case obtained by setting $w_\theta = 0.00$. The results show that there is a significant influence of the weighting factor w_θ on the optimized layouts. As w_θ is increased, the geometries feature a higher concentration of "porous rib" material close to the inlets while the "porous channels" migrate towards the external edges and outlets. The vertical channel at the center of the cell get thinner while two diagonal long and wide channels are created for $w_\theta \geq 5.00$, linking the inlet to the outlets. This suggests that more reactants are able to reach the regions close to the outlets through convective transport. To demonstrate these design trends, we consider the following performance metric:

$$\tilde{V} = \frac{\int_{\Omega_2} \rho_s \, d\mathbf{x}}{\int_{\Omega_1} \rho_s \, d\mathbf{x}}, \tag{8.38}$$

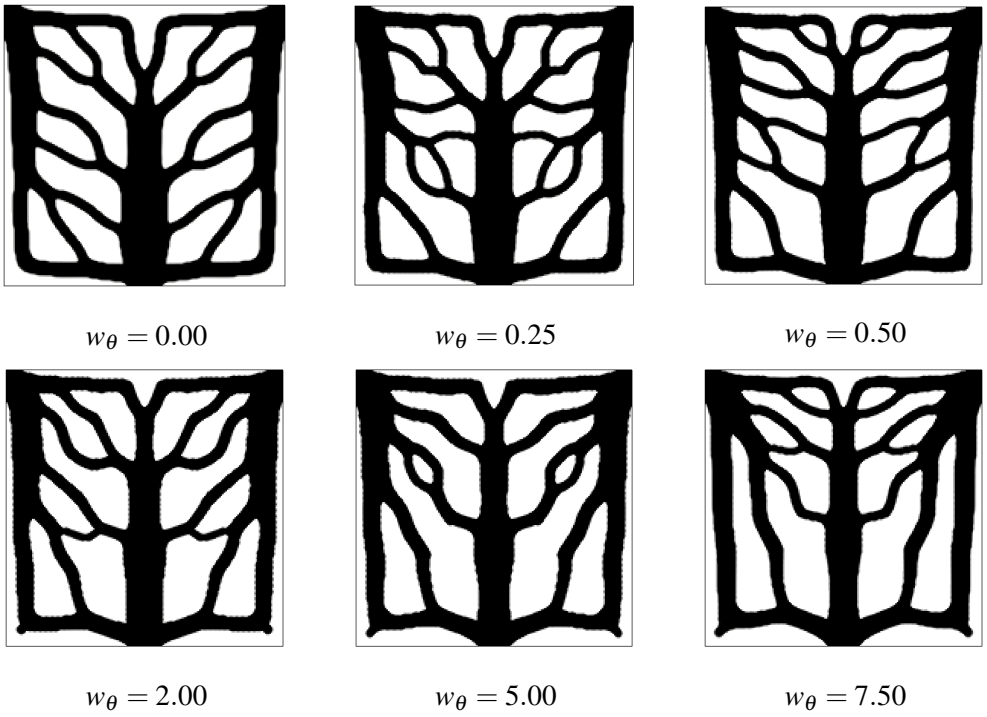

Fig. 8.17. Optimized designs obtained for different values of the current standard deviation weight, w_θ, with $F_{in} = 5$ Pa and $w_{\bar{W}} = 1.00$

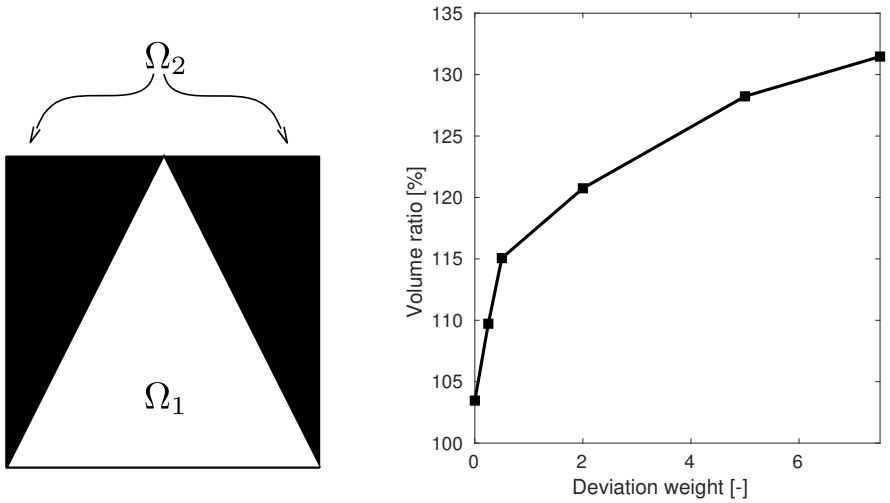

(a) (b)

Fig. 8.18. (a): Domain splitting in close-to-inlet region (Ω_1) and close-to-outlets region (Ω_2); (b): effect of w_θ on volume ratio $\tilde{V}$

where Ω_1 and Ω_2 are the portions of the design domain shown in Figure 8.18(a). The parameter $\tilde{V}$ quantifies the "density" of channels in the regions close to the outlets as compared to its value in the region connected to the inlet. We will refer to $\tilde{V}$ as volume ratio hereafter. The influence of w_θ on the volume ratio of the optimized layouts is shown in Figure 8.18(b). In the range of values considered, $\tilde{V}$ increases monotonically. When the power is the unique optimization criteria ($w_\theta = 0.00$), the flow field complexity in Ω_2 is comparable to that of Ω_1 such that $\tilde{V} = 103.5$ %. Obtaining a more homogeneous current density distribution requires more channels to be located close to the outlets. Setting $w_\theta = 7.50$ yields a layout in which the total volume of the channels in Ω_2 is 31.5 % higher than the one measured in Ω_1. Figure 8.19(a) shows that these design modifications are effective in lowering our criterion of current density dispersion: $\theta_{i_{CL}}$ is decreased from 86.87 A/m^2 to 79.78 A/m^2, corresponding to a 8.16 % reduction. The amount of power generated by the optimized layouts reveals to be slightly sensitive to the choice of w_θ (Figure 8.19(b)). We obtain a reduction of only 0.28 % when raising w_θ from 0.00 to 7.50, suggesting that the power generation is marginally affected by the design features promoting homogeneity. This indicates that the inclusion of current density dispersion measures in flow field design optimization frameworks has the potential to indicate promising routes for practical technological development.

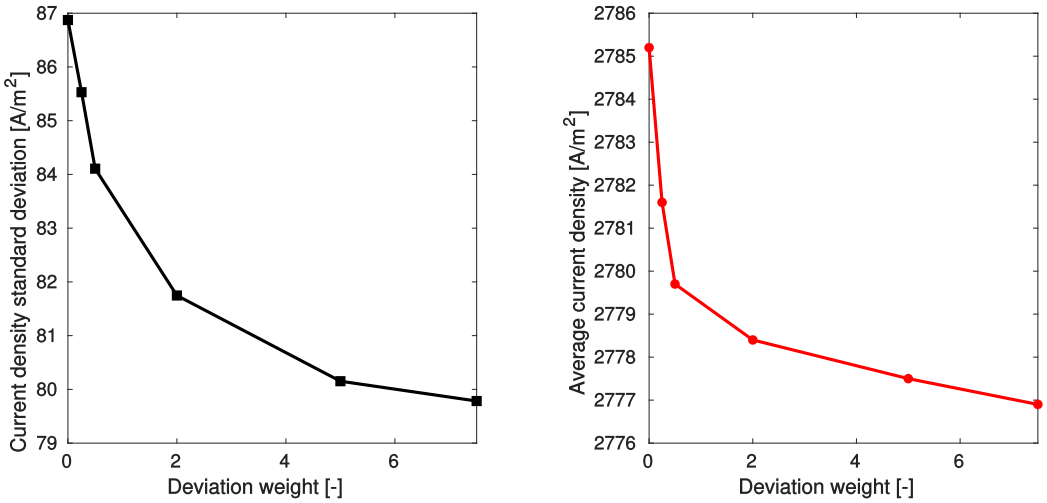

(a) (b)

Fig. 8.19. (a): Effect of w_θ on the standard deviation of current density; (b): effect of w_θ on the average current density

8.5 Conclusions

This chapter demonstrated the use of density-based topology optimization for the practical design of flow fields in PEMFCs. The objective function was formulated to maximize both the power output and homogeneity of the current density distribution, permitting reduced costs and higher durability. The gas dynamics, transport of chemical species, and electrochemical interactions in the cathodic portion of the PEMFC were computed using a 2D finite element model. The 3D transport effects were accounted for in the 2D model through an original depth-averaging procedure, which was verified against the predictions of a full 3D model calibrated using experimental and numerical results available in literature. Our analysis model framework did not account for liquid water transport. For this reason, the optimization results are considered realistic mostly for high temperature systems, in which flooding is seldom an issue [83].

A graphical summary of the main application-oriented advances is presented in Figure 8.20. Topology optimization yielded layouts with unintuitive and non-trivial features. Our reference flow field obtained considering an inlet pressure of 5 Pa has similarities with various design concepts such as parallel, mesh and bio-inspired geometries. Its performance was found to be superior to the one of

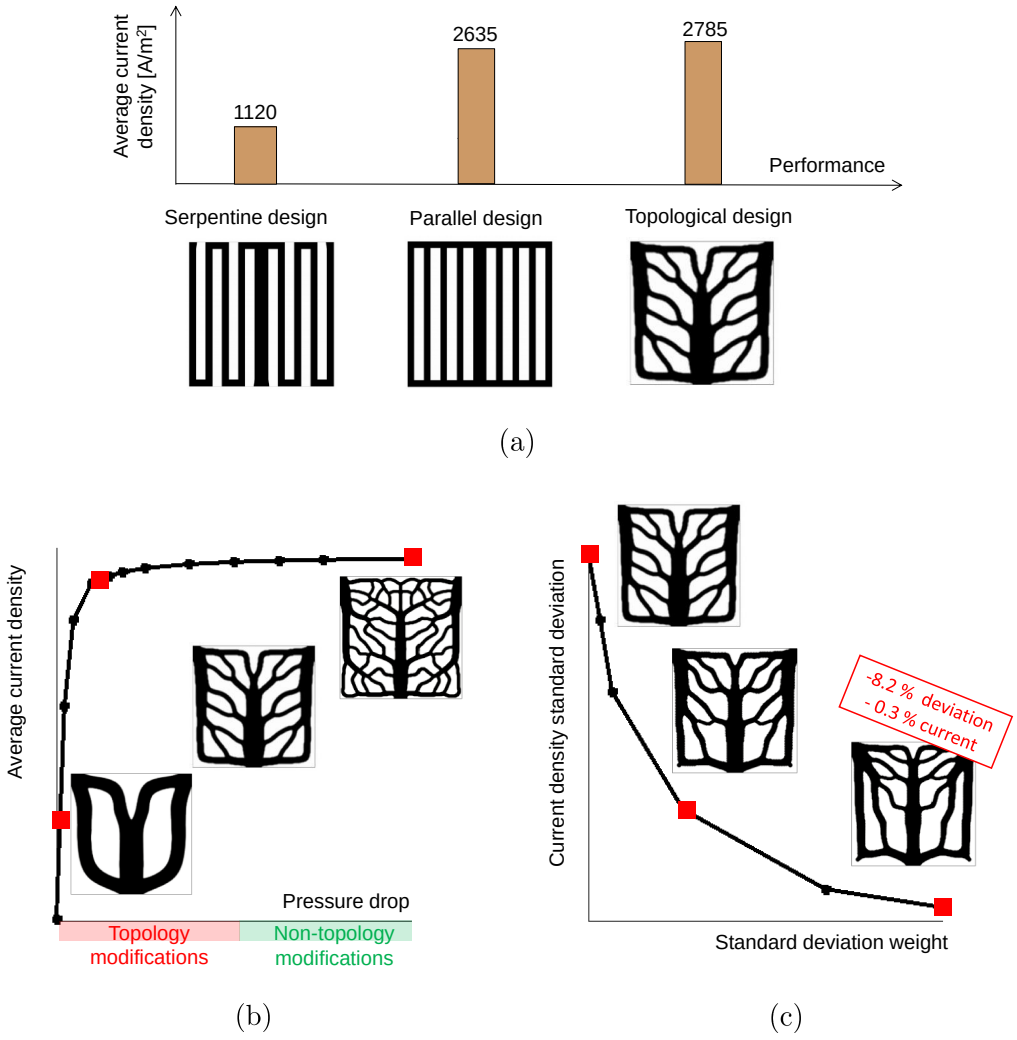

Fig. 8.20. Graphical summary of the main application-oriented advances of the chapter. (a): Performance comparison of the reference topology-optimized design with the conventional geometries; (b): design trend pressure drop/power generation; (c): design features promoting the homogeneity of the current density with minimal impact on the power generation

both parallel and serpentine flow fields, yielding a 5.7 % and a 248.6 % increase in the average current density (Figure 8.20(a)). The smaller fluid-dynamic resistance of our layout allows a much higher air flow rate as compared to the serpentine geometry. Furthermore, its effective reactants distribution avoids the creation of regions with a large oxygen depletion, which arise in the parallel geometry due to the uneven fluid-dynamic resistance of the flow paths. The trade-off between pressure drop and power generation was then explored to study the influence of the inlet pressure on both the optimized designs and performance (Figure 8.20(b)). The results showed that, at low inlet pressures, substantial power output improvements are achievable through topological modifications of the flow distributor. In this case, the optimization process yielded large enhancements with respect to the conventional flow fields. At higher inlet pressures, no topology modifications were observed and only moderate enhancements could be obtained through the increase of the tortuosity of the channels. In this case, the performance was found to be slightly sensitive to the flow field layout and the topology-optimized designs performed similarly to the serpentine and parallel flow fields. Adding a measure of the current density dispersion to the optimization objective led to design features capable of decreasing the current density standard deviation by 8.16 % with negligible impact on the amount of power generated (Figure 8.20(c)). This finding suggests a viable route for the future development of these systems with the aim of increasing the durability.

Chapter 9

Conclusions

In this chapter, we summarize the work presented in this thesis, highlighting the main research contributions. Finally, we give recommendations and identify directions for future developments.

9.1 Contributions

This dissertation developed a systematic framework for the optimal design of energy systems via topology optimization, yielding both method-related and application-oriented advances. The method-related advances stem from the modification of topology optimization approaches to allow practical improvements to LHTES, DHNs and PEMFCs. The application-oriented advances comprise the identification of geometries that greatly outperform the current industrial solutions and of design trends and guidelines that could be of interest to design engineers. The research objectives of this thesis were formulated according to the four fundamental research questions discussed in Chapter 1. Here, we present how it is possible to address them through the main contributions of our work.

Q1 *How and how much can we improve the performance of LHTES units through the design of high conducting structures?*

We first developed a density-based topology optimization framework for the optimal design of fins in shell-and-tube systems. We formulated the design optimization

problem in order to respond to three design criteria of practical interest. The unit dynamics was predicted using a simplified phase change model based on transient nonlinear diffusion. Then, we proposed a multi-scale multi-material design framework based on geometric primitive level-sets to obtain assemblies of periodic cellular materials that can be manufactured using conventional machining techniques, permitting reduced costs and mass production. To achieve this goal, the analysis and design capabilities were extended using forward and inverse computational homogenization. The topology optimization results demonstrated that the optimized layouts strongly depend on the desired level of discharge of the unit and that there is room for manipulation of the energy history towards a steadier power output. Hence, powerful design approaches are crucial in order to reduce costs and increase the efficiency of this technology. Considering a reduced dimensionality led to suboptimal configurations. The geometries optimized in three dimensions presented unique features that were not apparent in 2D, yielding an average performance improvement of 20 % with respect to the 2D layouts. The multi-scale optimization results indicated that the performance of a limited number of cellular materials with optimized microstructure strongly depends on the designer assumptions on the materials aggregation layout. Our tentative configurations yielded inferior performance with respect to the topology-optimized fins. However, when the aggregation layout was also controlled during the optimization, we obtained "machinable" structures responsible for substantial enhancements, ranging from a 12 % to a 31 % reduction in the discharge time as compared to the topology-optimized fins.

Q2 *How are optimized fin layouts and performance affected by natural convection, storage unit configuration and materials choice?*

To understand the effect of physics reductions in the analysis, we augmented the finite element model to include the effect of natural convection in the liquid PCM. Both the phase transition and geometry variations were accounted for in the flow analysis using a porosity approach. The effect of the material interpolation strategies and continuation trajectories on the penalization parameters was assessed by means of simplified conjugate heat transfer examples, revealing that incorrect choices may easily lead to unsatisfactory local minima. In the effort to produce results of greater interest for practical installations, we then considered the design of units with multiple tubes immersed in the shell. In this realistic setup, we investigated the effect of the unit configuration (by analyzing systems with unique or separate hydraulic

loops for the hot and cold HTFs) and of the materials choice (by considering different popular combinations of PCMs and HCMs). The numerical results demonstrate that accounting for fluid flow in the analysis is crucial for melting. The topology-optimized layout allows unobstructed liquid motion in the regions subject to strong convective currents. Diffusive-like geometries evolved in those regions that cannot be reached by the fluid. This layout led to a 26 % reduction in the charge time as compared to a benchmark diffusive geometry. For solidification, both the design and performance differences with respect to the diffusive structure were moderate. The structure optimized for solidification yielded only an 11 % reduction in the discharge time. This indicates that a simplified phase change model may be a viable route for the preliminary design of geometries enhancing solidification. When tested on a real-world single-tube storage unit for DHNs, topological geometries, as well as their post-processed versions for easier manufacturing, were found to be superior to the conventional longitudinal fins, yielding enhancements between 7.3 % and 32.3 %. Multi-tube units with unique or separate hydraulic loops for the hot and cold HTFs required ad-hoc designs. Using finned tubes optimized by considering circular periodicity or a different loop configuration was found to lead to sudden degradations of the heat transfer rate. The cost-constrained design studies conducted with different HCM-PCM combinations revealed that using steel is never convenient in terms of both the energy and power density of the unit. Furthermore, the optimized layouts were found to be slightly sensitive to the choice of PCM, suggesting that a modular fin configuration can be adopted for both low, intermediate and high temperature installations.

Q3 *How can we enhance the resilience of district heating infrastructures through the design of the network layout and the control of user valves?*

We considered improvements to the robustness and rapidity aspects of the resilience of the infrastructure. We developed a topology optimization framework for the robust design of looping paths in existing DHNs for maximized absorption of external perturbations. The robustness was quantified with a sensitivity metric computed through adjoint calculus. This fully deterministic route did not require the characterization of the input uncertainty, which may be hard to achieve in real-world installations. The rapidity was improved using a centralized control framework of user valves constructed with the MMA and discrete adjoint sensitivities. This was devised to quickly restore acceptable levels of service after a disruptive mechanical failure

event. The fluid-dynamic and thermal analyses at each optimization iteration were conducted using a validated computational model based on a graph representation of the network. The robust design results suggest that our sensitivity metric leads to layouts that are more capable of withstanding fluid-dynamic noise than those obtained using a minimum power dissipation formulation. Robustness and investment cost lie on a Pareto front, where large resilience improvements (+ 38.8 %) are obtained at a limited cost (400 k€) by modifying the connectivity of the network. Our control optimization studies reveal that a centralized management represents a substantial progress with respect to the approach in use today. Among the different failure cases analyzed, we obtained improvements to the thermal deficit of the most critical user between 5.89 % and 56.38 %. All the mechanical failures simulated could be handled to limit the impact on service with minimal backup pumping power. This strategy is suitable for integration within an RTI framework, where a continuous feedback from metering devices can be used to improve the accuracy of both the forward and sensitivity analyses.

Q4 *How and how much can we improve the efficiency and durability of PEMFCs through the design of reactants flow paths?*

We developed a density-based topology optimization framework for the design of flow fields in PEMFCs to obtain efficient and durable devices. The physical response of the system was predicted using a 2D finite element model, accounting for the fluid dynamics, transport of chemical species and electrochemistry at the cathode. The three-dimensional effects were reproduced in 2D using a depth-averaging procedure, whose accuracy was verified against the 3D predictions. The efficiency was improved by maximizing the power generation at a fixed pressure drop. The durability was improved by minimizing a measure of dispersion of the current density so that steep thermal gradients and stresses are avoided. The power maximization results demonstrate that the topology-optimized layouts are superior to conventional flow fields due to an increased reactants flow rate and improved distribution effectiveness. For a reference design case with a pressure drop of 5 Pa, the topology-optimized design led to a 5.7 % and a 248.6 % increase in the average current density compared to the parallel and serpentine flow fields, respectively. When our measure of homogeneity was included in the objective, we obtained design features that slightly influence power generation. The optimization process led to a layout yielding a 8.16

% reduction of the current density standard deviation with only a 0.28 % degradation of the power generated.

9.2 Perspectives

This thesis answered a few research questions but raised many others. We foresee and recommend future research in the following five areas.

Experimental validation of the optimization results
Various discussions with scholars within the applied heat transfer community revealed that most practitioners are impressed by the topology optimization results but seldom believe in the method for real-world problems. In our view, experimental testing to validate the topology optimization results is essential to win over skepticism and make a real step forward in innovating the outdated design methodologies. Future researches should focus on assessing whether the optimized designs presented in this thesis perform as expected and improving both the analysis and design models using feedbacks from experiments. In all the applications considered in this thesis, we observed some basic principles and formulated preliminary technology concepts. This collocates the proposed enhancement techniques to a Technology Readiness Level (TRL) of 2 according the classification adopted by the European Union [123]. Experimental testing and technology validation at the laboratory scale has the potential to raise the optimized layouts to a TRL of 4.

Advances using the presented analysis and design framework
Here, we include the researches that can be conducted in the field of LHTES and DHNs using the computational tools developed in this thesis. First, some recent numerical results [477] show that needle-like HCM formations are superior to tree structures for both thermal compliance and maximum temperature minimization. Future researches should assess whether this trend is valid also for heat transfer enhancement in LHTES systems by repeating our optimization studies with different initial guesses and periodicity assumptions. Second, the design studies that considered natural convection in the liquid PCM were limited to two dimensions and to the macroscopic scale. Combining heat transfer enhancements due to the 3D and convective design features with the developed multi-scale capabilities has the potential for dramatic improvements to the structures in use today. We are currently working in this direction. Furthermore, we speculate that the utilization of

multi-scale structures allows a finer manipulation of the process dynamics. Hence, the design of multi-scale structures may merit further investigations in view of the applications that are particularly sensitive to the power level. Last, it may be of interest to obtain optimized layouts and provide guidelines for mechanical design under different conditions and configurations such as the melting of units with high Rayleigh number, the simultaneous charge and discharge in multi-tube systems and the enhancement of shell-and-tube units with a large number of immersed pipes. The presented work in the field of district heating revealed that our demonstrative robust design and centralized control framework may have interesting capabilities on the small subnetwork considered. However, the method is better suited to larger and more complex transportation networks due to it its scalability properties. Future studies should consider this possibility.

Extensions of the analysis and optimization capabilities

Here, we include some possible extensions of the analysis and design tools developed in this thesis that can greatly contribute to advances in the field of LHTES, DHNs and PEMFCs. LHTES units are often operated with variable operating conditions of the HTF and using a sequence of partial charge/discharge cycles. The design of high conducting structures for stable performance with respect to different utilization strategies and conditions is certainly of interest to commercial installations. For this purpose, we plan on augmenting our design framework with computationally efficient ways for analysis and design under uncertainty such as the Polynomial Chaos Expansion (PCE) or perturbation methods. Advances in the topology optimization of shape memory alloys with programmed dynamics [294] and some recent experiments [200] for pool boiling enhancement are paving the way to the field of deformable smart structures. Our numerical experiments suggested that the length of the optimized fins increases with the amount of energy to be charged and discharged into and from the unit. Designing fins with prescribed dynamics that open and close like flowers by motion in the liquid PCM is a challenging but exciting possible future development. Also advances in the field of DHNs and PEMFCs require the development of additional analysis and optimization capabilities. First, the network model for control applications should be augmented to account for dynamics. This will allow to develop control algorithms based on formal MPC frameworks that are suited to both daily planning and on-line control in ordinary operating conditions. Second, neglecting water management in PEMFC may yield non-realistic results in low temperature systems. For this reason, the model should be improved to account

for multi-phase flow. Last, preliminary studies that were not presented in this thesis suggest that the optimized 3D flow field layouts present unintuitive features able to further boost performance. However, the physical model should also consider electrical conduction since ohmic losses may become predominant in some geometric configurations.

Advances in topology optimization for energy applications

Here, we discuss recommendations for future research in the field of topology optimization that can increase its employability to solve energy problems. Most of the optimization experiments presented in this thesis involved coupled flow and transport phenomena. For these multi-physics problems, the selection of proper continuation trajectories on the penalization parameters is by no mean a trivial task. Our analysis demonstrated that improper choices may lead to poorly-performing local minima due to an imbalance between transport mechanisms at early continuation steps. This issue is generally solved by an endless and frustrating parameters tuning. Our study provided insights into the methodological problem but did not identify any suitable solution. We are convinced that future researches should look at rigorous methods for the proper selection of the continuation schemes in coupled problems. The accuracy of our novel multi-scale multi-material topology optimization framework based on geometric primitive level-sets was found to be affected by the issue of the interface superposition, which is inherent in the Ersatz material approach for the geometry representation. Although this created limited problems in the design examples considered in this thesis, we welcome future developments using design models that retain a crisp definition of the interfaces, such as the XFEM level-set approach. Last, we observed a wide acceptance among practitioners of our topology optimization framework based on geometric primitives. Well-behaved shapes of structures are easy to understand, fabricate and verify. Since the method is still in its infancy, large efforts should be taken in the future to explore and improve this promising route.

Broadening the range of energy problems

This thesis focused only on three representative energy applications. There is a large number of high potential technologies in the energy field that demand advanced design methodologies to reduce costs, improve the efficiency and increase the resilience. We plan on broadening the spectrum of energy applications to: the design of 3D printed plastic blades for small hydro turbines; the design of flow fields in

redox flow batteries; the design of ceramic multi-scale absorbers for volumetric CSP receivers; the design and control of large electricity and gas distribution networks.

References

[1] Niels Aage, Thomas H. Poulsen, Allan Gersborg-Hansen, and Ole Sigmund. Topology optimization of large scale stokes flow problems. *Structural and Multidisciplinary Optimization*, 35(2):175–180, jun 2007. doi:10.1007/s00158-007-0128-0. [Cited on page 200]

[2] Ammar M. Abdulateef, Sohif Mat, Jasim Abdulateef, Kamaruzzaman Sopian, and Abduljalil A. Al-Abidi. Geometric and design parameters of fins employed for enhancing thermal energy storage systems: a review. *Renewable and Sustainable Energy Reviews*, 82:1620–1635, feb 2018. doi:10.1016/j.rser.2017.07.009. [Cited on pages 50 and 53]

[3] Ammar M. Abdulateef, Sohif Mat, Kamaruzzaman Sopian, Jasim Abdulateef, and Ali A. Gitan. Experimental and computational study of melting phase-change material in a triplex tube heat exchanger with longitudinal/triangular fins. *Solar Energy*, 155:142–153, oct 2017. doi:10.1016/j.solener.2017.06.024. [Cited on page 181]

[4] R. Adinberg, D. Zvegilsky, and M. Epstein. Heat transfer efficient thermal energy storage for steam generation. *Energy Conversion and Management*, 51(1):9–15, jan 2010. doi:10.1016/j.enconman.2009.08.006. [Cited on page 50]

[5] E. Afshari, M. Mosharaf-Dehkordi, and H. Rajabian. An investigation of the PEM fuel cells performance with partially restricted cathode flow channels and metal foam as a flow distributor. *Energy*, 118:705–715, jan 2017. doi:10.1016/j.energy.2016.10.101. [Cited on pages 325 and 354]

[6] Francis Agyenim, Philip Eames, and Mervyn Smyth. Heat transfer enhancement in medium temperature thermal energy storage system using a multitube heat transfer array. *Renewable Energy*, 35(1):198–207, jan 2010. doi:10.1016/j.renene.2009.03.010. [Cited on pages 47 and 48]

[7] Francis Agyenim, Neil Hewitt, Philip Eames, and Mervyn Smyth. A review of materials, heat transfer and phase change problem formulation for latent heat thermal energy storage systems (LHTESS). *Renewable and Sustainable Energy Reviews*, 14(2):615–628, feb 2010. doi:10.1016/j.rser.2009.10.015. [Cited on pages 47, 240, and 243]

[8] Dewan Hasan Ahmed and Hyung Jin Sung. Effects of channel geometrical configuration and shoulder width on PEMFC performance at high current density. *Journal of Power Sources*, 162(1):327–339, nov 2006. doi:10.1016/j.jpowsour.2006.06.083. [Cited on pages 324 and 327]

[9] Ararimeh Aiyejina and M. K. S. Sastry. PEMFC flow channel geometry optimization: A review. *Journal of Fuel Cell Science and Technology*, 9(1):011011, 2012. doi:10.1115/1.4005393. [Cited on pages 321, 323, and 324]

[10] Maher A. R. Sadiq Al-Baghdadi and Haroun A. K. Shahad Al-Janabi. Effect of design parameters on the hygro-thermal stresses in proton exchange membranes of the fuel cells. *Engineering Applications of Computational Fluid Mechanics*, 1(2):71–87, jan 2007. doi:10.1080/19942060.2007.11015183. [Cited on page 323]

[11] Saleh Nasser AL-Saadi and Zhiqiang (John) Zhai. Modeling phase change materials embedded in building enclosure: A review. *Renewable and Sustainable Energy Reviews*, 21:659–673, may 2013. doi:10.1016/j.rser.2013.01.024. [Cited on page 59]

[12] M. R. Albert and K. O'Neill. Moving boundary-moving mesh analysis of phase change using finite elements with transfinite mappings. *International Journal for Numerical Methods in Engineering*, 23(4):591–607, apr 1986. doi:10.1002/nme.1620230406. [Cited on page 56]

[13] Joe Alexandersen, Niels Aage, Casper Schousboe Andreasen, and Ole Sigmund. Topology optimisation for natural convection problems. *International Journal for Numerical Methods in Fluids*, 76(10):699–721, sep 2014. doi:10.1002/fld.3954. [Cited on pages v, 184, 200, 201, 203, 208, 209, and 344]

[14] Joe Alexandersen and Boyan S. Lazarov. Topology optimisation of manufacturable microstructural details without length scale separation using a spectral coarse basis preconditioner. *Computer Methods in Applied Mechanics and Engineering*, 290:156–182, jun 2015. doi:10.1016/j.cma.2015.02.028. [Cited on page 126]

[15] Joe Alexandersen and Boyan Stefanov Lazarov. Tailoring macroscale response of mechanical and heat transfer systems by topology optimization of microstructural details. In *Computational Methods in Applied Sciences*, pages 267–288. Springer International Publishing, 2015. doi:10.1007/978-3-319-18320-6_15. [Cited on page 126]

[16] Joe Alexandersen, Ole Sigmund, and Niels Aage. Large scale three-dimensional topology optimisation of heat sinks cooled by natural convection. *International Journal of Heat and Mass Transfer*, 100:876–891, sep 2016. doi:10.1016/j.ijheatmasstransfer.2016.05.013. [Cited on pages 200, 201, 203, 209, and 344]

[17] E. Alizadeh, M. Rahimi-Esbo, S.M. Rahgoshay, S.H.M. Saadat, and M. Khorshidian. Numerical and experimental investigation of cascade type serpentine flow field of reactant gases for improving performance of PEM fuel cell. *International Journal of Hydrogen Energy*, 42(21):14708–14724, may 2017. doi:10.1016/j.ijhydene.2017.04.212. [Cited on page 329]

[18] Grégoire Allaire. A brief introduction to homogenization and miscellaneous applications. *ESAIM: Proceedings*, 37:1–49, sep 2012. doi:10.1051/proc/201237001. [Cited on pages 113, 114, 115, 116, and 117]

[19] Grégoire Allaire, François Jouve, and Anca-Maria Toader. Structural optimization using sensitivity analysis and a level-set method. *Journal of Computational Physics*, 194(1):363–393, feb 2004. doi:10.1016/j.jcp.2003.09.032. [Cited on page 15]

[20] Yosr Allouche, Szabolcs Varga, Chiheb Bouden, and Armando C. Oliveira. Validation of a CFD model for the simulation of heat transfer in a tubes-in-tank PCM storage unit. *Renewable Energy*, 89:371–379, apr 2016. doi:10.1016/j.renene.2015.12.038. [Cited on page 260]

[21] Saleh Almsater, Alemu Alemu, Wasim Saman, and Frank Bruno. Development and experimental validation of a CFD model for PCM in a vertical triplex tube heat exchanger. *Applied Thermal Engineering*, 116:344–354, apr 2017. doi:10.1016/j.applthermaleng.2017.01.104. [Cited on page 47]

[22] Guruprasad Alva, Yaxue Lin, and Guiyin Fang. An overview of thermal energy storage systems. *Energy*, 144:341–378, feb 2018. doi:10.1016/j.energy.2017.12.037. [Cited on page 1]

[23] Guruprasad Alva, Lingkun Liu, Xiang Huang, and Guiyin Fang. Thermal energy storage materials and systems for solar energy applications. *Renewable and Sustainable Energy Reviews*, 68:693–706, 2017. doi:10.1016/J.RSER.2016.10.021. [Cited on pages 244, 245, 246, 247, and 269]

[24] Luigi Ambrosio and Giuseppe Buttazzo. An optimal design problem with perimeter penalization. *Calculus of Variations and Partial Differential Equations*, 1(1):55–69, mar 1993. doi:10.1007/bf02163264. [Cited on page 31]

[25] Refrigerating American Society of Heating, Air-Conditioning Engineers, and Ashrae. *2013 ASHRAE Handbook: Fundamentals*. ASHRAE Handbook Fundamentals Systems-International Metric System. ASHRAE, 2013. [Cited on page 288]

[26] Patrick R. Amestoy, Iain S. Duff, Jean-Yves L'Excellent, and Jacko Koster. A fully asynchronous multifrontal solver using distributed dynamic scheduling. *SIAM Journal on Matrix Analysis and Applications*, 23(1):15–41, jan 2001. doi:10.1137/s0895479899358194. [Cited on page 343]

[27] Casper Schousboe Andreasen, Allan Roulund Gersborg, and Ole Sigmund. Topology optimization of microfluidic mixers. *International Journal for Numerical Methods in Fluids*, 61(5):498–513, oct 2009. doi:10.1002/fld.1964. [Cited on page 200]

[28] Casper Schousboe Andreasen and Ole Sigmund. Saturated poroelastic actuators generated by topology optimization. *Structural and Multidisciplinary Optimization*, 43(5):693–706, dec 2010. doi:10.1007/s00158-010-0597-4. [Cited on page 152]

[29] Erik Andreassen and Casper Schousboe Andreasen. How to determine composite material properties using numerical homogenization. *Computational Materials Science*, 83:488–495, feb 2014. doi:10.1016/j.commatsci.2013.09.006. [Cited on pages 118 and 119]

[30] Simone Arena, Efisio Casti, Jaume Gasia, Luisa F. Cabeza, and Giorgio Cau. Numerical simulation of a finned-tube LHTES system: influence of the mushy zone constant on the phase change behaviour. *Energy Procedia*, 126:517–524, sep 2017. doi:10.1016/j.egypro.2017.08.237. [Cited on pages 181 and 196]

[31] J.S. Arora and Q. Wang. Review of formulations for structural and mechanical system optimization. *Structural and Multidisciplinary Optimization*, 30(4):251–272, jun 2005. doi:10.1007/s00158-004-0509-6. [Cited on page 17]

[32] A. Arvay, J. French, J.-C. Wang, X.-H. Peng, and A.M. Kannan. Nature inspired flow field designs for proton exchange membrane fuel cell. *International Journal of Hydrogen Energy*, 38(9):3717–3726, mar 2013. doi:10.1016/j.ijhydene.2012.12.149. [Cited on pages 323, 331, and 343]

[33] A Arvay, J French, J-C Wang, X-H Peng, and A M Kannan. Modeling and simulation of biologically inspired flow field designs for proton exchange membrane fuel cells. *The Open Electrochemistry Journal*, 6(1), 2015. [Cited on page 332]

[34] Moosa Ashrafi, Homayoon Kanani, and Mehrzad Shams. Numerical and experimental study of two-phase flow uniformity in channels of parallel PEM fuel cells with modified z-type flow-fields. *Energy*, 147:317–328, mar 2018. doi:10.1016/j.energy.2018.01.064. [Cited on pages 327 and 330]

[35] Donald R Askeland and Pradeep Prabhakar Phulé. *The science and engineering of materials*. Springer, 2006. [Cited on page 248]

[36] Aditya Atal, Yuping Wang, Mayur Harsha, and Subrata Sengupta. Effect of porosity of conducting matrix on a phase change energy storage device. *International Journal of Heat and Mass Transfer*, 93:9–16, feb 2016. doi:10.1016/j.ijheatmasstransfer.2015.09.033. [Cited on page 109]

[37] Bilal M. Ayyub. Systems resilience for multihazard environments: Definition, metrics, and valuation for decision making. *Risk Analysis*, 34(2):340–355, jul 2013. doi:10.1111/risa.12093. [Cited on page 278]

[38] Artem V. Babayan, Dragan A. Savic, Godfrey A. Walters, and Zoran S. Kapelan. Robust least-cost design of water distribution networks using redundancy and integration-based methodologies. *Journal of Water Resources Planning and Management*, 133(1):67–77, jan 2007. doi:10.1061/(asce)0733-9496(2007)133:1(67). [Cited on pages 280 and 281]

[39] Ruben Baetens, Bjørn Petter Jelle, and Arild Gustavsen. Phase change materials for building applications: A state-of-the-art review. *Energy and Buildings*, 42(9):1361–1368, sep 2010. doi:10.1016/j.enbuild.2010.03.026. [Cited on page 241]

[40] John Banhart. Manufacture, characterisation and application of cellular metals and metal foams. *Progress in Materials Science*, 46(6):559–632, jan 2001. doi:10.1016/s0079-6425(00)00002-5. [Cited on page 108]

[41] R. Baños, C. Gil, J. Reca, and F.G. Montoya. A memetic algorithm applied to the design of water distribution networks. *Applied Soft Computing*, 10(1):261–266, jan 2010. doi:10.1016/j.asoc.2009.07.010. [Cited on page 281]

[42] Tilman Barz, Christoph Zauner, Daniel Lager, Diana C. López Cárdenas, Florian Hengstberger, Mariano Nicolás Cruz Bournazou, and Klemens Marx. Experimental analysis and numerical modeling of a shell and tube heat storage unit with phase change materials. *Industrial & Engineering Chemistry Research*, 55(29):8154–8164, jul 2016. doi:10.1021/acs.iecr.6b01080. [Cited on page 240]

[43] Biswajit Basu and A W Date. Numerical modelling of melting and solidification problems—a review. *Sadhana*, 13(3):169–213, nov 1988. doi:10.1007/bf02812200. [Cited on page 179]

[44] Michael Bauccio et al. *ASM metals reference book*. ASM international, 1993. [Cited on page 248]

[45] Anton Beck, Martin Koller, Heimo Walter, and Michael Hameter. Transient numerical analysis of different finned tube designs for the use in latent heat thermal energy storage devices. In *Proceedings of the ASME*, 2015. doi:10.1115/es2015-49145. [Cited on pages 50 and 54]

[46] Anton Beck, Martin Koller, Heimo Walter, and Michael Hameter. Transient numerical analysis of different finned tube designs for use in latent heat thermal energy storage devices. In *Proceedings of the ASME 2015 9th International Conference on Energy Sustainability*. ASME International, jun 2015. doi:10.1115/es2015-49145. [Cited on pages 176 and 248]

[47] C Beckermann and R Viskanta. Double-diffusive convection during dendritic solidification of a binary mixture. *PhysicoChemical Hydrodynamics*, 10(2):195–213, 1988. [Cited on page 179]

[48] N. Beemkumar, A. Karthikeyan, D. Yuvarajan, and S. Lakshmi Sankar. Experimental investigation on improving the heat transfer of cascaded thermal storage system using different fins. *Arabian Journal for Science and Engineering*, 42(5):2055–2065, mar 2017. doi:10.1007/s13369-017-2455-9. [Cited on page 53]

[49] M. Behandish and Z.Y. Wu. Concurrent pump scheduling and storage level optimization using meta-models and evolutionary algorithms. *Procedia Engineering*, 70:103–112, 2014. doi:10.1016/j.proeng.2014.02.013. [Cited on page 284]

[50] M. Belusko, N.H.S. Tay, M. Liu, and F. Bruno. Effective tube-in-tank PCM thermal storage for CSP applications, part 2: Parametric assessment and impact of latent fraction. *Solar Energy*, 139:744–756, dec 2016. doi:10.1016/j.solener.2015.09.034. [Cited on page 240]

[51] M. P. Bendsøe. Optimal shape design as a material distribution problem. *Structural Optimization*, 1(4):193–202, dec 1989. doi:10.1007/bf01650949. [Cited on pages 12 and 27]

[52] M. P. Bendsøe and A. R. Díaz. Optimization of material properties for mindlin plate design. *Structural Optimization*, 6(4):268–270, dec 1993. doi:10.1007/bf01743387. [Cited on page 126]

[53] M. P. Bendsøe and O. Sigmund. Material interpolation schemes in topology optimization. *Archive of Applied Mechanics (Ingenieur Archiv)*, 69(9-10):635–654, nov 1999. doi:10.1007/s004190050248. [Cited on page 28]

[54] Martin P. Bendsøe and Ole Sigmund. *Topology Optimization: theory, methods and applications*. Springer Berlin Heidelberg, 2004. doi:10.1007/978-3-662-05086-6. [Cited on pages 17, 29, and 293]

[55] Martin Philip Bendsøe and Noboru Kikuchi. Generating optimal topologies in structural design using a homogenization method. *Computer Methods in Applied Mechanics and Engineering*, 71(2):197–224, nov 1988. doi:10.1016/0045-7825(88)90086-2. [Cited on pages 12, 31, and 125]

[56] W.D. Bennon and F.P. Incropera. A continuum model for momentum, heat and species transport in binary solid-liquid phase change systems i. model formulation. *International Journal of Heat and Mass Transfer*, 30(10):2161–2170, oct 1987. doi:10.1016/0017-9310(87)90094-9. [Cited on page 179]

[57] M. S. Bhat, D. R. Poirier, and J. C. Heinrich. Permeability for cross flow through columnar-dendritic alloys. *Metallurgical and Materials Transactions B*, 26(5):1049–1056, oct 1995. doi:10.1007/bf02654107. [Cited on page 179]

[58] Lorenz T. Biegler, Omar Ghattas, Matthias Heinkenschloss, and Bart van Bloemen Waanders. Large-scale PDE-constrained optimization: An introduction. In *Large-Scale PDE-Constrained Optimization*, pages 3–13. Springer Berlin Heidelberg, 2003. doi:10.1007/978-3-642-55508-4_1. [Cited on page 17]

[59] John Adrian Bondy and Uppaluri Siva Ramachandra Murty. *Graph theory with applications*, volume 290. Citeseer, 1976. doi:10.1007/978-1-349-03521-2. [Cited on page 290]

[60] R Bonnerot and P Jamet. Numerical computation of the free boundary for the two-dimensional stefan problem by space-time finite elements. *Journal of Computational Physics*, 25(2):163–181, oct 1977. doi:10.1016/0021-9991(77)90019-5. [Cited on page 56]

[61] Gratien Bonvin, Sophie Demassey, Claude Le Pape, Nadia Maïzi, Vincent Mazauric, and Alfredo Samperio. A convex mathematical program for pump scheduling in a class of branched water networks. *Applied Energy*, 185:1702–1711, jan 2017. doi:10.1016/j.apenergy.2015.12.090. [Cited on page 283]

[62] T. Borrvall. Topology optimization of elastic continua using restriction. *Archives of Computational Methods in Engineering*, 8(4):351–385, dec 2001. doi:10.1007/bf02743737. [Cited on page 32]

[63] Thomas Borrvall and Joakim Petersson. Topology optimization of fluids in stokes flow. *International Journal for Numerical Methods in Fluids*, 41(1):77–107, 2002. doi:10.1002/fld.426. [Cited on pages 199, 200, and 201]

[64] A. D. Brent, V. R. Voller, and K. J. Reid. Enthalpy-porosity technique for modeling convection-diffusion phase change: Application to the melting of a pure metal. *Numerical Heat Transfer, Part B: Fundamentals*, 13(3):297–318, 1988. doi:10.1080/10407798808551388. [Cited on pages 180 and 181]

[65] D. R. Broad, H. R. Maier, and G. C. Dandy. Optimal operation of complex water distribution systems using metamodels. *Journal of Water Resources Planning and Management*, 136(4):433–443, jul 2010. doi:10.1061/(asce)wr.1943-5452.0000052. [Cited on page 283]

[66] Darren R. Broad, Graeme C. Dandy, and Holger R. Maier. A systematic approach to determining metamodel scope for risk-based optimization and its application to water distribution system design. *Environmental Modelling & Software*, 69:382–395, jul 2015. doi:10.1016/j.envsoft.2014.11.015. [Cited on page 280]

[67] Alexander N. Brooks and Thomas J.R. Hughes. Streamline upwind/petrov-galerkin formulations for convection dominated flows with particular emphasis on the incompressible navier-stokes equations. *Computer Methods in Applied Mechanics and Engineering*, 32(1-3):199–259, sep 1982. doi:10.1016/0045-7825(82)90071-8. [Cited on pages 188 and 189]

[68] Michel Bruneau, Stephanie E. Chang, Ronald T. Eguchi, George C. Lee, Thomas D. O'Rourke, Andrei M. Reinhorn, Masanobu Shinozuka, Kathleen Tierney, William A. Wallace, and Detlof von Winterfeldt. A framework to quantitatively assess and enhance the seismic resilience of communities. *Earthquake Spectra*, 19(4):733–752, nov 2003. doi:10.1193/1.1623497. [Cited on page 278]

[69] T.E. Bruns. A reevaluation of the SIMP method with filtering and an alternative formulation for solid–void topology optimization. *Structural and Multidisciplinary Optimization*, 30(6):428–436, aug 2005. doi:10.1007/s00158-005-0537-x. [Cited on page 29]

[70] Tyler E. Bruns and Daniel A. Tortorelli. Topology optimization of nonlinear elastic structures and compliant mechanisms. *Computer Methods in Applied Mechanics and Engineering*, 190(26-27):3443–3459, mar 2001. doi:10.1016/s0045-7825(00)00278-4. [Cited on page 33]

[71] I. M. Bugaje. Enhancing the thermal response of latent heat storage systems. *International Journal of Energy Research*, 21(9):759–766, 1997. doi:10.1002/(SICI)1099-114X(199707)21:9<759::AID-ER254>3.0.CO;2-7. [Cited on page 111]

[72] L.F. Cabeza, H. Mehling, S. Hiebler, and F. Ziegler. Heat transfer enhancement in water when used as PCM in thermal energy storage. *Applied Thermal Engineering*, 22(10):1141–1151, jul 2002. doi:10.1016/s1359-4311(02)00035-2. [Cited on page 108]

[73] L.F. Cabeza, J. Roca, M. Nogués, H. Mehling, and S. Hiebler. Immersion corrosion tests on metal-salt hydrate pairs used for latent heat storage in the 48 to 58°c temperature range. *Materials and Corrosion*, 53(12):902–907, dec 2002. doi:10.1002/maco.200290004. [Cited on page 246]

[74] Joseph E. Cadman, Shiwei Zhou, Yuhang Chen, and Qing Li. On design of multi-functional microstructural materials. *Journal of Materials Science*, 48(1):51–66, jul 2012. doi:10.1007/s10853-012-6643-4. [Cited on pages 122 and 123]

[75] William D Callister and David G Rethwisch. *Materials science and engineering*, volume 5. John Wiley & Sons NY, 2011. [Cited on pages 246, 247, and 248]

[76] Y. Cao and A. Faghri. A numerical analysis of phase-change problems including natural convection. *Journal of Heat Transfer*, 112(3):812, 1990. doi:10.1115/1.2910466. [Cited on pages 177 and 179]

[77] Bruno Cárdenas and Noel León. High temperature latent heat thermal energy storage: Phase change materials, design considerations and performance enhancement techniques. *Renewable and Sustainable Energy Reviews*, 27:724–737, nov 2013. doi:10.1016/j.rser.2013.07.028. [Cited on pages 243, 246, and 247]

[78] Philip Crosbie Carman. Fluid flow through granular beds. *Transactions-Institution of Chemical Engineeres*, 15:150–166, 1937. [Cited on pages 180 and 181]

[79] L. Carrette, K. A. Friedrich, and U. Stimming. Fuel cells - fundamentals and applications. *Fuel Cells*, 1(1):5–39, may 2001. doi:10.1002/1615-6854(200105)1:1<5::aid-fuce5>3.0.co;2-g. [Cited on page 321]

[80] G Cembrano, G Wells, J Quevedo, R Pérez, and R Argelaguet. Optimal control of a water distribution network in a supervisory control system. *Control Engineering Practice*, 8(10):1177–1188, oct 2000. doi:10.1016/s0967-0661(00)00058-7. [Cited on page 284]

[81] Firat C. Cetinbas, Suresh G. Advani, and Ajay K. Prasad. Three dimensional proton exchange membrane fuel cell cathode model using a modified agglomerate approach based on discrete catalyst particles. *Journal of Power Sources*, 250:110–119, mar 2014. doi:10.1016/j.jpowsour.2013.10.138. [Cited on pages 334, 338, and 345]

[82] Vivien J. Challis, James K. Guest, Joseph F. Grotowski, and Anthony P. Roberts. Computationally generated cross-property bounds for stiffness and fluid permeability using topology optimization. *International Journal of Solids and Structures*, 49(23-24):3397–3408, nov 2012. doi:10.1016/j.ijsolstr.2012.07.019. [Cited on page 152]

[83] Amrit Chandan, Mariska Hattenberger, Ahmad El-kharouf, Shangfeng Du, Aman Dhir, Valerie Self, Bruno G. Pollet, Andrew Ingram, and Waldemar Bujalski. High temperature (HT) polymer electrolyte membrane fuel cells (PEMFC) – a review. *Journal of Power Sources*, 231:264–278, jun 2013. doi:10.1016/j.jpowsour.2012.11.126. [Cited on pages 324, 354, and 366]

[84] Denver Cheddie and Norman Munroe. Review and comparison of approaches to proton exchange membrane fuel cell modeling. *Journal of Power Sources*, 147(1-2):72–84, sep 2005. doi:10.1016/j.jpowsour.2005.01.003. [Cited on page 323]

[85] Shizhong Chen, Xuyang Zhang, and Hongtan Liu. Effect of pressure difference between adjacent channels in an adjustable flow field in PEM fuel cells. *International Journal of Hydrogen Energy*, 42(7):4667–4672, feb 2017. doi:10.1016/j.ijhydene.2016.10.164. [Cited on page 329]

[86] Stephen Chen, James Montgomery, and Antonio Bolufé-Röhler. Measuring the curse of dimensionality and its effects on particle swarm optimization and differential evolution. *Applied Intelligence*, 42(3):514–526, nov 2014. doi:10.1007/s10489-014-0613-2. [Cited on page 281]

[87] Shan-Jen Cheng, Jr-Ming Miao, and Sheng-Ju Wu. Use of metamodeling optimal approach promotes the performance of proton exchange membrane fuel cell (PEMFC). *Applied Energy*, 105:161–169, may 2013. doi:10.1016/j.apenergy.2013.01.001. [Cited on page 321]

[88] Jong Chan Choi and Sang Done Kim. Heat-transfer characteristics of a latent heat storage system using MgCl2 · 6h2o. *Energy*, 17(12):1153–1164, dec 1992. doi:10.1016/0360-5442(92)90004-j. [Cited on page 52]

[89] Mohammad Ziauddin Chowdhury and Yahya Erkan Akansu. Novel convergent-divergent serpentine flow fields effect on PEM fuel cell performance. *International Journal of Hydrogen Energy*, 42(40):25686–25694, oct 2017. doi:10.1016/j.ijhydene.2017.04.079. [Cited on page 330]

[90] Doina Cioranescu and Patrizia Donato. An introduction to homogenization, volume 17 of oxford lecture series in mathematics and its applications. *The Clarendon Press Oxford University Press, New York*, 4:118, 1999. [Cited on page 114]

[91] Joe K. Cochran, Kevin Hurysz, Kon Juin Lee, and Thomas H. Jr. Sanders. Extrusion and thermo-chemical processing of layered linear cellular alloys. *Materials Science Forum*, 426-432:4295–4300, 2003. doi:10.4028/www.scientific.net/msf.426-432.4295. [Cited on pages 110 and 112]

[92] Ramon Codina. A discontinuity-capturing crosswind-dissipation for the finite element solution of the convection-diffusion equation. *Computer Methods in Applied Mechanics and Engineering*, 110(3-4):325–342, dec 1993. doi:10.1016/0045-7825(93)90213-h. [Cited on page 343]

[93] P. G. Coelho, P. R. Fernandes, J. M. Guedes, and H. C. Rodrigues. A hierarchical model for concurrent material and topology optimisation of three-dimensional structures. *Structural and Multidisciplinary Optimization*, 35(2):107–115, jun 2007. doi:10.1007/s00158-007-0141-3. [Cited on page 125]

[94] P. G. Coelho and H. C. Rodrigues. Hierarchical topology optimization addressing material design constraints and application to sandwich-type structures. *Structural and Multidisciplinary Optimization*, 52(1):91–104, jan 2015. doi:10.1007/s00158-014-1220-x. [Cited on pages 125 and 127]

[95] P.G. Coelho, P.R. Fernandes, H.C. Rodrigues, J.B. Cardoso, and J.M. Guedes. Numerical modeling of bone tissue adaptation—a hierarchical approach for bone apparent density and trabecular structure. *Journal of Biomechanics*, 42(7):830–837, may 2009. doi:10.1016/j.jbiomech.2009.01.020. [Cited on page 125]

[96] P.G. Coelho, J.M. Guedes, and H.C. Rodrigues. Multiscale topology optimization of bi-material laminated composite structures. *Composite Structures*, 132:495–505, nov 2015. doi:10.1016/j.compstruct.2015.05.059. [Cited on page 125]

[97] Peter Coffin and Kurt Maute. A level-set method for steady-state and transient natural convection problems. *Structural and Multidisciplinary Optimization*, 53(5):1047–1067, dec 2015. doi:10.1007/s00158-015-1377-y. [Cited on page 144]

[98] Francesco Colella, Adriano Sciacovelli, and Vittorio Verda. Numerical analysis of a medium scale latent energy storage unit for district heating systems. *Energy*, 45(1):397–406, sep 2012. doi:10.1016/j.energy.2012.03.043. [Cited on pages 243, 267, and 268]

[99] G. Comini, S. Del Giudice, and O. Saro. A conservative algorithm for multidimensional conduction phase change. *International Journal for Numerical Methods in Engineering*, 30(4):697–709, sep 1990. doi:10.1002/nme.1620300410. [Cited on page 62]

[100] G. Comini, S. Del Guidice, R. W. Lewis, and O. C. Zienkiewicz. Finite element solution of non-linear heat conduction problems with special reference to phase change. *International Journal for Numerical Methods in Engineering*, 8(3):613–624, 1974. doi:10.1002/nme.1620080314. [Cited on page 60]

[101] COMSOL. *version 5.0*. COMSOL Inc., Burlington, MA, USA, 2014. [Cited on pages 38, 76, 193, 197, and 343]

[102] Luis A. Crivelli and Sergio R. Idelsohn. A temperature-based finite element solution for phase-change problems. *International Journal for Numerical Methods in Engineering*, 23(1):99–119, jan 1986. doi:10.1002/nme.1620230109. [Cited on pages 63 and 64]

[103] H.T. Cui. Experimental investigation on the heat charging process by paraffin filled with high porosity copper foam. *Applied Thermal Engineering*, 39:26–28, jun 2012. doi:10.1016/j.applthermaleng.2012.01.037. [Cited on page 109]

[104] G. W. Wei D. C. Wan, B. S. V. Patnaik. A new benchmark quality solution for the buoyancy-driven cavity by discrete singular convulution. *Numerical Heat Transfer, Part B: Fundamentals*, 40(3):199–228, sep 2001. doi:10.1080/104077901752379620. [Cited on page 193]

[105] Maria da Conceição Cunha and Joaquim José de Oliveira Sousa. Robust design of water distribution networks for a proactive risk management. *Journal of Water Resources Planning and Management*, 136(2):227–236, mar 2010. doi:10.1061/(asce)wr.1943-5452.0000029. [Cited on page 281]

[106] Cesar E. Damian-Ascencio, Adriana Saldaña-Robles, Abel Hernandez-Guerrero, and Sergio Cano-Andrade. Numerical modeling of a proton exchange membrane fuel cell with tree-like flow field channels based on an entropy generation analysis. *Energy*, 133:306–316, aug 2017. doi:10.1016/j.energy.2017.05.139. [Cited on page 332]

[107] Devendra Dandotiya and N. D. Banker. Numerical investigation of heat transfer enhancement in a multitube thermal energy storage heat exchanger using fins. *Numerical Heat Transfer, Part A: Applications*, 72(5):389–400, sep 2017. doi:10.1080/10407782.2017.1376976. [Cited on page 48]

[108] A. Ali Rabienataj Darzi, Mahmoud Jourabian, and Mousa Farhadi. Melting and solidification of PCM enhanced by radial conductive fins and nanoparticles in cylindrical annulus. *Energy Conversion and Management*, 118:253–263, jun 2016. doi:10.1016/j.enconman.2016.04.016. [Cited on page 50]

[109] A. Ali Rabienataj Darzi, Mahmoud Jourabian, and Mousa Farhadi. Melting and solidification of PCM enhanced by radial conductive fins and nanoparticles in cylindrical annulus. *Energy Conversion and Management*, 118:253–263, jun 2016. doi:10.1016/j.enconman.2016.04.016. [Cited on pages 176 and 248]

[110] G. De Vahl Davis. Natural convection of air in a square cavity: A bench mark numerical solution. *International Journal for Numerical Methods in Fluids*, 3(3):249–264, may 1983. doi:10.1002/fld.1650030305. [Cited on page 193]

[111] G. De Vahl Davis and I. P. Jones. Natural convection in a square cavity: A comparison exercise. *International Journal for Numerical Methods in Fluids*, 3(3):227–248, may 1983. doi:10.1002/fld.1650030304. [Cited on page 193]

[112] Niek de Kruijf, Shiwei Zhou, Qing Li, and Yiu-Wing Mai. Topological design of structures and composite materials with multiobjectives. *International Journal of Solids and Structures*, 44(22-23):7092–7109, nov 2007. doi:10.1016/j.ijsolstr.2007.03.028. [Cited on page 122]

[113] Jiadong Deng, Jun Yan, and Gengdong Cheng. Multi-objective concurrent topology optimization of thermoelastic structures composed of homogeneous porous material. *Structural and Multidisciplinary Optimization*, 47(4):583–597, nov 2012. doi:10.1007/s00158-012-0849-6. [Cited on page 129]

[114] A. Díaz and O. Sigmund. Checkerboard patterns in layout optimization. *Structural Optimization*, 10(1):40–45, aug 1995. doi:10.1007/bf01743693. [Cited on page 30]

[115] Alejandro R. Diaz and Ole Sigmund. A topology optimization method for design of negative permeability metamaterials. *Structural and Multidisciplinary Optimization*, 41(2):163–177, jul 2009. doi:10.1007/s00158-009-0416-y. [Cited on page 122]

[116] Moritz Diehl, H.Georg Bock, Johannes P. Schlöder, Rolf Findeisen, Zoltan Nagy, and Frank Allgöwer. Real-time optimization and nonlinear model predictive control of processes governed by differential-algebraic equations. *Journal of Process Control*, 12(4):577–585, jun 2002. doi:10.1016/s0959-1524(01)00023-3. [Cited on page 285]

[117] J N Reddy Dr. *An Introduction to the Finite Element Method*. McGraw-Hill Education, 2005. [Cited on page 71]

[118] Oleinik O. A. E., Shamaev A. S., and Yosifian G. A. *Mathematical Problems in Elasticity and Homogenization*. Elsevier, 1992. doi:10.1016/s0168-2024(08)x7009-2. [Cited on page 114]

[119] Yalchin Efendiev and Tom Hou. *Multiscale Finite Element Methods*. Springer New York, 2009. doi:10.1007/978-0-387-09496-0. [Cited on page 126]

[120] M. Esapour, M.J. Hosseini, A.A. Ranjbar, Y. Pahamli, and R. Bahrampoury. Phase change in multi-tube heat exchangers. *Renewable Energy*, 85:1017–1025, jan 2016. doi:10.1016/j.renene.2015.07.063. [Cited on page 240]

[121] Mehmet Esen, Aydin Durmuş, and Ayla Durmuş. Geometric design of solar-aided latent heat store depending on various parameters and phase change materials. *Solar Energy*, 62(1):19–28, jan 1998. doi:10.1016/s0038-092x(97)00104-7. [Cited on page 47]

[122] EUCO (European Council). Council decision establishing the specific programme implementing horizon 2020—the framework programme for research and innovation (2014–2020), 2013. [Cited on page 1]

[123] EUCO (European Council). Horizon 2020: Work programme 2016-2017, 2016. [Cited on page 373]

[124] EUCO (European Council). The strategic energy technology (set) plan, 2017. [Cited on page 3]

[125] Muzaffar M. Eusuff and Kevin E. Lansey. Optimization of water distribution network design using the shuffled frog leaping algorithm. *Journal of Water Resources Planning and Management*, 129(3):210–225, may 2003. doi:10.1061/(asce)0733-9496(2003)129:3(210). [Cited on page 282]

[126] A. Evgrafov. Topology optimization of slightly compressible fluids. *ZAMM*, 86(1):46–62, jan 2006. doi:10.1002/zamm.200410223. [Cited on page 200]

[127] Anton Evgrafov. The limits of porous materials in the topology optimization of stokes flows. *Applied Mathematics and Optimization*, 52(3):263–277, oct 2005. doi:10.1007/s00245-005-0828-z. [Cited on page 200]

[128] Anton Evgrafov. Simultaneous optimization of topology and geometry of flow networks. *Structural and Multidisciplinary Optimization*, 32(2):99–109, may 2006. doi:10.1007/s00158-005-0590-5. [Cited on pages 282 and 293]

[129] Víctor D. Fachinotti and Michel Bellet. Linear tetrahedral finite elements for thermal shock problems. *International Journal of Numerical Methods for Heat & Fluid Flow*, 16(5):590–601, jul 2006. doi:10.1108/09615530610669120. [Cited on pages 69 and 70]

[130] Víctor D Fachinotti, Alberto Cardona, and Alfredo E Huespe. A fast convergent and accurate temperature model for phase-change heat conduction. *International Journal for Numerical Methods in Engineering*, 44(12):1863–1884, 1999. [Cited on pages 63 and 64]

[131] Amir Faghri and Yuwen Zhang. *Transport phenomena in multiphase systems*. Academic Press, 2006. [Cited on page 242]

[132] Li-Wu Fan, Zi-Qin Zhu, Sheng-Lan Xiao, Min-Jie Liu, Hai Lu, Yi Zeng, Zi-Tao Yu, and Ke-Fa Cen. An experimental and numerical investigation of constrained melting heat transfer of a phase change material in a circumferentially finned spherical capsule for thermal energy storage. *Applied Thermal Engineering*, 100:1063–1075, may 2016. doi:10.1016/j.applthermaleng.2016.02.125. [Cited on page 247]

[133] Raziyeh Farmani, Godfrey A. Walters, and Dragan A. Savic. Trade-off between total cost and reliability for anytown water distribution network. *Journal of Water Resources Planning and Management*, 131(3):161–171, may 2005. doi:10.1061/(asce)0733-9496(2005)131:3(161). [Cited on pages 280 and 281]

[134] D. Fernandes, F. Pitié, G. Cáceres, and J. Baeyens. Thermal energy storage: "how previous findings determine current research priorities". *Energy*, 39(1):246–257, mar 2012. doi:10.1016/j.energy.2012.01.024. [Cited on page 2]

[135] Y FERNG and A SU. A three-dimensional full-cell CFD model used to investigate the effects of different flow channel designs on PEMFC performance. *International Journal of Hydrogen Energy*, 32(17):4466–4476, dec 2007. doi:10.1016/j.ijhydene.2007.05.012. [Cited on pages 325 and 327]

[136] Gerard Ferrer, Aran Solé, Camila Barreneche, Ingrid Martorell, and Luisa F. Cabeza. Corrosion of metal containers for use in PCM energy storage. *Renewable Energy*, 76:465–469, apr 2015. doi:10.1016/j.renene.2014.11.036. [Cited on page 247]

[137] Joel H. Ferziger and Milovan Perić. *Computational Methods for Fluid Dynamics*. Springer Berlin Heidelberg, 1996. doi:10.1007/978-3-642-97651-3. [Cited on page 291]

[138] Frédéric Feyel and Jean-Louis Chaboche. FE2 multiscale approach for modelling the elastoviscoplastic behaviour of long fibre SiC/ti composite materials. *Computer Methods in Applied Mechanics and Engineering*, 183(3-4):309–330, mar 2000. doi:10.1016/s0045-7825(99)00224-8. [Cited on page 126]

[139] Thomas Fiedler, Andreas Öchsner, Irina V. Belova, and Graeme E. Murch. Thermal conductivity enhancement of compact heat sinks using cellular metals. In *Diffusion in Solids and Liquids III*, pages 222–226. Trans Tech Publications Ltd., feb 2008. doi:10.4028/3-908451-51-5.222. [Cited on page 111]

[140] Evan Fleming, Shaoyi Wen, Li Shi, and Alexandre K. da Silva. Experimental and theoretical analysis of an aluminum foam enhanced phase change thermal storage unit. *International Journal of Heat and Mass Transfer*, 82:273–281, mar 2015. doi:10.1016/j.ijheatmasstransfer.2014.11.022. [Cited on page 109]

[141] C. Fleury. CONLIN: An efficient dual optimizer based on convex approximation concepts. *Structural Optimization*, 1(2):81–89, jun 1989. doi:10.1007/bf01637664. [Cited on page 20]

[142] Claude Fleury and Vincent Braibant. Structural optimization: A new dual method using mixed variables. *International Journal for Numerical Methods in Engineering*, 23(3):409–428, mar 1986. doi:10.1002/nme.1620230307. [Cited on page 20]

[143] Victor Fontalvo, Danny Illera, Humberto Gómez, and Marco Sanjuan. CFD multiphysics modeling and performance evaluation of PEM fuel cells. In *Volume 6: Energy*. ASME, nov 2017. doi:10.1115/imece2017-72160. [Cited on page 338]

[144] Éliton Fontana, Erasmo Mancusi, Adriano da Silva, Viviana Cocco Mariani, Antônio Augusto Ulson de Souza, and Selene M.A. Guelli Ulson de Souza. Study of the effects of flow channel with non-uniform cross-sectional area on PEMFC species and heat transfer. *International Journal of Heat and Mass Transfer*, 54(21-22):4462–4472, oct 2011. doi:10.1016/j.ijheatmasstransfer.2011.06.037. [Cited on pages 326 and 327]

[145] F. Fornarelli, S.M. Camporeale, B. Fortunato, M. Torresi, P. Oresta, L. Magliocchetti, A. Miliozzi, and G. Santo. CFD analysis of melting process in a shell-and-tube latent heat storage for concentrated solar power plants. *Applied Energy*, 164:711–722, feb 2016. doi:10.1016/j.apenergy.2015.11.106. [Cited on pages 267 and 268]

[146] Leopoldo Penna Franca and Eduardo Gomes Dutra Do Carmo. The galerkin gradient least-squares method. *Computer Methods in Applied Mechanics and Engineering*, 74(1):41–54, sep 1989. doi:10.1016/0045-7825(89)90085-6. [Cited on page 70]

[147] Alessandro Franco and Michele Versace. Optimum sizing and operational strategy of CHP plant for district heating based on the use of composite indicators. *Energy*, 124:258–271, apr 2017. doi:10.1016/j.energy.2017.02.062. [Cited on page 277]

[148] Luciana S. Freire, Ermete Antolini, Marcelo Linardi, Elisabete I. Santiago, and Raimundo R. Passos. Influence of operational parameters on the performance of PEMFCs with serpentine flow field channels having different (rectangular and trapezoidal) cross-section shape. *International Journal of Hydrogen Energy*, 39(23):12052–12060, aug 2014. doi:10.1016/j.ijhydene.2014.06.041. [Cited on pages 325 and 327]

[149] Okitsugu Fujiwara and Do Ba Khang. A two-phase decomposition method for optimal design of looped water distribution networks. *Water Resources Research*, 26(4):539–549, apr 1990. doi:10.1029/wr026i004p00539. [Cited on page 282]

[150] Jun Fukai, Yuichi Hamada, Yoshio Morozumi, and Osamu Miyatake. Effect of carbon-fiber brushes on conductive heat transfer in phase change materials. *International Journal of Heat and Mass Transfer*, 45(24):4781–4792, nov 2002. doi:10.1016/s0017-9310(02)00179-5. [Cited on page 49]

[151] Jun Fukai, Makoto Kanou, Yoshikazu Kodama, and Osamu Miyatake. Thermal conductivity enhancement of energy storage media using carbon fibers. *Energy Conversion and Management*, 41(14):1543–1556, sep 2000. doi:10.1016/s0196-8904(99)00166-1. [Cited on page 49]

[152] S. Ganesan and D. R. Poirier. Conservation of mass and momentum for the flow of interdendritic liquid during solidification. *Metallurgical Transactions B*, 21(1):173–181, feb 1990. doi:10.1007/bf02658128. [Cited on page 179]

[153] Dongyan Gao, Zhenqian Chen, Dongliang Zhang, and Linghai Chen. Lattice boltzmann modeling of melting of phase change materials in porous media with conducting fins. *Applied Thermal Engineering*, 118:315–327, may 2017. doi:10.1016/j.applthermaleng.2017.03.002. [Cited on pages 109 and 113]

[154] D. K. Gartling, C. E. Hickox, and R. C. Givler. Simulation of coupled viscous and porous flow problems. *International Journal of Computational Fluid Dynamics*, 7(1-2):23–48, jul 1996. doi:10.1080/10618569608940751. [Cited on page 180]

[155] DK Gartling. Finite element analysis of convective heat transfer problems with change of phase. Technical report, Sandia Labs, 1978. [Cited on page 179]

[156] DK Gartling and RE Hogan. Coyote ii-a finite element computer program for nonlinear heat conduction problems. part i-theoretical background. Technical report, Sandia National Labs., Albuquerque, NM (United States), 1994. doi:10.2172/6590258. [Cited on pages 190 and 191]

[157] C. Gau and R. Viskanta. Melting and solidification of a pure metal on a vertical wall. *Journal of Heat Transfer*, 108(1):174, 1986. doi:10.1115/1.3246884. [Cited on page 195]

[158] A. Gersborg-Hansen, O. Sigmund, and R.B. Haber. Topology optimization of channel flow problems. *Structural and Multidisciplinary Optimization*, 30(3):181–192, jun 2005. doi:10.1007/s00158-004-0508-7. [Cited on page 199]

[159] Bissan Ghaddar, Joe Naoum-Sawaya, Akihiro Kishimoto, Nicole Taheri, and Bradley Eck. A lagrangian decomposition approach for the pump scheduling problem in water networks. *European Journal of Operational Research*, 241(2):490–501, mar 2015. doi:10.1016/j.ejor.2014.08.033. [Cited on page 284]

[160] A. Ghanbarian and M.J. Kermani. Enhancement of PEM fuel cell performance by flow channel indentation. *Energy Conversion and Management*, 110:356–366, feb 2016. doi:10.1016/j.enconman.2015.12.036. [Cited on pages 327 and 328]

[161] Carlo Giacomello, Zoran Kapelan, and Matteo Nicolini. Fast hybrid optimization method for effective pump scheduling. *Journal of Water Resources Planning and Management*, 139(2):175–183, mar 2013. doi:10.1061/(axes)wr.1943-5452.0000239. [Cited on page 284]

[162] Leonid V. Gibiansky and Ole Sigmund. Multiphase composites with extremal bulk modulus. *Journal of the Mechanics and Physics of Solids*, 48(3):461–498, mar 2000. doi:10.1016/s0022-5096(99)00043-5. [Cited on pages 122 and 129]

[163] Antoni Gil, Eduard Oró, Laia Miró, Gerard Peiró, Álvaro Ruiz, José Manuel Salmerón, and Luisa F. Cabeza. Experimental analysis of hydroquinone used as phase change material (PCM) to be applied in solar cooling refrigeration. *International Journal of Refrigeration*, 39:95–103, mar 2014. doi:10.1016/j.ijrefrig.2013.05.013. [Cited on page 246]

[164] Michael B Giles and Niles A Pierce. An introduction to the adjoint approach to design. *Flow, turbulence and combustion*, 65(3-4):393–415, 2000. [Cited on page 25]

[165] Loïc Giraud, Massinissa Merabet, Roland Baviere, and Mathieu Vallée. Optimal control of district heating systems using dynamic simulation and mixed integer linear programming. In *Proceedings of the 12th International Modelica Conference, Prague, Czech Republic, May 15-17, 2017*. Linköping University Electronic Press, jul 2017. doi:10.3384/ecp17132141. [Cited on page 284]

[166] Orazio Giustolisi, Daniele Laucelli, and Andrew F. Colombo. Deterministic versus stochastic design of water distribution networks. *Journal of Water Resources Planning and Management*, 135(2):117–127, mar 2009. doi:10.1061/(asce)0733-9496(2009)135:2(117). [Cited on pages 280 and 281]

[167] Wenping Gong, Sara Khoshnevisan, and C. Hsein Juang. Gradient-based design robustness measure for robust geotechnical design. *Canadian Geotechnical Journal*, 51(11):1331–1342, nov 2014. doi:10.1139/cgj-2013-0428. [Cited on page 281]

[168] Theodore R. Goodman and John J. Shea. The melting of finite slabs. *Journal of Applied Mechanics*, 27(1):16, 1960. doi:10.1115/1.3643893. [Cited on page 56]

[169] R. Greco, A. Di Nardo, and G. Santonastaso. Resilience and entropy as indices of robustness of water distribution networks. *Journal of Hydroinformatics*, 14(3):761, jul 2012. doi:10.2166/hydro.2012.037. [Cited on page 279]

[170] P. M. Gresho and R. L. Sani. *Incompressible Flow and the Finite Element Method, Volume 1, Advection-Diffusion and Isothermal Laminar Flow*. Wiley, 2000. [Cited on page 190]

[171] Sébastien Gros, Mario Zanon, Rien Quirynen, Alberto Bemporad, and Moritz Diehl. From linear to nonlinear MPC: bridging the gap via the real-time iteration. *International Journal of Control*, pages 1–19, sep 2016. doi:10.1080/00207179.2016.1222553. [Cited on page 285]

[172] Oliver Gröger, Hubert A. Gasteiger, and Jens-Peter Suchsland. Review—electromobility: Batteries or fuel cells? *Journal of The Electrochemical Society*, 162(14):A2605–A2622, 2015. doi:10.1149/2.0211514jes. [Cited on page 2]

[173] JoséMiranda Guedes and Noboru Kikuchi. Preprocessing and postprocessing for materials based on the homogenization method with adaptive finite element methods. *Computer Methods in Applied Mechanics and Engineering*, 83(2):143–198, oct 1990. doi:10.1016/0045-7825(90)90148-f. [Cited on page 118]

[174] Elisa Guelpa, Adriano Sciacovelli, and Vittorio Verda. Thermo-fluid dynamic model of large district heating networks for the analysis of primary energy savings. *Energy*, aug 2017. doi:10.1016/j.energy.2017.07.177. [Cited on page 292]

[175] Elisa Guelpa, Claudia Toro, Adriano Sciacovelli, Roberto Melli, Enrico Sciubba, and Vittorio Verda. Optimal operation of large district heating networks through fast fluid-dynamic simulation. *Energy*, 102:586–595, may 2016. doi:10.1016/j.energy.2016.02.058. [Cited on pages 284 and 292]

[176] J. K. Guest, J. H. Prévost, and T. Belytschko. Achieving minimum length scale in topology optimization using nodal design variables and projection functions. *International Journal for Numerical Methods in Engineering*, 61(2):238–254, aug 2004. doi:10.1002/nme.1064. [Cited on pages 34 and 344]

[177] James K. Guest. Topology optimization with multiple phase projection. *Computer Methods in Applied Mechanics and Engineering*, 199(1-4):123–135, dec 2009. doi:10.1016/j.cma.2009.09.023. [Cited on page 36]

[178] James K. Guest, Alireza Asadpoure, and Seung-Hyun Ha. Eliminating beta-continuation from heaviside projection and density filter algorithms. *Structural and Multidisciplinary Optimization*, 44(4):443–453, jul 2011. doi:10.1007/s00158-011-0676-1. [Cited on pages 36 and 345]

[179] James K. Guest and Jean H. Prévost. Optimizing multifunctional materials: Design of microstructures for maximized stiffness and fluid permeability. *International Journal of Solids and Structures*, 43(22-23):7028–7047, nov 2006. doi:10.1016/j.ijsolstr.2006.03.001. [Cited on page 200]

[180] James K. Guest and Jean H. Prévost. Topology optimization of creeping fluid flows using a darcy–stokes finite element. *International Journal for Numerical Methods in Engineering*, 66(3):461–484, 2006. doi:10.1002/nme.1560. [Cited on pages 200 and 202]

[181] James K. Guest and Jean H. Prevost. Design of maximum permeability material structures. *Computer Methods in Applied Mechanics and Engineering*, 196(4-6):1006–1017, jan 2007. doi:10.1016/j.cma.2006.08.006. [Cited on page 122]

[182] James K. Guest and Jean H. Prévost. Design of maximum permeability material structures. *Computer Methods in Applied Mechanics and Engineering*, 196(4-6):1006–1017, jan 2007. doi:10.1016/j.cma.2006.08.006. [Cited on page 200]

[183] Indra Gunawan, Frank Schultmann, and Seyed Ashkan Zarghami. The four rs performance indicators of water distribution networks. *International Journal of Quality & Reliability Management*, 34(5):720–732, may 2017. doi:10.1108/ijqrm-11-2016-0203. [Cited on page 279]

[184] Nannan Guo, Ming C. Leu, and Umit O. Koylu. Network based optimization model for pin-type flow field of polymer electrolyte membrane fuel cell. *International Journal of Hydrogen Energy*, 38(16):6750–6761, may 2013. doi:10.1016/j.ijhydene.2013.03.066. [Cited on page 331]

[185] Nannan Guo, Ming C. Leu, and Umit O. Koylu. Bio-inspired flow field designs for polymer electrolyte membrane fuel cells. *International Journal of Hydrogen Energy*, 39(36):21185–21195, dec 2014. doi:10.1016/j.ijhydene.2014.10.069. [Cited on page 332]

[186] Shaopeng Guo, Jun Zhao, Weilong Wang, Jinyue Yan, Guang Jin, Zhiyu Zhang, Jie Gu, and Yonghong Niu. Numerical study of the improvement of an indirect contact mobilized thermal energy storage container. *Applied Energy*, 161:476–486, jan 2016. doi:10.1016/j.apenergy.2015.10.032. [Cited on page 240]

[187] Xu Guo, Weisheng Zhang, Jian Zhang, and Jie Yuan. Explicit structural topology optimization based on moving morphable components (MMC) with curved skeletons. *Computer Methods in Applied Mechanics and Engineering*, 310:711–748, oct 2016. doi:10.1016/j.cma.2016.07.018. [Cited on page 140]

[188] Xu Guo, Weisheng Zhang, and Wenliang Zhong. Doing topology optimization explicitly and geometrically—a new moving morphable components based framework. *Journal of Applied Mechanics*, 81(8):081009, may 2014. doi:10.1115/1.4027609. [Cited on pages 15, 140, and 141]

[189] Xu Guo, Weisheng Zhang, and Wenliang Zhong. Stress-related topology optimization of continuum structures involving multi-phase materials. *Computer*

Methods in Applied Mechanics and Engineering, 268:632–655, jan 2014. doi:10.1016/j.cma.2013.10.003. [Cited on page 131]

[190] Xu Guo, Xiaofang Zhao, Weisheng Zhang, Jun Yan, and Guomin Sun. Multi-scale robust design and optimization considering load uncertainties. *Computer Methods in Applied Mechanics and Engineering*, 283:994–1009, jan 2015. doi:10.1016/j.cma.2014.10.014. [Cited on page 129]

[191] R.S. Gupta and Dhirendra Kumar. A modified variable time step method for the one-dimensional stefan problem. *Computer Methods in Applied Mechanics and Engineering*, 23(1):101–109, jul 1980. doi:10.1016/0045-7825(80)90081-x. [Cited on page 56]

[192] Kjell Gustafsson. Control-theoretic techniques for stepsize selection in implicit runge-kutta methods. *ACM Transactions on Mathematical Software*, 20(4):496–517, dec 1994. doi:10.1145/198429.198437. [Cited on page 190]

[193] Simon Moritz Göhler, Tobias Eifler, and Thomas J. Howard. Robustness metrics: Consolidating the multiple approaches to quantify robustness. *Journal of Mechanical Design*, 138(11):111407, sep 2016. doi:10.1115/1.4034112. [Cited on pages 280 and 306]

[194] E Haber. A multilevel, level-set method for optimizing eigenvalues in shape design problems. *Journal of Computational Physics*, 198(2):518–534, aug 2004. doi:10.1016/j.jcp.2004.01.031. [Cited on page 14]

[195] E. Hachem, H. Digonnet, N. Kosseifi, E. Massoni, and T. Coupez. Enriched finite element spaces for transient conduction heat transfer. *Applied Mathematics and Computation*, 217(8):3929–3943, dec 2010. doi:10.1016/j.amc.2010.09.057. [Cited on pages 69 and 70]

[196] Raphael T. Haftka and Zafer Gürdal. *Elements of Structural Optimization*. Springer Netherlands, 1992. doi:10.1007/978-94-011-2550-5. [Cited on pages 16, 25, and 84]

[197] Marjan Haghayegh, Mohammad H. Eikani, and Soosan Rowshanzamir. Modeling and simulation of a proton exchange membrane fuel cell using computational fluid dynamics. *International Journal of Hydrogen Energy*, 42(34):21944–21954, aug 2017. doi:10.1016/j.ijhydene.2017.07.098. [Cited on pages xxxii, xxxvi, 346, 348, and 349]

[198] J.S. Han and B.M. Kwak. Robust optimization using a gradient index: MEMS applications. *Structural and Multidisciplinary Optimization*, 27(6), may 2004. doi:10.1007/s00158-004-0410-3. [Cited on page 281]

[199] Xiao-Hong Han, Qin Wang, Young-Gil Park, Christophe T'Joen, Andrew Sommers, and Anthony Jacobi. A review of metal foam and metal matrix composites for heat exchangers and heat sinks. *Heat Transfer Engineering*, 33(12):991–1009, sep 2012. doi:10.1080/01457632.2012.659613. [Cited on pages 107, 108, and 110]

[200] Wei Hao, Tao Wang, Yu yan Jiang, Cong Guo, and Chao hong Guo. Pool boiling heat transfer on deformable structures made of shape-memory-alloys. *International Journal of Heat and Mass Transfer*, 112:236–247, sep 2017. doi:10.1016/j.ijheatmasstransfer.2017.04.113. [Cited on page 374]

[201] B. Hassani and E. Hinton. A review of homogenization and topology opimization II—analytical and numerical solution of homogenization equations. *Computers & Structures*, 69(6):719–738, dec 1998. doi:10.1016/s0045-7949(98)00132-1. [Cited on page 118]

[202] B. Hassani and E. Hinton. A review of homogenization and topology optimization i—homogenization theory for media with periodic structure. *Computers & Structures*, 69(6):707–717, dec 1998. doi:10.1016/s0045-7949(98)00131-x. [Cited on pages 114, 115, and 117]

[203] G. Hauke and T.J.R. Hughes. A unified approach to compressible and incompressible flows. *Computer Methods in Applied Mechanics and Engineering*, 113(3-4):389–395, mar 1994. doi:10.1016/0045-7825(94)90055-8. [Cited on page 343]

[204] Alethea M. Hayes, Aijun Wang, Benjamin M. Dempsey, and David L. McDowell. Mechanics of linear cellular alloys. *Mechanics of Materials*, 36(8):691–713, aug 2004. doi:10.1016/j.mechmat.2003.06.001. [Cited on page 107]

[205] Zhongjie He, Hua Li, and Karl Erik Birgersson. *Reduced Modelling of Planar Fuel Cells*. Springer International Publishing, 2017. doi:10.1007/978-3-319-42646-4. [Cited on page 334]

[206] Hadi Heidary, Mohammad J. Kermani, and Bahram Dabir. Influences of bipolar plate channel blockages on PEM fuel cell performances. *Energy Conversion and Management*, 124:51–60, sep 2016. doi:10.1016/j.enconman.2016.06.043. [Cited on pages 326, 327, 328, and 331]

[207] Hadi Heidary, Mohammad J. Kermani, Ajay K. Prasad, Suresh G. Advani, and Bahram Dabir. Numerical modelling of in-line and staggered blockages in parallel flowfield channels of PEM fuel cells. *International Journal of Hydrogen Energy*, 42(4):2265–2277, jan 2017. doi:10.1016/j.ijhydene.2016.10.076. [Cited on pages 323, 327, 328, and 331]

[208] C.J. Hoogendoorn and G.C.J. Bart. Performance and modelling of latent heat stores. *Solar Energy*, 48(1):53–58, 1992. doi:10.1016/0038-092x(92)90176-b. [Cited on page 111]

[209] M.J. Hosseini, A.A. Ranjbar, M. Rahimi, and R. Bahrampoury. Experimental and numerical evaluation of longitudinally finned latent heat thermal storage systems. *Energy and Buildings*, 99:263–272, jul 2015. doi:10.1016/j.enbuild.2015.04.045. [Cited on page 50]

[210] Seyedmohsen Hosseini, Kash Barker, and Jose E. Ramirez-Marquez. A review of definitions and measures of system resilience. *Reliability Engineering & System Safety*, 145:47–61, jan 2016. doi:10.1016/j.ress.2015.08.006. [Cited on page 278]

[211] Henry Hu and Stavros A Argyropoulos. Mathematical modelling of solidification and melting: a review. *Modelling and Simulation in Materials Science and Engineering*, 4(4):371–396, jul 1996. doi:10.1088/0965-0393/4/4/004. [Cited on pages 55, 56, and 60]

[212] X. Huang and Y. M. Xie. Bi-directional evolutionary topology optimization of continuum structures with one or multiple materials. *Computational Mechanics*, 43(3):393–401, jul 2008. doi:10.1007/s00466-008-0312-0. [Cited on page 126]

[213] Thomas J.R. Hughes, Leopoldo P. Franca, and Marc Balestra. A new finite element formulation for computational fluid dynamics: V. circumventing the babuška-brezzi condition: a stable petrov-galerkin formulation of the stokes problem accommodating equal-order interpolations. *Computer Methods in Applied Mechanics and Engineering*, 59(1):85–99, nov 1986. doi:10.1016/0045-7825(86)90025-3. [Cited on pages 189 and 342]

[214] S. Hyun and S. Torquato. Designing composite microstructures with targeted properties. *Journal of Materials Research*, 16(01):280–285, jan 2001. doi:10.1557/jmr.2001.0042. [Cited on page 122]

[215] Nasiru I. Ibrahim, Fahad A. Al-Sulaiman, Saidur Rahman, Bekir S. Yilbas, and Ahmet Z. Sahin. Heat transfer enhancement of phase change materials for thermal energy storage applications: A critical review. *Renewable and Sustainable Energy Reviews*, 74:26–50, jul 2017. doi:10.1016/j.rser.2017.01.169. [Cited on pages 48, 49, 50, and 246]

[216] F. Ilinca and J.-F. Hétu. Galerkin gradient least-squares formulations for transient conduction heat transfer. *Computer Methods in Applied Mechanics and Engineering*, 191(27-28):3073–3097, apr 2002. doi:10.1016/s0045-7825(02)00242-6. [Cited on pages 69 and 70]

[217] Gerardo Martín Imbrioscia and Héctor José Fasoli. Simulation and study of proposed modifications over straight-parallel flow field design. *International Journal of Hydrogen Energy*, 39(16):8861–8867, may 2014. doi:10.1016/j.ijhydene.2013.11.079. [Cited on page 330]

[218] Kamal A.R. Ismail, Fátima A.M. Lino, Raquel C.R. da Silva, Antonio B. de Jesus, and Louryval C. Paixão. Experimentally validated two dimensional numerical model for the solidification of PCM along a horizontal long tube. *International Journal of Thermal Sciences*, 75:184–193, jan 2014. doi:10.1016/j.ijthermalsci.2013.08.008. [Cited on page 240]

[219] K.A.R Ismail, C.L.F Alves, and M.S. Modesto. Numerical and experimental study on the solidification of PCM around a vertical axially finned isothermal cylinder. *Applied Thermal Engineering*, 21(1):53–77, jan 2001. doi:10.1016/s1359-4311(00)00002-8. [Cited on page 240]

[220] Hamid Jannesari and Naeim Abdollahi. Experimental and numerical study of thin ring and annular fin effects on improving the ice formation in ice-on-coil thermal storage systems. *Applied Energy*, 189:369–384, mar 2017. doi:10.1016/j.apenergy.2016.12.064. [Cited on page 181]

[221] Long Jian-you. Numerical and experimental investigation for heat transfer in triplex concentric tube with phase change material for thermal energy storage. *Solar Energy*, 82(11):977–985, nov 2008. doi:10.1016/j.solener.2008.05.006. [Cited on page 47]

[222] Imen Jmal and Mounir Baccar. Numerical study of PCM solidification in a finned tube thermal storage including natural convection. *Applied Thermal Engineering*, 84:320–330, jun 2015. doi:10.1016/j.applthermaleng.2015.03.065. [Cited on pages 48 and 52]

[223] Zdeněk Johan and Thomas JR Hughes. A globally convergent matrix-free algorithm for implicit time-marching schemes arising in finite element analysis in fluids. *Computer Methods in Applied Mechanics and Engineering*, 87(2-3):281–304, 1991. doi:10.1016/0045-7825(91)90009-u. [Cited on page 190]

[224] Claes Johnson. *Numerical solution of partial differential equations by the finite element method*. Courier Corporation, 2012. [Cited on page 74]

[225] Mark C Johnson, David P Wilkinson, John Kenna, Olen R Vanderleeden, Joerg Zimmerman, and Mehrzad Tabatabaian. Differential pressure fluid flow fields for fuel cells, July 1 2003. US Patent 6,586,128. [Cited on page 330]

[226] David Rayner Hunkin Jones and Michael F Ashby. *Engineering materials 2: an introduction to microstructures, processing and design*. Butterworth-Heinemann, 2005. [Cited on page 248]

[227] Mahmood Mastani Joybari, Fariborz Haghighat, and Saeid Seddegh. Numerical investigation of a triplex tube heat exchanger with phase change material: Simultaneous charging and discharging. *Energy and Buildings*, 139:426–438, mar 2017. doi:10.1016/j.enbuild.2017.01.034. [Cited on page 47]

[228] Donghwi Jung, Kevin E. Lansey, Younghwan Choi, and Joong Hoon Kim. Robustness-based optimal pump design and scheduling for water distribution systems. *Journal of Hydroinformatics*, page jh2015091, nov 2015. doi:10.2166/hydro.2015.091. [Cited on pages 280 and 281]

[229] Huseyin Kahraman and Mehmet F. Orhan. Flow field bipolar plates in a proton exchange membrane fuel cell: Analysis & modeling. *Energy Conversion and*

Management, 133:363–384, feb 2017. doi:10.1016/j.enconman.2016.10.053. [Cited on pages 324, 329, 331, and 356]

[230] Babak Kamkari and Hamid Jahedi Amlashi. Numerical simulation and experimental verification of constrained melting of phase change material in inclined rectangular enclosures. *International Communications in Heat and Mass Transfer*, 88:211–219, nov 2017. doi:10.1016/j.icheatmasstransfer.2017.07.023. [Cited on page 181]

[231] D. Kang. Real-time optimal control of water distribution systems. *Procedia Engineering*, 70:917–923, 2014. doi:10.1016/j.proeng.2014.02.102. [Cited on page 284]

[232] Doosun Kang and Kevin Lansey. Scenario-based robust optimization of regional water and wastewater infrastructure. *Journal of Water Resources Planning and Management*, 139(3):325–338, may 2013. doi:10.1061/(asce)wr.1943-5452.0000236. [Cited on page 281]

[233] Zoran S. Kapelan, Dragan A. Savic, and Godfrey A. Walters. Multiobjective design of water distribution systems under uncertainty. *Water Resources Research*, 41(11), nov 2005. doi:10.1029/2004wr003787. [Cited on pages 280 and 281]

[234] P. Karthikeyan, R.J. Vasanth, and M. Muthukumar. Experimental investigation on uniform and zigzag positioned porous inserts on the rib surface of cathode flow channel for performance enhancement in PEMFC. *International Journal of Hydrogen Energy*, 40(13):4641–4648, apr 2015. doi:10.1016/j.ijhydene.2015.01.175. [Cited on pages 329 and 330]

[235] M. Kazemi, M.J. Hosseini, A.A. Ranjbar, and R. Bahrampoury. Improvement of longitudinal fins configuration in latent heat storage systems. *Renewable Energy*, 116:447–457, feb 2018. doi:10.1016/j.renene.2017.10.006. [Cited on pages 52 and 246]

[236] Robert J. Kee, Michael E. Coltrin, and Peter Glarborg. *Chemically Reacting Flow*. John Wiley & Sons, Inc., feb 2003. doi:10.1002/0471461296. [Cited on pages 337 and 353]

[237] C. T. Kelley and David E. Keyes. Convergence analysis of pseudo-transient continuation. *SIAM Journal on Numerical Analysis*, 35(2):508–523, apr 1998. doi:10.1137/s0036142996304796. [Cited on page 74]

[238] D. W. Kelly, S. Nakazawa, O. C. Zienkiewicz, and J. C. Heinrich. A note on upwinding and anisotropic balancing dissipation in finite element approximations to convective diffusion problems. *International Journal for Numerical Methods in Engineering*, 15(11):1705–1711, nov 1980. doi:10.1002/nme.1620151111. [Cited on page 189]

[239] Zakir Khan, Zulfiqar Khan, and Abdul Ghafoor. A review of performance enhancement of PCM based latent heat storage system within the context of materials, thermal stability and compatibility. *Energy Conversion and Management*, 115:132–158, may 2016. doi:10.1016/j.enconman.2016.02.045. [Cited on pages 48, 49, and 50]

[240] Ali C. Kheirabadi and Dominic Groulx. Simulating phase change heat transfer using comsol and fluent: effect of the mushy-zone constant. *Computational Thermal Sciences: An International Journal*, 7(5-6):427–440, 2015. doi:10.1615/computthermalscien.2016014279. [Cited on page 196]

[241] Ah-Reum Kim, Seungho Shin, and Sukkee Um. Multidisciplinary approaches to metallic bipolar plate design with bypass flow fields through deformable gas diffusion media of polymer electrolyte fuel cells. *Energy*, 106:378–389, jul 2016. doi:10.1016/j.energy.2016.03.073. [Cited on pages 324 and 327]

[242] C. Kim and H. Sun. Topology optimization of gas flow channel routes in an automotive fuel cell. *International Journal of Automotive Technology*, 13(5):783–789, jul 2012. doi:10.1007/s12239-012-0078-4. [Cited on page 321]

[243] Nam-Kyung Kim, Dong-Hun Kim, Dong-Wook Kim, Heung-Geun Kim, David A. Lowther, and Jan K. Sykulski. Robust optimization utilizing the second-order design sensitivity information. *IEEE Transactions on Magnetics*, 46(8):3117–3120, aug 2010. doi:10.1109/tmag.2010.2043719. [Cited on page 281]

[244] Yong-Sang Kim and Jung-Gu Kim. Failure analysis of a thermally insulated pipeline in a district heating system. *Engineering Failure Analysis*, 83:193–206, jan 2018. doi:10.1016/j.engfailanal.2017.09.014. [Cited on page 2]

[245] Uri Kirsch. *Structural Optimization*. Springer Berlin Heidelberg, 1993. doi:10.1007/978-3-642-84845-2. [Cited on pages 16 and 17]

[246] Anders Klarbring, Joakim Petersson, Bo Torstenfelt, and Matts Karlsson. Topology optimization of flow networks. *Computer Methods in Applied Mechanics and Engineering*, 192(35-36):3909–3932, aug 2003. doi:10.1016/s0045-7825(03)00393-1. [Cited on pages 282 and 293]

[247] Jason P. Kloess, Xia Wang, Joan Liu, Zhongying Shi, and Laila Guessous. Investigation of bio-inspired flow channel designs for bipolar plates in proton exchange membrane fuel cells. *Journal of Power Sources*, 188(1):132–140, mar 2009. doi:10.1016/j.jpowsour.2008.11.123. [Cited on page 332]

[248] Adriano A. Koga, Edson Comini C. Lopes, Helcio F. Villa Nova, Cícero R. de Lima, and Emílio Carlos Nelli Silva. Development of heat sink device by using topology optimization. *International Journal of Heat and Mass Transfer*, 64:759–772, sep 2013. doi:10.1016/j.ijheatmasstransfer.2013.05.007. [Cited on page 206]

[249] A. Kopanidis, A. Theodorakakos, M. Gavaises, and D. Bouris. Pore scale 3d modelling of heat and mass transfer in the gas diffusion layer and cathode channel of a PEM fuel cell. *International Journal of Thermal Sciences*, 50(4):456–467, apr 2011. doi:10.1016/j.ijthermalsci.2010.11.014. [Cited on page 324]

[250] J.P. Kotzé, T.W. von Backström, and P.J. Erens. Simulation and testing of a latent heat thermal energy storage unit with metallic phase change material. *Energy Procedia*, 49:860–869, 2014. doi:10.1016/j.egypro.2014.03.093. [Cited on page 240]

[251] Gerhard Kreisselmeier and Reinhold Steinhauser. Application of vector performance optimization to a robust control loop design for a fighter aircraft. *International Journal of Control*, 37(2):251–284, feb 1983. doi:10.1080/00207179.1983.9753066. [Cited on pages 140 and 142]

[252] R. Krishna and J.A. Wesselingh. The maxwell-stefan approach to mass transfer. *Chemical Engineering Science*, 52(6):861–911, mar 1997. doi:10.1016/s0009-2509(96)00458-7. [Cited on page 337]

[253] Sebastian Kuboth, Andreas König-Haagen, and Dieter Brüggemann. Numerical analysis of shell-and-tube type latent thermal energy storage performance with different arrangements of circular fins. *Energies*, 10(3):274, feb 2017. doi:10.3390/en10030274. [Cited on page 52]

[254] Atul Kumar and Ramana G Reddy. Effect of channel dimensions and shape in the flow-field distributor on the performance of polymer electrolyte membrane fuel cells. *Journal of Power Sources*, 113(1):11–18, jan 2003. doi:10.1016/s0378-7753(02)00475-5. [Cited on pages 321, 324, 325, and 327]

[255] Mathura Kumar and D. Jaya Krishna. Influence of mushy zone constant on thermohydraulics of a PCM. *Energy Procedia*, 109:314–321, mar 2017. doi:10.1016/j.egypro.2017.03.074. [Cited on page 181]

[256] Marcel Lacroix. Study of the heat transfer behavior of a latent heat thermal energy storage unit with a finned tube. *International Journal of Heat and Mass Transfer*, 36(8):2083–2092, jan 1993. doi:10.1016/s0017-9310(05)80139-5. [Cited on page 240]

[257] Doerte Laing, Thomas Bauer, Nils Breidenbach, Bernd Hachmann, and Maike Johnson. Development of high temperature phase-change-material storages. *Applied Energy*, 109:497–504, sep 2013. doi:10.1016/j.apenergy.2012.11.063. [Cited on page 54]

[258] James Larminie and Andrew Dicks. Fuel cell systems analysed. In *Fuel Cell Systems Explained*, pages 369–389. John Wiley & Sons, Ltd,., dec 2013. doi:10.1002/9781118878330.ch11. [Cited on pages 324 and 338]

[259] E. C. Lemmon. Phase-change techniques for finite element conduction codes. In R. W. Lewis and K. Morgan, editors, *Numerical Methods in Thermal Problems*, pages 149–158, 1979. [Cited on page 62]

[260] Bin Li and Xiaoqiang Zhai. Experimental investigation and theoretical analysis on a mid-temperature solar collector/storage system with composite PCM. *Applied Thermal Engineering*, 124:34–43, sep 2017. doi:10.1016/j.applthermaleng.2017.06.002. [Cited on page 181]

[261] Hao Li, Zhen Luo, Liang Gao, and Qinghua Qin. Topology optimization for concurrent design of structures with multi-patch microstructures by level sets. *Computer Methods in Applied Mechanics and Engineering*, 331:536–561, apr 2018. doi:10.1016/j.cma.2017.11.033. [Cited on page 113]

[262] X LI and I SABIR. Review of bipolar plates in PEM fuel cells: Flow-field designs. *International Journal of Hydrogen Energy*, 30(4):359–371, mar 2005. doi:10.1016/j.ijhydene.2004.09.019. [Cited on pages 330 and 331]

[263] Yemao Li, Jianjun Xia, Hao Fang, Yingbo Su, and Yi Jiang. Case study on industrial surplus heat of steel plants for district heating in northern china. *Energy*, 102:397–405, may 2016. doi:10.1016/j.energy.2016.02.105. [Cited on page 277]

[264] Yong Li, Bei Guo, Guanfei Huang, Shuichi Kubo, and Pengcheng Shu. Characterization and thermal performance of nitrate mixture/SiC ceramic honeycomb composite phase change materials for thermal energy storage. *Applied Thermal Engineering*, 81:193–197, apr 2015. doi:10.1016/j.applthermaleng.2015.02.008. [Cited on page 108]

[265] Zhuo Li and Zhi-Gen Wu. Numerical study on the thermal behavior of phase change materials (PCMs) embedded in porous metal matrix. *Solar Energy*, 99:172–184, jan 2014. doi:10.1016/j.solener.2013.11.017. [Cited on page 111]

[266] Johan Lie, Marius Lysaker, and Xue-Cheng Tai. Piecewise constant level set methods and image segmentation. In *Lecture Notes in Computer Science*, pages 573–584. Springer Berlin Heidelberg, 2005. doi:10.1007/11408031_49. [Cited on page 131]

[267] B. H. Lim, E. H. Majlan, W. R. W. Daud, T. Husaini, and M. I. Rosli. Effects of flow field design on water management and reactant distribution in PEMFC: a review. *Ionics*, 22(3):301–316, feb 2016. doi:10.1007/s11581-016-1644-y. [Cited on page 330]

[268] B.H. Lim, E.H. Majlan, W.R.W. Daud, M.I. Rosli, and T. Husaini. Numerical analysis of modified parallel flow field designs for fuel cells. *International Journal of Hydrogen Energy*, 42(14):9210–9218, apr 2017. doi:10.1016/j.ijhydene.2016.03.189. [Cited on pages 323, 328, and 330]

[269] Min-Der Lin, Yu-Hsin Liu, Gee-Fon Liu, and Chien-Wei Chu. Scatter search heuristic for least-cost design of water distribution networks. *Engineering Optimization*, 39(7):857–876, oct 2007. doi:10.1080/03052150701503611. [Cited on page 281]

[270] Michael Lindstrom and Brian Wetton. A comparison of fick and maxwell–stefan diffusion formulations in PEMFC gas diffusion layers. *Heat and Mass Transfer*, 53(1):205–212, apr 2016. doi:10.1007/s00231-016-1812-7. [Cited on page 338]

[271] Chang Liu and Dominic Groulx. Experimental study of the phase change heat transfer inside a horizontal cylindrical latent heat energy storage system. *International Journal of Thermal Sciences*, 82:100–110, aug 2014. doi:10.1016/j.ijthermalsci.2014.03.014. [Cited on page 52]

[272] H.C. Liu, W.M. Yan, C.Y. Soong, Falin Chen, and H.S. Chu. Reactant gas transport and cell performance of proton exchange membrane fuel cells with tapered flow field design. *Journal of Power Sources*, 158(1):78–87, jul 2006. doi:10.1016/j.jpowsour.2005.09.017. [Cited on pages 326 and 327]

[273] Hui-Chung Liu, Wei-Mon Yan, Chyi-Yeou Soong, and Falin Chen. Effects of baffle-blocked flow channel on reactant transport and cell performance of a proton exchange membrane fuel cell. *Journal of Power Sources*, 142(1-2):125–133, mar 2005. doi:10.1016/j.jpowsour.2004.09.037. [Cited on page 327]

[274] Ling Liu, Jun Yan, and Gengdong Cheng. Optimum structure with homogeneous optimum truss-like material. *Computers & Structures*, 86(13-14):1417–1425, jul 2008. doi:10.1016/j.compstruc.2007.04.030. [Cited on pages 127 and 128]

[275] Ming Liu, Wasim Saman, and Frank Bruno. Review on storage materials and thermal performance enhancement techniques for high temperature phase change thermal storage systems. *Renewable and Sustainable Energy Reviews*, 16(4):2118–2132, may 2012. doi:10.1016/j.rser.2012.01.020. [Cited on pages 246 and 247]

[276] Justo Lobato, Pablo Cañizares, Manuel A. Rodrigo, F. Javier Pinar, Esperanza Mena, and Diego Úbeda. Three-dimensional model of a 50 cm2 high temperature PEM fuel cell. study of the flow channel geometry influence. *International Journal of Hydrogen Energy*, 35(11):5510–5520, jun 2010. doi:10.1016/j.ijhydene.2010.02.089. [Cited on page 331]

[277] Justo Lobato, Pablo Cañizares, Manuel A. Rodrigo, F. Javier Pinar, and Diego Úbeda. Study of flow channel geometry using current distribution measurement in a high temperature polymer electrolyte membrane fuel cell. *Journal of Power Sources*, 196(9):4209–4217, may 2011. doi:10.1016/j.jpowsour.2010.10.017. [Cited on page 331]

[278] Sina Lohrasbi, Mofid Gorji-Bandpy, and Davood Domiri Ganji. Thermal penetration depth enhancement in latent heat thermal energy storage system in the presence of heat pipe based on both charging and discharging processes. *Energy Conversion and Management*, 148:646–667, sep 2017. doi:10.1016/j.enconman.2017.06.034. [Cited on page 53]

[279] Jian-You Long and Dong-Sheng Zhu. Numerical and experimental study on heat pump water heater with PCM for thermal storage. *Energy and Buildings*, 40(4):666–672, jan 2008. doi:10.1016/j.enbuild.2007.05.001. [Cited on page 260]

[280] Manuel López-Ibáñez, T. Devi Prasad, and Ben Paechter. Ant colony optimization for optimal control of pumps in water distribution networks. *Journal of Water Resources Planning and Management*, 134(4):337–346, jul 2008. doi:10.1061/(asce)0733-9496(2008)134:4(337). [Cited on page 284]

[281] Henrik Lund, Sven Werner, Robin Wiltshire, Svend Svendsen, Jan Eric Thorsen, Frede Hvelplund, and Brian Vad Mathiesen. 4th generation district heating (4gdh). *Energy*, 68:1–11, apr 2014. doi:10.1016/j.energy.2014.02.089. [Cited on pages 2 and 283]

[282] Zhen Luo, Liyong Tong, Junzhao Luo, Peng Wei, and Michael Yu Wang. Design of piezoelectric actuators using a multiphase level set method of piecewise constants. *Journal of Computational Physics*, 228(7):2643–2659, apr 2009. doi:10.1016/j.jcp.2008.12.019. [Cited on page 131]

[283] Daniel R. Lynch and Kevin O'Neill. Continuously deforming finite elements for the solution of parabolic problems, with and without phase change. *International Journal for Numerical Methods in Engineering*, 17(1):81–96, jan 1981. doi:10.1002/nme.1620170107. [Cited on pages 56 and 57]

[284] Zhanhua Ma and Yuwen Zhang. Solid velocity correction schemes for a temperature transforming model for convection phase change. *International Journal of Numerical Methods for Heat & Fluid Flow*, 16(2):204–225, feb 2006. doi:10.1108/09615530610644271. [Cited on page 178]

[285] Jasim M. Mahdi and Emmanuel C. Nsofor. Melting enhancement in triplex-tube latent heat energy storage system using nanoparticles-metal foam combination. *Applied Energy*, 191:22–34, apr 2017. doi:10.1016/j.apenergy.2016.11.036. [Cited on page 47]

[286] Helena Mala-Jetmarova, Nargiz Sultanova, and Dragan Savic. Lost in optimisation of water distribution systems? a literature review of system operation. *Environmental Modelling & Software*, 93:209–254, jul 2017. doi:10.1016/j.envsoft.2017.02.009. [Cited on page 284]

[287] D.J. Malan, R.T. Dobson, and F. Dinter. Solar thermal energy storage in power generation using phase change material with heat pipes and fins to enhance heat transfer. *Energy Procedia*, 69:925–936, may 2015. doi:10.1016/j.egypro.2015.03.176. [Cited on page 246]

[288] Erasmo Mancusi, Éliton Fontana, Antônio Augusto Ulson de Souza, and Selene M.A. Guelli Ulson de Souza. Numerical study of two-phase flow patterns in the gas channel of PEM fuel cells with tapered flow field design. *International Journal of Hydrogen Energy*, 39(5):2261–2273, feb 2014. doi:10.1016/j.ijhydene.2013.11.106. [Cited on pages 326 and 327]

[289] A.P. Manso, F.F. Marzo, J. Barranco, X. Garikano, and M. Garmendia Mujika. Influence of geometric parameters of the flow fields on the performance of a PEM fuel cell. a review. *International Journal of Hydrogen Energy*, 37(20):15256–15287, oct 2012. doi:10.1016/j.ijhydene.2012.07.076. [Cited on pages 323, 325, and 343]

[290] Gilles Marck, Maroun Nemer, and Jean-Luc Harion. Topology optimization of heat and mass transfer problems: Laminar flow. *Numerical Heat Transfer, Part B: Fundamentals*, 63(6):508–539, jun 2013. doi:10.1080/10407790.2013.772001. [Cited on pages 200 and 206]

[291] J. Marques, M. C. Cunha, J. Sousa, and D. Savić. Robust optimization methodologies for water supply systems design. *Drinking Water Engineering and Science Discussions*, 5(1):173–192, apr 2012. doi:10.5194/dwesd-5-173-2012. [Cited on page 281]

[292] MATLAB. *version R2017a*. The MathWorks Inc., Natick, Massachusetts, 2017. [Cited on page 38]

[293] K. Maute, M. Nikbay, and C. Farhat. Sensitivity analysis and design optimization of three-dimensional non-linear aeroelastic systems by the adjoint method. *International Journal for Numerical Methods in Engineering*, 56(6):911–933, 2003. doi:10.1002/nme.599. [Cited on pages 25 and 26]

[294] Kurt Maute, Anton Tkachuk, Jiangtao Wu, H. Jerry Qi, Zhen Ding, and Martin L. Dunn. Level set topology optimization of printed active composites. *Journal of Mechanical Design*, 137(11):111402, oct 2015. doi:10.1115/1.4030994. [Cited on page 374]

[295] David A. Mayne, Asif S. Usmani, and Martin Crapper. h-adaptive finite element solution of high rayleigh number thermally driven cavity problem. *International Journal of Numerical Methods for Heat & Fluid Flow*, 10(6):598–615, sep 2000. doi:10.1108/09615530010347187. [Cited on pages 193 and 195]

[296] Harald Mehling and Luisa F Cabeza. *Heat and cold storage with PCM*. Springer, 2008. [Cited on pages 45, 48, 60, 108, 241, 242, 244, 245, and 246]

[297] R. Mehrabian, M. Keane, and M. C. Flemings. Interdendritic fluid flow and macrosegregation influence of gravity. *Metallurgical and Materials Transactions B*, 1(5):1209–1220, may 1970. doi:10.1007/bf02900233. [Cited on page 179]

[298] Kevin Merlin, Didier Delaunay, Jérôme Soto, and Luc Traonvouez. Heat transfer enhancement in latent heat thermal storage systems: Comparative study of different solutions and thermal contact investigation between the exchanger and the PCM. *Applied Energy*, 166:107–116, mar 2016. doi:10.1016/j.apenergy.2016.01.012. [Cited on page 2]

[299] Osama Mesalhy, Khalid Lafdi, Ahmed Elgafy, and Keith Bowman. Numerical study for enhancing the thermal conductivity of phase change material (PCM) storage using high thermal conductivity porous matrix. *Energy Conversion and Management*, 46(6):847–867, apr 2005. doi:10.1016/j.enconman.2004.06.010. [Cited on page 111]

[300] Andrew Mills, Mohammed Farid, J.R. Selman, and Said Al-Hallaj. Thermal conductivity enhancement of phase change materials using a graphite matrix. *Applied Thermal Engineering*, 26(14-15):1652–1661, oct 2006. doi:10.1016/j.applthermaleng.2005.11.022. [Cited on page 108]

[301] M. Mirzaei and M.H. Paydar. A novel process for manufacturing porous 316 l stainless steel with uniform pore distribution. *Materials & Design*, 121:442–449, may 2017. doi:10.1016/j.matdes.2017.02.069. [Cited on page 108]

[302] Tamerabet Monsaf, Ben Moussa Hocine, Sahli Youcef, and Mohammedi Abdallah. Unsteady three-dimensional numerical study of mass transfer in PEM fuel cell with spiral flow field. *International Journal of Hydrogen Energy*, 42(2):1237–1251, jan 2017. doi:10.1016/j.ijhydene.2016.12.084. [Cited on page 329]

[303] K. Morgan. A numerical analysis of freezing and melting with convection. *Computer Methods in Applied Mechanics and Engineering*, 28(3):275–284, sep 1981. doi:10.1016/0045-7825(81)90002-5. [Cited on page 178]

[304] K. Morgan, R. W. Lewis, and O. C. Zienkiewicz. An improved algrorithm for heat conduction problems with phase change. *International Journal for Numerical Methods in Engineering*, 12(7):1191–1195, 1978. doi:10.1002/nme.1620120710. [Cited on pages 62 and 63]

[305] Jiwon Mun, Byoung-Gwan Yun, Jaehyung Ju, and Byung-Moon Chang. Indirect additive manufacturing based casting of a periodic 3d cellular metal – flow simulation of molten aluminum alloy. *Journal of Manufacturing Processes*, 17:28–40, jan 2015. doi:10.1016/j.jmapro.2014.11.001. [Cited on pages 110 and 112]

[306] Robynne E. Murray and Dominic Groulx. Experimental study of the phase change and energy characteristics inside a cylindrical latent heat energy storage system: Part 1 consecutive charging and discharging. *Renewable Energy*, 62:571–581, feb 2014. doi:10.1016/j.renene.2013.08.007. [Cited on page 246]

[307] K Nagano, K Ogawa, T Mochida, K Hayashi, and H Ogoshi. Performance of heat charge/discharge of magnesium nitrate hexahydrate and magnesium chloride hexahydrate mixture to a single vertical tube for a latent heat storage system. *Applied Thermal Engineering*, 24(2-3):209–220, feb 2004. doi:10.1016/j.applthermaleng.2003.09.002. [Cited on page 246]

[308] P.B. Nakshatrala, D.A. Tortorelli, and K.B. Nakshatrala. Nonlinear structural design using multiscale topology optimization. part i: Static formulation. *Computer Methods in Applied Mechanics and Engineering*, 261-262:167–176, jul 2013. doi:10.1016/j.cma.2012.12.018. [Cited on page 125]

[309] K.C. Nayak, S.K. Saha, K. Srinivasan, and P. Dutta. A numerical model for heat sinks with phase change materials and thermal conductivity enhancers. *International Journal of Heat and Mass Transfer*, 49(11-12):1833–1844, jun 2006. doi:10.1016/j.ijheatmasstransfer.2005.10.039. [Cited on page 111]

[310] Donald Nield and Adrian Bejan. Convection in porous media. In *Convection Heat Transfer*, pages 537–605. John Wiley & Sons, Inc., mar 2013. doi:10.1002/9781118671627.ch12. [Cited on pages 180 and 351]

[311] Bin Niu, Jun Yan, and Gengdong Cheng. Optimum structure with homogeneous optimum cellular material for maximum fundamental frequency. *Structural and Multidisciplinary Optimization*, 39(2):115–132, nov 2008. doi:10.1007/s00158-008-0334-4. [Cited on page 129]

[312] Fuxin Niu, Long Ni, Yang Yao, Yuebin Yu, and Haorong Li. Performance and thermal charging/discharging features of a phase change material assisted heat pump system in heating mode. *Applied Thermal Engineering*, 58(1-2):536–541, sep 2013. doi:10.1016/j.applthermaleng.2013.04.042. [Cited on page 260]

[313] Jorge Nocedal and S. Wright. *Numerical Optimization*. Springer New York, 2006. doi:10.1007/978-0-387-40065-5. [Cited on page 24]

[314] J. Norato, R. Haber, D. Tortorelli, and M. P. Bendsøe. A geometry projection method for shape optimization. *International Journal for Numerical Methods in Engineering*, 60(14):2289–2312, jul 2004. doi:10.1002/nme.1044. [Cited on page 139]

[315] J.A. Norato, B.K. Bell, and D.A. Tortorelli. A geometry projection method for continuum-based topology optimization with discrete elements. *Computer Methods in Applied Mechanics and Engineering*, 293:306–327, aug 2015. doi:10.1016/j.cma.2015.05.005. [Cited on pages 139 and 140]

[316] Donald A. Norman and Roberto Verganti. Incremental and radical innovation: Design research vs. technology and meaning change. *Design Issues*, 30(1):78–96, jan 2014. doi:10.1162/desi_a_00250. [Cited on page 3]

[317] Tijs Van Oevelen and Martine Baelmans. Numerical topology optimization of heat sinks. In *Proceedings of the 15th International Heat Transfer Conference*. Begellhouse, 2014. doi:10.1615/ihtc15.opt.009168. [Cited on page 206]

[318] Kyeongmin Oh, Purushothama Chippar, and Hyunchul Ju. Numerical study of thermal stresses in high-temperature proton exchange membrane fuel cell (HT-PEMFC). *International Journal of Hydrogen Energy*, 39(6):2785–2794, feb 2014. doi:10.1016/j.ijhydene.2013.01.201. [Cited on page 323]

[319] Ryan O'Hayre, Suk-Won Cha, Whitney Colella, and Fritz B. Prinz. *Fuel Cell Fundamentals*. John Wiley & Sons, Inc, may 2016. doi:10.1002/9781119191766. [Cited on pages 338 and 348]

[320] M. Olcese. Echangeur thermique pour systeme de stockage thermique, April 17 2014. WO Patent App. PCT/EP2013/070,849. [Cited on page 54]

[321] Curtis M. Oldenburg and Frank J. Spera. Hybrid model for solification and convection. *Numerical Heat Transfer, Part B: Fundamentals*, 21(2):217–229, mar 1992. doi:10.1080/10407799208944917. [Cited on page 178]

[322] Laurits Højgaard Olesen, Fridolin Okkels, and Henrik Bruus. A high-level programming-language implementation of topology optimization applied to steady-state navier-stokes flow. *International Journal for Numerical Methods in Engineering*, 65(7):975–1001, 2006. doi:10.1002/nme.1468. [Cited on pages 199 and 200]

[323] J OWEJAN, T TRABOLD, D JACOBSON, M ARIF, and S KANDLIKAR. Effects of flow field and diffusion layer properties on water accumulation in a PEM fuel cell. *International Journal of Hydrogen Energy*, 32(17):4489–4502, dec 2007. doi:10.1016/j.ijhydene.2007.05.044. [Cited on pages 325 and 327]

[324] Debabrata Pal and Yogendra K Joshi. Melting in a side heated tall enclosure by a uniformly dissipating heat source. *International Journal of Heat and Mass Transfer*, 44(2):375–387, aug 2001. doi:10.1016/s0017-9310(00)00116-2. [Cited on pages xxxiv, 195, and 196]

[325] S. Paria, S. Baradaran, Ahmad Amiri, A. A. D. Sarhan, and S. N. Kazi. Performance evaluation of latent heat energy storage in horizontal shell-and-finned tube for solar application. *Journal of Thermal Analysis and Calorimetry*, 123(2):1371–1381, sep 2015. doi:10.1007/s10973-015-5006-1. [Cited on page 52]

[326] M. F. K. Pasha and K. Lansey. Optimal pump scheduling by linear programming. In *World Environmental and Water Resources Congress 2009*. American Society of Civil Engineers, may 2009. doi:10.1061/41036(342)38. [Cited on page 284]

[327] S.V Patankar and D.B Spalding. A calculation procedure for heat, mass and momentum transfer in three-dimensional parabolic flows. *International Journal of Heat and Mass Transfer*, 15(10):1787–1806, oct 1972. doi:10.1016/0017-9310(72)90054-3. [Cited on page 292]

[328] A. L. R. Paulino, E. F. Cunha, E. Robalinho, M. Linardi, I. Korkischko, and E. I. Santiago. CFD analysis of PEMFC flow channel cross sections. *Fuel Cells*, 17(1):27–36, feb 2017. doi:10.1002/fuce.201600141. [Cited on pages 325 and 327]

[329] Gerard Peiró, Jaume Gasia, Laia Miró, and Luisa F. Cabeza. Experimental evaluation at pilot plant scale of multiple PCMs (cascaded) vs. single PCM configuration for thermal energy storage. *Renewable Energy*, 83:729–736, nov 2015. doi:10.1016/j.renene.2015.05.029. [Cited on page 49]

[330] Shiang-Wuu Perng and Horng-Wen Wu. A three-dimensional numerical investigation of trapezoid baffles effect on non-isothermal reactant transport and cell net power in a PEMFC. *Applied Energy*, 143:81–95, apr 2015. doi:10.1016/j.apenergy.2014.12.059. [Cited on pages 327 and 328]

[331] W. T. Perrins, D. R. McKenzie, and R. C. McPhedran. Transport properties of regular arrays of cylinders. *Proceedings of the Royal Society A: Mathematical, Physical and Engineering Sciences*, 369(1737):207–225, dec 1979. doi:10.1098/rspa.1979.0160. [Cited on pages xxii, 120, 121, 123, and 124]

[332] Joakim Petersson. A finite element analysis of optimal variable thickness sheets. *SIAM Journal on Numerical Analysis*, 36(6):1759–1778, jan 1999. doi:10.1137/s0036142996313968. [Cited on page 31]

[333] Q. T. Pham. Comparison of general-purpose finite element methods for the stefan problem. *Numerical Heat Transfer, Part B: Fundamentals*, 27(4):417–435, jun 1995. doi:10.1080/10407799508914965. [Cited on pages 57 and 62]

[334] Q. T. Pham. Finite element procedure for heat conduction problems with internal heating. *Numerical Heat Transfer, Part A: Applications*, 27(5):611–619, may 1995. doi:10.1080/10407789508913721. [Cited on page 62]

[335] Q.T. Pham. The use of lumped capacitance in the finite-element solution of heat conduction problems with phase change. *International Journal of Heat and Mass Transfer*, 29(2):285–291, feb 1986. doi:10.1016/0017-9310(86)90235-8. [Cited on pages 62 and 63]

[336] Kinga Pielichowska and Krzysztof Pielichowski. Phase change materials for thermal energy storage. *Progress in Materials Science*, 65:67–123, aug 2014. doi:10.1016/j.pmatsci.2014.03.005. [Cited on page 245]

[337] Georg Pingen, Matthias Waidmann, Anton Evgrafov, and Kurt Maute. A parametric level-set approach for topology optimization of flow domains. *Structural and Multidisciplinary Optimization*, 41(1):117–131, jun 2009. doi:10.1007/s00158-009-0405-1. [Cited on pages 14 and 15]

[338] A. Pizzolato, F. Donato, V. Verda, M. Santarelli, and A. Sciacovelli. CSP plants with thermocline thermal energy storage and integrated steam generator – techno-economic modeling and design optimization. *Energy*, 139:231–246, nov 2017. doi:10.1016/j.energy.2017.07.160. [Cited on page 267]

[339] D. R. Poirier. Permeability for flow of interdendritic liquid in columnar-dendritic alloys. *Metallurgical Transactions B*, 18(1):245–255, mar 1987. doi:10.1007/bf02658450. [Cited on page 180]

[340] William K. Pratt. *Digital Image Processing*. John Wiley & Sons, Inc., jan 2007. doi:10.1002/0470097434. [Cited on page 234]

[341] GD Puccini, LE Blaser, CA Bonetti, and A Butarelli. Robustness-based design of water distribution networks. *Water Utility Journal*, 13:13–28, 2016. [Cited on page 281]

[342] Alfio Quarteroni. *Numerical Models for Differential Problems*. Springer Milan, 2009. doi:10.1007/978-88-470-1071-0. [Cited on pages 59 and 68]

[343] Daniel Quiggin and Richard Buswell. The implications of heat electrification on national electrical supply-demand balance under published 2050 energy scenarios. *Energy*, 98:253–270, mar 2016. doi:10.1016/j.energy.2015.11.060. [Cited on page 1]

[344] Tran Dinh Quoc, Carlo Savorgnan, and Moritz Diehl. Real-time sequential convex programming for optimal control applications. In *Modeling, Simulation and Optimization of Complex Processes*, pages 91–102. Springer Berlin Heidelberg, 2012. doi:10.1007/978-3-642-25707-0_8. [Cited on page 285]

[345] Bladimir Ramos-Alvarado, Abel Hernandez-Guerrero, Daniel Juarez-Robles, and Peiwen Li. Numerical investigation of the performance of symmetric flow distributors as flow channels for PEM fuel cells. *International Journal of Hydrogen Energy*, 37(1):436–448, jan 2012. doi:10.1016/j.ijhydene.2011.09.080. [Cited on page 330]

[346] Zhengfu Rao and Elad Salomons. Development of a real-time, near-optimal control process for water-distribution networks. *Journal of Hydroinformatics*, 9(1):25, jan 2007. doi:10.2166/hydro.2006.015. [Cited on page 284]

[347] Manish K. Rathod and Jyotirmay Banerjee. Thermal performance enhancement of shell and tube latent heat storage unit using longitudinal fins. *Applied Thermal Engineering*, 75:1084–1092, jan 2015. doi:10.1016/j.applthermaleng.2014.10.074. [Cited on page 50]

[348] Lord Rayleigh. LVI.on the influence of obstacles arranged in rectangular order upon the properties of a medium. *Philosophical Magazine Series 5*, 34(211):481–502, dec 1892. doi:10.1080/14786449208620364. [Cited on page 120]

[349] J. N. Reddy. *An Introduction to Continuum Mechanics*. Cambridge University Press, 2007. doi:10.1017/cbo9780511800894. [Cited on page 177]

[350] Junuthula Narasimha Reddy and David K Gartling. *The finite element method in heat transfer and fluid dynamics*. CRC press, 2010. [Cited on pages 68, 73, 74, 184, and 187]

[351] Ph. Renard and G. de Marsily. Calculating equivalent permeability: a review. *Advances in Water Resources*, 20(5-6):253–278, oct 1997. doi:10.1016/s0309-1708(96)00050-4. [Cited on page 336]

[352] U. T. Ringertz. On finding the optimal distribution of material properties. *Structural Optimization*, 5(4):265–267, dec 1993. doi:10.1007/bf01743590. [Cited on page 126]

[353] M Haralick Robert and G SHAPIRO Linda. Computer and robot vision. *Vol. I, Addison-Wesley*, pages 28–48, 1992. [Cited on page 234]

[354] Claudio Rochas, Tatjana Kuzņecova, and Francesco Romagnoli. The concept of the system resilience within the infrastructure dimension: application to a latvian case. *Journal of Cleaner Production*, 88:358–368, feb 2015. doi:10.1016/j.jclepro.2014.04.081. [Cited on page 278]

[355] H. Rodrigues, J.M. Guedes, and M.P. Bendsoe. Hierarchical optimization of material and structure. *Structural and Multidisciplinary Optimization*, 24(1):1–10, aug 2002. doi:10.1007/s00158-002-0209-z. [Cited on pages 31 and 125]

[356] Susana Rojas-Labanda and Mathias Stolpe. Benchmarking optimization solvers for structural topology optimization. *Structural and Multidisciplinary Optimization*, 52(3):527–547, may 2015. doi:10.1007/s00158-015-1250-z. [Cited on page 17]

[357] W. Donald Rolph and Klaus-JÜRgen Bathe. An efficient algorithm for analysis of nonlinear heat transfer with phase changes. *International Journal for Numerical Methods in Engineering*, 18(1):119–134, jan 1982. doi:10.1002/nme.1620180111. [Cited on pages 62 and 63]

[358] J. Roose and O. Storrer. Modelization of phase changes by fictitious-heat flow. *International Journal for Numerical Methods in Engineering*, 20(2):217–225, feb 1984. doi:10.1002/nme.1620200203. [Cited on pages 62 and 63]

[359] R. Roshandel, F. Arbabi, and G. Karimi Moghaddam. Simulation of an innovative flow-field design based on a bio inspired pattern for PEM fuel cells. *Renewable Energy*, 41:86–95, may 2012. doi:10.1016/j.renene.2011.10.008. [Cited on page 332]

[360] A. Rozenfeld, Y. Kozak, T. Rozenfeld, and G. Ziskind. Experimental demonstration, modeling and analysis of a novel latent-heat thermal energy storage unit with a helical fin. *International Journal of Heat and Mass Transfer*,

110:692–709, jul 2017. doi:10.1016/j.ijheatmasstransfer.2017.03.020. [Cited on page 54]

[361] Hanxia Ruan, Chaoqun Wu, Shuliang Liu, and Tao Chen. Design and simulation of novel flow field plate geometry for proton exchange membrane fuel cells. *Heat and Mass Transfer*, 52(10):2167–2176, dec 2015. doi:10.1007/s00231-015-1737-6. [Cited on pages 332 and 354]

[362] Santosh Kumar Sahoo, Mihir Kumar Das, and Prasenjit Rath. Application of TCE-PCM based heat sinks for cooling of electronic components: A review. *Renewable and Sustainable Energy Reviews*, 59:550–582, jun 2016. doi:10.1016/j.rser.2015.12.238. [Cited on page 53]

[363] Uktam R. Salomov, Eliodoro Chiavazzo, and Pietro Asinari. Gas-dynamic and electro-chemical optimization of catalyst layers in high temperature polymeric electrolyte membrane fuel cells. *International Journal of Hydrogen Energy*, 40(15):5425–5431, apr 2015. doi:10.1016/j.ijhydene.2015.01.059. [Cited on pages 351 and 354]

[364] Enrique Sanchez-Palencia and André Zaoui, editors. *Homogenization Techniques for Composite Media*. Springer Berlin Heidelberg, 1987. doi:10.1007/3-540-17616-0. [Cited on pages 12 and 114]

[365] G. Sandou, S. Font, S. Tebbani, A. Hiret, C. Mondon, S. Tebbani, A. Hiret, and C. Mondon. Predictive control of a complex district heating network. In *Proceedings of the 44th IEEE Conference on Decision and Control*. IEEE, 2005. doi:10.1109/cdc.2005.1583351. [Cited on page 284]

[366] Ahmet Sarı. Eutectic mixtures of some fatty acids for low temperature solar heating applications: Thermal properties and thermal reliability. *Applied Thermal Engineering*, 25(14-15):2100–2107, oct 2005. doi:10.1016/j.applthermaleng.2005.01.010. [Cited on page 244]

[367] Ahmet Sarı, Alper Biçer, and Ali Karaipekli. Synthesis, characterization, thermal properties of a series of stearic acid esters as novel solid–liquid phase change materials. *Materials Letters*, 63(13-14):1213–1216, may 2009. doi:10.1016/j.matlet.2009.02.045. [Cited on page 244]

[368] Ahmet Sarı, Hayati Sarı, and Adem Önal. Thermal properties and thermal reliability of eutectic mixtures of some fatty acids as latent heat storage materials. *Energy Conversion and Management*, 45(3):365–376, feb 2004. doi:10.1016/s0196-8904(03)00154-7. [Cited on page 244]

[369] Bhaskar P. Saripella, Umit O. Koylu, and Ming C. Leu. Comparisons of performances and liquid water distributions within bio-inspired and single-serpentine PEM fuel cell channels. In *ASME 2015 13th International Conference on Fuel Cell Science, Engineering and Technology*. ASME, jun 2015. doi:10.1115/fuelcell2015-49099. [Cited on page 332]

[370] M.A. Sayegh, J. Danielewicz, T. Nannou, M. Miniewicz, P. Jadwiszczak, K. Piekarska, and H. Jouhara. Trends of european research and development in district heating technologies. *Renewable and Sustainable Energy Reviews*, 68:1183–1192, feb 2017. doi:10.1016/j.rser.2016.02.023. [Cited on page 2]

[371] Tobias A. Schaedler and William B. Carter. Architected cellular materials. *Annual Review of Materials Research*, 46(1):187–210, jul 2016. doi:10.1146/annurev-matsci-070115-031624. [Cited on pages 107 and 112]

[372] Fabian Schury, Michael Stingl, and Fabian Wein. Efficient two-scale optimization of manufacturable graded structures. *SIAM Journal on Scientific Computing*, 34(6):B711–B733, jan 2012. doi:10.1137/110850335. [Cited on page 126]

[373] Gerald Schweiger, Jonatan Rantzer, Karin Ericsson, and Patrick Lauenburg. The potential of power-to-heat in swedish district heating systems. *Energy*, feb 2017. doi:10.1016/j.energy.2017.02.075. [Cited on page 277]

[374] A. Sciacovelli, F. Gagliardi, and V. Verda. Maximization of performance of a PCM latent heat storage system with innovative fins. *Applied Energy*, 137:707–715, jan 2015. doi:10.1016/j.apenergy.2014.07.015. [Cited on pages 53 and 76]

[375] Adriano Sciacovelli and Vittorio Verda. Second-law design of a latent heat thermal energy storage with branched fins. *International Journal of Numerical Methods for Heat & Fluid Flow*, 26(2):489–503, mar 2016. doi:10.1108/hff-01-2015-0040. [Cited on pages 53 and 234]

[376] Mehmet Seyhan, Yahya Erkan Akansu, Miraç Murat, Yusuf Korkmaz, and Selahaddin Orhan Akansu. Performance prediction of PEM fuel cell with wavy serpentine flow channel by using artificial neural network. *International Journal of Hydrogen Energy*, 42(40):25619–25629, oct 2017. doi:10.1016/j.ijhydene.2017.04.001. [Cited on page 330]

[377] H. Shabgard, T.L. Bergman, N. Sharifi, and A. Faghri. High temperature latent heat thermal energy storage using heat pipes. *International Journal of Heat and Mass Transfer*, 53(15-16):2979–2988, jul 2010. doi:10.1016/j.ijheatmasstransfer.2010.03.035. [Cited on page 48]

[378] Xiaofang Shan, Peng Wang, and Weizhen Lu. The reliability and availability evaluation of repairable district heating networks under changeable external conditions. *Applied Energy*, 203:686–695, oct 2017. doi:10.1016/j.apenergy.2017.06.081. [Cited on page 2]

[379] Omar Z. Sharaf and Mehmet F. Orhan. An overview of fuel cell technology: Fundamentals and applications. *Renewable and Sustainable Energy Reviews*, 32:810–853, apr 2014. doi:10.1016/j.rser.2014.01.012. [Cited on page 2]

[380] Nourouddin Sharifi, Theodore L. Bergman, Michael J. Allen, and Amir Faghri. Melting and solidification enhancement using a combined heat pipe, foil approach. *International Journal of Heat and Mass Transfer*, 78:930–941, nov 2014. doi:10.1016/j.ijheatmasstransfer.2014.07.054. [Cited on page 247]

[381] Ashesh Sharma. *Advances in Design and Optimization using Immersed Boundary Methods*. PhD thesis, Colorado University, 11 2017. [Cited on pages 16 and 141]

[382] R.K. Sharma, P. Ganesan, V.V. Tyagi, and T.M.I. Mahlia. Accelerated thermal cycle and chemical stability testing of polyethylene glycol (PEG) 6000 for solar thermal energy storage. *Solar Energy Materials and Solar Cells*, 147:235–239, apr 2016. doi:10.1016/j.solmat.2015.12.023. [Cited on page 245]

[383] Mohsen Sheikholeslami, Sina Lohrasbi, and Davood Domairry Ganji. Response surface method optimization of innovative fin structure for expediting discharging process in latent heat thermal energy storage system containing nano-enhanced phase change material. *Journal of the Taiwan Institute of Chemical Engineers*, 67:115–125, oct 2016. doi:10.1016/j.jtice.2016.08.019. [Cited on page 53]

[384] Byung Chul Shin, Sang Done Kim, and Won-Hoon Park. Ternary carbonate eutectic (lithium, sodium and potassium carbonates) for latent heat storage medium. *Solar Energy Materials*, 21(1):81–90, nov 1990. doi:10.1016/0165-1633(90)90044-2. [Cited on page 246]

[385] H. Shmueli, G. Ziskind, and R. Letan. Melting in a vertical cylindrical tube: Numerical investigation and comparison with experiments. *International Journal of Heat and Mass Transfer*, 53(19-20):4082–4091, sep 2010. doi:10.1016/j.ijheatmasstransfer.2010.05.028. [Cited on pages 181, 184, and 196]

[386] O. Sigmund. Design of multiphysics actuators using topology optimization – part II: Two-material structures. *Computer Methods in Applied Mechanics and Engineering*, 190(49-50):6605–6627, oct 2001. doi:10.1016/s0045-7825(01)00252-3. [Cited on page 129]

[387] O. Sigmund and J. Petersson. Numerical instabilities in topology optimization: A survey on procedures dealing with checkerboards, mesh-dependencies and local minima. *Structural Optimization*, 16(1):68–75, aug 1998. doi:10.1007/bf01214002. [Cited on pages 30 and 31]

[388] O. Sigmund and S. Torquato. Design of materials with extreme thermal expansion using a three-phase topology optimization method. *Journal of the Mechanics and Physics of Solids*, 45(6):1037–1067, jun 1997. doi:10.1016/s0022-5096(96)00114-7. [Cited on pages 122 and 129]

[389] Ole Sigmund. Materials with prescribed constitutive parameters: An inverse homogenization problem. *International Journal of Solids and Structures*, 31(17):2313–2329, sep 1994. doi:10.1016/0020-7683(94)90154-6. [Cited on page 122]

[390] Ole Sigmund. Tailoring materials with prescribed elastic properties. *Mechanics of Materials*, 20(4):351–368, jun 1995. doi:10.1016/0167-6636(94)00069-7. [Cited on page 31]

[391] Ole Sigmund. On the design of compliant mechanisms using topology optimization. *Mechanics of Structures and Machines*, 25(4):493–524, jan 1997. doi:10.1080/08905459708945415. [Cited on page 32]

[392] Ole Sigmund. Morphology-based black and white filters for topology optimization. *Structural and Multidisciplinary Optimization*, 33(4-5):401–424, jan 2007. doi:10.1007/s00158-006-0087-x. [Cited on pages 34 and 217]

[393] Ole Sigmund. On the usefulness of non-gradient approaches in topology optimization. *Structural and Multidisciplinary Optimization*, 43(5):589–596, mar 2011. doi:10.1007/s00158-011-0638-7. [Cited on pages 16, 33, and 36]

[394] Ole Sigmund and Kurt Maute. Sensitivity filtering from a continuum mechanics perspective. *Structural and Multidisciplinary Optimization*, 46(4):471–475, jun 2012. doi:10.1007/s00158-012-0814-4. [Cited on page 32]

[395] Ole Sigmund and Kurt Maute. Topology optimization approaches. *Structural and Multidisciplinary Optimization*, 48(6):1031–1055, aug 2013. doi:10.1007/s00158-013-0978-6. [Cited on pages 12, 13, 16, 29, 36, 41, and 360]

[396] Debanand Singdeo, Tapobrata Dey, Shrihari Gaikwad, Søren Juhl Andreasen, and Prakash C. Ghosh. A new modified-serpentine flow field for application in high temperature polymer electrolyte fuel cell. *Applied Energy*, 195:13–22, jun 2017. doi:10.1016/j.apenergy.2017.03.022. [Cited on page 329]

[397] Raghavendra Sivapuram, Peter D. Dunning, and H. Alicia Kim. Simultaneous material and structural optimization by multiscale topology optimization. *Structural and Multidisciplinary Optimization*, 54(5):1267–1281, jul 2016. doi:10.1007/s00158-016-1519-x. [Cited on page 126]

[398] Dean Snelling, Qian Li, Nicolas Meisel, Christopher B. Williams, Romesh C. Batra, and Alan P. Druschitz. Lightweight metal cellular structures fabricated via 3d printing of sand cast molds. *Advanced Engineering Materials*, 17(7):923–932, mar 2015. doi:10.1002/adem.201400524. [Cited on page 111]

[399] Gustaf Söderlind. Automatic control and adaptive time-stepping. *Numerical Algorithms*, 31(1-4):281–310, 2002. [Cited on page 190]

[400] Aran Solé, Hannah Neumann, Sophia Niedermaier, Luisa F. Cabeza, and Elena Palomo. Thermal stability test of sugar alcohols as phase change materials for medium temperature energy storage application. *Energy Procedia*, 48:436–439, 2014. doi:10.1016/j.egypro.2014.02.051. [Cited on page 245]

[401] Gnanadurai Ravikumar Solomon and Ramalingam Velraj. Analysis of the heat transfer mechanisms during energy storage in a phase change material filled vertical finned cylindrical unit for free cooling application. *Energy Conversion and Management*, 75:466–473, nov 2013. doi:10.1016/j.enconman.2013.06.044. [Cited on page 50]

[402] Farah Souayfane, Farouk Fardoun, and Pascal-Henry Biwole. Phase change materials (PCM) for cooling applications in buildings: A review. *Energy and Buildings*, 129:396–431, oct 2016. doi:10.1016/j.enbuild.2016.04.006. [Cited on page 241]

[403] Lenko Stanev, Mihail Kolev, Boris Drenchev, and Ludmil Drenchev. Open-cell metallic porous materials obtained through space holders—part i: Production methods. a review. *Journal of Manufacturing Science and Engineering*, 139(5):050801, nov 2016. doi:10.1115/1.4034439. [Cited on page 108]

[404] J. Stegmann and E. Lund. Discrete material optimization of general composite shell structures. *International Journal for Numerical Methods in Engineering*, 62(14):2009–2027, 2005. doi:10.1002/nme.1259. [Cited on page 130]

[405] Wolf-Dieter Steinmann, Doerte Laing, and Rainer Tamme. Development of PCM storage for process heat and power generation. *Journal of Solar Energy Engineering*, 131(4):041009, 2009. doi:10.1115/1.3197834. [Cited on pages 246, 247, and 248]

[406] M. Stolpe and K. Svanberg. An alternative interpolation scheme for minimum compliance topology optimization. *Structural and Multidisciplinary Optimization*, 22(2):116–124, sep 2001. doi:10.1007/s001580100129. [Cited on pages 28 and 30]

[407] Douglas F. Surco, Thelma P. B. Vecchi, and Mauro A. S. S. Ravagnani. Optimization of water distribution networks using a modified particle swarm optimization algorithm. *Water Science and Technology: Water Supply*, page ws2017148, jul 2017. doi:10.2166/ws.2017.148. [Cited on page 284]

[408] C. R. Suribabu and T. R. Neelakantan. Design of water distribution networks using particle swarm optimization. *Urban Water Journal*, 3(2):111–120, jun 2006. doi:10.1080/15730620600855928. [Cited on page 281]

[409] Krister Svanberg. The method of moving asymptotes—a new method for structural optimization. *International Journal for Numerical Methods in Engineering*, 24(2):359–373, feb 1987. doi:10.1002/nme.1620240207. [Cited on pages 21 and 22]

[410] Krister Svanberg. A class of globally convergent optimization methods based on conservative convex separable approximations. *SIAM Journal on Optimization*, 12(2):555–573, jan 2002. doi:10.1137/s1052623499362822. [Cited on pages 21, 22, 23, and 24]

[411] Krister Svanberg. Mma and gcmma-two methods for nonlinear optimization. Technical report, KTH, Stockholm, 2007. [Cited on pages 21, 22, and 24]

[412] Rodolfo Taccani and Nicola Zuliani. Effect of flow field design on performances of high temperature PEM fuel cells: Experimental analysis. *International Journal of Hydrogen Energy*, 36(16):10282–10287, aug 2011. doi:10.1016/j.ijhydene.2010.10.026. [Cited on pages 330 and 356]

[413] Genichi Taguchi, Subir Chowdhury, Yuin Wu, et al. *Taguchi's quality engineering handbook*, volume 1736. Wiley Online Library, 2005. [Cited on page 280]

[414] Xue-Cheng Tai and Hongwei Li. A piecewise constant level set method for elliptic inverse problems. *Applied Numerical Mathematics*, 57(5-7):686–696, may 2007. doi:10.1016/j.apnum.2006.07.010. [Cited on page 131]

[415] T. T. Tanyimboh and A. B. Templeman. Calculating maximum entropy flows in networks. *Journal of the Operational Research Society*, 44(4):383–396, apr 1993. doi:10.1057/jors.1993.68. [Cited on page 280]

[416] Tiku T. Tanyimboh. Informational entropy: a failure tolerance and reliability surrogate for water distribution networks. *Water Resources Management*, 31(10):3189–3204, may 2017. doi:10.1007/s11269-017-1684-8. [Cited on page 280]

[417] N.H.S. Tay, F. Bruno, and M. Belusko. Comparison of pinned and finned tubes in a phase change thermal energy storage system using CFD. *Applied Energy*, 104:79–86, apr 2013. doi:10.1016/j.apenergy.2012.10.040. [Cited on pages 53, 267, and 268]

[418] T. Texduyar and T. Hughes. Finite element formulations for convection dominated flows with particular emphasis on the compressible euler equations. In *21st Aerospace Sciences Meeting*. American Institute of Aeronautics and Astronautics, jan 1983. doi:10.2514/6.1983-125. [Cited on page 189]

[419] T.E. Tezduyar, S. Mittal, S.E. Ray, and R. Shih. Incompressible flow computations with stabilized bilinear and linear equal-order-interpolation velocity-pressure elements. *Computer Methods in Applied Mechanics and Engineering*, 95(2):221–242, mar 1992. doi:10.1016/0045-7825(92)90141-6. [Cited on pages 188, 189, and 342]

[420] J. Tian, T. Kim, T.J. Lu, H.P. Hodson, D.T. Queheillalt, D.J. Sypeck, and H.N.G. Wadley. The effects of topology upon fluid-flow and heat-transfer within cellular copper structures. *International Journal of Heat*

and Mass Transfer, 47(14-16):3171–3186, jul 2004. doi:10.1016/j.ijheatmasstransfer.2004.02.010. [Cited on pages 110 and 111]

[421] Ezio Todini. Looped water distribution networks design using a resilience index based heuristic approach. *Urban Water*, 2(2):115–122, jun 2000. doi:10.1016/s1462-0758(00)00049-2. [Cited on page 279]

[422] Xinglin Tong, Jamil A. Khan, and M. RuhulAmin. Enhancement oh heat transfer by inserting a metal matrix into a phase change material. *Numerical Heat Transfer, Part A: Applications*, 30(2):125–141, aug 1996. doi:10.1080/10407789608913832. [Cited on page 111]

[423] André Jacomel Torii and Rafael Holdorf Lopez. Reliability analysis of water distribution networks using the adaptive response surface approach. *Journal of Hydraulic Engineering*, 138(3):227–236, mar 2012. doi:10.1061/(asce)hy.1943-7900.0000504. [Cited on pages 279 and 280]

[424] Mindaugas Valinčius, Mindaugas Vaišnoras, and Algirdas Kaliatka. Study and demonstration of pressure wave-based leak detection in a district heating network. *Structure and Infrastructure Engineering*, 14(2):151–162, may 2017. doi:10.1080/15732479.2017.1330892. [Cited on page 283]

[425] AMP Valli, GF Carey, and ALGA Coutinho. Control strategies for timestep selection in finite element simulation of incompressible flows and coupled reaction–convection–diffusion processes. *International Journal for numerical methods in fluids*, 47(3):201–231, 2005. doi:10.1002/fld.805. [Cited on page 190]

[426] Ioannis Vallios, Theocharis Tsoutsos, and George Papadakis. An applied methodology for assessment of the sustainability of biomass district heating systems. *International Journal of Sustainable Energy*, 35(3):267–294, mar 2014. doi:10.1080/14786451.2014.895005. [Cited on page 277]

[427] N. P. van Dijk, K. Maute, M. Langelaar, and F. van Keulen. Level-set methods for structural topology optimization: a review. *Structural and Multidisciplinary Optimization*, 48(3):437–472, mar 2013. doi:10.1007/s00158-013-0912-y. [Cited on pages 14, 15, and 134]

[428] N. P. van Dijk, G. H. Yoon, F. van Keulen, and M. Langelaar. A level-set based topology optimization using the element connectivity parameterization method. *Structural and Multidisciplinary Optimization*, 42(2):269–282, feb 2010. doi:10.1007/s00158-010-0485-y. [Cited on page 14]

[429] K. Vasant Kumar Varma, Shankar Narasimhan, and S. Murty Bhallamudi. Optimal design of water distribution systems using an NLP method. *Journal of Environmental Engineering*, 123(4):381–388, apr 1997. doi:10.1061/(asce)0733-9372(1997)123:4(381). [Cited on page 282]

[430] R. Velraj, R.V. Seeniraj, B. Hafner, C. Faber, and K. Schwarzer. Heat transfer enhancement in a latent heat storage system. *Solar Energy*, 65(3):171–180, feb 1999. doi:10.1016/s0038-092x(98)00128-5. [Cited on page 49]

[431] Alexander Verbart, Matthijs Langelaar, and Fred van Keulen. A unified aggregation and relaxation approach for stress-constrained topology optimization. *Structural and Multidisciplinary Optimization*, 55(2):663–679, jul 2016. doi:10.1007/s00158-016-1524-0. [Cited on pages 142 and 308]

[432] Francesca Verrilli, Seshadhri Srinivasan, Giovanni Gambino, Michele Canelli, Mikko Himanka, Carmen Del Vecchio, Maurizio Sasso, and Luigi Glielmo. Model predictive control-based optimal operations of district heating system with thermal energy storage and flexible loads. *IEEE Transactions on Automation Science and Engineering*, 14(2):547–557, apr 2017. doi:10.1109/tase.2016.2618948. [Cited on page 284]

[433] Henk Kaarle Versteeg and Weeratunge Malalasekera. *An introduction to computational fluid dynamics: the finite volume method*. Pearson Education, 2007. [Cited on pages 73, 188, and 291]

[434] Luminita A. Vese and Tony F. Chan. A multiphase level set framework for image segmentation using the mumford and shah model. *International Journal of Computer Vision*, 50(3):271–293, 2002. doi:10.1023/a:1020874308076. [Cited on page 131]

[435] S. Vigdergauz. Two-dimensional grained composites of extreme rigidity. *Journal of Applied Mechanics*, 61(2):390, 1994. doi:10.1115/1.2901456. [Cited on page 122]

[436] J. Vogel, J. Felbinger, and M. Johnson. Natural convection in high temperature flat plate latent heat thermal energy storage systems. *Applied Energy*, 184:184–196, dec 2016. doi:10.1016/j.apenergy.2016.10.001. [Cited on pages 176 and 248]

[437] V. R. Voller, M. Cross, and N. C. Markatos. An enthalpy method for convection/diffusion phase change. *International Journal for Numerical Methods in Engineering*, 24(1):271–284, jan 1987. doi:10.1002/nme.1620240119. [Cited on pages 178, 179, 180, and 181]

[438] V. R. Voller and C. R. Swaminathan. ERAL source-based method for solidification phase change. *Numerical Heat Transfer, Part B: Fundamentals*, 19(2):175–189, jan 1991. doi:10.1080/10407799108944962. [Cited on page 63]

[439] V. R. Voller, C. R. Swaminathan, and B. G. Thomas. Fixed grid techniques for phase change problems: A review. *International Journal for Numerical Methods in Engineering*, 30(4):875–898, sep 1990. doi:10.1002/nme.1620300419. [Cited on pages 58, 59, 62, and 63]

[440] VR Voller. An overview of numerical methods for solving phase change problems. *Advances in numerical heat transfer*, 1(9):341–380, 1997. [Cited on pages 55, 56, 57, 58, 59, and 60]

[441] V.R. Voller, A.D. Brent, and C. Prakash. The modelling of heat, mass and solute transport in solidification systems. *International Journal of Heat and Mass Transfer*, 32(9):1719–1731, sep 1989. doi:10.1016/0017-9310(89)90054-9. [Cited on pages 178, 179, and 181]

[442] H. N.G Wadley. Multifunctional periodic cellular metals. *Philosophical Transactions of the Royal Society A: Mathematical, Physical and Engineering Sciences*, 364(1838):31–68, jan 2006. doi:10.1098/rsta.2005.1697. [Cited on pages 110 and 112]

[443] H.N.G. Wadley. Cellular metals manufacturing. *Advanced Engineering Materials*, 4(10):726–733, oct 2002. doi:10.1002/1527-2648(20021014)4:10<726::aid-adem726>3.0.co;2-y. [Cited on page 107]

[444] Chao Wang, Qinglei Zhang, Jiabin Lu, Shuiyun Shen, Xiaohui Yan, Fengjuan Zhu, Xiaojing Cheng, and Junliang Zhang. Effect of height/width-tapered flow fields on the cell performance of polymer electrolyte membrane fuel cells. *International Journal of Hydrogen Energy*, 42(36):23107–23117, sep 2017. doi:10.1016/j.ijhydene.2017.07.136. [Cited on pages 326 and 327]

[445] Chao Wang, Qinglei Zhang, Shuiyun Shen, Xiaohui Yan, Fengjuan Zhu, Xiaojing Cheng, and Junliang Zhang. The respective effect of under-rib convection and pressure drop of flow fields on the performance of PEM fuel cells. *Scientific Reports*, 7:43447, mar 2017. doi:10.1038/srep43447. [Cited on pages 324, 325, 327, and 354]

[446] Fengwen Wang, Boyan Stefanov Lazarov, and Ole Sigmund. On projection methods, convergence and robust formulations in topology optimization. *Structural and Multidisciplinary Optimization*, 43(6):767–784, dec 2010. doi:10.1007/s00158-010-0602-y. [Cited on page 36]

[447] Haichao Wang, Elnaz Abdollahi, Risto Lahdelma, Wenling Jiao, and Zhigang Zhou. Modelling and optimization of the smart hybrid renewable energy for communities (SHREC). *Renewable Energy*, 84:114–123, dec 2015. doi:10.1016/j.renene.2015.05.036. [Cited on page 277]

[448] J. Wang and H. Wang. Flow-field designs of bipolar plates in PEM fuel cells: Theory and applications. *Fuel Cells*, 12(6):989–1003, nov 2012. doi:10.1002/fuce.201200074. [Cited on page 331]

[449] Jifen Wang, Huaqing Xie, and Zhong Xin. Thermal properties of paraffin based composites containing multi-walled carbon nanotubes. *Thermochimica Acta*, 488(1-2):39–42, may 2009. doi:10.1016/j.tca.2009.01.022. [Cited on page 49]

[450] Junye Wang. Theory and practice of flow field designs for fuel cell scaling-up: A critical review. *Applied Energy*, 157:640–663, nov 2015. doi:10.1016/j.apenergy.2015.01.032. [Cited on pages 323 and 331]

[451] Michael Yu Wang and Xiaoming Wang. Color level sets: a multi-phase method for structural topology optimization with multiple materials. *Computer Methods in Applied Mechanics and Engineering*, 193(6-8):469–496, feb 2004. doi:10.1016/j.cma.2003.10.008. [Cited on page 131]

[452] Wei-Wei Wang, Liang-Bi Wang, and Ya-Ling He. Parameter effect of a phase change thermal energy storage unit with one shell and one finned tube on its energy efficiency ratio and heat storage rate. *Applied Thermal Engineering*, 93:50–60, jan 2016. doi:10.1016/j.applthermaleng.2015.08.108. [Cited on pages 52 and 220]

[453] Xianglei Wang, Quangui Guo, Yajuan Zhong, Xinghai Wei, and Lang Liu. Heat transfer enhancement of neopentyl glycol using compressed expanded natural graphite for thermal energy storage. *Renewable Energy*, 51:241–246, mar 2013. doi:10.1016/j.renene.2012.09.029. [Cited on page 49]

[454] Xiao-Dong Wang, Yu-Xian Huang, Chin-Hsiang Cheng, Jiin-Yuh Jang, Duu-Jong Lee, Wei-Mon Yan, and Ay Su. An inverse geometry design problem for optimization of single serpentine flow field of PEM fuel cell. *International Journal of Hydrogen Energy*, 35(9):4247–4257, may 2010. doi:10.1016/j.ijhydene.2010.02.059. [Cited on pages 326 and 327]

[455] Xiao-Dong Wang, Xin-Xin Zhang, Wei-Mon Yan, Duu-Jong Lee, and Ay Su. Determination of the optimal active area for proton exchange membrane fuel cells with parallel, interdigitated or serpentine designs. *International Journal of Hydrogen Energy*, 34(9):3823–3832, may 2009. doi:10.1016/j.ijhydene.2008.12.049. [Cited on pages 328 and 330]

[456] Yaran Wang, Shijun You, Huan Zhang, Wandong Zheng, Xuejing Zheng, and Qingwei Miao. Hydraulic performance optimization of meshed district heating network with multiple heat sources. *Energy*, 126:603–621, may 2017. doi:10.1016/j.energy.2017.03.044. [Cited on page 284]

[457] Yiqiang Wang, Zhen Luo, Zhan Kang, and Nong Zhang. A multi-material level set-based topology and shape optimization method. *Computer Methods in Applied Mechanics and Engineering*, 283:1570–1586, jan 2015. doi:10.1016/j.cma.2014.11.002. [Cited on pages xxii, 131, and 133]

[458] Yu Wang, Jie Gao, Zhen Luo, Terry Brown, and Nong Zhang. Level-set topology optimization for multimaterial and multifunctional mechanical metamaterials. *Engineering Optimization*, 49(1):22–42, apr 2016. doi:10.1080/0305215x.2016.1164853. [Cited on page 131]

[459] Yulin Wang, Like Yue, and Shixue Wang. New design of a cathode flow-field with a sub-channel to improve the polymer electrolyte membrane fuel

cell performance. *Journal of Power Sources*, 344:32–38, mar 2017. doi:10.1016/j.jpowsour.2017.01.075. [Cited on page 330]

[460] Yun Wang, Ken S. Chen, Jeffrey Mishler, Sung Chan Cho, and Xavier Cordobes Adroher. A review of polymer electrolyte membrane fuel cells: Technology, applications, and needs on fundamental research. *Applied Energy*, 88(4):981–1007, apr 2011. doi:10.1016/j.apenergy.2010.09.030. [Cited on page 321]

[461] Jung-Ho Wee. Applications of proton exchange membrane fuel cell systems. *Renewable and Sustainable Energy Reviews*, 11(8):1720–1738, oct 2007. doi:10.1016/j.rser.2006.01.005. [Cited on page 321]

[462] Christopher B. Williams, Joe K. Cochran, and David W. Rosen. Additive manufacturing of metallic cellular materials via three-dimensional printing. *The International Journal of Advanced Manufacturing Technology*, 53(1-4):231–239, jul 2010. doi:10.1007/s00170-010-2812-2. [Cited on pages 110 and 112]

[463] James M Winget and Thomas JR Hughes. Solution algorithms for nonlinear transient heat conduction analysis employing element-by-element iterative strategies. *Computer Methods in Applied Mechanics and Engineering*, 52(1-3):711–815, 1985. doi:10.1016/0045-7825(85)90015-5. [Cited on page 190]

[464] Carlo Winterscheid, Jan-Olof Dalenbäck, and Stefan Holler. Integration of solar thermal systems in existing district heating systems. *Energy*, may 2017. doi:10.1016/j.energy.2017.04.159. [Cited on page 277]

[465] Robert Wright, Edo Abraham, Panos Parpas, and Ivan Stoianov. Control of water distribution networks with dynamic DMA topology using strictly feasible sequential convex programming. *Water Resources Research*, 51(12):9925–9941, dec 2015. doi:10.1002/2015wr017466. [Cited on pages 284 and 285]

[466] Robert Wright, Ivan Stoianov, Panos Parpas, Kevin Henderson, and John King. Adaptive water distribution networks with dynamically reconfigurable topology. *Journal of Hydroinformatics*, 16(6):1280, nov 2014. doi:10.2166/hydro.2014.086. [Cited on page 285]

[467] Dawei Wu, Junlong Chen, and Anthony P. Roskilly. Phase change material thermal storage for biofuel preheating in micro trigeneration application: A numerical study. *Applied Energy*, 137:832–844, jan 2015. doi:10.1016/j.apenergy.2014.09.087. [Cited on page 260]

[468] Jun Wu, Niels Aage, Rudiger Westermann, and Ole Sigmund. Infill optimization for additive manufacturing—approaching bone-like porous structures. *IEEE Transactions on Visualization and Computer Graphics*, 24(2):1127–1140, feb 2018. doi:10.1109/tvcg.2017.2655523. [Cited on page 126]

[469] Liang Xia and Piotr Breitkopf. Concurrent topology optimization design of material and structure within fe2 nonlinear multiscale analysis framework. *Computer Methods in Applied Mechanics and Engineering*, 278:524–542, aug 2014. doi:10.1016/j.cma.2014.05.022. [Cited on page 125]

[470] Liang Xia and Piotr Breitkopf. A reduced multiscale model for nonlinear structural topology optimization. *Computer Methods in Applied Mechanics and Engineering*, 280:117–134, oct 2014. doi:10.1016/j.cma.2014.07.024. [Cited on page 126]

[471] Liang Xia and Piotr Breitkopf. Recent advances on topology optimization of multiscale nonlinear structures. *Archives of Computational Methods in Engineering*, 24(2):227–249, jan 2016. doi:10.1007/s11831-016-9170-7. [Cited on page 125]

[472] Biao Xie, Wen long Cheng, and Zhi ming Xu. Studies on the effect of shape-stabilized PCM filled aluminum honeycomb composite material on thermal control. *International Journal of Heat and Mass Transfer*, 91:135–143, dec 2015. doi:10.1016/j.ijheatmasstransfer.2015.07.108. [Cited on page 108]

[473] Junling Xie and Chris Yuan. Parametric study of ice thermal storage system with thin layer ring by taguchi method. *Applied Thermal Engineering*, 98:246–255, apr 2016. doi:10.1016/j.applthermaleng.2015.12.038. [Cited on page 181]

[474] Yang Xu, Ming-Jia Li, Zhang-Jing Zheng, and Xiao-Dai Xue. Melting performance enhancement of phase change material by a limited amount of metal foam: Configurational optimization and economic assessment. *Applied Energy*, 212:868–880, feb 2018. doi:10.1016/j.apenergy.2017.12.082. [Cited on pages 109 and 112]

[475] Yang Xu, Qinlong Ren, Zhang-Jing Zheng, and Ya-Ling He. Evaluation and optimization of melting performance for a latent heat thermal energy storage unit partially filled with porous media. *Applied Energy*, 193:84–95, may 2017. doi:10.1016/j.apenergy.2017.02.019. [Cited on pages 109 and 112]

[476] Nurettin Yamankaradeniz. Thermodynamic performance assessments of a district heating system with geothermal by using advanced exergy analysis. *Renewable Energy*, 85:965–972, jan 2016. doi:10.1016/j.renene.2015.07.035. [Cited on page 277]

[477] Suna Yan, Fengwen Wang, and Ole Sigmund. On the non-optimality of tree structures for heat conduction. *International Journal of Heat and Mass Transfer*, 122:660–680, jul 2018. doi:10.1016/j.ijheatmasstransfer.2018.01.114. [Cited on pages 103, 164, and 373]

[478] Wei-Mon Yan, Hui-Chung Liu, Chyi-Yeou Soong, Falin Chen, and C.H. Cheng. Numerical study on cell performance and local transport phenomena of PEM fuel cells with novel flow field designs. *Journal of Power*

Sources, 161(2):907–919, oct 2006. doi:10.1016/j.jpowsour.2006.05.007. [Cited on pages 326 and 327]

[479] Libing Yang, Evgueniy Entchev, Antonio Rosato, and Sergio Sibilio. Smart thermal grid with integration of distributed and centralized solar energy systems. *Energy*, 122:471–481, mar 2017. doi:10.1016/j.energy.2017.01.114. [Cited on page 2]

[480] Xiaohu Yang, Zhao Lu, Qingsong Bai, Qunli Zhang, Liwen Jin, and Jinyue Yan. Thermal performance of a shell-and-tube latent heat thermal energy storage unit: Role of annular fins. *Applied Energy*, 202:558–570, sep 2017. doi:10.1016/j.apenergy.2017.05.007. [Cited on pages 52 and 240]

[481] L. Yin and G.K. Ananthasuresh. Topology optimization of compliant mechanisms with multiple materials using a peak function material interpolation scheme. *Structural and Multidisciplinary Optimization*, 23(1):49–62, dec 2001. doi:10.1007/s00158-001-0165-z. [Cited on page 130]

[482] Y YOON, W LEE, G PARK, T YANG, and C KIM. Effects of channel and rib widths of flow field plates on the performance of a PEMFC. *International Journal of Hydrogen Energy*, 30(12):1363–1366, sep 2005. doi:10.1016/j.ijhydene.2005.04.008. [Cited on pages 324 and 327]

[483] Yanping Yuan, Xiaoling Cao, Bo Xiang, and Yanxia Du. Effect of installation angle of fins on melting characteristics of annular unit for latent heat thermal energy storage. *Solar Energy*, 136:365–378, oct 2016. doi:10.1016/j.solener.2016.07.014. [Cited on page 52]

[484] Yanping Yuan, Nan Zhang, Wenquan Tao, Xiaoling Cao, and Yaling He. Fatty acids as phase change materials: A review. *Renewable and Sustainable Energy Reviews*, 29:482–498, jan 2014. doi:10.1016/j.rser.2013.08.107. [Cited on page 244]

[485] Nicholas Zabaras and Yimin Ruan. Moving and deforming finite-element simulation of two-dimensional stefan problems. *Communications in Applied Numerical Methods*, 6(7):495–506, oct 1990. doi:10.1002/cnm.1630060702. [Cited on page 56]

[486] Belen Zalba, Jose Ma Marin, Luisa F. Cabeza, and Harald Mehling. Review on thermal energy storage with phase change: materials, heat transfer analysis and applications. *Applied Thermal Engineering*, 23(3):251–283, feb 2003. doi:10.1016/s1359-4311(02)00192-8. [Cited on page 246]

[487] Christoph Zauner, Florian Hengstberger, Mark Etzel, Daniel Lager, Rene Hofmann, and Heimo Walter. Experimental characterization and simulation of a fin-tube latent heat storage using high density polyethylene as PCM. *Applied Energy*, 179:237–246, oct 2016. doi:10.1016/j.apenergy.2016.06.138. [Cited on page 247]

[488] Navid Zehtabiyan-Rezaie, Amir Arefian, Mohammad J. Kermani, Amir Karimi Noughabi, and M. Abdollahzadeh. Effect of flow field with converging and diverging channels on proton exchange membrane fuel cell performance. *Energy Conversion and Management*, 152:31–44, nov 2017. doi:10.1016/j.enconman.2017.09.009. [Cited on pages 324 and 327]

[489] Xiangbing Zeng, Ya Ge, Jun Shen, Lingping Zeng, Zhichun Liu, and Wei Liu. The optimization of channels for a proton exchange membrane fuel cell applying genetic algorithm. *International Journal of Heat and Mass Transfer*, 105:81–89, feb 2017. doi:10.1016/j.ijheatmasstransfer.2016.09.068. [Cited on pages 325 and 327]

[490] Huili Zhang, Jan Baeyens, Gustavo Cáceres, Jan Degrève, and Yongqin Lv. Thermal energy storage: Recent developments and practical aspects. *Progress in Energy and Combustion Science*, 53:1–40, mar 2016. doi:10.1016/j.pecs.2015.10.003. [Cited on pages 1 and 2]

[491] Jianlu Zhang, Zhong Xie, Jiujun Zhang, Yanghua Tang, Chaojie Song, Titichai Navessin, Zhiqing Shi, Datong Song, Haijiang Wang, David P. Wilkinson, Zhong-Sheng Liu, and Steven Holdcroft. High temperature PEM fuel cells. *Journal of Power Sources*, 160(2):872–891, oct 2006. doi:10.1016/j.jpowsour.2006.05.034. [Cited on page 328]

[492] P. Zhang, X. Xiao, and Z.W. Ma. A review of the composite phase change materials: Fabrication, characterization, mathematical modeling and application to performance enhancement. *Applied Energy*, 165:472–510, mar 2016. doi:10.1016/j.apenergy.2015.12.043. [Cited on pages xxvii and 243]

[493] Shanglong Zhang, Arun L. Gain, and Julián A. Norato. Stress-based topology optimization with discrete geometric components. *Computer Methods in Applied Mechanics and Engineering*, 325:1–21, oct 2017. doi:10.1016/j.cma.2017.06.025. [Cited on pages 140 and 141]

[494] Shanglong Zhang, Julián A. Norato, Arun L. Gain, and Naesung Lyu. A geometry projection method for the topology optimization of plate structures. *Structural and Multidisciplinary Optimization*, 54(5):1173–1190, may 2016. doi:10.1007/s00158-016-1466-6. [Cited on pages 107 and 140]

[495] Weisheng Zhang, Wenliang Zhong, and Xu Guo. Explicit layout control in optimal design of structural systems with multiple embedding components. *Computer Methods in Applied Mechanics and Engineering*, 290:290–313, jun 2015. doi:10.1016/j.cma.2015.03.007. [Cited on pages 140 and 141]

[496] Weisheng Zhang, Jianhua Zhou, Yichao Zhu, and Xu Guo. Structural complexity control in topology optimization via moving morphable component (MMC) approach. *Structural and Multidisciplinary Optimization*, 56(3):535–552, jun 2017. doi:10.1007/s00158-017-1736-y. [Cited on page 140]

[497] Hong-Kai Zhao, Barry Merriman, Stanley Osher, and Lihe Wang. Capturing the behavior of bubbles and drops using the variational level set approach. *Journal of Computational Physics*, 143(2):495–518, jul 1998. doi:10.1006/jcph.1997.5810. [Cited on pages 130 and 132]

[498] D. Zhou and C.Y. Zhao. Experimental investigations on heat transfer in phase change materials (PCMs) embedded in porous materials. *Applied Thermal Engineering*, 31(5):970–977, apr 2011. doi:10.1016/j.applthermaleng.2010.11.022. [Cited on page 109]

[499] D. Zhou, C.Y. Zhao, and Y. Tian. Review on thermal energy storage with phase change materials (PCMs) in building applications. *Applied Energy*, 92:593–605, apr 2012. doi:10.1016/j.apenergy.2011.08.025. [Cited on pages 241 and 245]

[500] M. Zhou and G.I.N. Rozvany. The COC algorithm, part II: Topological, geometrical and generalized shape optimization. *Computer Methods in Applied Mechanics and Engineering*, 89(1-3):309–336, aug 1991. doi:10.1016/0045-7825(91)90046-9. [Cited on page 12]

[501] Shiwei Zhou and Qing Li. Computational design of multi-phase microstructural materials for extremal conductivity. *Computational Materials Science*, 43(3):549–564, sep 2008. doi:10.1016/j.commatsci.2007.12.021. [Cited on page 122]

[502] Shiwei Zhou and Qing Li. Design of graded two-phase microstructures for tailored elasticity gradients. *Journal of Materials Science*, 43(15):5157–5167, jun 2008. doi:10.1007/s10853-008-2722-y. [Cited on page 122]

[503] Shiwei Zhou and Qing Li. A microstructure diagram for known bounds in conductivity. *Journal of Materials Research*, 23(03):798–811, mar 2008. doi:10.1557/jmr.2008.0101. [Cited on page 122]

[504] Feng Zhu, Chuan Zhang, and Xiaolu Gong. Numerical analysis and comparison of the thermal performance enhancement methods for metal foam/phase change material composite. *Applied Thermal Engineering*, 109:373–383, oct 2016. doi:10.1016/j.applthermaleng.2016.08.088. [Cited on page 109]

[505] Zi-Qin Zhu, Yuan-Kai Huang, Nan Hu, Yi Zeng, and Li-Wu Fan. Transient performance of a PCM-based heat sink with a partially filled metal foam: Effects of the filling height ratio. *Applied Thermal Engineering*, 128:966–972, jan 2018. doi:10.1016/j.applthermaleng.2017.09.047. [Cited on pages 109 and 112]

[506] Chungang Zhuang, Zhenhua Xiong, and Han Ding. Topology optimization of multi-material for the heat conduction problem based on the level set method. *Engineering Optimization*, 42(9):811–831, sep 2010. doi:10.1080/03052150903443780. [Cited on page 131]

[507] C. Zillober. A globally convergent version of the method of moving asymptotes. *Structural Optimization*, 6(3):166–174, sep 1993. doi:10.1007/bf01743509. [Cited on pages 20 and 22]

[508] Christian Zillober. Global convergence of a nonlinear programming method using convex approximations. *Numerical Algorithms*, 27(3):265–289, 2001. doi:10.1023/a:1011841821203. [Cited on page 22]

[509] B. Zivkovic and I. Fujii. An analysis of isothermal phase change of phase change material within rectangular and cylindrical containers. *Solar Energy*, 70(1):51–61, 2001. doi:10.1016/s0038-092x(00)00112-2. [Cited on page 47]